Rehabilitation of Sewer Pipes and Related Infrastructure with Geopolymer and Alkali-activated mortar

A thesis submitted in fulfilment of the requirements for the degree of

Doctor of Philosophy

by

CHERDPHONG SEEDAO

SID: [redacted]

School of Chemical and Biomolecular Engineering

The University of Sydney

August 2023

STATEMENT OF ORIGINALITY

This is to certify that, to the best of my knowledge, the content of this thesis is my original research work. This thesis has not been submitted elsewhere for any degree or other purposes.

I certify that the intellectual content of this thesis is the product of my own work and that all the assistance received in preparing this thesis and sources have been acknowledged.

Signature: _____

CHERDPHONG SEEDAO

AUTHORSHIP ATTRIBUTION STATEMENT

Part of the results from characterisation and performance data from chapters 4 and 5, respectively, of this thesis is contributed to the conference book chapter and conference papers:

Book chapter:

1. Cherdphong SEEDAO, M. E. FISHER and Marjorie VALIX, "Comparative Acid Resistance Of One-Part Geopolymer And Calcium Aluminate Cement Mortar" International Conference on Calcium Aluminates 2022, Cambridge, England

I and my supervisor designed the study, extracted and analysed the data, interpreted the analysis done by Cherdphong Seedao, Matthew Fisher and Marjorie Valix, and wrote the drafts of the manuscript.

Conference paper:

1. Cherdphong Seedao, Ye Jun In, Matthew Fisher, James Gardner and Marjorie Valix, "Evaluation of one-part geopolymer mortars as protective sewer coating for sewer assets," No-Dig Down Under 2021, Sydney, Australia

I and my supervisor designed the study, extracted and analysed the data, discussed and interpreted the analysis done by Cherdphong Seedao, Ye Jun In, Matthew Fisher, James Gardner and Marjorie Valix and wrote the drafts of the manuscript.

2. C.SEEDAO, Y.J.In, J. Sunarho, and M.Valix, "Comparison of corrosion resistance of one-part geopolymer and calcium aluminate cement mortar exposed to live aggressive sewer environment" Singapore International Water Week 2022, Singapore

I and my supervisor designed the study, extracted and analysed the data, discussed and interpreted the analysis done by Cherdphong Seedao, Ye Jun In, Jerry Sunarho, and Marjorie Valix and wrote the drafts of the manuscript.

In addition to the statements above, in cases where I am not the corresponding author of a published item, permission to include the published material has been granted by the corresponding author.

Signature: _____

Cherdphong seedao | 24 August 2023

As supervisor for the candidature upon which this thesis is based, I can confirm that the authorship attribution statements above are correct.

Signature: _____

Prof.Majorie Valix | 24 August 2023

ACKNOWLEDGEMENT

I would like to express my sincere gratitude to my supervisor, Professor. Marjorie Valix, for her guidance, encouragement, and support throughout my PhD journey. Her guidance, support, extensive knowledge, and constructive feedback have pushed me to improve and grow as a researcher. Thank you for allowing me to join the industrial research project and showing me how to conduct research, which faces many challenges.

I would also like to thank the faculty and staff of the School of Chemical and Biomolecular Engineering at The University of Sydney for their assistance and resources that have facilitated me in conducting my research. In addition to the grant provided by the Australian Government through the Cooperative Research Centres Project (CRC-P), this project was made possible by the following project partners, all of whom contributed expertise, labour, funding, products, or trial sites to assist in its delivery. I also want to thank the Thai government sponsorship for supporting the pursuit of my PhD at the University of Sydney.

I am grateful to all my friends and colleagues from the Material and Minerals Processing Research Unit (MMPRU) for their unwavering support, friendly, generous training, and assistance. I also want to acknowledge the contribution of all participants who generously gave their time and shared their experiences for this research.

Finally, I would like to thank my family for their faith in me and for allowing me to live far away from home with my ambitious dream. Importantly, I would like to extend my appreciation to myself for persistently pushing through the challenge of this PhD journey.

ABSTRACT

The concrete sewer pipe network, comprising approximately 122,000 km of infrastructure in Australia, is essential in ensuring the liveability and productivity of cities and communities. These sewer assets are designed with an intended service life of approximately 100 years. However, the durability of these assets is compromised due to the detrimental effects of deterioration caused by several factors. Among the factors contributing to sewer asset degradation, microbial-induced concrete corrosion (MICC) is the most aggressive and significant threat. MICC is a complex process characterised by various chemical and biological reactions, primarily involving the conversion of sulphide present in wastewater to sulfuric acid and other biogenic acids. These acidic by-products directly interact with the concrete material, leading to gradual deterioration and eventual failure of the sewer assets in a short period.

Various mitigation strategies have been implemented to mitigate the impact of MICC on sewer assets to extend the service life of existing sewer assets. For existing sewer infrastructure, mitigation efforts have focused on reducing hydrogen sulphide (H_2S) generation through chemical dosing and employing surface protective coatings to prevent concrete corrosion. However, effective H_2S reduction often necessitates the injection of chemicals at various locations along the sewer assets. Continuing a controllable H_2S level requires consistent chemical dosing, as a failure to maintain adequate doses results in H_2S production returning to previous levels. Unfortunately, this mitigation approach poses long-term operational and financial challenges, as the costs associated with maintenance and operation can be excessively high. On the other hand, surface protective linings have emerged as an intriguing strategy for protecting and extending the existing sewer assets. These linings served as effective barriers between concrete infrastructure and harsh environmental conditions. Sewer assets can be effectively preserved and extended their service

life by employing surface protective linings. The durability of the protective linings itself relies on its corrosion resistance capabilities.

Alkali-activated binders (AAB), including geopolymer, exhibit comparable or better properties to traditional construction materials like ordinary Portland cement (OPC) concrete. Geopolymer mortar often surpasses OPC mortar in terms of durability, with calcium content playing a crucial role in enhancing its performance. For several reasons, these materials have gained attention as potential protective lining mortar options for sewer asset rehabilitation. Firstly, they offer high chemical corrosion resistance, superior mechanical strength, and minimal shrinkage. Additionally, Alkali-activated binders (AAB), including geopolymer, were produced using industrial waste by-products, resulting in reduced energy consumption, lower CO_2 emissions and inexpensive.

Despite their promising qualities, these materials have not been utilised as protective linings in sewer asset applications for a few reasons. Firstly, there is a lack of corrosion resistance performance data. Secondly, there are no established guidelines for their application and selection. Thirdly, the design of protective systems based on geopolymers is complex due to limited kinetic corrosion data, especially in actual sewer environments. Lastly, understanding sewer requirements and defining sewer corrosivity to specify the durability features of the protective lining system remains a challenge, making the selection of the appropriate Alkali-activated binders. To address these challenges, this study developed the framework for predicting the service life and selection criteria for alkali-activated binders (AAB) and geopolymer mortar under specific sewer corrosivity. However, the lack of available information regarding using geopolymer as a protective lining material for sewer asset rehabilitation poses limitations.

Therefore, the objectives of this study were i) to provide an understanding of alkali-activated mortar, including geopolymer performance, specifically in live sewer environments, ii) to obtain

performance data for various commercial geopolymers and compare corrosion-resistant performance to high-performing calcium aluminate cement mortar (CACm) (100% CAC) that reflects the impact of the various sewer corrosion classification, and iii) to use the field performance data to develop the service life prediction models and lining mortar selection criteria.

To achieve the objectives of this study, four commercially available one-part geopolymer mortars (OGPm), denoted as OGPm-1, OGPm-2, OGPm-3, and OGPm-4, and one calcium aluminate cement mortar (CACm) were evaluated. 50 mm cured mortar cube in a laboratory and fresh shotcrete lining mortar were involved in this study. The lining mortar samples were tested for corrosion resistance under i) pH 1 sulphuric acid immersion test in the laboratory and ii) live sewer environmental conditions ranging from C1 (low corrosivity) to C5 (very high corrosivity) based on the sewer corrosivity classification. The acid immersion test aimed to simulate the last stage of the deterioration mechanism using sulphuric acid, which is presented as the main corrosive compound in MICC. Lining mortar sample preparation involved the shotcrete applied lining mortar and cured cube mortar. The corrosion resistance performance test of shotcrete applied lining under the live sewer was undertaken for the first time, reflecting the real corrosion resistance performance of lining mortar in live sewer systems. The corrosion resistance performance was estimated based on the corrosion depth and residual unconfined compressive strength (UCS) as a function of time.

The four geopolymer mortars (OGPm) and one CAC mortar (CACm) were characterised to reveal their composition, mineralogy, and corresponding physical properties to support the durability assessment. Based on the XRF results, the high calcium content of the geopolymer binders that ranged from 23.3 to 53.9 wt.% suggested the geopolymers involved in this study were alkali-activated binder (AAB) and hybrid geopolymer with blended aluminosilicate phases. The physical

and chemical properties such as initial UCS, initial porosity, acid neutralisation capacity (ANC), hydration products (C-S-H, C-A-S-H, C-N-A-S-H, and N-A-S-H), and chemical composition of aggregate (SiO_2, Al_2O_3, and CaO) were found to correlate with the corrosion resistance performance of mortar.

The corrosion resistance performance of OGPm and CACm in the live sewer was found to follow three-staged corrosion steps: initiation period or lag-phase, fast stage 1 corrosion propagation (R_1), and followed by slower stage 2 corrosion propagation (R_2). It needs to be noted that this is the first time that corrosion data and characterisation from live sewers have been obtained. The corrosion rates were used to compare the corrosion resistance performance. R_2 exhibited an essential feature of this protective lining mortar. These results suggest that the reduction of corrosion rate in the second stage could be attributed to the build-up of the corrosion product layer, reducing the acid diffusion rate due to pore blocking. The corrosion resistance performance of OGPm and CACm was associated with the chemical and physical properties of the mortar and sewer corrosivity of sewer environmental conditions. For example, the ANC of the mortar plays a crucial role in slowing mortar deterioration by neutralising the acids produced from MICC. This helps protect the mortar from acid attacks. At the same time, the porosity of the mortar affects its susceptibility to corrosion. Higher porosity allows for easier penetration of acids into the mortar matrix, leading to increased corrosion depth.

The hydration products in the mortar, such as C-S-H, C-A-S-H, C-N-A-S-H, and N-A-S-H, also play a significant role in corrosion resistance by improving the UCS, porosity, and ANC. These hydrates also contributed to the formation of gypsum and ettringite because of the Ca content in the hydration phases. The ANC, UCS, porosity, and hydration products in the mortar are interconnected factors that influence its corrosion resistance. CACm demonstrated superior

performance as a lining mortar compared to OGPm. The better corrosion resistance performance of CACm compared to OGPm can be attributed to its chemical composition, high ANC, low porosity, and high UCS. CACm, primarily composed of calcium aluminate, inherently possesses acid resistance properties. The denser microstructure of CACm reduces porosity and limits acid penetration. Additionally, CACm exhibits higher chemical stability in acidic environments, maintaining its structural integrity over time due to the buffering effect from $Al(OH)_3$ dissolution at pH approximately 3-4.

This study developed the service life prediction model for alkali-activated binder mortar, including geopolymer, based on the depth of corrosion with time, employing the semi-empirical approach using the power law model and following a solid-liquid kinetic model based on the shrinking core model. The corrosion depth prediction model incorporated several factors, including the sewer environment conditions, properties of the mortar including porosity, UCS, ANC, geopolymer hydration products, and chemical composition of the aggregates and time. Individual models were developed for the three stages of corrosion: the initial period, stage I corrosion propagation, and stage II corrosion propagation. These were combined to provide a holistic model to predict the overall service life, as presented below.

Initiation period : $t_i = k_{tiG} C_{ti} F_{tiG}$

Stage 1 Corrosion Propagation: $X_{S1\_G} = K_{S1\_G} C_{S1\_G} F_{S1\_G} (-p_{1\_S1G} t^{p_{2\_S1G}} + p_{3\_S1G} t - p_{4\_S1G})$

Stage 2 Corrosion Propagation: $X_{S2\_G} = K_{S2\_G} C_{S2\_G} F_{S2\_G} (-p_{1\_S2G} t^{p_{2\_S2G}} + p_{3\_S2G} t - p_{4\_S2G})$

Where: t = time, C= sewer corrosivity, F = mortar durability, K = Constant for depth of corrosion prediction model, p = Constant parameters for time

The final service life should be defined as t final = t_i + t (stage 1) + t (stage 2)

To establish the fit of these models, an independent variable significance test was performed for each model established using a partial F-test and justified with the p-value. If the p-value is less than the conventional 0.05 level, the independent variable was found to be a significant predictor in the predictive model. The goodness of fit of the models was determined using R^2, adjusted- R^2 and mean-square error (se), as presented below.

For the initial corrosion period: R^2 of 0.99, adjusted- R^2 of 0.98 and se of 0.04.

For stage I corrosion propagation: R^2 of 0.98, adjusted- R^2 of 0.75 and se of 2.87.

For Stage II corrosion propagation: R^2 of 0.90, adjusted- R^2 of 0.82 and se of 4.0

These statistical parameters suggested that the model adequately fits the mortar corrosion behaviour under all stages of corrosion. The corrosion depth prediction models were verified by comparing the predicted and 10% of the external data. The verified corrosion depth was observed to be a reliable fit along with the diagonal line. It is important to note that this study represents the first instance of developing a service life prediction model that considers real-world field applications, encompassing diverse live sewer corrosivity classifications and mortar durability.

The selection criteria input in the service life prediction model were the mortar durability and sewer corrosivity. The mortar durability could be predicted from porosity, UCS, ANC, binder hydrations (C-S-H, C-A-S-H, C-N-A-S-H, and N-A-S-H), and chemical composition of aggregate (CaO, SiO_2, and Al_2O_3) and sewer corrosivity conditions, as defined by sewer environmental conditions, could be predicted from H_2S, CO_2, temperature, and %RH.

TABLE OF CONTENTS

STATEMENT OF ORIGINALITY ii
AUTHORSHIP ATTRIBUTION STATEMENT iii
ACKNOWLEDGEMENT v
ABSTRACT vi
TABLE OF CONTENTS xii
LIST OF FIGURE xviii
LIST OF TABLE xxviii
1 INTRODUCTION 1
1.1 BACKGROUND 1
1.2 PROBLEM STATEMENT 3
1.3 RESEARCH OF OBJECTIVE 4
1.4 THESIS ORGANISATION 5
1.5 LIST OF PUBLICATIONS 7
1.5.1 BOOK SECTION 7
1.5.2 CONFERENCES 7
1.5.3 CONTRIBUTION OF THE RESULT 7
2 LITERATURE REVIEWS 8
2.1 INTRODUCTION 8
2.2 SANITARY SEWER NETWORK SYSTEM 8
2.2.1 SEWER PIPE NETWORK 8
2.2.2 SEWER GASES BUILD UP IN SEWER PIPE 10

2.2.3 SEWER PIPE CONSTRUCTION MATERIALS 12
2.3 SEWER STRUCTURE DETERIORATION 12
2.3.1 SEQUENTIAL GROWTH OF MICROORGANISMS 13
2.3.2 MICROBIAL-INDUCED CONCRETE CORROSION (MICC) 15
2.3.3 DETERIORATION OF CONCRETE MATERIALS 21
2.4 MITIGATION STRATEGIES FOR CORROSION 22
2.4.1 CHEMICAL MITIGATION STRATEGIES FOR HYDROGEN SULPHIDE EMISSION 22
2.4.2 LINING APPLICATIONS 23
2.5 TYPICAL CONCRETE SEWER PIPE 25
2.5.1 ORDINARY PORTLAND CEMENT 25
2.5.2 HYDRATION REACTION 26
2.6 ALKALI-ACTIVATED BINDERS 27
2.6.1 HIGH-CALCIUM ALKALI-ACTIVATED BINDERS 27
2.6.2 LOW-CALCIUM ALKALI-ACTIVATED BINDERS (GEOPOLYMER) 29
2.6.3 ALUMINOSILICATE SOURCES 31
2.6.4 ACTIVATED REAGENT 34
2.6.5 DETERIORATION OF GEOPOLYMER 35
2.7 ONE-PART AND TWO-PART GEOPOLYMER 39
2.8 CALCIUM ALUMINATE CEMENT 40

2.9 PRACTICAL REQUIREMENT 42
2.10 TYPES OF AGGREGATE 43
2.10.1 FINE AGGREGATE 44
2.10.2 COARSE AGGREGATE 44
2.11 CONDITION ASSESSMENT OF CONCRETE CORROSION 45
2.12 FACTORS INFLUENCING THE CORROSION RESISTANCE OF GEOPOLYMER 47
2.12.1 PARTICLE SIZE DISTRIBUTION OF MORTAR POWDER 49
2.13 SERVICE LIFE MODELS FOR CONCRETE-BASED MATERIAL 49
2.14 ASSESSMENT OF LITERATURE REVIEW 51
3 MATERIAL AND METHODOLOGY 56
3.1 INTRODUCTION 56
3.2 MORTAR LINING MATERIALS 57
3.3 SAMPLE PREPARATION 59
3.3.1 COUPON SAMPLE PREPARATION 59
3.3.2 SHOTCRETE APPLICATION 62
3.4 CORROSION RESISTANCE PERFORMANCE TEST 62
3.4.1 ACID IMMERSION TEST 62
3.4.2 DIGESTER CHAMBER TEST 65
3.4.3 FIELD APPLICATION TEST (SHOTCRETE APPLICATION) 70

3.5 CHARACTERISATION OF LINING MORTAR 85
3.5.1 CHEMICAL PROPERTIES 85
3.5.2 PHYSICAL AND MECHANICAL PROPERTIES 91
3.6 EVALUATION OF CORROSION RESISTANCE PERFORMANCE 93
3.6.1 DEPTH OF CORROSION 93
3.6.2 RESIDUAL UCS 95
4 CHARACTERISATION OF GEOPOLYMER AND CAC PROTECTIVE LINING MATERIALS 97
4.1 INTRODUCTION 97
4.2 CHEMICAL COMPOSITION OF ONE-PART GEOPOLYMER AND CAC MORTAR 99
4.2.1 BINDERS 100
4.2.2 FINE AGGREGATES 111
4.3 MORTAR MIX DESIGN AND PARTICLE SIZE DISTRIBUTION OF BINDER AND FINE AGGREGATES 118
4.3.1 MORTAR DESIGN 119
4.3.2 PARTICLE SIZE DISTRIBUTION 122
4.3.3 FINE AGGREGATE GRADING 122
4.4 PHYSICAL PROPERTIES OF MORTARS 128
4.4.1 POROSITY 129
4.4.2 UNCONFINED COMPRESSIVE STRENGTH (UCS) 132

4.5 CHEMICAL PROPERTIES OF THE LINING MATERIAL 134

4.5.1 HYDRATION PRODUCTS GEOPOLYMER 135

4.5.2 ACID NEUTRALISATION CAPACITY (ANC) 153

4.6 SUMMARY 160

5 THE DURABILITY OF LINING MORTAR UNDER LABORATORY AND FIELD TEST 163

5.1 INTRODUCTION 163

5.2 EVALUATION OF CORROSION RESISTANCE PERFORMANCE OF MORTARS 166

5.2.1 ACID IMMERSION TEST 166

5.2.2 SEWER CORROSIVITY CLASSIFICATION 188

5.2.3 DIGESTER CHAMBER TEST 192

5.2.4 FIELD APPLICATION TEST 230

5.3 DURABILITY TEST AS A FUNCTION OF MORTAR PROPERTIES 249

5.3.1 PHYSICAL PROPERTIES 250

5.3.2 CHEMICAL PROPERTIES 252

5.4 SUMMARY 256

6 SERVICE LIFE PREDICTION MODELS FOR ALKALI-ACTIVATED BINDERS, INCLUDING GEOPOLYMER EXPOSED TO SEWER CONDITIONS OF VARIOUS CORROSIVITY 259

6.1 INTRODUCTION 259

6.2 SCOPE OF SERVICES LIFE PREDICTION MODEL 260

6.3 PREVIOUS SERVICE LIFE MODEL 260

6.4 SERVICE LIFE MODELS 262

6.4.1 ERROR ANALYSIS OF THE MODELS 265

6.4.2 MODEL OF THE CORROSION INITIATION PERIOD 268

6.4.3 CORROSION PROPAGATION MODELS BASED ON THE DEPTH OF CORROSION 278

6.4.4 RATE-DETERMINING STEP AND MODEL FITTING 286

6.4.5 SENSITIVITY ANALYSIS 302

6.4.6 VERIFICATION OF SERVICE LIFE PREDICTION MODEL 312

6.5 SUMMARY 314

7 CONCLUSION AND RECOMMENDATIONS 317

7.1 CONCLUSIONS 317

7.2 RECOMMENDATIONS 321

8 REFERENCES 322

LIST OF FIGURE

Figure 2-1 Schematic diagram of a sewer pipe network (Mackenzie L. Davis, 2020)..... 9

Figure 2-2 Type of sewer network: gravity sewers and pressure sewers (Hvitved-Jacobsen et al., 2013) 10

Figure 2-3 Approximate pH range for the growth of different classes of the pH-specific microbiome 15

Figure 2-4 Microbial-induced corrosion of concrete (MICC) (Ling et al., 2014, Roberts et al., 2002, Jiang et al., 2015b, Wu et al., 2020, Grengg et al., 2018)..... 16

Figure 2-5 Schematic illustration of the different zones in the corrosion layer (Wu et al., 2020) 21

Figure 2-6 Reaction mechanism in an alkali-activated slag particle (Palomo et al., 2015)..... 28

Figure 2-7 Structure of Sialate monomer (Davidovits, 1994) 30

Figure 2-8 Schematic diagram of the geopolymerisation process (Davidovits, 1991)..... 31

Figure 2-9 SEM micrograph of fly ash sample..... 32

Figure 2-10 SEM micrograph of Blast Furnace Slag..... 33

Figure 2-11 Leaching process after acid attacks..... 36

Figure 2-12 Re-occupied by silicon atoms process 36

Figure 2-13 Degree of particle roundness..... 44

Figure 3-1 Coupons sample preparation 61

Figure 3-2 Example of mortar coupon: (a) Front view and (b) Side view 61

Figure 3-3 Accelerated corrosion test..... 65

Figure 3-4 Basket with all clips attached..... 66

Figure 3-5 Photos of Digester Chambers at North Head Wastewater Treatment Plant (NH-WWTP), Sydney Water..... 68

Figure 3-6. Basket with length adjustment (left) and Cube coupons installed on the wires inside an access chamber (right)..... 68
Figure 3-7 Field test schedule for NH-WWTP..... 69
Figure 3-8 Acid neutralisation capacity (ANC) of OPC..... 74
Figure 3-9. Photos of access chamber surface pH with phenolphthalein indicator (left) and Universal indicator (right)..... 74
Figure 3-10 Schematic diagram of lining application in an access chamber for field test..... 77
Figure 3-11. Schematic diagram of coating application in a personnel-entry pipe field test..... 79
Figure 3-12. Measuring the coating thickness with a ruler..... 80
Figure 3-13 Ni-Al alloy rebars (top-left); false rebar installation in access chamber (top-right); false rebar installation in sewer pipe (bottom-left); cover meter testing of coating thickness (bottom-right)..... 81
Figure 3-14 Core sampling in a manhole (left) and personnel-entry pipe (right)..... 82
Figure 3-15 Field test schedule for coating performance assessment..... 84
Figure 3-16 Thermo Scientific, Nicolet 6700-FTIR..... 87
Figure 3-17 Thermogravimetric Analysis (TGA)..... 88
Figure 3-18. Phenom XL Desktop Scanning Electron Microscope..... 89
Figure 3-19 Surface pH Testing Apparatus..... 90
Figure 3-20 UTEST Automatic Compression Machine Model UTC-4231 (Left) and concrete coupons before and after crushing test (right)..... 92
Figure 3-21 Lortone inc Model FS8 Lapidary Trim Saw equipped with an 8-inch diamond blade..... 93
Figure 3-22 Colour scale for the Universal indicator..... 94

Figure 3-23 a.Leica DM2500 optical microscope and b.Photo of the depth of acid permeation . 94
Figure 3-24 Depth of corrosion calculation 95
Figure 3-25 Corroded mortar sample (Left) and Measured Sides of Sample (Right) for UCS Testing..... 96
Figure 4-1 SiO_2, Al_2O_3, and CaO from XRF analysis of mortar binders 104
Figure 4-2 SEM image of unhydrated OGPm-1, OGPm-2, OGPm-3, and OGPm-4 and CACm 109
Figure 4-3 SiO_2, Al_2O_3, and CaO from XRF analysis of mortar aggregates 114
Figure 4-4 SEM images of mortar aggregate and corresponding EDS analyses: i) quartz sand, ii) glass and iii) CAC aggregate 116
Figure 4-5 Shape of fine aggregates in geopolymer mortars 118
Figure 4-6 Charts for the visual assessment of particle shape provided by Powers (1953) 118
Figure 4-7 Mixed proportion between binder and aggregate of OGPm and CACm mortar 120
Figure 4-8 Aggregate gradings adopted from Lee and Estrada (2020). 124
Figure 4-9 Particle size distribution of OGPm and CACm: (a).binder and (b). aggregate..... 125
Figure 4-10 Correlation of coefficient of curvature and UCS at 28 days of curing 127
Figure 4-11 Development of porosity of OGPm and CACm 130
Figure 4-12 Correlation between porosity and water and mortar ratio (W/M) and aggregate grading 132
Figure 4-13 Unconfined compressive strength (UCS) of the lining material 134
Figure 4-14 FTIR spectrum of OGPm-4 after curing 28 days..... 137
Figure 4-15 Development of geopolymer as a function of time up to 28 days: (a).OGPm-1, (b).OGPm-2, (c).OGPm-3, and (d).OGPm-4..... 141

Figure 4-16 the example of deconvolution of the peak to quantify the amount of the geopolymer based on the Levenberg-Marquardt equation 143
Figure 4-17 Development of hydration phases of geopolymer as a function of time..... 146
Figure 4-18 The correlation between hydration phases with Si/Al ratio (a) N-A-S-H and (b) C-A-S-H 146
Figure 4-19 the example of deconvolution of the TGA-DTG peak to quantify the amount of the geopolymer based on the Levenberg-Marquardt equation. 148
Figure 4-20 Correlation of FTIR and TGA-DTG result from OGPm-4 149
Figure 4-21 Correlation of hydration product and porosity 150
Figure 4-22 Correlation of hydration product and UCS 152
Figure 4-23 Characterisation of Acid Neutralisation Capacity (ANC) 154
Figure 4-24 Characterisation of Acid Neutralizing Capacity (ANC) of geopolymer 155
Figure 4-25 Correlation of practical ANC and CaO, MgO, and Al_2O_3 159
Figure 5-1 Post Acid Immersion Image of Corroded Surface 168
Figure 5-2 Thickness of mortar before and after 28 days of corrosion in sulfuric acid pH 1 and 27 °C 169
Figure 5-3 Acid attack on the cross-section of mortar from acid immersion test..... 170
Figure 5-4 Schematic diagram of the depth of corrosion calculation 170
Figure 5-5 Progression of Corrosion surface for OGPm and CACm after acid immersion up to 28 day 172
Figure 5-6 Plot of the depth of corrosion of OGPm and CACm as a function of time of exposure to sulphuric acid (pH 1, 30 °C) 173
Figure 5-7 Fitted rates of corrosion 173

Figure 5-8 The a) initial and b) final rates of corrosion of geopolymer and CAC exposed to H_2SO_4 at pH 1.0 and 30 °C 175
Figure 5-9 Correlation between stage I and Stage II corrosion rate and initial porosity 176
Figure 5-10 Correlation between stage I and stage II corrosion rate and CaO content 178
Figure 5-11 The SEM/EDS of OGPm-1 and OGPm-3 after 28 days of acid immersion test 179
Figure 5-12 Correlation between the rate of corrosion and UCS 181
Figure 5-13 Correlation between the rate of corrosion and porosity 181
Figure 5-14 Correlation between the rate of corrosion and ANC 182
Figure 5-15 Correlation between the rate of corrosion and hydration binders 184
Figure 5-16 Compressive strengths of OGPm and CACm exposed to H_2SO_4 pH 1.0 at 27°C .. 186
Figure 5-17 Loss of UCS of OGPm and CACm with respect to exposure time in acid solution (pH 1) with 27 °C 188
Figure 5-18 Environmental conditions in chamber 1: a) H2S and T, (b) %RH and T, (c) CO_2. 194
Figure 5-19 Corroded OGPm-1 and OGPm-2 after 42 months in C4 of sewer corrosivity 196
Figure 5-20 Visual corrosion depth in C1 sewer corrosivity classification after 31 and 42 months 199
Figure 5-21 Visual corrosion depth in C3 sewer corrosivity classification after 31 and 42 months 200
Figure 5-22 Visual corrosion depth in C4 sewer corrosivity classification after 31 and 42 months 201
Figure 5-23 Depth of corrosion after exposure to the aggressive environment in the three digester chambers. 204

Figure 5-24 Effect of initial porosity and UCS on the corrosion performance after 42 months of exposure to C1, C3, and C4 of sewer corrosivity classification 207
Figure 5-25 Effect of ANC on the corrosion performance after 42 months of exposure to C1, C3, and C4 of sewer corrosivity classification 209
Figure 5-26 Effect of hydration phases on the corrosion performance after 42 months of exposure to C1, C3, and C4 of sewer corrosivity classification..... 211
Figure 5-27 Schematic diagrams of corrosion depth as a function of time. 212
Figure 5-28 Comparison of corrosion characteristics of OGPm-1 at C4 and C1 sewer corrosivity classification 214
Figure 5-29 (a) Stage I corrosion rate and (b) Stage II corrosion rate of OGPm and CACm exposed to H_2SO_4 at pH 1.0 and 30 °C and three corrosivity classification..... 217
Figure 5-30 Correlation between CaO and $CaSO_4$ formation from C4 sewer corrosivity classification after 31 months of exposure..... 218
Figure 5-31 SEM backscattering images and Ca and S maps of the corroded sections of OGPm-1 and OGPm-3 after 12 months of corrosion field test (129 ppm H2S, 26 °C and 99% RH 220
Figure 5-32 SEM backscattering images and Ca and S maps of the uncorroded sections of OGPm-1 and OGPm-3 after 12 months of corrosion field test (129 ppm H2S, 26 °C and 99% RH 221
Figure 5-33 Correlation of R_2 from field test and R_2 from accelerated corrosion test 222
Figure 5-34 Comparison of the corrosion rate of low Ca geopolymer 224
Figure 5-35 Residual UCS of OGPm and CACm from the three digestion chambers, which presented C1, C3, and C4 of sewer corrosivity classification 226
Figure 5-36 Loss of UCS of OGPm and CACm after exposure to C1, C3, and C4 of sewer corrosivity classification 229

Figure 5-37 Collation of 4 environmental surveys of H_2S, T, RH and CO_2 in SWC NOOS from 4th March to 13th September 2020..... 232
Figure 5-38 Depth of corrosion of cored sample..... 235
Figure 5-39 Depth of corrosion of OGPm and CACm exposed to live sewer assets..... 237
Figure 5-40 Correlation between the depth of corrosion of OGPm and CACm exposed to C1 live sewer assets for 13 months..... 238
Figure 5-41 Correlation between the depth of corrosion and ANC of OGPm exposed to C1 live sewer assets for 13 months..... 239
Figure 5-42 Correlation between the depth of corrosion and hydration product of OGPm exposed to C1 live sewer assets for 13 months..... 240
Figure 5-43 Lag phase, stage I corrosion rate (R_1) and stage II corrosion rate (R_2) of OGPm-1, OGPm-2, OGPm-3, OGPm-4 and CACm..... 243
Figure 5-44 SEM backscattering images and S maps of the uncorroded and corroded sections of OGPm-1 and OGPm-3 after 16 months of exposure to C2 sewer corrosion classification..... 244
Figure 5-45 Comparison of corrosion rate of practical application and cube sample preparation under C1 of sewer corrosivity classification..... 247
Figure 5-46 Correlation between the corrosion rate of shotcrete application and acid immersion test (pH 1 sulphuric acid)..... 249
Figure 5-47 Correlation of R_1 and initial porosity at C1 of sewer corrosivity classification 251
Figure 5-48 Correlation of R_1 and initial UCS at C1 of sewer corrosivity classification..... 252
Figure 5-49 Correlation of R_1 and practical ANC at C1 of sewer corrosivity classification..... 253
Figure 5-50 Correlation of R_1 and C-S-H, C-A-S-H, and N-A-S-H at C1 of sewer corrosivity classification 256

Figure 6-1 Corrosion of geopolymer coating (OGPm-3) as a function of time and sewer classifications 263
Figure 6-2. Conceptual model of cement mortar corrosion 264
Figure 6-3. pH dependence of microbiome growth 269
Figure 6-4. Biogenic acid generation as a function of pH on polymeric coatings installed in sewers for 18 months (Valix and Shanmugarajah, 2015) 269
Figure 6-5. Corrosion of geopolymer coating (OGPm-3) as a function of time and sewer classifications 270
Figure 6-6. Corrosion data fitted to the corrosion initiation period model (see Table 6-3)..... 275
Figure 6-7. Example of a cross-section of corroded geopolymer demonstrating core-shrinking model..... 278
Figure 6-8. Schematic of the core shrinking model for corroding geopolymer and/or alkali-activated mortar 281
Figure 6-9. Cumulative sulphuric acid generated in epoxy mortars installed in large-diameter sewer pipes at various H_2S concentrations and with time (Valix and Shanmugarajah, 2015) 283
Figure 6-10. The plot of mortar corrosion data under propagation stage 1 fitted to the core shrinking model based on: a) chemical controlled (C1), b) pore diffusion-controlled reaction (C1), c) chemical controlled (C2, C5) and d) pore diffusion-controlled reaction (C2, C5)..... 287
Figure 6-11. R^2 of fitted mortar corrosion data under propagation stage 1 to core shrinking models 288
Figure 6-12. Mortar data under propagation stage 1 fitted to Model 2 – mixed chemical and pore diffusion- controlled model (see Equation 6-41) 291

Figure 6-13. Plot of mortar corrosion data under propagation stage 2 fitted to the core shrinking model based on: a) chemical-controlled (C1), b) pore diffusion-controlled (C1), c) chemical-controlled (C2) and d) pore diffusion-controlled reaction (C2), e) chemical controlled (C3), f) pore diffusion-controlled reaction (C3), g) chemical controlled (C5) and h) pore diffusion-controlled reaction (C5) 295

Figure 6-14. R^2 of fitted mortar corrosion data under propagation stage 2 to core shrinking models 296

Figure 6-15. Mortar data under propagation stage 2 fitted to Model 2 – mixed chemical and pore diffusion-controlled model (see equation 25) 300

Figure 6-16 Impact of changes in the relative humidity on the depth of corrosion as a function of service life under Category 1 exposure conditions 305

Figure 6-17 Impact of changes in UCS and porosity on the depth of corrosion as a function of service life under Category 1 exposure conditions (C1:15 ppm H_2S, 9500 ppm CO_2, T= 28 °C and 99 %RH) and chemical properties (ANC at 1 mmol H^+ /g substrate,0.68 wt.% C-S-H, 0.42 wt.% C-A-S-H, 0.99 wt.% C-N-A-S-H, and 0.69 wt.% N-A-S-H, 0.36 wt.% Al_2O_3.in aggregate, 0.10 wt.% CaO in the aggregate, and 96.95 wt.% SiO_2 in aggregate) 307

Figure 6-18 Impact of changes in ANC on the depth of corrosion as a function of service life under Category 1 exposure conditions (15 ppm H_2S, 9500 ppm CO_2, T at 28 °C, and 99 %RH) and physical properties (35.4 MPa UCS and 22.3 vol.% porosity) and The chemical properties (0.68 wt.% C-S-H, 0.42 wt.% C-A-S-H, 0.99 wt.% C-N-A-S-H, and 0.69 wt.% N-A-S-H, 0.36 wt.% Al_2O_3.in aggregate, 0.10 wt.% CaO in the aggregate, and 96.95 wt.% SiO_2 in aggregate) 309

Figure 6-19 Impact of changes C-S-H, C-A-S-H, C-N-A-S-H, and N-A-S-H on the depth of corrosion as a function of service life under Category 1 exposure conditions (15 ppm H_2S, 9500

ppm CO_2, T at 28 °C, and 99 %RH) and physical properties (35.4 MPa UCS and 22.3 vol.% porosity) and The chemical properties (ANC at 1 mmol H+ /g substrate, 0.36 wt.% Al_2O_3.in aggregate, 0.10 wt.% CaO in the aggregate, and 96.95 wt.% SiO_2 in aggregate) 311

Figure 6-20 Impact of changes in the chemical composition of aggregate SiO2, Al_2O_3 and CaO on the depth of corrosion as a function of service life under Category 1 exposure conditions (15 ppm H_2S, 9500 ppm CO_2, T at 28 °C, and 99 %RH) and physical properties (35.4 MPa UCS and 22.3 vol.% porosity) and The chemical properties (ANC at 1 mmol H+ /g substrate,0.68 wt.% C-S-H, 0.42 wt.% C-A-S-H, 0.99 wt.% C-N-A-S-H, and 0.69 wt.% N-A-S-H) 312

Figure 6-21 Correlation between predicted corrosion depth and actual corrosion depth 313

Figure 6-22 Difference between actual and predicted corrosion depth 314

LIST OF TABLE

Table 2-1 Types of Sewers pipe in a typical collection system (Mackenzie L. Davis, 2020)..... 10

Table 2-2 Physiological characteristics of some sulphur-oxidising bacteria in concrete corrosion layers by Sun (2015) 20

Table 2-3 Typical Chemical compositions of CAC (Ideker et al., 2019)..... 42

Table 2-4 Factors affecting sewer pipeline condition (Hawari et al., 2017)..... 46

Table 2-5 A summary of some essential factors influencing the corrosion resistance of geopolymer 48

Table 2-6 Service lift modelling equations..... 50

Table 3-1 List of one-part geopolymer and calcium aluminate cement mortar..... 58

Table 3-2 Water and mortar ratio (W/M) by weight..... 60

Table 3-3 Environmental parameter analysis of sewer assets 67

Table 3-4 Site Locations and Environmental Conditions..... 71

Table 3-5 The list of the protective lining mortar..... 75

Table 3-6 Coatings Applied for Field Tests and Biogenic Digester..... 76

Table 3-7 Example of manhole rehabilitation using OGPm and CACm..... 78

Table 4-1 XRF analysis of the chemical composition of OGPm and CACm binder 101

Table 4-2 Chemical compositions of fly ash, Blast furnace slag by XRF..... 105

Table 4-3 SEM-EDS of bulk mortar binder..... 106

Table 4-4 SEM images of mortar precursors and corresponding EDS analyses: i) fly-ash, ii) blast furnace slags, iii) calcium aluminate cement..... 110

Table 4-5 Chemical composition (wt%) of the composition of OGPm and CACm based on quantitative EDS microanalysis..... 111

Table 4-6 Bulk chemical composition of aggregates from OGPm and CACm by XRF 113
Table 4-7 Chemical composition (wt.%) of aggregate based on quantitative EDS microanalysisMortar Components 115
Table 4-8 Particle size of binder and aggregate for geopolymer mortars 121
Table 4-9 The particle size of a binder and aggregates of OGPm and CACm (this study) 124
Table 4-10 Coefficient of curvature of the mortar used in this study 126
Table 4-11 FTIR bands for geopolymer 138
Table 4-12 FTIR wavenumber for deconvolution of the FTIR spectrum 144
Table 4-13 Acid Neutralizing Capacity (ANC) of geopolymer 156
Table 5-1 Classification of Sewer Corrosivity adopted from Valix (2021) 191
Table 5-2 Environmental conditions of each digestor chamber 195
Table 5-3 The rate of corrosion phases of OGPm and CACm at the digester tank 215
Table 5-4 Measured corrosion depth per year (mm/yr) within geopolymers exposed to sewer environment in previous case studies. 223
Table 5-5 Site Locations and Environmental Conditions 231
Table 5-6 The core sample of OGPm and CACm from QUU at different time 234
Table 5-7 The corrosion phases of OGPm and CACm 241
Table 6-1. Error functions 267
Table 6-2. Environmental conditions for OGPm-3 270
Table 6-3. Semi-empirical model for the corrosion initiation period 273
Table 6-4. Fitted parameters for the corrosion initiation period model (Table 6-3) 276
Table 6-5. Statistical significance analysis of Model 1 parameters (n = 11, p = 8) 277

Table 6-6. Model for Stage 1 Corrosion Propagation of Alkali Activated Binders (AAB) including Geopolymers under Mixed Chemical and Pore Diffusion Controlled..... 289

Table 6-7. Fitted parameters for mortar corrosion data under propagation stage 1..... 292

Table 6-8 Statistical significance analysis of Model 2 parameters fitted to propagation stage 1 corrosion data (n = 17, p = 15)..... 293

Table 6-9. Model for Stage 2 Corrosion Propagation of AAB and Geopolymer Mortar under Mixed Chemical and Pore Diffusion Controlled..... 297

Table 6-10 Fitted parameters for AAB and geopolymer mortar corrosion data under propagation stage 2 301

Table 6-11. Statistical significance analysis of Model 2 parameters fitted to propagation stage 2 data (n = 30, p = 15)..... 302

1 INTRODUCTION

1.1 BACKGROUND

In Australia, there are approximately 122,000 km of concrete sewer pipe networks and related infrastructures are referred to as “sewer assets” (WSA-201, 2017). The sewer assets are valuable and essential infrastructure, ensuring our cities and communities are liveable and productive. The purpose of the sewer assets is to collect, convey and treat domestic and industrial wastewater. Sewer assets are constructed from various materials, such as Bricks, Vitrified Clays, Cement Concrete, Cast Iron, Steel Pipes, and Plastics, depending on the operational criteria (Kim et al., 2012). However, most assets have been constructed using Ordinary Portland Cement (OPC) concrete.

The sewer assets are designed to have a service life of approximately 100 years (Wu et al., 2020). Unfortunately, sewer assets experience deterioration because of various factors, including operational conditions, the impact of microbial-induced concrete corrosion (MICC), and external soil corrosion. The most aggressive factor is MICC, which significantly decreases the service life of sewer assets. The MICC is a complex process with various chemical and biological reactions that convert sulphide within the wastewater to sulfuric and other biogenic acids. The sulfuric acid and other biogenic acids from the MICC process will directly react with concrete material, resulting in the gradual deterioration of sewer assets.

The failure of the sewer asset caused by MICC increasingly triggers high economic expenses and severe health and environmental concerns (Grengg et al., 2018). For example, the replacement and rehabilitation of sewer assets cost 14 billion dollars annually in the USA, 103 million dollars in the UK and over 458 million dollars in Germany to keep the existing wastewater infrastructure operational (Grengg et al., 2018, Berger et al., 2003). Furthermore, the leakage of sewer gases such

as nitrous oxide (N_2O), methane (CH_4) and carbon dioxide (CO_2) into the atmosphere would also contribute to climate change since they consider greenhouse gases formed within sewer assets (Jensen et al., 2016). In addition, hazardous gas production such as hydrogen sulphide (H_2S) and carbon dioxide (CO_2), methane (CH_4), ammonia (NH_3) and other volatile organic compounds (VOCs) associated with MICC present a severe health risk for community workers and wastewater system operators.

Sewer assets management is challenging because the sewer assets are usually buried under cities, and over 50 percent of the sewer assets are aged about 80-100 years old (WSA-201, 2017). Therefore, various mitigation strategies have been applied to reduce the impact of MICC. The mitigation strategies for existing sewer assets can target reducing the H_2S generation by chemical dosing and avoiding the development of concrete corrosion by a surface protective lining. However, To reduce the H_2S generation by chemical dosing, injecting the chemical in the various locations along the sewer assets is often required. Furthermore, once the chemical dose is not maintained at the desired H_2S level, the H_2S will return to the previous production level (Gutierrez et al., 2008). From a practical point of view, this mitigation strategy becomes expensive to maintain and operate in the long term (Hvitved-Jacobsen, 2001).

On the other hand, to avoid the concrete corrosion deterioration impacted by MICC, the use of surface protective lining has become a fascinating strategy to protect the existing sewer assets, extend the service life of the sewer assets, and work in the long term. The surface protective lining acts as a barrier between sewer assets and aggressive environmental conditions. The sewer asset can be protected using a surface protective lining, and the service life of the protective lining depends on the corrosivity of the sewer environment and the durability of the lining material.

1.2 PROBLEM STATEMENT

Alkali-activated binders (AAB) are a new class of binder material prepared by activating an aluminosilicate precursor with an alkali medium such as sodium silicate (waterglass) ($Na_2O \cdot mSiO_2 \cdot xH_2O$), Sodium hydroxide (NaOH) or Potassium hydroxide (KOH) (Ibrahim and Maslehuddin, 2021, Brough and Atkinson, 2002). The aluminosilicate precursors are utilised from industrial by-products such as fly ash (FA), Metakaolin, and Ground granulated blast furnace slag (GGBFS). The AAB can be classified into high-Calcium AAB and low-Calcium AAB, depending on the calcium content within the aluminosilicate precursors.

The reaction between low-calcium aluminosilicate precursors (FA and Metakaolin) and an alkali-activated medium can be developed in a three-dimensional crosslinked poly-sialate amorphous and semi-crystalline structure of sodium aluminosilicate hydrate gel (N-A-S-H) (Davidovits, 1991, Liew et al., 2016, Majidi, 2013, Liguori et al., 2017). The product of low-calcium aluminosilicate with alkali activation is also known as a "geopolymer" (Davidovits and Cordi, 1979). On the other hand, alkali activation of high-calcium aluminosilicate precursors can formulate the hydration product as disordered tobermorite-like (C-S-H), which can be partially substituted by aluminium or sodium/potassium to form calcium aluminium silicate hydrate gel (C-A-S-H) or calcium (sodium) aluminium silicate hydrate gel (C-(N)-A-S-H) (Provis and Van Deventer, 2013, Herrmann et al., 2018). However, if the aluminosilicate precursor is mixed with fly ash, slag, or other material, with often contains approximately 10-20 %wt CaO. Therefore, the reaction product potentially contains a Ca-rich phase and sodium aluminosilicate hydrate (N-A-S-H), providing better strength and durability (Herrmann et al., 2018).

Geopolymer and calcium-rich AAB provided comparable properties to ordinary portland cement (OPC) concrete as a traditional construction material (Davidovits, 1994). In many cases, the

durability of geopolymer concrete is better than OPC concrete, and calcium content significantly affects the durability mechanism (Chen et al., 2021). They become more attractive to utilise as a protective coating material for sewer assets rehabilitation because:

i) High chemical corrosion resistance, high mechanical strength, low shrinkage

ii) Geopolymer and calcium-rich AAB binder produced with industrial by-products with lower energy and CO_2 emission

iii) Low cost of Geopolymer and calcium-rich AAB binder production

There are various commercially available geopolymer and calcium-rich AAB products in the market. However, it has never been used as a protective coating material in sewer assets applications because:

i. There is a lack of corrosion resistance performance data.

ii. There are no guidelines for application and selection.

iii. The design of protective systems based on geopolymers is complex because of the lack of kinetic corrosion data, particularly relevant to the live sewer environment.

iv. There is a lack of understanding of sewer requirements or the definition of sewer corrosivity to specify the durability features of the protective coating system. Therefore, choosing the right geopolymer and calcium-rich AAB that fits the specific sewer environment becomes more challenging.

1.3 RESEARCH OF OBJECTIVE

The lack of information restricts the use of geopolymer as a protective coating material for sewer asset rehabilitation. Therefore, the objectives of this study are as follows:

- To understand the performance of geopolymer and alkali-activated binder coatings and in a live sewer environment.
- To obtain performance data for various commercial geopolymers and compare corrosion-resistant performance to high-performing calcium aluminate cement mortar (CACm) (100% CAC) that reflects the impact of the various sewer corrosion classification
- To use the field performance data to develop the service life prediction models and coating selection criteria

1.4 THESIS ORGANISATION

This thesis is organised into seven chapters, as shown below

Chapter 1 Introduction

- This chapter provides a brief overview of the background regarding the deterioration process of sewer assets, followed by a clear statement of the problem and the specific objectives of this investigation.

Chapter 2 Literature review

- This chapter provides an literature review of background information on sewer assets, the principle of concrete corrosion by microbial-induced concrete corrosion (MICC), mitigation strategies to inhibit the extent of the corrosion, protective coating material, and service life model for sewer rehabilitation.

Chapter 3 Material and methodology

- This chapter presents comprehensive information on the protective lining mortars utilised in this study, including details about the corrosion resistance performance tests conducted,

the characterization methods employed, and the evaluation of the protective coating material's corrosion resistance performance.

Chapter 4 Characterisation of geopolymer and calcium aluminate cement protective lining materials

- This chapter focuses on the characterisation of geopolymer and calcium aluminate cement mortar prior to their exposure to live sewer assets. The chapter highlights the important chemical and physical properties of these lining mortars, providing their initial condition before subjecting them to the challenging sewer environment.

Chapter 5 The durability of lining mortar under laboratory and field test

- This chapter presents the performance of alkali-activated binder mortar, including geopolymer to acid immersion test and different sewer corrosivity environmental classifications in live sewer assets.

Chapter 6 Service life prediction models for alkali-activated binders, including geopolymer exposed to sewer conditions of various corrosivity

- This chapter presents the service life model developed using corrosion resistance performance data obtained from live sewer assets. The model aims to accurately predict the expected service life of these assets based on the gathered data.

Chapter 7 Conclusion and Recommendation

- This chapter provides a concise summary of the key findings and results obtained in this study related to the objectives outlined. It aims to present the essential outcomes that have emerged from this study, highlighting their significance and relevance to the overall study.

1.5 LIST OF PUBLICATIONS

1.5.1 BOOK SECTION

1. Cherdphong SEEDAO, M. E. FISHER and Marjorie VALIX, “Comparative Acid Resistance Of One-Part Geopolymer And Calcium Aluminate Cement Mortar” International Conference on Calcium Aluminates 2022, Cambridge, England

1.5.2 CONFERENCES

1. Cherdphong Seedao, Ye Jun In, Matthew Fisher, James Gardner and Marjorie Valix, “Evaluation of one-part geopolymer mortars as protective sewer coating for sewer assets” No-Dig Down Under 2021, Sydney, Australia
2. C.SEEDAO, Y.J.In, J. Sunarho, and M.Valix, “Comparison of corrosion resistance of one-part geopolymer and calcium aluminate cement mortar exposed to live aggressive sewer environment” Singapore International Water Week 2022, Singapore

1.5.3 CONTRIBUTION OF THE RESULT

1. Factsheet: Corrosion Classification for Concrete Wastewater Infrastructure
2. WSA 161-2021 - Water Industry Standard for Alkali Activated Binder Including Geopolymer Cement Mortar used for the renovation of wastewater structures and large diameter pipes Version 1.0
3. WSA 201:2020 Manual for Selection and Application of Protective Coatings Version 2.3

2 LITERATURE REVIEWS

2.1 INTRODUCTION

A concrete sewer pipe network, including pipes, pumping stations, and access chambers, referred to as “Sewer assets”, is the valuable and essential urban infrastructure in ensuring our cities and communities are liveable. However, the sewer assets are seriously experiencing corrosion due to microorganism activities known as “microbial-induced concrete corrosion (MICC)”. In order to address the issues of corrosion of the sewer assets, understanding the context of assets management and the causes of the corrosion would be helpful information for future development. Therefore, this chapter will present state of the art on sewer network systems, the MICC process, chemistry, and the corrosion mechanism behind concrete corrosion. Moreover, this chapter will also highlight the history of experiments to analyse the corrosion-resistance performance of geopolymers, including alkali-activated binders, against chemical and biological corrosion.

2.2 SANITARY SEWER NETWORK SYSTEM

Sanitary sewage is wastewater generated by human activities from residential (e.g., toilets, sinks, showers, washing machines, dishwashers) and industrial wastewater. It is a complex mixture of inorganic and organic materials. The sewage is collected and conveyed to a wastewater treatment plant by a sewer network between the sewage and wastewater treatment plants (Hvitved-Jacobsen et al., 2013).

2.2.1 SEWER PIPE NETWORK

Generally, there are various types of sewers in the typical sewer pipe network: lateral, main, trunk, and interceptor, as shown in Figure 2-1. The difference between the various pipe type is described

in Table 2-1. The sewage flow can be controlled by either gravity or pressure as shown in Figure 2-2 (Hvitved-Jacobsen et al., 2013).

- Gravitational sewer system – the sanitary wastewater flows by gravity force
- Pressure sewer system - the sanitary wastewater from the sewage collection tank are pumped to another main sewer network

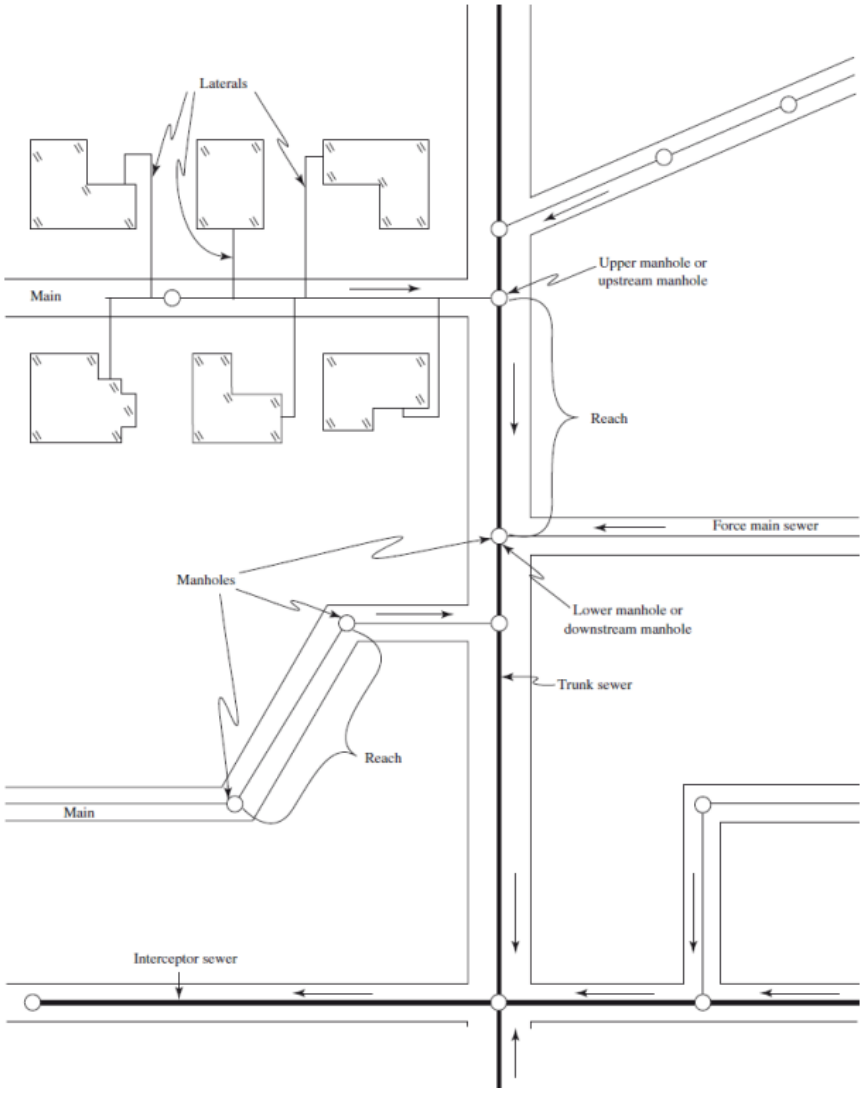

Figure 2-1 Schematic diagram of a sewer pipe network (Mackenzie L. Davis, 2020)

Table 2-1 Types of Sewers pipe in a typical collection system (Mackenzie L. Davis, 2020)

Sewer type	Description
Lateral	Lateral sewers form the first element of a wastewater collection system. They collect the wastewater from buildings and convey it to a main sewer.
Main	The main sewer conveys wastewater to trunk sewers or intercepting sewers.
Trunk	Trunk sewers are large-diameter sewers that are used to convey wastewater from main sewers to treatment facilities or to intercept sewers.
Interceptor	The interceptors are very large diameter sewers that are used to intercept a number of main or trunk sewers and convey wastewater to treatment facilities.

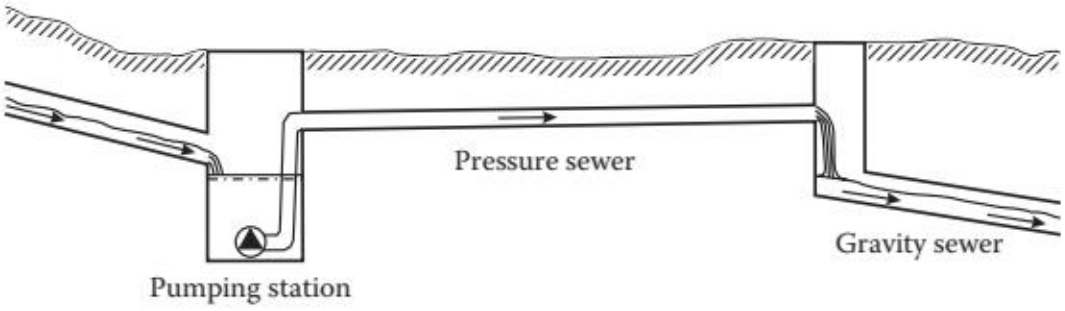

Figure 2-2 Type of sewer network: gravity sewers and pressure sewers (Hvitved-Jacobsen et al., 2013)

2.2.2 SEWER GASES BUILD UP IN SEWER PIPE

In sewage, it is an extensive range of pollutants and various microbial presence within the sewage. These are “microbial reactors” that potentially transform and degrade substances to gases and soluble substances based on their chemical and biological reactivity (Hvitved-Jacobsen et al., 2013). Sewage typically contains high sulphate concentration and supports sulphate-reducing

bacteria (SRB) growth. The SRB transforms sulphate (SO_4^{2-}) to sulphide (S^{2-}) in sewage sludge under anaerobic conditions (Petersen and Ahring, 1990, Roberts et al., 2002). The microorganism utilises SO_4^{2-} as an external electron acceptor in the absence of oxygen and nitrate (Barton and Fauque, 2009, Grengg et al., 2018). The sulphide (S^{2-}) that is formed is converted to hydrogen sulphide (H_2S) in sewers as a significant compound and plays a significant role in the MICC process (Grengg et al., 2018). Carbon dioxide (CO_2), methane (CH_4) and other volatile organic carbons (VOCs) are also generated by the anaerobic microorganisms as part of their catabolic reactions. Nitrogen-fixing microorganisms may also form NH_3 in the sewer. Sewer gases are transferred to the atmosphere within sewer pipes depending on pH and flow rate. Once in the headspace of the sewer pipe, the H_2S gas is either spontaneously abiotically or biotically oxidised by Sulfur-oxidising bacteria (SOB) in the crown and tidal regions of the pipe to form sulfuric acid (H_2SO_4) (Jensen et al., 2009). At this stage, the high surface alkalinity provides an antimicrobial environment. The surface pH of concrete is first reduced by an abiotic acid-base reaction, resulting in carbonation and the formation of weak acids (thiosulfuric and polythionic acid) (Grengg et al., 2018). The dissolved H_2S and intermediate sulphur species such as elemental sulphur (S_0) and thiosulfate ($S_2O_3^-$) are oxidised to sulphuric acid (H_2SO_4) by the microorganisms, which highly corrodes the concrete sewer pipes (Ling et al., 2014, Okabe et al., 2007a). Changes in mineralogical compositions during this stages of corrosion are indicated by + (newly formed minerals). At this stage, the corrosion process is profoundly affected by the environmental factors of hydrogen sulphide concentration, humidity, and temperature (Jiang et al., 2014). In the concrete sewer pipe, the corrosion of concretes mostly occurs in the region right above the sewage level (tidal) and at the ceiling (crown region) (Li et al., 2017).

2.2.3 SEWER PIPE CONSTRUCTION MATERIALS

In managing sewer assets, effective sewer asset management plans must be implemented to simultaneously address long-term sustainability principles, i.e., economic growth, human health and safety, and environmental protection. One of the keys to this solution is using the right material to convey the sewage to the sewer network. Sewer pipe is manufactured with different materials such as cement-based material (i.e., Ordinary Portland Cement, Sulfur-resistant cement, Brick, sandstone, clay), Metal (i.e., Cast Iron (CI), Ductile Iron (DI), Mild Steel (MS), Cast Iron Cement lined (CICL), Ductile Iron Cement lined (DICL)), and plastics (i.e., Polyethylene (PE), Polyvinyl chloride (PVC), High-Density Polyethylene (HDPE),). The material selection depends on the operational criteria (i.e., location, pressure, sewage flow, and environmental condition). Cast iron is employed to transfer the sewage under high pressure (Kim et al., 2012). Plastics are used for many sewer piping applications. The most known are polyvinyl chloride (PVC), polyethylene (PE), polypropylene (PP), acrylonitrile–butadiene–styrene (ABS), polybutylene (PB) and glass–fibre-reinforced polyester (GRP or FRP). However, PVC has been extensively used for urban drainage systems because of its cost-efficiency, ease of installation, range of available diameters (40–630 mm) and high chemical resistance (Makris et al., 2020).

2.3 SEWER STRUCTURE DETERIORATION

The concrete sewer asset is one of modern urban society's most critical infrastructure assets. It typically comprises three components: water, aggregate and cement binder. The cement binder is usually referred to as Ordinary Portland Cement (OPC) and is the most widely used material for sewer pipe construction. When the cement powder is mixed with water, it formulates hydration products as a binder that could hold together the aggregates and other additional components named concrete (Monteiro et al., 2017). However, additives may also include altering the rate of

the hydration reaction. Deterioration of sewer assets is possibly associated with varied factors such as sewer asset aging, microbiologically induced concrete corrosion (MICC), inflow and infiltration (I/I), abrasion, tree intrusion, and external corrosion from acidic soil.

Nevertheless, the corrosion of sewer assets problem is primarily linked to sewer gases, mainly hydrogen sulphide from the microbiological process within the sewer pipe network known as MICC. The MICC can cause the loss of concrete mass, cracking of sewer pipes, and, finally, the sewer asset collapse. The sequential growth of microorganisms, MICC, and Corrosion chemistry will be reviewed to improve understanding of concrete deterioration.

2.3.1 SEQUENTIAL GROWTH OF MICROORGANISMS

The generation of the corrosive compound is related to biological activity. The successful growth of the microbiome and proliferation depends on different parameters such as cell pH requirement, nutrient availability, environmental condition, and comparability microbiome (Auguet et al., 2015, Valix et al., 2012). Therefore, it is essential to understand the consequential growth of microorganisms on the concrete surface. Microorganisms can grow on concrete sewer pipe walls as a biofilm. However, it has a specific pH growth range and pH growth optimum, as shown in Figure 2-3 (Valix and Shanmugarajah, 2015, Nevarez et al., 2009, Willey et al., 2016). The sequential growth of the microbiome occurs approximately in the following order. Fresh concrete has a pH of approximately 12.0. Each strain of microorganisms, with the exception of alkaliphiles, works cooperatively by growing and metabolising their specific biogenic acids successively to bring down the surface pH of concrete to promote its corrosion. At highly alkali concrete surface, alkaliphile bacteria and fungi can colonise and grow above pH 9, such as *Bacillus pseudofirmus* and *Trichoderma reesei*, which heals the concrete by filling in the microcracks and growing at high alkaline conditions (pH > 10) (Jonkers and Schlangen, 2008, Ryparová et al., 2021, Luo et

al., 2018). When the surface pH of the sewer pipe is abiotically reduced below 9, The colonisation of various strains of neutrophilic microorganisms commences colonising on the surface of the concrete, such as *Thiobacillus thioparus, Thiobacillus novellus* and *Thiobacillus neapolitanus,* and *Thiobacillus intermedius,* which promote the conversion of thiosulphate to elemental sulphur grow optimally at pH 5.5 to 8.0 (Islander et al., 1991a) while generating low concentrations of sulphuric acid. These are also referred to as neutrophilic sulphur-oxidising microorganisms (NSOMs). As the surface pH of concrete is reduced below 4, acidophilic bacteria, specifically *Acidithiobacillus thiooxidans,* begin colonising on the surface (Roberts et al., 2002, Valix and Shanmugarajah, 2015). At this pH, there are five species of *Acidithiobacillus* found to play essential roles as a key on corroded and corroding concrete, including *T. thioparus, T. novellus, T. neapolitanus, T. intermedius* and *T. thiooxidans* (Behnood et al., 2016, Bertron, 2013, Valix and Shanmugarajah, 2015, Mackenzie L. Davis, 2020). They have their growth optimum at pH 1.0 to 3.5 (Okabe et al., 2007b, Hernandez et al., 2002, Leduc and Ferroni, 1994). These are also referred to as acidophilic sulphur-oxidising bacteria (ASOB). Neutrophilic sulphur-oxidising microorganisms (NSOMs) and acidophilic Sulfur-oxidising microorganisms (ASOMs) play an essential role in sewer corrosion. Both microorganisms used a reduced form of sulphur as an energy source (Roberts et al., 2002). ASOB and NSOB oxidise the dissolved H_2S and intermediate sulphur species such as elemental sulphur (S^0) and thiosulfate ($S_2O_3^-$) to sulphuric acid (H_2SO_4), which corrodes the concrete (Ling et al., 2014, Okabe et al., 2007a).

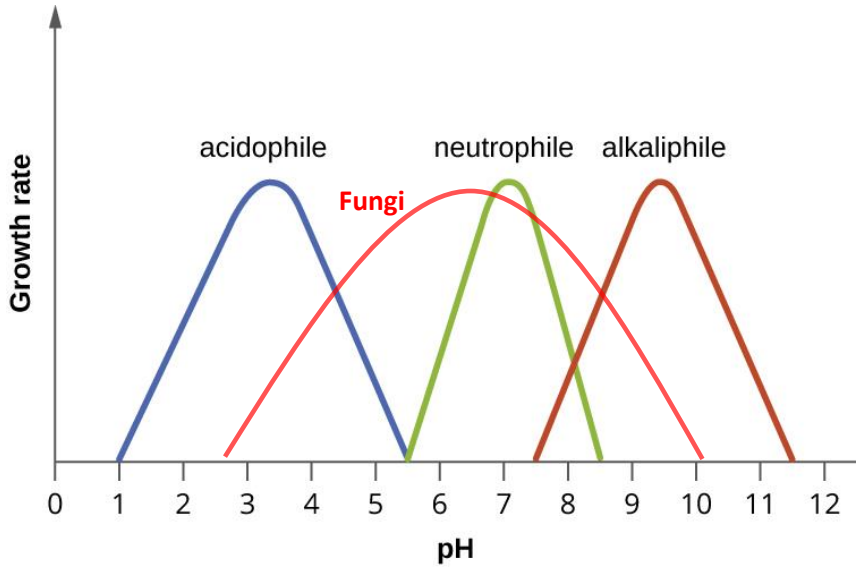

Figure 2-3 Approximate pH range for the growth of different classes of the pH-specific microbiome

2.3.2 MICROBIAL-INDUCED CONCRETE CORROSION (MICC)

Microbial-induced concrete corrosion (MICC) is a multi-stage concrete deterioration process related to microorganism activities in wastewater collection, storage, and treatment infrastructure. Long residence time or slow sewage flow initiates the anaerobic conditions within the sewer pipe, referred to as the sewer environment. The microorganism activities in the sewer environment generated sewer gases typically consisting of Nitrogen (N_2), Methane (CH_4), Hydrogen Sulphide (H_2S), Carbon dioxide (CO_2), Ammonia (NH_3), Sulphur dioxide (SO_2) and other volatile organic compounds (VOCs) as shown in Figure 2-4 (a) (Grengg et al., 2018). The concrete sewer pipes and other related infrastructure has been mainly deteriorated by biogenic strong/weak acid from microorganism metabolism under sewer environmental condition. MICC is considered to be a three stages corrosion process, which is surface pH reduction (pH 12.5-9), the establishment of biofilm (pH 10-4) and finally, concrete deterioration (pH <4), as shown in Figure 2-4 (b) (C1894-19, 2019).

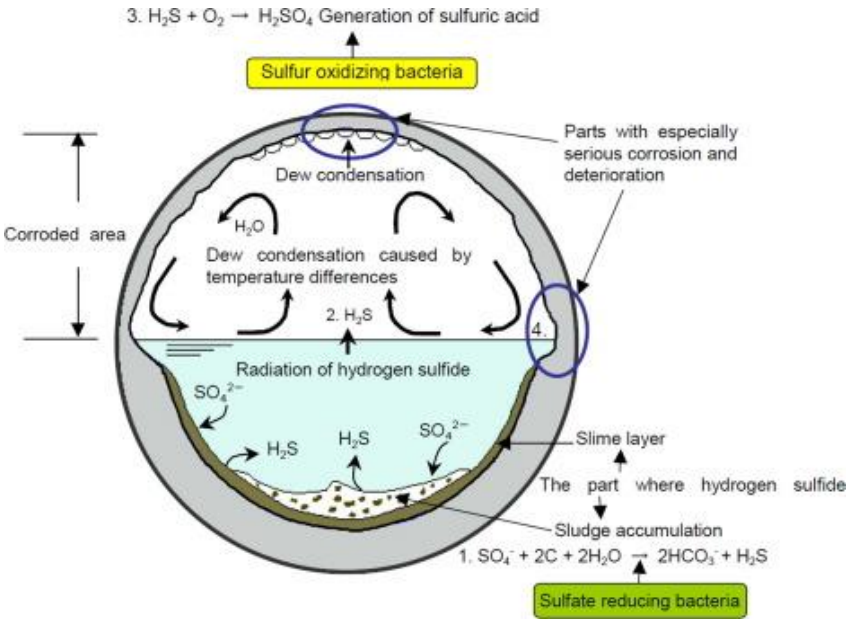

(a)

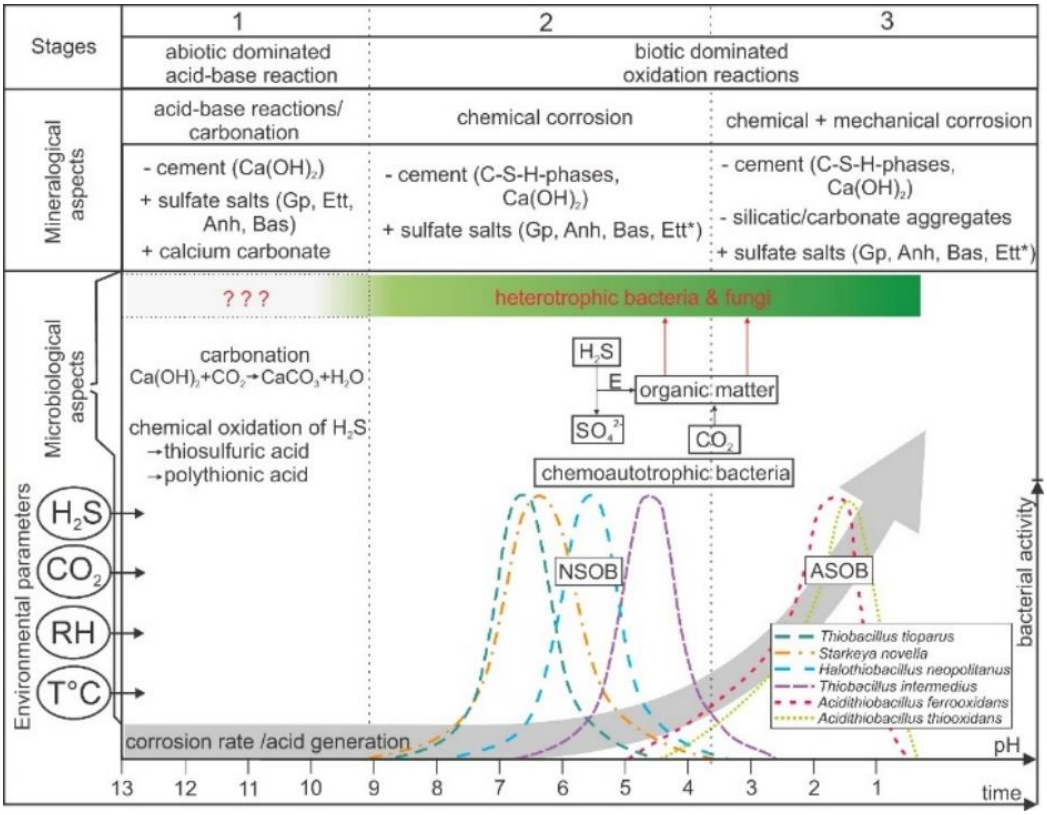

(b)

Figure 2-4 Microbial-induced corrosion of concrete (MICC) (Ling et al., 2014, Roberts et al., 2002, Jiang et al., 2015b, Wu et al., 2020, Grengg et al., 2018)

Stage 1: Chemical surface pH reduction - this stage of deterioration of concrete sewer pipe occurs by chemical corrosion. Fresh concrete sewer pipes are typically porous material and highly alkaline, with pH in the range of 11 to 13 (Behnood et al., 2016, Bertron, 2013, Valix and Shanmugarajah, 2015, Mackenzie L. Davis, 2020). The initial surface pH reduction of concrete is typically contributed by carbonation. The carbonation of the concrete will reduce the concrete surface pH from 11-13 to 8.2, which is a natural pH of calcium carbonate ($CaCO_3$) as the carbonation product (Kurda et al., 2019, Wu et al., 2018a). Potential corrosive sewer gases and humidity have accumulated in space above the sewage level within concrete sewer pipes. The CO_2 reacts with water and forms carbonic acid (H_2CO_3), as shown in Equation 2.1. The H_2CO_3 solution continues to react with calcium hydroxide ($Ca(OH)_2$) and calcium silicate hydrate (C-S-H) to form calcium carbonate, as shown in Equation 2.2 and Equation 2.3. This process is usually known as the carbonation process.

$$CO_2 + H_2O \rightarrow H_2CO_3 \qquad \text{Equation 2.1}$$

$$Ca(OH)_2 + H_2CO_3 \rightarrow CaCO_3 + 2H_2O \qquad \text{Equation 2.2}$$

$$CaO \cdot SiO_2 \cdot 2H_2O + H_2CO_3 \rightarrow CaCO_3 + Si(OH)_2 + 2H_2O \qquad \text{Equation 2.3}$$

Aside from the carbonation process, hydrolysis of other sewer gases commences forming both weak and strong acids as shown in Equation 2.4 - Equation 2.8 (Sand, 1997a, Valix and Shanmugarajah, 2015, Gutierrez et al., 2014). The weak and strong acid contributes to the leaching of $Ca(OH)_2$, reducing surface pH to lower the initial pH of concrete from pH ~12.5 to ~9(C1894-19, 2019).

$$H_2S + H_2O \rightarrow H_3O^+ + HS^- \qquad \text{Equation 2.4}$$

$$HS^- + H_2O \rightarrow H_3O^+ + S^- \qquad \text{Equation 2.5}$$

$$2NO_2 + H_2O \rightarrow HNO._2 + HNO._3 \qquad \text{Equation 2.6}$$

$$2NO + 3O_2 + 2H_2O \rightarrow 4HNO_3$$ Equation 2.7

$$SO_2 + H_2O \rightarrow H_2SO_3$$ Equation 2.8

Moreover, the surface pH of the concrete sewer pipe is likely to reduce faster by carbonation when the sewer environment contains a high concentration of CO_2 with relative humidity in the range of 40% to 80% (Roberts et al., 2002, von Greve-Dierfeld et al., 2020, Elsalamawy et al., 2019). Another further reaction to reduce the surface pH from 10 to 8 is mainly by the dissolution of H_2S reduction (Joseph et al., 2012), as shown in reaction Equation 2.9.

$$2CaCO_3 + 2H_2S \rightarrow Ca(HCO_3)_2 + Ca(HS)_2$$ Equation 2.9

Stage 2: Chemical corrosion by biogenic acid - when the surface pH is approximately low to 9, the concrete surface becomes appropriate for colonisation and the growth of bacteria and fungi. Biogenic strong/weak acids are initially produced by sulphur-oxidising bacteria (SOB) and fungi. Based on the culturing of bacteria from corrosion samples (Sun, 2015) suggested that SOB is important for sewer corrosion, including *Thiobacillus thioparus*, *Thiobacillus plumbophilus*, S*tarkeya novella*, *Halothiobacillus neapolitanus*, *Thiomonas intermedius* (formerly *Thiobacillus intermedius*), *Acidithiobacillus thiooxidans* (formerly *Thiobacillus thiooxidans*), *Thiomonas perometabolis* (formerly *Thiobacillus perometabolis*), *Paracoccus versutus* (formerly *Thiobacillus versutus*) and *Acidiphilium acidohilum*. The product of H_2S oxidation by SOB can generate an oxidation product with various sulphur states depending on the local pH condition, e.g. S^0, $S_2O_3^{2-}$, Polythionic acid, SO_4^{2-} as shown in Table 2-2 (Sun, 2015). However, there are two types of SOB: neutrophilic sulphur-oxidising bacteria (NSOB) and Acidictrophilic sulphur-oxidising bacteria (ASOB). Once the surface pH is approximately reduced to 9, NSOB, e.g. *Thiobacillus thioparus*, commences colonising on the concrete surface and oxidising H_2S. This led to a decrease in the surface pH to 4-5. When the surface pH reduces to 4-5, ASOB is started to

colonise, and at the same time, the NSOB activities are gradually inhibited due to environmental conditions is not support the growth of NSOB. At this point, ASOB can directly oxidise H_2S to H_2SO_4 and low the surface pH to 1-2. The H_2SO_4 dissolution starts to attack the cementitious paste portion of the concrete matrix and calcium carbonate. It formulates expansive corrosion products such as gypsum and ettringite, as shown in Figure 2-5 (Wu et al., 2020).

Stage 3: Chemical and mechanical corrosion - at this stage, the corrosion of concrete sewer pipe is basically related to chemical and mechanical corrosion, resulting in a massive loss of material and continued expansion of gypsum and ettringite as corrosion product into concrete sewer pipe due to the reaction of the biogenic acid with the cementitious material. The structural stabilisation of concrete is obviously weakened by a transformation to a corrosion product. It eventually results in a collapse of the concrete sewer pipe. Additionally, The corroded concrete may be divided into several zones, as shown in Figure 2-5. The transition of corroded concrete starts from the uncorroded concrete (sound concrete), transition zone, ettringite layer at high pH value areas (>10.7) and gypsum near the corroded front facing corrosive environment (Wu et al., 2020). The deterioration of concrete under the biogenic acid will be reviewed in section 2.3.3.

Table 2-2 Physiological characteristics of some sulphur-oxidising bacteria in concrete corrosion layers by Sun (2015)

SOB Species	pH range for growth	Sulphur substrate	Product
Thiobacillus thioparus	6–10	H_2S, S^0, $S_2O_3^{2-}$	Polythionic acids, S^0
Halothiobacillusneapolitanus (former *Thiobacillusneapolitanus*)	6–8	S^0, $S_2O_3^{2-}$	Polythionic acids, SO_4^{2-}
Starkeyanovella (former *Thiobacillusnovellus*)	6–8	$S_2O_3^{2-}$	S^0
Starkeyaintermedius	5–7	$S_2O_3^{2-}$	Polythionic acids, SO_4^{2-}
Thiobacillusplumbophilus	4–6.5	H_2S	–
Acidiphilium spp. (former *Thiobacillusacidophilus*)	3–10	H_2S, S^0	SO_4^{2-}
Thiomonas spp. (former *Thiobacillusintermedius*)	3–9	H_2S, $S_2O_3^{2-}$	SO_4^{2-}
Acidithiobacillusferrooxidans (former *Thiobacillusferrooxidans*)	~3	H_2S	S^0,SO_4^{2-}
Thiobacillusacidophilus	~3	H_2S	S^0,SO_4^{2-}
Acidithiobacillusthiooxidans	<3	H_2S, S^0	S^0,$S_2O_3^{2-}$
Sulfobacillus spp.	1–3	H_2S, $S_2O_3^{2-}$	–
Thermothiobacillus	Poorly characterised	H_2S, $S_2O_3^{2-}$,$S_nO_6^{2-}$	SO_4^{2-}
Metallibacterium spp.	Poorly characterised		
Burkholderiales spp.	Poorly characterised		
Sphingobacteriales spp.	Poorly characterised		
Xanthomonadales spp.	No cultured representative		

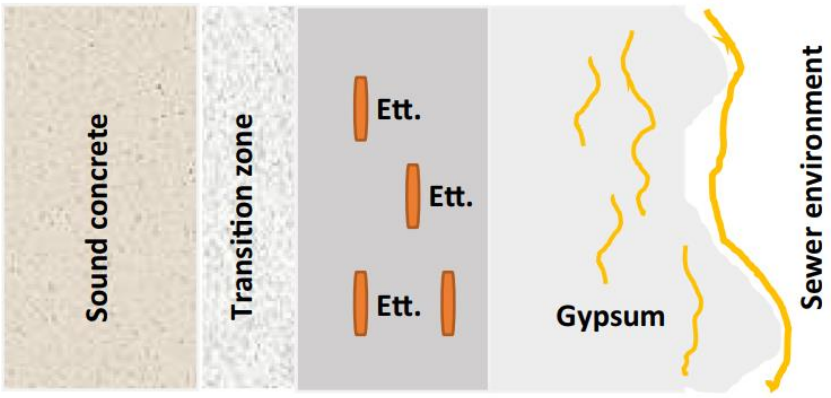

Figure 2-5 Schematic illustration of the different zones in the corrosion layer (Wu et al., 2020)

2.3.3 DETERIORATION OF CONCRETE MATERIALS

Concrete-based ordinary portland cement (OPC) is a highly alkaline material in nature. The concrete-based OPC initially deteriorate when exposed to the acidic condition. The chemistry of concrete corrosion is comprised of three principal corrosion mechanisms i) dissolution of cement matrix components, ii) expansive reaction and iii) decomposition of hydrates. The process of corrosion begins with the diffusion of sulphuric acid generated by SOB into the concrete sewer pipe. Calcium hydroxide, carbonate compound, and calcium silicate hydrate (C-S-H) are first started to dissolve by hydrogen ions from H_2SO_4 solution and formulate gypsum and consequently (see Equation 2.10 - Equation 2.12), the gypsum can continually react with C_3AH_6 to form ettringite as shown in chemical reaction in Equation 2.13 (Wu et al., 2020, Aragaw, 2018, Davis et al., 1998, Monteny et al., 2000). The main corrosion product, expansive gypsum and ettringite, can significantly increase the pore volume of concrete, resulting in structural destabilisation and internal crack formation.

$$H_2SO_4 + CaCO_3 \rightarrow CaSO_4 + H_2CO_3 \quad \text{Equation 2.10}$$

$$H_2SO_4 + Ca(OH)_2 \rightarrow CaSO_4 + 2H_2O \quad \text{Equation 2.11}$$

$$H_2SO_4 + 3CaO{\cdot}SiO_2{\cdot}2H_2O \rightarrow CaSO_4 + Si(OH)_4 + H_2O \quad \text{Equation 2.12}$$

$3CaSO_4 + 3CaO{\cdot}Al_2O_3{\cdot}6H_2O + 26H_2O \rightarrow 3CaO{\cdot}Al_2O_3{\cdot}\ 3CaSO_4{\cdot}32H_2O$ Equation 2.13

2.4 MITIGATION STRATEGIES FOR CORROSION

The concrete sewer pipe networks are seriously deteriorated by microbial-induced concrete corrosion (MICC), associated with biogenic sulfuric acid (H_2SO_4) as a final product in the MICC process. H_2SO_4 is considered an aggressive compound for concrete sewer pipes that have been converted from hydrogen sulphide (H_2S) by Sulfate Oxidising Bacteria (SOB) under anaerobic conditions. Several methodologies presently respond to the corrosion of concrete sewer pipe mitigation by controlling the hydrogen sulphide emission/oxidation and sewer pipe protection using coating material.

2.4.1 CHEMICAL MITIGATION STRATEGIES FOR HYDROGEN SULPHIDE EMISSION

The hydrogen sulphide emission into the headspace of the concrete sewer pipe usually happens under anaerobic conditions. The generation of hydrogen sulphide depends on several factors, such as the concentration of biodegradable organic matter (BOM), temperature, pH of sewage, and sewage hydraulics (Park et al., 2014). The hydrogen sulphide emission needs to reduce from wastewater to avoid biogenic acid generation from SOB oxidation. Dissolved sulphide in wastewater is originally from sulphate reduction within anaerobic regions of the biofilm and sediments under the submerged part of the concrete sewer, as shown in Equation 2.14 (Park et al., 2014).

$$SO_4^{2-} + 2C + 2H_2O \xrightarrow{SRB} 2HCO_3^- + H_2S \qquad \text{Equation 2.14}$$

The dissolved hydrogen sulphide gradually diffuses to the wastewater phase and emits to the sewer headspace as hydrogen sulphide (H_2S) gas. However, the dissolved hydrogen sulphide can be converted back to sulphate or element sulphur (S^0) again by chemical and biological oxidation if

there are O_2 (Zhang et al., 2008) and NO_3^- (Hvitved-Jacobsen et al., 2013) as electron acceptors, as shown in Equation 2.15- Equation 2.17. Moreover, adding some metal compounds such as iron, zinc, and copper can precipitate the dissolved sulphide as metallic sulphide (Nielsen et al., 2005b). However, chemical dosing required various points to control hydrogen sulphide production. This would be considered a short-term solution because it is expensive and difficult to maintain the dosing operation.

$$H_2S + 2O_2 \rightarrow SO_4^{2-} + 2H^+ \quad \text{Equation 2.15}$$

$$H_2S + 2O_2 \rightarrow 2S^0 + 2H_2O \quad \text{Equation 2.16}$$

$$H_2S + NO_3^- + H_2O \rightarrow SO_4^{2-} + H^+ + NH_3 \quad \text{Equation 2.17}$$

2.4.2 LINING APPLICATIONS

The conversational method for controlling concrete sewer corrosion emphasises hydrogen sulphide production and emission to headspace from wastewater. Likewise, it deactivates the sulphide-oxidising bacteria on the crown region of the sewer pipe. Mortar lining is used to extend the service life of concrete sewer assets. The lining mortar act as a barrier between a corrosive environment and concrete sewer pipe. Some of the primary lining mortar are cement-based lining and polymeric-based lining.

2.4.2.1 CEMENT-BASED LINING

Cement-based linings are protective coatings or linings applied to the inner surfaces of pipes or structures using cementitious materials. It enhances the corrosion resistance and durability of concrete, steel, or iron substrates in various applications, such as water and wastewater pipes and sewer systems (Valix, 2011, Kodagoda and Thiyagarajan, 2018). Cement-based linings are typically known as mortar, which is mainly composed of cement binder and fined aggregates (Arulmoly et al., 2021, De Schutter and Poppe, 2004). Ordinary portland cement binder, calcium

aluminate cement binder, and alkali-activated binder, including geopolymer, have been evaluated as cement binder for use as mortar in many studies (Alexander and Fourie, 2011, Ali et al., 2022, Khan et al., 2019a, Khan et al., 2018).

2.4.2.2 POLYMERIC BASED COATING

Polymeric-based linings refer to polymer materials as protective coatings or linings applied to various surfaces, such as pipes, tanks, structures, or substrates, to enhance their performance and durability. These linings are designed to provide a barrier between the substrate and its surrounding environment, protecting it from corrosion, chemical attack, abrasion, and other forms of degradation (Nazemi and Valix, 2016, Liu and Vipulanandan, 2001, Kohankar Kouchesfehani et al., 2020). It is typically based on epoxy, polyurethane, polyurea, and their hybrids (Zhu et al., 2021a, Nazemi and Valix, 2016). All polymeric lining methods require extensive cleaning of the internal pipe surface, especially for sewage systems. Different types of polymeric lining/coating has been developed to protect the concrete surface against MICC (Nazemi and Valix, 2016, Liu and Vipulanandan, 2001, Kohankar Kouchesfehani et al., 2020, Pazoki et al., 2016). They can be applied to a wide range of pipe materials, including concrete (Liu and Vipulanandan, 2001, Nazemi and Valix, 2016), and steel (Kohankar Kouchesfehani et al., 2020). Despite the polymeric-based linings showing excellent corrosion resistance performance, they show variable performance in corrosive sewer environments due to their unique chemical composition, physical forms, mechanical properties and applications, exposure environment and time (Nazemi and Valix, 2016, Gu, 2003).

2.5 TYPICAL CONCRETE SEWER PIPE

2.5.1 ORDINARY PORTLAND CEMENT

Ordinary Portland cement (OPC) is a binder material that has been used for construction. OPC is produced by burning limestone minerals (limestone, chalk, dolomites) and clay minerals (clays and marbles, silica sand, and bauxites at elevated temperatures of 1400-1600 °C (El Mogahzy, 2009, Aragaw, 2018). The product of burning is called clinker stone, which is ground to dust finesse with additional gypsum ($CaSO_4 \cdot 2H_2O$). The gypsum is added to the clinker in order to control the setting time (Biczok and Blasovszky, 1964). The chemical composition of cement contained generally four metal oxides as Calcium Oxide (CaO, C), Silicon Oxide (SiO_2, S), Aluminum Oxide (Al_2O_3, A) and Iron Oxide (Fe_2O_3, F). The clinker undergoes chemical reactions during the calcination process to produce the key mineral constituents of OPC, which are: Alite: Tri-calcium silicate ($3CaO.SiO_2$, C_3S), Belite: Dicalcium Silicate ($2CaO.SiO_2$, C_2S), Celite II: Tricalcium Aluminate ($3CaO.Al_2O_3$, C_3A) and Celite I: Tetracalcium Aluminoferrite ($4CaO.Al_2O_3.Fe_2O_3$, C_4AF).

The clinker production typically comprises 60–65 wt.% CaO (Lime), 21–25 wt.% SiO_2 (silica), 4–8 wt.% Al_2O_3 (Aluminum Oxide), 2–4 wt.% Fe_2O_3 (ferrous oxide), 1-3 wt.% MgO (Magnesium Oxide), 1-4 wt.% SO_3 (Sulphur trioxide) and other impurities from raw materials such as magnesia and sulphur trioxide (Ojovan and Lee, 2005, Aragaw, 2018). The quality of cement will depend on its composition, as higher tricalcium silicate provides better cement (Aragaw, 2018). According to ASTM C150/C150M-18, ordinary Portland cement is classified into five (5) types. Type I—For the general purpose, which has high C_3S; Type II – for moderate sulphate resistance, which has less than 8% of C_3A, Type III – for high early strength; type IV – for low heat of

hydration and Type V – for high sulphate resistance (Kurdowski, 2014). RC reinforced concrete-large gravity sewer.

2.5.2 HYDRATION REACTION

Cement hydration is the reaction of the anhydrous Portland cement with water to produce a hydrated cement. The hydrated cement is entirely changed at the chemical and physicomechanical levels in the system. When cement is in contact with water, a hydration reaction occurs with mainly C_3S, C_2S, C_3A, and C_4AF cement composition react with water; the hydration reaction will occur (Kurdowski, 2014).

Tricalcium silicate hydration

$$2C_3S + 6H \rightarrow C_3S_2H_3 + 3CH \qquad \text{Equation 2.18}$$

Dicalcium silicate hydration

$$2C_2S + 4H \rightarrow C_3S_2H_3 + CH \qquad \text{Equation 2.19}$$

Calcium aluminate hydration

Absence of Calcium Sulphate ($CaSO_4$):

$$C_3A + 6H \rightarrow 2C_3AH_6 \qquad \text{Equation 2.20}$$

Presence of Calcium Sulphate ($C\bar{S}H_2$): the main product of hydration of C_3A is Ettringite ($C_6A\bar{S}_3H_{32}$) is formed as the main product of hydration

$$C_3A + 3C\bar{S}H_2 + 26H \rightarrow C_6A\bar{S}_3H_{32}\ (\text{Ettringite}) \qquad \text{Equation 2.21}$$

$$2C_3A + C_6A\bar{S}_3H_{32} + 4H \rightarrow 3C_4A\bar{S}H_{12} \qquad \text{Equation 2.22}$$

Tetracalcium Aluminoferrite hydration

$$C_4AF + 10H \rightarrow C_3AH_6 + FH_3 + CH \qquad \text{Equation 2.23}$$

2.6 ALKALI-ACTIVATED BINDERS

2.6.1 HIGH-CALCIUM ALKALI-ACTIVATED BINDERS

OPC is a cement binder that is commonly used as a construction material. However, it needs to find a new cement binder due to environmental and durability performance problems (Pacheco-Torgal et al., 2008). Presently, alkali-activated binders (AAB) are alternative cement binders to OPC. Still, it is in the early stage of development to become technically and economically available as the primary construction material in the market.

AABs are a new class of binder material prepared by activating an aluminosilicate precursor with an alkali medium such as Sodium silicate (waterglass) ($Na_2O{\cdot}mSiO_2{\cdot}xH_2O$), Sodium hydroxide (NaOH) or Potassium hydroxide (KOH) (Ibrahim and Maslehuddin, 2021, Brough and Atkinson, 2002). The AABs hydration product depends on the availability of calcium content of the precursor; high calcium aluminosilicate precursors (CaO > 10 %wt) such as Blast furnace slag (BFS) can formulate Calcium aluminosilicate hydrate (C-A-S-H) with tobermorite like (mostly Q_2, some Q_1 and Q_3) structure based on NMR analysis (Richardson et al., 1994b, Provis et al., 2015, Richardson et al., 1994a), while low-calcium aluminosilicate precursors (CaO < 10%wt) such as fly ash or metakaolin tend to formulate sodium aluminosilicate hydrate (N-A-S-H) gel with a highly crosslinked (mainly Q_4) (Brough and Atkinson, 2002). The activation product of low calcium aluminosilicate precursors was given the term Geopolymer by Davidovits in 1979 (Davidovits and Cordi, 1979). The geopolymer will be explained more in section 2.6.2. AABs-based high-calcium aluminosilicate precursors such as blast furnace slag (BFS) and other industrial

by-product has been generated for over ten years. Most development of AABs is based on BSF. It is a heterogeneous reaction process, and it is not well understood. However, the general mechanisms for formulating the AABs are covered by i) dissolution of the glassy precursor particles, ii) nucleation and growth of the initial solid phases, and iii) transportation and polycondensation (Provis and Van Deventer, 2013). The reaction mechanism of high-Ca AABs can be referred to as both hydration and polymerisation processes (Herrmann et al., 2018). The hydration of AAB started from rapid hydration of soluble Na and Si, followed by small and reactive particles, and finally, the formation of a layer of C-S-H around the particle with slowly increasing the thickness of C-S-H as shown in Figure 2-6.

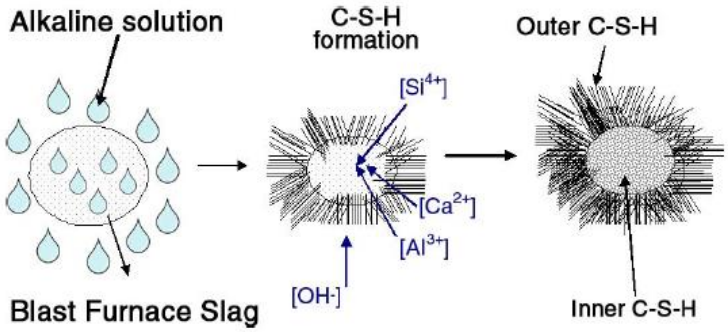

Figure 2-6 Reaction mechanism in an alkali-activated slag particle (Palomo et al., 2015).

This hydration process leads to a dense and strong AAB matrix. The main reaction product is a disordered tobermorite-like (C-S-H (I)) with low Ca/Si ratio (0.9-1.2), which can be partially substituted by aluminium or sodium/potassium to form calcium aluminium silicate hydrate gel (C-A-S-H) or calcium (sodium) aluminium silicate hydrate gel (C-(N)-A-S-H) (Provis and Van Deventer, 2013, Herrmann et al., 2018). Followed by the secondary reaction product such as alumina ferric oxide mono sulphate (AFm) ($3CaO\cdot(Al, Fe)_2O_3\cdot CaSO_4\cdot nH_2O$) depending on the activator types and concentration, Hydrotalcite ($Mg_6Al_2(OH)_{16}CO_3\ 4H_2O$) when containing high

MgO, and Zeolite (gismondine and garronite) when activated BSF with high Al_2O_3 and low MgO (<5%wt) (Provis and Van Deventer, 2013). However, if the aluminosilicate precursor is mixed with fly ash, slag, or other material, with often contains approximately 10-20 %wt CaO. The reaction product may contain a Ca-rich phase along with sodium aluminosilicate hydrate (N-A-S-H) or geopolymer. All hydration products would contribute to better strength and durability (Herrmann et al., 2018).

2.6.2 LOW-CALCIUM ALKALI-ACTIVATED BINDERS (GEOPOLYMER)

Geopolymer is an inorganic polymer synthesised from aluminosilicate precursors and an alkaline activator solution (Cong and Cheng, 2021). It is also known for their high strength, excellent durability, and resistance to chemical and environmental degradation, making them an attractive alternative to traditional cement-based materials in a variety of applications (Aiken et al., 2018, Aliques-Granero et al., 2019, Lahoti et al., 2019, Shill et al., 2020, Vafaei et al., 2018).It was synthesised by polymerising low-Ca aluminosilicate with a strongly alkaline solution (Davidovits, 1991, Liew et al., 2016, Majidi, 2013, Liguori et al., 2017). Davidovits (1979) led the early development of low-Ca of AAB in France (Davidovits and Cordi, 1979). It consists of a repeating unit of sialate monomer (–Si–O–Al–O–) as shown in Figure 2-7 to form a three-dimensional crosslinked poly-sialate amorphous and semi-crystalline structure material. The sialate monomer is composed of alumina (AlO_4^-) and silica (SiO_4^-) tetrahedra and links together by sharing the oxygen between alternating tetrahedra of SiO_4 and AlO_4^-. Alkali metal ions are required in the geopolymer structure framework to balance the negative charge in IV-fold coordination (Davidovits, 1994, Majidi, 2013). The geopolymer structure can be amorphous or semi-crystalline, depending on condensation temperature. The amorphous polymer can be obtained at 20-90 °C, whereas semi-crystalline geopolymer is obtained at 150-1200 °C (Majidi, 2013, Cioffi et al.,

2003). The monomer of geopolymer can be classified based on Si/Al ratio, as shown in Figure 2-7. Geopolymers have an empirical formula as

$$M_n[-(SiO_2)_z - AlO_2]_n \cdot \mathrm{w}H_2O \qquad \text{Equation 2.24}$$

Where: M is an alkali metal (K^+, Na^+, Ca^{2+}), n is the degree of polymerisation, z is 1, 2 or 3 w is the amount of binding water (Duxson et al., 2006, Liew et al., 2016).

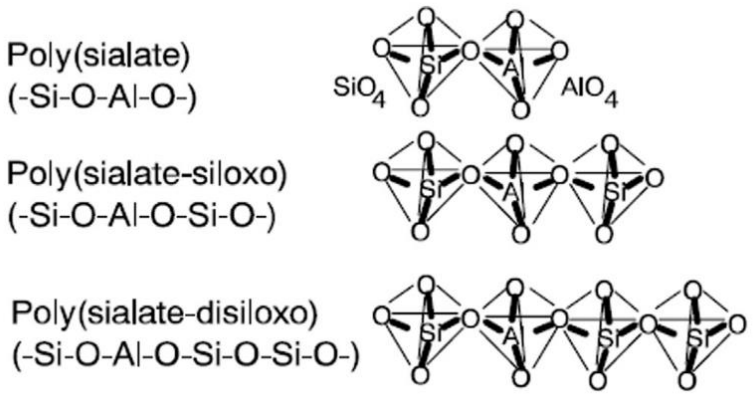

Figure 2-7 Structure of Sialate monomer (Davidovits, 1994)

2.6.2.1 GEOPOLYMERISATION MECHANISM

The geopolymerisation reaction is a chemical process rapidly transforming partially or totally amorphous aluminosilicate sources into three-dimensional polymeric networks. It is an exothermic reaction, and it has been assumed that the synthesis is carried out through oligomers (dimer, trimer) that provide the actual unit structures of the three-dimensional macromolecular edifices. The geopolymerization reaction is suggested to occur in multistep, which occurs simultaneously as dissolution of aluminosilicates in the highly alkaline reactant, re-organisation and diffusion of dissolved ions with the formation of small coagulated structures, polycondensation to form aluminosilicate gel phases solid-state transformation, and hardening to form hard solid (Liew et al., 2016). The equations of geopolymer formation are shown in Figure 2-8. The final product has

a Si-O-Al backbone. The three-dimensional network of alkali-aluminosilicate geopolymer is configured with the negative $[AlO_4]^{5-}$ and $[SiO_4]^{4-}$ tetrahedrons in addition to positive alkali metal ions (e.g., Na^+ or K^+).

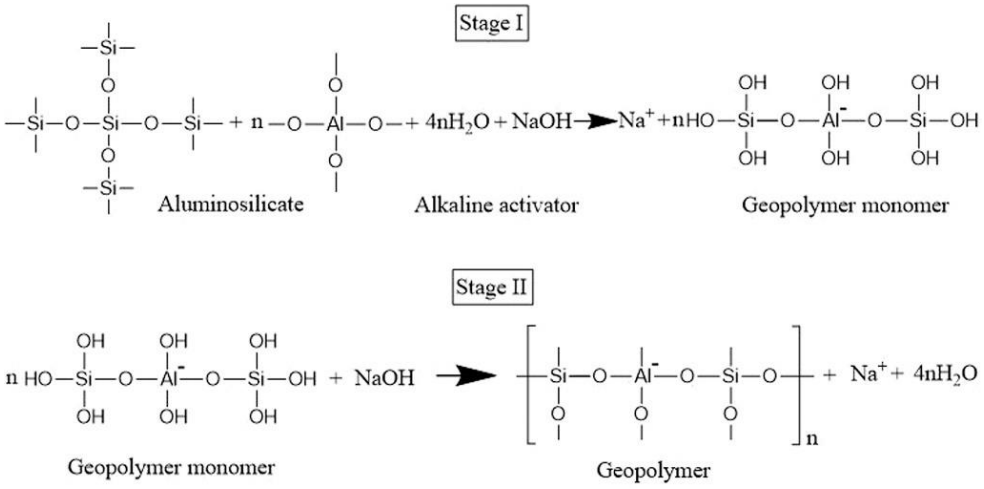

Figure 2-8 Schematic diagram of the geopolymerisation process (Davidovits, 1991)

2.6.3 ALUMINOSILICATE SOURCES

Geopolymer concrete mainly comprises aluminosilicates. The aluminosilicates come from different resources such as fly ash, slag cement or metakaolin. The selection criteria for aluminosilicate resources are based on performance, supply and cost. The strengths and weaknesses, supply, demand, and cost of each raw material are discussed.

2.6.3.1 FLY ASH

Fly ash is a toxic waste material produced primarily from coal-fired power production as shown in Figure 2-9. It is produced by burning finely ground coal in a boiler to produce electricity and is captured in a power plant's chimney through a particulate control device (e.g., electrostatic precipitators or fabric filters). Fly ash consists mostly of silt-sized and clay-sized glassy spheres, giving it a consistency somewhat like talcum powder. There are two types of fly ash defined by

ASTM standard C618, which are Class C (high calcium content) and Class F (low calcium content) (ASTM-C618, 2022). Class F fly ash is typically produced from burning anthracite or bituminous coal but may also be produced from sub-bituminous coal and lignite. Class C fly ash is typically produced from burning lignite or sub-bituminous coal and may also be produced from anthracite or bituminous coal. The majority of the fly ash used as precursors for geopolymer production is class F, while class C is less used due to rapid setting time and availability (Duxson, 2009).

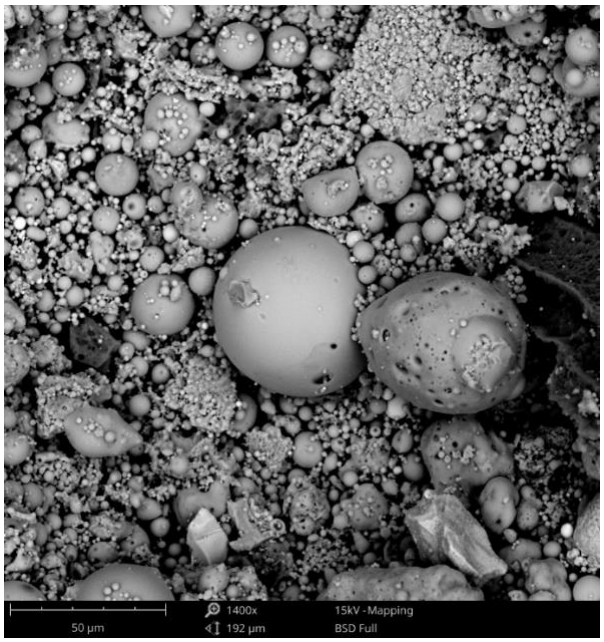

Figure 2-9 SEM micrograph of fly ash sample

2.6.3.2 METAKAOLIN

Metakaolin (MK) is a pozzolanic material. Metakaolin originated from kaolinite clay ($Al_2O_3 \cdot 2SiO_2 \cdot 2H_2O$). It is not a waste by-product of industrial activities, nor is it completely natural. Kaolinite clay is processed by thermal treatment for different uses and applications, including cementitious systems (Khatib et al., 2018). Metakaolin can obtain from the calcination of kaolinite clay at elevated temperatures between 500 °C and 800 °C, as seen in the equation below.

$$Al_2O_3 \cdot 2SiO_2 \cdot 2H_2O \rightarrow Al_2O_3 \cdot 2SiO_2 + 2H_2O \uparrow \quad \text{Equation 2.25}$$

The chemical composition of MK typically consists of 50-55 %wt SiO2, 40-45 %wt Al_2O_3, and other oxides such as TiO_2, Fe_2O_3, MgO, and CaO are also present in smaller amounts (Khatib et al., 2018). MK can react with $Ca(OH)_2$ (CH) to produce C-S-H gel at ambient temperature and reacts with CH to produce alumina-containing phases, including C_4AH_{13}, C_2ASH_8, and C_3AH_6 (Siddique and Klaus, 2009).

2.6.3.3 BLAST FURNACE SLAG

Blast furnace slag is a high calcium (>40%wt) by-product of iron production and occurs when iron, iron scrap, coal, coke, and fluxes (limestone or dolomite) are melted together at around 1500 °C (Assi et al., 2020, Amran et al., 2020). Chemical compositions of blast furnace slag (slag cement), which is approximately composed of calcium oxide, silicon dioxide, and aluminium oxide etc. There are three forms of blast furnace slag; air-cooled blast furnace slag (ACBFS), pelletised slag, and granulated blast furnace slag (slag cement) (Assi et al., 2020). Blast furnace slag is commonly mixed with Fly ash (class F) in one-part geopolymer mixtures due to calcium-rich aluminosilicate, which induces rapid setting and high early strength (Luukkonen et al., 2018b).

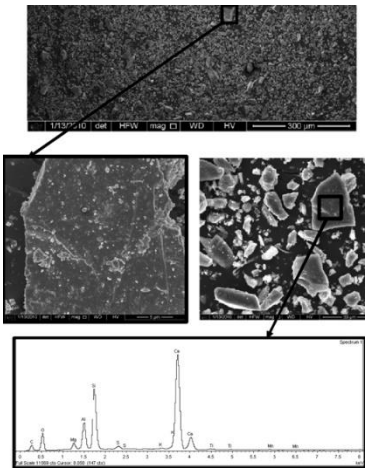

Figure 2-10 SEM micrograph of Blast Furnace Slag

2.6.4 ACTIVATED REAGENT

Alkali-activated reactant can be any substance that provides alkali cations, raises the pH of the reaction mixture, and facilitates the dissolution of aluminosilicate. It can be in a solid or solution reactant, depending on the type of geopolymer. Under a strongly alkaline medium, the aluminosilicates rapidly dissolve to release SiO_4 and AlO_4 tetrahedral units and promote the dissolved species for geopolymerization.

2.6.4.1 NA- OR K-BASED ALKALI SOLUTION

The NaOH or KOH solutions are used for alkalinity. The leaching ability of various aluminosilicate sources in NaOH and KOH solutions has been extensively carried out. Generally, the dissolution of aluminosilicate sources increases with increasing concentration of alkali solution. Dissolution ability is usually associated with the ultimate strength of geopolymers. However, most of the researchers agreed that aluminosilicate sources are more readily dissolved in NaOH solution than in KOH solution (Liew et al., 2016). Despite higher dissolution in NaOH solution, the geopolymers produced from the aluminosilicate minerals possess higher compressive strength in KOH solution rather than in NaOH solution.

2.6.4.2 NA- OR K-BASED ALKALI SOLID REACTANT

The solid-activated reagent is used in a one-part geopolymer. Activators employed in one-part geopolymer mixes include solid NaOH, Na_2SiO_3, $Na_2SiO_3 \cdot 5H_2O$, Na_2CO_3, $NaAlO_2$, $CaSO_4$, Na_2SO_4, K.O.H., red mud, and maise stalk and cob ash (Luukkonen et al., 2018b).

2.6.4.3 A MIXTURE OF ALKALI HYDROXIDE AND ALKALI SILICATE SOLUTIONS

While alkali hydroxide is required for the dissolution of aluminosilicates, alkali silicate acts as a binder, alkali reactant, and dispersant or plasticiser. Apart from sodium/potassium silicate solution, silica fume can also be used as an alternative or supplement to the metal silicate. Sometimes, they were added to modify the silica composition in the mixture and promote the gelation and precipitation of silicates (Liew et al., 2016).

2.6.5 DETERIORATION OF GEOPOLYMER

Geopolymer materials are prone to degradation when exposed to aggressive environments, reducing their durability and service life. Various chemical and physical processes contribute to the deterioration of geopolymer. One of the primary chemical agents responsible for this degradation is sulphuric acid (H_2SO_4), which can react with the geopolymer binder matrix and weaken its structure. In addition to sulphuric acid, exposure to other acidic substances and carbon dioxide (CO_2) can also contribute to the deterioration of geopolymer materials.

2.6.5.1 ACID ATTACKS

An interesting property of geopolymer cement is its relatively high resistance to acidic solution. The resistance of geopolymer to chemical attack by acids such as nitric, sulphuric, or hydrochloric has been claimed to be far better than that of Portland cement mortar or concrete due to lack of $Ca(OH)_2$ (Provis and van Deventer). The corrosion mechanism of geopolymer concrete in solution could mainly involve two steps: the leaching process and silicon atoms re-occupied (Allahverdi and Skvara, 2001). The mechanism of corrosion of hardened paste of geopolymer cement in a solution of nitric acid involves two steps, as shown below

Step 1: Leaching process (see Figure *2-11*) - the alkali cations included in the aluminosilicate framework to charge-balance the tetrahedral aluminium are exchanged by H^+ ions from an acidic solution. This occurs along with electrophilic attack by H^+ ions on framework Si-O-Al bonds, resulting in the ejection of tetrahedral aluminium from the aluminosilicate framework.

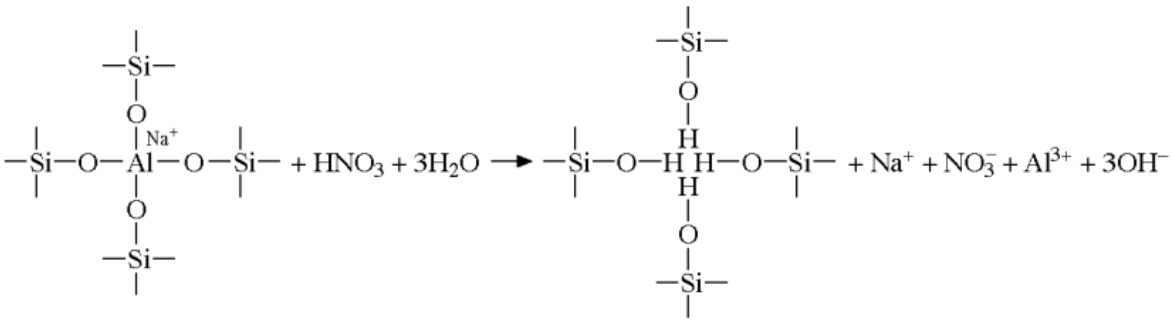

Figure 2-11 Leaching process after acid attacks

Step 2: The framework vacancies are mostly re-occupied by silicon atoms (see Figure 2-12), forming an imperfect, highly siliceous framework. The ejected aluminium, converted to octahedral coordination, mainly accumulates in the intra-framework space.

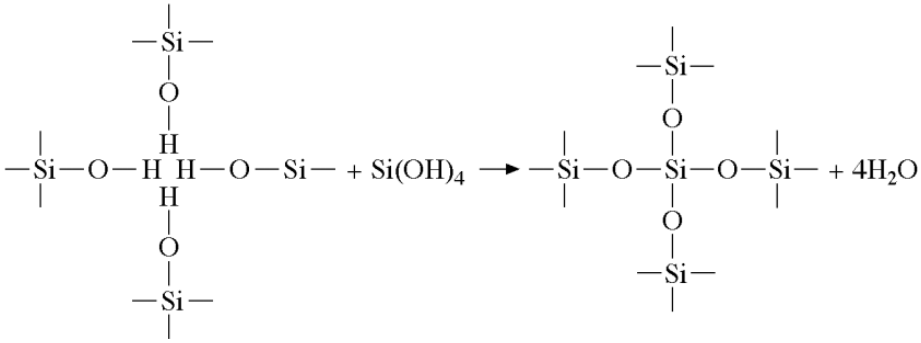

Figure 2-12 Re-occupied by silicon atoms process

2.6.5.2 SULFURIC ACID ATTACK

The sulfuric attack of geopolymer is similar to the acid attack in section 2.6.5.1. However, the exchanged calcium ions diffusing in the case of high calcium-based geopolymer toward the acid solution react with the counter-diffusing sulphate anions resulting in the formation and deposition

of gypsum crystals inside the corroding layer (Khan et al., 2020b, Provis and van Deventer). The degradation of concrete resulting from corrosion reactions is manifested by physical damage, including expansion, cracking, and delamination. In this process, sulfuric acid reacts first with the calcium hydroxide and calcium silicate hydrate in the concrete to form gypsum, as shown in Equation 2.26-Equation 2.27 (Monteny et al., 2000).

$$Ca(OH)_2 + H_2SO_4 \rightarrow CaSO_4 + 2H_2O \qquad \text{Equation 2.26}$$

$$CaO.SiO_2.2H_2O + H_2SO_4 \rightarrow CaSO_4 + Si(OH)_2 + H_2O \qquad \text{Equation 2.27}$$

The formation of gypsum contributes to the loss of strength and adhesion of the cement paste due to the decalcification of calcium silicate hydrate responsible for binding the cement paste (Collepardi, 2003). The reaction between gypsum and calcium aluminate hydrate to form ettringite (see Equation 2.28) is considered much more detrimental due to the ettringite being more expansive than gypsum, resulting in increased internal pressures and concrete breakdown (Monteny et al., 2000, Wafa, 1994, Attiogbe and Rizkalla, 1988).

$$3CaO.Al_2O_3.6H_2O + 3CaSO_4.2H_2O + 24H_2O \rightarrow 3CaO.Al_2O_3.3CaSO_4.32H_2O \qquad \text{Equation 2.28}$$

The dominating reactions, whether the formation of gypsum or ettringite, is determined by the sulphate concentration (Cohen and Mather, 1991, Biczok and Blasovszky, 1964). At low concentrations of sulphate lower than 1000 mg/L, concrete deterioration is considered to occur by ettringite formation. Whilst at higher sulphate concentrations of more than 8000 mg/L, concrete deterioration occurs by the formation of gypsum.

2.6.5.3 HYDROGEN SULPHIDE (H_2S) ATTACKS

Hydrogen sulphide (H_2S) in sewers primarily originates from the microbial decomposition of organic matter, particularly under anaerobic conditions. When wastewater containing organic

substances, such as human waste and organic debris, flows through the sewer assets, it undergoes degradation by bacteria and other microorganisms. As a byproduct of this microbial activity, H_2S gas is produced. The H_2S gas is released into the sewer atmosphere, contributing to the characteristic odour of sewers. The presence of H_2S in sewer environments poses challenges due to its corrosive nature and potential health risks. The H_2S contributes to the reduction of mortar surface pH by reacting with $Ca(OH)_2$ to form CaS (Hudon et al., 2011, Cerny and Rovnanikova, 2002, Joseph et al., 2012).

$$Ca(OH)_2 + H_2S \rightarrow CaS + 2H_2O \qquad \text{Equation 2.29}$$

It can also react with calcite to form calcium sulphide and calcium bicarbonate.

$$2CaCO_3 + H_2S \rightarrow CaS + Ca(HCO_3)_2 \qquad \text{Equation 2.30}$$

Both reactions achieve a pH of around 9.0 and thus H_2S impact on corrosion is considered low.

2.6.5.4 CARBON DIOXIDE (CO_2) ATTACKS

Carbon dioxide (CO_2) is typically microbial activity and the degradation of organic matter. As wastewater flows through the sewer system, organic compounds present in the wastewater are broken down by bacteria and other microorganisms (Grengg et al., 2018). This microbial activity produces CO_2 as a byproduct. The CO_2 can dissolve in moisture in under the sewer environment from carbonic acid (H_2CO_3) (see Equation 2.31)and accumulate in the pore space in the mortar matrix (Yuan et al., 2015) when the mortar matrix reacts with the acid leaching the $CaOH_2$ (see Equation 2.32). It could formulate the calcium carbonate, resulting in a surface pH reduction from 12 to approximately 8.4 (Joseph et al., 2012).

$$CO_2 + H_2O \rightarrow H_2CO_3 \qquad \text{Equation 2.31}$$

$$CO_2 + Ca(OH)_2 \rightarrow CaCO_3 + H_2O \qquad \text{Equation 2.32}$$

However, Elsalamawy et al. (2019) have investigated the effect of variation of relative humidity (RH) on the carbonation resistance of concrete made with different cementitious materials. The study found that RH is a very important factor in the carbonation resistance of concrete structures, where carbonation effectively stops when concrete is saturated and dry enough to prevent the ingress of CO_2. The results also indicated that carbonation reaches its maximum level at %RH between 50 and 70%.

2.7 ONE-PART AND TWO-PART GEOPOLYMER

Extensive investigation on geopolymer to replace OPC concluded that geopolymer could be prepared by two-part of the component; i) aluminosilicate precursor and ii) strong alkali solution. This AAB is called a two-part geopolymer. Additionally, the combination of sodium hydroxide and sodium silicate solutions can be a good application for activators and a higher concentration of sodium hydroxide solution and curing temperature enable the concrete compressive strength to be higher (Hardjito et al., 2004). However, the alkali solution can cause rapid setting time and lead to quick workability and loss of mortar or concrete against the elapsed time. It would establish an obstacle for practical applications (Yang et al., 2008). Therefore, the one-part geopolymer mixtures are a newly introduced class of geopolymeric binders developed to simplify the difficulties in handling silicate solution-activated geopolymers. The one-part geopolymers are made by blended aluminosilicate precursors with solid activators. It only needs to add just water, which is similar to OPC.

2.8 CALCIUM ALUMINATE CEMENT

Calcium aluminate cement (CAC) is a binder consisting predominantly of monocalcium aluminate ($CaAl_2O_4$, CA; $CaO{\cdot}Al_2O_3$), which is the leading hydraulic phase in this binder (Khaliq and Khan, 2015, Ideker et al., 2019). CAC is manufactured by calcining limestone and bauxite between 1450 and 1600 °C in an open-heart furnace (Ideker et al., 2019). Bauxite is a high alumina content ore mineral, which consists mainly of aluminium minerals as gibbsite ($Al(OH)_3$), boehmite (γ-AlO(OH)) and diaspore (α-AlO(OH)), mixed with the two iron oxides goethite (FeO(OH)) and hematite (Fe_2O_3) (Kloprogge et al., 2006). The chemical composition of standard CAC for making concrete is shown in Table 2-3. Formulated mortar and peri-refractory. It is also known for its rapid strength gain, especially at low temperatures, superior durability across several categories and high-temperature resistance (Ideker et al., 2019). Calcium aluminate cement is used in a wide variety of applications. For sewer liner application, pure calcium aluminate (CA) will be applied. The hydration reactions between CA and water are shown in Equation 2.33-Equation 2.35 (Shirani et al., 2020). It is well established that the hydration reactions of $CaAl_2O_4$ strongly depend on temperature (Scrivener et al., 1999). At the initial stage, metastable phase of hydrated CAC (C_2AH_8 ($Ca_2Al_2O_5{\cdot}8H_2O$) and CAH_{10} ($CaAl_2O_4{\cdot}10H_2O$)) are formed resulting in a high early strength followed by a slow decline to a minimum because of conversion of metastable phase to stable phase C_3AH_6 ($Ca_3Al_2(OH)_{12}$) and AH_3 ($Al(OH)_3$-gibbsite)(generally amorphous) at a temperature above 15°C is shown in Equation 2.36-Equation 2.37 before a further increase (Scrivener et al., 1999, Ideker et al., 2019, Shirani et al., 2020). Both CAH_{10} and C_2AH_8 have a low density and fill space rapidly (Ideker et al., 2019). The hydration of calcium aluminate is shown below

$$CA + 10H \rightarrow CAH_{10} \qquad \text{Equation 2.33}$$

$$2CA + 11H \rightarrow C_2AH_8 + AH_3 \quad \text{Equation 2.34}$$

$$3CA + 12H \rightarrow C_3AH_6 + 2AH_3 \quad \text{Equation 2.35}$$

$$3C_2AH_8 \rightarrow 2C_3AH_6 + AH_3 + 9H \quad \text{Equation 2.36}$$

$$3CAH_{10} \rightarrow C_3AH_6 + 2AH_3 + 18H \quad \text{Equation 2.37}$$

The main vital properties of calcium aluminate cement, particularly alumina hydrate (C_3AH_6) are superior to acid resistance in sewer and wastewater systems. The chemistry of CAC deterioration involves the diffusion, dissolution and precipitation reactions after an acid attack on the CAC matrix. A longer chain of dissolution and neutralisation was provided by various CAC hydrates (CAH_{10}, C_2AH_8, C_3AH_6, and AH_3) (Fan et al., 2020). The C_3AH_6 is stable down to a pH of about 3-4. The acid attack of C_3AH_6 resulted in the dissolution of the calcium component and formulation of aluminium hydroxide ($Al(OH)_3$) gel, as shown in Equation 2.38. Both calcite (Ca ions and the atmospheric CO_2 interaction) and ($Al(OH)_3$) gel infill the pore in the CAC matrix and act as a buffer under acid attack to prevent corrosion of CAC (Ukrainczyk et al., 2019, Scrivener et al., 1999). At the same time, ($Al(OH)_3$) also neutralised more acid, as shown in Equation 2.39 (Ukrainczyk et al., 2019). The overall neutralisation reaction is shown in Equation 2.40.

$$C_3AH_6 + 6H^+ \rightarrow 3Ca^{2+} + 2Al(OH)_3\downarrow + 6H_2O \quad \text{Equation 2.38}$$

$$AH_3 + 6H^+ \rightarrow 2Al^{3+} + 6H_2O \quad \text{Equation 2.39}$$

$$C_3AH_6 + 2AH_3 + 24H^+ \rightarrow 3Ca^{2+} + 6Al^{3+} + 24H_2O \quad \text{Equation 2.40}$$

Consequently, alumina ions can directly suppress the action of bacteria. The CAC material is made with calcium aluminate aggregates and calcium aluminate cement. It is considered to be 100% calcium aluminate material. The 100% CAC will last longer as the aggregates can also limit microorganisms' growth and inhibit acid generation (Scrivener et al., 1999).

Table 2-3 Typical Chemical compositions of CAC (Ideker et al., 2019)

Chemical Compositions	Percent Weight (%wt)
Al_2O_3	36-42
CaO	36-42
SiO_2	3-8
Fe_2O_3	12-20
TiO_2	<3
MgO	<1
Na_2O	~0.1
K_2O	~0.1

2.9 PRACTICAL REQUIREMENT

Sewer rehabilitation is one of the critical sewer management for deteriorated concrete sewer pipes. A typical rehabilitation process of the sewer pipes usually commences with collecting information about the project requirements and constraints (i.e., diameter, type of defect, sewer environmental condition) (Shehab-Eldeen and Moselhi, 2001). The survey information is then processed to select the most suitable rehabilitation method(s) that efficiently extend the service life of the concrete sewer pipes. Presently, this selection process relies on the decision-maker's experience without computer-assisted tools. Increasing the deteriorated concrete sewer pipes, selection in this manner may suffer from the decision-makers limited knowledge and (or) experience. It could result in overlooking technically suitable and cost-effective methods. Because concrete sewer pipes are usually buried underground, discovering the damage caused by chemical erosion is difficult. Further, the repair work needs to be quick, and the repair material must have watertightness and acid resistance. For manhole and large-scale concrete sewer pipes in the live sewer, using the

wet/dry spray coating technique for sewer pipe rehabilitation must be suitable. The performance requirement of cement mortar includes placement test (setting time, rebound test, and slump test), cured mortar properties test (amount of hydration phase, acid neutralisation capacity (ANC), unconfined compressive strength (UCS),self-compaction, tensile strength).

2.10 TYPES OF AGGREGATE

Concrete is generally referred to as a heterogeneous material and is formed primarily by mixing three constituents: aggregate, cement and water. The concrete volume contains around 75 to 80 percent of fine and coarse aggregate, which could significantly influence the characteristic of concrete, freshness, and hardness (Smith et al., 2001a). The aggregate, shape, and texture type significantly affect the workability, findability, bleeding, pump ability, and segregation of fresh concrete (Mermerdaş et al., 2017, Provis and van Deventer). The interface zone between cement paste and aggregate is the most important interface in concrete and is known as The interfacial transition zone (ITZ) (Scrivener et al., 2004). It has been well-recognised that ITZ negatively influences the mechanical behaviour and durability of Portland cement concrete (Peng et al., 2019). The aggregate that has been used for concrete material is fine and coarse aggregate. The coarse and fine aggregates are bound together by the adhesive character of cement paste into a rock-like mass. Concrete suffers from microcracks and flaws, including pores, air voids, lenses of bleed water and shrinkage cracks even in the unloaded stage. When external loading is applied, these microcracks grow and coalesce with new microcracks leading to the failure of the structure or member (Caliskan, 2003).

2.10.1 FINE AGGREGATE

Fine aggregates are small particle sizes between 4.75 to 0.075 mm. it used as admixture material for concrete. The primary fine aggregate sources are river or machine sand, crushed stone sand, and crushed gravel sand. The voids between the coarse aggregate are filled up by fine aggregate. The degree of particle roundness (see Figure *2-13*) for sediment grains with each category showing low and high sphericity (Smith et al., 2001b).

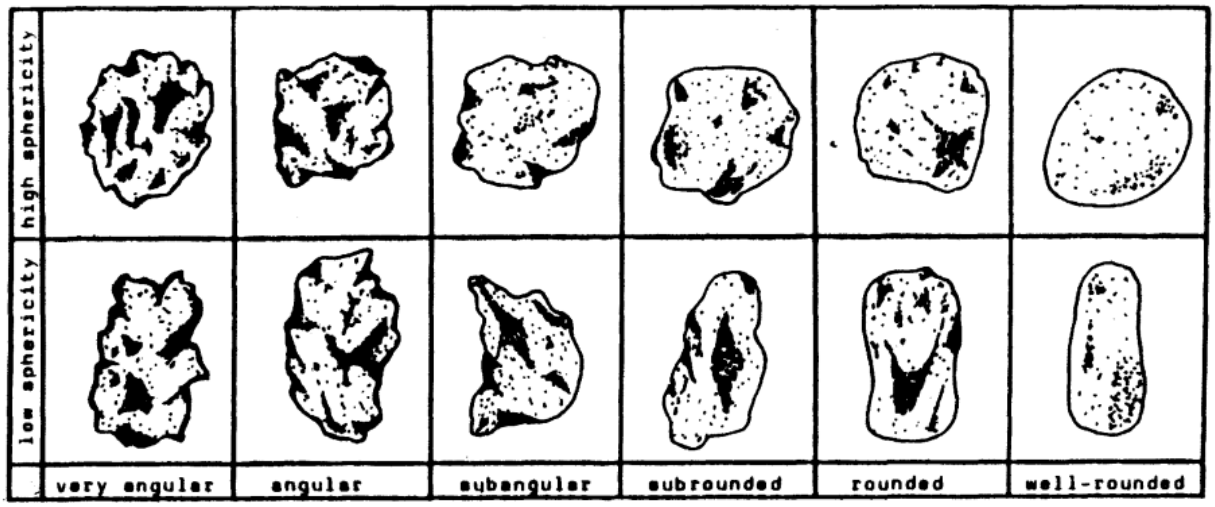

Figure 2-13 Degree of particle roundness

2.10.2 COARSE AGGREGATE

Coarse aggregates are larger-size filler materials in construction. Coarse aggregates are the particles that retain on a 4.75 mm sieve. Brick chips (broken bricks), stone chips (broken stones), gravels, pebbles, clinkers, cinders etc. are used as coarse aggregate in concrete. Coarse aggregate acts as inert filler material for concrete.

2.11 CONDITION ASSESSMENT OF CONCRETE CORROSION

Condition assessment of concrete sewer pipes is a high priority for water utilities that proactively protect and maintain the sewer assets to work with less interruption (McDonald and Zhao, 2020). Failure in sewer asset management may result in a catastrophic impact on the community, business, transportation, public, and environment (Hawari et al., 2020). Currently, most water utilities are moving towards the proactive approach to preventive repair strategies for sewer asset networks (Fenner, 2000). It is more cost-effective than reactive sewer asset maintenance. However, developing a condition assessment tool is challenging for water utilities. The collected data must be organised, analysed, and kept in an established database system to develop condition assessment tools successfully. Condition assessment tools can facilitate users deciding on the intervention required, such as sewer assets prioritisation of inspection, rehabilitation, or replacement of sewer assets for certain sewer assets based on their state of deterioration (Hawari et al., 2020). The condition of the sewer assets can be affected by the physical, operational, and environmental conditions, as shown in Table 2-4. The concrete condition assessment prediction model can be formulated based on the depth of corrosion or the remaining UCS of the sewer assets as a dependent variable versus physical, operation, and environmental factors as an independent variable.

Table 2-4 Factors affecting sewer pipeline condition (Hawari et al., 2017)

Main factors	Sub-factors	Description
Physical	Age	The effects of pipeline degradation become more significant over time.
	Diameter	The larger the pipeline diameter, the larger is its thickness, the lower is its deterioration rate and vice versa.
	Length	Longer pipes are more likely to suffer from bending stresses.
	Buried depth	Live loads impact increases at shallow depths and the soil overburden impact increases at high depths. Moderate depths increase the life of sewers.
	Material	Different pipeline materials show different failure patterns.
	Coating conditions	Pipelines with good coating conditions have higher resistance against corrosion.
	Installation quality	Pipeline installation should be done according to certain standards and qualifications. High deterioration rates result from poor installation quality.
Operational	Flow rate	High velocity water corrodes the internal walls of the pipe and causes disturbances especially when moving between pipes of different diameters. Low velocity water causes deposition and accumulation of sediments.
	Blockages	Accumulation of deposits and sediments, intrusion of trees roots and other types of blockages have a significant effect on the structural and operational condition of a sewer pipeline.
	Infiltration and inflow	Infiltration washes soil particles and reduces the support along a pipeline.
	Corrosive impurities	Chemicals and substances (such as salts and micro-bio species) present in water while being transported decrease water quality. They can also corrode the internal surface of the pipe and cause its breakage.

Main factors	Sub-factors	Description
	Maintenance and break strategies	The service life of sewer pipelines is increased by a good maintenance and break strategies.
	Operating pressure	The pressure resulting from transients in the water distribution system may cause pump and device failure, system fatigue, or pipe ruptures.
Environmental	Soil type	This factor refers to the type of soil in direct contact with the pipe surface. Soils have different physical and chemical properties, which have different impacts on the pipeline. Some soils are corrosive; others experience significant volume changes in response to moisture changes, resulting in changes to pipe loading. The presence of hydrocarbons and solvents in soil may cause pipe deterioration.
	Bedding conditions	Sewer pipeline failure chances increase with improper bedding conditions.
	Location	The pipeline location is related to the installation zone being residential, industrial, school, etc. Pipelines in residential areas are exposed to different conditions than those located in industrial areas or cities because they may be located under different surface types (e.g. asphalt, seal, unpaved etc.). City pipelines are subject to heavy traffic, adding more dynamic load on the pipeline.
	Groundwater	The amount of water in the soil affects the soil resistivity, which inversely relates to the corrosion rate. The ground water may lead to corroding the pipe directly when salts and some corrosive substances exist.

2.12 FACTORS INFLUENCING THE CORROSION RESISTANCE OF GEOPOLYMER

As mentioned above, biogenic weak and strong acids have been generated under the MICC process. The durability of a geopolymer depends on the properties of the geopolymer itself. It can resist or slowly change the properties of geopolymer during exposure to a corrosive environment. The effects of the essential factors under consideration are summarised in Table 2-5.

Table 2-5 A summary of some essential factors influencing the corrosion resistance of geopolymer

Factors	Description	References
SiO_2/Al_2O_3	A Higher Si/Al ratio resulted in a higher amount of Si-O-Si bonds, and Si-O-Si bonds were well known to be stronger than Si-O-Al bonds. The residual silica particles played the role of reinforcement due to the strong interface bonding between the binder phase and silica.	(Amran et al., 2020)
CaO	The amount of CaO affects the geopolymer's alkalinity, compressive strength, and porosity. The high CaO content in geopolymer powder, coexistence of geopolymer gel (C-A-S-H), and calcium silicate hydrate (C-S-H) are generated through hydration and polymerisation. Voids and pores of geopolymer matric filled with the C-S-H gel resulting in an increase in mechanical strength. However, remaining unreacted CaO with excess hydroxide can be promoted precipitation of calcium hydroxide ($Ca(OH)_2$). $Ca(OH)_2$ can be responsible for increasing the alkalinity of the geopolymer binder	(Yip et al., 2005)
Alkalinity	High alkalinity provides more substances to react with the generated biogenic acids, thus slowing down the MIC rate (penetration depth)	(De Belie et al., 2004)
Bacteriostatic	Heavy metal ions (Me^+) can be toxic to bacteria due to Me^+ reactions with the negatively charged cell walls of bacteria and the associated formation of complex compounds within the bacterial membrane. Therefore, the bacteriostatic effect is exhibited depending on the heavy metal concentration as an admixture in geopolymer.	(Grengg et al., 2018)

2.12.1 PARTICLE SIZE DISTRIBUTION OF MORTAR POWDER

The geopolymer mortar can be developed physical properties by adjusting the chemical composition and the curing process. However, many researchers have agreed that the particle size of the aluminosilicate sources is one of the essential parameters in the strength development, durability properties and microstructure of geopolymer (Assi et al., 2018, Li et al., 2021, He et al., 2013). Generally, finer binder particles are more reactive and produce geopolymers with denser microstructures and higher compressive strength (Nazari et al., 2011). The fine particle of the geopolymer binder is usually measured as particle size distribution. Assi et al. (2018) reported that the particle size distribution directly affects the strength and reduction of the permeation void ratio. The finer the particle revealed better strength and denser geopolymer.

2.13 SERVICE LIFE MODELS FOR CONCRETE-BASED MATERIAL

The service life prediction model is an essential management tool to proactively plan for sewer maintenance and rehabilitation on concrete sewer pipe networks. Water utilities proactively use sewer condition prediction models and condition ratings to manage concrete sewer pipes and other related infrastructures. The service life prediction model is used to prioritise the inspection plan and provide valuable information to forecast the short-term and long-term behaviour of sewer pipes. In contrast, condition rating for sewer pipe is used to evaluate the current condition of sewer pipe to take action to renew or repair the sewer pipe based on the deterioration state (Hawari et al., 2020, Mohammadi et al., 2020). Predicting concrete corrosion under sewer environment conditions is very challenging due to the scarcity of assessment and complex systems. The concept behind the deterioration model is to find the relationship between the corrosion factors affecting the deterioration process of the concrete sewer pipe and sewer pipe condition. Service life prediction of deteriorated concrete sewer pipe has developed using several models, which are

based on different deterioration factors such as the physical properties of sewer pipe, the environmental condition, and the operational and characterisation of wastewater. Recently, the deterioration model has been developed, as shown in Table 2-6.

Table 2-6 Service lift modelling equations

Type of chemical attack	Model equations	Remarks	Reference
Mixed chemical	$L = \frac{t_i}{12} + \frac{D}{r}$	The bi-linear corrosion model was proposed based on the loss of concrete material. L= sewer service life (year). The model was not parameterised for application to different sewer conditions because it was based on very limited field data. t_i = time for corrosion to initiate (month), r = rate of concrete depth lost (mm/year), D is the concrete depth (mm) that can be sacrificed before the end of sewer service life	(Jiang et al., 2016, Wells and Melchers, 2014)
Hydrogen sulphide (H_2S) and wastewater characteristics	$C_r = \frac{11.5k\phi_{sw}}{\text{alk}}$	The Pomeroy model is constructed based on the loss of concrete material by the Hydrogen sulphide (H_2S) and wastewater characteristics in sewer networks. The parameter of the model identified as C_r = corrosion rate	(Pomeroy, 1990)

Type of chemical attack	Model equations	Remarks	Reference
		(mm/year); k = factor related to the acid formation, based on climate conditions, 0.8 in moderate climates; ϕ_{sw} = sulphide flux at the air-wall interface [g $H_2S/(m^2$ hr)]; and alk = alkalinity of the pipe material (g $CaCO_3$/g concrete).	
Sewer gases environment (H_2S, CO_2, T and % RH.)	$C = A \times [H_2S]^{0.5} \times \frac{(0.1602H - 0.1355)}{(1 - 0.9770H)} \times e^{(-45000/RT)}$	This model is based on loss of concrete material with time. The parameters the model identified as C is the rate of corrosion (mm yr^{-1}), [H_2S] is the concentration of hydrogen sulphide in the sewer atmosphere (ppm). H is the percent relative humidity of the sewer atmosphere (-). R is the universal gas constant (= 8.314 J mol^{-1} K^{-1}). T is the temperature of the sewer atmosphere (K).	(Wells and Melchers, 2015)

2.14 ASSESSMENT OF LITERATURE REVIEW

In order to achieve an efficient and successful operation and maintenance plan for concrete sewer pipes and other infrastructure assets, water utilities must have information on the condition of the assets to make informed strategic decisions and adequately plan expenditure of capital

investments. Water utilities are proactively using sewer condition prediction models and condition rating methods for sewer pipes to facilitate water utilities or decision-makers managing the sewer pipe and other related infrastructure. The sewer condition prediction model is used to produce a prioritised inspection plan and provide valuable information to forecast sewer pipes' short- and long-term behaviour. In contrast, condition rating for sewer pipe is used to evaluate the current condition of sewer pipe to take action to renew or repair the sewer pipe based on the deterioration state (Hawari et al., 2020, Mohammadi et al., 2020).

The condition assessment models are usually developed by incorporating sewer pipe conditions and factors that influence the condition of sewer pipe. Hawari et al. (2020) have classified the factors that affect concrete sewer pipes into three main categories: physical, operational, and environmental. Based on the potential factors that could affect sewer pipe deterioration, prediction of sewer pipe condition is considered a very complex system. Therefore, valid information on the condition of the assets is essential and requires keeping a record in the proficient information system.

There are two types of inspection methodology to assess the condition of the concrete sewer pipe: destructive and non-destructive. This inspection method breaks down the sewer asset using the destructive test to determine the change in physical and chemical properties (Alzraiee et al., 2015, Khan et al., 2020b). For non-destructive inspection methods, many new technologies such as closed-circuit television (CCTV), robotics, ground piercing radar, sonar and infrared thermography involve facilitating water utilities to collect valid information on internal sewer pipe conditions (Fenner, 2000, Wirahadikusumah et al., 1998, Liu and Kleiner, 2013). The condition assessment data obtained from the destructive or non-destructive test will be analysed to find the relationship between sewer pipe condition and influence concrete deterioration factors. First

approach, the prediction of sewer conditions based on the age and other deterioration factors of the sewer pipe is considered a very complicated process. The deterioration of sewer assets can be affected by multiple factors at once. Therefore, the development of the sewer concrete deterioration model will be based on the concepts and different data requirements. Currently, the deterioration models have been classified into three different groups of the model as physical, statistical, and artificial intelligence models (Hawari et al., 2020). The second approach to the concrete sewer condition assessment model is to develop the condition rating. The condition rating is used to evaluate the current condition of sewer pipes in order to identify the action for deterioration of sewer pipes. The sewer pipe condition rating is usually developed based on the result of sewer pipe inspection using CCTV and/or walk-through surveys and condition assessment data (Ana et al., 2009, Opila, 2011, Chughtai and Zayed, 2008).

Severe concrete sewer pipe deterioration needs to take rehabilitation action immediately to extend the service life of the sewer pipe. It is very challenging because some of the rehabilitation technology is expensive and would disrupt many social activities. However, the protective coating technique seems to be a promising technology in the short and long term (Wang et al., 2020b). At this stage, the condition assessment or service life model and condition rating have become an essential tool for water utilities to decide what type of coating material, when and how to rehabilitate the deteriorated concrete sewer pipe surface needs to be removed before applying a surface protective coating. Protection of the inner surface of concrete sewer pipes and related infrastructures with a corrosion-resistant coating material has been implemented in many field locations and underdeveloped coating materials for aggressive sewer environments and tests their performance in field and laboratory tests (Khan et al., 2019a, Heikal et al., 2015, Roghanian and Banthia, 2019, Valix et al., 2012). There are several cement-based application methods like

shotcrete, cast-in-place concrete, and spin-cast that can be used to increase the service life of deteriorated concrete sewer pipes and other related infrastructure (Kaushal et al., 2020, Wu et al., 2018b). For selection rehabilitation methods, water utilities will use criteria such as cost, inflow, and infiltration (I&I), pipe cleaning, corrosion resistance, by-pass possibility, level of deterioration (structural or non-structural), access, above-ground conditions (i.e., access and traffic limitations), and underground conditions (i.e., depth of the pipe, groundwater, and crossing utilities) (Wu et al., 2018b). There are many potential coating materials suitable to be coating material. It could be classified as cement-based material (e.g. Calcium aluminated cement) and polymeric-based material (e.g. CIPP, Epoxy, epoxy mortar, PVC). Water utilities select suitable coating materials based on the aggressiveness of environmental conditions. Currently, there is only one environmental classification for concrete sewer pipes (WSAA, 2017). The acid resistance of coating material is an essential selection criterion for water utilities to select coating material (Wu et al., 2018b).

Based on the literature reviews, there remains a research gap in the development of corrosion classification, condition assessment or service life model and material selection criteria of the coating material. Presently, there is only one classification of sewer environmental conditions, while the concentrations of sewer gases are different. The condition assessment model is considered physical, operational, and environmental, but it does not include sewer environmental conditions. The development of corrosion classification based on different sewer environmental conditions will help researchers accurately develop a service life model for sewer pipe networks and other related infrastructure management. The development of selection criteria there also requires testing the acid resistance based on the different corrosion classifications. It is also an excellent opportunity to develop more sensibility in terms of accelerated corrosion tests due to the

lack of acid resistance standard tests of the coating material. To our knowledge, this is the first study on corrosion performance based on different corrosion classifications in order to develop a decision tool for concrete sewer pipe rehabilitation. Moreover, this study will involve one-part geopolymer as one of the commercial coating materials to be tested in both long-term corrosions in the real scenario of sewer environmental conditions and accelerated corrosion test at a laboratory in order to develop decision tools around the use of one-part geopolymer at different sewer corrosion classification. The use of geopolymer as a lining material could represent a significant step towards the development of sustainable materials for the MICC problem. In summary, this research study would be able to deliver a decision tool by means of sewer corrosion classification, selection criteria, and service life model around the use of geopolymers as a coating material. It would be the first study that facilitates water utilities to select a different type of geopolymer as a coating material for concrete sewer pipes and related infrastructure rehabilitation.

3 MATERIAL AND METHODOLOGY

3.1 INTRODUCTION

This chapter presents the materials and methodology used for conducting the experiments in the laboratory and field test, which are divided into five main sections:

- **Materials:** This section provides an overview of the materials used in the study, including the specific types of materials, their sources, and their properties. It includes information on the geopolymer mortar (OGPm), calcium aluminate cement mortar (CACm), and any additional additives or components used in the experiments.
- **Sample preparation and curing:** This section outlines the process of preparing the samples for testing, including the mixing of materials, sample moulding, and curing conditions. It describes the procedures followed to ensure consistency and accuracy in sample preparation, which is essential for obtaining reliable and reproducible results.
- **Corrosion resistance performance test:** This section describes the two main types of tests conducted to assess the corrosion resistance performance of the materials: field performance tests and laboratory tests. It provides details on the test setups, conditions, and measurement parameters used to evaluate the performance of the materials under different environmental conditions and stressors.
- **Characterisation of samples:** This section focuses on the characterization techniques used to analyse the samples before and after exposure to an aggressive environment. It discusses various analytical methods, such as microscopy, spectroscopy, and mechanical testing, which provide insights into the structural, chemical, and mechanical changes that occur in the materials due to corrosion or other factors.

- **Evaluation of Corrosion Performance:** this section describes the two main methods to evaluate the corrosion resistance performance of the lining mortar after exposure to an aggressive environment.

3.2 MORTAR LINING MATERIALS

This study involved four commercially available one-part geopolymer mortars (OGPm) to evaluate the corrosion resistance performance as mortar lining material and develop the decision tool for concrete sewer pipe rehabilitation. In addition, calcium aluminate cement mortar (CACm) was used as comparable mortar lining material.

This study received four commercially available OGPm and one CACm from different manufacturers. The mortar lining materials were pre-mixed between mortar binder and aggregate and supplied to The University of Sydney in a 20 kg/bag. Aluminosilicate precursors, admixture, and fine aggregate were partially indicated based on the safety data sheet (SDS) and technical note of each lining mortar, as shown in **Table 3-1.**

Table 3-1 List of one-part geopolymer and calcium aluminate cement mortar

Type of Coating	Coating name	Description	Designation	Aggregate Type
Geopolymer	OGPm-1	single component, polymer–modified mortar with micro silica geopolymer, pozzolan, fly ash and select admixtures	One-part Geopolymer	Silicaceous
	OGPm-2	one-component cement powder, which requires only the addition of water to form an acid-resistant structural mortar	One-part Geopolymer	Recycled Glass
	OGPm-3	One-part corrosion-resistant geopolymer mortar based on waste materials such as fumed silica, blast furnace slag and fly ash	One-part Geopolymer	Silicaceous
	OGPm-4	Fibre-reinforced one-part structural and corrosion-resistant geopolymer mortar	One-part Geopolymer	Silicaceous + Fibre
Calcium aluminate cement	CACm	Single component, high alumina cement-based shotcrete mix with a reduced rebound.	100% CAC	CAC Clinker

3.3 SAMPLE PREPARATION

3.3.1 COUPON SAMPLE PREPARATION

Four commercially available one-part geopolymers mortar as sewer rehabilitation lining products were investigated in this study. It is denoted as OGPm-1, OGPm-2, OGPm-3, and OGPm-4. One comparison non-geopolymer product was a commercially available calcium aluminate cement mortar denoted as CACm.

The specimen sample can be prepared as cubic or cylindrical for the acid immersion test following ASTM C 267-20. However, in many immersion tests, the specimen size varied from 50 to 20 mm cubic, 40×40×80 mm or 25×25×285 prism, and or 2x25 cylinder (Sata et al., 2012, Chindaprasirt et al., 2004, Mohamed, 2022, Sturm et al., 2018, Khan et al., 2020b, Zhuang et al., 2017). This is because the specification of the further test after the immersion test depends on the standard the researcher used. In this study, the mortar specimens were purposed to test the corrosion depth and compressive strength after the acid immersion test removal. Therefore, the 50 mm cube was selected to prepare as it meet the requirement to estimate the compressive strength and chemical resistance test according to ASTM C109/C109M – 21 and ASTM C 267-20, respectively.

This study prepared the 50×50×50 mm cube mortar specimens following ASTM C 305-20, ASTM C109/C109M – 21 and ASTM C 267-20, as shown in Figure 3-1. The unhydrated mortar powder was mixed with tap water based on a water and mortar ratio (W/M) from the manufacturer's instruction (2.2-3.6 L/20 kg concrete) (see Table 3-2). After that, the freshly mixed mortars were poured into 50 x 50 mm prism steel concrete moulds and packed with a compactor and a shaker table. Finally, the packed mortar allows for smoothing of the surface with a trowelful. The cast mortars were immediately covered with moisture-woven fabric and allowed to be set in the mound for 24 hours. The mortars were demolded and allowed to cure for another 28 days in a humidity

chamber based on ASTM C192/C192M at 23±2 °C and relative humidity (%RH) of not less than 98 %RH (ASTMC192/C192M, 2019).

Following a curing period of 28 days in a humidity chamber, the coupons underwent an application of Sika High Strength Epoxy Adhesive Concrete Fix Kit on all four sides of the specimens. This adhesive effectively sealed and protected the edges, exposing only the top and bottom surfaces for subsequent testing, as shown in Figure 3-2.

Table 3-2 Water and mortar ratio (W/M) by weight

Lining mortar	**W/M ratio (w/w)**	**References**
OGPm-1	0.125	Manufacturer
OGPm-2	0.125	Manufacturer
OGPm-3	0.150	Manufacturer
OGPm-4	0.160	Manufacturer
CACm	0.108	Manufacturer

a.Sample preparation

b. Finished sample

Figure 3-1 Coupons sample preparation

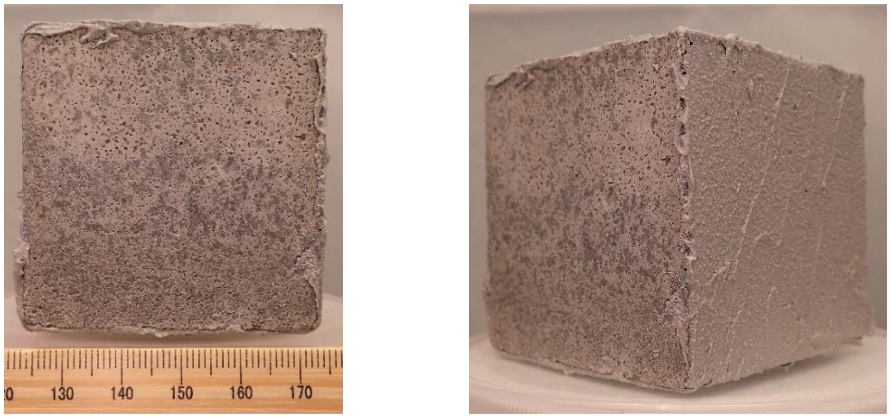

Front view

Side view

Figure 3-2 Example of mortar coupon: (a) Front view and (b) Side view

3.3.2 SHOTCRETE APPLICATION

The mortar application in this study can be referred to as 'shotcrete', a term adopted in Australia from American Concrete Institute (ACI) conventions. This refers to concrete delivered by the 'spray' method or projection by compressed air through a nozzle so that the concrete is delivered at a sufficiently high velocity capable of achieving consolidation at the receiving surface (Australia, 2010). There are two processes for spraying shotcrete, dry spray and wet spray. The dry spray method is the pre-mixed mortar powder that is put into the pump hopper and fed to the nozzle using compressed air to the point of application. Additionally, pre-mixed mortar powder is mixed with water at the back of the nozzle and combined with an accelerator to dissipate the mortar to the substrate. While the wet spray method, the pre-mixed mortar powder is mixed with water in the hopper and fed to the point of application by a pump. The compressed air is added to the nozzle to dissipate to mortar into the substrate. Shotcrete application has been made under a water utility sub-contractor as part of the CRC-P: Smart Linings for Pipe and Infrastructure Project (Smart Linings Project).

3.4 CORROSION RESISTANCE PERFORMANCE TEST

3.4.1 ACID IMMERSION TEST

3.4.1.1 SAMPLE PREPARATION

The preparation of mortar coupons for the acid immersion test followed the procedures outlined in section 3.3.1, which detailed the steps for sample preparation.

3.4.1.2 CORROSION CONDITIONS

The acid immersion test was combined with media solution, temperature and corrosion period. This is to simulate the acid attack at a controllable condition. The media solution used in the acid immersion test was sulfuric acid (H_2SO_4) in this study. It was found as the main corrosive compound in the final stage of the MICC process within the sewer network (Stanaszek-Tomal

and Fiertak, 2016). The H_2SO_4 solution was widely used as a media solution in several studies but in different concentrations, such as 1%, 3%, 5%, and 10 % sulfuric solution depending on their purpose of simulation (Sata et al., 2012, Chindaprasirt et al., 2004) (Mohamed, 2022, Sturm et al., 2018, Khan et al., 2020b). However, serval media solutions were used depending on the specific application and the simulated corrosion type. For example, hydrochloric acid can be used to simulate conditions where chlorides are present, such as in seawater or industrial environments where chlorine is used (Mohit et al., 2021, Senhadji et al., 2019). Nitric acid can be used to simulate conditions where nitrates are present, such as in groundwater, seawater, fertiliser production or wastewater treatment plants (Senhadji et al., 2019, Fan et al., 2012). Other acids, such as acetic and phosphoric acids, may also be used for specific applications (Chatveera and Lertwattanaruk, 2014, Chen et al., 2022, Ren et al., 2022). It is important to note that the choice of acid used in the acid immersion test should be carefully considered based on the simulated conditions. The concentration of the sulphuric acid solution was used at 1% w/v, having a pH of approximately 1±0.05 for the acid immersion test. This concentration was selected for the test to mimic the final stage of MICC, where the acidophilic bacteria take place and produce more sulphuric acid, resulting in the most severe degradation of concrete (Grengg et al., 2018). The testing temperature is usually tested at 23±2 °C in accordance with ASTM C267-20 (Sata et al., 2012, Chindaprasirt et al., 2004, Mohamed, 2022, Sturm et al., 2018, Khan et al., 2020b). However, the temperature was modified from 23±2 °C to 28±2 °C in order to better simulate the corrosion development. The temperature at 28±2 °C were derived from the environmental survey at various sewer asset across water utility within Australia established in corrosion classifications under the CRC-P: Smart Linings for Pipes and Infrastructure from the University of Sydney, School of Chemical and Biomolecular Engineering (Valix, 2021). The period of immersion test indicated to remove the sample from the acid solution chamber was 1,7,14,28,56 and 84 days to determine the corrosion rate in

accordance with ASTM C267-20. However, the immersion time was modified in several studies to be longer or shorter to suit their material to determine the rate of corrosion (Sata et al., 2012, Chindaprasirt et al., 2004, Mohamed, 2022, Sturm et al., 2018, Khan et al., 2020b). Based on the preliminary test, the acid immersion test was performed for up to 28 days in this study.

3.4.1.3 PROCEDURE OF ACID IMMERSION TEST

The acid immersion test was performed in sulphuric acid at pH 1±0.05 and 28±2 °C for up to 28 days (see Figure 3-3). The pH of the solution was changed over time by a neutralisation reaction between mortar and acid solution. Therefore, the pH of the acid solution was monitored through the test with pH-temperature probes with a TPS WP-80D pH meter, and the pH of the solution was adjusted using 98% w/w H_2SO_4 to maintain the pH at 1±0.05. The pH adjustment was made every day for the first week and once a week for the following week.

The mortar sample was periodically removed from the acid for up to 28 days. Then, the specimens were immediately rinsed with distilled water to remove the access acid and debris material. The mortar specimens were sliced into sections to analyse the corrosion depth using a universal indicator and optical microscope (if the depth corrosion is less than 5 mm) or callipers (if the depth corrosion is less than 5 mm) and residual UCS (see 3.6.1) a durability performance. This method has been widely used in many studies (Khan et al., 2020b, Sturm et al., 2018).

Figure 3-3 Accelerated corrosion test

3.4.2 DIGESTER CHAMBER TEST

3.4.2.1 SAMPLE PREPARATION

Three commercially available one-part geopolymers mortar as sewer rehabilitation lining products were investigated in this study. It is denoted as OGPm-1, OGPm-2, and OGPm-3. One comparison non-geopolymer product was a commercially available calcium aluminate cement mortar denoted as CACm. The preparation of mortar coupons for the acid immersion test followed the procedures outlined in section 3.3.1, which detailed the steps for sample preparation.

For the mortar durability test in the digester chamber, the cube mortar specimens were hung in the overflow drain of each digester chamber. The digester chamber is described in the following section 3.4.2.2. The cubes mortar specimen was set up as shown in Figure 3-4. The stainless steel wire, HDPE net, and Snap Hook were assembled to hold the cube sample and hang it within the overflow drains of the digester chamber. The proposed setup had to be durable and, at the same time, easy to handle, considering the aggressiveness of the environment and the duration of the experiment.

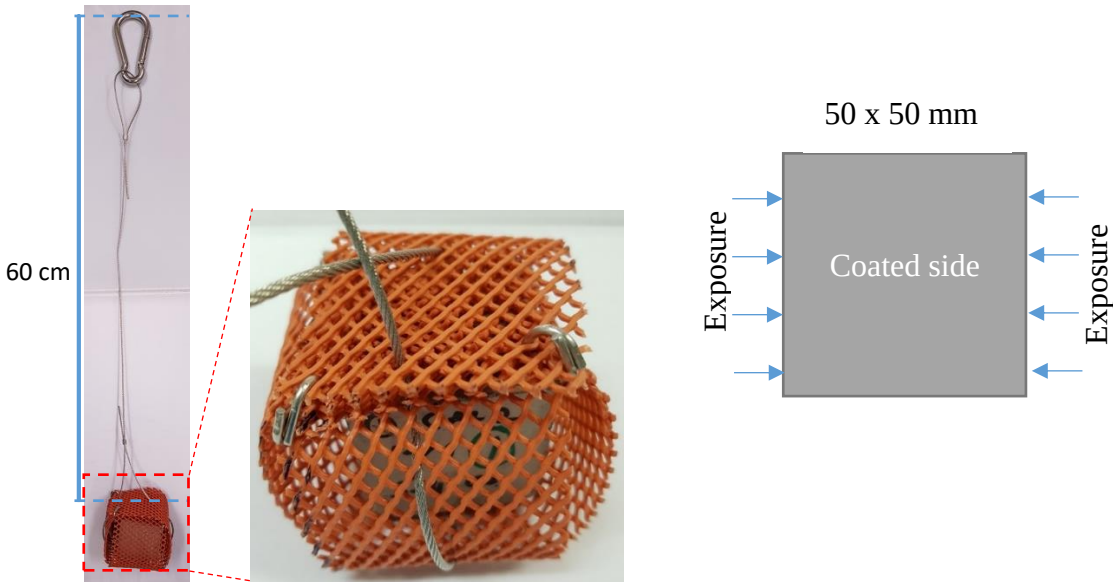

(a) Sample setup (b) Exposure surface

Figure 3-4 Basket with all clips attached

3.4.2.2 DIGESTER CHAMBER ENVIRONMENTAL SURVEY

For the field test, the coupons were also installed in three (3) digestor tanks based on the installation procedures at the wastewater treatment plant (WWTP), Sydney Water. The digester tank received the sewage from the sewer network. The gases produced along the sewer network and digester tank were the same main composition, known as sewer gas. The sewer gases typically comprise N_2, CH_4, H_2S, CO_2, NH_3, and SO_2. The latter four gases are corrosive when hydrolysed and oxidised in humid sewer environments. These sewer gases will form both weak and strong acids, specifically H_2CO_3, HNO_2, HNO_3 and H_2SO_3 (Sand, 1997b).

The environmental condition of the three digester chambers was monitored H_2S, CO_2, %RH, and temperature. They were monitored during 2018 – 2022. Each selected site for the performance test monitored the sewer gases (H_2S and CO_2) and the condition that promotes the growth of bacteria and other microbes (temperature and humidity). The lists of the environmental parameters show in Table 3-3. The table also includes the methods, monitoring

period and statistical measure for each parameter. The 90th percentile provided a single statistical estimate of each parameter that defined the environmental condition.

Table 3-3 Environmental parameter analysis of sewer assets

Parameters	Measurement Methods	Periods of Monitoring	Statistical Measure
H_2S (ppm)	Odalog (e.g., AppTek Odalog 0-200ppm H_2S logger)	7-30 days	90th percentile
Temperature (gas) (°C)	Odalog (e.g., AppTek Odalog 0-200ppm H_2S logger)	7-30 days	90th percentile
Relative humidity (RH %)	Optic fibre, photonics	7-30 days	90th percentile
CO_2 (ppm), SO_2 (ppm), NO_2 (ppm), O_2 (ppm)	MultiRae multigas analyser	Up to 2 days	90th percentile
Infiltration	Visual	Spot check before application and before coring	NA

3.4.2.3 SAMPLE INSTALLATION

The specimens prepared from section 3.4.2.1 were hung in the overflow drains of three digester chambers, which have different environmental conditions, as shown in Figure 3-5. Each mortar type was designated with colours for better identification during exposure. Tapes of those designated colours were placed on top with the identification number written over them. OGPm-1, OGPm-2, OGPm-3, and CACm were identified by labelling the sample, as shown in Figure 3-6.

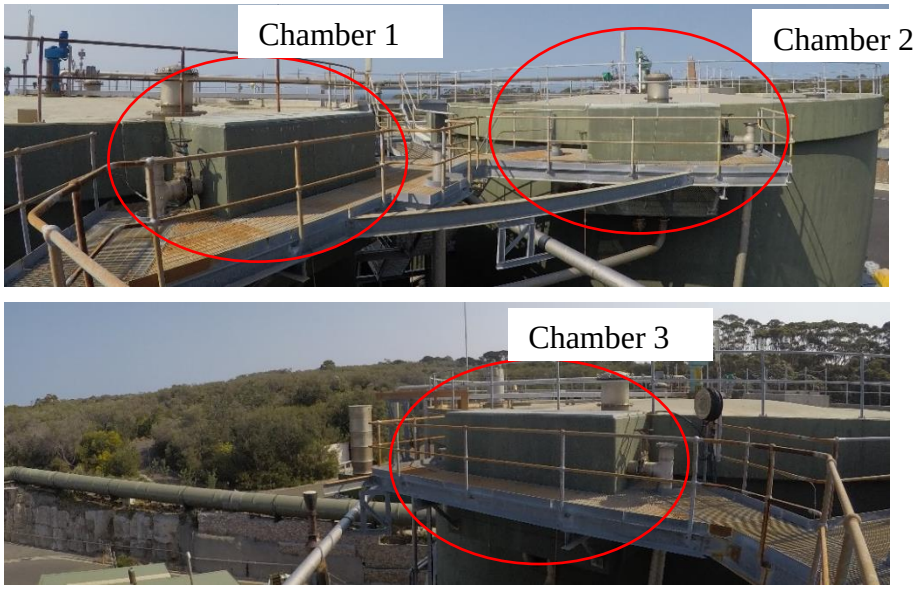

Figure 3-5 Photos of Digester Chambers at North Head Wastewater Treatment Plant (NH-WWTP), Sydney Water

Figure 3-6. Basket with length adjustment (left) and Cube coupons installed on the wires inside an access chamber (right)

3.4.2.4 SCHEDULES

The initial field test plan was scheduled to commence in June 2018 to complete the work by the end of 2022. As demonstrated in Figure 3-7, the sample collection was planned every six months. However, the sample collection schedule was impacted and rescheduled due to the COVID-19 pandemic, resulting in an extension of the sample collection period from NH-WWTP to March 2022.

Year		2018										2019										2020										2021										2022		
Month		March	April	May	June	July	August	September	October	November	December	January	February	March	April	May	June	July	August	September	October	November	December	January	February	March	April	May	June	July	August	September	October	November	December	January	February	March	April	May	June	July	August	September	October	November	December	January	February	March
Product	Date of collection and installation							11-Sep-18						20-Mar-19						5-Sep-19																			20-Apr-21												10-Mar-22
OGPm-1								2	6 months					2	6 months					2	20 months																2	11 months										2
OGPm-2								2						2						2																	2										2
OGPm-3								2						2						2																	2										2
CACm								2						2						2																	2										2

Figure 3-7 Field test schedule for NH-WWTP

3.4.3 FIELD APPLICATION TEST (SHOTCRETE APPLICATION)

The corrosion resistance performance of OGPm and CACm as protective lining mortars under the impact of MICC was carried through the live sewer assets. The protective lining mortars directly applied the coatings on live sewer assets. The direct application of protective coatings on the sewer asset allows both the corrosion resistance and the requirements of applying the protective coating to be examined. This section provides essential information to approach the performance of OGPm and CACm under live sewer assets. It will be divided into four parts as

- site selection
- sewer environment monitoring
- surface preparation
- coating application
- cored sample transport and analysis

3.4.3.1 MATERIALS

Four commercially available one-part geopolymers mortar as sewer rehabilitation lining products were investigated in this study as presented mortar lining material in section 3.2. It is denoted as OGPm-1, OGPm-2, OGPm-3 and OGPm-4. One comparison non-geopolymer product was a commercially available calcium aluminate cement mortar denoted as CACm.

3.4.3.2 LIVE SEWER ASSET ENVIRONMENTAL SURVEY

Each selected site for the performance test monitored the sewer gases (H_2S and CO_2) and the condition that promotes the growth of bacteria and other microbes (temperature and humidity). The environmental survey was conducted for each asset using the same method in section 3.4.2.2. The summary of environmental conditions is presented in Table 3-4.

Table 3-4 Site Locations and Environmental Conditions

City	Utility	Address	Type of Asset	Asset ID	Date of Construction	Asset Age (years)	T_{gas}(°C)	RH%	H_2S (ppm)	CO_2 (ppm)
Perth	Water Corporation	Hordern Street, Victoria Park in Western Australia	Access Chamber	AC3	1976	43	21.92	99.99	170	12880
			Access Chamber	AC7	1938	81	21.56	99.99	180	6180
			Access Chamber	AC9	1938	81	20.21	99.99	190	7800
Brisbane	QUU	Forest Lake Blvd, Forest Lake	Access Chamber	MH101132	1994	25	21.3	100	26	4500
			Access Chamber	MH233216	2001	18	20.6	100	16	4500
			Access Chamber	MH233215	2001	18	20.5	100	24	4500
			Access Chamber	MH233213	2001	18	21.3	100	26	4500
Melbourne	Melbourne Water	58 Afton St, Essendon West	Pipe	MW	1997	22	23	98	4.5	7700
Sydney	Sydney Water	254 Toongabbie Rd, Girraween	Pipe	SWC	1963	56	24	98.7	1.6	6250

3.4.3.3 FIELD SITE SELECTION

The selection of field sites was based on: i) asset condition assessment and ii) environmental conditions of the assets. The criteria used in selecting sites were the corrosivity of the asset (H_2S, CO_2, T, and %RH) and the deteriorated concrete host and its accessibility. The field sites were selected to ensure a broad representation of corrosivity from Australian sewers. Assets were also chosen to ensure they have a suitable remaining life over the project's time frame. The ease of accessibility to permit safe monitoring of the applied coatings was also considered. Corrosivity of the asset was established through asset condition assessment. The corrosion classification of the sewer asset was based on the sewer corrosion classification established by Valix (2021).

3.4.3.4 SEWER ASSETS

The field tests provide two personnel-entry pipes (1.8 m ID x 100 m length and 3.0 m ID x 20 m in length) and 16 maintenance holes (approximately 1.0 m ID and 2-3 m in height) as field test beds for assessing coating performance.

3.4.3.5 SURFACE PREPARATION

One of the essential steps in rehabilitating deteriorated sewer assets is surface preparation to promote the adhesion between the host structure (concrete substrate) and protective coating mortar (overlay) that affect the reliability and durability of the repair mortar. The adhesion depends on many phenomena taking place at the interface zone for bond-detrimental layers (including bleeding), wettability of concrete substrate by repair materials, secondary physical attraction forces induced in the system, the roughness of surface (an interlocking mechanism), and moisture content in the concrete substrate versus the repair system (Garbacz et al., 2005). To achieve the adequate adhesion between the host structure and protective coating mortar, the deteriorated concrete sewer

assets surface needs to remove all the unsound concrete until sound and homogeneous concrete is reached (Garbacz et al., 2006). Mechanical treatments (e.g. sandblasting, shotblasting) and water blasting are commonly used for concrete surface preparation. Unsound concrete is defined as laitance materials where the concrete section has lost its alkalinity and protective function.

The criteria used to determine the depth of deteriorated concrete surface removal is the alkalinity of concrete, which can be represented by surface pH in the field. The criteria for the surface pH analysis are based on the acid neutralisation capacity (ANC) of the host structure. Figure 3-8 shows the ANC of OPC. It shows that OPC can resist the acid until pH 8. Below pH 8, there is a rapid decline in pH with a further increase in acid to substrate ratio. To maintain the protective feature of OPC, the pH of the OPC structure must be at least pH 8.0. Therefore, surface pH > 8 is assessed when sound concrete is reached.

A liquid pH indicator was sprayed on the host structure to assess the asset surface pH rapidly. Two types of indicators, Phenolphthalein and Universal indicator, were tested. However, using Phenolphthalein is more practical as it uses only one colour change; the indicator pH > 8.0 shows a pink colour, while pH < 8 is colourless. This indicator test was used for all the tests (see Figure 3-9). After laitance materials removal, the concrete repair mortar was applied before the protective lining application.

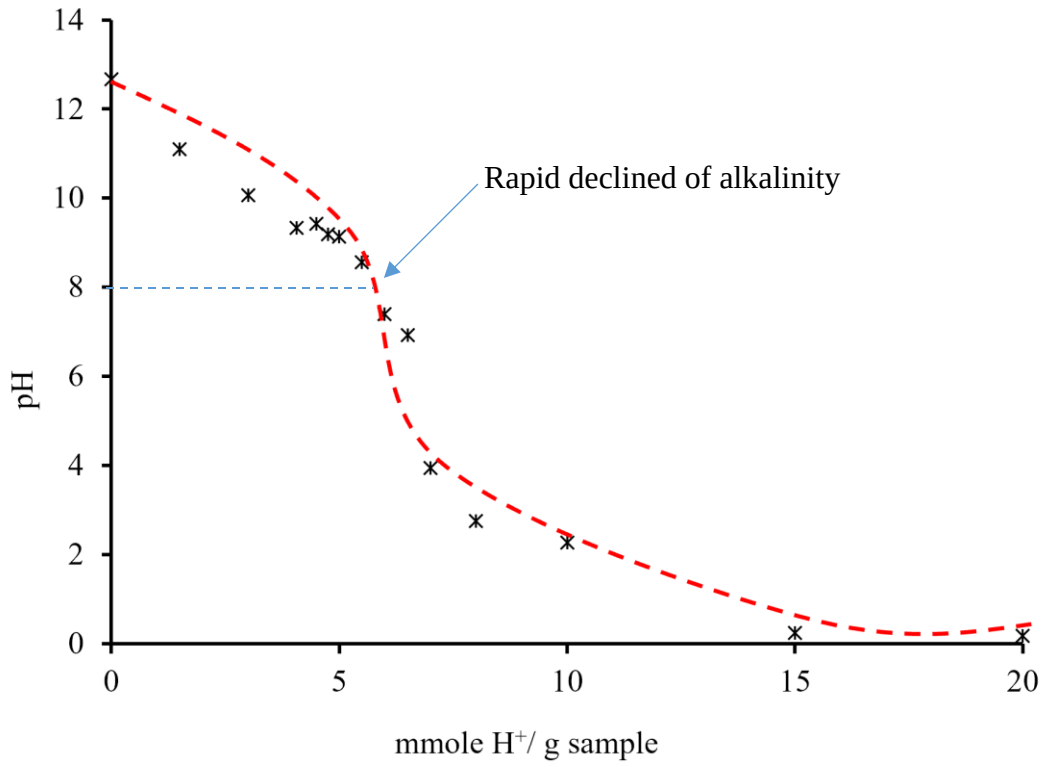

Figure 3-8 Acid neutralisation capacity (ANC) of OPC

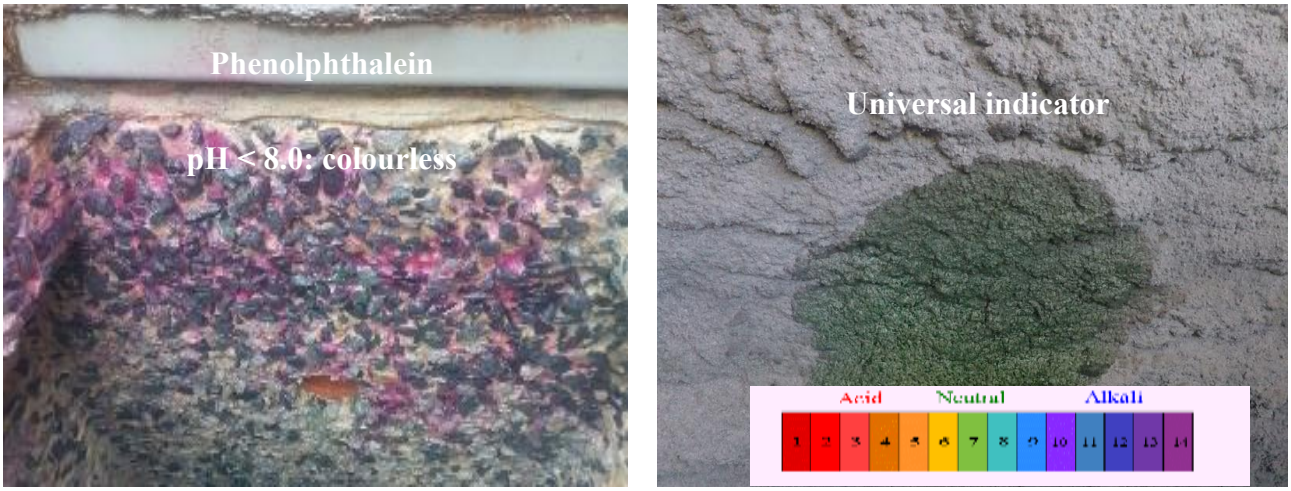

Figure 3-9. Photos of access chamber surface pH with phenolphthalein indicator (left) and Universal indicator (right)

3.4.3.6 SHOTCRETE APPLICATION IN LIVE SEWER ASSET

Deteriorated sewer assets were cleaned and prepared prior to mortar lining application. Then, the geopolymer and calcium aluminate cement lining material (see Table 3-5) was applied on the surface repair mortar using the dry and wet spray technique, as described in shotcrete application in section 3.3.2. The number of protective linings that were applied to each asset for the field test trial is shown in Table 3-6. It is important to note that a surface repair motor (SRm) was applied between each lining. All lining mortar was uniformly applied with at least 20 mm thickness.

Table 3-5 The list of the protective lining mortar

Type of Coating	Coating Names	Water to Mortar ratio (W/M) (L/20 Kg Concrete)	Application Method	Bulk Density (kg/m^3)
Geopolymer	OGPm-1	2.6	Dry spray and coupon	2101
	OGPm-2	2-3	Dry spray and coupon	2233
	OGPm-3	2.2	Dry spray and coupon	2143
	OGPm-4	3.2-3.4	Wet- Spray	2160
Calcium aluminate cement	CACm	1.8-2.5	Dry spray and coupon	2482
Surface Repair	SRm	2	Dry spray	2037

Table 3-6 Coatings Applied for Field Tests and Biogenic Digester

Trial Site Location	Type	Number of Assets	Geopolymer				CAC	Surface Repair	TOTAL
			OGPm-1	OGPm-2	OGPm-3	OGPm-4	CACm	RPm	
Melbourne Water	Pipe	1	1		1	1	1	1	**5**
Sydney Water	Pipe	1	1	1	1	1	1	1	**6**
Water Corporation	Access Chamber	5	1		1	1	1	1	**5**
Water Corporation	Access Chamber	4	1	1			1	1	**4**
SA Water	Access Chamber	5	1		1	1	1	1	**5**
QUU	Access Chamber	4	1		1	1	1	1	**5**
TOTAL		**20**	**6**	**2**	**5**	**5**	**6**	**6**	**30**

3.4.3.6.1 MAINTENANCE HOLES

After removing deteriorated material from the sewer asset, shotcrete as surface repair mortar (SRm) was applied to the pre-cleaned asset at approximately 10 mm above the highest exposed aggregate before lining applications. As shown in a schematic diagram of lining application in an access chamber in Figure 3-10, each manhole is divided into four sections. Two coatings were applied through the depth of the access chambers with a thickness of 20 mm on two opposite sections. In between each coating, shotcrete was applied at the same thickness (20 mm) as the coating to provide a control material for the test. Moreover, under each coating mortar, including shotcrete between the coating mortar, were embedded Ni-Ag alloy rebars for the cover meter to measure thickness later in the future. The stainless steel labels were then installed to identify each

coating. the Table 3-7 shows the example of complete rehabilitation of access chambers in QUU utility, Brisbane, QLD.

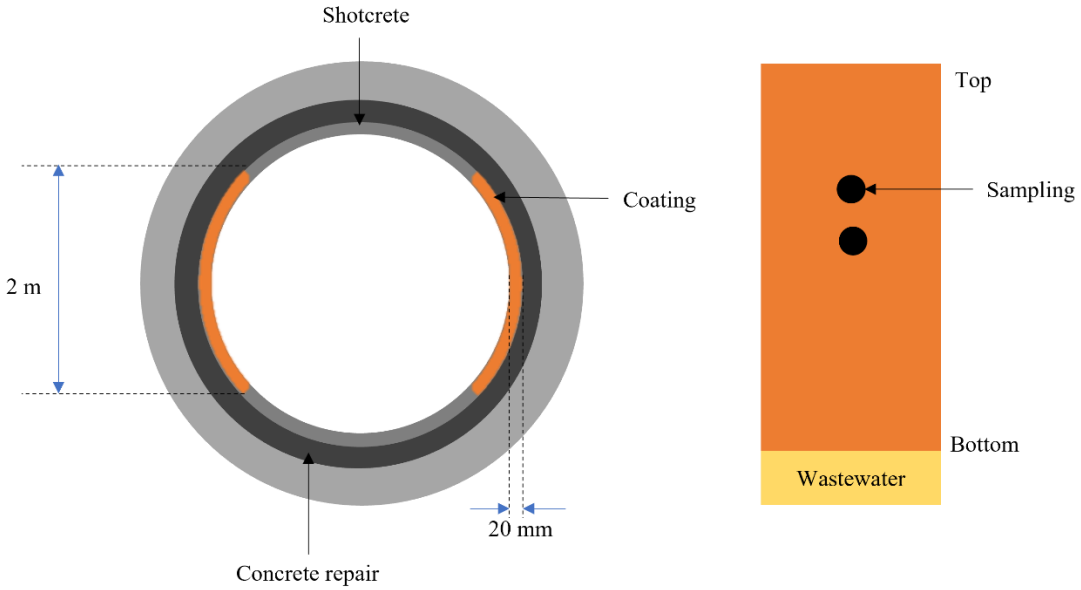

Figure 3-10 Schematic diagram of lining application in an access chamber for field test

Table 3-7 Example of manhole rehabilitation using OGPm and CACm

Manhole No.	Location of coating material	Real scenario
MH233216	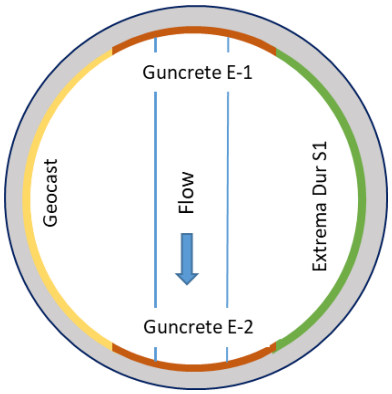	
MH101132	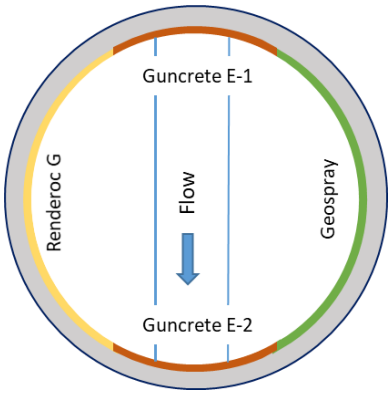	
MH233213	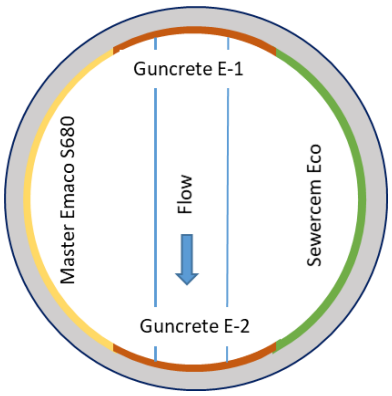	

3.4.3.6.2 PERSONNEL-ENTRY PIPES

In personnel-entry pipes, shotcrete as surface repair mortar was applied through the whole test section of the pipe to cover any exposed aggregates after the laitance material was removed with a thickness of 10 mm above the highest exposed aggregate. The surface was smoothed after application. The linings were then applied with a length of about 5 m and a thickness of 20 mm with a gap of 2 m. Shotcrete was applied in the gap between each coating with the same thickness of 20 mmm. The first and last 5 m section of the pipe was left uncoated to indicate the extent of corrosion of the pipe in the absence of lining and verify if uncoated sections directly after linings are more aggressively attacked by MICC. Similar to the maintenance holes, under each coating mortar, including shotcrete between the lining mortar, were embedded Ni-Ag alloy rebars for the cover meter to measure the thickness. The Stainless steel labels were then installed to identify each coating. Figure 3-11 shows the schematic diagram of the coating and shotcrete application in the personnel-entry pipe.

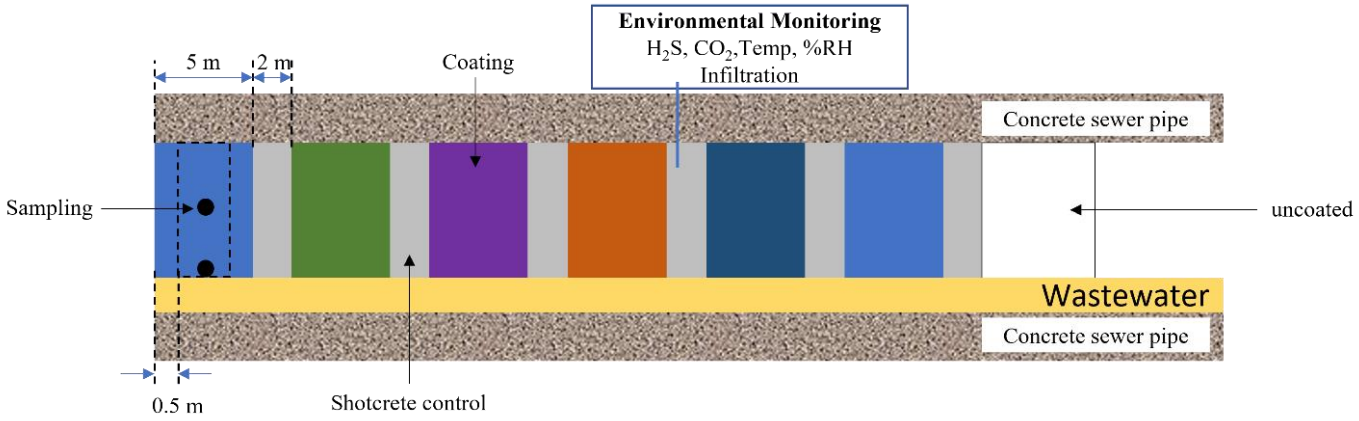

Figure 3-11. Schematic diagram of coating application in a personnel-entry pipe field test

3.4.3.7 LINING THICKNESS

The coating thickness during application was randomly tested by inserting a metal ruler in the uncured non-set concrete (see Figure 3-12). Another method that was adopted was the insertion of false rebars between the host structure and coating and the reading of the coating thickness with a cover meter. Various alloys, including stainless steel, copper and Ni-Ag alloys and dimensions, were tested as false rebars were considered. Ni-Ag alloy was chosen because it provided a strong signal and was sufficiently strong to allow thin bars to be used to minimise its interference with the coating and host structure adhesion and corrosion resistance that would enable its use over the project period. Ni-Ag alloy bars (10mm x 30 cm x 0.5 mm) were embedded between the coating and the host structure as false rebars (see Figure 3-13). The coating thickness was measured post-application and during the monitoring period using a Profoscope cover meter.

Figure 3-12. Measuring the coating thickness with a ruler

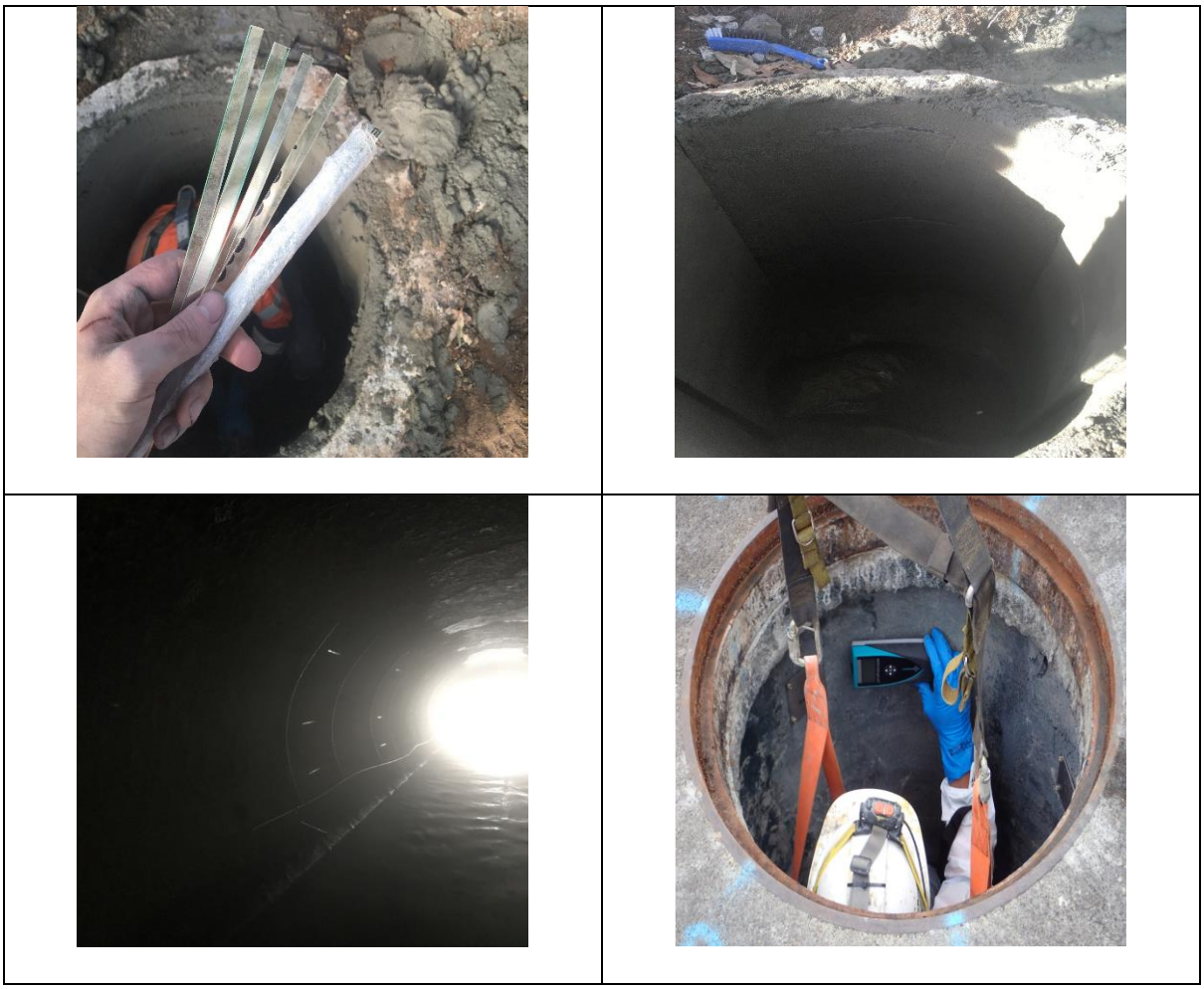

Figure 3-13 Ni-Al alloy rebars (top-left); false rebar installation in access chamber (top-right); false rebar installation in sewer pipe (bottom-left); cover meter testing of coating thickness (bottom-right)

3.4.3.8 CORE SAMPLING

After the protective lining mortar application, the corrosion resistance performance of the protective lining was assessed by the core test. The cored sample was stored in plastic bags with as much of the air expelled then, followed by bubble wrap. The packed cores are then stored in a plastic bottle for mailing to The University of Sydney (USYD). There are two types of sewer assets; i) Manhole and ii) personnel-entry pipe. The core sampling area is located at a different position. Figure 3-14 shows the schematic diagram for the coring sample in the sewer asset. The number of cores taken from maintenance holes is limited by the size of the asset. When sampling

maintenance holes, 2 x cores (5 cm ID x 3-5 cm in length) are extracted at least 10 cm below the top of the manhole. At the same time, the personnel-entry pipe, 2x cores (5 cm ID x 3-5 cm in length) are taken from the tidal, wall and crown. Subsequent samplings were extracted at least 10-15 cm from the previous cored areas. In man entry pipes, 2x cores (5 cm ID x 3-5 cm in length) are taken from the tidal, wall and crown. Subsequent samplings were extracted at least 10-15 cm from the previous cored areas. The cores were stored in plastic bags with as much of the air expelled then, followed by bubble wrap. The packed cores are then stored in a plastic bottle for mailing to the University of Sydney (USYD).

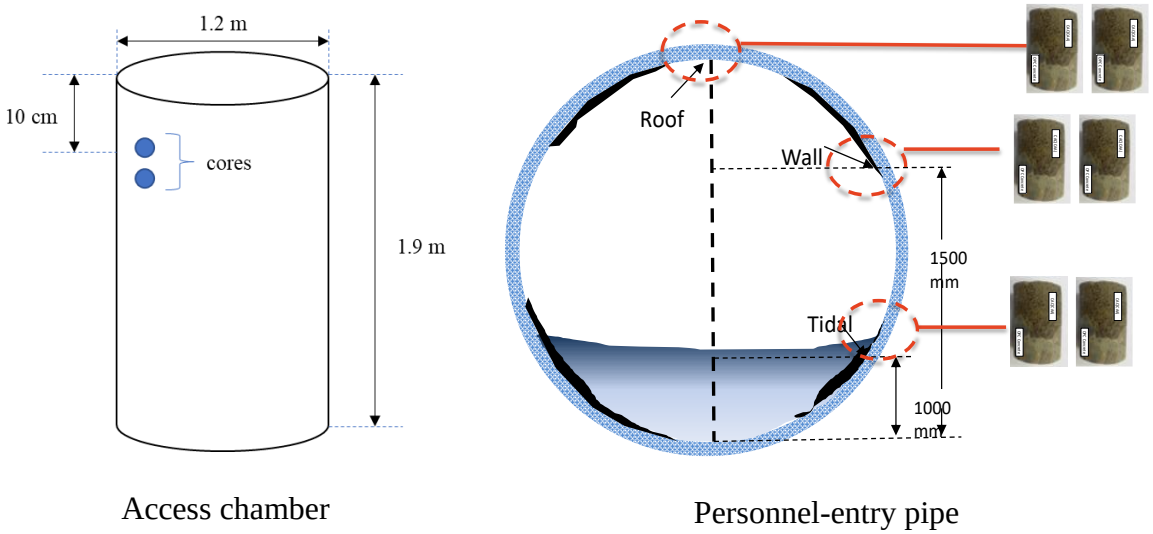

Access chamber

Personnel-entry pipe

Figure 3-14 Core sampling in a manhole (left) and personnel-entry pipe (right)

3.4.3.8.1 SAMPLE CORING SCHEDULE

The schedule for the field test included: i) the condition assessment of the asset; ii) surface preparation; iii) coating application; iv) monitoring; and v) reinstatement of the asset. The initial plan was to start the work in June 2018, with the completion by the end of 2020 within four sampling to occur every 7-8 months. However, given the challenges of organising the field test in live sewers and unforeseen disruptions such as COVID-19, the schedule for the field test has been a work in progress. Figure 3-15 shows the latest schedule. As a result, the field test was extended until February 2022, allowing the period between some of the sampling to be between 5-6 months. However, given the challenges of organising the field test in live sewers and unforeseen disruptions such as COVID-19, the schedule for the field test has been delayed. Finally, the field test schedule will be extended until February 2022.

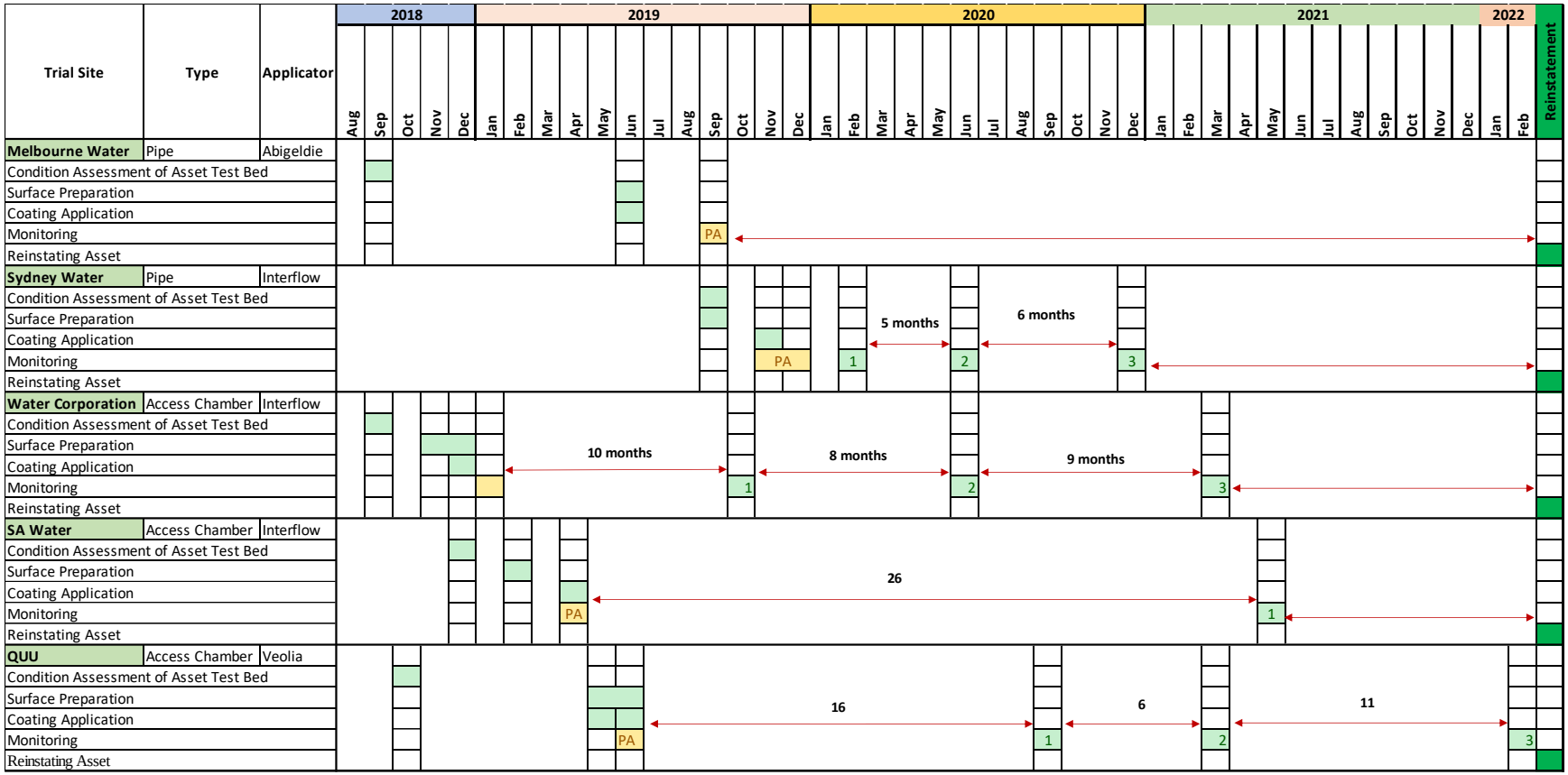

Figure 3-15 Field test schedule for coating performance assessment

3.5 CHARACTERISATION OF LINING MORTAR

3.5.1 CHEMICAL PROPERTIES

3.5.1.1 X-RAY FLUORESCENCE SPECTROSCOPY (XRF)

The mineral components and composition of the mortar, both the mortar binder and aggregates, influence its performance. The chemical composition of the mortar is used to identify its quality and, hence its application. Although the mineral composition may be more important in establishing the quality of the mortar, its analysis is more challenging. Elemental analysis by X-ray fluorescence spectroscopy can be more straightforward, but it estimates the mineral composition by converting the elementals to their corresponding mineral oxides. Establishing the nature of the mineral oxides will, therefore, require other test methods, including SEM-EDS, TGA and FTIR.

X-ray fluorescence analyses of the mortar binders and aggregates were carried out by a commercial laboratory at the University of New South Wales, using a PANalytical Philips Axios-Advanced XRF spectrometer with a 4kW Rhodium (Rh) anode end window and super sharp ceramic technology X-ray tube. The sample preparation involved dissolving the concrete powder in a lithium tetraborate flux at high temperatures (> 1000 °C), which was then cast in a platinum/gold crucible to form homogenous fused beads (32 mm). Quantitative elemental analysis was carried out using the PANalytical SuperQ system with IQ+ and WROXI programs.

3.5.1.2 ACID NEUTRALISATION CAPACITY (ANC)

Acid neutralisation capacity reflects the ability of lining mortar to resist the change in pH. It is determined by the amount of acid/base consumed to achieve specific pH (Giampaolo et al., 2002a). The ANC has often been considered a fundamental property in determining the

durability or resistance of concrete to chemical attack. The method used in this study followed the standard according to EN 14429:2015 (EN14429:2015, 2015, 14429, 2005).

The test used a separate batch test with a fixed L/S ratio of 1 gram of milled concrete with 10 ml nitric acid. Concrete samples were pre-milled using a Planetary Mono Mill Pulverisette 6-ball mill to generate a particle size of 200 microns. A minimum of 8 batch tests were performed to cover a final pH of 4 to 12. The amounts of acid added were based on preliminary titration of the concrete to establish maximum acid consumption. The ANC tests were carried out for 48 hours in a rotating shaker. After 48 hours, the pH of the solutions was analysed and then repeated after 4 hours. If the pH changes by more than 0.3 pH unit, the shaking test is resumed for another 24 hours until the change in pH unit is less than 0.3. The data are represented by plotting the measured pH against the ratio of the amount of acid added (in milli-mole) per gram of substrate used in the test. The results were also plotted as a differential curve to identify the buffering pH regions.

3.5.1.3 FOURIER TRANSFORM INFRARED (FTIR) SPECTROSCOPY

The Fourier Transform Infrared (FTIR) Spectroscopy has been used to identify the functional groups in both organic and inorganic materials. The FTIR has shown to be a great technique to analyse the extent of geopolymer by revealing the Al-O and Si-O bond inside the three-dimensional framework of SiO_4 and AlO_4 interlink with O atom and charge balance at Al^{3+} coordinator with alkali metal within the network of geopolymer (Lee and Van Deventer, 2003). The extent of geopolymerisation was estimated using Thermo Scientific Nicolet 6700-FTIR with attenuated total reflection (ATR) mode, as shown in Figure 3-16.

Figure 3-16 Thermo Scientific, Nicolet 6700-FTIR

Powder of uncorroded and corroded samples was prepared by crushing and grinding into very fine powder. Background spectra were taken before the powder samples were directly pressed onto a diamond crystal, and their specific spectra were collected. The sample was placed in a sample holder and scanned with different wavelength numbers. The FTIR spectra were collected using a resolution of 4 cm^{-1}, wavelength numbers between 550 cm^{-1} to 4000 cm^{-1}, and scanned over 32 scans to obtain the average FTIR data. The FTIR data were processed with OMNIC Specta data processing software, followed by deconvoluting the peak solving the baseline adjusted multi-component spectra bands associated with the minerals phases according to a Gauss-Lorentz sum function as shown in Equation 3.1 (Jain et al., 2018). Parameters for the Gauss-Lorentz sum function are the wavelength (x), the specific component peak wavelength (x_o), the component peak height (H), the component width (w) and the degree of mixing between Gaussian and Lorentzian functions (L).

$$\sum f\,(\mathrm{x},\mathrm{x_o}\mathrm{H},\mathrm{w},\mathrm{L}) = (1-\mathrm{L})\mathrm{H}e^{-\left[4ln2\left(\frac{x-x_o}{w}\right)^2\right]} + \frac{LH}{1+4\left(\frac{x-x_o}{w}\right)^2} \quad \text{Equation 3.1}$$

3.5.1.4 THERMOGRAVIMETRIC ANALYSIS (TGA)

Thermogravimetric Analysis (TGA) is a quantitative analysis technique to study the thermal decomposition of materials. It is used to identify the mineral phases in cement and concrete from their decomposition temperature resulting in the release of water in the case of hydrates and CO_2 in mineral carbonates (e.g., calcite). It can quantitatively measure hydration and some corrosion products from geopolymers and calcium aluminate cement. However, overlaps between phases can make establishing an accurate quantitative analysis challenging. For example, C-S-H (OPC hydrate) overlaps with the gypsum, ettringite and AFm phases. This was addressed using a deconvolution algorithm similar to FTIR deconvolution described in section 3.5.1.3.

In this study, TGA was utilised to investigate the change of minerals on the OGPm and CACm using Perkin Elmer TGA 4000, as shown in Figure 3-17. Approximately 5-10 mg of the sample was heated at 15°C/min from 50 °C to 900 °C under 15 ml/min N_2 gas. The result from TGA can provide a quantitative analysis of the fresh lining materials and corrosion products after exposure to aggressive environmental conditions.

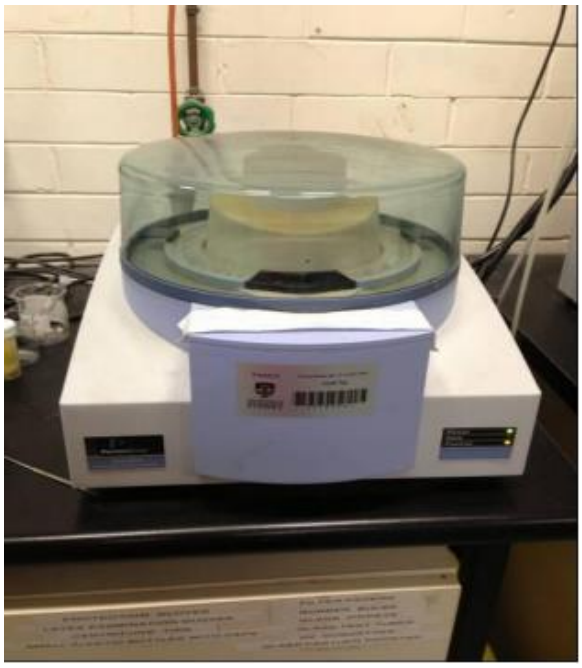

Figure 3-17 Thermogravimetric Analysis (TGA)

3.5.1.5 SCANNING ELECTRON MICROSCOPE (SEM-EDS)

This study analysed the microstructure of hydrates and corroded concrete specimens using scanning electron microscopes (SEM). Phenom XL G2 Desktop SEM is equipped with an EDS detector and a basic identification software package (EID) to control the fully integrated EDS detector. This unit is a low vacuum and low resolution (< 10 nm) that provided rapid SEM analysis. The cored sample was visually used to confirm the depth of acid permeation by observing the change of morphology and corrosion products from a backscatter SEM image and the concrete specimen's area and line element mapping. The backscatter SEM-EDS images and elemental analysis were obtained using Phenom XL Desktop Scanning Electron Microscope (SEM) with integrated EDS, as shown in Figure 3-18.

The mortar sample preparation involved sectioning the mortar samples using the diamond saw and mounted on the sample holder (aluminium mounds) using carbon tape. SEM-EDS backscatter images of the corroded and uncorroded sections were taken, and elemental mapping was conducted over the corrosion surface to identify the elements lost and sulphur deposition due to the neutralisation reaction with sulphuric acid. Microstructure and other corrosion products such as gypsum, ettringite, and calcite were also analysed.

Figure 3-18. Phenom XL Desktop Scanning Electron Microscope

3.5.1.6 SURFACE pH

The surface pH of mortar plays a crucial role in assessing its corrosion resistance and durability. The surface pH value indicates the level of acidity or alkalinity of a lining mortar surface, which has significant implications for its performance and long-term stability. The surface pH of mortars was randomly performed at the surface using a pH meter connected with a Metrohm flat membrane electrode, as shown in Figure 3-19. One exposed side of the cube was sprayed with DI water for surface pH measurement until hydrated. A pH probe was then applied to the centre of the hydrated surface, ensuring the probe only contacted the water but not the actual material surface. The pH reading was allowed to stabilise for 60 seconds before recording, and the pH measuring process was repeated at least three times at different places on the same exposure surface.

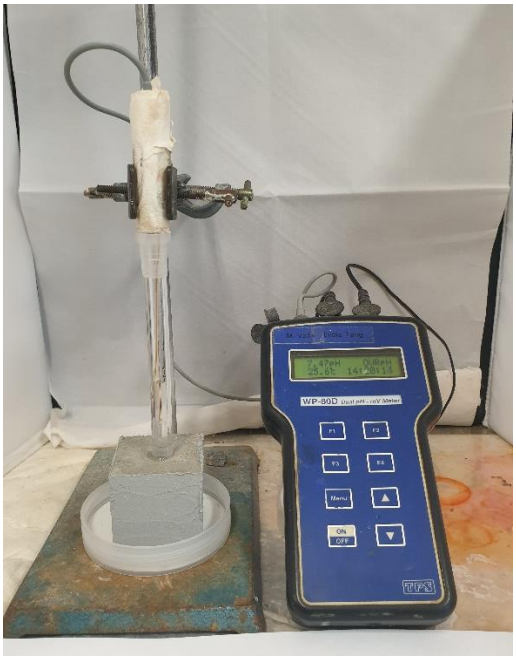

Figure 3-19 Surface pH Testing Apparatus

3.5.2 PHYSICAL AND MECHANICAL PROPERTIES

3.5.2.1 PARTICLE SIZE DISTRIBUTION

The particle size distribution of mortar is a critical parameter that significantly influences its workability, mechanical properties, and overall performance. Understanding and analysing the particle size distribution is essential for optimizing mortar mixtures, ensuring proper material selection, and achieving desired properties in construction applications. In this study, the particle size distribution of mortar binder was determined by laser diffraction technique using the Malvern mastersizer 3000 instruments. At the same time, the particle size distribution of the aggregate was determined based mechanical sieve analysis technique.

3.5.2.2 POROSITY

The porosity of mortar is the ratio of voids or pore volume to the total volume of the concrete specimen. Porosity tests were conducted using the modified ASTM C642 (ASTM-C642, 2013). The volumetric porosity can be estimated using water absorption methods. The mortar specimens used for the test were cut into 1 cm cubes. The dimensions were measured using a Vernier calliper to estimate the bulk volume (V_b). After that, the sample was dried at 45 °C for 24 hours in the air oven. After removing the sample from the oven, allow it to cool down to approximately 25 °C and determine the mass of the sample. The sample was then returned to the oven. After another hour, the sample was measured again. If the mass was within 0.5% of the previous measurement, then the final mass was recorded as dry mass (M_d). The dry sample was immediately immersed in water at 25 °C for not less than 48 h. The sample was removed from the water, tab dried the surface with a towel, and determined the mass of the sample. The sample was returned to immersion in water for another 24 hours. The sample was determined the mass again. The final mass was recorded as wet mass (M_w) if the mass was within 0.5% of the previous measurement as a wet sample. The mass of water is multiplied by water density (ρ) to convert to the volume. The porosity was calculated based on Equation 3.2. The Porosity

tests were conducted on uncorroded and corroded samples to compare porosity between corroded and uncorroded samples.

$$\text{Porosity (\%)} = \frac{(M_w - M_w) \times \rho_w}{V_b} \times 100 \qquad \text{Equation 3.2}$$

3.5.2.3 UNCONFINED COMPRESSIVE STRENGTH

Unconfined Compressive strength (UCS) of the lining mortar measures the resistance of the concrete to an axially applied crushing force. The UCS was determined in accordance with ASTM C109/C109M-21 for cube specimens (ASTM-C109/C109M-21, 2021) and ASTM C39/C39M-21 for cylindrical specimens (ASTM-C39/C39M-21, 2021) using A UTEST Automatic Compression Machine Model UTC-4231, as presented in Figure 3-20. The pacing rate of the load is 0.6 MPa/s for the cube and cylinder. The dimension of the samples was measured before the UCS test, and the height of the sample should not be less than 20 mm.

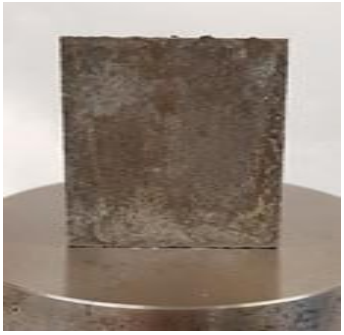

(a) Mortar coupon

(b) Crushed mortar coupon

Figure 3-20 UTEST Automatic Compression Machine Model UTC-4231 (Left) and concrete coupons before and after crushing test (right)

3.6 EVALUATION OF CORROSION RESISTANCE PERFORMANCE

3.6.1 DEPTH OF CORROSION

Depth of acid permeation is used to evaluate the durability of the lining material. It was measured based on the neutralisation of acid and the distance into intact lining material. The samples were slice perpendicular to the exposed sewer surface using a Lortone inc Model FS8 Lapidary Trim Saw equipped with an 8-inch diamond blade, as shown in Figure 3-21. The sliced sample was immediately dried and cleaned to eliminate any loose material from cutting. A universal indicator was sprayed on the crossed section of the sample to depict the depth of corrosion. The colour of the lining material surface is changed based on the alkalinity of the material. The non-acid permeation zone turns purple, while the acid permeation zone turns green to red depending on the residual alkalinity, as shown in Figure 3-22. The corrosion depth was measured using Leica DM2500 optical microscope integrated Leica Application Suite (LAS) software if the corrosion depth was less than 5 mm, while the depth of carrion was over 5 mm using a calliper, as shown in Figure 3-23.

Figure 3-21 Lortone inc Model FS8 Lapidary Trim Saw equipped with an 8-inch diamond blade

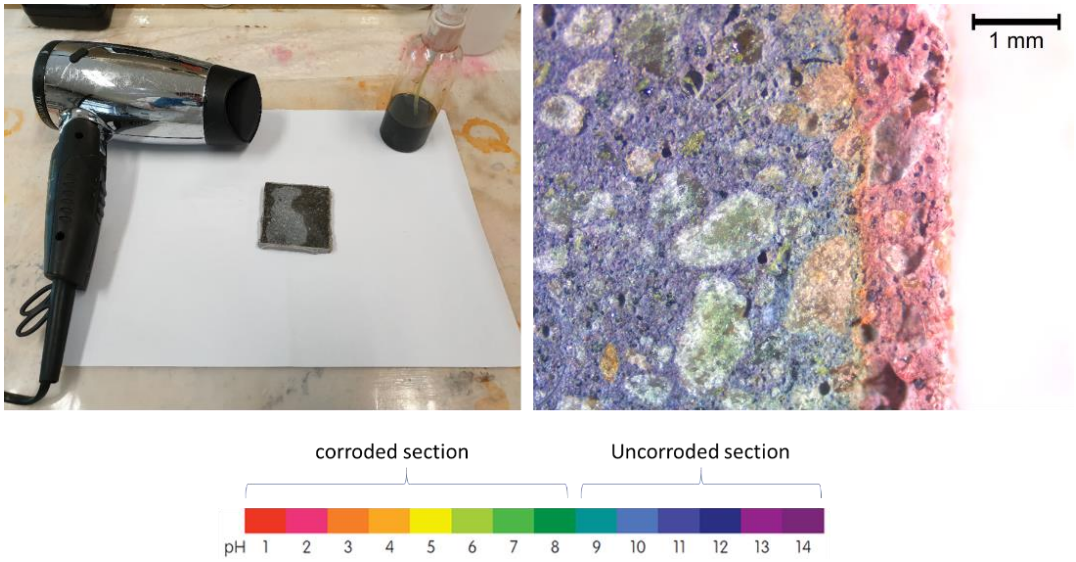

Figure 3-22 Colour scale for the Universal indicator

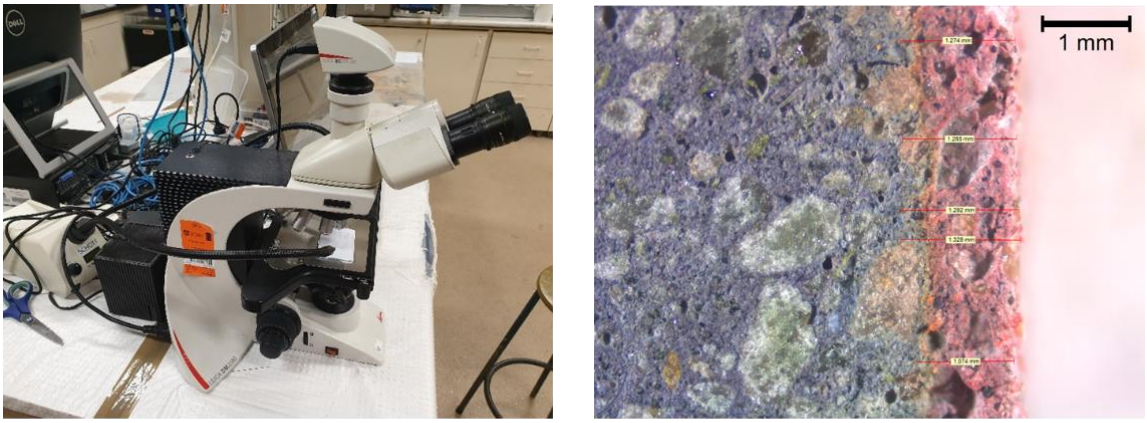

a. Leica DM2500 optical microscope b. Measured depth of corrosion

Figure 3-23 a.Leica DM2500 optical microscope and b.Photo of the depth of acid permeation

The corrosion depth was determined by measuring from the centre of the original cube, considering the expansion that occurred during the test, as shown in Figure 3-24. The depth of corrosion was calculated based on Equation 3.3.

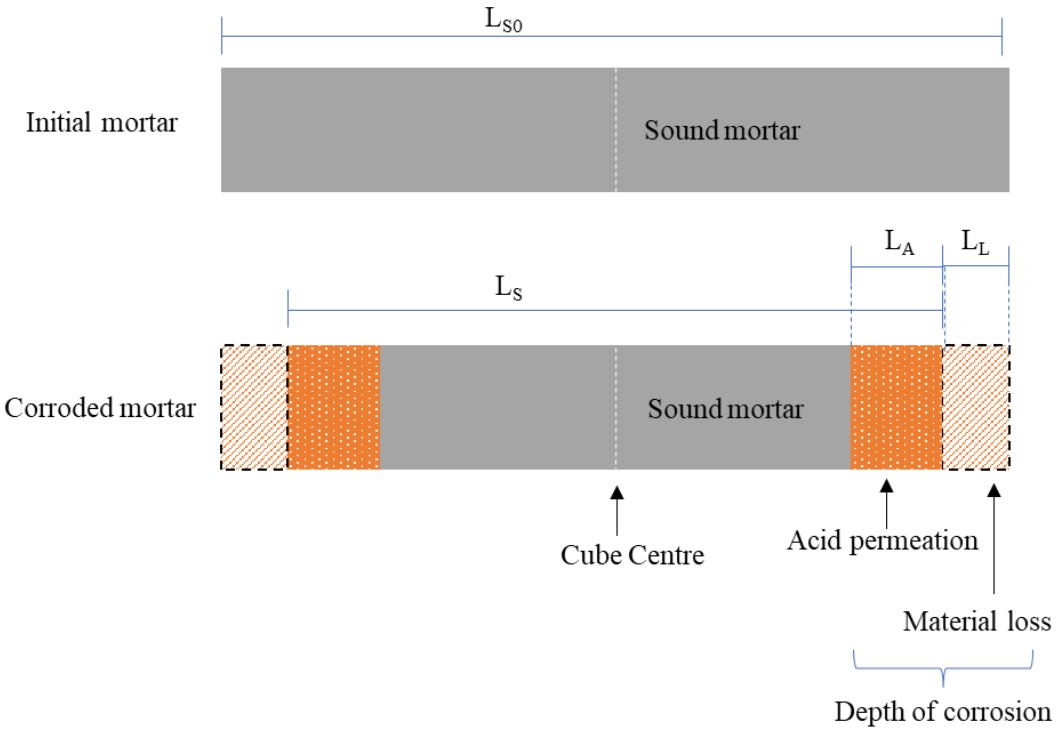

Figure 3-24 Depth of corrosion calculation

The corroded section of the concrete is known to expand because of the expansive nature of the corrosion products and may experience loss of material. Therefore, the total depth of corrosion (DoC) was estimated from the difference between the original thickness of the lining mortar ($L_{original}$) and the thickness of the intact lining mortar minus the depth of acid permeation ($L_{acid\ permeation}$) as following the equation below.

$$DoC = \left(\frac{L_{S0}}{2} - \frac{L_S}{2}\right) + L_A \qquad \text{Equation 3.3}$$

3.6.2 RESIDUAL UCS

The corroded mortar sample collected from the corrosion resistance performance test was measured by the residual UCS. The corroded mortar sample was prepared for measuring residual UCS by removing two sides of the corroded layer and four epoxy sides, as shown in Figure 3-25. After that, the length and width of the cube were measured three times on each

side using Kincromec K11100 callipers at least three times at different locations along width and length. The average measurement is used to calculate the cross-sectional area of the cube. The residual UCS were performed as described in section 3.5.2.3.

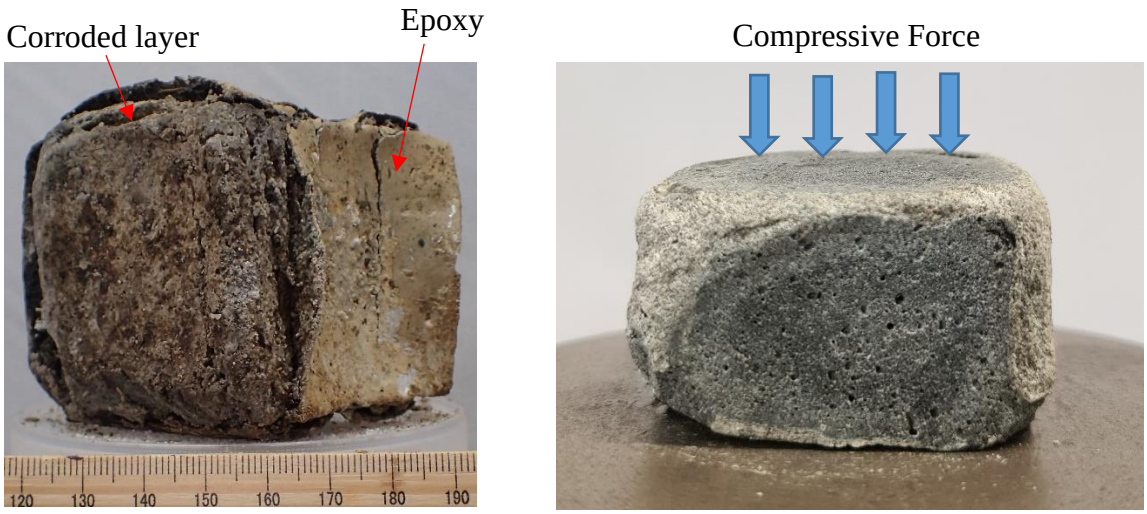

(a) Corroded mortar sample

(b) Removed corrosion layer and epoxy mortar sample

Figure 3-25 Corroded mortar sample (Left) and Measured Sides of Sample (Right) for UCS Testing

4 CHARACTERISATION OF GEOPOLYMER AND CAC PROTECTIVE LINING MATERIALS

4.1 INTRODUCTION

Geopolymers are of interest in being used as a lining material. There are various commercial geopolymer lining products, but their uptake has been slow. This problem is attributed to a lack of performance data, service life models that could be used to design the protective system, and material specifications that could be used to select lining material. The lack of performance data and understanding of the critical properties that contribute to the corrosion resistance of cement-based coating materials, including geopolymers, have hampered the selection of fit-for-purpose lining materials that would suit sewer applications.

It should be noted that geopolymers are a subset of the broader family of alkali-activated binders (AAB). The feature distinguishing geopolymers from AAB is their 3D sialate network, while AAB tends to form linear structures (Sun et al., 2022, Lecomte et al., 2006). Most commercial products, however, regardless of the nature of hydrate phases, are referred to as geopolymers. Therefore, for this study, the products will be referred to as geopolymers.

This section examined the properties that impact the durability of commercially available geopolymer and calcium aluminate cement mortar as protective linings for the first time. The impact of physical, mechanical and chemical characteristics of geopolymer and calcium aluminate cement mortars on their performance or corrosion resistance for sewer applications is accepted but not well established, in particular where it relates to commercial products. Studies have shown the impact of unconfined compressive strength (UCS) and porosity on the durability of the mortar (Khan et al., 2020b, Thokchom et al., 2009, Chindaprasirt et al., 2004, Sata et al., 2012). Chemical features, including mortar binder and aggregate ratio, binder hydration phases, acid neutralisation

capacity, efflorescent, alkali-aggregate reaction (AAR), impacted the corrosion resistance of the mortar (Khan et al., 2020b, Thokchom et al., 2009, Sturm et al., 2018, Xue et al., 2018, Hyeok-Jung et al., 2018). These studies have examined the impact of mortar manufacturing conditions on the properties of the mortar, and some have extended the study also to evaluate the effect of these properties on the durability of the mortar. The manufacturing conditions considered have included the type of binder precursors, precursor composition, activating reagents, mortar mix design, water-to-cement ratio, aggregate quality and curing conditions (Part et al., 2015, Jegan et al., 2023, Parthiban et al., 2022). However, most of these manufacturing conditions are research-based material products rather than commercial ones. This is understandable because such information would be commercial in confidence. This industry-led research focussed on the evaluation of commercial products to ensure outcomes can be commercially translated. Many of the manufacturing features of the mortars, including mortar mix design, were not available in this study. This study focussed on identifying the specific mortar properties that impact the durability of the mortar coatings specific to sewer conditions instead of the manufacturing conditions.

This chapter presents the physical and chemical characteristics of the four commercial geopolymers (OGPm) and the calcium aluminate cement mortar (CACm) control mortars used in this study. The characterisations of the geopolymers are presented in four (4) sections. The first section presents the chemical composition of binder and aggregate, which is primarily characterised by elemental compositions. The second section presents a mix of design and particle size before proceeding further with chemical and physical characterisation. The third section presents the physical properties and their early development during curing, specifically porosity and unconfined compressive strength (UCS). Finally, the fourth section presents the analysis of the microstructure of the cured mortar, including cement hydrates formed during curing and

alkalinity. Although features including conversion and efflorescence are also considered necessary, their effects were not included in the mortar evaluation. Tests were, however, performed to ensure these features were absent in the mortars tested.

4.2 CHEMICAL COMPOSITION OF ONE-PART GEOPOLYMER AND CAC MORTAR

The elemental composition of the binder and aggregate from each mortar was analysed by X-ray fluorescence spectroscopy (XRF) (Javed et al., 2022). The XRF test was carried out by a commercial laboratory at the University of New South Wales (UNSW), using a PANalytical Philips Axios-Advanced XRF spectrometer with a 4kW Rhodium (Rh) anode end window and super sharp ceramic technology X-ray tube. In this study, commercial geopolymer and calcium aluminate cement mortar were supplied in a pre-mixed binder and aggregate with 20 kg/bag size. The pre-mixed mortars were reduced to the sample size for laboratory testing using the coning and quartering methods. Afterwards, the binder and aggregate were separated using a sieve analysis technique. Particles smaller than 75 µm sieve were considered components of the binder, while particles greater than 75 µm were considered an aggregate. This is justified based on the lowest fine aggregate use for masonry mortar from ASTM C144-18 (ASTM-C144-18, 2019). After separation, the binder and aggregate samples were milled to reduce the particle size to approximately 50-70 µm. Following this, the samples were dried at 100 °C before delivery to the laboratory at UNSW for XRF analysis.

4.2.1 BINDERS

Based on the literature on OGPm and CACm, the primary chemical composition associated with geopolymer formation is Silicon dioxide (SiO_2) and Aluminium oxide (Al_2O_3). However, the inclusion of Calcium oxide (CaO) has been recognized as a beneficial component in improving the performance of geopolymer mortar, particularly in strength and durability (Cong and Cheng, 2021, Amran et al., 2020). In the case of CACm, the composition is primarily focused on Al_2O_3 and CaO, which are vital components responsible for their properties (Ideker et al., 2019).

This study investigated their properties and performance using commercially available OGPm and CACm. Four types of OGPm and one type of CACm were specifically chosen for the study. The bulk chemical compositions of the OGPm and CACm binders were determined and shown in Table 4-1. The XRF analysis of the OGPm revealed notable percentages of SiO_2, Al_2O_3, and CaO, indicating their significance as principal components. As expected, the CACm binder predominantly comprised Al_2O_3 and CaO, aligning with previous expectations. The chemical composition of CACm was consistent with the standard of CACm (Scrivener et al., 1999). However, the OGPm was observed to have varied chemical compositions (SiO_2, Al_2O_3, and CaO) because it can be produced from various raw aluminosilicate precursors. Based on the technical data sheet (TDS) from OGPm, which is not present in this thesis due to the confidentiality of the product used in this study. The TDS of the OGPm indicated the OGPm were produced based on blending different aluminosilicate precursors such as Fly ash (FA) and ground granulated blast slag (BSF). The Si/Al ratio of OGPm in this study was observed to be between 0.69 and 4.63, consistent with the Si/Al ratio of geopolymers reported by Fletcher et al. (2005).

Table 4-1 XRF analysis of the chemical composition of OGPm and CACm binder

Binder (wt%)					
Components	**OGPm-1**	**OGPm-2**	**OGPm-3**	**OGP-4**	**CACm**
	Binder	**Binder**	**Binder**	**Binder**	**Binder**
Na_2O	0.37	0.44	0.52	0.54	0.19
MgO	1.35	3.19	2.03	8.69	0.52
Al_2O_3	5.95	27.60	14.41	9.01	43.70
SiO_2	27.55	19.16	48.11	26.18	8.57
SO_3	2.38	1.10	0.77	4.38	0.01
K_2O	0.76	0.17	0.67	0.41	0.22
CaO	53.85	37.43	23.26	44.52	36.97
Fe_2O_3	1.84	8.99	4.92	2.13	6.65
LOI.	5.16	0.27	2.57	5.16	1.20

The OGPm is produced from raw materials that contain silica (SiO_2) and alumina (Al_2O_3), known as aluminosilicate. The aluminosilicate source used for the production of geopolymer can be divided into two categories: i) natural minerals such as metakaolin and volcanic ash and ii) industrial by-products that are rich in silicon and aluminium components such as fly ash (low-Ca aluminosilicate), blast furnace slag (high-Ca aluminosilicate) and waste glass cullets (Cong and Cheng, 2021, Castillo et al., 2021, Ma et al., 2022). Fly ash can be derived from various sources; the most important are coal power stations and other combustion and gasification plants, including biomass gasification and waste-to-energy plants (Khan et al., 2019b, Kaur et al., 2018). Slag is typically sourced from blast furnaces, but slags can also be sourced from steel, ferronickel and copper processing (Maragkos et al., 2009, Zhu et al., 2021b). This type of material is known for its properties, such as strength, durability, and eco-friendliness, as it uses industrial waste materials as an alternative to natural resources, reducing the carbon footprint of construction and manufacturing processes (Chowdhury et al., 2021, Wong, 2022).

Calcium aluminate cement (CAC) is produced from a mixture of bauxite (source of aluminium oxide (Al_2O_3)) and limestone (source of calcium oxide (CaO) as a raw material. The raw materials are fused at 1450 °C – 1550 °C depending on the chemical composition of the raw materials (Scrivener and Capmas, 1998). After cooling, The fused cement clinker is milled to a fine CAC cement powder. This type of cement is known for its high early strength, fast setting time, and acid resistance (Zapata et al., 2022). In general, the nature of the raw material used in manufacturing CAC binders is consistent. On the other hand, geopolymers are complicated by the variety of raw aluminosilicate precursor materials, as mentioned above.

Figure 4-1 compares SiO_2, Al_2O_3, and CaO in OGPm and CACm binder from XRF analysis and with chemical com. The SiO_2 concentration among the geopolymer mortar shows that OGPm-1, OGPm-2, and OGPm-4 have concentrations of approximately 19.16 - 27.55 wt.%, while OGPm-3 has a higher SiO_2 content of 48.11 wt.%. These results suggest that the OGPm-3 binders may have been prepared from high SiO_2 aluminosilicate material and additional SiO_2 sources such as silica fume. The Al_2O_3 content is generally low in OGPm-1, OGPm-3, and OGPm-4 from 5.95 to 27.60 wt.%, while OGPm-2 shows significant content at 27.60 wt.%. These results suggest that the OGPm-2 is prepared from high Al_2O_3 aluminosilicate material. The CaO content of OGPm was found to vary approximately from 23.26 -53.85 wt.%, with OGPm-1 having the highest CaO content. The high calcium aluminosilicate precursors (CaO > 10 % wt.) such as blast furnace slag (BFS) have been proposed to preferentially form calcium aluminosilicate hydrate (C-A-S-H) with tobermorite like (mostly Q_2, some Q_1 and Q_3) structure based on NMR analysis (Richardson et al., 1994b, Provis et al., 2015, Richardson et al., 1994a), while low-calcium aluminosilicate precursors (CaO < 10% wt.) such as fly ash or metakaolin tend to form sodium aluminosilicate hydrate (N-A-S-H) gel with a highly crosslinked 3D sialate (mainly Q_4) network associated with geopolymer

(Brough and Atkinson, 2002). The presence of high-CaO material suggests that the binders are most likely to combine AAB and geopolymer phases. This is considered a high-Ca geopolymer. The aluminosilicate precursors for geopolymer production are typically metakaolin mineral and/or aluminosilicate waste, such as blast furnace slags and fly ash (Cong and Cheng, 2021).

Comparing SiO_2, Al_2O_3, and CaO composition of OGPm in this study with an average chemical composition of blast furnace slag (BSF) and fly ash (FA) as common aluminosilicate precursors from literature (see Table 4-2) in Figure 4-1, it was observed that the chemical compositions are comparable. For example, the CaO content of BSF within the concentrations found in OGPm-1 and the OGPm-3 have similar CaO content to FA, while the SiO_2 content in FA is similar concentration to OGPm-3 and other geopolymers has a similar SiO_2 concentration to BSF. The mortar mix design cannot be decoupled from the bulk analysis of the binder. However, the comparable composition of the geopolymer binders with FA and BSF suggests these could be potentially produced from single or blends of FA and BSF. For the CACm binder, the CaO and Al_2O_3 contents are 36.97 wt.% and 43.70 wt.%, respectively. This composition is consistent with a standard grade for CAC, containing around 40-50 %wt Al_2O_3 generated from limestone and bauxite (Scrivener et al., 1999).

The bulk elemental analysis of the mortars established from SEM-EDS of unhydrated bulk mortars is shown in Table 4-3. Although the oxide compositions are not expected to be similar to those established by XRF (see Table 4-1), these results show the main components in the OGPm are SiO_2, Al_2O_3, and CaO and CACm consist mainly of Al_2O_3 and CaO.

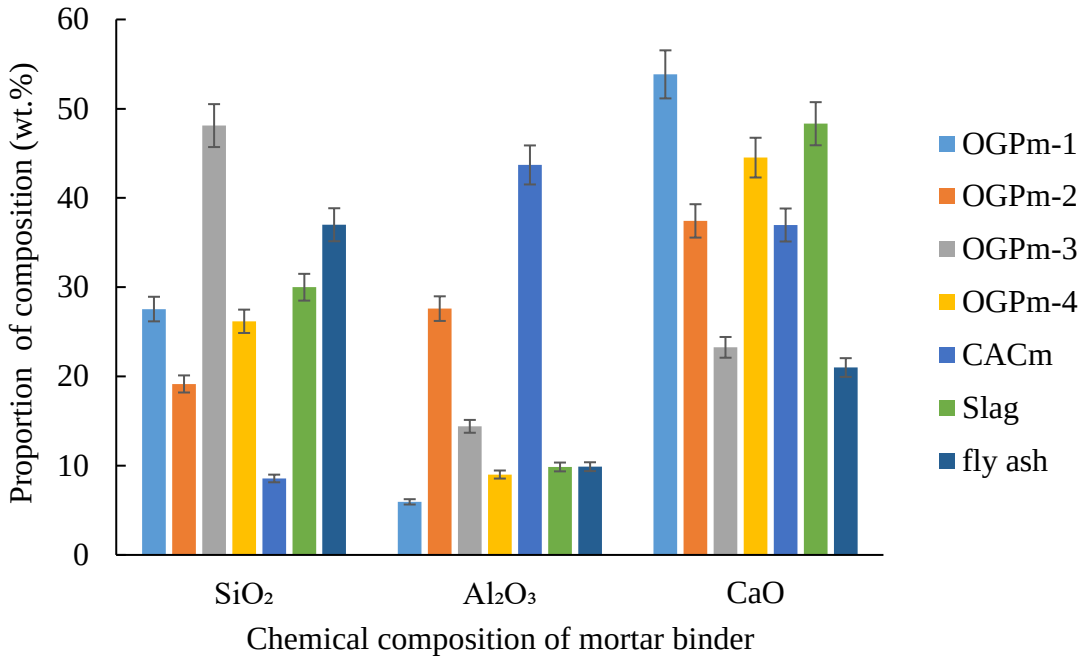

Figure 4-1 SiO_2, Al_2O_3, and CaO from XRF analysis of mortar binders

Table 4-2 Chemical compositions of fly ash, Blast furnace slag by XRF

Material	Chemical component (wt.%)								References
	SiO_2	Al_2O_3	CaO	Fe_2O_3	MgO	N_2O	K_2O	SO_3	
Slag	21.32	5.61	61.72	3.12	3.94		0.79	2.51	(Kim et al., 2019)
Slag	30.40	10.50	50.37	0.53	3.20				(Aziz et al., 2020)
Slag	28.70	9.50	52.60	0.60	2.10			4.10	(Park et al., 2017)
Slag	35.33	9.94	34.65	0.62	14.63	0.31	0.44	3.97	(Shi and Xie, 1998)
Slag	34.24	13.75	42.26	1.10	5.88	0.28	0.32	0.24	(Karri et al., 2022)
slag	31.63	13.42	36.35	1.32	9.12	0.34	0.46	0.00	(Yang et al., 2016)
slag	40.00	5.91	46.98	0.32	5.87	0.64	0.50	1.62	(Krivenko et al., 2014)
Slag	31.00	18.00	37.20	5.45	9.70	0.09	1.04	1.40	(Samantasinghar and Singh, 2018)
Slag	35.7	11.21	39.40	0.42	10.74	0.26	0.48	0.58	(Puligilla and Mondal, 2013)
Slag	31.85	17.31	41.20	0.34	6.13	0.03	0.33	1.78	(Wang et al., 2022b)
Fly ash	37.00	9.89	21.00	4.45	3.50	0.56		1.91	(Karri et al., 2022)
Fly ash	50.94	24.56	2.86	13.25	1.98	0.69	2.69	0.00	(Krivenko et al., 2014)
Fly ash	57.41	28.50	2.143	5.45	0.54	0.60	1.26	0.90	(Samantasinghar and Singh, 2018)
Fly ash	60.17	21.91	1.81	7.57	1.28	0.81	2.13	0.17	(Puligilla and Mondal, 2013)
Fly ash	57.02	32.35	2.88	3.01	0.58	0.03	2.07	0.41	(Wang et al., 2022b)

Table 4-3 SEM-EDS of bulk mortar binder

Mortar	SEM	EDS	Chemical compositions
OGPm-1	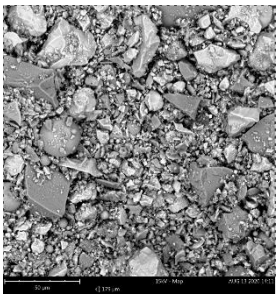	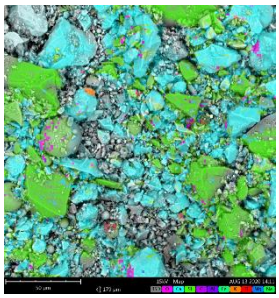	
OGPm-2	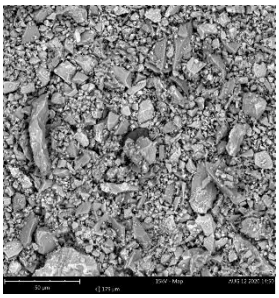	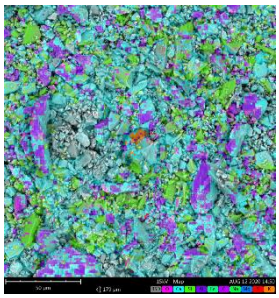	
OGPm-3	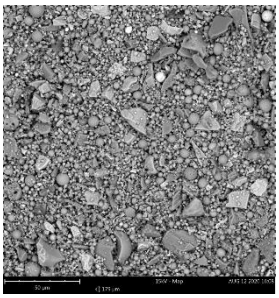	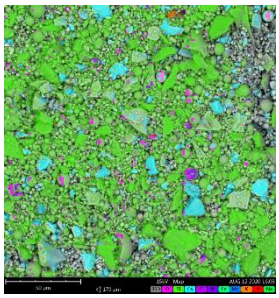	
OGPm-4	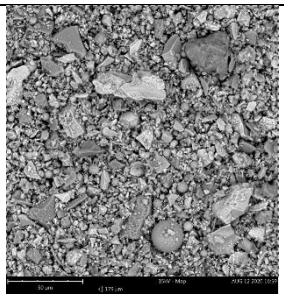	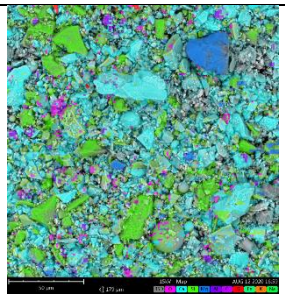	
CACm	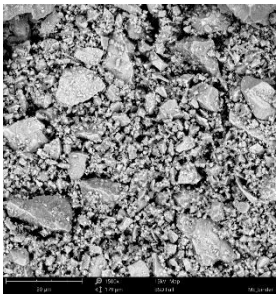	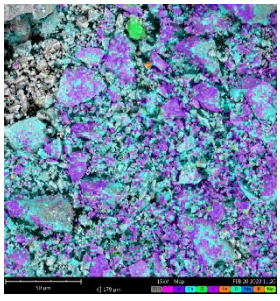	

Composition	Element (wt.%)	Oxide (wt.%)
Si	18.92	46.32
Al	2.81	6.08
Ca	25.75	16.19
Fe	1.37	2.27
Mg	0.41	0.00
Na	0.14	0.40
S	1.10	0.00

Composition	Element (wt.%)	Oxide (wt.%)
Si	12.35	28.15
Al	11.30	22.75
Ca	23.96	35.72
Fe	5.64	8.59
Mg	1.04	1.84
Na	1.29	1.85
S	0.41	1.09

Composition	Element (wt.%)	Oxide (wt.%)
Si	26.11	63.88
Al	5.91	12.77
Ca	9.98	15.97
Fe	2.62	4.28
Mg	0.76	1.44
Na	0.18	0.28
S	0.48	1.37

Composition	Element (wt.%)	Oxide (wt.%)
Si	15.74	36.76
Al	3.88	8.00
Ca	24.38	37.25
Fe	1.38	2.15
Mg	5.87	10.63
Na	0.09	0.13
S	1.86	5.07

Composition	Element (wt.%)	Oxide (wt.%)
Si	8.63	17.59
Al	20.42	36.75
Ca	28.69	38.24
Fe	4.97	6.77
Mg	0.38	0.60
Na	0.04	0.05
S	0.00	0.00

Figure 4-2 shows the microscopic characterisation of the binder contained in OGPm-1, OGPm-2, OGPm-3, OGPm-4, and CACm using Scanning electron microscopy and energy dispersive spectroscopy (SEM-EDS). In general, bulk SEM images of the mortars show non-uniform materials. Superimposed on these photos are identification of the mineral phases. To identify the materials in the binder, the elemental composition of the mortar components was analysed using SEM-EDS. The SEM-BSE image with EDS analysis of specific binder material is shown in Table 4-4. The composition of the components was compared with reported compositions of fly ash, blast furnace slag, silica fume, and calcium aluminate cement (see Table 4-5).

The fly ash particles in Table 4-4 have a notable spherical shape. The elemental analysis of the fly ash is consistent with the chemical composition of fly ash reported (Mohammed Razzaq et al., 2017, Wang et al., 2022a, Kuri et al., 2022, Gomaa et al., 2020). Table 4-5 reports the four principal constituents of fly ash based on SEM/EDS analysis as SiO_2 (39.95-65.50 wt%), CaO (0.17-18.28 wt%), Al_2O_3 (31.92–37.06 wt%) and Fe_2O_3 (0.93-6.60 wt%). In this study, the chemical composition of fly ash is 53.29 wt.% SiO_2, 2.43 wt.% CaO, 49.11 wt.% Al_2O_3 and 4.48 wt% Fe_2O_3. These compositions are within the range of chemical fly ash composition from other studies reported in Table 4-5.

According to ASTM C618, low and high calcium fly ash were classified as class F when the total composition of fly ash contained a minimum of 50 wt.% of $SiO_2 + Al_2O_3 + Fe_2O_3$ with a maximum of 18 wt.% CaO and class C if the total composition of fly ash contained a minimum of 50 wt.% of $SiO_2 + Al_2O_3 + Fe_2O_3$ containing more than 18 wt.% CaO (ASTM-C618, 2022). Therefore, this result suggested that the fly ash used in this study is low calcium fly ash (class F). Fly ash was also observed in OGPm-1, OGPm-3, and OGPm-4 (see Figure 4-2). The light colour of the angular particle shape was analysed using SEM-EDS in Table 4-4. This is expected to be blast furnace slag (BFS). The BFS is one of the common aluminosilicate precursors for geopolymer production. It is a by-product of iron production in blast furnaces

where iron ore, coke and limestone are used as feed (Cwirzen, 2020). The BFS mainly comprises silica, calcium oxide, magnesium oxide, ferrite and aluminium oxides with highly cementitious properties (Cwirzen, 2020). Slag is considered a high calcium aluminosilicate precursor for alkali-activated binders (AAB). The elemental analysis of the particle using EDS is consistent with the chemical composition of BSF reported in Table 4-5. In this study, the chemical composition of the angular particle-shaped particles is 36.66 wt.% SiO_2, 34.65 wt.% CaO, 14.93 wt.% Al_2O_3 and 5.95 wt.% MgO. The chemical composition of BSF is reported to be in the range of 37.33-52.68 wt.% SiO_2, 8.20-20.07 wt.% Al_2O_3, 28.74-34.55wt.% CaO, and 0-13.10 wt.% MgO (Zhang et al., 2022, Matalkah and Soroushian, 2022). This suggests that the light-coloured angular-shaped particles appear to be BSF. The BSF was observed in OGPm-1, OGPm-2, OGPm-3, and OGPm-4 (see Figure 4-2).

The shapes of fly ash and slag particles are different primarily because they are produced from different processes and materials, resulting in different shapes and physical and chemical properties. One of the main processes is the cooling rate of the material. Fly ash is created as a by-product. The shape of fly ash particles is spherical due to surface tension, and its structure is dependent on particle size, which is influenced by the cooling rate (Matsunaga et al., 2002).

In contrast, slag is a by-product of the steel manufacturing industry (Saberian et al., 2022). It contained a calcium-silicate-based product removed from the top of molten iron during its extraction from ore in a blast furnace (Wang et al., 2020a). The slag is rapidly cooled, which inhibits the formation of rounded or spherical particles, leading to characteristic glassy and irregular shapes (Provis et al., 2015, Pal et al., 2003).

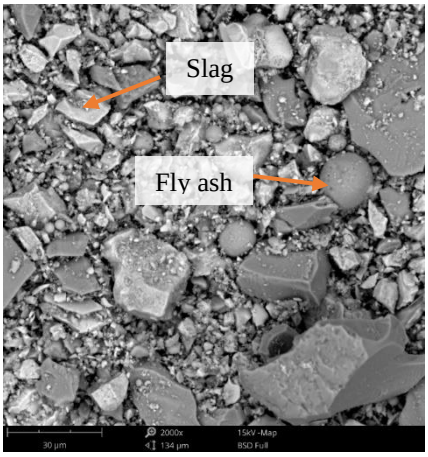

a. OGPm-1

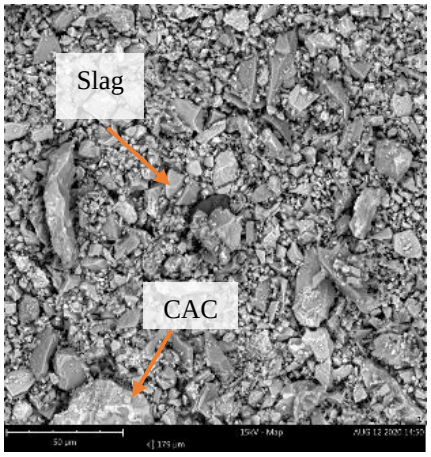

b.OGPm-2

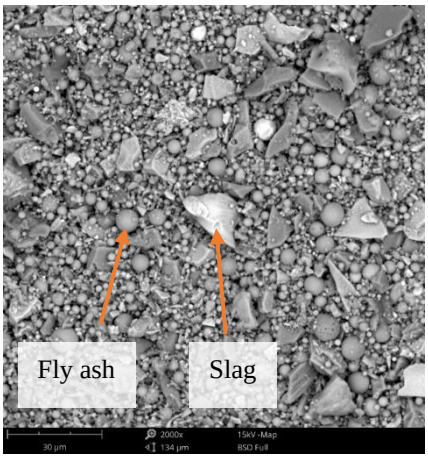

c.OGPm-3

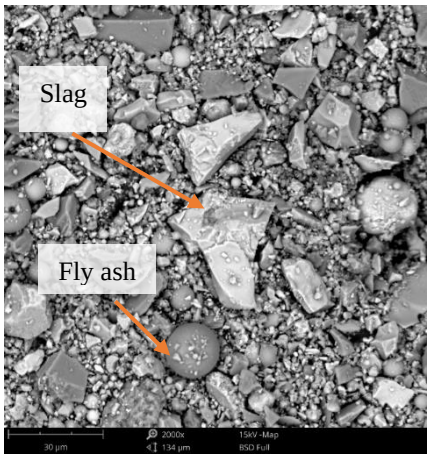

d.OGPm-4

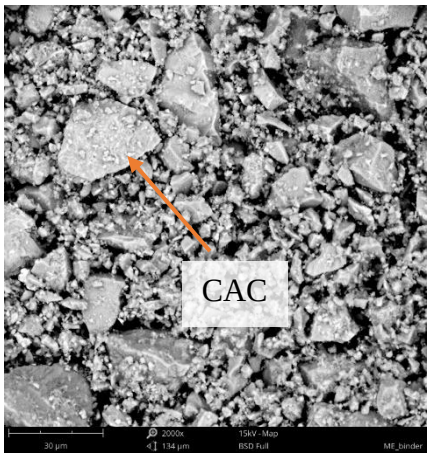

e.CACm

Figure 4-2 SEM image of unhydrated OGPm-1, OGPm-2, OGPm-3, and OGPm-4 and CACm

Table 4-4 SEM images of mortar precursors and corresponding EDS analyses: i) fly-ash, ii) blast furnace slags, iii) calcium aluminate cement

<table>
<tr><th>Particle</th><th>SEM</th><th>Chemical compositions</th></tr>
<tr><td>Fly ash</td><td> 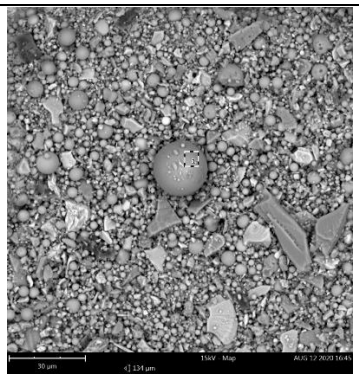 </td><td>
<table>
<tr><th>Component</th><th>Element (wt.%)</th><th>Oxide (wt.%)</th></tr>
<tr><td>Si</td><td>28.08</td><td>55.14</td></tr>
<tr><td>Al</td><td>20.68</td><td>35.87</td></tr>
<tr><td>Ca</td><td>1.21</td><td>1.55</td></tr>
<tr><td>Fe</td><td>4.56</td><td>5.98</td></tr>
<tr><td>Mg</td><td>0.69</td><td>1.05</td></tr>
<tr><td>Na</td><td>0.33</td><td>0.41</td></tr>
<tr><td>S</td><td>0.00</td><td>0.00</td></tr>
</table>
</td></tr>
<tr><td>Slag</td><td> 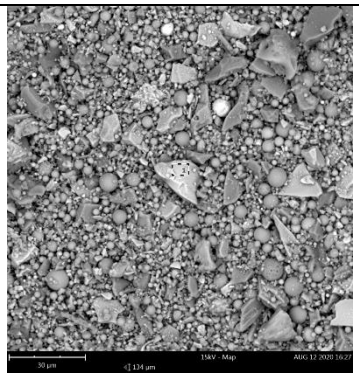 </td><td>
<table>
<tr><th>Component</th><th>Element (wt.%)</th><th>Oxide (wt.%)</th></tr>
<tr><td>Si</td><td>18.67</td><td>36.66</td></tr>
<tr><td>Al</td><td>8.61</td><td>14.93</td></tr>
<tr><td>Ca</td><td>26.98</td><td>34.65</td></tr>
<tr><td>Fe</td><td>0.12</td><td>0.16</td></tr>
<tr><td>Mg</td><td>3.67</td><td>5.59</td></tr>
<tr><td>Na</td><td>0.07</td><td>0.09</td></tr>
<tr><td>S</td><td>0.51</td><td>1.17</td></tr>
</table>
</td></tr>
<tr><td>Calcium aluminate cement</td><td> 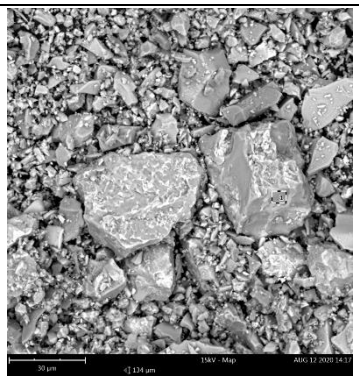 </td><td>
<table>
<tr><th>Component</th><th>Element (wt.%)</th><th>Oxide (wt.%)</th></tr>
<tr><td>Si</td><td>3.31</td><td>6.54</td></tr>
<tr><td>Al</td><td>16.06</td><td>28.04</td></tr>
<tr><td>Ca</td><td>40.39</td><td>52.22</td></tr>
<tr><td>Fe</td><td>8.79</td><td>11.61</td></tr>
<tr><td>Mg</td><td>0.52</td><td>0.80</td></tr>
<tr><td>Na</td><td>0.50</td><td>0.62</td></tr>
<tr><td>S</td><td>0.07</td><td>0.16</td></tr>
</table>
</td></tr>
</table>

Table 4-5 Chemical composition (wt%) of the composition of OGPm and CACm based on quantitative EDS microanalysis

Mortar Components	SiO_2	Al_2O_3	CaO	Fe_2O_3	MgO	Na_2O	SO_3	References
Fly ash	65.50	31.82	0.33	2.36	0.00	0.00	0.00	(Mohammed Razzaq et al., 2017)
Fly ash	49.79	48.77	0.22	1.22	0.00	0.00	0.00	(Wang et al., 2022a)
Fly ash	49.23	32.66	10.24	5.61	1.41	0.86	0.00	(Kuri et al., 2022)
Fly ash	39.95	26.94	15.37	5.55	1.91	10.28	0.00	(Gomaa et al., 2020)
Slag	46.79	11.89	34.55	0.00	6.56	0.21	0.00	(Zhang et al., 2022)
Slag	52.68	18.61	28.71	0.00	0.00	0.00	0.00	(Humad et al., 2019)
Slag	36.99	8.20	33.12	0.00	11.77	9.93	0.00	(Matalkah and Soroushian, 2022)
Slag	37.33	20.07	29.31	0.19	13.10	0.00	0.00	(Wang et al., 2022a)
CAC	4.5	48.8	33.6	9.9	0.3	0.4	0.9	(Adesanya et al., 2023)
CAC	3.1	49.7	39.2	2.7	0.5	0.3	1.3	(Adesanya et al., 2023)

4.2.2 FINE AGGREGATES

4.2.2.1 CHEMICAL COMPOSITION

Sand, including some crushed stone, is generally used as the fine aggregate for mortar (Young, 2021). However, the fine aggregates for specialty mortars can often be sand, similar siliceous materials, or clinker (Ng and Foster, 2013, Darvish et al., 2020). The elemental composition of the fine aggregates from OGPm and CACm mortar used in this study is shown in Table 4-6. The aggregates mixed in OGPm were mostly high SiO_2 aggregates containing more than 91wt.% SiO_2 except for the aggregated mixed in OGPm-2 containing only 71 wt.% SiO_2. Figure 4-3 compares the composition of SiO2, Al_2O_3, and CaO from aggregate mixed in mortars with glass and sand from literature (See Table *4-7*). It suggested that the fine aggregate that mixed in the OGPm-1, OGPm-3, and OGPm-4 was sand. The aggregates mixed in OGPm-1, OGPm-3, and OGPm-4 are

composed mainly of 91.61 to 97 wt.% SiO_2. Meanwhile, the aggregate in OGPm-2 contained 71.24 wt.% SiO_2, 14.85 wt.% Na_2O, and 9.33 wt.% CaO, which is consistent with the glass composition (Rajabipour et al., 2010, Abalouch et al., 2021, Gorospe et al., 2019). The aggregate composition in CACm is similar to Aluminous Aggregate (ALAG), which is referred to as synthetic calcium aluminate aggregate (ALAG). It contains mainly 39.5 wt.% Al_2O_3 and 36.1 wt.% CaO (see Table *4-7*) (Strauss Rambo et al., 2019, Scrivener et al., 1999). It was observed that the CACm binder and CACm aggregate presented similar chemical compositions (see Table 4-1 and Table 4-6). The similarity in the composition of binder and aggregate suggested that the CACm used in this study is 100% CAC.

As mentioned, mortars are mixtures of cement binder, aggregate (sand and gravel), and water. The chemical composition of aggregates can significantly impact the properties and performance of mortars. The aggregate containing reactive minerals or chemical compounds can lead to chemical reactions within the mortar known as Alkali activated reaction (AAR). There are two main types of AAR: Alkali-Silica Reaction (ASR) and Alkali-Carbonate Reaction (ACR). ASR results from a chemical reaction between hydroxyl ions in pore water and silica from aggregates and cement of the concrete matrix (Paudel et al., 2020). This reaction forms a gel that absorbs water and swells, leading to the expansion of the concrete. The expansion can result in cracking and reduced durability of the concrete. However, it must be noted that the ASR effect usually takes several years due to slow reaction (Paudel et al., 2020). ACR is the reaction between the carbonate aggregates, such as dolomite or limestone, with typical texture used as a coarse aggregate of concrete with alkalis in the concrete (Qian et al., 2002). Dedolomitization was thought to be the underlying mechanism leading to expansion without any reactive silica involvement. However,

the ACR is less common than ASR but can still be problematic. This reaction forms a gel, which can also cause expansion and cracking.

Table 4-6 Bulk chemical composition of aggregates from OGPm and CACm by XRF

Aggregate (wt%)					
Components	**OGPm-1**	**OGPm-2**	**OGPm-3**	**OGP-4**	**CACm**
	Aggregate	**Aggregate**	**Aggregate**	**Aggregate**	**Aggregate**
Na_2O	0.21	14.85	0.07	0.09	0.36
MgO	0.03	4.01	0.02	0.07	1.00
Al_2O_3	2.62	0.50	0.36	0.31	39.54
SiO_2	91.61	71.24	96.95	96.99	4.9
SO_3	0.07	0.20	<0.01	0.04	0.03
K_2O	1.47	0.06	0.02	0.02	0.28
CaO	0.82	9.33	0.10	0.30	36.14
Fe_2O_3	0.52	0.38	0.39	0.35	15.75
LOI.	0.28	(+0.07)	0.06	0.01	0.21

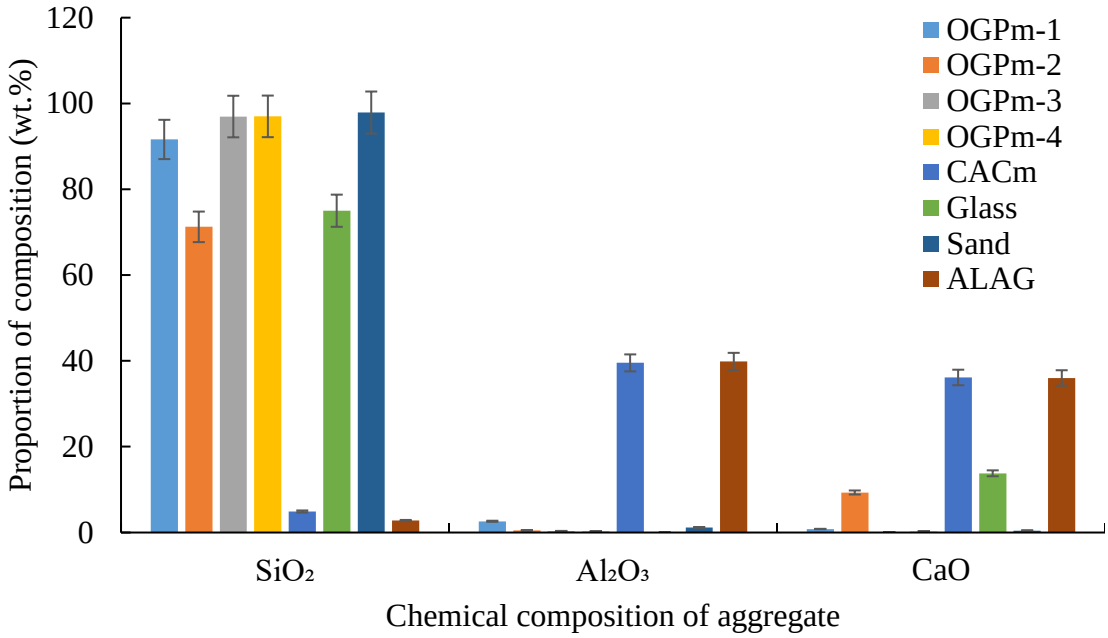

Figure 4-3 SiO_2, Al_2O_3, and CaO from XRF analysis of mortar aggregates

Table 4-7 Chemical composition (wt.%) of aggregate based on quantitative EDS microanalysisMortar Components

Mortar Components	SiO_2	Al_2O_3	CaO	Fe_2O_3	MgO	Na_2O	SO_3	References
Glass	73.78	0.00	5.70	0.00	0.00	20.52	0.00	This study
Glass	75.00	0.00	13.80	0.00	0.00	9.00	0.00	(Rajabipour et al., 2010)
Glass	73.00	0.00	14.20	0.00	0.00	10.10	0.00	(Rajabipour et al., 2010)
Glass	71.14	0.00	10.66	0.00	0.00	18.21	0.00	(Abalouch et al., 2021)
Glass	81.62	0.00	10.02	0.00	0.00	8.36	0.00	(Gorospe et al., 2019)
Sand	97.89	1.19	0.45	0.00	0.04	0.44	0.00	This study
River sand	83.90	16.10	0.00	0.00	0.00	0.00	0.00	(Badapalli et al., 2022)
Lake sand	100.00	0.00	0.00	0.00	0.00	0.00	0.00	(Badapalli et al., 2022)
Beach sand	82.14	17.86	0.00	0.00	0.00	0.00	0.00	(Badapalli et al., 2022)
Quartz sand	96.25	3.75	0.00	0.00	0.00	0.00	0.00	(Sulistiyono et al., 2020)
Quartz sand	87.05	3.59	0.02	1.29	0.00	0.13	0.00	(Temuujin et al., 2010)
Quartz sand	71.60	15.36	7.58	0.72	4.73	0.00	0.00	(Taciroğlu et al., 2022)
ALuminous AGgregate (ALAG)	2.79	39.88	36.02	14.48	0.00	0.00	1.05	(Strauss Rambo et al., 2019)

The elemental composition of specific aggregate was analysed using SEM-EDS, as shown in Figure 4-4. The fine aggregates used in OGPm-1, OGPm-3, and OGPm-4 showed a chemical composition of 97.83 wt.% SiO_2, 1.25 wt.%Al_2O_3, and 0.32 wt.%CaO are consistent with the chemical composition of sand reported in Table 4-7. The aggregate use in OGPm-2 shows a chemical composition of 73.78 wt.% SiO_2, 20.52 wt.% Na_2O, and 5.70 wt.% CaO is consistent with recycled glass from other studies and XRF analysis in this study (see Table 4-6 and Table 4-7). For aggregate mixed in CACm presents 29.40 wt.% CaO and 33.34 wt.% Al_2O_3, the chemical

composition was consistent with the chemical composition obtained from XRF analysis and reported in the literature (see Table 4-6 and Table 4-7). These results confirmed that sand was used as fine aggregate for OGPm-1, OGPm-3, and OGPm-4, Glass was used as fine aggregate for OGPm-2, and ALuminous AGgregate (ALAG) was used as fine aggregate for CACm.

Materials

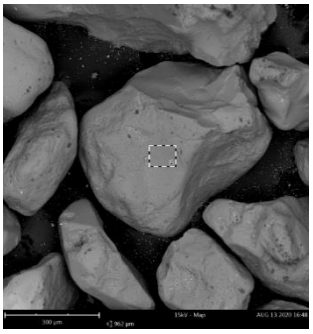

Quartz sand

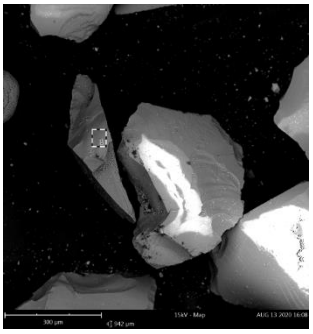

Glass

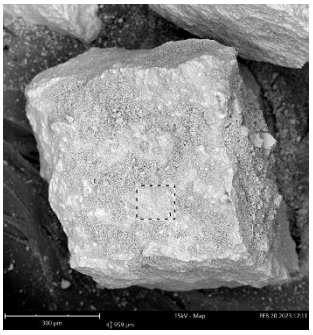

CAC aggregate

EDS

Component	Element (wt.%)	Oxide (wt.%)
Si	29.70	96.65
Al	0.43	1.24
Ca	0.15	0.32
Fe	0.00	0.00
Mg	0.02	0.05
Na	0.26	0.53
S	0.32	1.22

EDS

Component	Element (wt.%)	Oxide (wt.%)
Si	26.69	69.48
Al	0.00	0.00
Ca	3.15	5.36
Fe	0.00	0.00
Mg	2.89	5.83
Na	11.78	19.32
S	0.00	0.00

EDS

Component	Element (wt.%)	Oxide (wt.%)
Si	6.95	11.70
Al	22.43	33.34
Ca	21.95	29.40
Fe	6.08	6.84
Mg	0.34	0.44
Na	0.21	0.22
S	0.01	0.02

Figure 4-4 SEM images of mortar aggregate and corresponding EDS analyses: i) quartz sand, ii) glass and iii) CAC aggregate

4.2.2.2 SHAPE OF AGGREGATE

The aggregate particle shape characteristics and variations can affect the workability and strength of mortar and concrete (Hewlett and Liska, 2019). The shapes of aggregate particles can be described with the two principal parameters being "sphericity" and "roundness"(Hewlett and Liska, 2019). The particle surface texture also influences the strength of the mortar. The rough surface particle will have a high bonding area with mortar binder compared to the smooth surface particle of the same volume. However, the smooth surface particle influences the density of the mortar. The smooth surface particle requires a thin layer of paste to lubricate their movement during the packing process, allowing it to be the denser packing of mortar sample (Bashar et al., 2014).

The morphology of fine aggregates from geopolymer and calcium aluminate cement mortar was analysed using the Leica DM2500 optical microscope. The microscope image showing the aggregate morphology and corresponding elemental composition based on SEM/EDS analysis is provided in Figure 4-5 and Figure 4-4, respectively. The images and colour of the aggregates shown in Figure 4-5 suggest that the aggregate used varied for each mortar. The visual assessment of a particle grain shape based on the method by Powers (1953) is shown in Figure 4-6. The aggregate shapes in OGPm-1, OGPm-3, and OGPm-4 all have similar shapes, and these are sub-rounded with high sphericity compared to the charts used for shape assessment. Meanwhile, the aggregate in OGPm-2 was observed to be very angular with low sphericity.

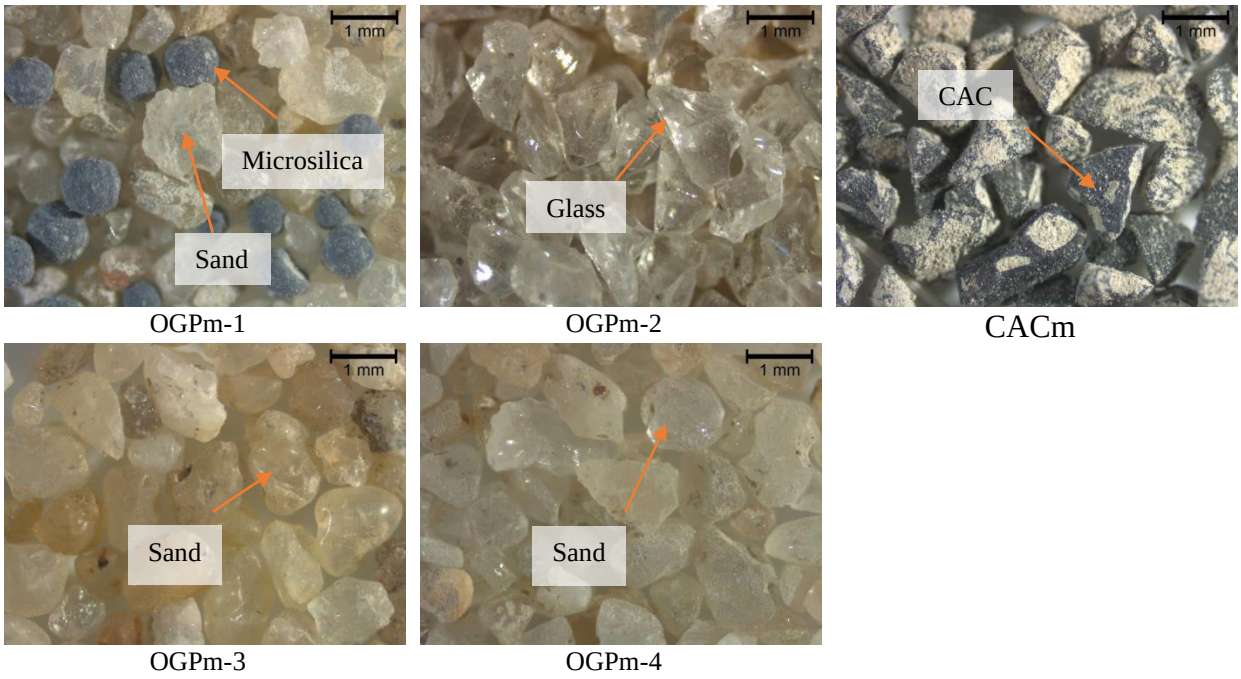

Figure 4-5 Shape of fine aggregates in geopolymer mortars

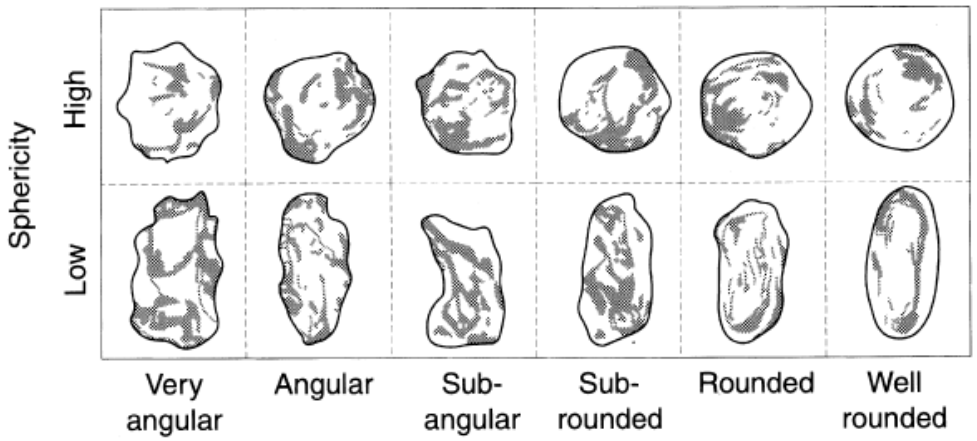

Figure 4-6 Charts for the visual assessment of particle shape provided by Powers (1953)

4.3 MORTAR MIX DESIGN AND PARTICLE SIZE DISTRIBUTION OF BINDER AND FINE AGGREGATES

The particle size distribution of both the binder and aggregates mortar and the mix design directly affected the fresh and hardened characteristics of the mortars (Mehdipour and Khayat, 2017).

Mortar design with the appropriate mix of binder, fine aggregates, admixtures, fibres, and other additives can improve physical-chemical properties and mechanical properties (John et al., 2021). Therefore, the design of the mortar is an important consideration in its selection because the mix affects the mortar's physical properties, including mechanical properties (Beall, 2012, Mehdipour and Khayat, 2017). Most geopolymer designs consist of a binder that is composed of aluminosilicate precursor (e.g. fly ash, slag, geothermal silica), activators consisting of alkali (NaOH, KOH) and water glass or sodium silicate ($NaSiO_3$) and additives (e.g.fibre, plasticiser) (Luukkonen et al., 2018b). Therefore, this section presents the mixed design of mortar used in this study, including the particle size distribution of aggregate and binder and aggregate grading

4.3.1 MORTAR DESIGN

Geopolymer mortars are prepared from activating aluminosilicate precursors using an alkali solution (Davidovits, 2020). As shown in Table 4-8, the key aluminosilicate precursors used are low-Ca aluminosilicate precursor (e.g. fly ash, metakaolin) and high-Ca aluminosilicate precursor (blast furnace slag). However, geopolymers can be made from single or multi-aluminosilicate precursors. This blended geopolymer provides several advantages, including improved mechanical strength, waste utilisation, durability, and sustainability (Zhang et al., 2020). The primary reaction of blended low-Ca and high-Ca aluminosilicate precursors can formulate various hydration products, including calcium silicate hydrate (C–S–H gel), calcium aluminosilicate hydrate (C-A-S-H) gel, calcium-sodium aluminosilicate hydrate (C-N-A-S-H) gel and sodium aluminosilicate hydrate (N-A-S-H) gel (Zhuang et al., 2016). Moreover, geopolymer binders can be blended with other binders, such as ordinary Portland cement (OPC) or calcium aluminate cement (CAC), to improve mechanical strength (Cao et al., 2018).

Figure 4-7 shows the mixed proportion of binder to aggregate from OGPm and CACm in this study. The binder and aggregate ratio (B/A) affected the chemical and physical properties, such as the formation of hydration phases, shrinkage, and microcrack (Gameiro et al., 2014). This study's B/A of OGPm and CACm varied from 0.47–0.80. The B/A ratio closely follows other studies' reported B/A ratio values between 0.25 and 1.00 (see Table 4-8). These results confirmed that this study's B/A of OGPm and CACm agreed with other studies.

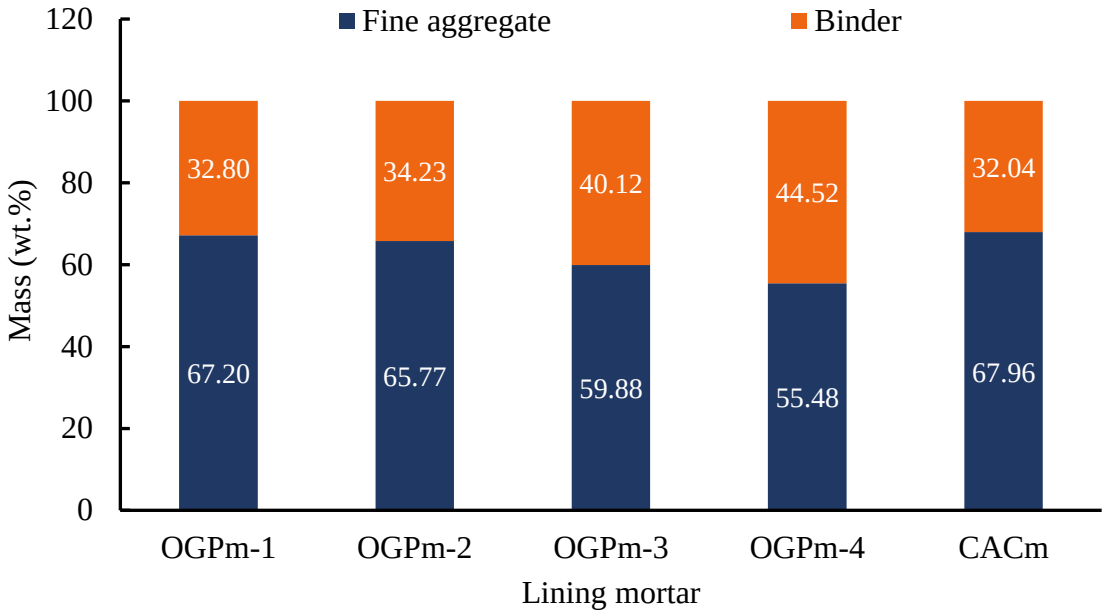

Figure 4-7 Mixed proportion between binder and aggregate of OGPm and CACm mortar

Table 4-8 Particle size of binder and aggregate for geopolymer mortars

Precursors	Binder size (μm)			Aggregate size (μm)			Fineness modulus of aggregate	Binder/Aggregate ratio	References
	D_{10}	D_{50}	D_{90}	D_{10}	D_{50}	D_{90}			
Fly ash	8.10	32.80	92.78				1.25	0.33	(Görhan and Kürklü, 2014)
Fly ash	0.35	3.40	18.25						(Kumar and Kumar, 2011)
Fly ash		14.40		250	450	700		0.50	(Temuujin et al., 2010)
Fly ash			45.00	150	800	1500		0.33	(Atiş et al., 2015)
Fly ash	5.00	24.80	75.00					0.36	(Hadi et al., 2018)
Fly ash	5.00	20.50	60.00					0.36	(Hadi et al., 2018, Sitarz et al., 2020)
Fly ash	4.00	17.00	43.00					0.36	(Hadi et al., 2018, Sitarz et al., 2020)
Fly ash	0.35	9.00	25.00					0.36	(Hadi et al., 2018, Sitarz et al., 2020)
Fly ash								0.77	(Hardjito et al., 2008)
Fly ash		8.50					1.8	1	(Phoo-ngernkham et al., 2015)
Fly ash	1.50	15.00	90.00				1.94	0.62	(Kuri et al., 2022)
BFS	0.50	20.00	45.00	170	1000	2000		0.25	(Islam et al., 2014)
BFS	1.30	6.50	60.00	150	600	2000		0.9	(Huseien et al., 2018)
BFS		10.80		140	750	1580		0.50	(Luukkonen et al., 2018a)
BFS	1.11	25.75	84.24						(Kumar et al., 2010)
Fly ash + Slag				125	750	1500		0.67	(Sitarz et al., 2020)

4.3.2 PARTICLE SIZE DISTRIBUTION

The particle size distribution of the binder and aggregate mortars are shown in Figure 4-9. D_{10}, D_{90}, and D_{50} are terms used in particle size analysis to describe the size distribution of a sample of aggregate material. D_{10} represents the particle size such that 10% of the sample is smaller than this size. D_{50} is the median particle size distribution meaning that 50% of the total particle are smaller than this size and another 50% are larger than this size. D_{90} represents the particle size such that 90% of the sample is smaller than this size. In this study, D_{50} is used as representative of average particle size. The summary of the particle size analysis is presented in Table 4-9.

Table 4-9 shows the median diameter (D_{50}) of the OGPm binders is from 12.70-15.40 µm, and the control CACm is 14.70 µm. These are similar to the reported binder particle size, varied from 3.40 - 32.80 µm (see Table 4-8). The mortar binders are prepared by milling the aluminosilicate precursor, specifically blast furnace slag and calcium aluminate clinkers, to a particle size of less than 75 µm (Usha et al., 2016, Ng and Foster, 2013, Khan, 2019). It is generally agreed that binder particles larger than 45 µm are challenging to hydrate thoroughly (al-Swaidani et al., 2016). Therefore, based on their size, the mortar binder for the commercial geopolymers used in this study is expected to hydrate well over the required curing period.

4.3.3 FINE AGGREGATE GRADING

The grading of aggregates is based on the distribution of particle size that will reduce void formation when the mortar is compacted (Mehta and Monteiro, 2014). The particle size distribution of the aggregates significantly impacts the performance and the properties of the mortar, such as workability, compressive strength, shrinkage, and porosity (Lee and Estrada, 2020, Nazari et al., 2011, Assi et al., 2018, Mehdipour and Khayat, 2017). If the aggregate size is uniform, more voids will form with the compacter mortar, while aggregates of different sizes will generate fewer voids and form stronger mortars (Mehta and Monteiro, 2014). In addition,

adequately graded aggregates will also require less cement to generate high-quality mortars without reducing the strength and workability of mortar, which can result in significant economic benefits. Moreover, the specific surface area of the aggregate controls the amount of water needed to wet and lubricate the mix. Increasing the fine aggregate content can affect the cohesion of the mortar mix between binder and aggregate. Therefore, controlling the aggregate grading will assist in achieving high concrete densities and strengths with minimum cement contents and this also reduces the risks of segregation and bleeding.

The grading curves are represented by a cumulative percentage of mass passing through a sieve size plotted as a function of the sieve opening on a logarithmic scale (Lee and Estrada, 2020). There are essentially four (4) grading of aggregates:

i) Well-graded aggregate – this type of graded aggregate is one where the aggregate sizes are present in approximately equal weights.
ii) Gap-graded aggregate – this type of graded aggregate is characterised by a wide range of particle sizes but missing middle particle sizes.
iii) Uniformly graded aggregate –this type of graded aggregate contains a large number of particles that approximately have the same size.
iv) Open-graded aggregate – this type of graded aggregate presents a small percentage of small-size particles.

The grading chart shown in Figure 4-8 can be used to characterise the aggregate grading curve. In this study, the aggregate grading curve is shown in Figure 4-9b. It is characterised using the grading chart. As shown, the mortars in this study follow the ‘well’ grading and are considered suitable. The aggregate analysis shows that the median particle size (D_{50}) of OGPm and CACm mixed within the OGPm varies from 0.40 mm to 0.80 mm, and CACm is 0.90 mm (See Table

4-9). The particle size of the aggregate showed a similar size to the reported aggregate particle size, varying from 0.45- 0.8 mm (see Table 4-8).

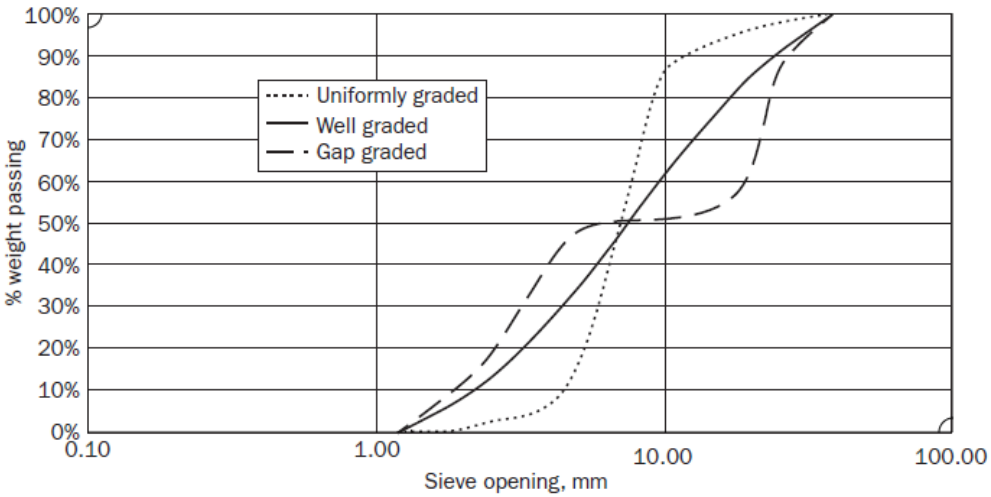

Figure 4-8 Aggregate gradings adopted from Lee and Estrada (2020).

Table 4-9 The particle size of a binder and aggregates of OGPm and CACm (this study)

Materials	**The particle size of the binder (µm)**			**The particle size of aggregate (µm)**		
	D_{10}	**D_{50}**	**D_{90}**	**D_{10}**	**D_{50}**	**D_{90}**
OGPm-1	3.17	14.70	38.80	110	400	900
OGPm-2	2.94	15.40	46.90	130	800	2700
OGPm-3	2.64	13.80	48.90	110	460	2000
OGPm-4	2.54	12.70	38.00	100	400	1100
CACm	2.03	14.70	50.80	140	900	3000

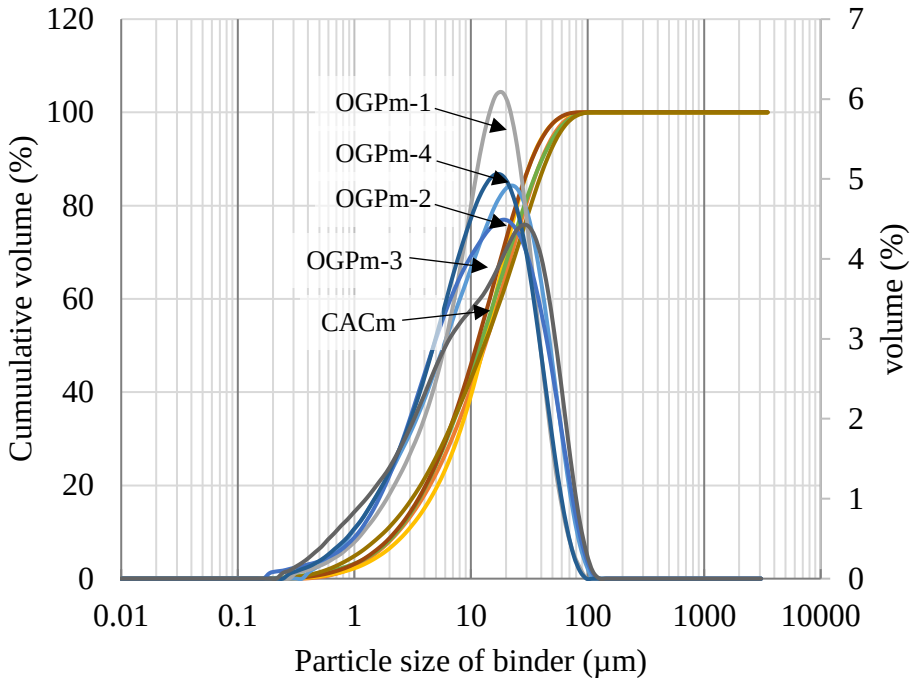

a. Binder

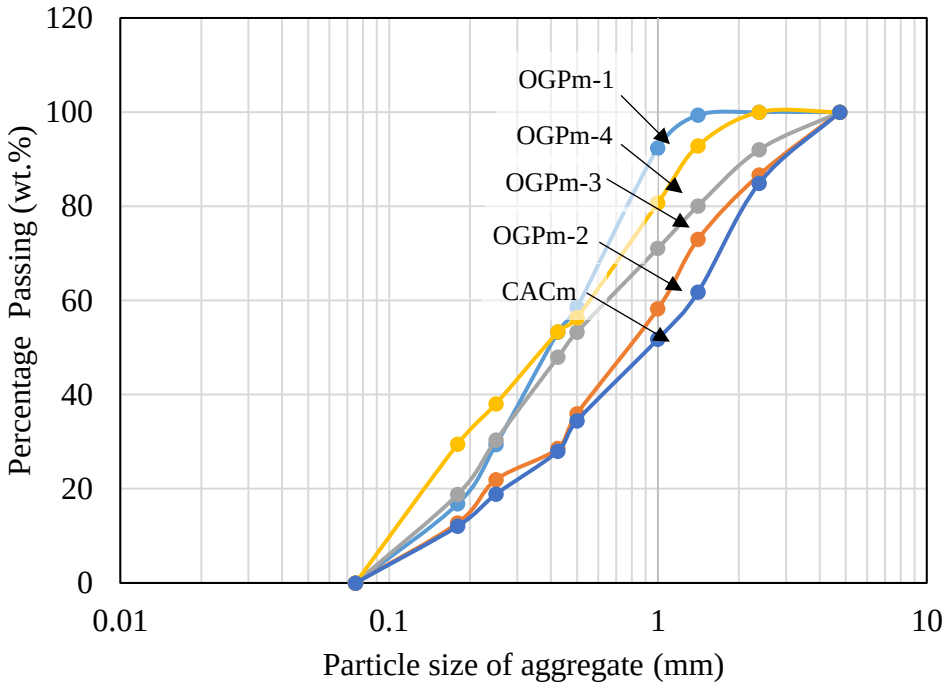

b. grading curve of aggregate

Figure 4-9 Particle size distribution of OGPm and CACm: (a).binder and (b). aggregate

Aside from determining aggregate grading using an aggregate grading chart, as shown in Figure 4-8, an alternative assessment of the aggregate grading uses the coefficient of curvature (Cc). The coefficient of curvature is a measure of the aggregate grading curve at a specific point. (Islam et al., 2014). It is calculated using Equation 4.1.

$$C_C = \frac{{D_{30}}^2}{D_{10} \times D_{60}} \qquad \text{Equation 4.1}$$

Where D_{10} represents the particle size such that 10% of the sample is smaller than this size. D_{30} is the particle size distribution, meaning that 30% of the total particles are smaller than this size, and another 70% are larger than this size. D_{60} represents the particle size such that 60% of the sample is smaller and another 40% is larger than this size.

The coefficient of curvature value lies between 1 and 3, indicating a well-graded aggregate (Islam et al., 2014). The C_C calculated in this study is presented in Table *4-10*. It reveals that the OGPm-2 is the most well-graded aggregate, followed by CACm, OGPm-1, OGPm-3, and OGPm-4, respectively.

Table 4-10 Coefficient of curvature of the mortar used in this study

Material	D_{10}	D_{30}	D_{60}	C_C
OGPm-1	0.14	0.25	0.52	0.90
OGPm-2	0.16	0.44	1.05	1.17
OGPm-3	0.13	0.25	0.69	0.67
OGPm-4	0.11	0.18	0.58	0.53
CACm	0.16	0.45	1.34	0.93

Figure 4-10 shows the correlation between the coefficient of curvature and the initial UCS of mortar. The result is highly scatted, but the UCS value appears to increase trend when the coefficient of curvature increases. This correlation confirmed that the mortar prepared from

well-graded aggregate exhibited better initial UCS due to well-graded aggregate mixed in the mortar, leading to optimum porosity and more dense material (Jamil et al., 2022).

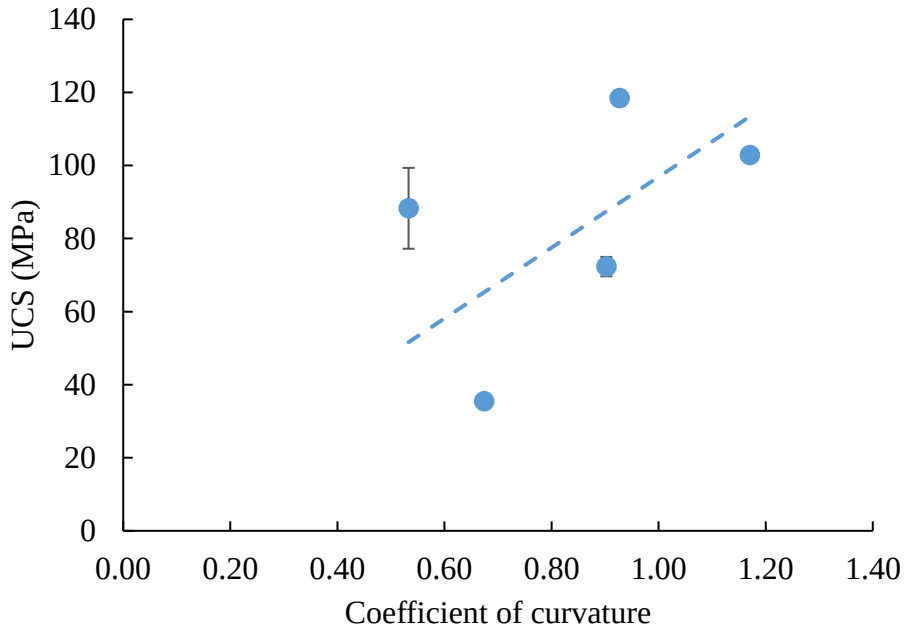

Figure 4-10 Correlation of coefficient of curvature and UCS at 28 days of curing

Aside from the impact on physical and chemical properties, the aggregate particle size also impacts the application technique. In this study, the geopolymer mortars were applied using shotcrete technology in the field trial test, either by wet-spray or dry-spray methods. Wet spray involves the pre-mixed mortar mixed with water, and then the fresh mortar is pumped to the nozzle, where the compressed air accelerates it and is sprayed onto the application surface (Kaufmann et al., 2013, Taylor, 2011). Dry spray involves pre-mixed mortar and then conveys the dry pre-mixed mortar through a pipe to the nozzle, where water is added to hydrate mortar and is sprayed onto the application surface (Taylor, 2011). Controlling the application, for example, to ensure the correct build or thickness is achieved and the lining adheres to the host material will determine the long-term durability of the lining materials. Mortar application was not addressed in this study. However, it is essential to control this feature from the mortar mix design and the particle size distribution of the mortar components. A key requirement to reduce

blockage during the shotcrete application based on WSA 161-2021 is that the maximum size of the aggregates must be less than 5 mm or 75% of the nozzle. WSA 161 is the Water Industry Standard for Alkali Activated Binder, Including Geopolymer Cement Mortar used to renovate wastewater structures and large diameter pipes Version 1.0 (WSA161-2021, 2021).

Therefore, the particle size of the aggregate of all the mortars used in this study reaches the particle size requirement based on WSA 161-2021.

4.4 PHYSICAL PROPERTIES OF MORTARS

The two crucial physical properties that impact the performance of protective mortars are the initial porosity and strength, specifically unconfined compressive strength (UCS). The initial UCS of the mortar is considered an essential factor, even if it is not subject to support an external load. Nevertheless, the UCS reflects the inherent strength and integrity of the mortar material itself. High UCS has generally been directly correlated to higher corrosion resistance (Ng et al., 2018). The porosity is related to the void that potentially absorbs the corrosive compound and reacts further with the mortar binder. Moreover, It is usually linked to the UCS. Previous studies revealed that the UCS decreased when the porosity of the material increased (Rong-rong and Dong-dong, 2020, Jia et al., 2019). Therefore, determining the initial porosity and UCS as important physical properties is essential before the corrosion resistance performance test. The UCS was determined in accordance with ASTM C109/C109M-21 for cube specimens (ASTM-C109/C109M-21, 2021) and ASTM C39/C39M-21 for cylindrical specimens (ASTM-C39/C39M-21, 2021) and porosity was determine using modified ASTM C642 (ASTM-C642, 2013)

4.4.1 POROSITY

The porosity of mortar refers to the amount of void within hydrated mortar material. It considers an essential physical property of mortar because higher porosity can promote acid permeation and deterioration of geopolymer. This section presents the porosity development of OGPm and CACm. The porosity was evaluated up to 28 days of curing under controlled humidity conditions at 25°C and 99% relative humidity using a water immersion test based on modified ASTM C642 (ASTM-C642, 2013).

Figure 4-11 presents the development of the porosity of OGPm and CACm up to 28 days of curing. The porosity of OGPm at 28 days of curing was observed in the range of 15.6 to 24.5 vol.%, with the lowest and highest porosity observed in OGPm-2 and OGPm-3, respectively. CACm showed porosity at 13.8 vol %, which is lower than OGPm and expected to have more excellent corrosion resistance. The porosity development trend in Figure 4-11 shows that porosity had formed within 24 hours and continues to change following curing time. Most of the mortar showed a general decline in porosity with time except for OGPm-3, which appears to increase with time. This could be attributed to the low final setting times of OGPm-3 (measured at 48 hours – data not reported in this thesis) compared to less than 4 hours final setting times of the other mortars. However, the chemical composition of the binder could affect the development of porosity due to the hydration product filling the pore structure of geopolymer mortar. For example, OGPm-1 and OGPm-2 were commercially available geopolymers prepared from different aluminosilicate precursors. OGPm-1 is prepared from a high CaO aluminosilicate precursor. Meanwhile, the OGPm-2 is a hybrid geopolymer prepared from aluminosilicate precursors blended with calcium aluminate cement.

For OGPm-1, the geopolymerisation process forms amorphous and semi-crystalline hydration products. These hydration products may not always pack together as efficiently as the crystalline phases, leading to higher porosity in the geopolymer matrix in OGPm-1. At the

same time, the OGPm-2 is considered a hybrid geopolymer as a geopolymer blended with CAC. The hydration products in CAC, such as calcium aluminate hydrates (e.g., C_2AH_8 and C_3AH_6) (Scrivener et al., 1999, Ideker et al., 2019, Shirani et al., 2020), tend to have a more ordered crystalline structure, which results in a more compact microstructure with lower porosity over time as the hydration product produce. Besides the chemical composition of mortar binder, several other factors influence the porosity of mortar, including the water-to-mortar ratio (W/M), size of aggregates, curing conditions, and mixing method (Shamsai et al., 2012, Lafhaj et al., 2006, Pavía and Toomey, 2008). Because the curing conditions and mixing method used were constant for all mortars, it would be anticipated that the W/M and particle size of aggregate impact the porosity.

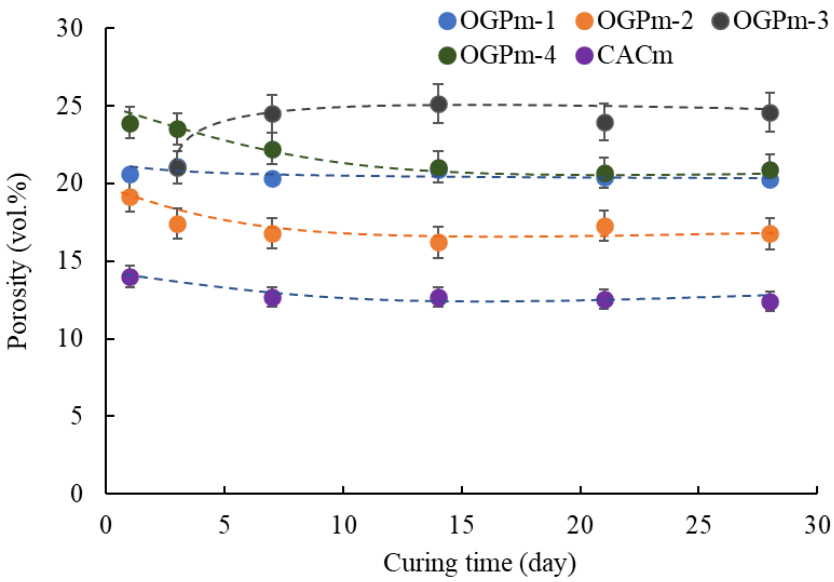

Figure 4-11 Development of porosity of OGPm and CACm

The W/M refers to the weight of water to mortar weight ratio for mixing mortar. As shown in Figure 4-12 (a), increasing the W/M resulted in higher porosity of the mortars. The completed 28 days cured mortar was observed with the porosity values of OGPm in the range of 15.6 to 24.5 vol.% and 13.8 vol.% for CACm. These were agreed and consistent with previous works (Shamsai et al., 2012, Lafhaj et al., 2006). The porosity is observed to increase with the W/M

ratio. Kim et al. (2014), Shamsai et al. (2012) and Lafhaj et al. (2006) tested the impact of water to mortar ratio and found that durability performance, especially porosity and compressive strength, were changed. Increased porosity exhibited low compressive strength. The porosity increased as the water increased due to the excess water filling in the space between the mortar paste and aggregate, resulting in a low-durability mortar (Kim et al., 2014). Adding water in the mortar is necessary for hydration reaction and mixing with other components such as aggregate and admixture. However, as mentioned above, adding too much water could result in low-durability mortar due to high porosity and low UCS.

Figure 4-12 (b) shows the correlation between porosity and the coefficient of curvature (C_C) of aggregate within OGPm-1, OGPm-2, OGPm-3, OGPm-4, and CACm. These plots showed the reduction in the porosity of hardened mortar as the C_C increased from 0.53 to 1.17. These results agreed with those reported by Pavía and Toomey (2008), where the aggregate grade was linked to mortar porosity and strength. Uniform aggregates were found to have higher porosity, while distributed or well-graded aggregates resulted in higher packing density, low porosity, and higher strength, as observed in this study.

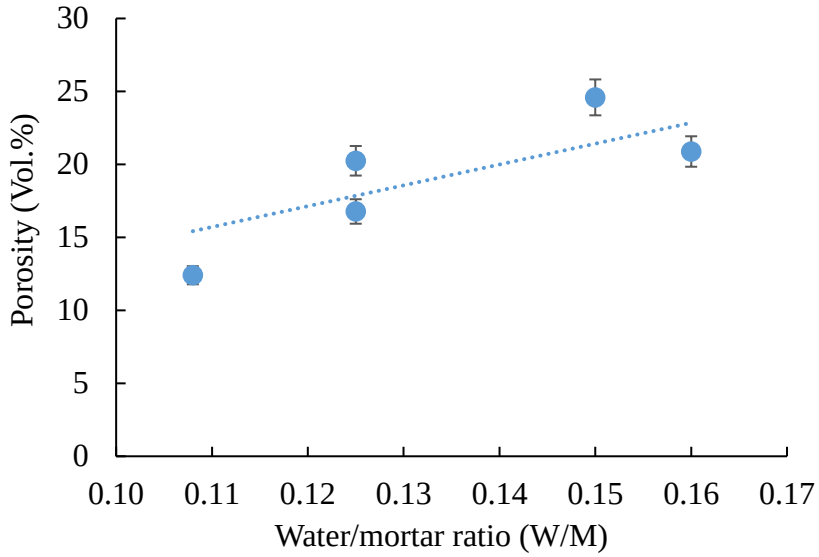

(a).Water and mortar ratio

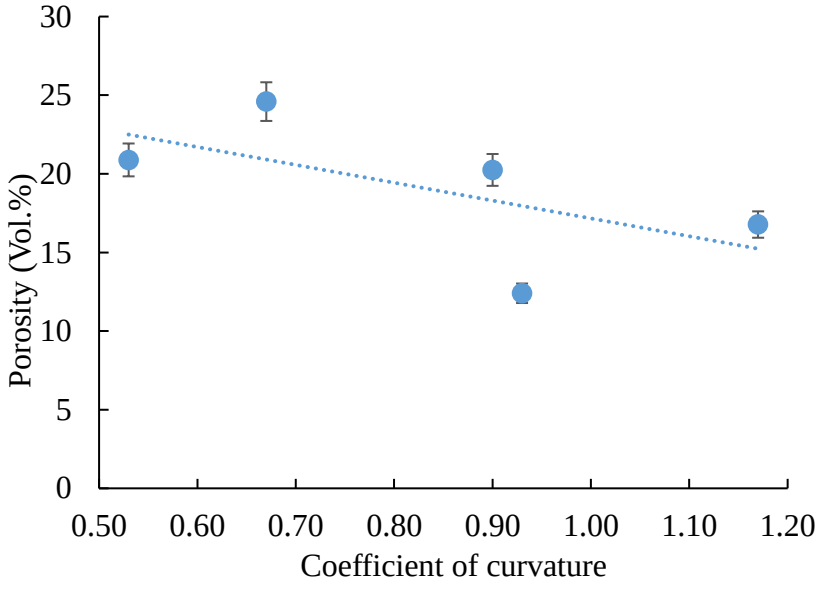

(b). Aggregate grading

Figure 4-12 Correlation between porosity and water and mortar ratio (W/M) and aggregate grading

4.4.2 UNCONFINED COMPRESSIVE STRENGTH (UCS)

Unconfined compressive strength (UCS) is a term commonly used to describe the strength of a mortar. The UCS of all samples were tested based on the ASTM C109/C109M-21 for cube specimens (ASTM-C109/C109M-21, 2021) using A UTEST Automatic Compression Machine Model UTC-4231 based on Australian Standards AS 1012.9 (AS1012.9:2014, 2014). The early

strength development of mortar is essential for application in live sewer asset rehabilitation. Repair of live assets can occur over a limited period (4 hours), requiring mortars that can demonstrate early strength. Therefore, measurements of UCS over 28 days from 24 hours are essential to determining the suitability of the mortar for live sewer application. In this study, the UCS of mortar was determined after 1, 7, 14 and 28 days of curing at 21 ºC and 99 %RH.

The strength development of OGPm and CACm can be influenced by various factors, including the chemical composition of the binder, W/C ratio, aggregate grading, and curing conditions (Amran et al., 2020). The UCS development results from the formation of hydration products such as C-S-H, C-A-S-H, N-A-S-H and C-N-A-S-H, where C=CaO, N=Na_2O, A=Al_2O_3, S=SiO_2, and H=H_2O. Figure 4-13 shows the development of UCS of OGPm and CACm as a function of time. The results show that UCS depends on the mortar type after one day. The UCS of the geopolymers OGPm-1, OGPm-2, OGPm-3, and OGPm-4 were 44.2 MPa, 73.1 MPa, 8.7 MPa, 54.2 MPa, while CACm showed 79.4 MPa, which was generally higher compared to OGPm. Over time, the UCS continued to increase but at a slower pace. However, the relative difference in UCS between geopolymer and CAC mortars remained the same. After 28 days of hydration, The UCS of geopolymers OGPm-1, OGPm-2, OGPm-3, OGPm-4 were 72.3 MPa, 102.8 MPa, 35.4 MPa, and 88.3 MPa, and CACm was 110 MPa. CACm showed generally greater strength than OGPm, which suggested its more excellent corrosion resistance.

Among the geopolymers, the OGPm-3 has the lowest UCSs. It did not reach the minimum UCS requirement of 17 MPa after one day and 55 MPa after 28 days for alkali-activated binders and geopolymers (WSSA, 2021).

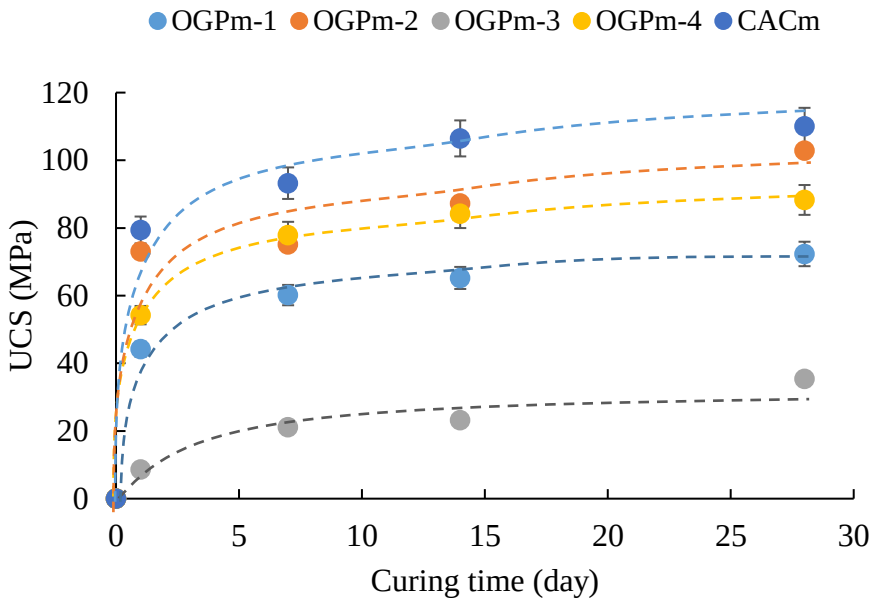

Figure 4-13 Unconfined compressive strength (UCS) of the lining material

4.5 CHEMICAL PROPERTIES OF THE LINING MATERIAL

This study used four commercially available one-part geopolymers to develop the service life prediction model. Additionally, one calcium aluminated cement mortar was used as a comparison mortar for corrosion resistance performance. These geopolymers were manufactured by blending low-calcium aluminosilicate precursors, such as fly ash, with high-calcium precursors, such as slag. Besides, the geopolymers are combined with calcium aluminate cement (CAC) and ordinary Portland cement (OPC) to accelerate strength development at ambient conditions. The chemical properties of the protective mortar lining material are essential for its strength, durability, and high corrosion resistance when exposed to corrosive environmental conditions such as sewer environments. Therefore, chemical properties in this study focused on the hydration products and acid neutralisation capacity. The commercial OGPm and CACm were prepared using the recommended water-to-mortar ratio, compacted into 5 mm cube moulds and allowed to harden for 24 hours. The demolded mortars were then further cured at 21 ºC at 99 % relative humidity for up to 28 days. The hydration

phase development study of OGPm and CACm involved collecting specimens from 1, 7, 14, 21, and 28 days of curing, followed by mineralogical analysis using Fourier transform infrared spectroscopy (FTIR) and thermogravimetric analysis (TGA). The acid neutralization capacity (ANC) was performed using mortars cured for 28 days following the standard according to CENT/TS 14429 (EN14429:2015, 2015).

4.5.1 HYDRATION PRODUCTS GEOPOLYMER

4.5.1.1 HYDRATION PRODUCTS

Hydration of geopolymer occurs when dry OGPm power is mixed with water resulting in various hydration products such as Sodium aluminosilicate hydrate (N-A-S-H), Calcium aluminosilicate hydrate (C-A-S-H), Calcium Sodium aluminosilicate hydrate (C-N-A-S-H), and Calcium silicate hydrate (C-S-H). This study defines the hydration product's nomenclature as C=CaO, N=Na_2O, A=Al_2O_3, S=SiO_2, and H=H_2O. Low-calcium precursors for geopolymers primarily form a three-dimensional amorphous aluminosilicate network (N-A-S-H, Q^4) (Duxson et al., 2005). The use of high-calcium aluminosilicate precursor will tend to generate linear aluminosilicate hydrate structures Q^1, Q^2 and Q^3 of (C-S-H, C-A-S-H and C-N-A-S-H) (Wong et al., 2021). Increasing the Ca content of the aluminosilicate precursor will tend to yield calcium silicate hydrate (C-S-H) (Yip et al., 2005). Aside from the main hydration product, additional products such as smaller alumina and silica species, alkali-metal hydroxides, and water can also be generated and remain in the hydrate mortar (Khale and Chaudhary, 2007, Van Jaarsveld et al., 1998).

The hydration product of OGPm is related to the strength and durability of its mortar. Therefore, it is essential to understand how specific hydration products are developed as a function of time and contribute to their performance. For example, most literature suggests the N-A-S-H phase of geopolymer is higher durability than the C-S-H phase in geopolymer or

OPC (Yang et al., 2022, García-Lodeiro et al., 2013, Zhao et al., 2019). This result was attributed to lower calcium content and structure of the hydrate. The lower calcium reduced the formation of expansive gypsum and ettringite as corrosion products, increasing the mortar's durability. Therefore, controlling the Ca content in the geopolymer mix is essential as it affects its hydration phases.

Hydration phases of geopolymer are usually identified using FTIR. The FTIR spectrum of hydrate geopolymer is generally collected from 550-4000 cm^{-1}. Generally, the spectra regions are divided into two regions: i). functional group region, and ii) fingerprint region. A peak higher than 1300 cm^{-1} is a characteristic “functional group region” (Medupin et al., 2017). The peak below 1300 cm^{-1} is known to be a characteristic “fingerprint region” of the binding gel (Revathi and Jeyalakshmi, 2021, Medupin et al., 2017). Most of the literature on geopolymer analysis suggested that the fingerprint region plays an essential wavenumber in identifying the specific absorption bands of the hydrate phases present in the geopolymer. Thus, the fingerprint region is utilised to analyse the hydration phases of geopolymer based on FTIR spectra in this study, and the identified wavenumber of each hydrate phase is shown in Table 4-11. Figure 4-14 shows the FTIR spectrum for OGPm-4 cured for 28 days as representative of protective lining mortar in this study. The spectrum shows the specific functional groups of interest identified using the wavenumber of hydration phases in Table 4-11.

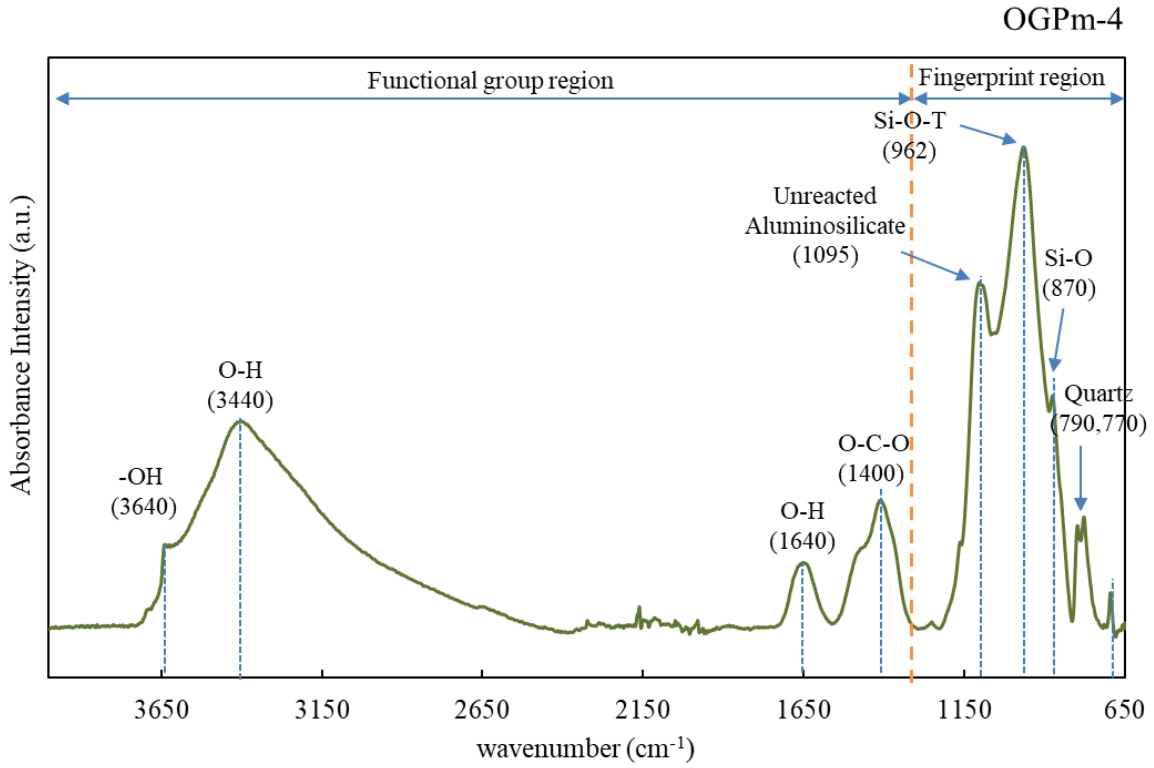

Figure 4-14 FTIR spectrum of OGPm-4 after curing 28 days

Table 4-11 FTIR bands for geopolymer

Wavelength (cm^{-1})	Assignments	Interpretation	References
precursors			
1060-1100		Unreacted aluminosilicate	(Puertas and Fernández-Jiménez, 2003, Palomo et al., 1999, Hajimohammadi et al., 2010, Hajimohammadi et al., 2008) (Cong and Mei, 2021)
930-965		Unreacted Slag	(Cong and Mei, 2021)
Hydrates and carbonate			
940-960	Si–O stretching vibrations	C-S-H	(Puligilla et al., 2019, Revathi and Jeyalakshmi, 2021, Zhao et al., 2019)
960-970	asymmetric stretching vibrations of Si-O-T bonds (T: tetrahedral Si or Al)	C-A-S-H	(Ramos et al., 2020, Walkley et al., 2016, Komljenović et al., 2020)
1005	asymmetric stretching vibrations of Si–O-T bonds (T: tetrahedral Si or Al)	C-(N)-A-S-H	(Aboulayt et al., 2020)
1036-1058	attributed to asymmetric stretching of Al–O/Si–O bonds	N-A-S-H	(Zhao et al., 2019, Guo et al., 2010, Ahmad et al., 2022)
3400-3450	stretching vibration and bending vibration of O–H bonds	N-A-S-H, C-A-S-H, C-S-H (water)	(Ismail et al., 2012, Ramos et al., 2020, Lecomte et al., 2006, Kapeluszna et al., 2017)
1650	stretching vibration and bending vibration of O–H bonds	N-A-S-H, C-A-S-H, C-S-H (water)	(Ismail et al., 2012, Ramos et al., 2020, Lecomte et al., 2006, Kapeluszna et al., 2017)
3630-3640	-OH stretching vibrations	$Ca(OH)_2$	(Lecomte et al., 2006, Beaino et al., 2022)
Carbonate			
1410-1450,870-875	Carbonate mineral		(Yaseri et al., 2019, Ramos et al., 2020, Ismail et al., 2012, Dong et al., 2014, Pasupathy et al., 2016)

The FTIR spectra of the geopolymer mortars (OGPm-1, OGPm-2, OGPm-3, and OGPm-4) as a function of curing periods (from 1 to 28 days) are shown in Figure 4-15. It needs to be noted that the geopolymer mortars used in this study are high-Ca geopolymers.

The main absorption bands are located between 900 and 1200 cm^{-1}. The FTIR spectra of all geopolymer samples exhibited a broad and intense peak around 960-970 cm^{-1}, which is assigned to the asymmetric stretching vibrations of Si-O-T bonds (T: tetrahedral Si or Al) in the chain structure of C-A-S-H (Hanjitsuwan et al., 2017, Alexander and Shashikala, 2022, Ismail et al., 2012, Hajimohammadi et al., 2008, Ramos et al., 2020, García-Lodeiro et al., 2008). García-Lodeiro et al. (2008) also suggested that when the peak is centred at approximately 960-970 cm^{-1}, C-A-S-H type gel is likely to be present, and when it is centred at approximately 1000 cm^{-1}, N-A-S-H gel is likely to be present. As the curing time increases, the peak at 960-970 cm^{-1} becomes sharper in all geopolymer samples, indicating the evolution of C-A-S-H as the primary hydration progresses. During the development of all geopolymers, there is a shift towards lower and higher wavenumbers depending on the high or low calcium (Ca) aluminosilicate precursor. The high-Ca aluminosilicate precursors were activated and slightly displaced by the main absorption band toward the higher wavenumber due to the formation of C-S-H and C-A-S-H. Mikhailova et al. (2019) mentioned that the hydration peak of slag as a high-Ca aluminosilicate precursor shifts towards higher wavelengths. It is typical of alkali-activated slag pastes with silicon-rich solutions. Therefore, the C-S-H phases would be expected to form at a lower wavenumber than 960-970 cm^{-1}. At the same time, the hydration peak shift of fly ash to a lower wavenumber is due to the precipitation of the geopolymer with an increased substitution of Si with Al (Puligilla and Mondal, 2015). The substitution of Al for Si led to a reduction of the Si–O–T angle. The smaller bonding force and the fact that the Al–O bond is longer than the Si–O bond results in the main band shift to the lower wavenumber (Fernández-Jiménez and Palomo, 2005, Puligilla and Mondal, 2015, Usman Kankia et al., 2021).

Another broad peak at 1100 cm^{-1} is related to Si−O−Si vibrations of unreacted aluminosilicate precursor (Hajimohammadi et al., 2010). The peak presented at 796 and 778 (double band) and

697 cm^{-1} is attributed to quartz in the geopolymers (Fernández-Jiménez and Palomo, 2005, Criado et al., 2007, Ramos et al., 2020).

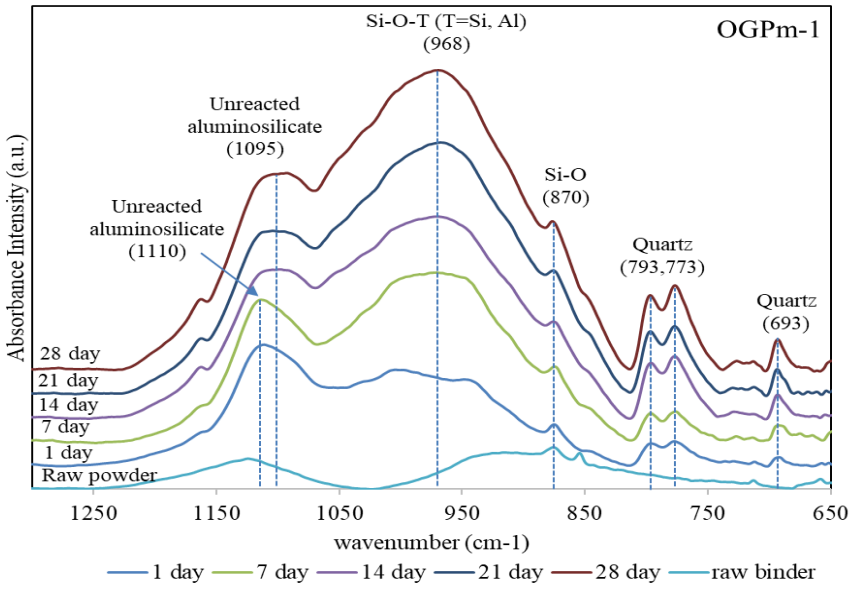

(a)

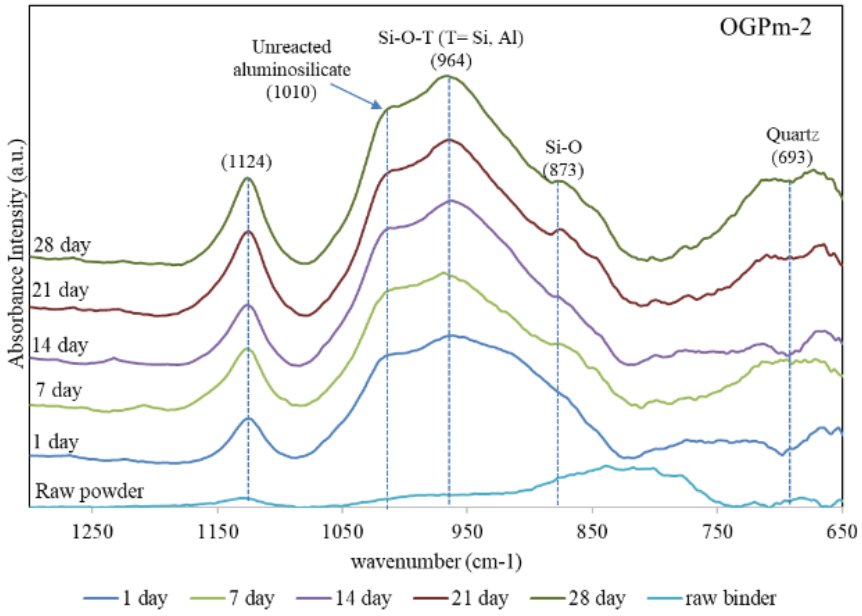

(b)

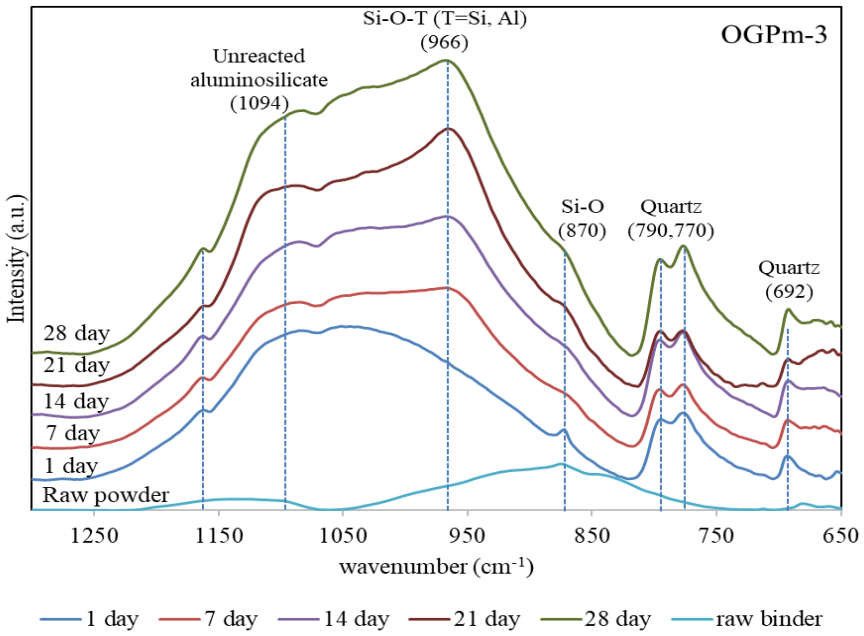

(c)

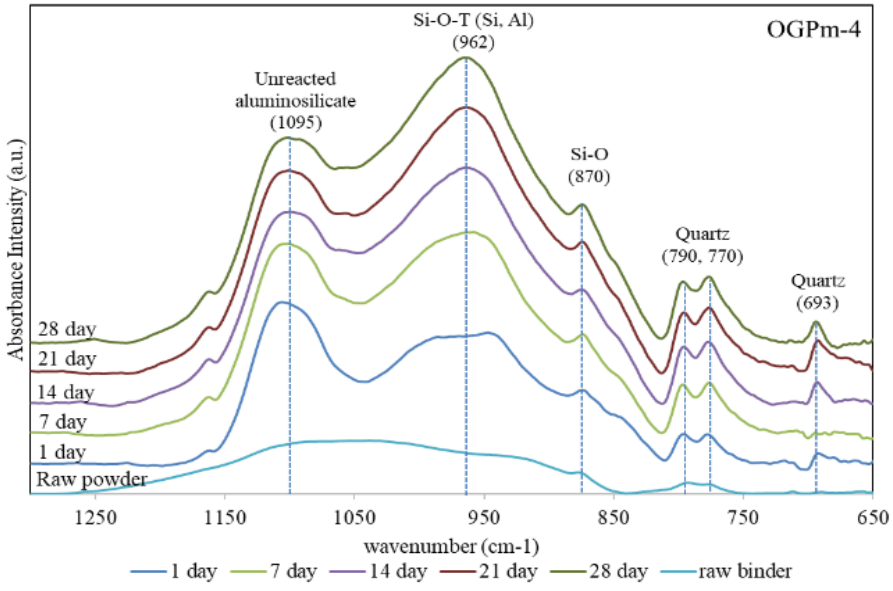

(d)

Figure 4-15 Development of geopolymer as a function of time up to 28 days: (a).OGPm-1, (b).OGPm-2, (c).OGPm-3, and (d).OGPm-4

As mentioned, the hydration process of mortar can lead to the formation of various types of gels, such as C-S-H, C-A-S-H, N-A-S-H, and C-N-A-S-H. Aboulayt et al. (2020) and studies on the hydration of blended fly ash and slag found that the slag-based geopolymer peak at 960 cm^{-1} was shifted to a higher wavenumber when mixed with fly ash, probably as the result of

the overlapping of several components, reaction products (C-S-H, C-A-S-H, N-A-S-H, and N-C-A-S-H). These results show that distinguishing between these different hydration products can be challenging. Infrared spectra obtained using FTIR can be complicated by overlapping peaks when two or more functional groups absorb at the same or similar wavenumber. Therefore, separating the overlapping peaks into their respective hydration phases requires deconvolution. The FTIR spectrums of geopolymer were deconvoluted to identify the hydrate phases using Microsoft Excel and the Levenberg-Marquardt method (see Equation 4-2) (Marquardt, 1963). The example of deconvolution is presented in Figure 4-16.

$$\sum f\,(x;x_0,H,W,L) = H * (1-L)\exp\left[-4\ln 2 \cdot \frac{(x-x_0)^2}{W^2}\right] + \frac{LH}{\left[1+4\frac{(x-x_0)^2}{W^2}\right]} \qquad \text{Equation 4-2}$$

Where x = wavelength, x_0 = the specific component peak wavelength, H = the component peak height, W = the component width, and L= the degree of mixing between Gaussian and Lorentzian functions.

Figure 4-16 shows an example of peak deconvolution in the fingerprint region to identify hydrate phases. The wavenumber can be attributed to the Si-O-Si and Si-O-Al stretching vibration (Hanjitsuwan et al., 2017, Alexander and Shashikala, 2022). This FTIR peak is collected from OGPm-4 curing for 28 days. The OGPm-4 is fabricated from the blended aluminosilicate from fly ash and slag. Blended fly ash and slag are usually known as “hybrid geopolymers” (Jiang and Jin, 2022). The broad peak centre is presented at 970 cm^{-1}. This peak is attributed to C-A-S-H formation. This proposed peak is agreed with other high-Ca geopolymers (Komljenović et al., 2020, Aboulayt et al., 2020, Aiken et al., 2018). The deconvoluted peak at the lower wavenumber is approximately 940 cm^{-1}. This peak is attributed to the C-S-H formation. The results of the deconvolute peak agree with other studies that the C-S-H is formulated at the peak around 940-960 (Puligilla et al., 2019, Revathi and Jeyalakshmi, 2021, Zhao et al., 2019). The deconvoluted peak at approximately 1040 cm-1 has

been attributed to the asymmetric stretching of Si–O–T, corresponding to N-A-S-H. This peak agreed with Longhi et al. (2019), Zhao et al. (2019), Guo et al. (2010). They suggested that N-A-S-H is present at the peak of approximately 1035-1058 cm^{-1}. In the hydration of high-Ca geopolymer studied by Aboulayt et al. (2020), the peak shift from 960-970 cm^{-1} to a higher wavenumber resulted from overlapping several hydrate phases such as N-A-S-H, C-A-S-H and C-N-A-S-H. Moreover, several studies agreed with these results, suggesting the hydration phases of hybrid geopolymer coexist with C-A-S-H, N-A-S-H, and additionally metastable C-N-A-S-H (Ismail et al., 2014, Jiang and Jin, 2022). Therefore, the C-N-A-S-H phase is potentially formulated between 1035 – 970 cm^{-1}. The deconvoluted peak of C-N-A-S-H is approximately 1000 cm^{-1}. This deconvoluted peak agrees with Aboulayt et al. (2020).

Therefore, the FTIR spectrums were deconvoluted to individual hydrate peaks based on wavenumber, as shown in Table 4-12.

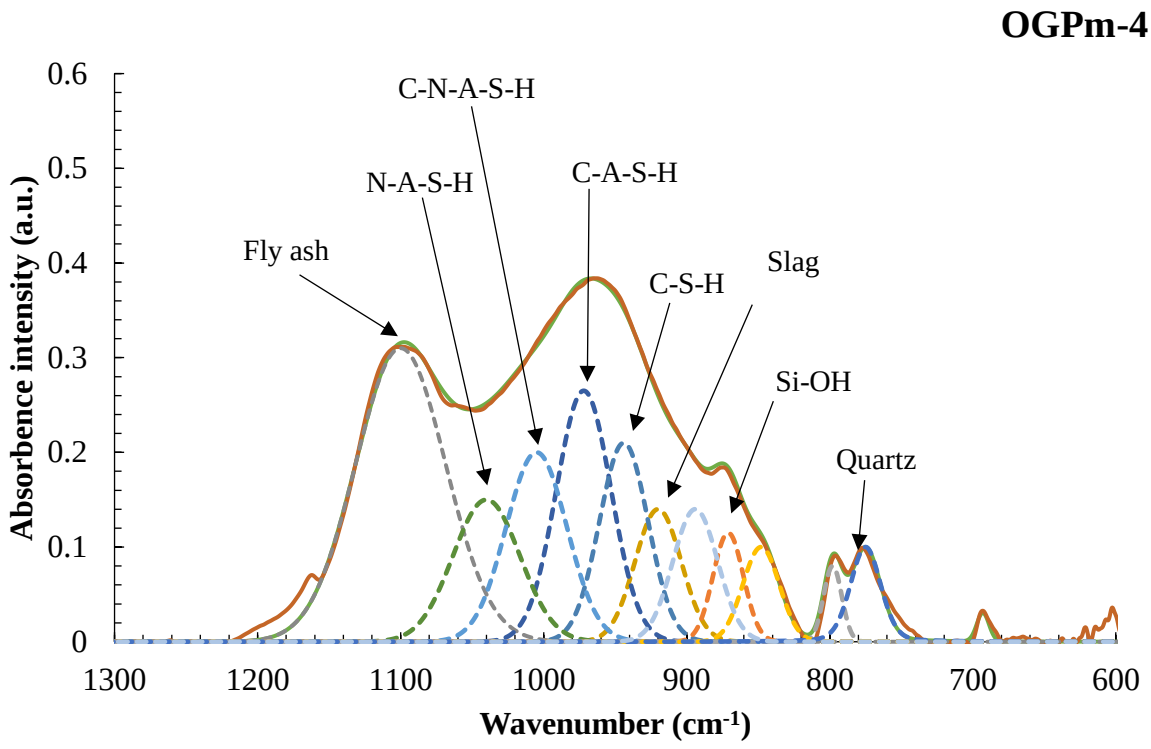

Figure 4-16 the example of deconvolution of the peak to quantify the amount of the geopolymer based on the Levenberg-Marquardt equation

Table 4-12 FTIR wavenumber for deconvolution of the FTIR spectrum

Wavenumber (cm^{-1})	Hydration phase
940	C-S-H
970	C-A-S-H
1000	C-N-A-S-H
1040	N-A-S-H

All geopolymer samples were formulated C-S-H, C-A-S-H, N-A-S-H, and C-N-A-S-H as the hydration products. The development of hydration phases as C-S-H, C-A-S-H, N-A-S-H, and C-N-A-S-H of geopolymer mortar at the curing age of 1, 7, 14, 21 and 28 days are plotted in Figure 4-17. The results observed that the evolution of the C-A-S-H phase in all samples increased over time, as indicated by the sharpening of the intense peak at approximately 960-970 cm^{-1} in all samples. These results suggested that C-A-S-H evolves as a function of time.

The development of the C-S-H phase was observed to form in high-Ca geopolymer but decreased with increasing the curing time. Cong et al. (2023) suggested this phenomenon occurred because of the decalcification of C-S-H, and the calcium component was consumed by forming C-A-S-H phases. The C-A-S-H phases are formed by the interaction between calcium hydroxide and N-A-S-H and C-N-A-S-H in geopolymer materials (Cong et al., 2023). The formation of C-S-H and/or C-A-S-H phases can improve the mechanical properties and durability of geopolymer materials by filling the pores and bridging the gaps in the geopolymer matrix. This reaction decreases the N-A-S-H and C-N-A-S-H phases, increasing the curing time, as shown in Figure 4-17.

Interestingly, the N-A-S-H is observed to have an extremely low percentage, approximately 1.4 % in OGPm-2, compared to other geopolymers. Other geopolymers formed between 20-27 % of N-A-S-H. This result may be due to the chemical composition of the aluminosilicate

precursor used in OGPm-2 being high calcium-sodium aluminosilicate precursors. It is well known that the basic structures of geopolymer are the network structures of [SiO_4] tetrahedrons and [AlO_4]$^-$ tetrahedrons connected by shared oxygen atoms (Wang et al., 2020c). Therefore, the N-A-S-H and C-A-S-H were correlated with the Si/Al ratio to prove this assumption. The correlation between hydration phases with Si/Al ratio (a) N-A-S-H and (b) C-A-S-H were plotted in Figure 4-18. The results indicated that N-A-S-H formation is favoured at higher Si/Al ratios (see Figure 4-18a), while C-A-S-H is favoured at lower Si/Al ratios (see Figure 4-18b). Incorporating Al into the geopolymer network can lead to more crosslinking, resulting in a denser and more crystalline structure of C-A-S-H (Luo et al., 2022b). On the other hand, a higher Si/Al ratio can form more N-A-S-H, which has a more open and disordered structure due to more Si-O-Si linkages resulting increase in porosity (Wang et al., 2021, Castillo et al., 2021). Thus, the Si/Al ratio can be used to consider a mixed design of geopolymer with specific desired properties.

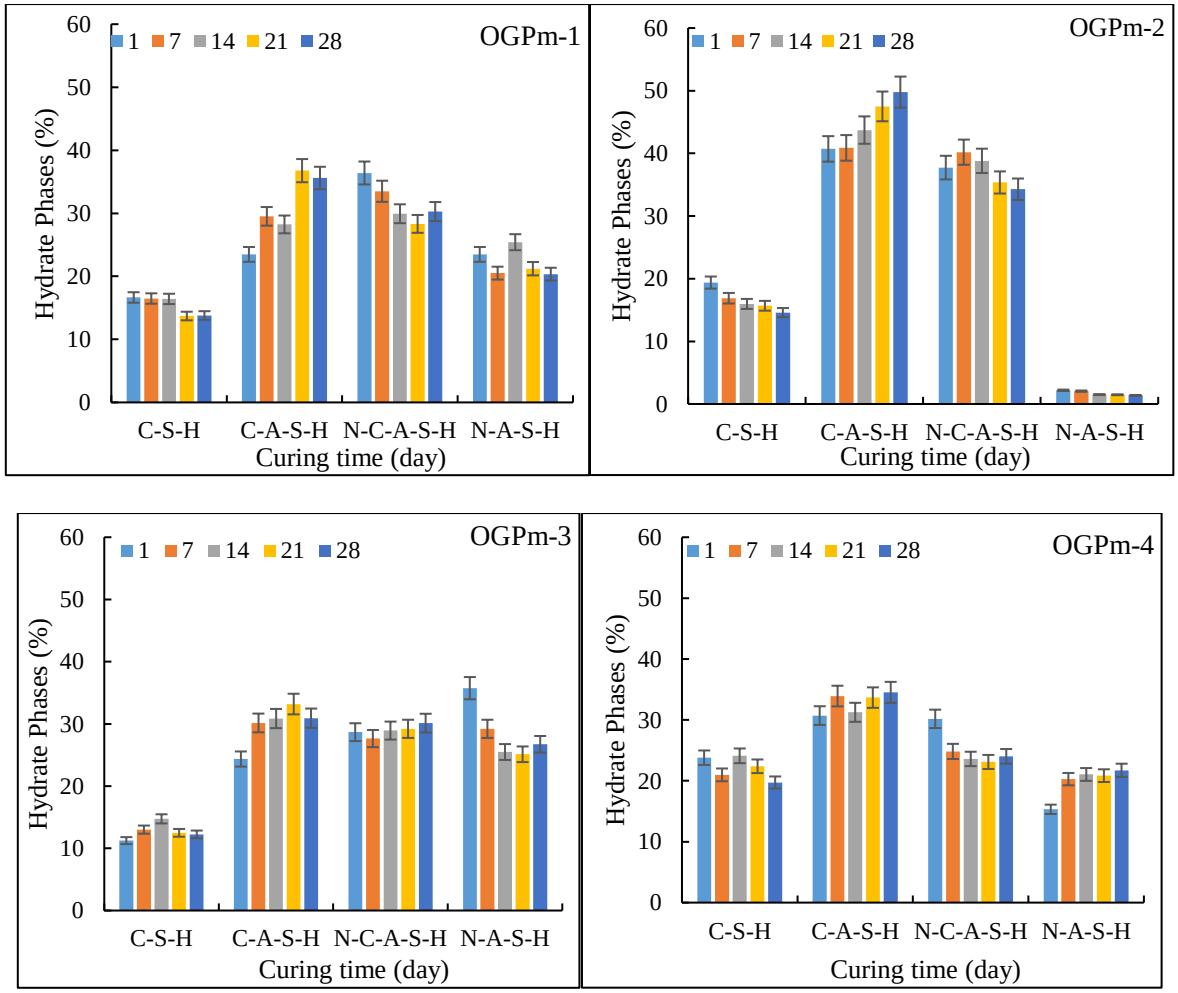

Figure 4-17 Development of hydration phases of geopolymer as a function of time

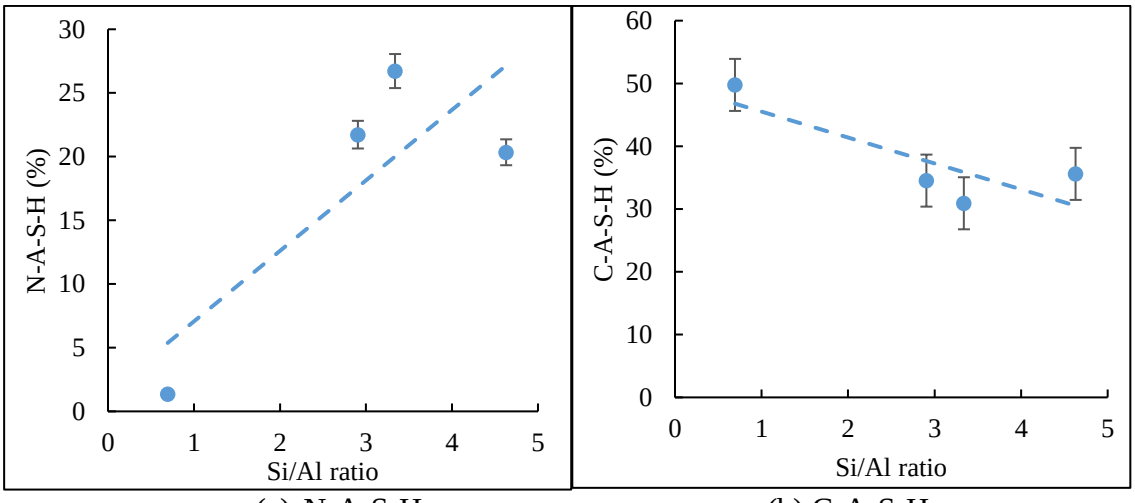

(a) N-A-S-H (b) C-A-S-H

Figure 4-18 The correlation between hydration phases with Si/Al ratio (a) N-A-S-H and (b) C-A-S-H

Following a qualitative examination of the geopolymer's hydration phase proportions, the subsequent step involved a quantitative analysis using TGA to determine the proportions of the various hydration phases (C-S-H, C-A-S-H, C-N-A-S-H, and N-A-S-H) present in the geopolymer. However, in this study, the commercially available geopolymer is blended with various aluminosilicate precursors, including fly ash, blast furnace slag, silica fume, and ordinary portland cement. Therefore, the additional peak shown suggests the presence of hydration products from the different chemical components of the aluminosilicate precursor.

Rosas-Casarez et al. (2014) suggested that the peak of TGA-DTG of geopolymer is generally shown in the three regions: i). free water evaporation, ii). water-associated with hydration/geopolymerisation product, and iii). carbonate mineral. The results from this study agree with the suggestion from Rosas-Casarez et al. (2014).

The first region is associated with free water evaporation, which is present in the pores of the hydration products. The temperature in this region was not more than 100 ℃ (Hosan et al., 2016, Ariffin et al., 2013, ul Haq et al., 2014, Valencia Saavedra and Mejía de Gutiérrez, 2017, Long et al., 2017, Ma et al., 2018). The second region occurs between 100-300 ℃. It is associated with hydration products with different phases depending on the decomposition temperature. The C-S-H were decomposed at 100-109 ℃ (Long et al., 2017, Qu et al., 2021). C-A-S-H were approximately decomposed at 160 ℃ (Gao et al., 2017, Luo et al., 2022a). The dehydration of C-N-A-S-H happened at 150-200 ℃ (Fořt et al., 2019). And finally, N-A-S-H were decomposed by loss of hydroxyl groups at high temperatures between 200-400 ℃ (Istuque et al., 2019). However, they still exhibited other phases such as hydrotalcite at 330-350 ℃ (Gao et al., 2017, Ma et al., 2018), $Ca(OH)_2$ at 425-440 (Chindaprasirt et al., 2014, Duan et al., 2017, Cong and Mei, 2021), and carbonate minerals at 550-700 ℃ (Ismail et al., 2012, Ariffin et al., 2013, Adesanya et al., 2018, Duan et al., 2017, Chindaprasirt et al., 2014), due to the different chemical composition within the geopolymer.

Therefore, the TGA-DTG of geopolymers were analysed in the hydration product by deconvoluting the spectrum of the TGA-DTG peak into individual hydration phases based on the decomposition temperature of each hydration phase using Microsoft Excel and the Levenberg-Marquardt method (see Equation 4-2) (Marquardt, 1963). Figure 4-19 shows an example of the deconvolution of the TGA-DTG peak of 28 days cured OGPm-4 based on the decomposition temperature mentioned above. The deconvolution of the peak exhibited the individual hydration phase presented in the geopolymer.

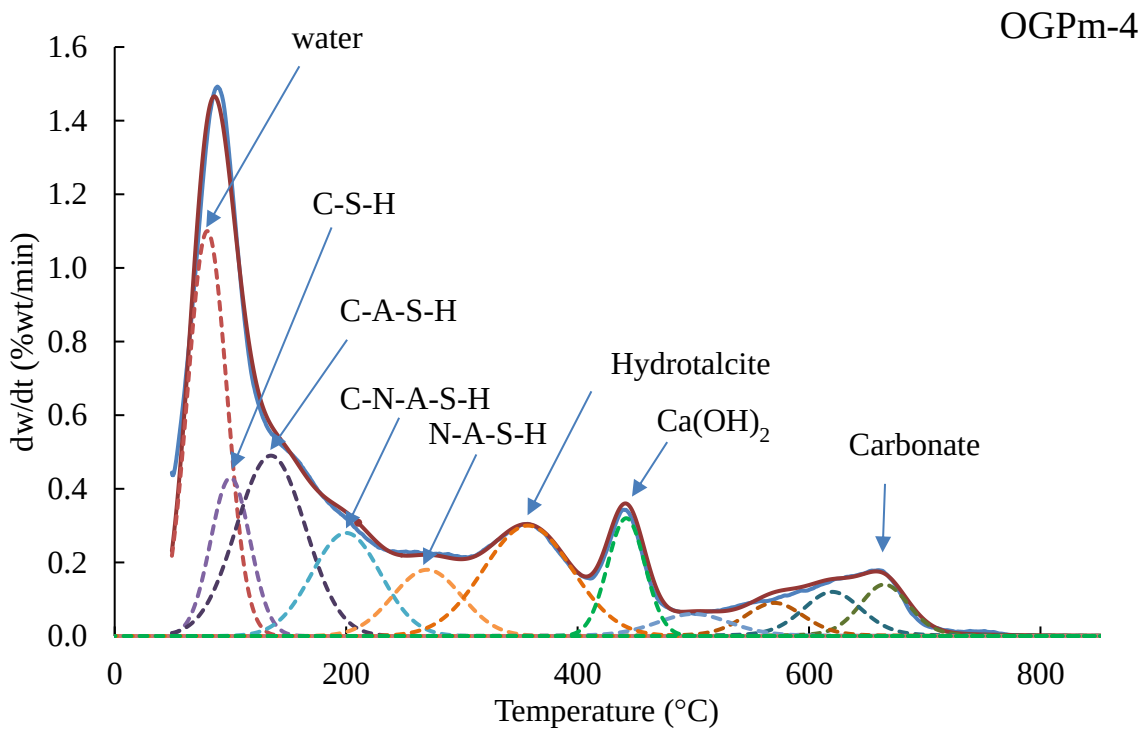

Figure 4-19 the example of deconvolution of the TGA-DTG peak to quantify the amount of the geopolymer based on the Levenberg-Marquardt equation.

Figure 4-20 presents the correlation of hydrate gel from OGPm-4 using FTIR and TGA analysis. The FTIR analysis was used to identify the formation of different hydrate gel phases based on chemical functional groups. In contrast, TGA analysis was used to measure the weight loss associated with the dehydration of these phases. The correlation of the hydrating gel analysed using FTIR and TGA revealed an interesting trend. It was observed that an increase in the FTIR peak area of C-S-H, C-A-S-H, C-N-A-S-H, and N-A-S-H results was consistent

with an increase in the TGA results. This observation indicates a direct relationship between the formation of hydrate gel and the weight loss associated with the dehydration of the gel. The strong correlation between the two results suggests that the FTIR analysis is a reliable method for identifying the formation of hydrate gel phases and that TGA analysis can quantify the amount of these phases present in the material. This correlation also indicates that the TGA technique is sensitive enough to detect the changes in the thermal properties of the material resulting from the formation of the hydrating gel.

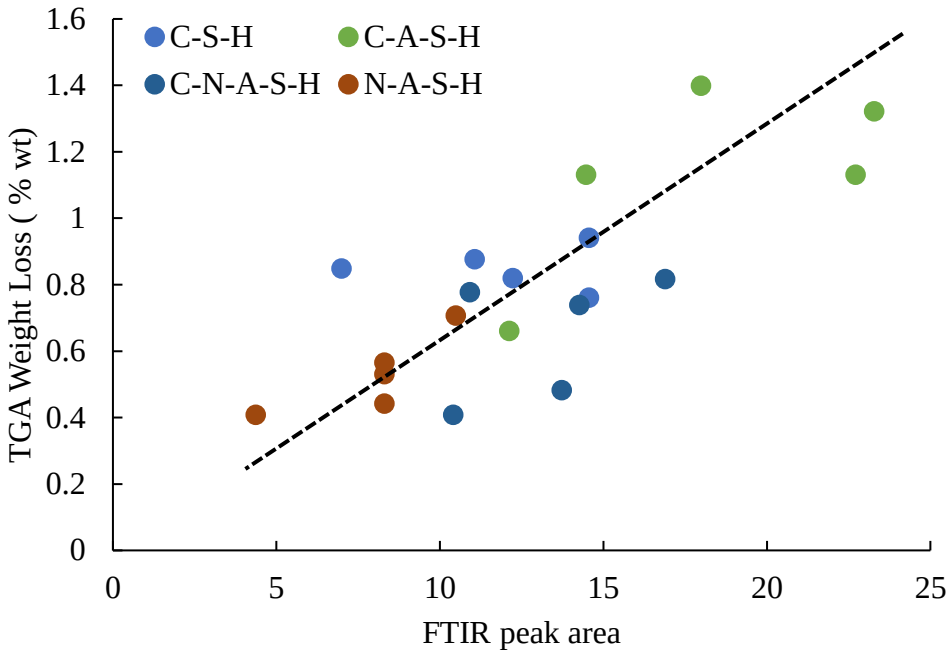

Figure 4-20 Correlation of FTIR and TGA-DTG result from OGPm-4

4.5.1.2 CORRELATION OF HYDRATION PRODUCT WITH POROSITY AND UCS

The hydration process of geopolymer leads to the formulation of the hydrate phase as C-S-H, C-A-S-H, C-N-A-S-H, and N-A-S-H. These hydrate phases play an essential role in the initial porosity and UCS. Porosity refers to voids or empty spaces within the mortar, as mentioned in section 4.4.1. The porosity can directly impact the mortar's durability resulting from corrosive compound's permeability, such as moisture, sewer gases and chemical attack.

Figure 4-21 shows the correlation between hydration products and the porosity of mortar. It has been observed that the C-A-S-H and N-A-S-H formation showed a strong correlation with porosity. This suggested that the increasing or decreasing porosity depends on the C-A-S-H and N-A-S-H formation. The N-A-S-H gel is a 3D structure in geopolymers that is often more open and less compact (Aiken et al., 2018). While the formation of coexisting hydration products such as C-S-H and C-A-S-H could fill the void, resulting in improved porosity and mechanical properties (Yip et al., 2005, Cong et al., 2023).

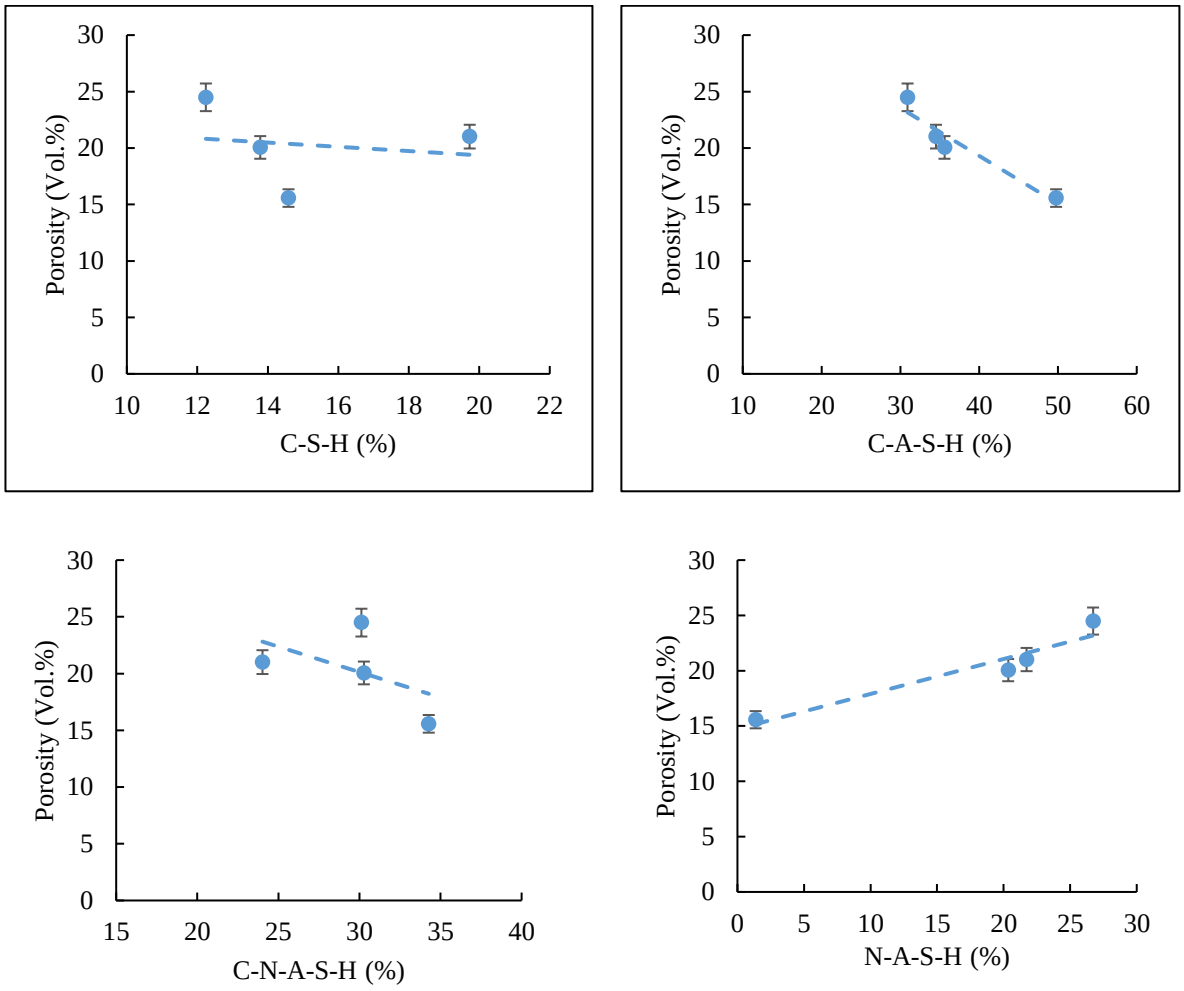

Figure 4-21 Correlation of hydration product and porosity

Figure 4-22 shows the correlation between the hydration product and the UCS. It observed that the C-S-H and C-A-S-H presented a strong positive correlation with the UCS. The UCS was increased when the amount of C-S-H and C-A-S-H were increased. These results agreed with Cong et al. (2023) that the UCS was improved by increasing the C-S-H and C-A-S-H in the mortar matrix. (Cong et al., 2023). It is because the C-S-H and C-A-S-H were formed and acted as fillers to fill the void spaces between the particles, enhancing the packing efficiency (Cong et al., 2023, Yip et al., 2005). This improved densification and reduced porosity contribute to the increased strength of the geopolymer.

The negative correlation observed between N-A-S-H and UCS highlights a clear trend where an increase in the N-A-S-H percentage correlates with a decrease in the UCS of the lining material. This outcome is attributed to the microstructure of N-A-S-H, characterised by high porosity, which adversely affects the UCS. An increase of N-A-S-H in the sample was observed to reduce the UCS due to The N-A-S-H gel is a 3D structure in geopolymers that is often more open, less compact (more porous) and a highly contained pore solution (Bernal et al., 2013, Aiken et al., 2018). Therefore, the highest N-A-S-H exhibited the lowest UCS. In contrast, C-N-A-S-H showed no discernible correlation with UCS, indicating that the addition of C-N-A-S-H does not directly influence the UCS of the lining material.

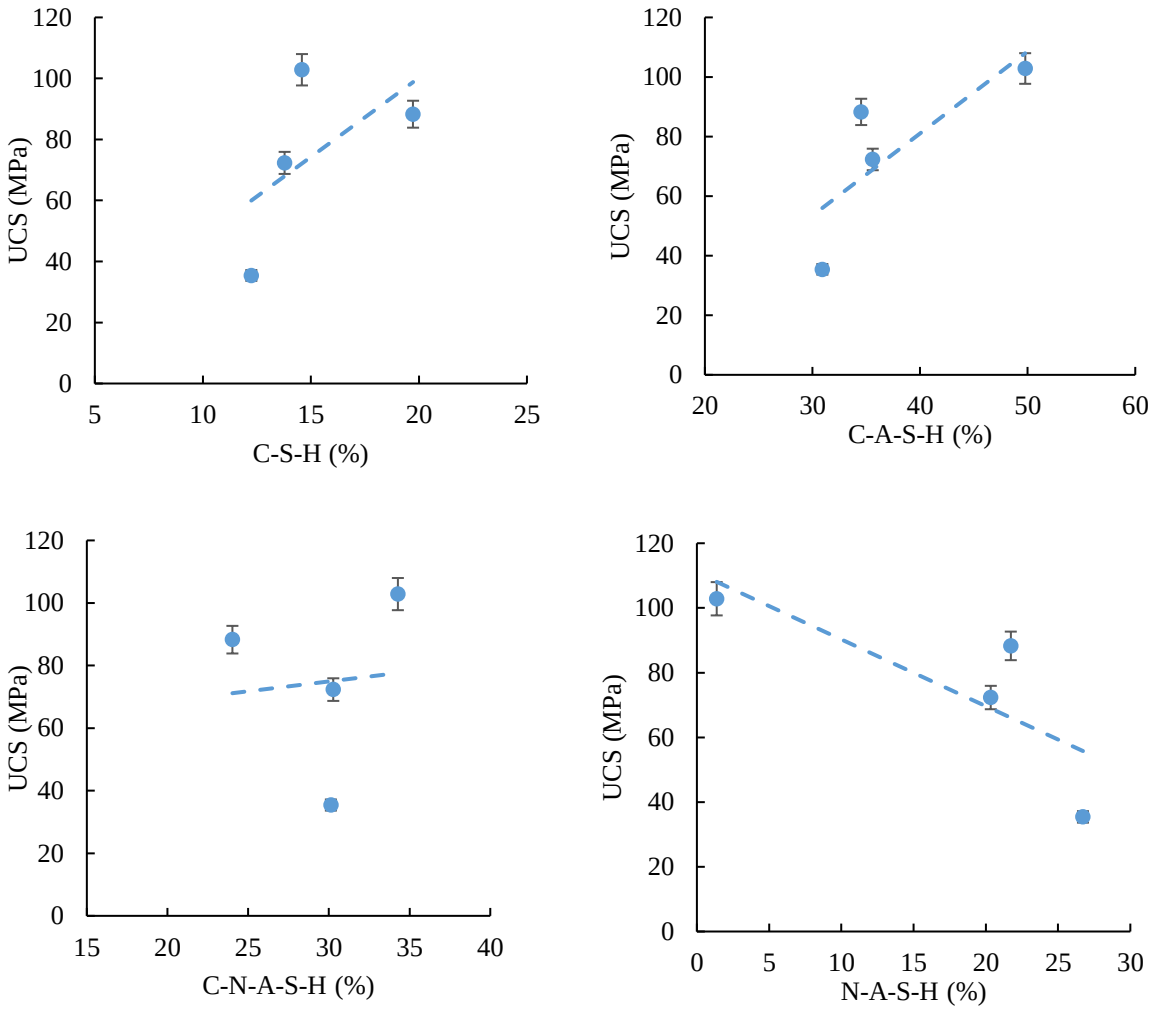

Figure 4-22 Correlation of hydration product and UCS

4.5.2 ACID NEUTRALISATION CAPACITY (ANC)

The acid neutralisation capacity (ANC) refers to the ability of the OGPm and CACm to resist the acid when exposed to aggressively corrosive environmental conditions such as sewer environment. The ANC of mortar is determined by bulk mortar against the change of pH of the solution. The ANC of mortar can be measured using various methods, including acid titration or pH measurements after exposure to acidic solutions (Wahlström et al., 2009). The acid neutralisation behaviour of the mortar was evaluated by plotting the pH of each extract as a function of milli-equivalents of acid added per gram of dry solid (Sanchez et al., 2000). In this study, the ANC was determined based on EN 14429:2015 standard (EN14429:2015, 2015, 14429, 2005).

4.5.2.1 CHARACTERISATION OF ANC

A high ANC is used to infer the resistance of the mortar to resist acid attack and maintain its structural integrity. A typical ANC curve is shown in Figure 4-23. It comprises three regions: ideal ANC, practical ANC, and the buffering region. The ideal ANC measured the acid concentration at the initial bending region when the mortar resisted changing the pH of the solution after adding the acid. The ideal ANC was identified around pH 10.4, which presented 1.3 mmol of H^+/g substrate. The practical pH was measured at pH 7.0. This pH is assumed to be when the mortar is still sound. The practical ANC showed approximately 1.9 mmol of H^+/g substrate. Both ANC ideal and ANC practical indicate the short-term front-end defence provided by the mortar. As noted in Figure 4-23, the later part of the ANC curve is characterised by the ability of the mortar to demonstrate a buffering effect or further resistance to change in pH. As shown in Figure 4-23, the buffering effect controls the pH between pH 3-4. This pH is important because the growth of sulphur-oxidising bacteria (SOB) is responsible for generating biogenic sulphuric acid, which is pH-dependent (Grengg et al., 2018). Their growth occurs at pH < 4. Therefore, the ability of the mortar to buffer may control the microorganism growth

and mortar corrosion. It needs to be noted that the ANC shown in Figure 4-23 is for calcium aluminate cement mortar (CACm). Therefore, the interpretation of ANC should consider the short-term corrosion resistance effects from ideal ANC or practical ANC and the longer-term corrosion resistance from the buffering pH.

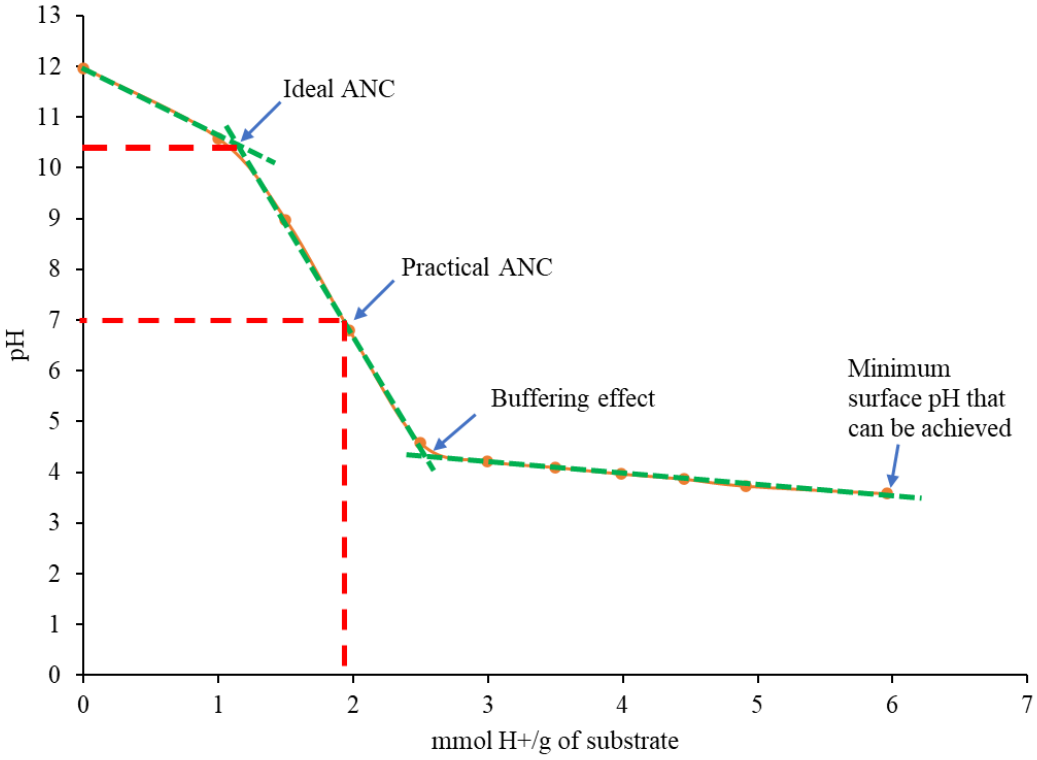

Figure 4-23 Characterisation of Acid Neutralisation Capacity (ANC)

4.5.2.2 ANC OF PROTECTIVE LINING MORTAR

The ANC curve of all OGPm and CACm was estimated and shown in Figure 4-24. It shows the amount of hydrogen ion (H^+) consumed by OGPm-1, OGPm-2, OGPm-3, OGPm-4, and CACm to resist the change in the acid solution.

Determination of ANC of the mortar used in this study was demonstrated by using OGPm-1 as representative of geopolymer lining mortar. OGPm-1 showed a gradual resistance to changes in the pH of the solution (approximately pH 12 to pH 10) up to the point of adding 4.2 mmol of H^+. However, upon further addition of acid, the pH of the solution decreased dramatically

to approximately pH 1. However, the ANC is typically measured at pH 7 as practical ANC because it represents a neutral solution, considered a baseline condition for measuring acid neutralisation capacity and sound mortar. Therefore, the practical ANC of OGPm-1 presented approximately 5.20 mmol of H^+/g substance. The summary of the practical ANC of all mortar is shown in Table *4-13*. However, it is essential to note that OGPm-2, OGPm-4, and CACm exhibited a buffering effect at pH approximately 4, which will be discussed in more detail below.

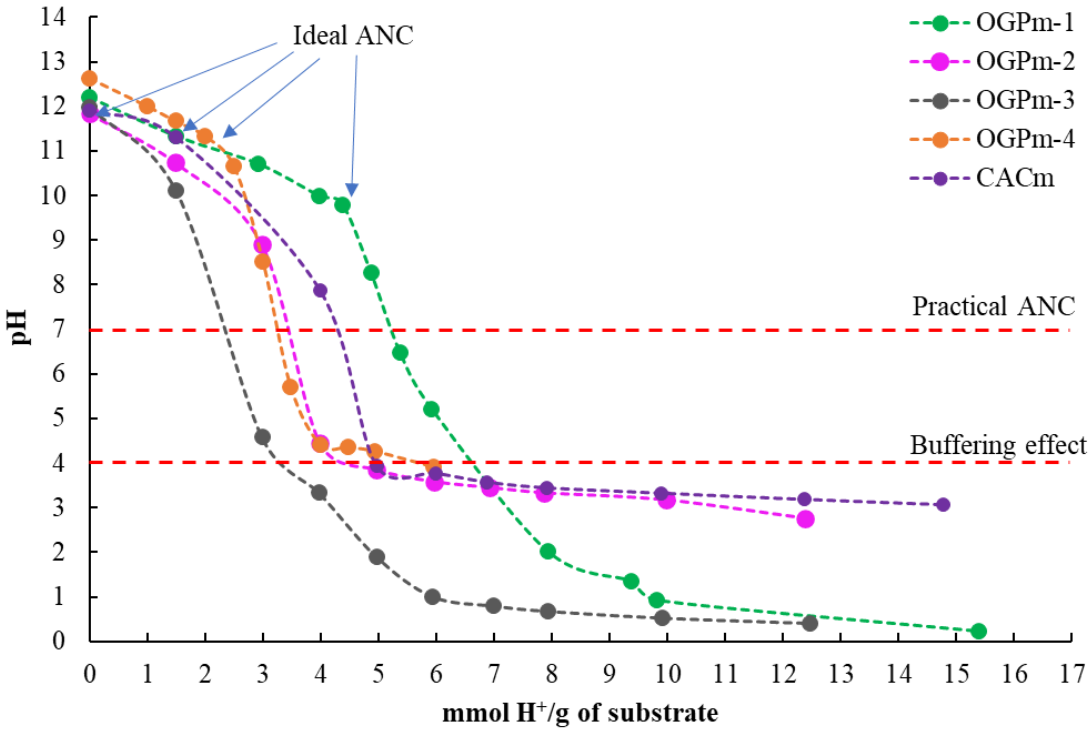

Figure 4-24 Characterisation of Acid Neutralizing Capacity (ANC) of geopolymer

Table 4-13 Acid Neutralizing Capacity (ANC) of geopolymer

Mortar	CaO (wt.%)	Al_2O_3 (wt.%)	MgO (wt.%)	ANC practical (mmol of H^+/g substrate)	Buffering effect (mmol of H^+/g substrate)
OGPm-1	53.85	5.95	1.35	5.4	n.a.
OGPm-2	37.43	27.60	3.19	3.8	12
OGPm-3	23.26	14.41	2.03	2.6	n.a.
OGPm-4	44.52	9.01	8.69	3.4	6
CACm	36.97	39.54	0.52	4.4	15

Table 4-13 shows the practical ANC and buffering effect for OGPm and CACm. Among the OGPm, the practical ANC presented 5.4, 3.8, 2.6, 3.4 and 4.2 mmol of H^+/g substance for OGPm-1, OGPm-2, OGPm-3, OGPm-4, and CACm, respectively. Among the OGPm, the OGPm-1 has the highest ANC, followed by OGPm-2, OGPm-4 and OGPm-3. The OGPm-2 and OGPm-4 have the capability to neutralise the acidic solution to reach approximately pH 4 and resist changing the pH of the solution. At this point, it is defined as the "buffering effect", which refers to the ability of a mortar to resist the changes in pH when an acid or base is added to the solution. The amount of acid added to the solution and the solution still maintained at pH 3-4 is defined as "buffering ANC". It indicated that from this point of buffering ANC, the additional acid could be neutralised without causing a significant change in pH. The OGPm-2 and OGPm-4 presented the buffering ANC at 12.5 and 6 mmol H^+ per gram substrate, respectively. Meanwhile, OGPm-1 and OGPm-3 can reach a pH of 0.22-0.41. They did not present the buffering ANC. The CACm revealed practical ANC around 4.2 mmol H^+ per gram substrate and buffered ANC at 15 mmol H^+/g. Interestingly, OGPm-2 and OGPm-4 have similar behaviours that resist pH reduction around pH 3-4 compared to CACm. These results may be attributed to the chemical composition of geopolymers and CAC mortar, such as CaO, MgO, and Al_2O_3.

Calcium oxide (CaO) is an alkaline compound that can react with acids to neutralise them, thereby increasing the ANC of the mortar. Therefore, mortars with higher CaO content can have higher ANC values (Scrivener et al., 1999). This is because the $Ca(OH)_2$ can be formulated and neutralised when the acid is attacked.

Aluminium oxide (Al_2O_3) can also contribute to ANC by forming aluminium hydroxide ($Al(OH)_3$) in the presence of water and acid and filling up the pore (Damion et al., 2022, Scrivener et al., 1999). In addition, The $Al(OH)_3$ is stable down to the pH of approximately 3-4, generating additional OH^- and neutralising further acid attacks (Scrivener et al., 1999). The $Al(OH)_3$ dissolved and consumed hydrogen ions (H^+) from the acid, known as neutralisation at this pH.

High MgO content in geopolymer mortar can form hydrotalcite during the hydration process. The $Mg(OH)_2$ and $Al(OH)_3$ were leached out from the hydrotalcite when the acid attacked and neutralised the acid solution. Jobbágy and Regazzoni (2011) suggested that in the range $5 \leq pH \leq 9$, $Mg(OH)_2$ were leached out. When the pH was below 4.7, total dissolution of hydrotalcite occurred and leached out $Mg(OH)_2$ and $Al(OH)_3$. the leached $Mg(OH)_2$ and $Al(OH)_3$ were used to neutralise the acid attack. This result leads to the OGPm-4 showing the buffering ANC.

4.5.2.3 CORRELATION OF CHEMICAL COMPOSITION AND ANC

The practical ANC and buffering ANC values from Table 4-13 were found to be correlated with the essential chemical composition, including CaO, MgO, and Al_2O_3, in OGPm and CACm. This correlation can be attributed to the generation of OH^- during the corrosion process, as these chemical components contribute to the neutralisation of acids.

Figure 4-25 shows the correlation between practical ANC and essential chemical compositions of mortar binders such as CaO, MgO, and Al_2O_3. The correlation observed reveals a different correlation between ANC and the primary chemical composition of mortar binders. The

practical ANC strongly correlated with CaO as a positive correlation. It suggested that CaO significantly affected the practical ANC and the overall performance of geopolymer mortar. The correlation between ANC and Al_2O_3 was an optimum non-linear correlation. The ANC was decreased when the Al_2O_3 increased to approximately 15 wt.%. After reaching the Al_2O_3 at about 15 wt.%, the ANC was increased. After the acid attack on the mortar sample, the Al_2O_3 were leached out as $Al(OH)_3$, which is stable down to the pH of approximately 3-4, generating additional OH^- and neutralising further acid attacks (Scrivener et al., 1999). The $Al(OH)_3$ dissolved and consumed hydrogen ions (H^+) from the acid, known as neutralisation at this pH. Therefore, if the chemical composition of the mortar sample is further increased, it is expected to achieve a higher ANC value. This study presented the lowest ANC at 2.6 mmol H^+/g substrate at Al_2O_3, approximately 15 wt.%. At the same time, the MgO presented a weak correlation with the ANC. Therefore, controlling the chemical compositions of aluminosilicate precursors such as CaO, MgO, and Al_2O_3 is essential in improving corrosion resistance performance and durable geopolymer mortars when exposed to corrosive environmental conditions such as sewer environments.

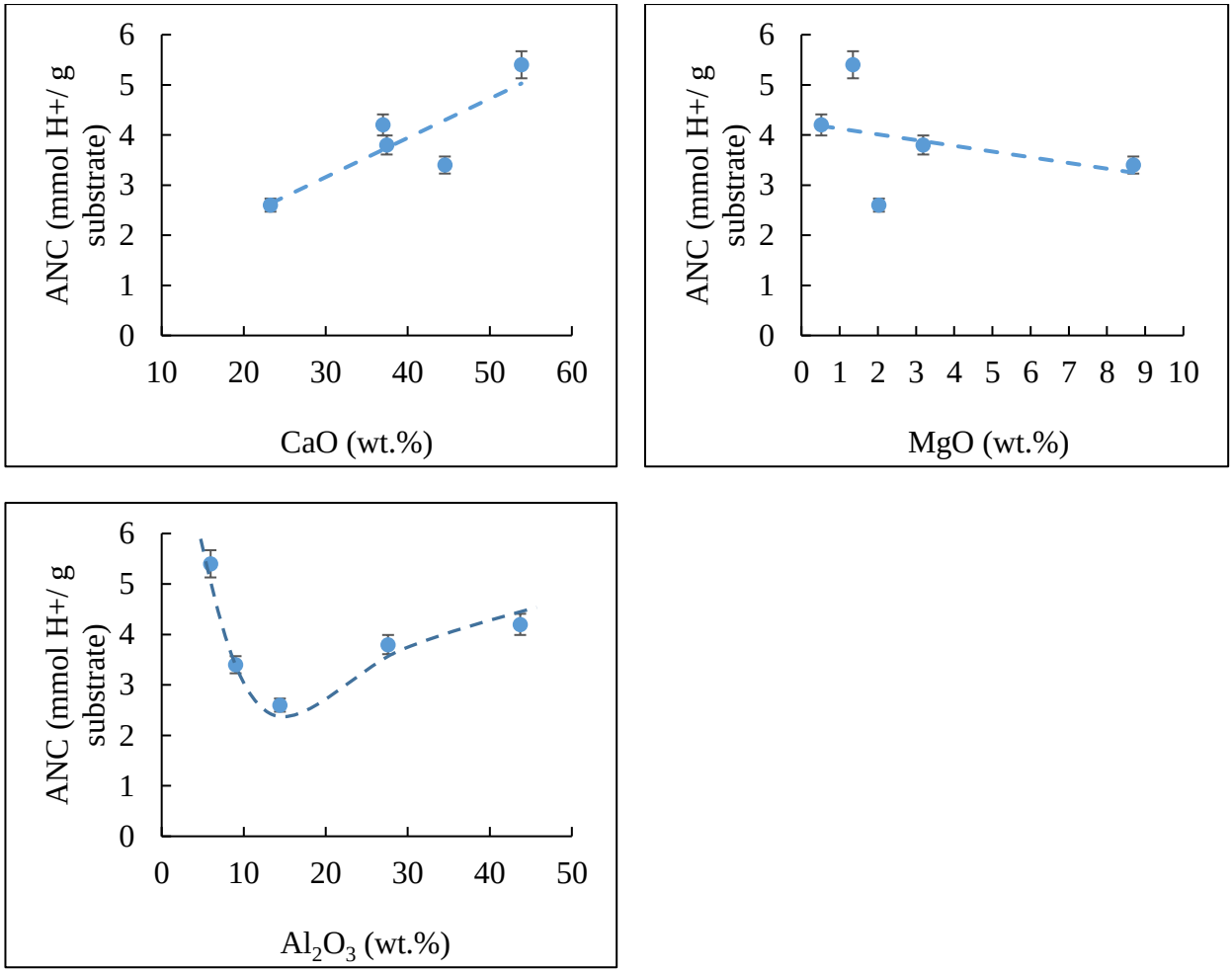

Figure 4-25 Correlation of practical ANC and CaO, MgO, and Al_2O_3

4.6 SUMMARY

In this chapter, four geopolymer mortars (OGPm) and one CAC mortar (CACm) were characterised to reveal their composition, mineralogy, and corresponding physical properties to support the durability assessment in Chapter 5. A key challenge noted at the beginning of this chapter is that because these are all commercially available mortar, there is very little information about their precursors and general properties. A summary of the learnings from these characterisations is provided below.

Cement Composition and Mineralogy

It was of interest to determine the nature of the cement binders. For example, most geopolymer coatings are marketed as geopolymer. However, the binder could be an Alkali-activated binder (AAB) or a hybrid geopolymer by blending different aluminosilicate precursors. Based on the XRF results, the high calcium content of the geopolymer binders that ranged from 23.3 to 53.9 wt.% suggest the precursors are high calcium aluminosilicate binders. This means that the hydrates from these binders are likely to be a blend of geopolymer and AAB hydrates. FTIR and TGA verified the composition of hydrates. The geopolymer phase (N-A-S-H) was found to be present in 1.4 to 26.7%. The rest of the hydrates established were 31-49.7 % C-A-S-H, 24-34.3 % C-N-A-S-H, and 12-19.7% C-S-H. On OGPm-2 was found to contain CAC hydrate. The fine aggregate mixed in OGPm-1, OGPm-3, and OGPm-4 was indicated as sand. The aggregate utilised in OGPm-2 was glass. The particle distribution of aggregate was the ‘well’ grading, which resulted in obtaining a higher density with minimum mortar binder content.

Based on the XRF of the CAC binder and aggregate as comparison mortar, it was found that the CAC binder showed standard grade composition of CAC binder, which contained approximately 37 wt% CaO and 43.7 wt.% Al_2O_3. While the aggregate of CAC mortar showed a composition of 39.5 wt.% Al_2O_3 and 36.1 wt.% CaO which is consistent with synthetic

calcium aluminate aggregate. This result suggested that the CAC used in this study was 100% CAC as standard grade CAC.

The chemical composition of binder and aggregate mortar, hydration phases, and particle size of binder and aggregates are essential parameters that impact the chemical and physical properties of mortar (ANC, hydration product, porosity, and UCS). These properties of mortar play a significant role in determining the corrosion resistance performance when subjected to aggressive sewer environmental conditions.

Physical properties

The porosity of mortar must be considered a significant factor in acid corrosion resistance performance because it directly affects the acid permeability of the mortar. It means there are more interconnected voids or pores within its mortar structure. The initial porosity of mortar in this study was observed to vary from 13 – 24.5 vol.%. The other factor that links to the porosity is UCS. The UCS of the mortar needs to be considered an essential factor to consider, even if it is not subject to an external load. However, the UCS reflects the inherent strength and integrity of the mortar itself. The UCS of the mortar used in this study varied from 35.4-110 MPa. High initial UCS improve corrosion resistance performance. The correlation between the initial UCS and porosity exhibited a negative correlation, which means that the initial UCS was increased when the initial porosity was decreased.

Chemical properties

As mentioned, the geopolymers used in this study were high-Ca geopolymers known as alkali-activated mortar (AAB) or hybrid geopolymers. N-A-S-H, C-A-S-H, C-N-A-S-H, and C-S-H were formulated during the hydration process as the main hydration products. The hydration products were related to the physical properties. The correlation between hydration products and physical properties such as initial porosity and UCS shows that the C-S-H, C-A-S-H, C-

N-A-S-H and N-A-S-H were important hydration phases because they strongly influence initial porosity and UCS. the C-S-H, C-A-S-H, and C-N-A-S-H could improve the mortar by reducing the initial porosity, leading to increase the initial UCS. In contrast, the N-A-S-H influenced high porosity and low UCS in mortar.

The acid neutralisation capacity (ANC) refers to the ability of the OGPm and CACm to resist the acid attack. The ANC of the OGPm and CACm varied from 2.6-5.4 mmol H^+ per gram substrate. The buffering effect was also observed on OGPm-2, OGPm-4, and CACm at pH approximately 3.5±0.7 due to the leaching of $Al(OH)_3$ from the mortar hydration product and dissolved at pH 3-4. At the buffering pH, it has been observed that the mortar consumed approximately 6-15 mmol of H^+ per gram of substrate based on this study. The ANC had a strong correlation with CaO and a weak correlation with MgO. At the same time, Al_2O_3 exhibited an optimum non-linear correlation. The ANC was decreased when the Al_2O_3 was increased to approximately 15 wt.%. After reaching the Al_2O_3, approximately 15 wt.%, the ANC was increased. Therefore, the practical ANC can influence the short-term corrosion resistance effects from practical ANC and the longer-term corrosion resistance from the buffering ANC and is highly influenced by CaO and Al_2O_3, respectively.

5 THE DURABILITY OF LINING MORTAR UNDER LABORATORY AND FIELD TEST

5.1 INTRODUCTION

The durability of OGPm and CACm was tested to identify properties of mortars that impact their corrosion resistance. This chapter presented the durability evaluation results. The durability of geopolymer and CAC mortars was tested through three different approaches: i) lab-based accelerated corrosion test of precast mortars, ii) corrosion testing of precast mortars in live digester tank tests, and iii) corrosion testing of shotcrete applied mortars in live sewer assets.

i) Lab-based accelerated corrosion test of precast mortars

The lab-based accelerated corrosion test involved acid immersion of precast mortars. The test was designed to simulate the effects of exposure to acidic solutions such as biogenic sulfuric acid found in sewer environments (Hvitved-Jacobsen et al., 2002, Joseph et al., 2012, Grengg et al., 2018). In this study, the lining mortar was purposed for use under sewer environmental conditions. Therefore, the test involved immersing the 50×50 mm lining mortar coupons in 1% w/v H_2SO_4, having a pH of approximately 1±0.05 for the acid immersion test for up to 28 days. The pH of the solution was changed over time by a neutralisation reaction between mortar and acid solution. The pH of the acid solution was monitored with a TPS WP-80D pH meter, and the pH of the solution was adjusted using 98% w/w H_2SO_4 to keep the pH at 1±0.05. The pH adjustment was made every day for the first week and once a week for the following week (see the details of the method in section 3.4.1 in Chapter 3).

ii) Corrosion testing of precast mortars in live digester tank tests

Field corrosion testing of precast coupon lining mortars in live digester chamber was tested at North Head Waste Treat Plant (NHWTP), Sydney Water. These corrosion testing results

reflected the corrosion resistance performance impacted by MICC. Three live digester tanks were involved in this test, which represented different serwer environmental conditions varying from 4-146 ppm H_2S, 2600-11900 ppm CO2, 28-30 °C, and 95-99.99 % relative humidity (RH). The mortar samples were exposed for up to 42 months in each digester chamber under the live sewer environment (see the details of the method in section 3.4.1 in Chapter 3). It had to be noted that the corrosion resistance performance test of the precast coupon of various new commercially available one-part geopolymers under a live sewer asset was performed for the first time. The corrosion resistance performance from this study contributed to a new result in the area of corrosion resistance performance of geopolymers impacted by MICC.

For this study, the corrosivity of the North Head Digesters was defined according to the sewer corrosivity classification of the gas phase in wastewater assets recently proposed to the WSAA (Water Services Association of Australia) (Valix, 2021). Therefore, the sewer environment conditions as surrogate measurements were used to assess sewer corrosivity classification, considering the causes of MICC.

To support the corrosivity classification of North Head digester tanks, gas surveys were performed following protocols described in section 3.4.2.2 in Chapter 3. During the environmental survey of the live sewer assets, various parameters were monitored to assess the environmental conditions that impacted the sewer corrosion. Key factors such as sewer gases (specifically H_2S and CO_2) and environmental conditions favourable for the growth of bacteria and other microbes, such as temperature (T) and relative humidity (%RH), were continuously monitored. This was achieved through the use of advanced environmental data loggers, including devices such as Odalog and MultiRae multigas analysers. (see section 3.4.2.2 in Chapter 3).

iii) Corrosion testing of shotcrete applied mortars in live sewer assets.

Corrosion testing of shotcrete applied mortars in live sewer assets as concrete manholes and pipes in Perth, Sydney, Adelaide, Brisbane, and Melbourne. These corrosion testing results reflected the real-world application of the lining mortar and the corrosion resistance performance impacted by MICC. The shotcrete lining mortars were exposed under different sewer environmental conditions across Australia. The sewer environmental condition varied from 1.6-190 ppm H_2S, 4500-12880 ppm CO_2, 20-25 °C, and 98-99 %RH (see the details of the method in section 3.4.3 in Chapter 3). The lining mortar was exposed to the live sewer environment for up to approximately 26 months and cored as a cylinder shape with the size of 5 cm ID x 3-5 cm in length (see section 3.4.3.8 Chapter 3). It had to be noted that the corrosion resistance performance test of shotcrete application under a live sewer asset was performed for the first time in this study. Therefore, the result from this study contributed to a new result in the area of corrosion resistance performance of geopolymers.

The corrosion resistance performance of lining mortar of all performance tests was assessed by the depth of corrosion and UCS as a function of time (see section 3.6 in Chapter 3). In the case of shotcrete lining mortar application, a layer of protective lining mortar was applied over the repaired mortar surface. During this process, Ni-Ag alloy rebars were embedded between the two layers. The thickness of the protective lining mortars was determined using a cover meter, which detected the presence and position of the Ni-Ag alloy rebars.

The corrosion resistance performance data obtained from the field tests analysis and geopolymer characterisation from Chapter 4 and the durability results in this chapter were used to develop a service life prediction model (see Chapter 6). The service life model established the coating selection criteria for ensuring the appropriate selection of materials based on sewer corrosivity classification requirements

5.2 EVALUATION OF CORROSION RESISTANCE PERFORMANCE OF MORTARS

5.2.1 ACID IMMERSION TEST

The acid immersion test is a widely used method for evaluating the effectiveness of lining mortar in protecting concrete from chemical attacks (Hvitved-Jacobsen et al., 2002, Joseph et al., 2012, Grengg et al., 2018). In this test, a sample of the lining mortar is placed in contact with an acid solution for a specified period, and the degree of chemical deterioration is then evaluated based on the depth of corrosion and residual UCS.

5.2.1.1 CORROSION RESISTANCE PERFORMANCES

The corrosion resistance performance of lining mortar is essential to evaluate when assessing durability and long-term performance in corrosive environments. It was evaluated based on the depth of corrosion and the residual UCS. However, for the depth of corrosion, Aiken et al. (2018) suggested that considering only the loss of surface material is not ideal for estimating corrosion depth. Therefore, the corrosion depth was estimated by considering the loss of surface material and acid permeation through mortar identified using a pH indicator applied to the cross-sectioned slide mortar sample and examined the depth of corrosion through a Leica DM2500 optical microscope (see section 3.9 in Chapter 3).

5.2.1.1.1 PHYSICAL APPEARANCES

OGPm-1, OGPm-2, OGPm-3, OGPm-4, and CACm were immersed in pH 1 of H_2SO_4 for up to 28 days. The mortar samples monitored the corrosion resistance performance at 1,3,7,14,21, and 28 days of immersion. Figure 5-1 presented the appearance changes observed in a mortar sample before and after exposure to a pH 1 acid solution for 28 days. Additionally, it presented a cross-section view of the corroded mortar sample.

All mortar samples observed that after 28 days immersed in the pH 1 of the sulfuric acid solution, the surface of all mortar samples changed from grey to white. This indicated the formation of corrosion products, such as gypsum, on the surface, which is investigated further in the next section. This was because the sulphuric acid reacted with the mortar binder, leaching Na+, $Ca^{2+,}$ and Al^{3+} toward the acid solution and forming expansive corrosion products such as gypsum and ettringite, which have little or no hydraulic properties and thus no structural integrity (Khan et al., 2020a, Mehta, 1983). At the same time, the OH^- diffused forward to the acid solution and reacted with available H^+ in mortar and acid solution as a neutralisation process (Khan et al., 2020b). While the bulk geopolymer coupons appeared to be structurally intact, noticeable degradation and material loss were observed on the surface of OGPm-1, OGPm-2, OGPm-3, and OGPm-4. Moreover, the mortar coupons showed a slight increase in thickness after 28 days of immersion in the acid solution in Figure 5-2, confirming the formation of expansive corrosion products (Okabe et al., 2007b).

The deterioration behaviour by visual observation at the same acid solution concentration suggested that OGPm-1 was the highest corrosion resistance and OGPm-3 was the lowest corrosion resistance to the acid attack. Since all lining mortar coupons were exposed to the same environmental condition, the deterioration of the mortar lining must depend on the chemical composition of the mortar. The CACm coupons maintained their initial smooth greyish surface and remained structurally intact, exhibiting only minor deterioration on the surface. Therefore, in the next section, the corrosion resistance performance was determined based on the corrosion depth and correlated with their chemical and physical properties to understand the impact of their properties.

Condition	OGPm-1	OGPm-2	OGPm-3	OGPm-4	CACm
0 day					
After 28 days immersed in acid solution			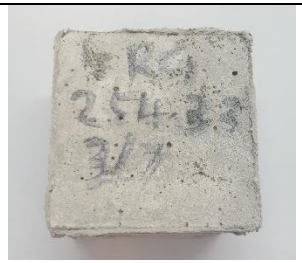		
Cross-section after 28 days		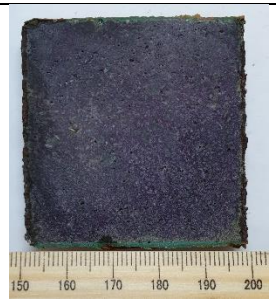	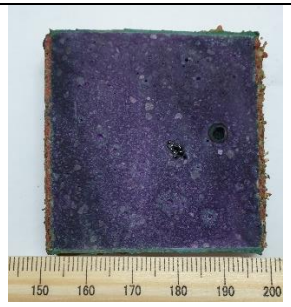	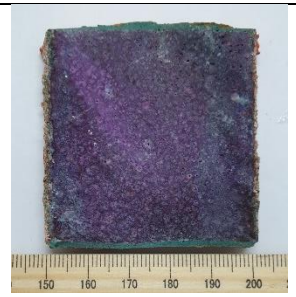	

Figure 5-1 Post Acid Immersion Image of Corroded Surface

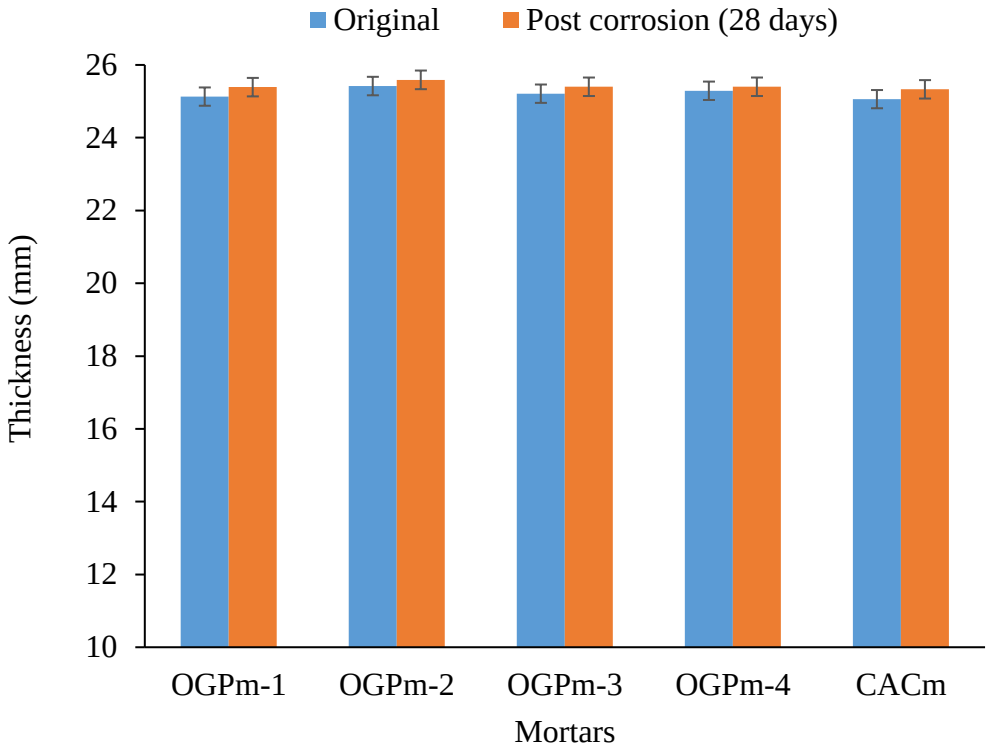

Figure 5-2 Thickness of mortar before and after 28 days of corrosion in sulfuric acid pH 1 and 27 °C

5.2.1.1.2 DEPTH OF CORROSION

During the acid immersion test, both OGPm and CACm exhibited corrosion that initiated from the surface, resulting in visible deterioration. The corrosion of coupon mortar was only forced to corrode in two directions by coating another four sides of the coupon with Sika High Strength Epoxy, as shown in Figure *5-3* (a). The corrosion depth was determined by examining the cross-section of coupon mortar by a spraying universal indicator, as presented in Figure *5-3* (b). The colour variations observed in the mortar samples provided indications of their corrosion levels. The purple colour represented uncorroded mortar, with a pH range of approximately 9-13. The green to red colour indicated the deterioration of the mortar, corresponding to a lower pH range of approximately 1-7. The optical microscope was utilised to help measure the acid permeation less than 5 mm, and the vernier calliper was used when the acid permeation was more than 5 mm. The schematic of the corrosion depth calculation is

shown in Figure 5-4. It is calculated based on the original cube centre and takes into account the expansion or loss of material. The depth of corrosion was calculated based on Equation 5.1.

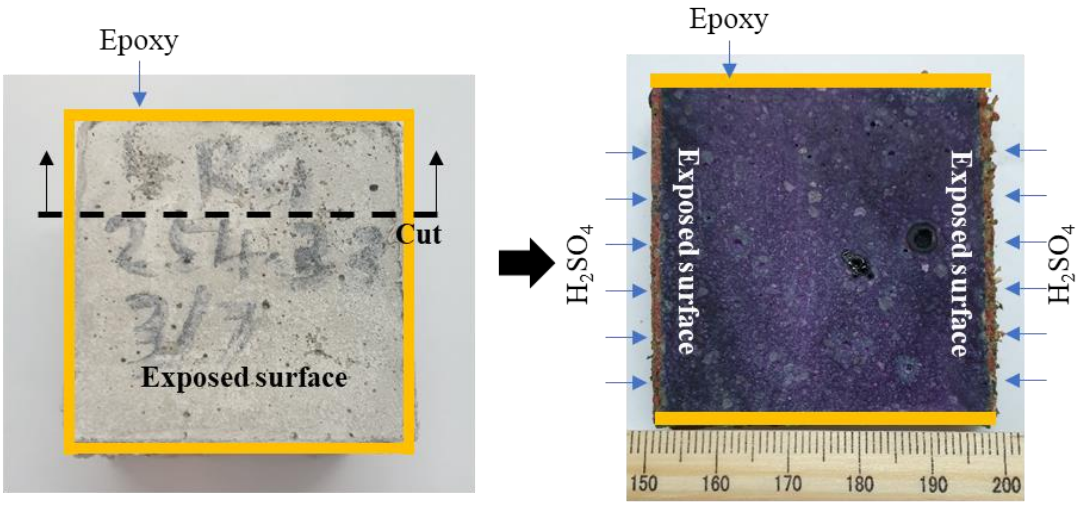

(a) Mortar after acid immersion test (b) Cross-section of coupon mortar

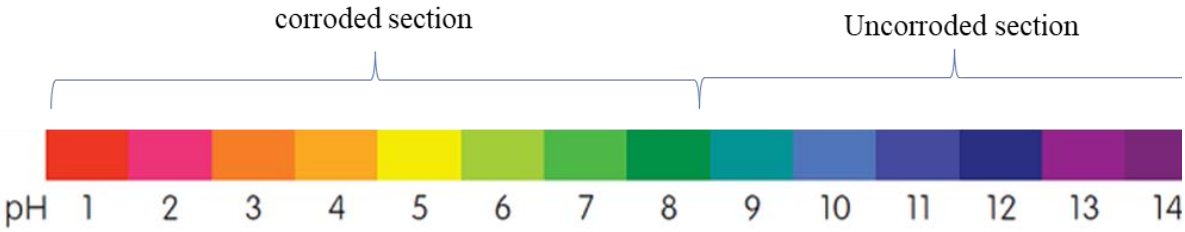

Figure 5-3 Acid attack on the cross-section of mortar from acid immersion test

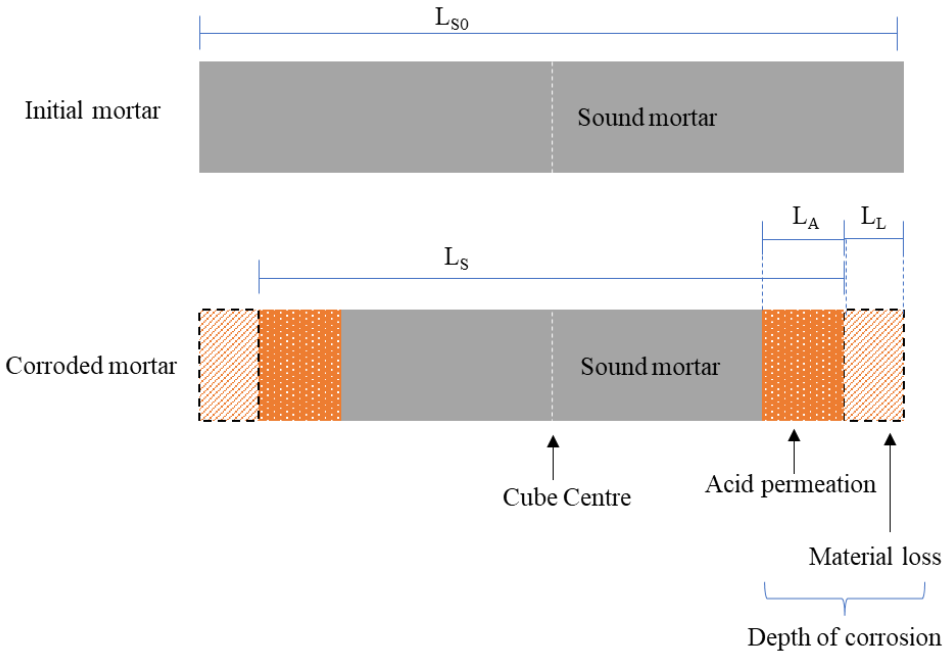

Figure 5-4 Schematic diagram of the depth of corrosion calculation

$$DoC = \left(\frac{L_{S0}}{2} - \frac{L_S}{2}\right) + L_A \qquad \text{Equation 5.1}$$

Figure 5-5 presented microscopic images of OGPm and CACm after acid immersion for up to 28 days after spraying the universal indicator. It visually observed that the acid permeation gradually progressed toward the mortar matrix as a function of time. Moreover, the acid permeation depth was exhibited differently between the lining mortar. This result suggested that the corrosion resistance differs depending on the lining mortar type. This suggestion agrees with Dorner (2000) that the corrosion resistance of concrete depends on the type and chemical composition of the cement as well as the pH of the attacking acid. Moreover, the porosity was also expected to influence the depth of permeation based on the study by Khan et al. (2020b).

The corrosion resistance performance of the mortar was examined from the depth of corrosion. Figure 5-6 shows the corresponding plots of the corrosion depths of the four OGPm and CACm as a function of time. It was observed that the corrosion depth was increased as a function of time. The corrosion behaviour was observed to occur in two stages. The initial stage exhibited accelerated corrosion, considered stage I corrosion, which persisted for a duration of up to 3 days. This was followed by a subsequent stage characterised by slow corrosion, considered stage II corrosion. Based on the corrosion depth after 28 days of acid immersion test in Figure 5-6, the CACm showed the highest resistance to corrosion as expected, followed by OGPm-1, OGPm-2, OGPm-4, and OGPm-3. The plot of corrosion depth as a function of time of all OGPm in Figure 5-6 was examined further by analysing the corrosion rates. The corrosion rates were estimated by fitting the line to the depth of the corrosion plot (see Figure 5-7). The slopes of the fitted line are reported as stage I corrosion rate (R_1) and stage II corrosion rate (R_2).

Immersion	OGPm-1	OGPm-2	OGPm-3	OGPm-4	CACm
1 Day	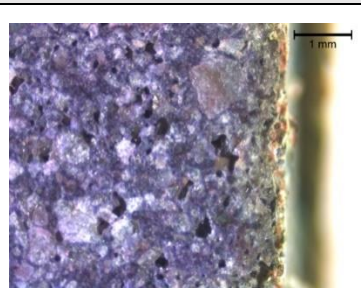	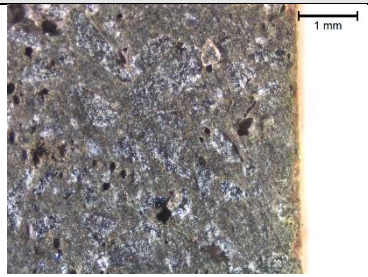	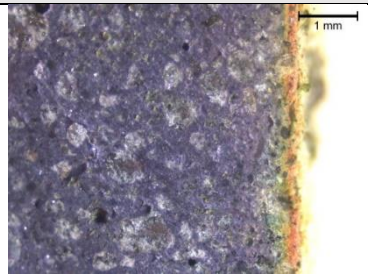	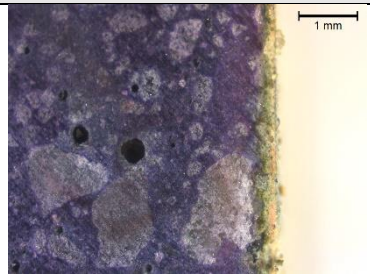	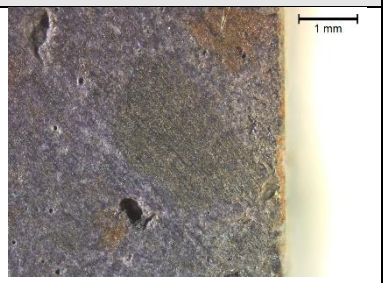
14 Days	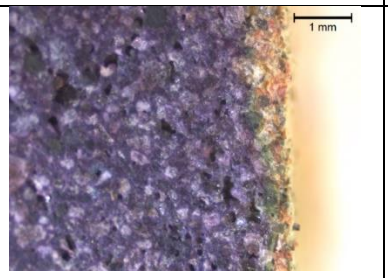	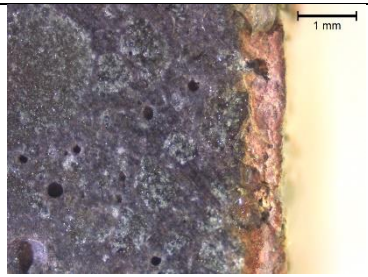	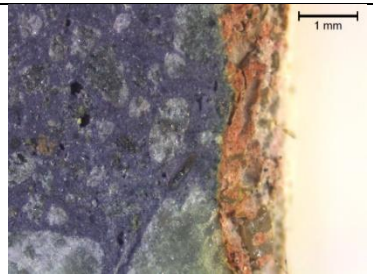	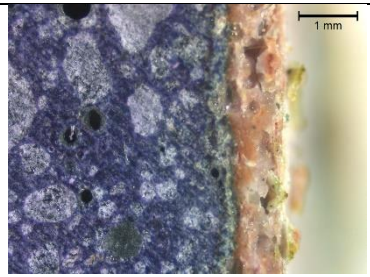	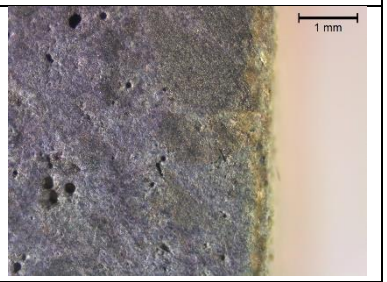
28 Days	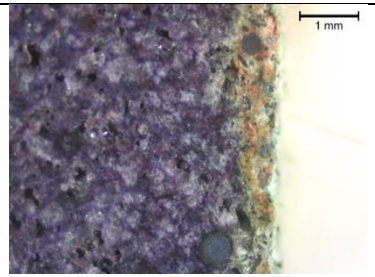	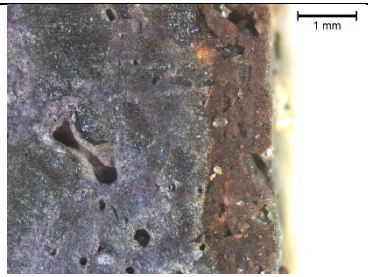	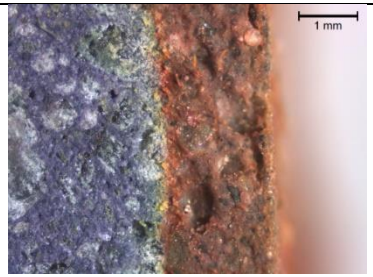	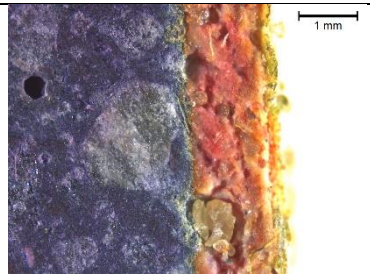	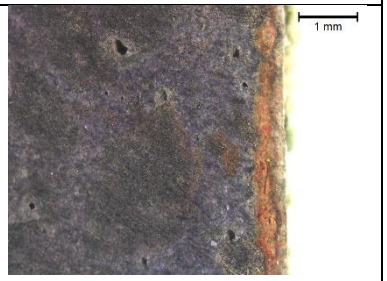

Figure 5-5 Progression of Corrosion surface for OGPm and CACm after acid immersion up to 28 day

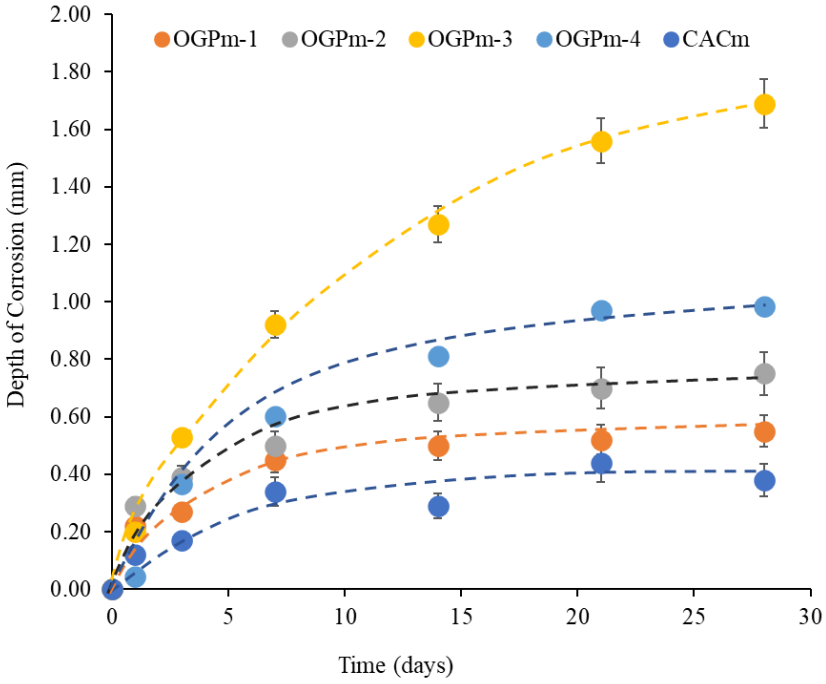

Figure 5-6 Plot of the depth of corrosion of OGPm and CACm as a function of time of exposure to sulphuric acid (pH 1, 30 °C)

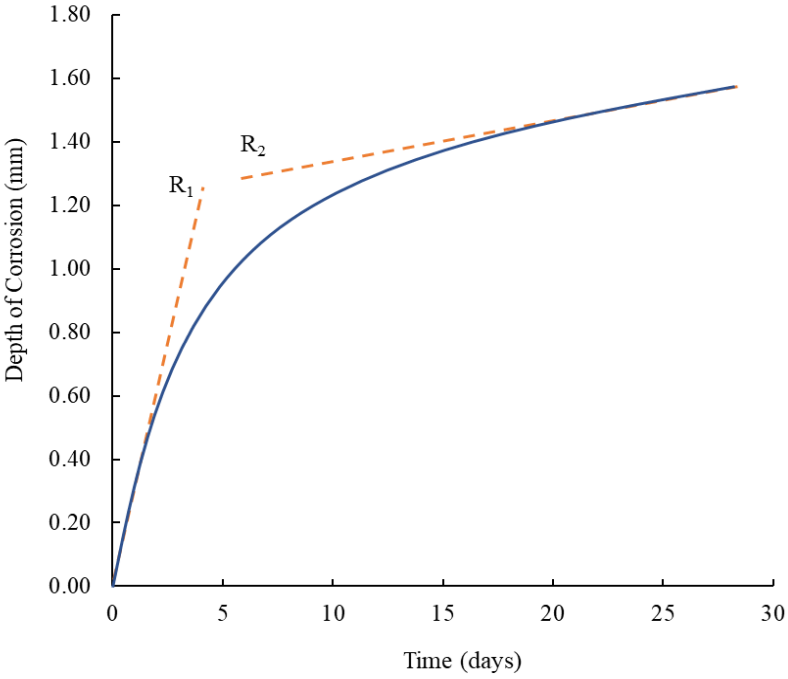

Figure 5-7 Fitted rates of corrosion

A comparison of relative corrosion resistance based on R_1 for the OGPm and CACm, shown in Figure 5-8(a), confirms their relative corrosion resistance established from the corrosion depth

in Figure 5-6. The relative corrosion resistance based on R_1 of the mortar is CACm > OGPm-1 > OGPm-2 > OGPm-4 > OGPm-3. In a similar comparison, the relative corrosion resistance based on R_2 in Figure 5-8 (b) showed a similar trend in R_1. Interestingly, The R_2 of OGPm-1 was comparable with CACm, which usually presented better performance and durability. The low R_2 rates observed for all OGPm and CACm were an exciting feature for estimating the service life of lining mortar. Additionally, it occurred over a period of time and could, therefore, have an important bearing on the durability of OGPm. This result highlighted that the corrosion rates exhibited by the second-stage corrosion were an important feature of these protective lining mortars, which is reflected by the values of R_2. The corrosion rate reduction in the second stage could be attributed to the increased diffusion resistance for the acid through the build-up of the corrosion layer and to pore blocking by gypsum.

Once the OGPm and CACm were immersed in an acid solution, The dissolution of important elements from hydrates phases such as Na^+, Ca^{2+}, Fe^{3+} and Al^{3+} occurred at lower pH values, resulting in increasing the porosity (Dorner, 2000, Dorner and Beddoe, 2002, Yuan et al., 2013, Khan et al., 2020b). The increasing porosity provided more H^+ and SO_4^{2-} permeation pathways and reacted further with mortar binder, especially Ca^{2+}. The SO_4^{2-} was reacted with $Ca^{2+,}$ formulating expansive corrosion products such as gypsum and ettringite (Beddoe and Dorner, 2005, Monteny et al., 2000, Khan et al., 2020b, Scrivener et al., 1999, Yuan et al., 2013). The corrosion products caused the deterioration of the lining mortar by generating more cracks and allowing more acid to penetrate the lining mortar matrix. Therefore, the corrosion resistance performance of the lining mortar depended on the transport mechanism and diffusion of sulphate and proton from the sulphuric acid solution (Albitar et al., 2017, Khan et al., 2020b). However, the corrosion products formed along the cracks limited acid diffusion through the pore by acting as a barrier between the sound mortar and acid solution. This phenomenon resulted in reducing the corrosion rate. Additionally, the OH^- that leached out from the lining

mortar matrix was reacted with H^+ as a neutralisation process, resulting in lower acid permeation. It is important to note that at a lower pH solution than 3.5, the $Al(OH)_3$ was dissolved and neutralised more acid as in this study (Scrivener et al., 1999).

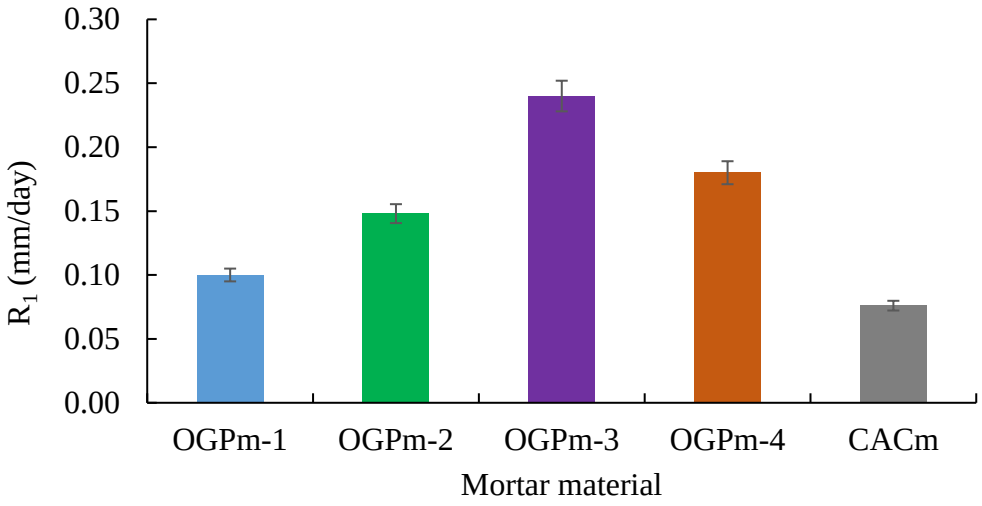

(a) R_1

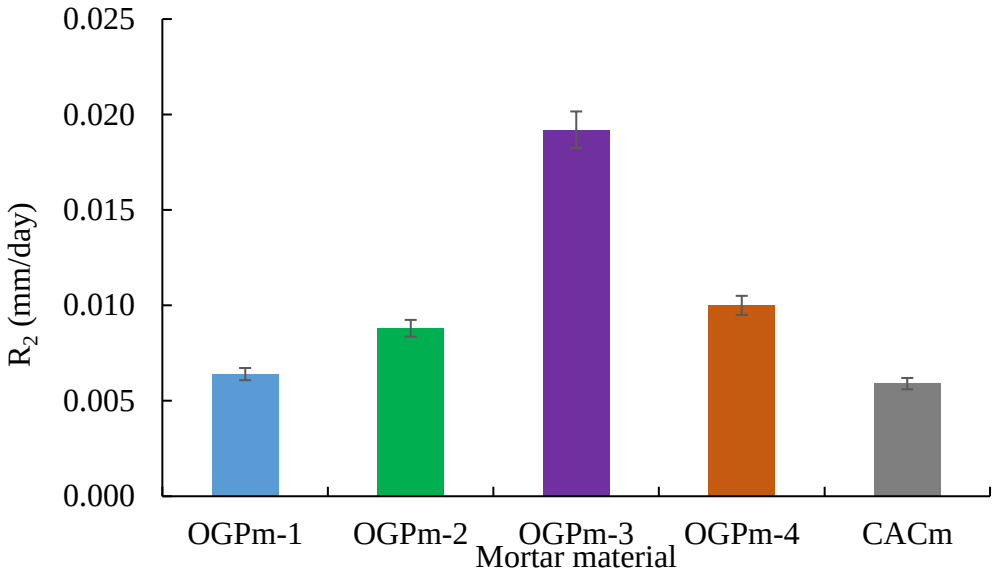

(b) R_2

Figure 5-8 The a) initial and b) final rates of corrosion of geopolymer and CAC exposed to H_2SO_4 at pH 1.0 and 30 °C

The initial porosity is relatively linked to the corrosion resistance performance of mortar. The porosity of the fresh OGPm ranged from 15.6% to 24.5%, whereas the fresh CACm exhibited a porosity of 13.8%. Figure 5-9 shows the correlation between R_1 and R_2 and initial porosity. They showed a strong linear correlation between R_1 and R_2 and initial porosity. The corrosion rate was increased with an increase in the initial porosity.

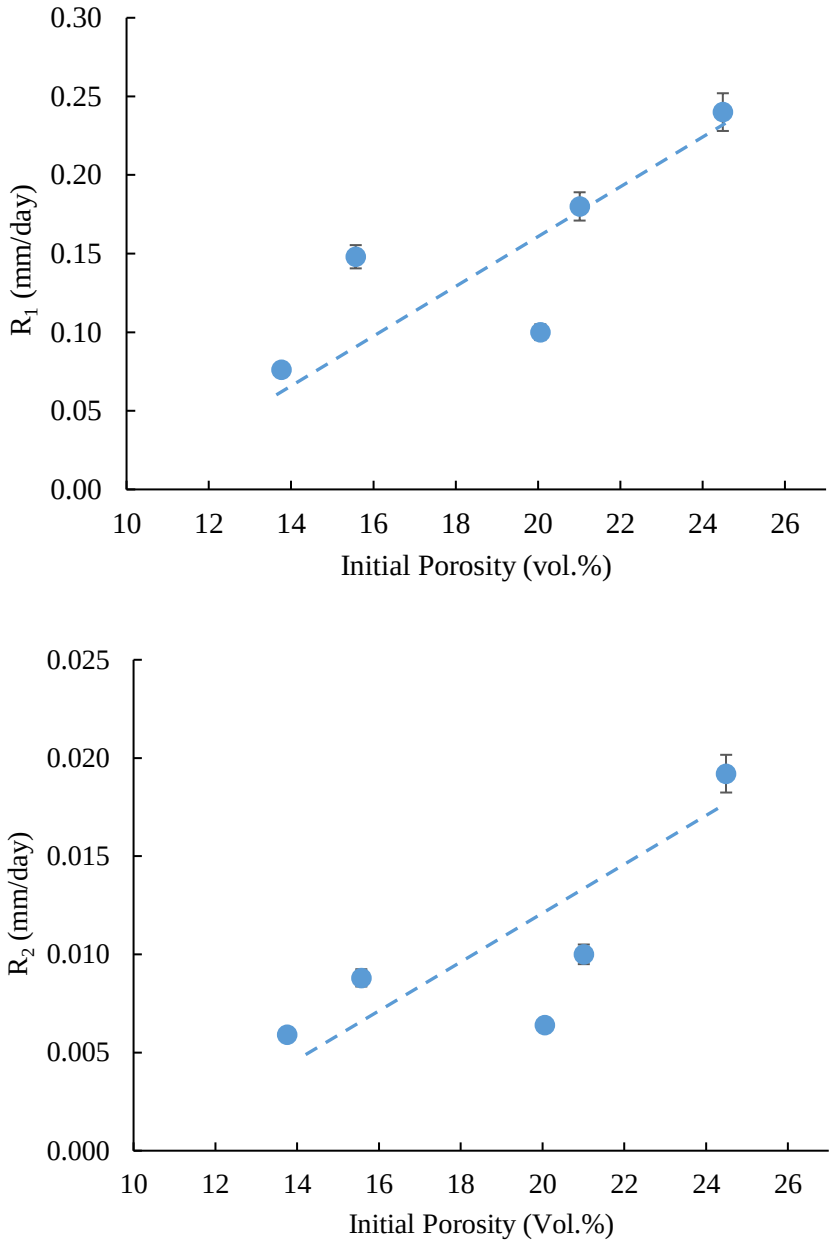

Figure 5-9 Correlation between stage I and Stage II corrosion rate and initial porosity

As noted, OGPm-1 has the highest calcium (Ca) content and OGPm-3 is the lowest calcium (Ca) content. Figure 5-10 shows the correlation between the CaO content in the mortar and R_1 and R_2. The Ca content in the lining mortar strongly correlated with R_1 and R_2. These results presented evidence to confirm that the CaO content in OGPm and CACm played an essential role in the corrosion resistance of the mortar. The corrosion rate in stages I and II revealed that the corrosion rate decreased when the Ca content in the mortar increased due to the formation of corrosion products such as gypsum and ettringite, as mentioned earlier.

The formation of gypsum was also observed using SEM/EDS. Figure 5-11 shows the corroded microstructure of OGPm-1 and OGPm-3 using SEM/EDS after 28 days of acid immersion test. The corroded section developed a 'mushy' crystalline texture on the surface due to the decalcification from hydrate mortar binder reacting with SO_4^{2-} to form expansive corrosion products such as gypsum and ettringite. The EDS line scan within the deteriorated region of OGPm-1 and OGPm-3 presented the high concentration of Sulphur (S) element as representative of gypsum on the surface and low concentration when the distance scanned further toward the sound mortar region. Moreover, It was noticed that the concentration of the S on the surface of OGPm-1 was more than OGPm-3, as expected. This is because the Ca content in OGPm-1 was higher than OGPm-3 based on the XRF analysis (See Table 4-1 XRF analysis of the OGPm and CACm binder chemical composition in Chapter 4). The Ca reacted with SO_4^{2-}, formed more gypsum, and deposited within the pore from the surface toward the sound mortar.

Another noticeable is that the depth of S permeation presented in OGPm-1 and OGPm-3 lining matric, the OGPm-3 observed a depth of S approximately 2 mm, while the OGPm-1 observed a depth of S approximately 0.8 mm. These results are attributed to the porosity of the lining mortar. The initial porosity of OGPm-3 was higher than OGPm-1, allowing more acid to permeate deeper toward the sound mortar.

This finding highlighted that the corrosion of lining mortar by acid attacks relied on the transport mechanism and diffusion of sulphate and proton from the sulphuric acid solution. However, the corrosion product, such as gypsum from the acid attacks, had an advantage in slowing down the corrosion rate by acting as a barrier to reduce acid diffusion. The formation of gypsum appears to depend on the calcium content of the binders. However, if the gypsum is formed excessively, it could accelerate the corrosion rate because gypsum and ettringite is expansive compounds and one of the most common causes of corrosion of lining mortar in sewer environments.

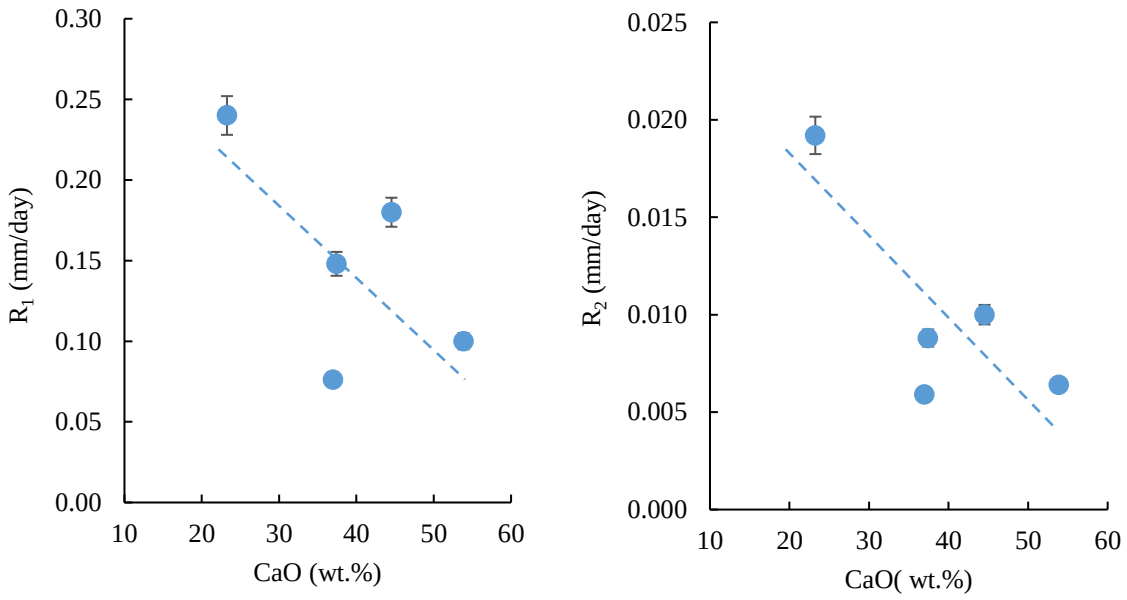

Figure 5-10 Correlation between stage I and stage II corrosion rate and CaO content

OGPm-1

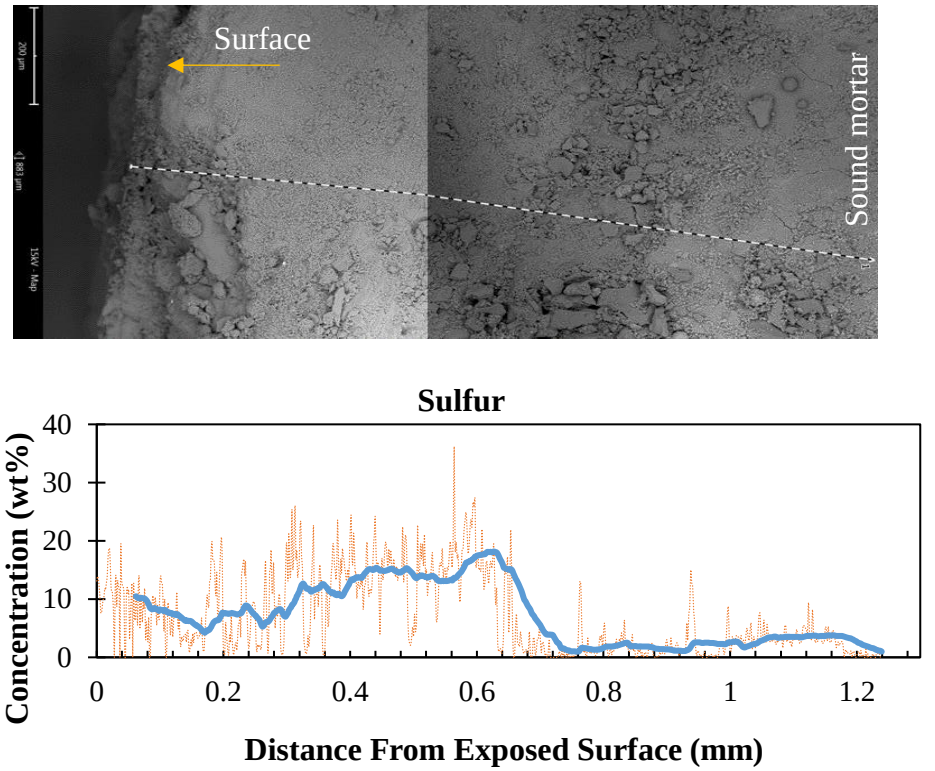

OGPm-3

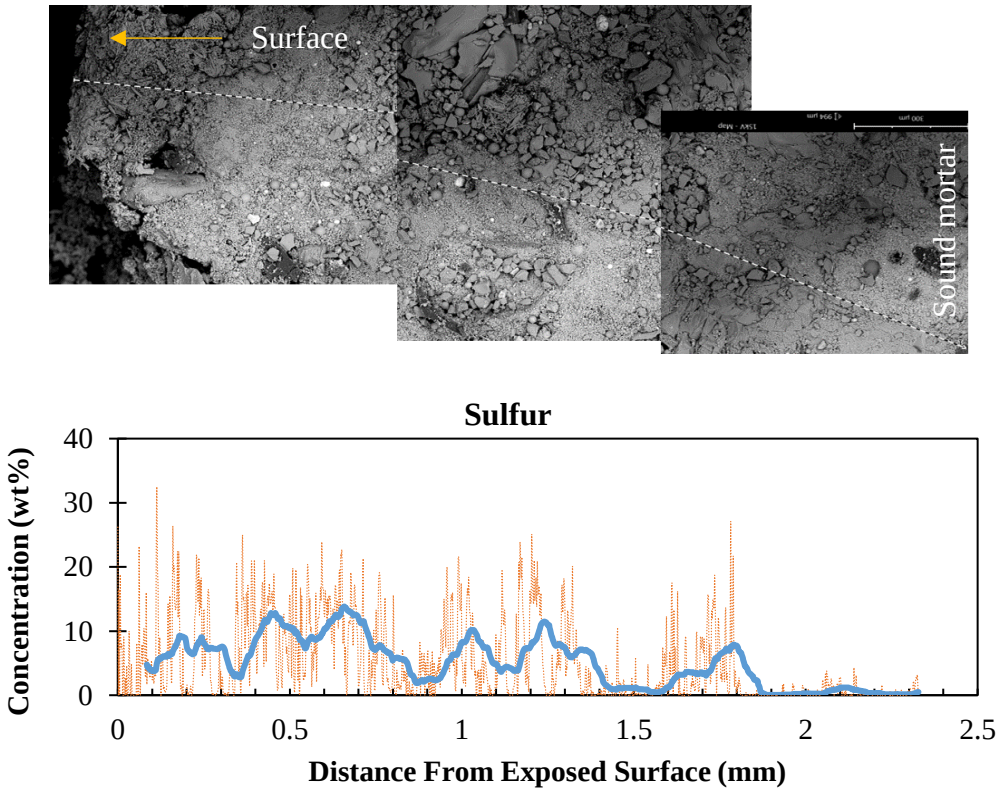

Figure 5-11 The SEM/EDS of OGPm-1 and OGPm-3 after 28 days of acid immersion test

Another parameter assessing the corrosion resistance performance is the initial UCS. Both stage I and stage II corrosion rates were correlated with the initial UCS to confirm the durability of mortar related to the initial UCS. Figure 5-12 shows a strong negative correlation between the initial UCS and R_1 and R_2. The corrosion rates were decreased with decreased initial UCS of lining mortar. These results confirmed that the durability of the mortar is related to its initial UCS. It is attributed to the physical and chemical properties of lining mortar.

High initial UCS is related to the low initial porosity and Ca content, which is key to the acid permeability of the mortar. As mentioned above, the Ca content is also presented as one of the essential elements in lining mortar. It could reveal the advantages or disadvantages of the corrosion resistance performance. Figure 5-13 shows the correlation between the corrosion rates at stage I and stage II and the initial porosity of the mortar. The results revealed a clear positive correlation between the corrosion rate and the initial porosity, indicating that both corrosion rates increased when the porosity increased. This suggests that a higher initial porosity in the mortar leads to greater corrosion in both stages. Combining the high porosity with low Ca content would lead to high corrosion depth. Therefore, A higher initial UCS generally corresponds to improved corrosion resistance, suggesting that a stronger mortar exhibits better durability in corrosive environments. However, it needs to control the Ca content appropriately in the lining mortar mix.

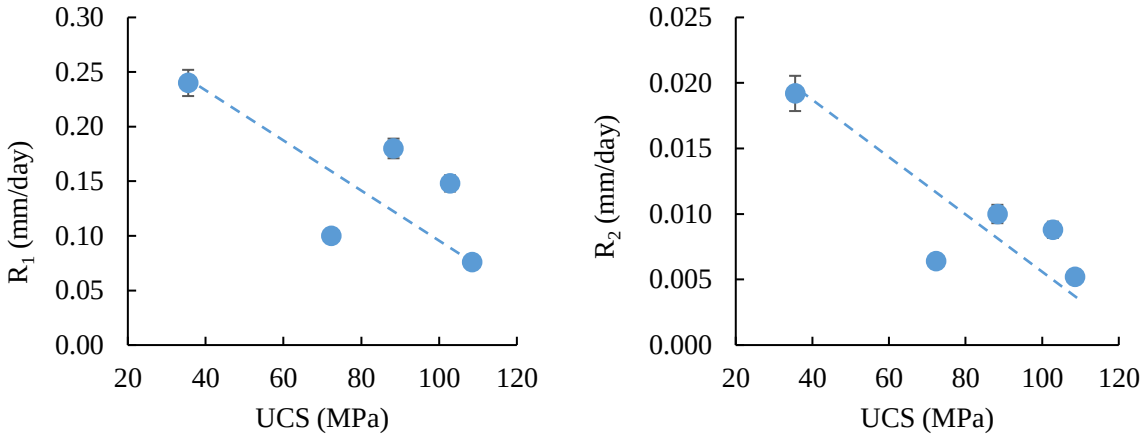

Figure 5-12 Correlation between the rate of corrosion and UCS

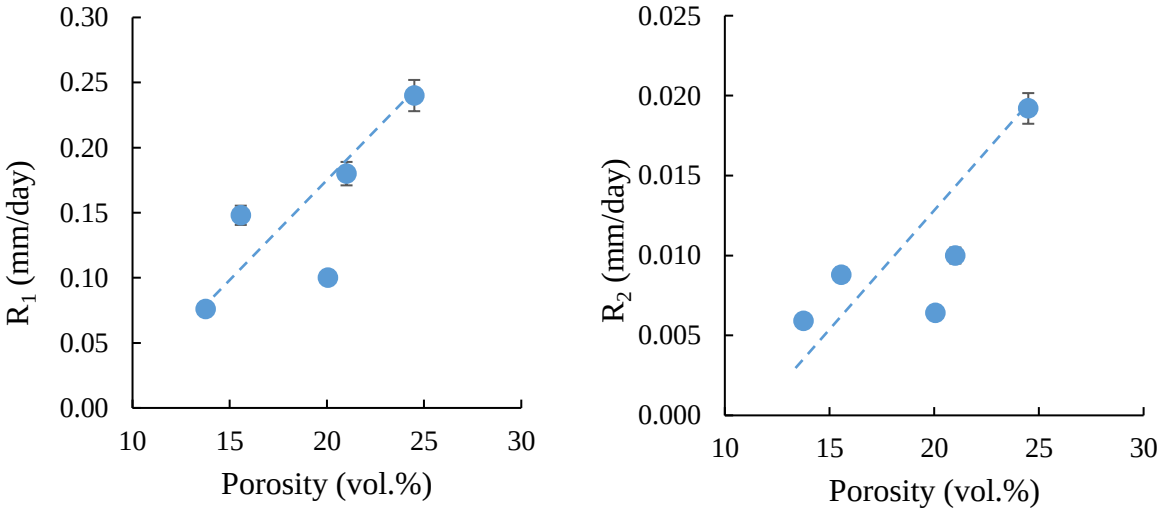

Figure 5-13 Correlation between the rate of corrosion and porosity

Figure 5-14 shows the correlation between the ANC of the lining mortar and the corrosion rate at stage I and stage II of corrosion. It observed optimal corrosion resistance performance in geopolymer mortar in both stages. The correlation suggested that both corrosion rates were decreased with increased ANC, followed by a slight increase after ANC reached 4.5 mmol H^+/g substrate. This behaviour is attributed to the available oxide composition, especially Ca, in the mortar (Giampaolo et al., 2002b). Once the acid attacks the mortar binder, several elements from the hydrate phase, such as Na^+, Fe^{3+}, Si^{4+}, Al^{3+}, and Ca^{2+}, leach out, increasing porosity and providing more pores, allowing acid to penetrate further toward sound lining

mortar. During the acid permeation, the formation of gypsum and neutralisation coincide. Increasing the ANC reduced the corrosion rate. Increasing ANC is related to the Ca content in the mortar (see 4.5.2.3). However, if the ANC excessively increases, it potentially increases the corrosion rate due to the reaction between Ca^{2+} and SO_4^{2-}, forming an expensive corrosion product such as gypsum.

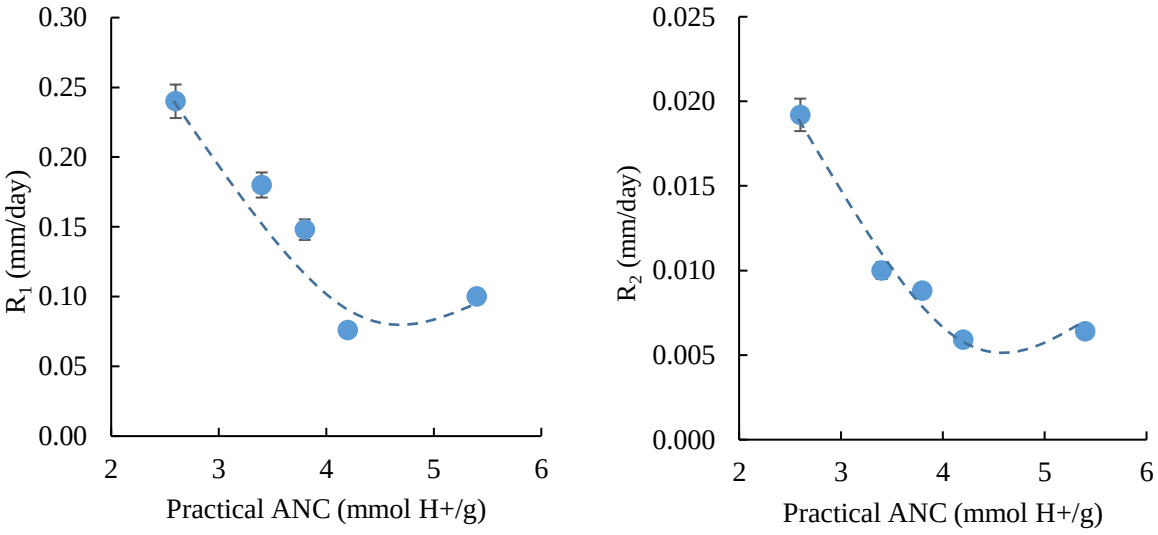

Figure 5-14 Correlation between the rate of corrosion and ANC

Figure 5-15 presents the correlation between the corrosion rates at both stages and the hydration binder products (C-S-H, C-A-S-H, C-N-A-S-H, and N-A-S-H). The plots show a negative optimal correlation between the corrosion rates and the amounts of C-S-H and C-A-S-H. As the content of C-S-H and C-A-S-H increases, the corrosion rates initially decrease. However, the levels of C-S-H and C-A-S-H immediately exceeded approximately 15% and 35%, respectively. The corrosion rates started to increase. These results attributed to the decalcification of hydrate products and the formation of gypsum. At the same time, C-N-A-S-H shows a weak negative correlation with the corrosion rates.

Additionally, the positive optimal correlation observed with N-A-S-H indicates that increased N-A-S-H content leads to higher corrosion rates in both stages. This relationship is likely due to the porosity of the mortar, as higher N-A-S-H content is associated with increased porosity (see section 4.5.1.2), allowing the corrosive compounds to penetrate and react with the mortar binder matrix. Therefore, optimizing the amount and type of hydration products is important for improving corrosion resistance performance.

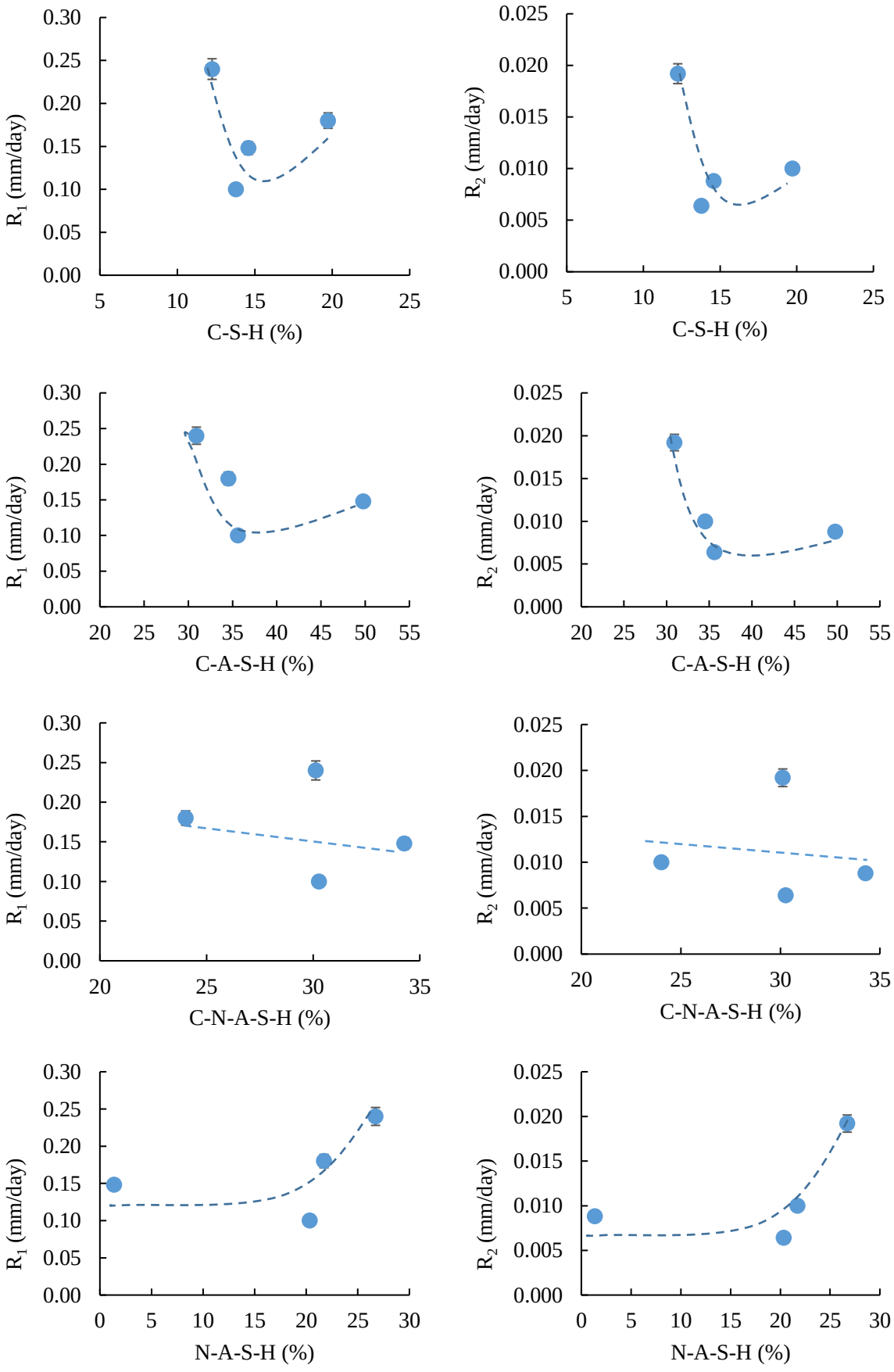

Figure 5-15 Correlation between the rate of corrosion and hydration binders

5.2.1.1.3 RESIDUAL UNCONFINED COMPRESSIVE STRENGTH (UCS)

The initial and residual UCS was measured with the corrosion progression to monitor the strength loss from the acid attack. The residual UCS were measured from the remaining sound concrete. Therefore, the corroded layer and the epoxy coating on all four sides of the corroded mortar sample were carefully removed, as shown in section 3.6.2. The UCS of deteriorated OGPm and CACm from acid immersion tests at different corrosion times were estimated to be similar to the initial UCS based on ASTM C109 (ASTM-C109/C109M-21, 2021). The initial compressive strengths of the OGPm-1, OGPm-2, OGPm-3, OGPm-4, and CACm are 72.3, 102.8, 35.4, 88.3 and 108.5 MPa, respectively.

The change of residual UCS of all lining mortar over time was plotted in Figure 5-16. Among the OGPm, the residual UCS of all lining mortars were initially increased and followed by a decrease with time. In the early period, the UCS was increased as the mortar absorbed the water and acid from the acid solution, leading to the development and deterioration of UCS. The initial increase in UCS is attributed to the hydration of calcium silicates and pozzolanic reactions (Albitar et al., 2017). For example, the OGPm-3 exhibited the highest increase in the UCS during the first 7 days after being exposed to acidic solutions, followed by a decrease in the UCS. The increase in UCS at the initial exposure time was similar to the study by Albitar et al. (2017). They suggested that the increase in UCS was attributed to C-S-H and C-A-H from the hydration of available calcium silicates and pozzolanic reactions (see Equation 5.2 and Equation 5.3) of fly ash or other silica sources, which result in internal confinement due to the pressure that the expanded elements exert and enhance the integrity of geopolymer mortar specimens (Sargent, 2015, Albitar et al., 2017). It needs to note that the pozzolanic reactions occur over long time scales (months to years) (Sargent, 2015), and according to Bergado et al. (1996) and Diamond and Kinter (1965), the pozzolanic reactions are not complete until five years post-mixing.

$$Ca^{2+} + 2(OH)^{-} + SiO_2 \rightarrow C - S - H \qquad \text{Equation 5.2}$$

$$Ca^{2+} + 2(OH)^{-} + Al_2O_3 \rightarrow C - A - H \qquad \text{Equation 5.3}$$

The reduction in UCS of OGPm and CACm was caused by the number of essential elements such as Al^{3+}, Si^{4+}, and Ca^{2+} leaching out, especially Ca^{2+}, which leads to the formation of gypsum and ettringite, resulting in strength reduction due to expansion, cracking and material loss (Alzeebaree et al., 2019, Xie et al., 2019, Khan et al., 2020b). These results indicated that acid attacks of the OGPm and CACm led to the deterioration of mortar based on UCS reduction.

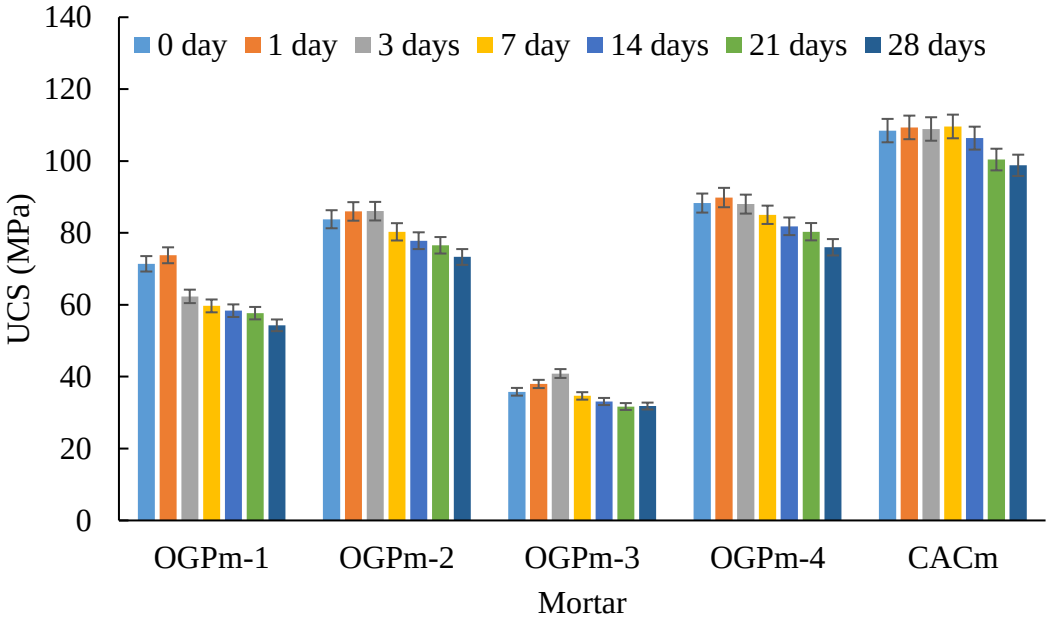

Figure 5-16 Compressive strengths of OGPm and CACm exposed to H_2SO_4 pH 1.0 at 27°C

Figure 5-17 presents the percentage of loss or gain UCS compared to the initial UCS. Initially, all mortar was increased in the UCS, followed by a decrease in the UCS. This phenomenon has been suggested by Yuan et al. (2013) and Albitar et al. (2017) that the increase of UCS was related to the continuing hydration of the matrix and the formation of corrosion products filling the pores, which results in internal confinement due to the expansion pressure. This internal pressure can exert forces on the surrounding material, causing it to crack, delaminate, or undergo mechanical damage (Vafaei and Allahverdi, 2017). The UCS loss of all OGPm and

CACm after 28 days in the acid immersion test exhibited a loss of UCS not more than 32% from their initial UCS. Among the OGPm, The OGPm-1 was the highest loss of the UCS, approximately 31% and OGPm-3 was the lowest loss of UCS, approximately 12.5%. This result would be attributed to the Ca content in the mortar lining.

Interestingly, despite having a denser matrix and high initial UCS, OGPm-2 experienced a loss of UCS of about 14%, which was more than OGPm-3. This indicated that OGPm-2 matrices started to lose their structural integrity, which is linked to the decalcification from the OGPm-2 matrices and the formation of a corrosion product such as gypsum. Lower UCS loss in OGPm-3 was potentially due to the lowest CaO content in the mix, resulting in the highest N-A-S-H matrix compared to other OGPm. Based on the literature, the cross-linked N-A-S-H usually has high acid corrosion resistance compared to C-A-S-H (Aiken et al., 2018, Khan et al., 2020b, Lee and Lee, 2016). Therefore, the acid immersion test revealed the highest acid resistance performance based on the reduction of UCS, which was OGPm -2, followed by OGPm-4, OGPm-3, and OGPm-1, respectively.

In comparison, CACm experienced a loss of UCS of about 9% with a decelerating trend. In a CACm acid attack, decalcification from CACm was leached, and $CaSO_4$ and $Al(OH)_3$ were formed (Scrivener et al., 1999). The $Al(OH)_3$ was further dissolved when the pH was below approximately 4. Specifically, in the experimental conditions of this study, the pH of the solution was maintained at 1. At this low pH, the presence of OH^- ions facilitated the neutralisation of H^+ ions, effectively slowing down the degradation process of CACm. This mechanism played a crucial role in preserving the integrity and durability of the CACm under the given acidic conditions. Furthermore, the observed loss of UCS in this study confirmed that CACm exhibited superior corrosion resistance compared to OGPm.

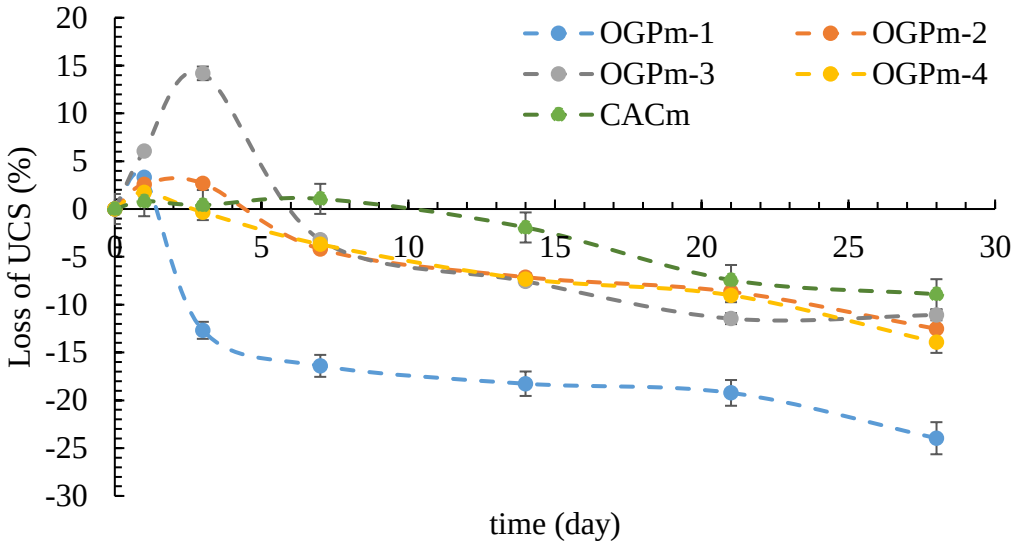

Figure 5-17 Loss of UCS of OGPm and CACm with respect to exposure time in acid solution (pH 1) with 27 °C

5.2.2 SEWER CORROSIVITY CLASSIFICATION

Concrete, protective linings and other materials are sensitive to corrosion when exposed to harsh sewer environments (Jacobs, 2019, Valix, 2018, Valix et al., 2012, Okabe et al., 2007b, Hudon et al., 2011, Valix et al., 2011, Nielsen et al., 2005a). This means that lining mortar depends on its corrosion resistance performance and exposed environmental conditions. Therefore, the environmental conditions must be considered in mortar lining selection. Currently, only one classification for sewer corrosivity is designated as a “severe environment” (WSA-201, 2017). The information on the corrosivity of the sewer environment is an essential requirement for selecting material, selecting mitigation strategies (e.g., type of protective linings), and estimating service life (Mikhailov et al., 2004, Knotková, 2007). Recently, sewer corrosivity classification of sewers was developed as part of the CRC-P Smart Linings for Pipes and Infrastructure project. It refers to the severity of sewer concrete corrosion when the concrete is exposed to corrosive or harsh environmental conditions.

Sewer deterioration can occur from the impact of Microbially Induced Concrete Corrosion (MICC) on the gas phase. It can also be impacted by tree root intrusion (Hawari et al., 2017),

soil corrosivity and chemical and abrasion in the submerged phase (Damvergis, 2014, De Belie et al., 2004). In general, the impact of MICC is considered the most aggressive. For the study undertaken in the CRCP, only the effect of MICC was classified. The impact of MICC is complex and will typically involve the growth of microbes, generation of acid, and acid attack (Grengg et al., 2018). The sewer corrosivity classification, therefore, used the environmental conditions as surrogate measures to infer the corrosivity of the sewer. Sewer environmental conditions included H_2S, CO_2, temperature, and relative humidity. This is because the H2S, CO2, temperature, and relative humidity significantly influenced the corrosion of the concrete sewer assets as a precursor of MICC in different stages. H_2S and CO_2 gases, through abiotic and biotic processes, can undergo conversions that lead to the formation of corrosive compounds such as H_2SO_4 (sulfuric acid) and H_2CO_3 (carbonic acid). These acids then attack the concrete matrix within sewer systems, forming calcium carbonate, gypsum, and ettringite. (Jiang et al., 2015a, Grengg et al., 2018).

To generate the classification, an environmental survey of 16 sewer assets (manhole and pipes) and a condition assessment of the concrete assets that have been in service for 20-81 years were undertaken. The classification was verified by the corrosion of various protective coatings under different exposure conditions.

The final classification recommended by the CRCP Smart Linings projects is shown in Table 5-1. As shown, the corrosivity is divided into five classifications. These are Classification 1: very low corrosivity (C1), classification 2: low corrosivity(C2), classification 3: Medium corrosivity (C3), classification 4: high corrosivity (C4), and classification 5: very high corrosivity (C5). These are correlated to the environmental condition limits, also referred to as the ‘dose’ and corrosion impact on the concrete sewer asset. The corrosion impact was reported as the range of corrosion depth (in mm) at 10 and 100 years of service. The corrosion impact was also reported in terms of residual UCS (in MPa) at 10 and 100 years of service. The

temperature and relative humidity were broadly reported from 15-28 and 95-99 %RH, respectively, with no specific correlation to H_2S. This was similar to the previous sewer environmental survey within Australia by Valix and Shanmugarajah (2015). However, sensitivity analysis showed that the changes in temperature and RH under specific categories do not affect the change in the corrosion rates to alter the classification (Valix, 2021). A sewer concrete corrosion model was developed for a more accurate corrosion prediction. This is embedded in the Sewer Decision Tool developed under the CRCP Smart Linings project.

Table 5-1 Classification of Sewer Corrosivity adopted from Valix (2021)

Corrosion Classification	Corrosion Impact	Environmental Conditions				Predicted Corrosion of Concrete Asset			
						Depth of Corrosion (mm)		Residual UCS (MPa)	
		H_2S (ppm)	CO_2 (ppm)	T_g(°C)	RH (%)	10 years of service	100 years of service	10 years of service	100 years of service
Category 5	Very High	>155	<2500	15-28	95-99	>61	>180	<25	<19
Category 4	High	135-155	2500-4000	15-28	95-99	54-61	158-180	25-34	19-26
Category 3	Medium	70-135	4000-9300	15-28	95-99	29-54	85-158	26-36	20-28
Category 2	Low	15-70	9300-9400	15-28	95-99	6.8-29	20-25	27-43	21-33
Category 1	Very Low	<15	9400-9500	15-28	95-99	2.4-6.8	7.0-20	33-49	25-38

5.2.3 DIGESTER CHAMBER TEST

This section presents the acid resistance performance of four lining mortars (OGPm-1, OGPm-2, OGPm-3, and CACm) under a digester tank which presented a sewer environment. The main focus of this section is to evaluate the corrosion resistance performance of lining mortar against the MICC under a sewer environment. The cured mortar cube of OGPm-1, OGPm-2, OGPm-3, and CACm were placed in the three digester tanks, presenting different environmental conditions. The mortar samples were periodically collected, and the corrosion resistance performance was from 6 to 42 months, with samples within this interval where possible. Regular sample collection was interrupted by the Covid-19 shutdown. The details of this test were presented in (see section 3.4.1 in Chapter 3). The corrosion depth and residual UCS were used to assess the corrosion resistance performance and compared to the initial mortar coupon. The test results provided the impact of MICC on the proper preparation of lining mortar samples under different corrosivity environmental conditions. This section also presented the visual of mortar samples after exposure to the digestion chamber under different aggressive environmental conditions. Moreover, the chemical and physical properties of lining mortar were also correlated to understand the impact of the properties on the durability of lining mortar.

5.2.3.1 CORROSIVITY CLASSIFICATION OF NORTH HEAD CHAMBERS

For the field test in the digester tanks, the lining mortar coupons were installed in three (3) digester tanks denoted as CC1, CC2, and CC3, based on the installation procedures at the wastewater treatment plant (WWTP), Sydney Water. The digester tank received the sewage from the sewer network (see 3.4.1 in Chapter 3). The gases produced in the digester tanks were consistent with the main gas composition in the sewer network, known as sewer gases. The sewer gases typically comprised N_2, CH_4, H_2S, CO_2, NH_3, and SO_2. The latter four gases are

corrosive when hydrolysed and oxidised in humid sewer environments. These sewer gases will form weak and strong acids, specifically H_2CO_3, HNO_2, HNO_3 and H_2SO_3 (Sand, 1997b).

The environmental condition of the three digester chambers was monitored, including H_2S, CO_2, %RH, and temperature. They were monitored during 2018 – 2022. Figure 5-18 presents the environmental condition in CC1 as representative of environmental condition measurement. The environmental survey data were analysed further with statistical analysis. The 90th percentile was used to provide statistical estimates of the gas compositions and conditions from the overall survey (see Table 5-2). The environmental condition of chamber 1, chamber 2, and chamber 3 was classified as C4, C1, and C3, respectively, using Table 5-1.

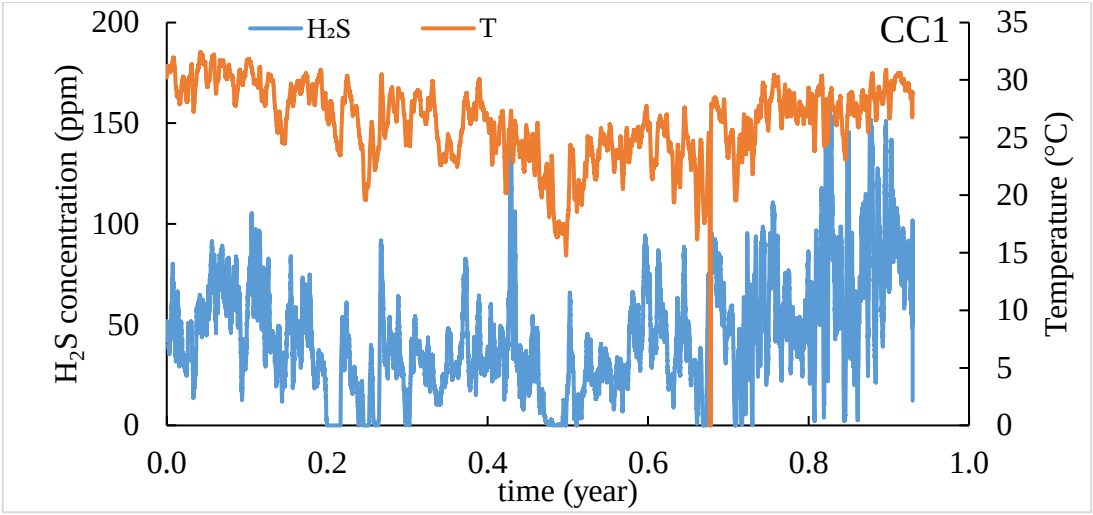

(a) H_2S and temperature

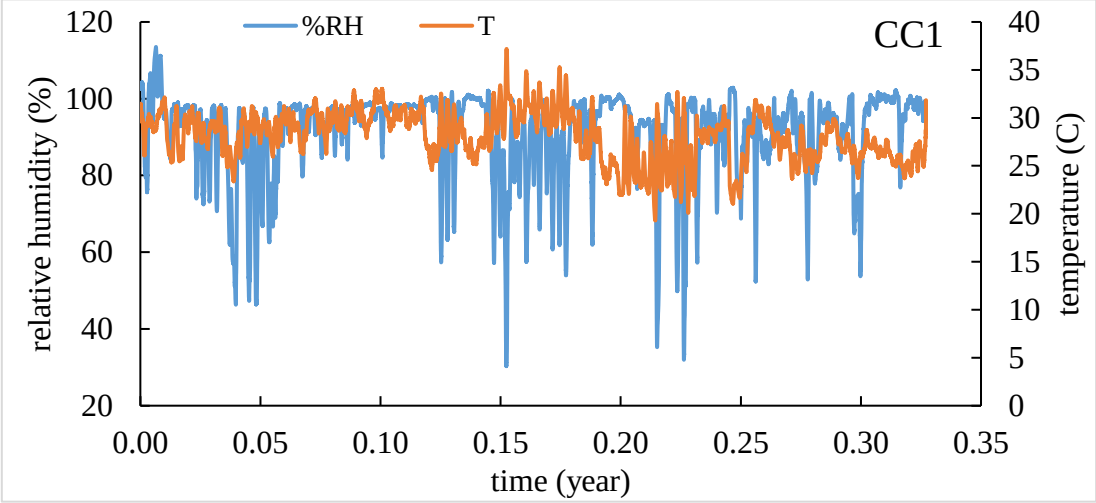

(b) %RH and temperature

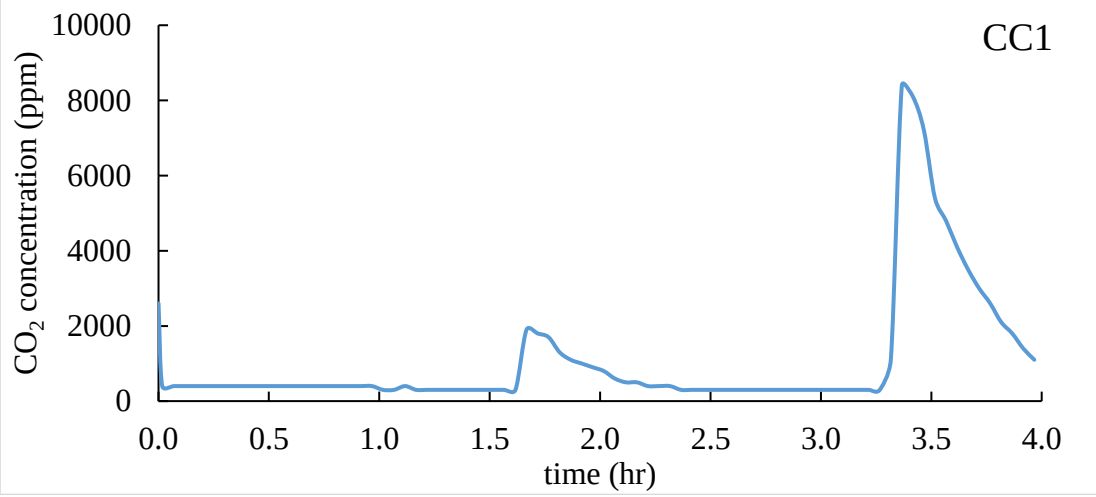

(c) CO_2 and temperature

Figure 5-18 Environmental conditions in chamber 1: a) H2S and T, (b) %RH and T, (c) CO_2

Table 5-2 Environmental conditions of each digestor chamber

Conditions	Chamber 1	Chamber 2	Chamber 3
H_2S (ppm)	146	4	94
CO_2 (ppm)	2600	11900	8150
Temperature (°C)	30.38	28	27.73
Humidity (%RH)	99.99	94.93	99.99
Corrosivity classification	C4	C1	C3

5.2.3.2 CORROSION RESISTANCE PERFORMANCE

5.2.3.2.1 PHYSICAL APPEARANCES

After exposure of the OGPm and CACm in three digester chambers, which presented sewer corrosivity classification of C1, C3, and C4 for up to 42 months, the OGPm and CACm were periodically collected and assessed the corrosion resistance performance based on corrosion depth and residual UCS.

Figure 5-19 presents corroded OGPm-1, a representative sample collected from C1, where the sewer corrosivity classification C4 was presented. The figure clearly shows the accumulation and expansion of corrosion products on the exposed surface of OGPm-1. The epoxy coating on the four sides of the lining cube was extremely cracked. Furthermore, the corroded surface of OGPm-1 exhibits noticeable material loss and expansion, indicating the extent of degradation caused by corrosion. It is important to note that not all geopolymers exhibit the same degree of deterioration as OGPm-1. The deterioration of lining mortar after exposure to sewer environmental conditions differed depending on the lining mortar and the corrosivity of environmental conditions (see Figure 5-20 - Figure 5-22).

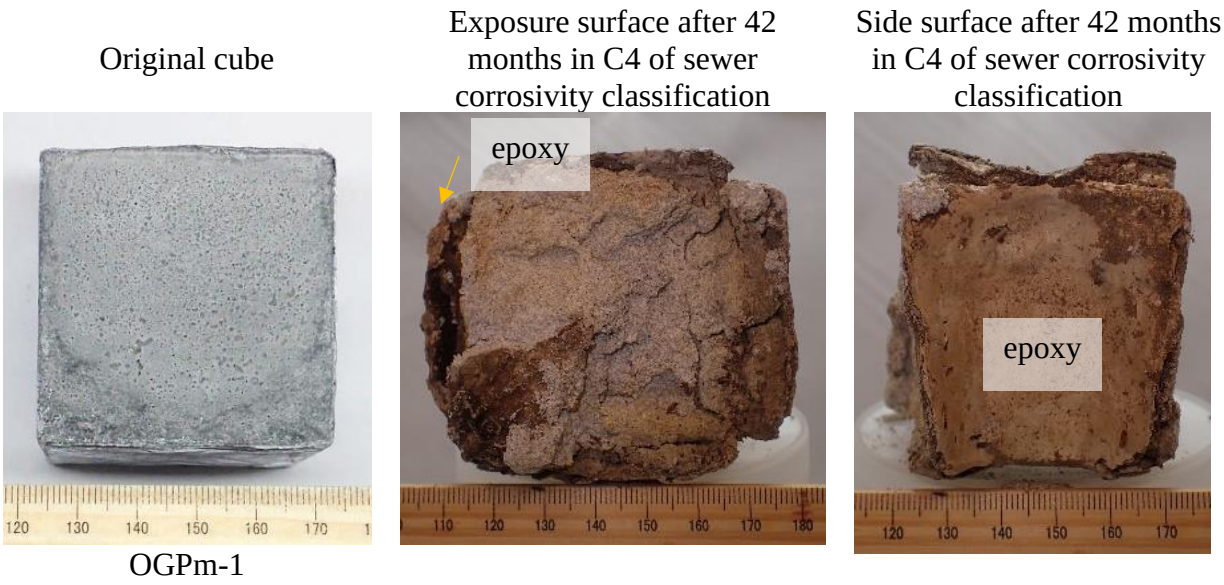

Figure 5-19 Corroded OGPm-1 and OGPm-2 after 42 months in C4 of sewer corrosivity

The visual acid permeation of OGPm and CACm exposed in C1, C3, and C4 sewer corrosivity was assessed based on the procedure explained in section 3.6.1. The corrosion depth of all mortar samples was determined using a universal indicator, providing a visual representation of the extent of corrosion.

Figure 5-20 presents the corrosion depth of OGPm and CACm samples after 31 and 42 months in C1 sewer corrosivity classification (very low corrosivity). The cross-sections of OGPm-1, OGPm-2, OGPm-3, and CACm were treated with universal indicators, allowing visual assessment. Surprisingly, all OGPm and CACm samples exhibited healthy structural integrity, indicating their high corrosion resistance performance at this corrosivity classification. However, upon evaluating the acid permeation of all mortar samples, it was evident that OGPm-3 exhibited green and yellow colours on the surface. This observation suggested that the pH of the mortar surface was lowered to approximately 5.5, indicating the initiation of deterioration. The colour change from purple to yellow or green indicated the acid attacks from the mortar surface toward the sound lining mortar of OGPm-3. Among the OGPm samples, OGPm-3 presented a significant acid permeation depth of approximately 7 mm compared to

other OGPm samples. Despite the high acid permeation, the OGPm-3 exhibited no material loss from the exposure surface.

Figure 5-21 shows the corrosion depth of OGP and CACm samples after 31 and 42 months in C3 sewer corrosivity classification (medium corrosivity). The cross-sections of OGPm-1, OGPm-2, OGPm-3, and CACm were sprayed with universal indicators, allowing visual assessment. All OGPm and CACm samples exhibited great structural integrity. Despite all the lining mortar showing great structural integrity, the OGPm-3 visually exhibited the highest acid permeation, approximately 8 mm, compared to other lining mortar samples. It presented green and yellow mixed with orange from the surface toward the sound mortar lining, indicating a surface pH of around 3. At the same time, the OGPm-2 exhibited orange on the surface, indicating a surface pH of around 3. The other lining mortar exhibited a purple colour on the surface of each lining mortar. This observation suggested that the surface pH of OGPm-2 and OGPm-3 were lower by approximately 3, while the surface pH of OGPm-1 and CACm were lower by approximately 8-9, suggesting mortar deterioration was presented at different stages of corrosion by MICC. The OGPm-2 and OGPm-3 were at stage 2 of corrosion, while the OGPm-1 and CACm were at stage 1 of corrosion (Islander et al., 1991b).

Figure 5-22 presents the corrosion depth of OGPm and CACm after 31 and 42 months in C4 of sewer corrosivity classification (high corrosivity). Comparing the OGPm-1, OGPm-2, and OGPm-3 at 31 and 42 months of exposure, it was observed that all OGPm significantly deteriorated from their surface toward sound mortar over time. All OGPm experienced the loss of material from the surface and the acid permeation toward sound mortar, assessing based on the colour of the universal indicators on the cross-section of mortar samples. The purple colour means sound mortar, with a pH of approximately 12. However, the extent of material loss and acid permeation varied among the OGPm samples. For example, OGPm-1 exhibited significant material loss from the exposure surface and showed acid permeation towards the sound mortar

at 42 months, as seen in the green colour from the surface. At the same time, OGPm-3 experienced severe mortar deterioration, where material loss and acid permeation from the exposure surface towards the sound mortar was almost 100% deteriorated. CACm demonstrated a low acid permeation level and a minor material loss at the deteriorated surface.

In summary, the visual assessment of acid permeation was conducted on OGPm and CACm samples exposed to different sewer corrosivity classifications (C1, C3, and C4). The results confirmed that sewer corrosivity classification significantly impacted the corrosion performance of both OGPm and CACm. Moreover, OGPm and CACm demonstrated different corrosion resistance performances within the same sewer corrosivity classification. These results are attributed to the variations in chemical and physical properties of the OGPm and CACm.

Time (months)	OGPm-1	OGPm-2	OGPm-3	CACm
31	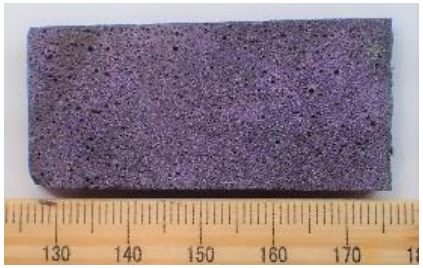		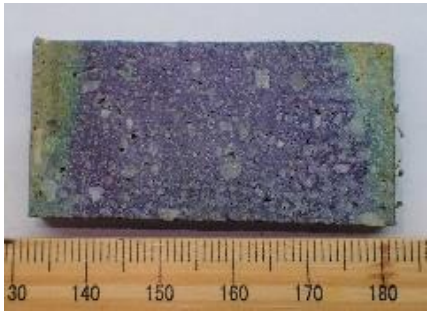	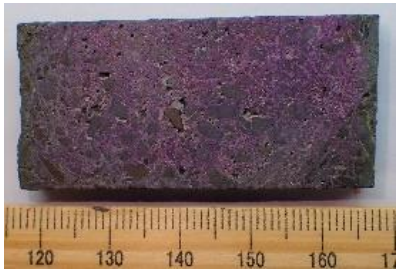
42	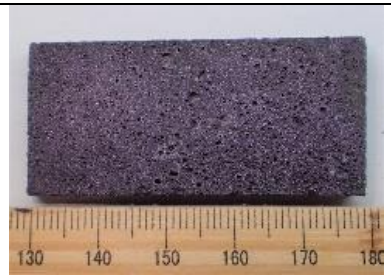		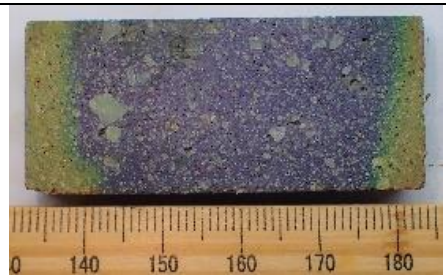	

Figure 5-20 Visual corrosion depth in C1 sewer corrosivity classification after 31 and 42 months

Time (months)	OGPm-1	OGPm-2	OGPm-3	CACm
31	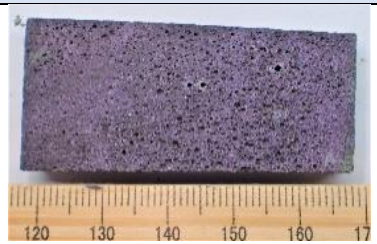		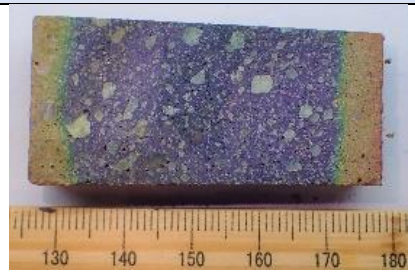	
42	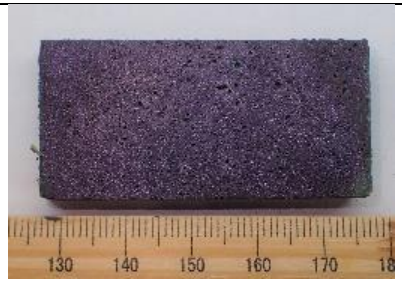	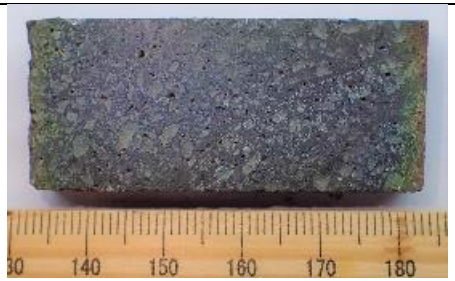	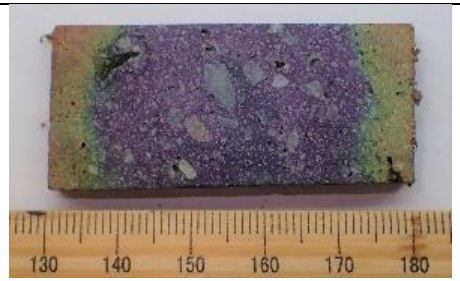	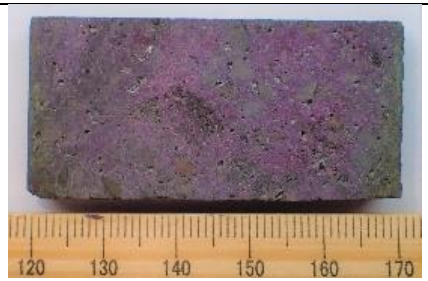

Figure 5-21 Visual corrosion depth in C3 sewer corrosivity classification after 31 and 42 months

Time (months)	OGPm-1	OGPm-2	OGPm-3	CACm
31	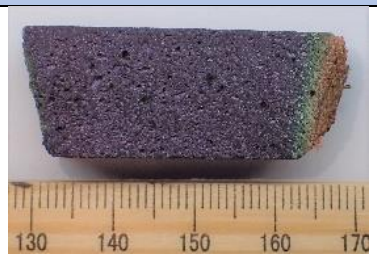			
42	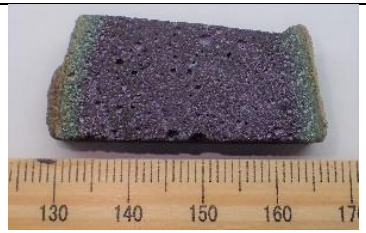			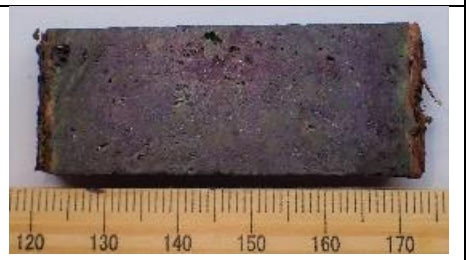

Figure 5-22 Visual corrosion depth in C4 sewer corrosivity classification after 31 and 42 months

5.2.3.2.2 DEPTH OF CORROSION

The corrosion resistance performance of OGPm-1, OGPm-2, OGPm-3 and CACm after exposure up to 42 months in three digestion chambers representing C1, C3, and C4 of sewer corrosivity classifications was assessed based on corrosion depth and residual UCS.

Figure 5-23 presents the corrosion depth of all mortar specimens exposed in three digestion chambers representing C1, C3, and C4 of sewer corrosivity classification (see Table 5-2) for up to 42 months. The OGPm-1, OGPm-2, OGPm-3, and CACm experienced an increase in corrosion depth with respect to time. However, low or high corrosion depth depends on the type of lining mortars. Among the OGPm, OGPm-3 showed the highest corrosion depth in all sewer corrosivity classifications compared to OGPm-1 and OGPm-2. The corrosion depth of OGPm-3 in C1, C3, and C4 were 29%, 33%, and 65% compared with initial thickness, respectively. The corrosion depth of OGPm-1 in C1, C3, and C4 were 1.7%, 2.9%, and 42% compared with initial thickness, respectively. The corrosion depth of OGPm-2 in C1, C3, and C4 were 0.3%, 0.4%, and 17% compared with initial thickness, respectively. The results of lining mortar deterioration exposed in C1, C3, and C4 of sewer corrosivity classification indicated a clear association between the environmental condition (H_2S, CO_2, temperature, and %RH) and chemical and physical properties of geopolymer lining mortar. These results also agreed with studies by Khan et al. (2020b) and (Grengg et al., 2020) that exposed geopolymer samples in higher H_2S influenced the higher corrosion depth. In CACm, the corrosion depth from C1, C3, and C4 of sewer corrosivity classifications was raised by approximately 0.4%, 0.6%, and 10% compared with the initial thickness. The long-term durability of the CACm result was compared to OGPm durability results and confirmed that CACm is the superior material for resisting acid corrosion in sewer environments. However, in comparison OGPm and CACm, it was observed that the corrosion resistance performance of OGPm-2 was comparable with CACm. This suggested that OGPm was able to provide comparable the acid

corrosion resistance to CACm. The depth of corrosion was also observed that at the same sewer corrosivity classification, the corrosion resistance performance of the OGPm in this study exhibited different depth of corrosion at the same exposure time. This can be attributed to chemical and physical properties of the mortar.

Corrosivity classification	OGPm-1	OGPm-2	OGPm-3	CACm
C1	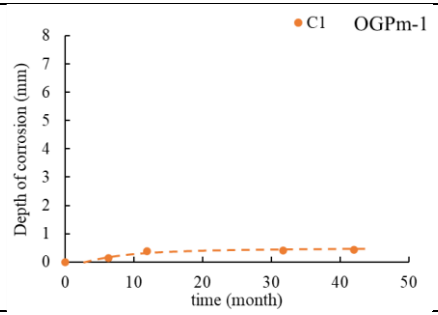	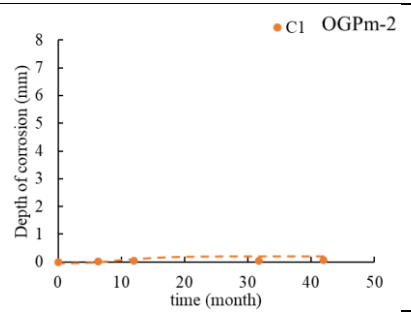	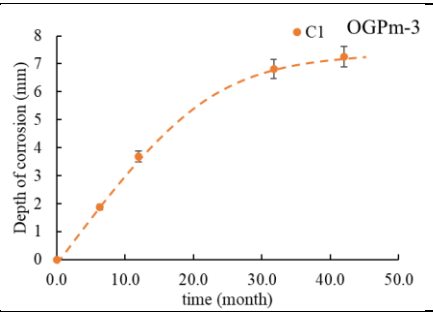	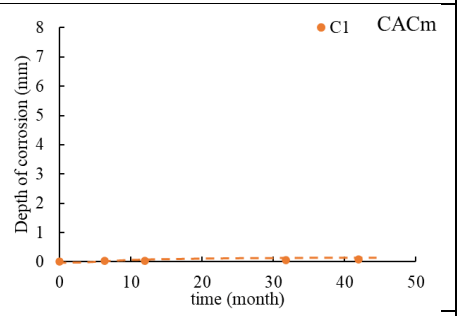
C3	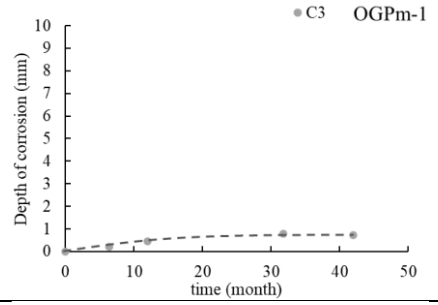	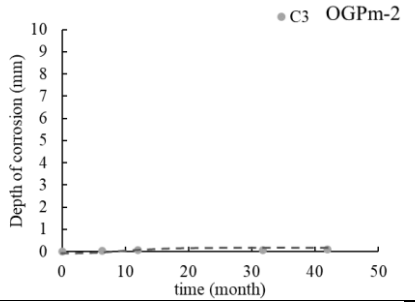	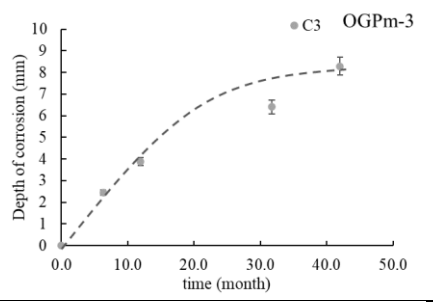	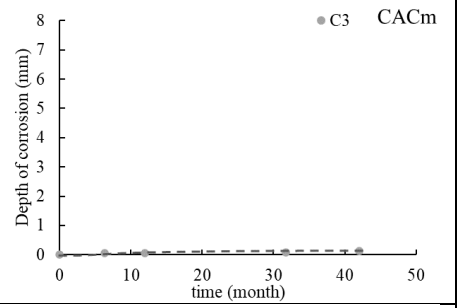
C4	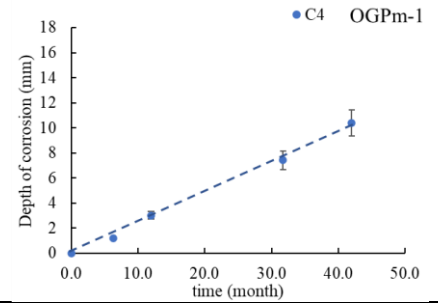	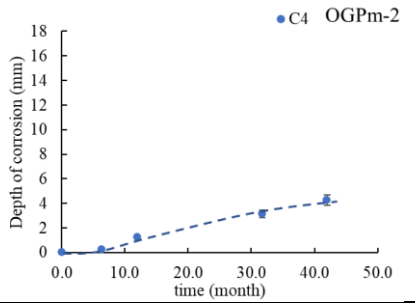	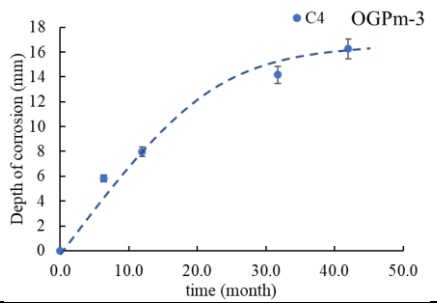	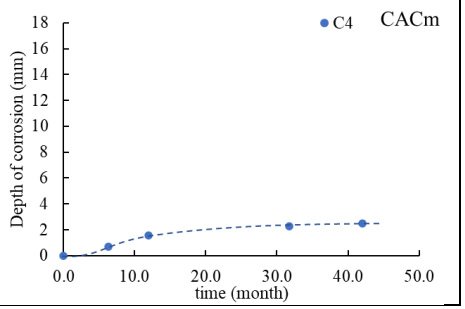

Figure 5-23 Depth of corrosion after exposure to the aggressive environment in the three digester chambers.

Physical properties

The corrosion depth in geopolymer lining mortars was correlated with two fundamental physical properties: the initial unconfined compressive strength (UCS) and the initial porosity to understand the impact of these properties.

Figure 5-24 presents the correlation between corrosion depth and initial porosity (a), and initial UCS (b) after 42 months of exposure in C1, C3, and C4 of sewer corrosivity classification. Figure 5-24 (a) generally shows a positive correlation between the corrosion depth and initial porosity. As the initial porosity of the geopolymer increases, the corrosion depth also increases. This result suggested that a higher initial porosity allowed biogenic sulfuric acid penetration into the OGPm and CACm matrix and formed corrosion products such as gypsum and ettringite. Scrivener et al. (2004), Albitar et al. (2017) and Khan et al. (2020b) suggested that when the proton (H^+) penetrated the mortar matrix, essential elements such as Ca^{2+}, Al^{3+}, Si^{4+}or Na^+ were leached out to pore space. At the same time, H^+ and sulphate (SO_4^{2-}) were neutralised and transferred into a mortar matrix, forming a corrosion product, respectively (Khan et al., 2020b). In contrast, a lower initial porosity limits acid penetration and improves corrosion resistance performance.

The sewer corrosivity classification distinguishedly influenced lining mortar deterioration by increasing the corrosion depth with increasing the sewer corrosivity. The correlation between corrosion depth and initial porosity revealed a strong negative correlation in C4 of the sewer corrosion classification. An optimal correlation was observed for the initial porosity in C1 and C3 of the sewer corrosivity classifications. These findings suggest that in C1 and C3, the initial porosity must be maintained below 20 vol.% to effectively mitigate excessive acid penetration and prevent subsequent corrosion damage permeation, while in C4 could generate more

biogenic sulphuric acid to attack the mortar binder, resulting in exhibiting severe deterioration and more severe when increasing more porosity.

Figure 5-24 (b) generally shows a negative correlation between the corrosion depth and initial UCS. The plot generally showed that the corrosion depth decreased when the initial UCS of the geopolymer increased. Moreover, corrosion depth was additionally impacted by the sewer corrosivity classification.

The correlation between corrosion depth and initial UCS revealed a strong negative correlation in C4 of sewer corrosion classification. At the same time, in C1 and C3 of sewer corrosivity classifications, an optimal correlation was observed between the initial UCS and corrosion depth. The results showed that the corrosion resistance performance of all lining mortars was generally improved with increasing the initial UCS but performed differently in different sewer corrosivity. As we mentioned, the UCS is used to reflect the inherent strength and integrity of the mortar material itself. It is significantly related to the density of lining mortar material; less dense lining mortar allows more acid to penetrate further into the mortar matrix (Ng et al., 2018, Rong-rong and Dong-dong, 2020, Jia et al., 2019). Therefore, high UCS revealed better corrosion resistance performance. However, the sewer corrosivity clearly shows the impact on the lining mortar performance. At C4 sewer corrosivity, all mortar showed the highest corrosion depth but lower with increased initial UCS. Meanwhile, the C1 and C3 sewer corrosivity showed optimal UCS of lining mortar. It exhibited that the initial UCS exceeded approximately 70 MPa, showing a corrosion depth of less than 2 mm. These results suggested that the mortar with initial UCS exceeding 70 MPa can effectively be used as lining mortar in C1 and C3 sewer corrosivity.

These findings highlight the importance of considering both the sewer corrosivity classification and the physical properties of materials in order to optimise corrosion resistance performance.

By considering an appropriate initial UCS and porosity, sewer lining materials can effectively mitigate the corrosion issue and enhance their durability in corrosive environments.

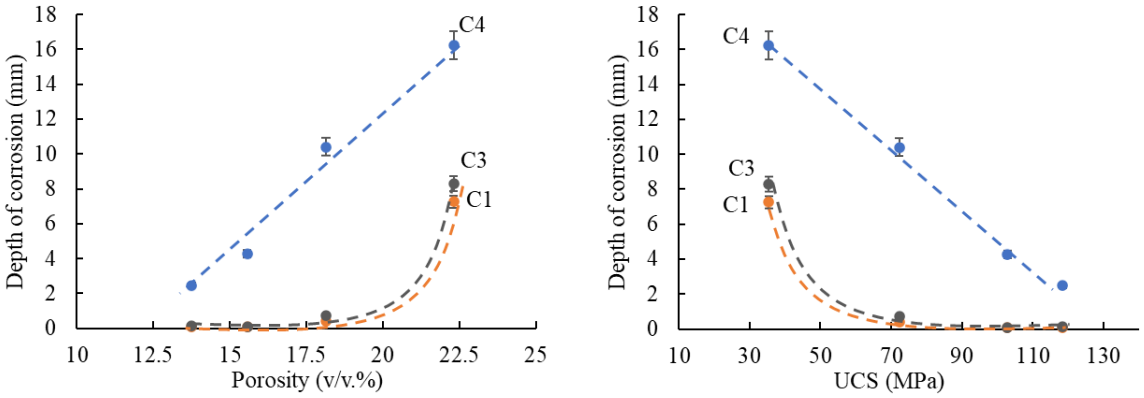

(a) Initial Porosity (b) Initial UCS

Figure 5-24 Effect of initial porosity and UCS on the corrosion performance after 42 months of exposure to C1, C3, and C4 of sewer corrosivity classification

Chemical properties

Aside from the impact of physical properties on corrosion resistance performance, chemical properties are also important. The two significant chemical properties of lining mortar considered in the study are Acid Neutralization Capacity (ANC) and the hydration products of the mortar (C-S-H, C-A-S-H, C-N-A-S-H, and N-A-S-H).

The ANC of lining mortar refers to its capacity to neutralise acidic substances (Damion and Chaunsali, 2022). In sewer systems, the presence of sulphur-oxidizing bacteria (SOB) and Sulphate-reducing bacteria (SRB) can lead to the presence of gases like hydrogen sulphide (H_2S) and carbon dioxide (CO_2) and strong and weak acid formation such as sulphuric acid (H_2SO_4) and carbonic acid (H_2CO_3) (Grengg et al., 2018, Okabe et al., 2007b). These acids potentially attack the mortar matrix, leading to lining mortar deterioration. The ANC of the mortar acts as a protection mechanism against deterioration by neutralising the acidic substances. Therefore, mortars with higher ANC can effectively reduce the acid attack and exhibit improved corrosion resistance.

Figure 5-25 presents the impact of ANC with corrosion performance based on corrosion depth after 42 months of exposure to C1, C3, and C4 of sewer corrosivity classification. It observed the optimum correlation between the depth of corrosion and ANC. Additionally, the correlation is similar in all sewer corrosivity classifications. The optimum value of ANC relied on 3.8-4.4 mmol H^+/g of mortar. The ANC lower than 3. 8 mmol H^+/g of mortar allowed acid compounds such as H_2SO_4 and H_2CO_3 to penetrate and attack the mortar matrix due to less neutralisation process. However, if the ANC is higher than 4.4, it shows higher acid permeation. This is because essential elements, particularly calcium (Ca), can be leached out when acids attack the mortar matrix. This leaching process can lead to the formation of gypsum, a corrosion product that tends to expand and generate cracks within the mortar (Albitar et al., 2017, Jiang et al., 2015b). These cracks provided more pathways and allowed more acid penetration. It is important to note the strong correlation between ANC and the calcium (Ca) content in the mortar, as discussed in section 4.5.2.3 of Chapter 4. The ANC of mortar is closely linked to the amount of Ca present. Specifically, higher levels of CaO in the mortar composition tend to result in a higher ANC. However, higher Ca content in the mortar binder composition generated more expansive corrosion products such as gypsum and ettringite when the sulphuric acid attacked. Therefore, considering the appropriate Ca content in the mortar formulation can improve the corrosion resistance performance by achieving appropriate ANC, providing a more effective defence mechanism against deterioration from MICC.

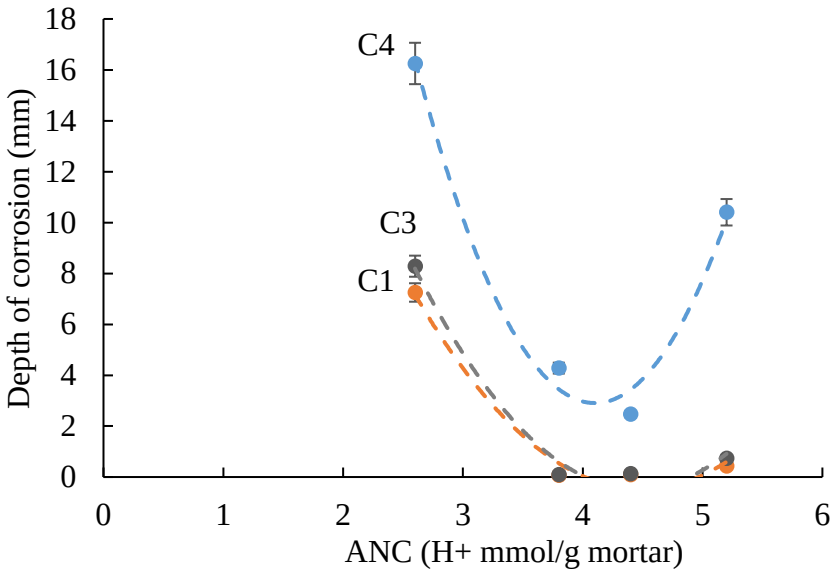

Figure 5-25 Effect of ANC on the corrosion performance after 42 months of exposure to C1, C3, and C4 of sewer corrosivity classification

Another chemical property affecting corrosion resistance performance is the hydration products (C-S-H, C-A-S-H, C-N-A-S-H, and N-A-S-H) of OGPm. Figure 5-26 presented a correlation between corrosion depth and the hydration products of OGPm after 42 months in the C1, C3, and C4 of sewer corrosivity classification.

The correlation between the corrosion depth and C-S-H, C-A-S-H and C-N-A-S-H observed a negative and optimum negative correlation dependent on the corrosivity classification. Generally, the corrosion depth was decreased when the content of C-A-S-H, C-S-H, and C-N-A-S-H increased. This is because the C-A-S-H, C-S-H, and C-N-A-S-H improved the physical properties, such as initial UCS and porosity, by filling the void with those hydration products to have higher UCS and lower porosity (Aiken et al., 2018). Moreover, the Ca^{2+} and Al^{3+} content that can leach out from hydration product during the acid attacks influenced to gain higher ANC, resulting in improving corrosion resistance performance of mortar by limiting the acid penetration and acid neutralisation. In contrast, the correlation between corrosion depth and N-A-S-H observed a positive and optimum positive correlation dependent on the

corrosivity classification. The corrosion depth was increased when the N-A-S-H content was increased. This is attributed to the nature of the N-A-S-H structure, which presents a 3D structure that is more porous and less dense (Aiken et al., 2018). The higher N-A-S-H remarkably allowed acid penetration into the mortar matrix, increasing corrosion depth.

The sewer corrosivity classification also impacted the depth of corrosion. Higher corrosivity classification exhibited a higher corrosion depth.

At C4 sewer corrosivity, deteriorated mortar showed a corrosion depth of approximately 4-16 mm. The corrosion depth exhibited a strong negative linear correlation with C-A-S-H, C-S-H, and C-N-A-S-H while exhibiting a positive linear correlation with N-A-S-H. At C3 and C1 sewer corrosivity, deteriorated mortar showed a corrosion depth of 0-8 mm and 0-7 mm, respectively. The optimum value of hydration phases provided the lowest corrosion depth, as shown in Figure 5-26. These results suggested that to achieve the best corrosion resistance performance of OGPm in C3 and C1, the C-A-S-H, C-S-H, and C-N-A-S-H content should not be lower than 35 wt.%, 14 wt.%, and 30 wt.%, respectively. On the other hand, it is essential to limit the N-A-S-H content to no more than 20 wt.%. These results can be used as guidelines for geopolymer mortar selection to achieve better corrosion resistance performance.

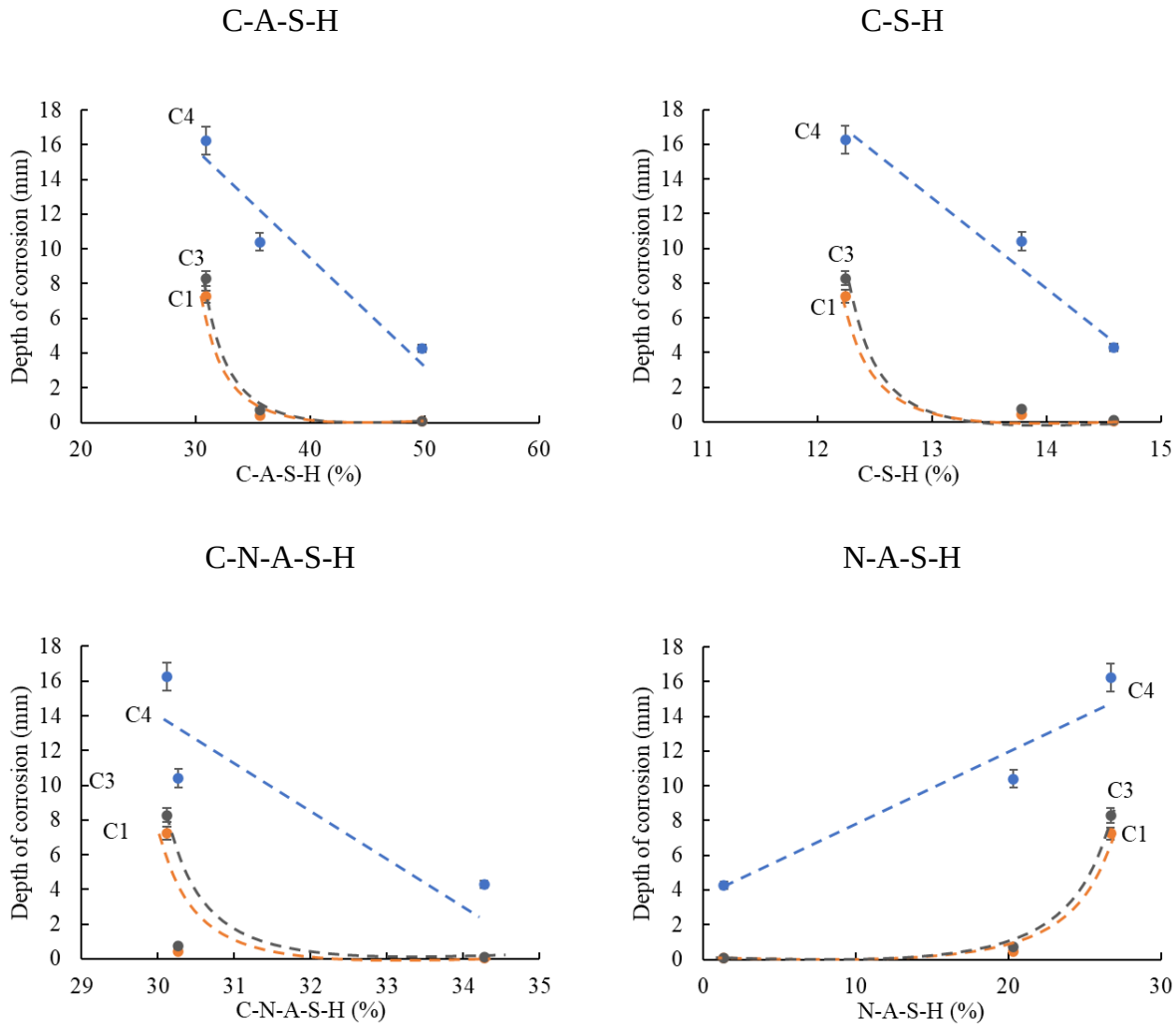

Figure 5-26 Effect of hydration phases on the corrosion performance after 42 months of exposure to C1, C3, and C4 of sewer corrosivity classification

5.2.3.2.3 STAGES OF CORROSION

The corrosion depth of OGPm-1, OGPm-2, OGPm-3, and CACm as a function of time up to 42 months after exposure to C1, C3, and C4 sewer corrosivity is shown in Figure 5-23. Three phases characterised the lining mortar corrosion: i) Lag phase, ii) stage I corrosion rate (R_1) and iii) stage II corrosion rate (R_2). A schematic diagram of these phases is shown in Figure 5-27. The R_1 and R_2 features are consistent with the corrosion observed under accelerated tests (see 5.2.1.1.2).

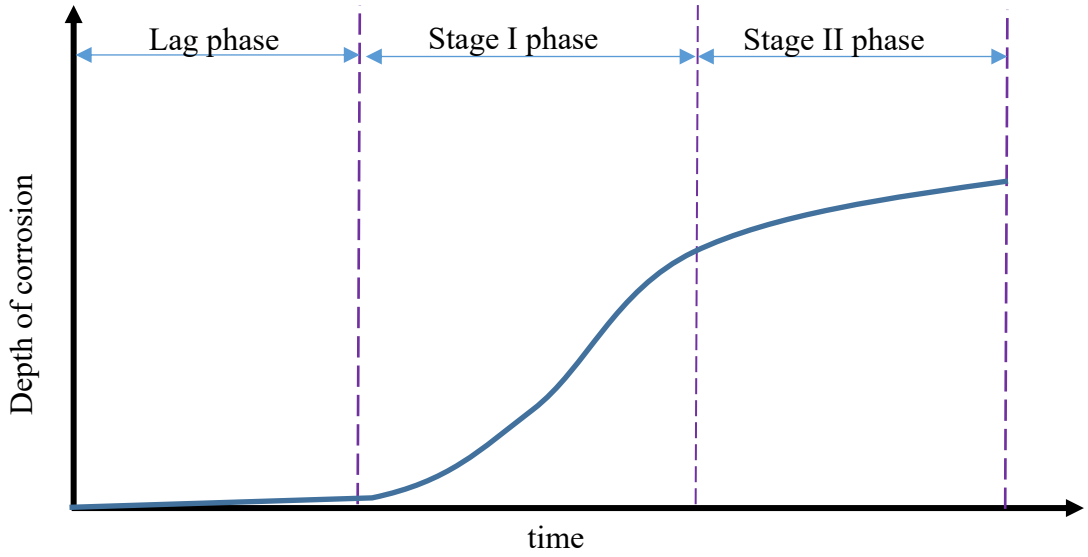

Figure 5-27 Schematic diagrams of corrosion depth as a function of time.

The lag phase represents the initial corrosion period, characterised by the initiation of microbially induced concrete corrosion (MICC). The absence of microorganisms in the accelerated test means the lag phase cannot be observed. During this stage, the corrosion process is primarily driven by abiotic acid-based carbonation reactions and the formation of weak acids (Grengg et al., 2018). In the lag phase, the acid neutralisation capacity of the mortar plays a vital role in controlling corrosion initiation. The alkalinity of the lining mortar strongly influences the corrosion resistance during the lag phase. The high alkalinity of mortar provides excellent corrosion resistance against acid attacks from MICC, effectively neutralising weak or strong acids and slowing down mortar deterioration.

The stage I corrosion phase represents the initial propagation of corrosion. During this stage, corrosion exhibits a rapid rate of corrosion, primarily driven by the colonisation of microorganisms such as fungi, neutrophile sulphur oxidising bacteria (NSOB), and Acidophil sulphur oxidising bacteria (ASOB), which generate biogenic sulphuric acid (Grengg et al., 2018). The interaction between biogenic sulfuric acid and the lining mortar matrix leads to mortar deterioration by forming expansive corrosion products such as gypsum and ettringite

(Grengg et al., 2018, Ling et al., 2015, Okabe et al., 2007b). In this phase, the corrosion behaviour is closely linked to the porosity and the quantity of hydration products within the lining mortar.

The stage II corrosion phase is characterised by a significant reduction in corrosion rates, indicating slower corrosion than stage I. During stage II corrosion, the presence of expansive corrosion products such as gypsum plays an important role in pore blocking and consequently reducing acid diffusion into the mortar matrix. This phenomenon results in slower mortar deterioration. The stage II corrosion phase offers protection by reducing acid permeation. It is essential to note that the lining mortar may still experience material loss or exhibit relatively higher corrosion depths.

The corrosion depth as a function of time of OGPm and CACm after exposure to C1, C3, and C4 of sewer corrosivity classification up to 42 months in Figure 5-23 was exhibited in the different phases of corrosion, either complete or partial corrosion characteristics. For example, in C4 of sewer corrosivity classification, OGPm-1 primarily showed only the stage I corrosion phase. OGPm-2 exhibited both the lag and stage I corrosion phases. OGPm-3 demonstrated corrosion characteristics throughout both the stage I and stage II corrosion phases. These results clearly suggested that different mortars exhibited varying corrosion behaviour under the same sewer corrosivity conditions. At the same time, the environmental condition was also observed to impact the corrosion characteristics. Figure 5-28 presents the corrosion characteristics of OGPm-1 at different corrosivity classifications. In C4, the OGPm-1 was observed only in the stage I corrosion phase, whereas, in C1, the OGPm-1 was observed in both stage I and II corrosion phases. These observations suggested that sewer corrosivity plays a significant role in corrosion behaviour, influencing the increase of corrosion depth over time.

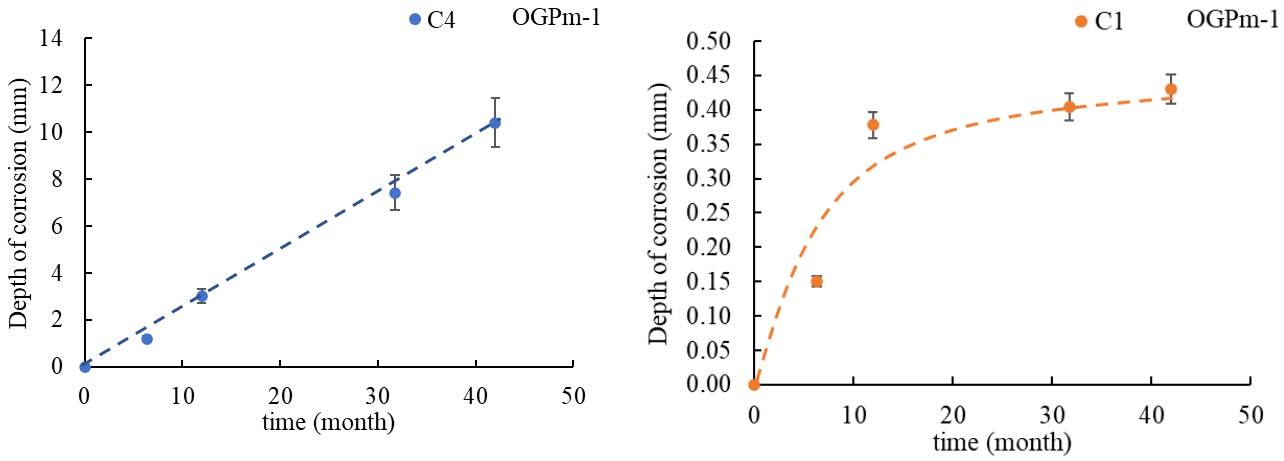

Figure 5-28 Comparison of corrosion characteristics of OGPm-1 at C4 and C1 sewer corrosivity classification

5.2.3.2.4 CORROSION RATE IN FIELD TEST

The corrosion rate was employed to assess and compare the corrosion resistance performance of OGPm at different sewer corrosivity classifications. The corrosion rate was calculated at the lag phase, stage I corrosion rate (R_1) and stage II corrosion rate (R_2), similar to the accelerated corrosion test in the laboratory (see Figure 5-7).

The corrosion rate of OGPm and CACm at three different digester tanks, represented for C1, C3, and C4 of sewer corrosivity classification, were determined based on corrosion depth in Figure 5-23. The corrosion phases are exhibited in Table 5-3.

Table 5-3 The rate of corrosion phases of OGPm and CACm at the digester tank

Mortar	Sewer Corrosivity Classification	Lag (day)	R_1 (mm/year)	R_2 (mm/year)
OGPm-1	C1	n.a.	0.27	0.06
	C3	n.a.	0.46	0.10
	C4	n.a.	3.04	n.a.
OGPm-2	C1	150	0.05	0.00
	C3	120	0.09	0.01
	C4	120	1.83	0.52
OGPm-3	C1	n.a.	3.65	0.43
	C3	n.a.	3.95	0.52
	C4	n.a.	9.13	1.22
CACm	C1	150	0.04	0.02
	C3	90	0.07	0.01
	C4	90	2.13	0.25

Figure 5-29 compares the lag phase and corrosion rate at R_1 and R_2 of OGPm-1, OGPm-2, OGPm-3, and CACm at different sewer corrosivity classifications. Overall for the lag phase, it appeared in OGPm-2 and CACm. while OGPm-1 and OPGm-3 vary from 90 to150 days. it was also observed that higher corrosivity classification impacted the lag phase period. The lag phase was shorter in C4 and longer in C1. This is highly attributed to the ANC of the mortar and the sewer corrosivity classification.

In the C4 sewer corrosivity classification, the stage I corrosion rate of OGPm appeared at various times depending on the type of OGPm. Among the geopolymers, OGPm-2 presented a lag phase for approximately two months before initiating the stage I corrosion phase, while OGPm-1 and OGPm-3 did not present the lag phase. The R_1 of all geopolymers have been observed as OGPm-3 > OGPm-1 > OGPm-2 > CACm. The R_1 of OGPm-2 was comparable to CACm. The R_2 refers to a slower corrosion rate after a stage I corrosion phase. It is an important feature because it could determine the durability of the lining material. The R_2 of all OGPm and CACm were determined and exhibited as OGPm-3 > OGPm-2 >CACm, but the R_2 of

OGPm-1 did not present, which means that under C4, OGPm-1 continued significant deterioration.

In the C1 and C3 sewer corrosivity classification, the R_1 presented OGPm-3 > OGPm-1 > OGPm-2 > CACm. The R_1 of OGPm in C1 and C3 were consistent with the R_1 in the C4 sewer corrosivity classification. The R_2 of OGPm-1, OGPm-2, and OGPm-3 presented that the corrosion rate of OGPm-3 > OGPm-1 > OGPm-2 > CACm. Moreover, comparing the R_2 of OGPm with CACm, it has been observed that the R_2 of OGPm-2 was comparable with CACm, which consisted of corrosion resistance performance based on R_2 in C4.

The corrosion rate at stage II corrosion was used to evaluate the corrosion resistance and durability of the geopolymer mortar. Based on the R_2 among the OGPm, it has been observed that OGPm-2 had high corrosion resistance, followed by OGPm-1 and OGPm-3 in the C1 and C3 sewer corrosivity classifications. While at a higher sewer corrosivity classification of C4, the OGPm-2 had high corrosion resistance, followed by OGPm-3 and OGPm-1. Since the R_2 of OGPm-1 was not presented in C4, it suggested that OGPm-1 were continuously attacked by the acid with a stage I corrosion rate.

As mentioned, the R_2 becomes an essential indicator to determine the corrosion resistance performance of mortar. The corrosion rate reduction was not only attributed to the neutralisation alone since freshly available biogenic sulphuric acid from microorganisms continuously produced and attacked the sound mortar. The other factor could be differences in permeability and pore blocking. The initial porosity of the OGPm mortars is from 15-23%, while the CACm mortar has a porosity of 13%. While porosity explains the corrosion resistance of CACm to be relatively higher than that of OGPm mortars, the similarity in the porosity of the OGPm cannot explain the relative difference in their corrosion resistance.

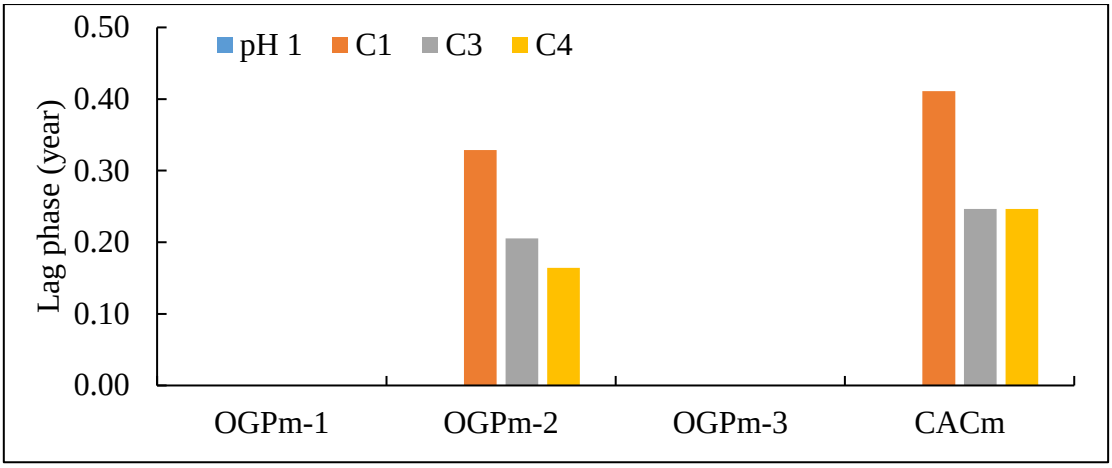

(a) Lag phase

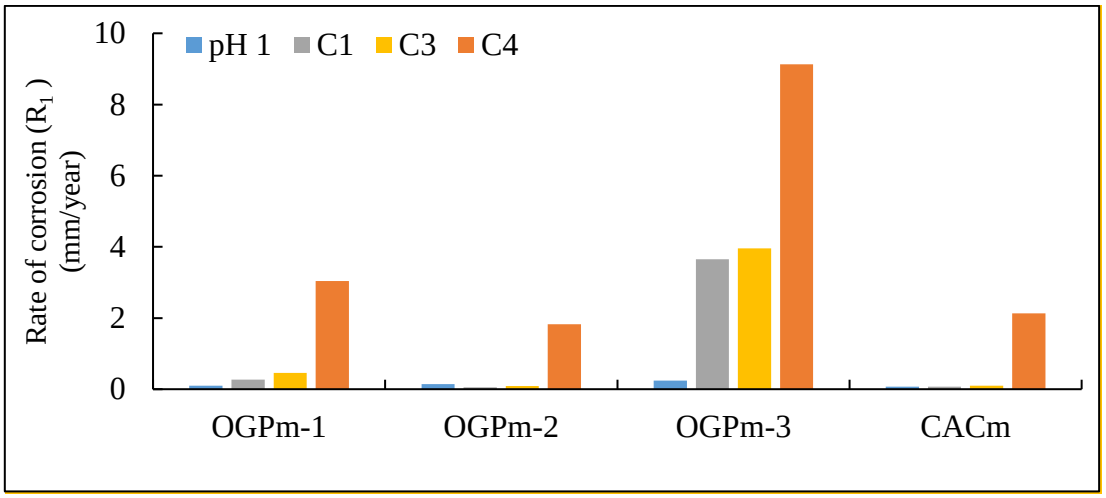

(b) The stage I corrosion rate (R_1)

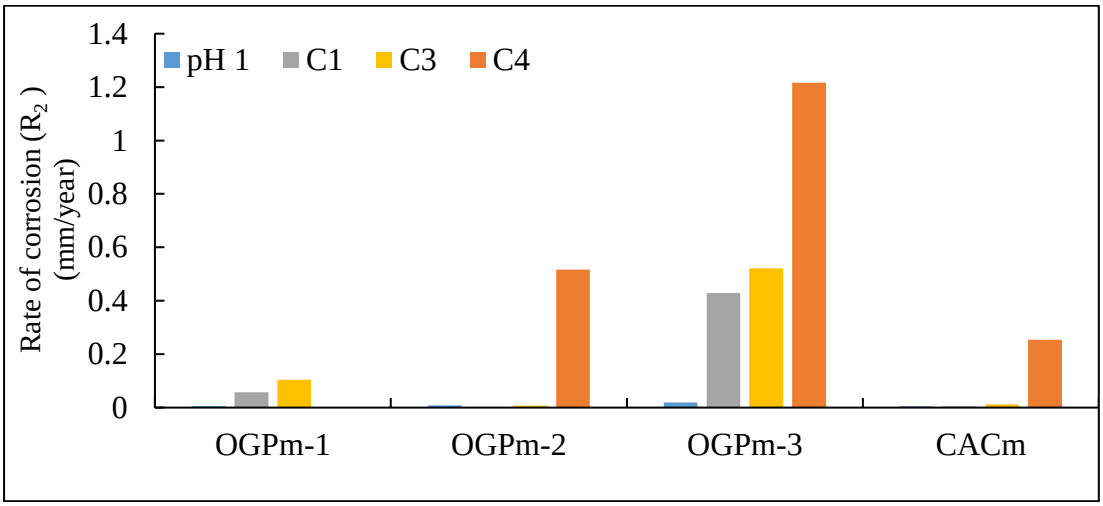

(c) The stage II corrosion rate (R_2)

Figure 5-29 (a) Stage I corrosion rate and (b) Stage II corrosion rate of OGPm and CACm exposed to H_2SO_4 at pH 1.0 and 30 °C and three corrosivity classification

As the acid decalcifies the binder, the dissolved calcium will primarily form an expansive corrosion product such as gypsum, mainly if corrosion occurs at low pH (Yuan et al., 2013). The expansive nature of gypsum will fill the concrete pores, contributing to the diffusion resistance to the acid. Based on the chemical composition of mortars in Chapter 4, OGPm-1 shows the highest calcium (Ca) content and OGPm-3 is the lowest. Figure 5-30 presented the correlation of Ca content in OGPm and CACm with $CaSO_4$ as corrosion production from 31 months of exposure in C4 of sewer corrosivity classification as representative of corroded mortar. The $CaSO_4$ content was obtained from TGA analysis. It observed that among the OGPm, Ca contents correspond to the formation of $CaSO_4$. These results suggested that the tendency to form gypsum appears to depend on the calcium content of the binders. Comparing the OGPm and CACm, despite the OGPm having similar Ca content with CACm, The CACm showed lower $CaSO_4$ formation due to lower porosity and high ANC of CACm, which led to low Ca leaching and $CaSO_4$ formation compared to OGPm.

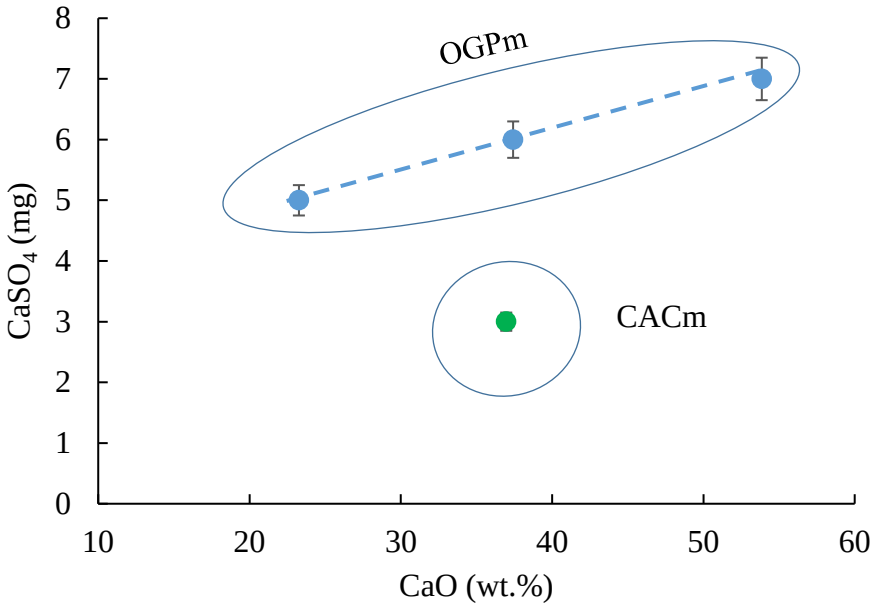

Figure 5-30 Correlation between CaO and $CaSO_4$ formation from C4 sewer corrosivity classification after 31 months of exposure

Figure 5-31 and Figure 5-32 show the SEM backscattering image and Ca and S maps of the uncorroded and corroded sections of OGPm-1 and OGPm-3 after 12 months of exposure to C4 sewer corrosivity classification. As shown, the formation of gypsum in OGPm-1 is more extensive than in OGPm-3. This observation is also consistent with the Ca content of OGPm. Moreover, we have also noticed that the formation of $CaSO_4$ in the OGPm-3 was formed along the crack in the OGPm-3 matrices. This evidence that the formation of $CaSO_4$ potentially slowed down the acid diffusion further into the OGPm-3 matrices, leading to the corrosion rate reduction. Comparing the formation of $CaSO_4$ in OGPm to CACm, the observation revealed the presence of formulated $CaSO_4$ within the pores or cracks. The $CaSO_4$ is known to have expansive properties, and its accumulation within the pore led to pore stress, mechanical damage, and increased permeability of the mortar.

Although the Ca content alone may not be the only factor affecting the corrosion resistance of the mortars, these results highlighted the importance of the Ca content on their durability. If it has too much Ca content in OGPm, It potentially forms more expansive corrosion products such as gypsum and ettringite, resulting in severe mortar deterioration. The CACm showed superior performance with high corrosion resistance based on the corrosion depth and is expected to retain high residual strengths.

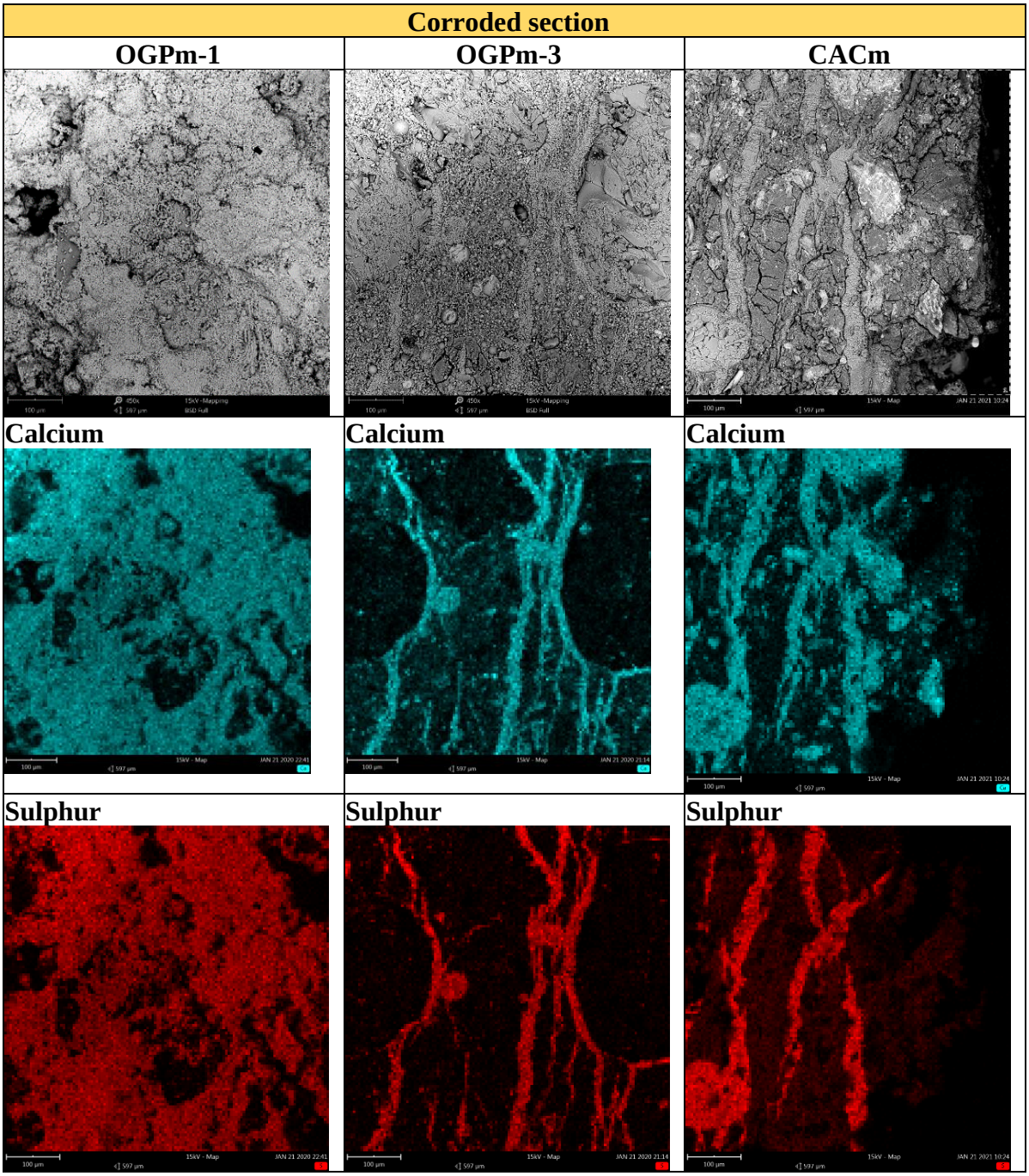

Figure 5-31 SEM backscattering images and Ca and S maps of the corroded sections of OGPm-1 and OGPm-3 after 12 months of corrosion field test (129 ppm H2S, 26 °C and 99% RH

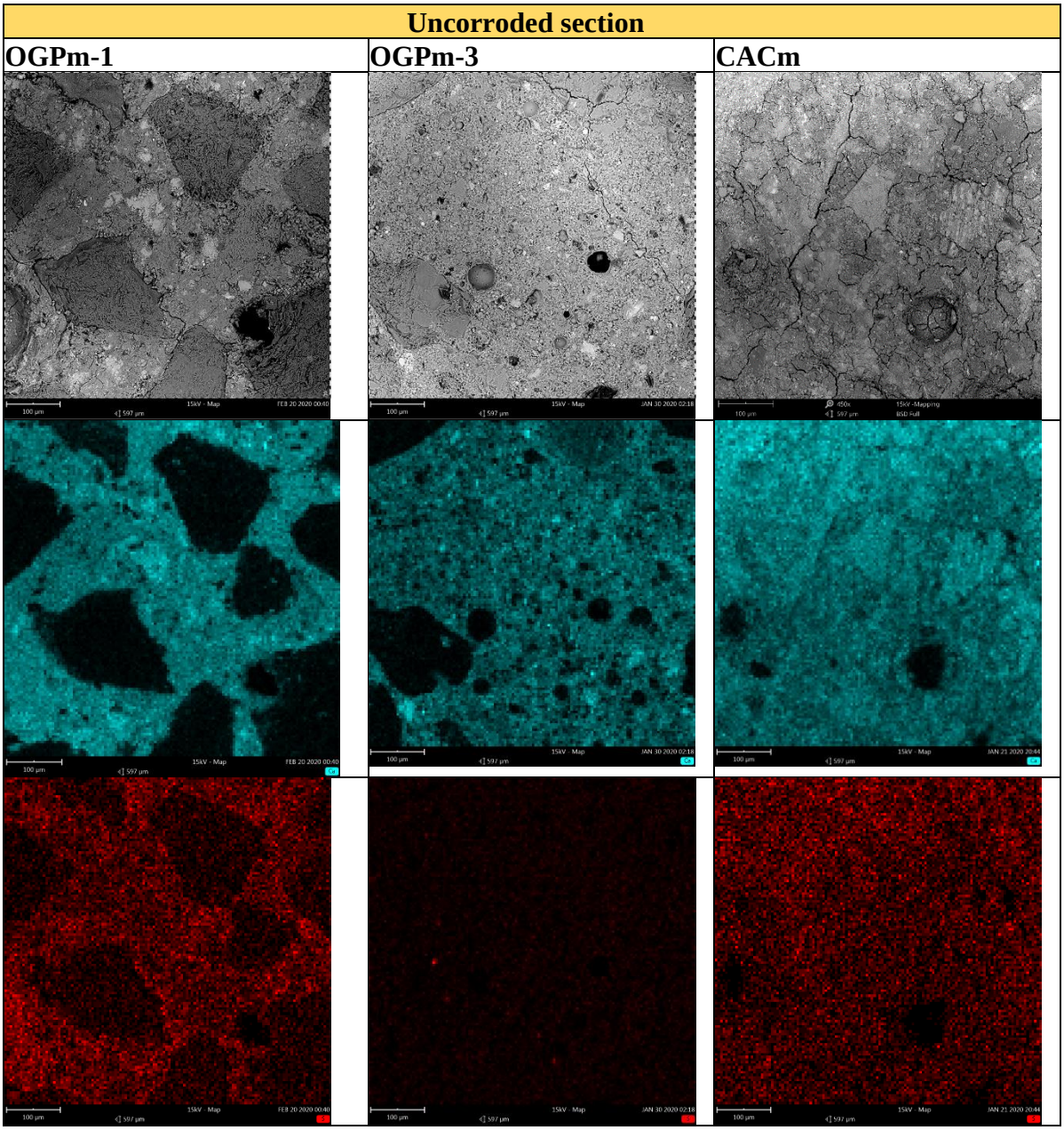

Figure 5-32 SEM backscattering images and Ca and S maps of the uncorroded sections of OGPm-1 and OGPm-3 after 12 months of corrosion field test (129 ppm H2S, 26 °C and 99% RH

5.2.3.2.5 COMPARISON OF CORROSION RESISTANCE IN LABORATORY AND FIELD TEST

The corrosion resistance performance from acid immersion tests, which simulate a chemical attack, and exposure to live sewer environments involve microbiologically induced concrete corrosion (MICC). Therefore, correlating the results of these different test methods provides valuable information to reflect the corrosion behaviour between the two methods. This study

investigated and presented the stage I and II corrosion rates observed in the acid immersion test and the live sewer environmental conditions in Figure 5-33. The positive correlation between these two test methods indicates that the acid immersion test is consistent with the corrosion behaviour experienced in live sewer environments. These results confirmed the impact of sewer corrosivity, higher sewer corrosivity revealed a higher corrosion rate in both stages of corrosion. Moreover, these results highlight the strong correlation of corrosion rate between the immersion test and field test.

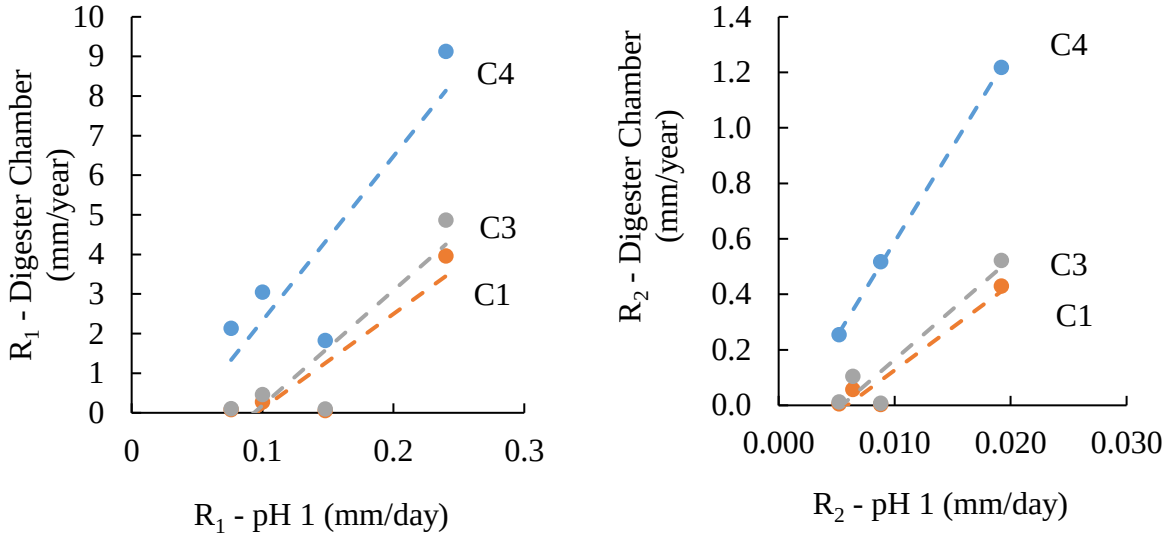

(a) Stage I corrosion rate (b) Stage II corrosion rate

Figure 5-33 Correlation of R_2 from field test and R_2 from accelerated corrosion test

Table 5-4 shows the measured depth of corrosion of geopolymers exposed within three digestion chambers, which presented the sewer corrosivity classifications from C1, C3, and C4 in this study and other field studies. The corrosion rate in this study was measured at both stage I and II corrosion rates. However, the directly calculated corrosion rate was also calculated to compare with other previous in-field case studies for comparison purposes. It is important to note that the directly calculated corrosion rate is determined by dividing the final corrosion

depth by the exposure time. This corrosion rate provides a measure of the average corrosion progression over the given duration of exposure.

The directly calculated corrosion rate was estimated after 42 months of exposure time for the purpose of comparison to other studies. The rate of corrosion presented in the different corrosion rates is due to the chemical and physical properties of the geopolymer. Due to the low-Ca geopolymer studies in the field, OGPm-3 was chosen as a representative for comparing corrosion rates with other studies that used low-Ca geopolymer in their study. The corrosion rate of OGPm-3 was compared to those reported in the literature, as shown in Figure 5-34. The scatter plot revealed a trend of higher corrosion rates associated with increased H_2S concentration.

Table 5-4 Measured corrosion depth per year (mm/yr) within geopolymers exposed to sewer environment in previous case studies.

Sample type	Field conditions	R_1 (mm/yr)	R_2 (mm/yr)	Direct calculated (mm/yr)	References
Coupon OGPm-1	106 ppm H_2S	3.01	N/A	3.01	This study
Coupon OGPm-2	106 ppm H_2S	1.83	0.52	1.23	This study
Coupon OGPm-3	106 ppm H_2S	9.13	1.22	4.71	This study
Coupon OGPm-1	2 ppm H_2S	0.27	0.06	0.12	This study
Coupon OGPm-2	2 ppm H_2S	0.06	0.00	0.02	This study
Coupon OGPm-3	2 ppm H_2S	3.65	0.43	2.10	This study
Coupon OGPm-1	81.7 ppm H_2S	0.46	0.10	0.21	This study
Coupon OGPm-2	81.7 ppm H_2S	0.09	0.00	0.03	This study
Coupon OGPm-3	81.7 ppm H_2S	3.95	0.52	2.4	This study
Coupons of FA- GPm	53 ppm H_2S	-	-	6	(Khan et al., 2020b)
Coupons of FA- GPm	27 ppm H_2S	-	-	3.5	(Khan et al., 2020b)

Sample type	Field conditions	R_1 (mm/yr)	R_2 (mm/yr)	Direct calculated (mm/yr)	References
Coupon Metakaolin GP-1	65 ppm H2S	-	-	28	(Grengg et al., 2020)
Coupon Metakaolin GP-1	65 ppm H2S	-	-	3.8	(Grengg et al., 2020)

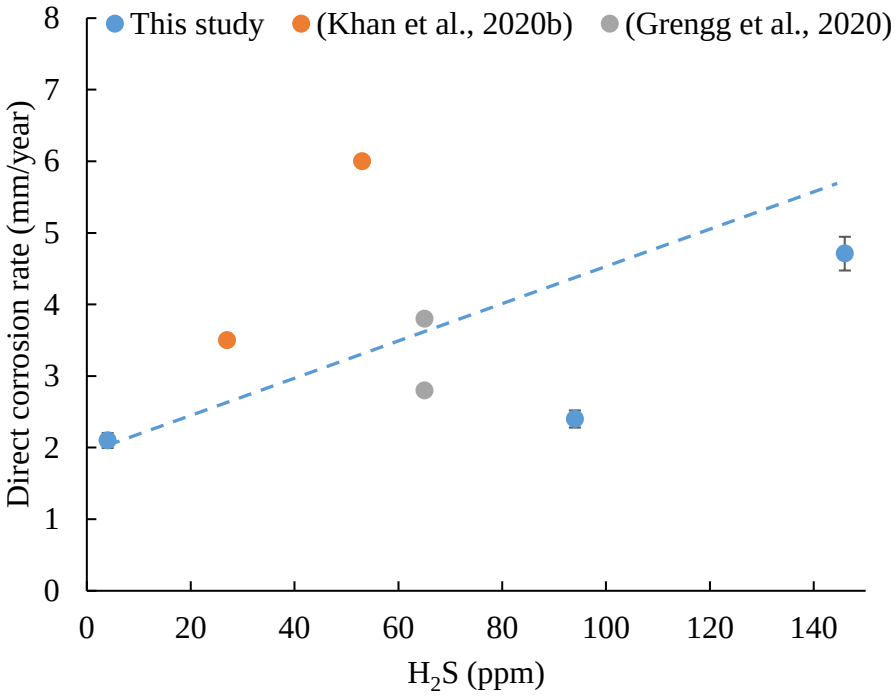

Figure 5-34 Comparison of the corrosion rate of low Ca geopolymer

5.2.3.2.6 RESIDUAL UCS

The UCS of lining mortar is an important factor used to assess the corrosion resistance performance of mortar due to its direct influence on the structural integrity and durability of the mortar material. The corrosion products, such as gypsum and ettringite, formed during the corrosion process, which mainly caused the deterioration of mortar. This study evaluated the UCS degradation of the specimens exposed to different sewer corrosivity by measuring compressive strength at different exposure times.

Figure 5-35 presents the development of the UCS of mortars before and after exposure in three different sewer corrosivity classifications, C1, C3, and C4, in the digestion chambers (see Table *5-2*) for up to 42 months. The initial UCS after 28 days of curing under a curing environment of OGPm-1, OGPm-2, OGPm-3, and CACm were achieved at 72.31, 102.85, 35.42, and 108.5 MPa, respectively. After OGPm-1, OGPm-2, OGPm-3, and CACm exposure to C1, C3, and C4 sewer corrosivity classification, the UCS of mortar generally degraded to a lower UCS over time. Remarkably, some of the mortar, such as OGPm-1 and OGPm-3, exhibited an initial increase in the UCS, followed by either an extreme or slight decrease.

The increase in UCS at the initial exposure time was similar to the study by Albitar et al. (2017). They suggested that the increase in UCS was attributed to C-S-H and C-A-H from the hydration of calcium silicates and pozzolanic reactions (see **Error! Reference source not found.** and REF _Ref137121012 \h **Error! Reference source not found.**). It needs to be noted that the pozzolanic reactions occur over long time scales (months to years) (Sargent, 2015), and according to Bergado et al. (1996) and Diamond and Kinter (1965), the pozzolanic reactions are not complete until five years post-mixing.

After the initial increase in UCS, the UCS gradually decreases over time due to the ongoing hydration process of the matrix, which fills the existing pores. This hydration process leads to internal confinement within the mortar, resulting in expansion pressure. The internal pressure generated by the expanding matrix can exert significant forces on the surrounding material, leading to various forms of damage, such as cracking, delamination, or mechanical deterioration. (Vafaei and Allahverdi, 2017). At the same time, the mortars were attacked by the acid, and expansive corrosion products such as gypsum and ettringite were formulated. Additionally, the UCS degradation was influenced by sewer corrosivity classification, which means the high sewer corrosivity generated more acid and attacked the mortar.

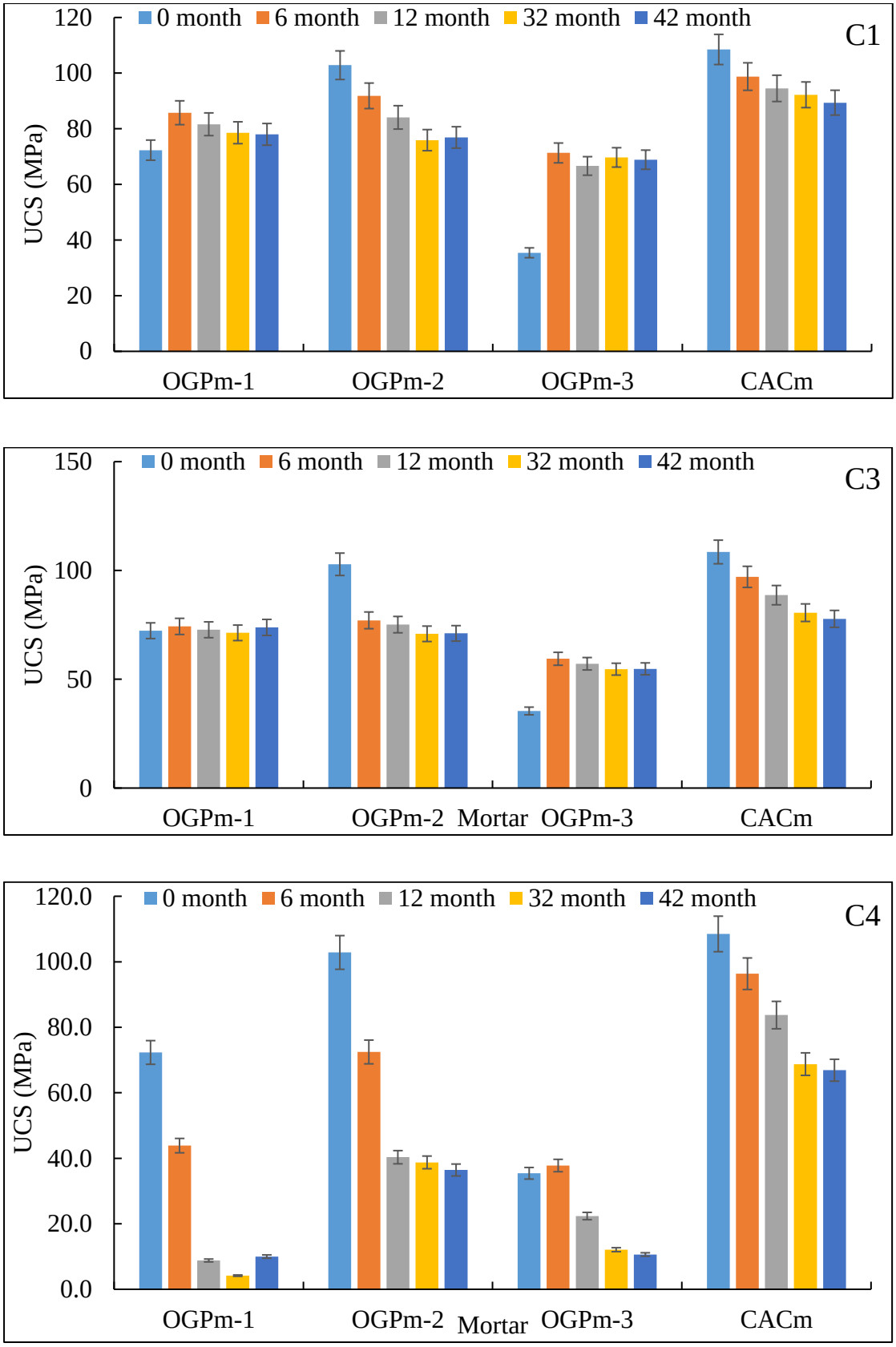

Figure 5-35 Residual UCS of OGPm and CACm from the three digestion chambers, which presented C1, C3, and C4 of sewer corrosivity classification

As mentioned, the corrosivity classification also influenced the severe UCS degradation. The loss of UCS of all sewer corrosivity classifications is shown in Figure 5-36. At the same mortar, the degradation of UCS was observed to be different at different corrosivity classifications.

At C1 of sewer corrosivity classification, OGPm-1 and OGPm-3, their UCS initially experienced an increase during the early phase of exposure time, followed by a subsequent decrease or stability. Meanwhile, the UCS of OGPm-2 and CACm were reduced over time. After 42 months, the UCS of OGPm-1 and OGPm-3 approximately increased 8% and 95% from the original UCS, respectively. Meanwhile, the UCS of OGPm-2 and CACm approximately lost 25% and 18% from the original UCS value, respectively. This suggested that in C1, OGPm-3 exhibited better corrosion resistance performance impacted by MICC, followed by OGPm-1, CACm and OGPm-2.

At C3 of sewer corrosivity classification, the UCS of OGPm-3 and OGPm-1 initially experienced an increase during the early phase of exposure time, followed by a subsequent decrease or stabilisation. This behaviour of OGPm-3 and OGPm-1 was similar in C1. Meanwhile, the UCS of OGPm-2 and CACm were reduced over time. After 42 months, the UCS of OGPm-3 and OGPm-1 were increased by approximately 55% and 2% from the original UCS. Meanwhile, the UCS of OGPm-2 and CACm approximately lost 30% and 28% from the original UCS value, respectively. These results suggested that in C3 sewer corrosivity, OGPm-3 exhibited better corrosion resistance performance, based on the residual UCS, impacted by MICC, followed by OGPm-1, CACm and OGPm-2. In comparison, C3 with C1, the corrosion resistance performance of mortar has remained consistent with C1 sewer corrosivity.

At C4 of sewer corrosivity classification, UCS of all mortar types exhibited a decreasing trend over time. However, the UCS of OGPm-3 initially increased during the early phase of exposure time, followed by a subsequent decrease. After 42 months, the UCS of OGPm-1, OGPm-2,

OGPm-3, and CACm were approximately lost 86%, 64%, 70%, and 38% from the original UCS, respectively. This suggested that in C4, CACm exhibited better corrosion resistance performance impacted by MICC, followed by OGPm -2, OGPm -3, and OGPm -1.

A comparison of all geopolymers in three sewer corrosivity classifications observed that OGPm-3 presented the best corrosion resistance based on the residual UCS, followed by OGPm-1 and OGPm-2 in C1 and C3. However, OGPm-2 exhibited the best corrosion resistance performance, followed by OGPm-3 and OGPm-1 in C4. This suggested that the OGPm-2 had better corrosion resistance performance for high sewer corrosivity classification. Although OGPm-2 showed better corrosion resistance performance than OGPm-1 and OGPm-3, after 42 months of exposure, it lost the UCS by approximately 64%. Comparing the corrosion resistance performance of OGPm-2 with CACm, it was observed that the CACm showed better corrosion resistance than OGPm-2 in all sewer corrosivity classifications.

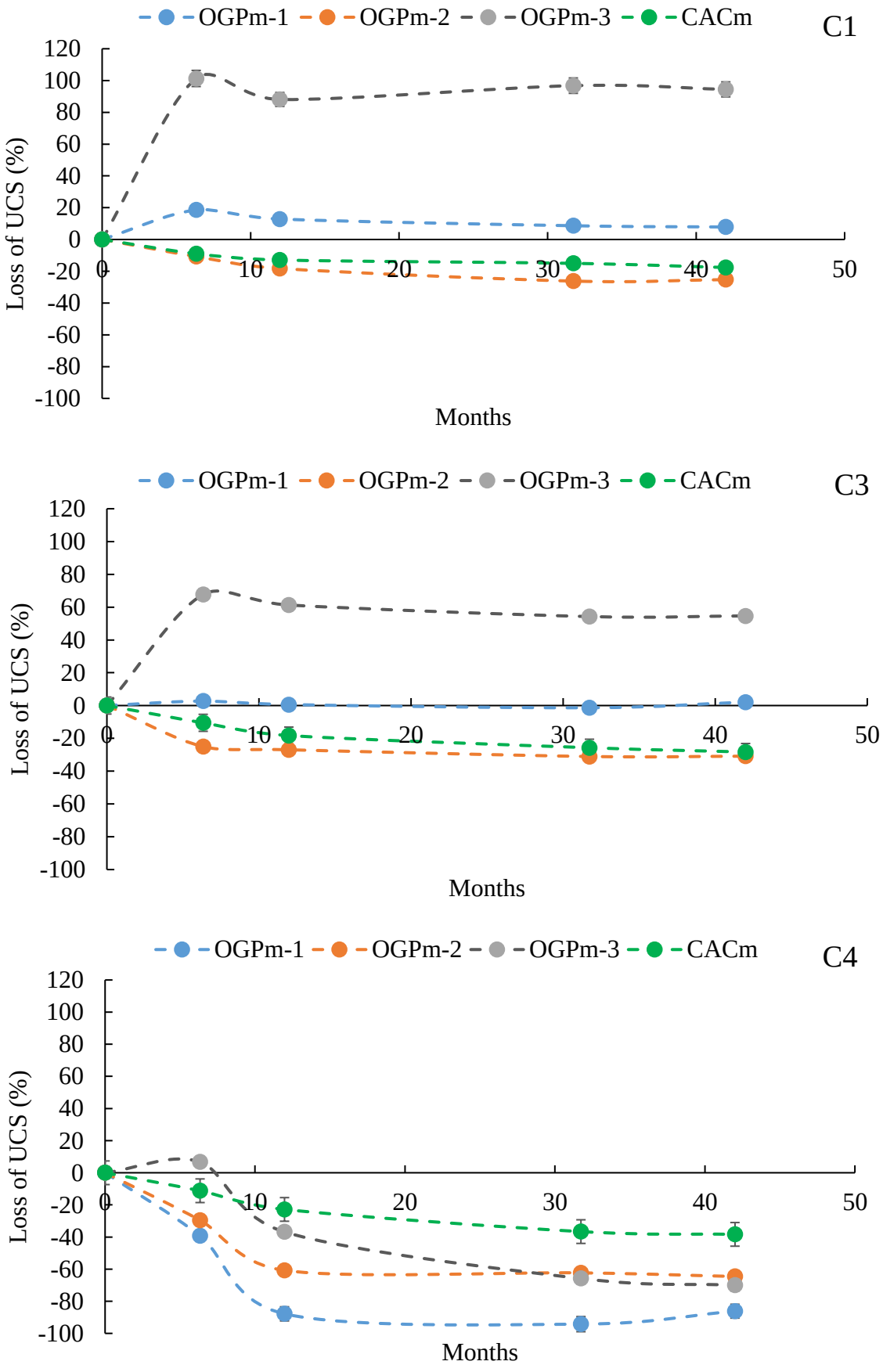

Figure 5-36 Loss of UCS of OGPm and CACm after exposure to C1, C3, and C4 of sewer corrosivity classification

5.2.4 FIELD APPLICATION TEST

This section presents the live sewer environment's experimental investigations of four lining mortars (OGPm-1, OGPm-2, OGPm-3, OGPm-4 and CACm). The main focus of this section is to evaluate the corrosion performance of lining mortar against the MICC under a live sewer environment and actual lining application. The depth of corrosion and residual UCS were used to assess the corrosion resistance performance throughout the monitor. The field lives sewer assets in different locations across Australia, including Sydney, Melbourne, Perth, Brisbane and Adelaide. The results from the actual field test provided real corrosion resistance performance under a live sewer environment. Moreover, this is the first time the corrosion resistance performance of geopolymers under a live sewer environment has been tested with a real lining application scenario.

5.2.4.1 CORROSION PERFORMANCE

Lining mortar as OGPm-1, OGPm-2, OGPm-3, OGPm-4, and CACm were applied in the live sewer assets such as concrete manholes and pipes in Perth, Sydney, Adelaide, Brisbane, and Melbourne. Corrosion performance was evaluated based on the depth of corrosion and the residual UCS, if possible.

5.2.4.1.1 CORROSIVITY CLASSIFICATION OF FIELD LOCATION

Each selected site in Sydney, Perth, and Brisbane (see Table *5-5*) for the performance test monitored the sewer gases (H_2S and CO_2) and the conditions that promote the growth of bacteria and other microbes (temperature and humidity). Figure *5-37* shows the example of sewer environmental data from Sydney Water. The sewer environmental data were analysed further with the 90^{th} percentile to estimate the representative data of each environmental parameter. The 90^{th} percentile was used to provide statistical estimates of the gas compositions and conditions from the overall survey (see Table *5-5*). Finally, each selection site for

corrosion resistance performance tests was classified using the sewer corrosion classification developed by Valix (2021) (see Table *5-2*). It observed that the location sites were classified as C5, C2, and C1 sewer corrosion classifications in Perth, Brisbane, and Sydney, respectively.

Table 5-5 Site Locations and Environmental Conditions

City	Utility	Asset ID	T_{gas}(°C)	RH%	H_2S (ppm)	CO_2 (ppm)	Corrosivity classification
Perth	Water Corporation	AC3	21.92	99.99	170	12880	C5
		AC7	21.56	99.99	180	6180	C5
		AC9	20.21	99.99	190	7800	C5
Brisbane	QUU	MH101132	21.3	100	26	4500	C2
		MH233216	20.6	100	16	4500	C2
		MH233215	20.5	100	24	4500	C2
		MH233213	21.3	100	26	4500	C2
Sydney	Sydney Water	SWC	24	98.7	1.6	6250	C1

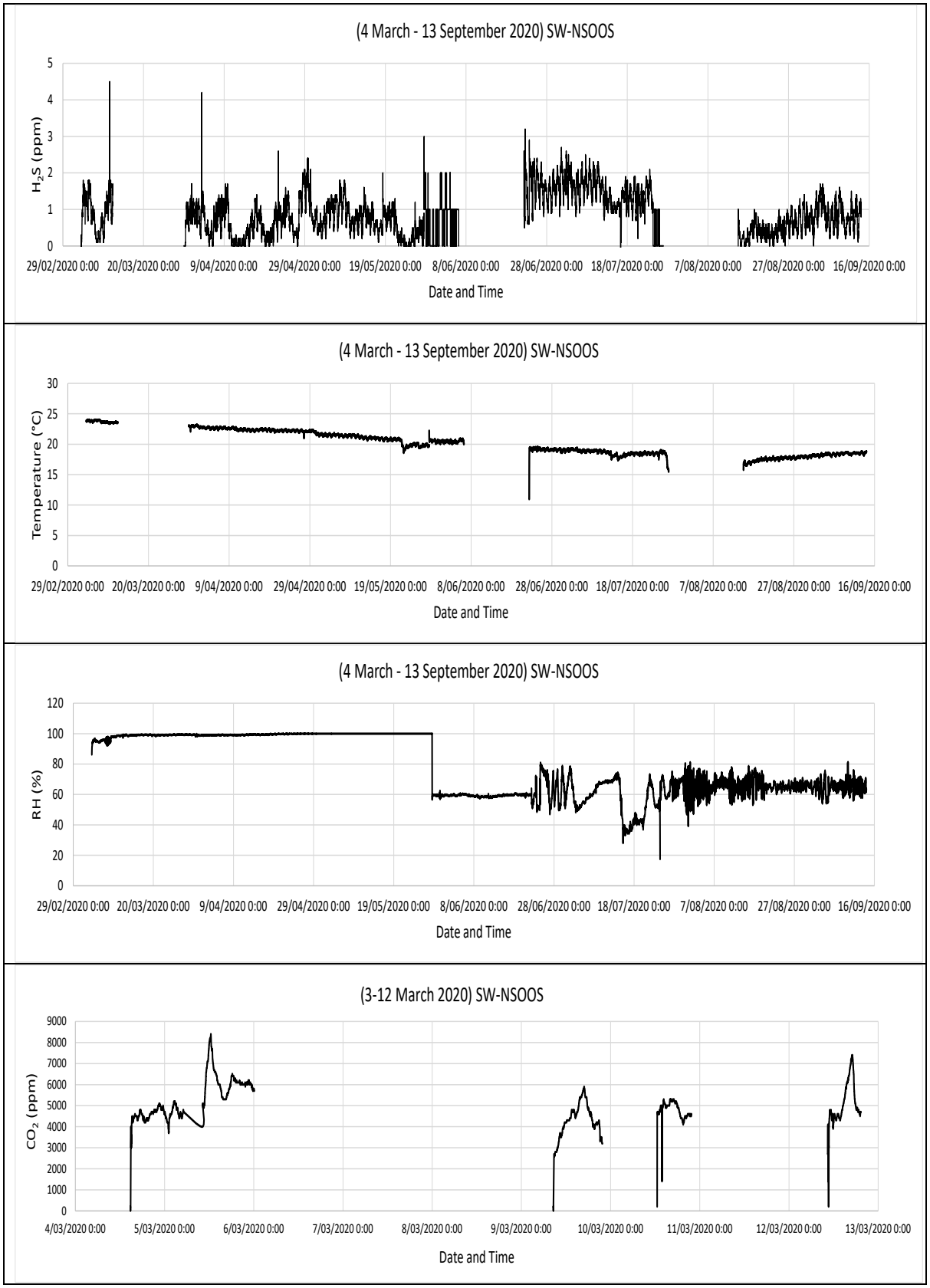

Figure 5-37 Collation of 4 environmental surveys of H_2S, T, RH and CO_2 in SWC NOOS from 4th March to 13th September 2020.

5.2.4.1.2 PHYSICAL APPEARANCE

Lining mortars were applied in a manhole and concrete pipe in Perth, Brisbane, and Sydney. The environmental condition of the field locations was classified C5, C2, and C1 (see Table *5-5*), respectively, based on the sewer corrosivity classification established by Valix (2021).

After exposing the lining mortar in the live sewer for up to 26 months, depending on the field location site, The lining mortar samples were periodically cored from various locations and delivered to the University of Sydney to evaluate the corrosion resistance performance based on the depth of corrosion. It needs to be noted that the residual UCS of mortars was not determined due to the insufficient thickness of the lining mortar. Table 5-6 presents an example of the physical appearance of up to 986 days of OGPm and CACm cored samples after application and being exposed to aggressive environmental conditions in the live sewer manhole at a sewer network managed by Queensland Urban Utilities (QUU), Brisbane, Australia. The environmental condition of the sewer assets exhibited 16-26 ppm H_2S, 4500 ppm CO_2, 20-22 °C and 100 %RH. This environmental condition was indicated to be a C2 sewer corrosivity classification. Overall, the core sample deteriorated over time, and the degree of deterioration depended on the type of geopolymer (chemical composition). The OGPm observed visually presents the corrosion depth from the surface, showing white or yellow at the corrosion layer. Qu et al. (2021) suggested that the white and yellow corrosion products were primarily attributed to the formation of gypsum and ettringite. The OGPm-1 and OGPm-4 exhibited a layer of corrosion and loss of their material when the exposure time was increased. However, the OGPm-3 had shown negligible material loss but noticeably presented the corrosion depth. The corrosion behaviour has consistently shown negligible material loss but a high corrosion depth from mortar coupon with acid immersion test and mortar coupon with digester chambers. CACm had no apparent change in visual appearance after 986 days. It suggested that CACm had higher corrosion resistance than OGPm.

Table 5-6 The core sample of OGPm and CACm from QUU at different time

Time (days)	OGPm-1	OGPm-3	OGPm-4	CACm
160				
471				
640				
986				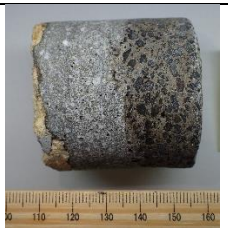

5.2.4.1.3 DEPTH OF CORROSION

The corrosion depth of cored samples from the field location test was similarly determined based on material loss and the depth of acid permeation suggested by Khan et al. (2020b) and Lloyd et al. (2012). The cored mortar sample was cut and sprayed with universal indicators (see Figure 5-38). the corrosion depth was estimated by considering the loss of surface material and acid permeation through mortar identified using a pH indicator applied to the cross-sectioned sample and examined through a Leica DM2500 optical microscope or vernier calliper (see section 3.6.1 in Chapter 3).

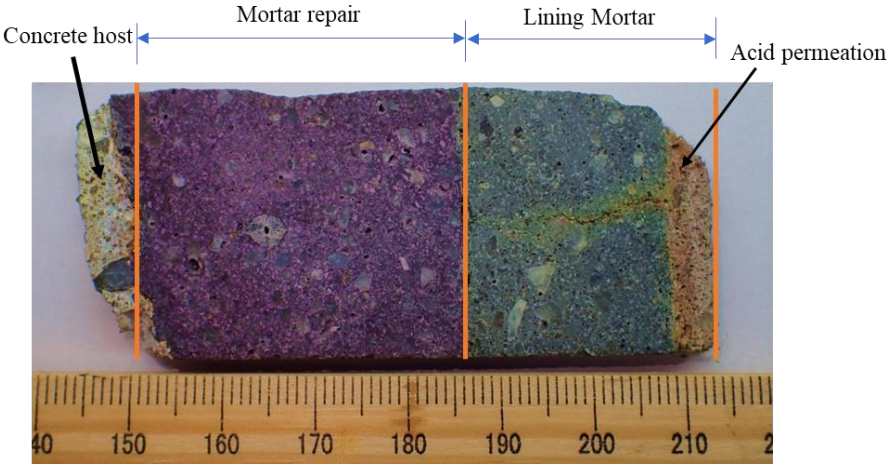

Figure 5-38 Depth of corrosion of cored sample

The corrosion depth of OGPm-1, OGPm-2, OGPm-3, OGPm-4 and CACm after exposure to C1, C2, and C5 sewer corrosivity classification is shown in Figure 5-39. Mortar corrosion-based corrosion depth is characterised by three phases, similar to section 5.2.3.2.3. The corrosion depth from the live sewer field test exhibited different stages of corrosion depending on the chemical and physical properties and sewer corrosivity classification. For example, corrosion of OGPm-3 at C2 in Figure 5-39, OGPm-3 exhibited three stages of corrosion: lag, stage I corrosion (R_1), and stage II corrosion (R_2). However, in higher sewer corrosivity classifications such as C5, OGPm-3 only exhibited R_1 and R_2 stages. This is because the acid

extremely attacked the mortar matrix and caused severe deterioration, leading to the inability to capture the lag phase of corrosion.

Figure 5-39 presents the corrosion depth of OGPm-1, OGPm-2, OGPm-3, OGPm-4, and CACm after the deterioration in live sewer assets, which has different sewer corrosivity classifications (C5-C1). All OGPm and CACm samples were observed to have high corrosion depth as the sewer corrosivity classification increased. These results exhibited a clear relationship between the severity of sewer corrosion and corrosion depth. The difference in corrosion depth was observed between OGPm-1, OGPm-2, OGPm-3, and OGPm-4 in the same sewer corrosivity classification. For example, at C1 with 13 months, the corrosion depth of OGPm-1, OGPm-2, OGPm-3, and OGPm-4 were presented 0.6, 0.65, 3.25, 0.37, and 0.09 mm, respectively. These results suggested the different corrosion depths attributed to the chemical and physical properties of the lining mortar. This will be explained further in the following section. Comparing the corrosion depth of OGPm and CACm, it was shown that CACm exhibited a low depth of corrosion, approximately 8 mm, after being exposed to C5 for 26.3 months, indicating a superior corrosion resistance performance compared to OGPm, which presented 22.8 mm corrosion depth after being exposed to C5 for 26.3 months.

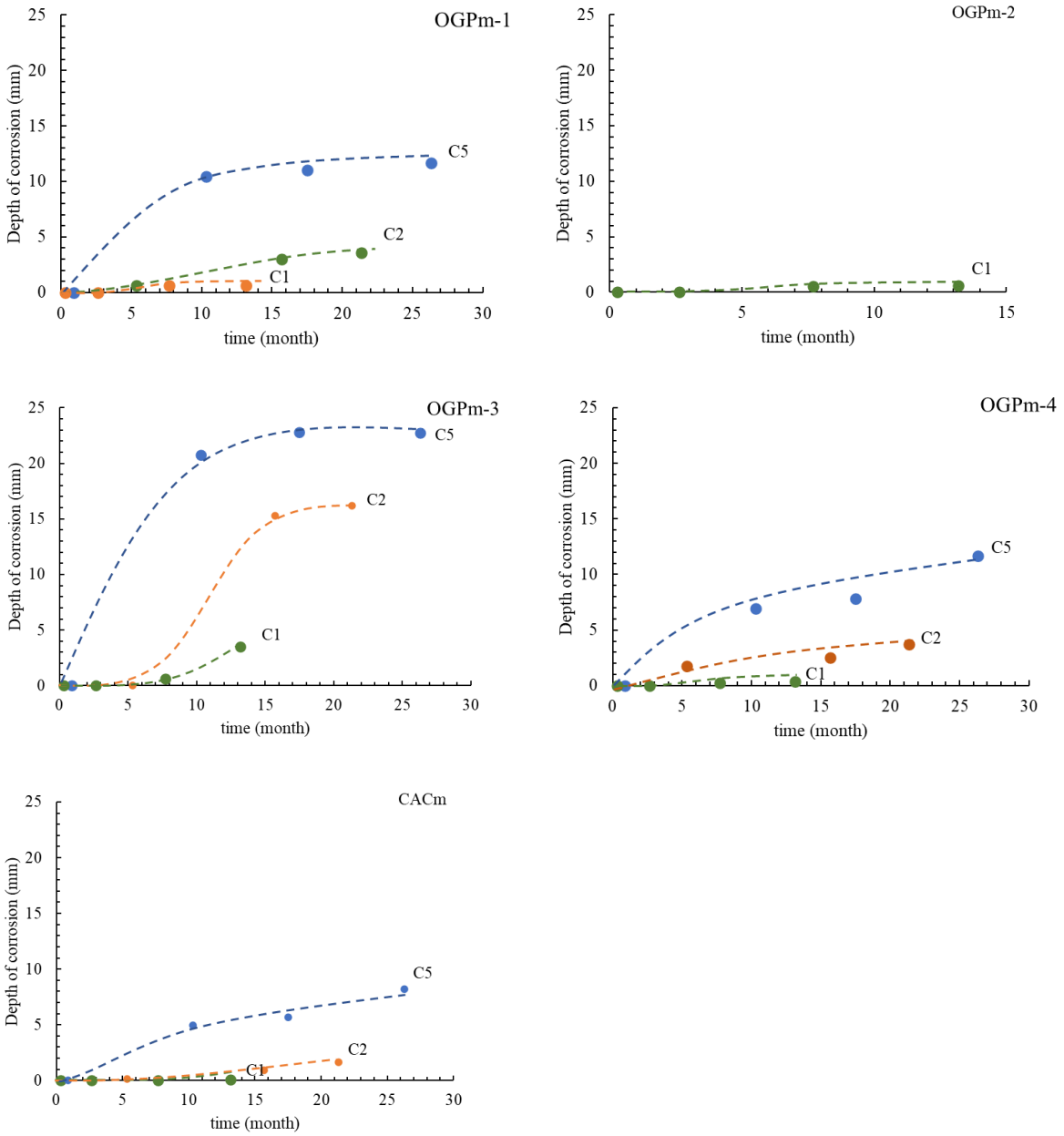

Figure 5-39 Depth of corrosion of OGPm and CACm exposed to live sewer assets

The corrosion depth was correlated with physical and chemical properties, as shown in Figure 5-40, Figure 5-41 and Figure 5-42. The correlation plot exhibited negative and positive correlations, indicating the impact of chemical and physical properties, such as ANC, hydration product, porosity, and UCS, on OGPm and CACm deterioration.

Porosity and UCS showed strong positive and negative correlations, respectively. Higher porosity influenced higher corrosion depth due to higher porosity allowing biogenic acid to

penetrate further and react with the mortar matrix, generating expansive corrosion products. While the UCS of lining mortars were used to reflect the inherent strength and integrity of the mortar material, the mortar performed better in resisting the acid corrosion when the mortar showed higher initial UCS due to the higher UCS reflected by the dense mortar and lower acid penetration, resulting in lower corrosion depth. These results agreed with Aiken et al. (2018) and Luna Galiano et al. (2016) that porosity and UCS were related to corrosion resistance performance. Lower porosity had greater compressive strength, resulting in lower deterioration. Aiken et al. (2018), Khan et al. (2020b), and Grengg et al. (2020) found that the corrosion resistance performance was significantly impacted by porosity and UCS after being exposed to a sewer environment.

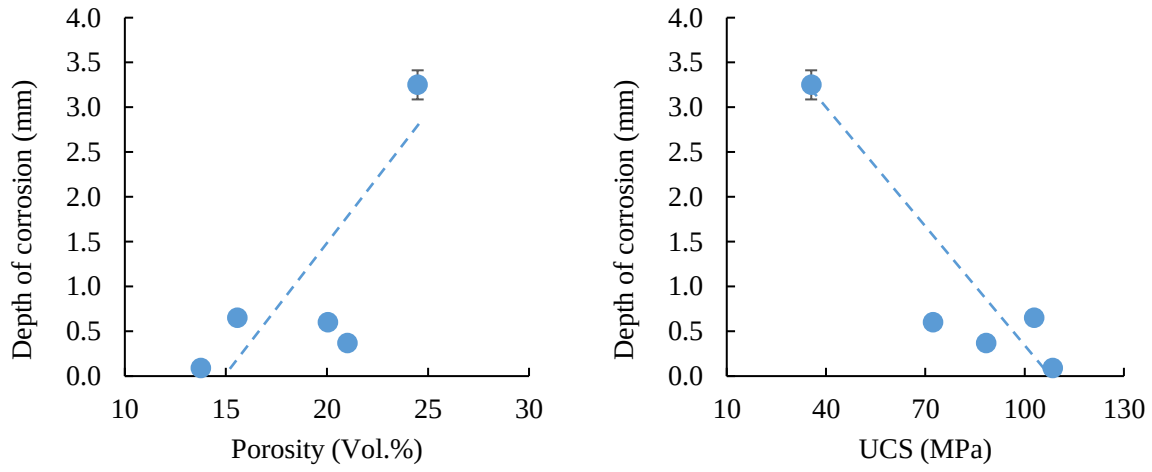

Figure 5-40 Correlation between the depth of corrosion of OGPm and CACm exposed to C1 live sewer assets for 13 months

Another factor that impacts the corrosion resistance performance of mortar is ANC. The ANC showed the optimum correlation (see Figure 5-41). It was observed that the ANC from 2.6-4.2 mmol H+/g substrate decreased the corrosion depth as the ANC increased, while the ANC increased by more than 4.2 mmol H+/g substrate, and the corrosion depth increased. This is attributed to decalcification and dealumination from the geopolymer matrix generating more

OH^- and forming gypsum and ettringite as corrosion products (Khan et al., 2020b, Grengg et al., 2020).

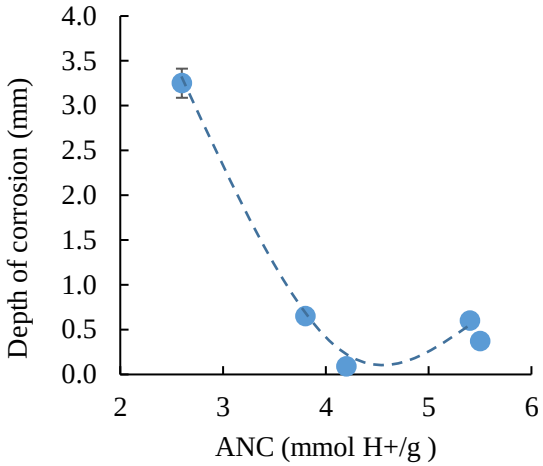

Figure 5-41 Correlation between the depth of corrosion and ANC of OGPm exposed to C1 live sewer assets for 13 months

Hydration products such as C-S-H, C-A-S-H, C-N-A-S-H, and N-A-S-H were correlated with the depth of corrosion and found positive and negative correlations, as presented in Figure 5-42. For C-S-H and C-A-S-H, the correlation has shown that the corrosion depth decreased as the C-S-H and C-A-S-H increased. However, the C-A-S-H slightly increased after C-A-S-H reached 40 %. The C-S-H and C-A-S-H had poor stability when the acid attacked and leached out as $Ca(OH)_2$ and $Al(OH)_3$ (Shi et al., 2003, Kong et al., 2022, Khan et al., 2020b). The OH^- was leached out and neutralised H^+, resulting in a lower corrosion depth. Even though the Ca content in the mortar improved its neutralised capacity, it also exhibited a disadvantage when it formulated the gypsum and ettringite, which expanded and generated more cracks and allowed acid to penetrate further and attack the mortar binder (Khan et al., 2020b, Wu et al., 2020). C-N-A-S-H was one of the main products in alkali-activated mortar (Ismail et al., 2014, Khan et al., 2020b). It improved the strength of the mortar (Yaghoubi et al., 2019, Ismail et al., 2014, Shoaei et al., 2019). The correlation of C-N-A-S-H and corrosion depth was shown as weak correlation. While N-A-S-H exhibited a positive correlation, increased N-A-S-H led to

an increase in the depth of corrosion. This is attributed to the N-A-S-H nature, which is less dense and more porous, which is generally found in low calcium geopolymer (Aiken et al., 2018, Khan et al., 2020b). This hydration phase allowed the acid to penetrate further and react with the mortar binder, increasing the corrosion depth. Moreover, Khan et al. (2020b) also explained that when the acid attacks the N-A-S-H. The N-A-S-H gel dealuminated and led to increased porosity and acid penetration, leading to the deterioration of pore structure, which increases the corrosion depth.

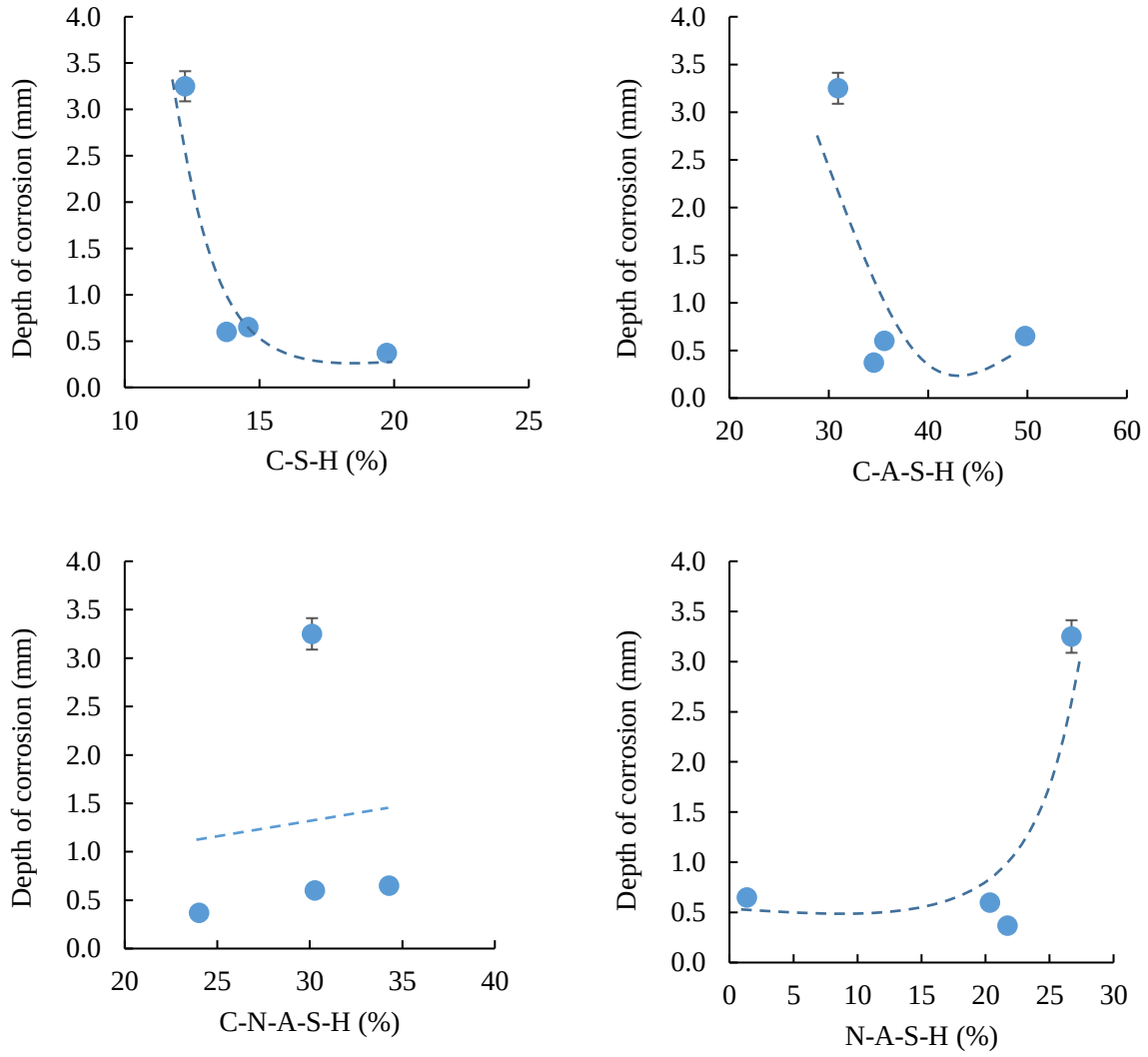

Figure 5-42 Correlation between the depth of corrosion and hydration product of OGPm exposed to C1 live sewer assets for 13 months

5.2.4.1.4 CORROSION RATE IN LIVE SEWER ASSETS

To assess the corrosion resistance performance of OGPm and CACm, the corrosion rates were determined using a similar methodology as described in the previous section (5.2.1.1.2). The corrosion behaviour was categorised into three phases: lag, stage I corrosion rate (R_1), and stage II corrosion rate (R_2). It needs to be noted that the corrosion characterisation is unable to capture all corrosion phases in all sewer corrosivity classifications (see Table 5-7). Among the OGPm, lag phases were revealed at low sewer corrosivity classification. For example, the lag phase could take up to 240 days before initiating the stage I corrosion rate. However, CACm was revealed to capture the lag phase in all sewer corrosivity classifications. This result suggested that the CACm was a superior material against acid corrosion due to its better chemical and physical properties, such as ANC, porosity, and UCS. This allowed the slowing down of the deterioration of CACm.

Table 5-7 The corrosion phases of OGPm and CACm

Mortar	Sewer Corrosivity Classification	Lag (day)	R_1 (mm/year)	R_2 (mm/year)
OGPm-1	C5	-	17.52	2.19
	C2	60	2.78	0.54
	C1	80	1.46	0.15
OGPm-2	C1	120	1.96	0.22
OGPm-3	C5	-	36.50	4.98
	C2	200	24.82	1.46
	C1	240	7.71	-
OGPm-4	C5	-	8.21	2.71
	C2	-	6.21	0.85
	C1	80	0.67	0.18
CACm	C5	60	7.58	1.14
	C2	200	1.39	-
	C1	280	0.30	-

Figure 5-43 compares the corrosion rate of R_1 and R_2 of OGPm-1, OGPm-2, OGPm-3, and CACm at C1, C2, and C5 sewer corrosivity classifications. Corrosion resistance performance

based on R_1 at C1 as representative corrosivity classification to compare all mortar was seen that OGPm-3 was the highest stage I corrosion rate, followed by OGPm-2, OGPm-1, and OGPm-4, respectively. At high sewer corrosivity classification, OGPm-3 was observed to have a high corrosion rate, as expected. The higher corrosivity classification produces more biogenic sulphuric acid due to high H_2S concentration in the gas phase and continuously attacks the mortar matrix. A similar comparison of R_2 observed that R_2 was lower than R_1. As mentioned earlier, the absence of R_2 indicates that the acid penetration continued to diffuse into the OGPm matrix and formed expansive corrosion products, such as gypsum, limiting the acid permeation. This observation was particularly noticeable in the low sewer corrosivity classification, suggesting that the mortar matrix remained sensitive to an acid attack without sufficient protection. Consequently, the corrosion depth is expected to continue to increase over time, eventually leading to the stage II corrosion phase.

Figure 5-44 shows the SEM backscattering image and sulphur (S) mapping of the uncorroded and corroded sections of OGPm-1 and OGPm-3 after 16 months of exposure to C2 sewer corrosivity classification as representative of a corroded sample. The S was mapped as representative of gypsum, which formed on the surface of the corroded section. The SEM with S mapping were evidence of the pore blocking by the corrosion product deposited on the corroded surface, similar to the cube sample exposure to the sewer corrosivity classification in the digester chamber. The uncorroded samples were shown low S concentration. The SEM image of OGPm-1 and OGPm-3 exhibited the gypsum deposit on the surface. However, the concentration of S on the surface of OGPm-3 was lower than OGPm-1 due to the OGPm-1 having Ca content more than OGPm-3, resulting in formulating less gypsum.

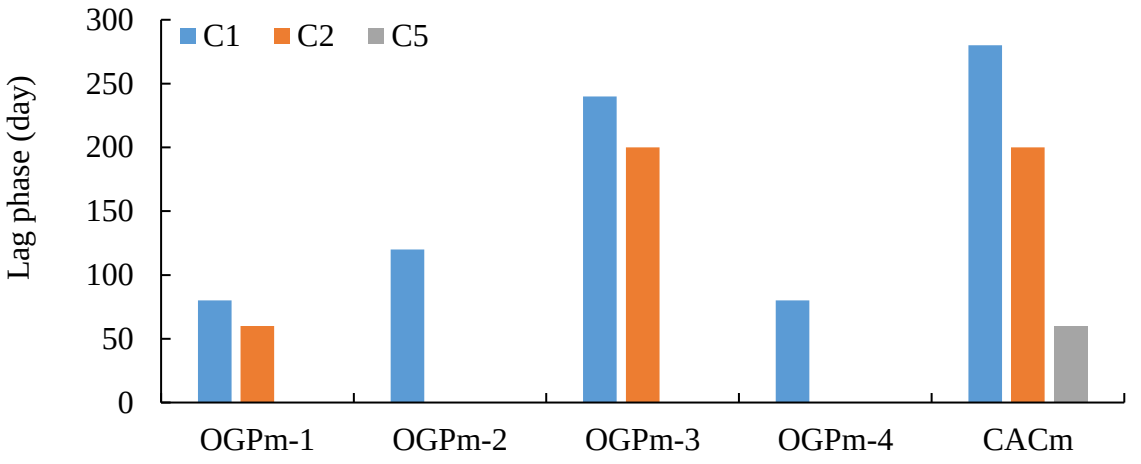

(a) Lag phase

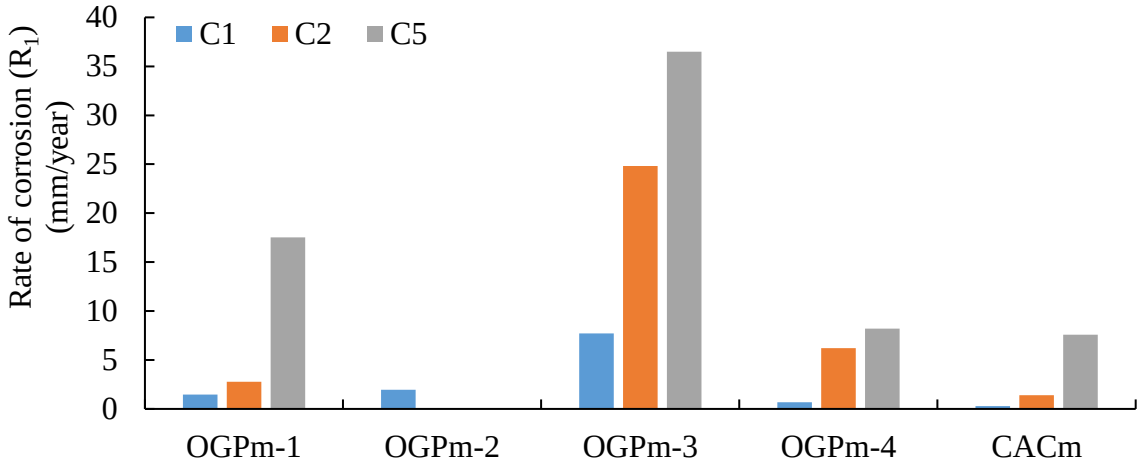

(b) Stage I corrosion rate

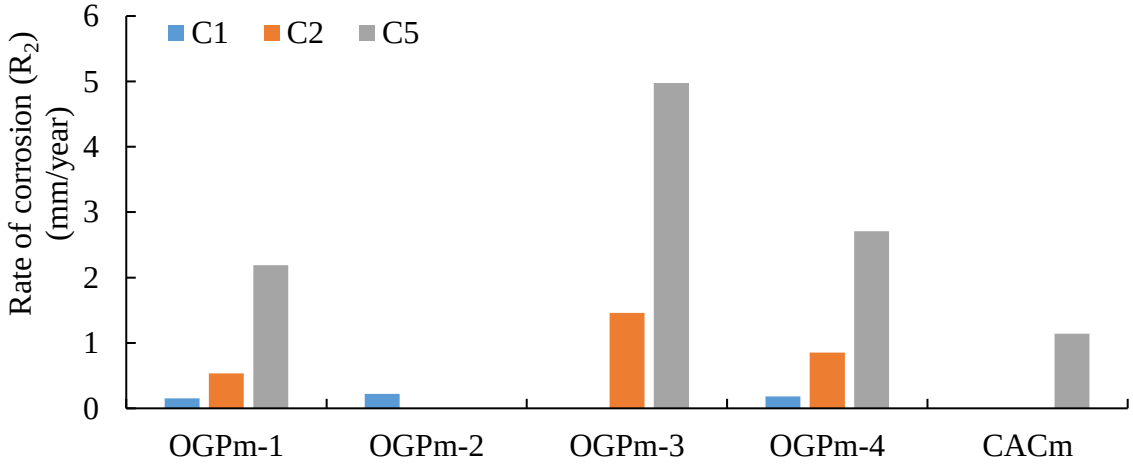

(c) Stage II corrosion rate

Figure 5-43 Lag phase, stage I corrosion rate (R_1) and stage II corrosion rate (R_2) of OGPm-1, OGPm-2, OGPm-3, OGPm-4 and CACm

OGPm-1		OGPm-3	
Uncorroded section	corroded section	Uncorroded section	corroded section
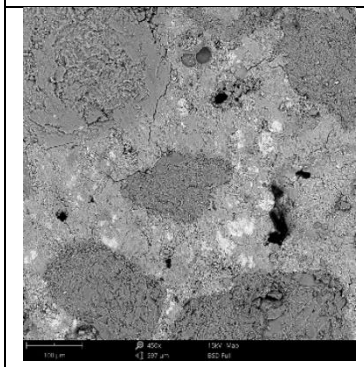	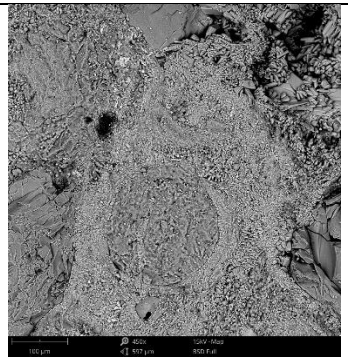	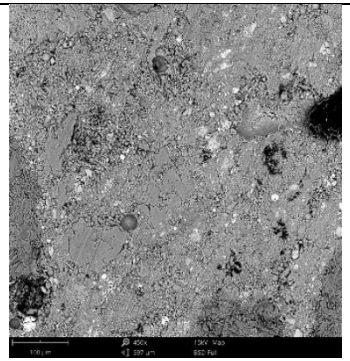	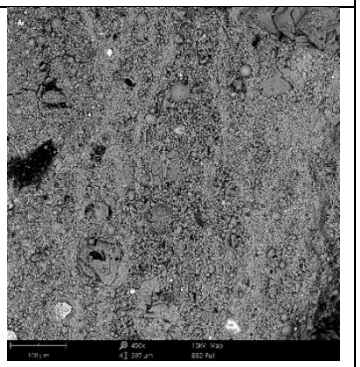
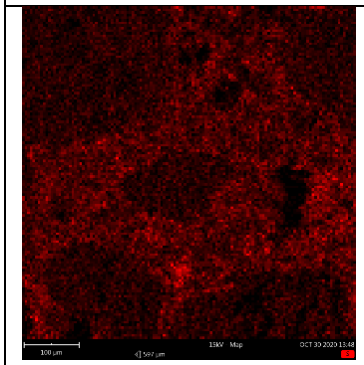	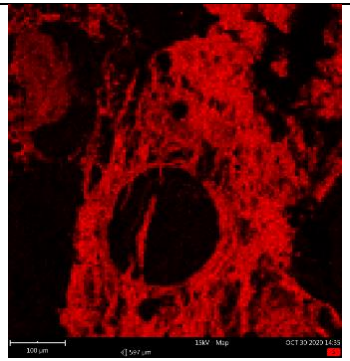	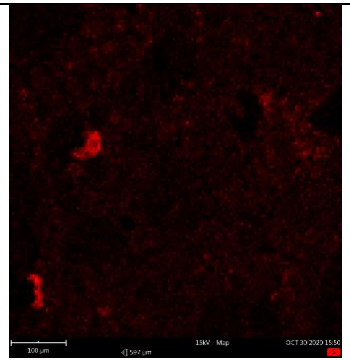	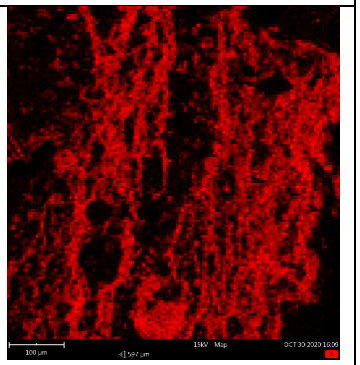
0.53 wt.% S	9.13 wt.% S	0.74 wt.% S	8.61 wt.% S

Figure 5-44 SEM backscattering images and S maps of the uncorroded and corroded sections of OGPm-1 and OGPm-3 after 16 months of exposure to C2 sewer corrosion classification

5.2.4.1.5 COMPARISON OF DIFFERENT CORROSION TESTS UNDER SEWER ENVIRONMENTAL CONDITIONS

The durability test of OGPm and CACm using wet and dry spray shotcrete provided a realistic corrosion resistance performance impacted by MICC. This test allowed a more accurate evaluation of their durability in shotcrete application. This section compares the corrosion resistance performance of OGPm and CACm obtained from shotcrete application and cured cube mortar samples after being exposed under the same sewer corrosivity classification to understand the impact of sample preparation methods. This section also compares the performance test method between the shotcrete field and immersion tests to understand the impact of MICC and chemical attack on the mortar.

Figure 5-45 compares the lag phase, R_1 and R_2 of shotcrete application and cube sample preparation of OGPm-1, OGPm-3, and CACm under C1 of sewer corrosivity classification. In comparing the lag phases of shotcrete and cube samples, the shotcrete appeared to have a more extended period before initiating the stag I of corrosion. Based on the knowledge that at the initial period of corrosion attributed to the practical ANC, the fresh mortar shotcrete would have a high ability to neutralise the acid generated under the sewer environment compared to cured mortar sample due to freshly applied mortar generally has a higher ability to neutralise acids compared to cured mortar due to factors such as its high alkalinity, presence of reactive components in the paste, high porosity, and active hydration process. The high alkalinity and availability of reactive components, such as fly ash and slag, in fresh mortar facilitate acid neutralisation reactions (Potgieter-Vermaak et al., 2006, Yan et al., 2000), while the increased porosity (see in section 4.4.1.) allows for better acid penetration and interaction with alkaline compounds (Chen et al., 2013, Huo et al., 2018). Additionally, the hydration process of fresh mortar contributes to the release of hydroxide ions and improves its acid neutralisation capacity of mortar. In contrast, cured mortar has low alkalinity, low reactivity, and low acid

neutralisation capacity compared to fresh mortar, simultaneously resulting in higher deterioration.

However, it exhibited that the corrosion rate in both R_1 and R_2 of OGPm-1, OGPm-3, and CACm obtained from the shotcrete application was higher than in both R_1 and R_2 obtained from the cured cube sample. This is because the cured mortar generally exhibits better acid resistance than fresh mortar due to the formation of hydration products, increased chemical stability, reduction in alkalinity, and improved density and porosity. The hydration process during curing leads to the formation of hardened products that create a denser and more compact matrix, providing a protective barrier against acid penetration. The chemical stability of the hydration products enhances the mortar's resistance to acid dissolution and degradation. Additionally, the reduced alkalinity and increased density of the cured mortar contribute to its improved acid resistance by limiting acid penetration. However, the R_2 has not appeared in all OGPm-3 and CACm because the mortar was still in stage I of corrosion.

Additionally, the corrosion resistance performance of CACm was compared with OGPm. It was observed that CACm was still a better corrosion-resistant lining mortar. Despite the field shotcrete application appearing to exhibit worse corrosion resistance performance, this is valuable data because this first corrosion performance data presented a real scenario of corrosion with practical sewer rehabilitation.

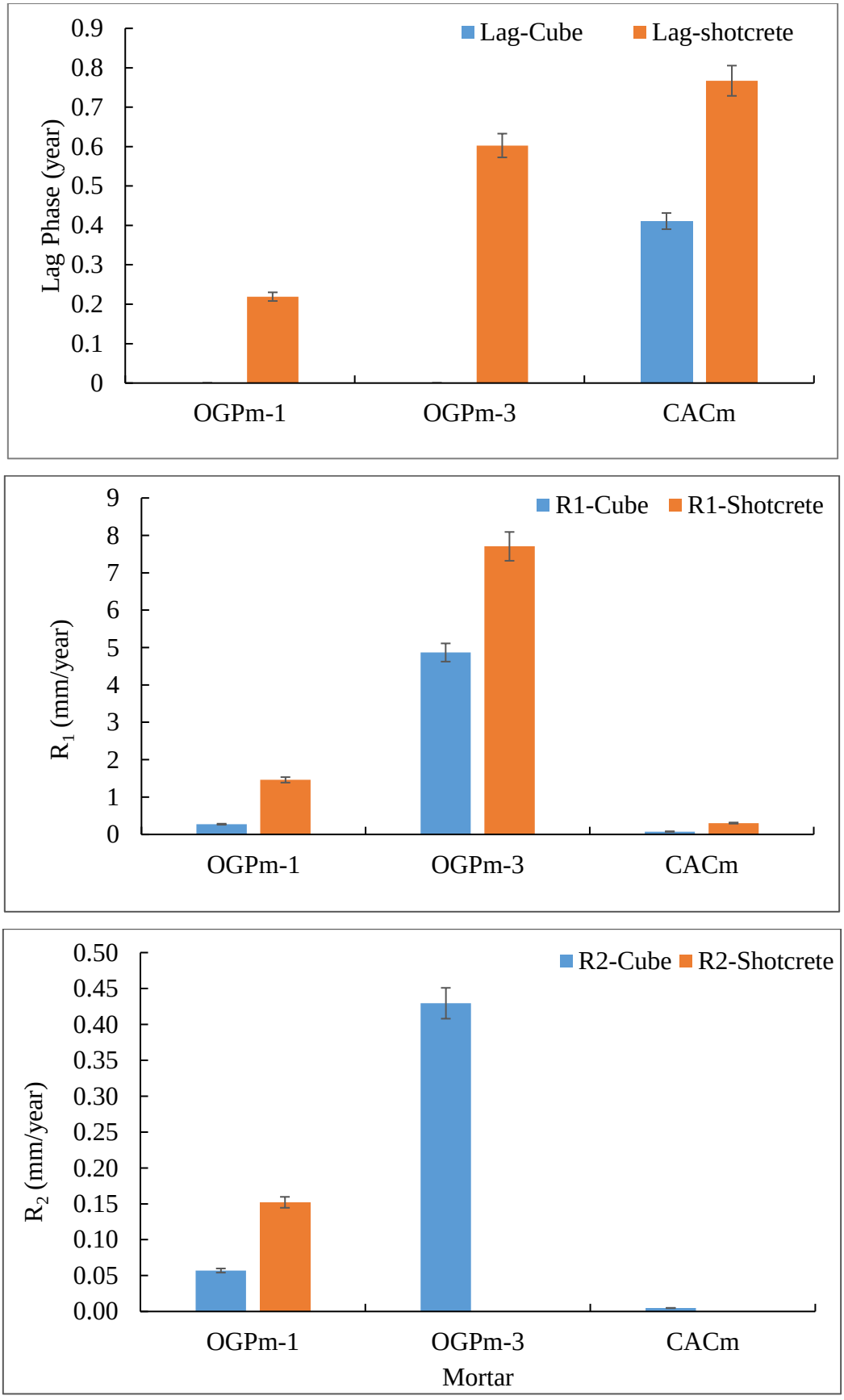

Figure 5-45 Comparison of corrosion rate of practical application and cube sample preparation under C1 of sewer corrosivity classification

The corrosion resistance performance from acid immersion tests, which simulate a chemical attack, and exposure to live sewer environments involve microbiologically induced concrete corrosion (MICC). This compared the R_1 and R_2 exposure to acid immersion tests and field live sewer assets. Stage I and stage II of corrosion, the corrosion rates observed in the acid immersion test and the live sewer environmental conditions are shown in Figure 5-46.

The positive correlation between these two test methods indicates that the acid immersion test is consistent with the corrosion behaviour experienced in live sewer environments. Moreover, the difference in sewer corrosivity classification also impacted the corrosion rate; higher sewer corrosivity exhibited a higher corrosion rate at C5 > C2 > C1. It was also noticed that all sewer corrosivity corrosion rates were aggressively higher in a live sewer than in the immersion test. This is related to the microorganism growth in the sewer environment, such as SOB, which produces biogenic sulphuric acid and plays an essential role in sewer corrosion (Grengg et al., 2018). Once the sulphuric acid attacked the mortar, the gypsum and ettringite were formulated as the primary corrosion product with increased porosity and presented as the corroded layer from the mortar surface (Monteny et al., 2000, Khan et al., 2020b).

In the case of pure sulphuric acid attacks, the formation of the corrosion layer acted as a barrier to further attack. The fresh sulphuric acid must penetrate through this layer before the acid reaches the sound mortar. In the case of sulphuric acid produced by SOB, the corrosion layer becomes an excellent condition for the growth of the SOB because the increasing porosity of the corroded layer allows the SOB to penetrate and grow further into the inner of the corroded layer (Monteny et al., 2000). Fresh biogenic sulphuric acid formation can occur near the sound mortar and immediately attack the mortar, resulting in more corrosion depth than pure sulphuric acid attacks.

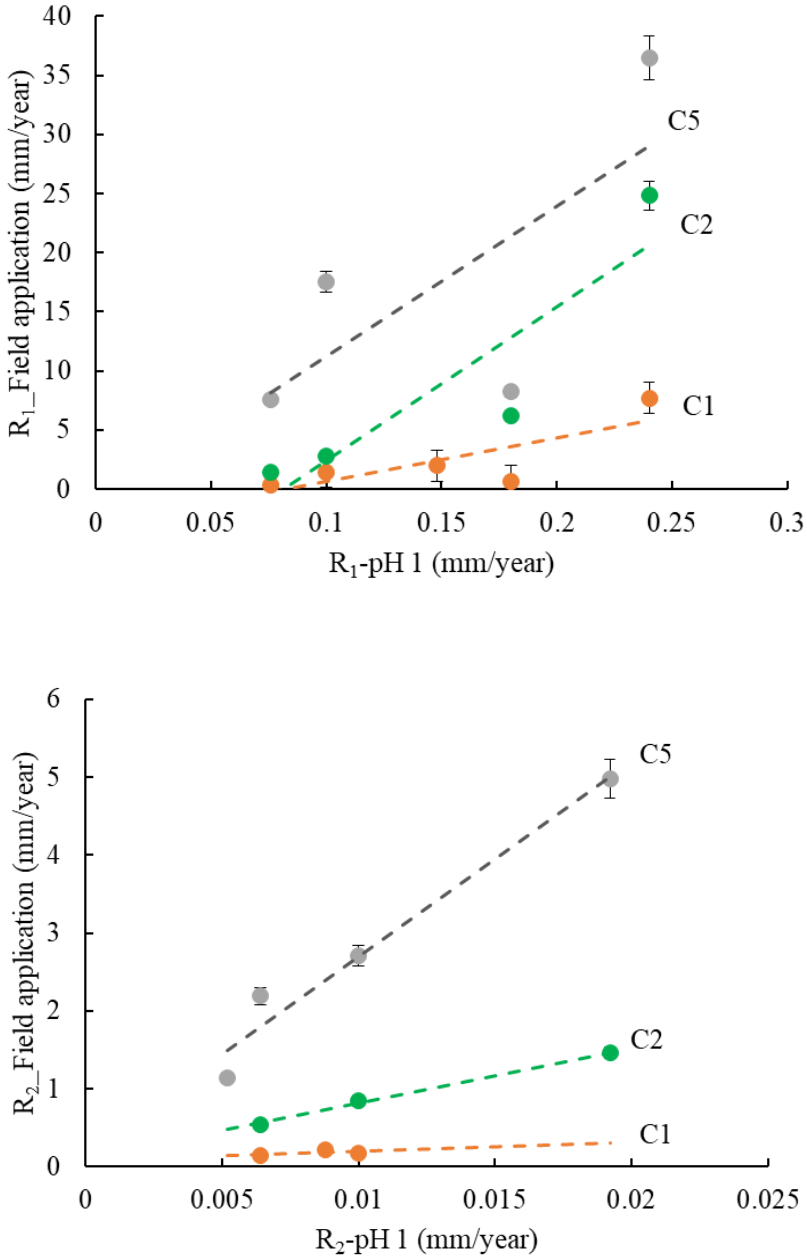

Figure 5-46 Correlation between the corrosion rate of shotcrete application and acid immersion test (pH 1 sulphuric acid)

5.3 DURABILITY TEST AS A FUNCTION OF MORTAR PROPERTIES

The field test showed that mortars' durability plays an essential role in ensuring long-term corrosion resistance performance. Various alkali-activated mortars, including geopolymer (OGPm-1, OGPm-2, OGPm-3, and OGPm-4) and CACm, were subjected to various sewer corrosivity and pH 1 sulphuric acid. The deterioration of the mortars was assessed based on the corrosion depth over time. Chemical and physical properties, sewer environmental conditions,

and time influence the durability of mortars. Therefore, this section aimed to understand the impact of the physical and chemical properties on the durability of lining mortar by correlating the chemical and physical properties and corrosion rate.

The ANC, hydration phases, porosity, and UCS as the initial properties of the lining mortar were correlated with the stage I corrosion rate (R_1) under the C1 sewer corrosivity classification to understand the impact on the corrosion resistance performance. Moreover, the corrosion resistance performance of different sample preparations was also compared based on R_1. It is important to note that this section only correlated the chemical and physical properties and R_1 under C1 of sewer corrosivity to compare corrosion resistance performance because all lining mortars could capture the R1. In contrast, only some lining mortars could capture R_2.

5.3.1 PHYSICAL PROPERTIES

5.3.1.1 POROSITY

Figure 5-47 presents a correlation between porosity and R_1. It shows a positive non-linear correlation. The correlation suggested that there was an optimum corrosion rate along with increasing the initial porosity of the protective lining. The corrosion rate dramatically increased after the initial porosity increased by more than 20 vol.%. This was because higher porosity allows more acid and other corrosive compounds to penetrate the mortar lining matrix and react with the mortar binders, enhancing the corrosion process and increasing R_1. Therefore, reducing porosity mitigates acid permeation and reduces the corrosion rate, improving the long-term corrosion resistance performance. These results agreed with Aiken et al. (2018), Khan et al. (2020b), and Grengg et al. (2020) that the corrosion resistance performance was impacted by porosity after exposure to a sewer environment. the corrosion depth was increased as the initial porosity increased. Comparing the corrosion rate of all sample preparation and performance tests, it showed consistent results. The shotcrete application samples exhibited the highest R_1 values after exposed C1 sewer corrosivity in the field, which was attributed to the

higher porosity of fresh lining mortar compared to the cured samples (see section 4.4.1), followed by 28 days cured cube exposed C1 sewer corrosivity in the field and 28 days cured cube exposed in pH 1 of sulphuric acid, respectively. Therefore, the results suggested that a maximum porosity of approximately 20 vol.% is recommended for optimal corrosion resistance performance in geopolymer mortar.

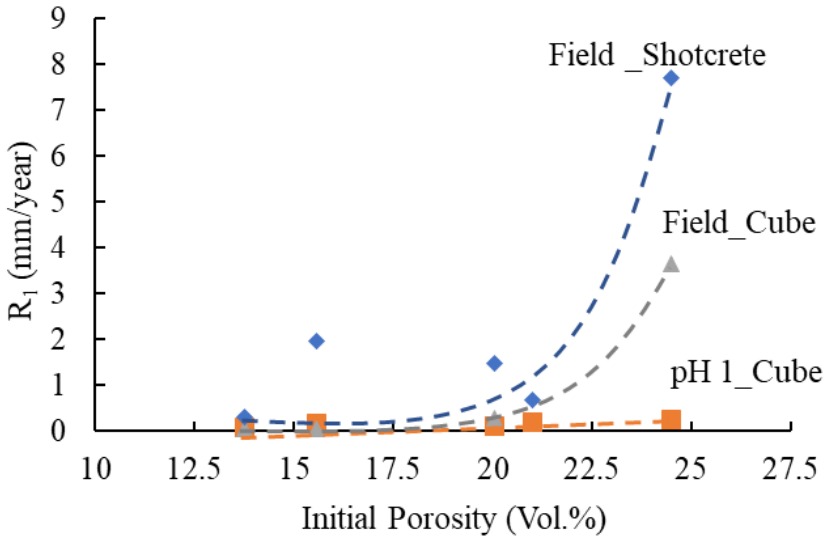

Figure 5-47 Correlation of R_1 and initial porosity at C1 of sewer corrosivity classification

5.3.1.2 UCS

Figure 5-48 shows the negative non-linear correlation between the initial UCS and R_1. Increasing the initial UCS observed that the corrosion resistance performance was improved. This is due to higher initial UCS attributed to low porosity and dense mortar material, which could provide better protection against corrosive compounds (He et al., 2021, Ali et al., 2022). The corrosion performance was also influenced by the sample preparation method, specifically the application of shotcrete and the use of cured cube mortar samples. This correlation indicated an optimal initial UCS enhanced the corrosion resistance performance. It was observed that a minimum UCS of 70 MPa was reached, a desirable UCS for better corrosion resistance performance.

Moreover, it is evident that the UCS is related to the porosity of the mortar material. Ali et al. (2022) suggested that higher porosity results in lower UCS. Therefore, initial porosity and UCS must be carefully considered to provide better corrosion resistance performance and more durable mortar.

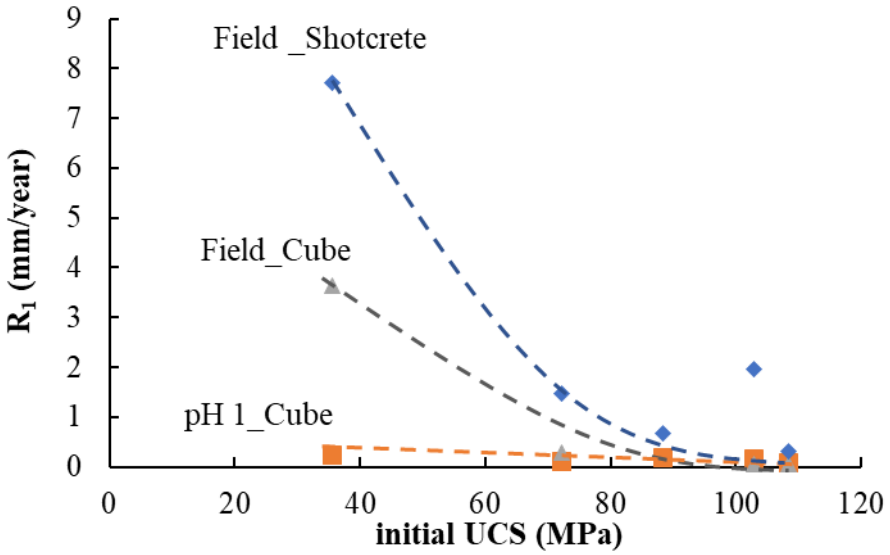

Figure 5-48 Correlation of R_1 and initial UCS at C1 of sewer corrosivity classification

5.3.2 CHEMICAL PROPERTIES

5.3.2.1 ANC

Figure 5-49 presents the non-linear correlation between practical ANC and R_1. The correlation indicated the optimum practical ANC at approximately 4.5 mmol H^+/g substrate. Lower and higher practical ANC than 4.5 mmol H^+/g substrate exhibited an increasing corrosion rate. As explained in section 4.5.2.3, the ANC was strongly correlated with CaO within the mortar binder. Decalcification from hydration phases from the lining mortar is attributed to acid neutralisation and formation of corrosion products such as gypsum and ettringite (Giampaolo et al., 2002b, Khan et al., 2020b). Therefore, increasing the practical ANC reflects an increased ability to neutralise acids that attack the mortar binder, providing improved protection against corrosive compounds. Nevertheless, if the ANC increases too much, the access leaching Ca^{2+}

will formulate the gypsum and ettringite, generating more cracks and providing a pathway for corrosive compounds to penetrate further and react with binder mortar (Khan et al., 2020b).

Comparing the corrosion resistance performance of both the shotcrete application and 28 days-cured cube samples showed a consistent correlation. However, it exhibited different corrosion resistance performances based on the R_1. The method of preparing the sample affected the practical ANC of the mortar as explained in section 5.2.4.1.5 that fresh shotcrete mortar has a higher ability to neutralise acids compared to cured mortar due to high alkalinity and availability of reactive components in fresh mortar facilitating acid neutralisation reactions (Potgieter-Vermaak et al., 2006, Yan et al., 2000). This correlation suggests that for optimal corrosion resistance performance in geopolymer mortar, it is recommended to have a minimum practical ANC of 4.5 mmol H+/g substrate.

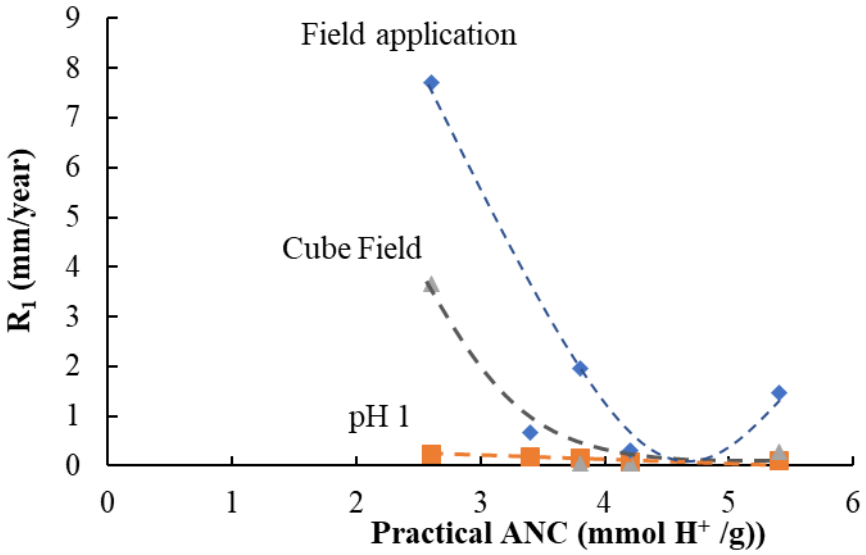

Figure 5-49 Correlation of R_1 and practical ANC at C1 of sewer corrosivity classification

5.3.2.2 HYDRATION PHASES

The hydration phases of alkali-activated mortar, including geopolymer, are C-S-H, C-A-S-H, C-N-A-S-H, and N-A-S-H. Figure 5-50 shows the correlation between the hydration phase (C-S-H, C-A-S-H, and N-A-S-H) and R_1. It exhibited a negative non-linear correlation between

C-S-H and C-A-S-H correlated with R_1 (see Figure 5-50 (a) and (b)). At the same time, N-A-S-H exhibited a positive non-linear correlation (see Figure 5-50 (d)). In contrast, The C-N-A-S-H appeared to have a very weak correlation with R_1 (see Figure 5-50 (c)). This correlation suggests that an increase in the content of the C-S-H and C-A-S-H phases is associated with an improvement in corrosion resistance performance. The presence of these hydrate phases in the mortar matrix contributes to the enhanced durability of the mortar because the C-S-H and C-A-S-H can improve the mortar by filling the void and acting as micro-aggregate in the microstructure of mortar, resulting in decreased porosity and increased UCS (Phoo-ngernkham et al., 2013). Increasing the N-A-S-H phase in the mortar appears to lower corrosion resistance performance. This is attributed to the nature of N-A-S-H phases which has a more open and disordered structure due to more Si-O-Si linkages, resulting in high porosity (Wang et al., 2021, Castillo et al., 2021). In the comparison of the corrosion rate from the shotcrete application and 28-day cured cubes, the shotcrete application exhibited the highest corrosion rate because the formation of the hydration phase was not completed, resulting in a lower ability to resist corrosion compared to 28-day cured cubes.

The correlation of hydration phases with R_1 suggested that alkali-activated mortar, including geopolymer mortar, must cautiously consider the hydration phases to achieve optimal corrosion resistance. This study recommends that the lining mortar have a minimum content of 14% C-S-H and 35% C-A-S-H phases. These hydrate phases contribute to the strength and durability of the mortar, enhancing its resistance to acid corrosion. At the same time, it advised limiting the content of N-A-S-H phases to a maximum of 22.5% because the excessive N-A-S-H phases may negatively affect the corrosion resistance properties of the mortar, potentially leading to reduced performance.

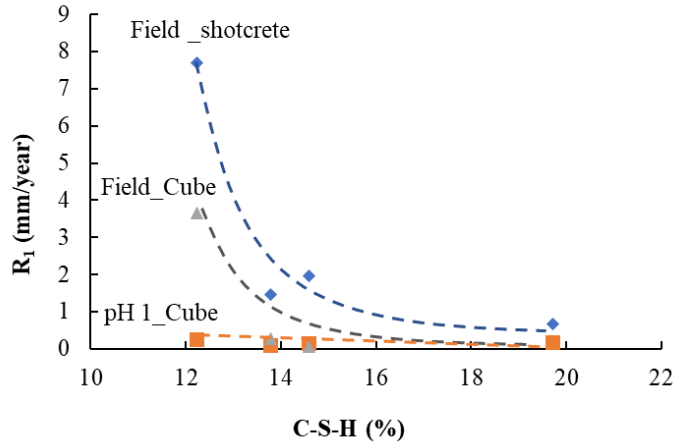

(a) C-S-H

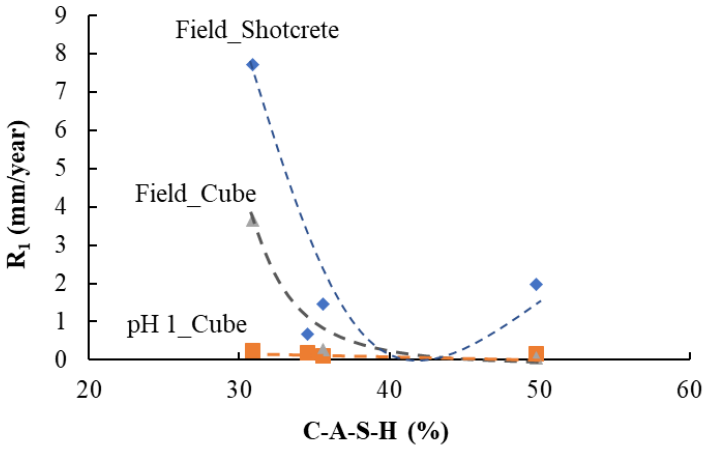

(b) C-A-S-H

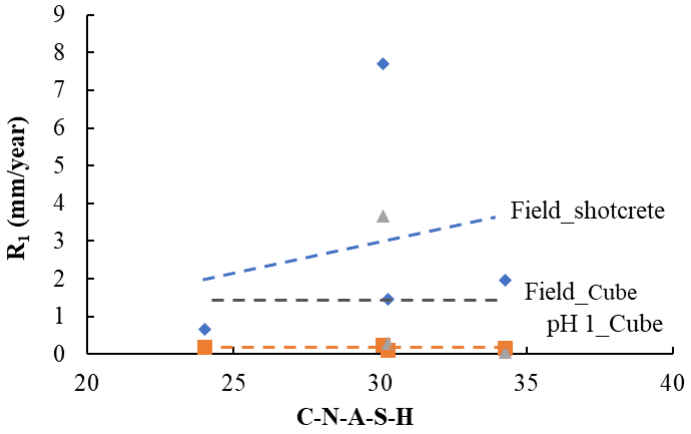

(c) C-N-A-S-H

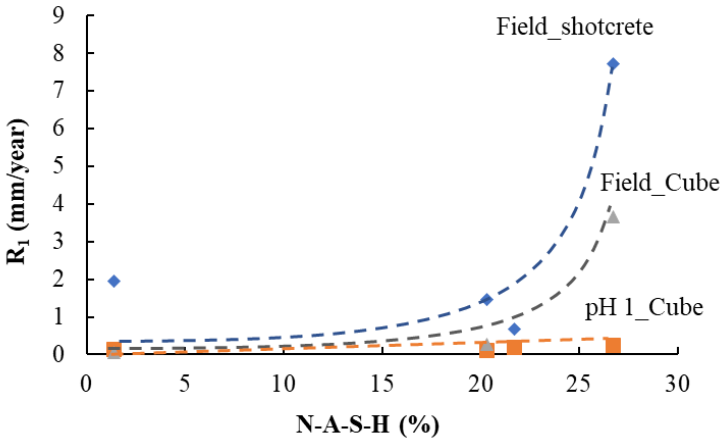

(d) N-A-S-H

Figure 5-50 Correlation of R_1 and C-S-H, C-A-S-H, and N-A-S-H at C1 of sewer corrosivity classification

Overall, when comparing the corrosion resistance performance based on the stage I corrosion rate (R_1), it was observed that the cube mortar samples performed better than the fresh lining mortar shotcrete application under C1 sewer corrosivity environment conditions. When comparing the corrosion resistance performance of cured mortar coupon exposed to C1 sewer corrosivity classification and pH 1 of the sulphuric acid immersion test, it was observed that the samples exposed to the sewer environment exhibited worse performance than the acid immersion test. These results suggested that mortar corrosion is more complicated under Microbially Induced Concrete Corrosion (MICC).

5.4 SUMMARY

This chapter focused on the evaluation of alkali-activated mortar durability, including one-part geopolymer mortar (OGPm) samples, specifically OGPm-1, OGPm-2, OGPm-3, and OGPm-4, along with calcium aluminate cement mortar (CACm), as a comparative analysis of their acid corrosion resistance performance. Durability was established from 3 measures, lag phase, R_1 and R_2. The durability of the mortars was correlated to the various 28 days physical and

chemical properties of the mortar to establish their relative influence on durability.

Performance of mortar lining material

Cured cube mortar samples and practical field applications were used to evaluate the corrosion resistance performance impacted by chemical attack and MICC.

Acid immersion test

Cured mortar coupons were exposed to sulphuric acid, simulating the final stage of corrosion impacted by MICC. The corrosion of mortar as a function of time was observed to have a stage I and stage II corrosion rate. The R_2 was an essential feature of these protective lining mortar. These results suggest that the reduction in corrosion rate in the second stage could be attributed to the increased diffusion resistance for the acid through the build-up of the corrosion layer and to pore blocking by gypsum. Therefore, the corrosion resistance performance of mortars was related to the CaO composition and porosity.

MICC

The cured mortar sample and practical field application were investigated to evaluate the corrosion resistance performance of geopolymer mortar impacted by MICC. After exposing the geopolymer mortar to aggressive sewer environments, which were classified as C1 (very low corrosivity) to C5 (very high corrosivity), the corrosion of geopolymer mortar of both sample preparation methods was characterised into three (3) phases characterised mortar corrosion: i) Lag phase, ii) stage I corrosion rate (R_1) and iii) stage II corrosion rate (R_2). However, the degree of deterioration of mortar was different. The shotcrete field application appeared to show higher degradation than cured mortar sample. It needs to note that not all lining mortar can capture all 3 phases of corrosion. It depends on the chemical and physical properties.

The durability of the mortar lining material

The chemical and physical properties were correlated with the stage I corrosion rate (R_1) to evaluate the properties of mortar, such as initial UCS, initial porosity, ANC, and hydration product impact on the mortar's durability. The results found that physical properties such as initial porosity and UCS had positive and negative impacts on the durability of the mortar. The initial porosity negatively impacted the mortar's durability, while the initial UCS had a positive impact. Similar to physical properties correlation, the chemical properties such as ANC and hydration phase were also correlated with the R_1. The C-S-H and C-A-S-H have a positive impact on mortar durability, while N-A-S-H has a negative impact on mortar durability. 14% C-S-H and 35% C-A-S-H phases N-A-S-H phases to a maximum of 22.5%. The practical ANC exhibited a positive impact on mortar durability.

Overall, the durability of mortar is related to its physical and chemical properties and its exposure to environmental conditions. Therefore, physical properties (porosity and UCS), chemical properties (ANC and hydration phases; C-S-H, C-A-S-H, C-N-A-S-H, and N-A-S-H) and sewer environmental condition were involved in developing the service life prediction model and presented in Chapter 6.

6 SERVICE LIFE PREDICTION MODELS FOR ALKALI-ACTIVATED BINDERS, INCLUDING GEOPOLYMER EXPOSED TO SEWER CONDITIONS OF VARIOUS CORROSIVITY

6.1 INTRODUCTION

The deterioration of sewer asset structures is a significant challenge for modern society. It is linked to the loss of the economy, health and environmental concerns (Wang et al., 2020b). Various mitigation strategies have been trialled and implemented to extend the service life of the sewer assets. Rehabilitation of sewer assets using mortar lining material is an effective mitigation strategy for long-term sewer asset protection.

Cement-based coatings have been of interest because of their potential to extend the life of assets by more than 50 years (Valix, 2011). In addition, cement-based linings are more likely to interact and bond with the existing concrete host. They are less likely to suffer from delamination attributed to water infiltration into the assets (Valix, 2011). Geopolymers have been interested in lining mortar applications because of their excellent corrosion resistance compared to ordinary Portland cement (OPC). Recently, many types of geopolymers have been available for sewer assets rehabilitation.

However, the geopolymer mortar as lining material can continue to deteriorate under sewer environmental conditions after rehabilitating sewer assets. Therefore, to facilitate water utilities in prioritising remedial and replacement of the lining material, service life prediction becomes an essential issue for water utilities. To obtain a reliable service life prediction model is required to understand the deterioration process and how the sewer environment and properties of geopolymer influence the deterioration process. Therefore, the two challenges in implementing geopolymers in sewer assets rehabilitation are i) lack of the selection criteria of geopolymer mortars to fit specific aggressive environmental conditions of the sewer assets and ii) the prediction of service life under the given conditions.

However, Chapter 5 shows geopolymers' performance under different corrosion classifications established under the CRC-P: Smart Linings for Pipes and Infrastructure from the University of Sydney, School of Chemical and Biomolecular Engineering (Valix, 2021). In this chapter, the service life model has been developed by observing the corrosion performance and relevant environmental and other potential parameters that influence the corrosion of geopolymers, such as hydration products, geopolymer properties, and aggregate composition.

6.2 SCOPE OF SERVICES LIFE PREDICTION MODEL

The service life prediction models were developed based on the three-stage corrosion behaviour of lining mortar for alkali-activated binders, including geopolymers. These models involved three main corrosion factors: time, sewer environmental conditions (H_2S, CO_2, %RH, and T), and chemical and physical properties of alkali-activated binders, including geopolymers (porosity, UCS, ANC and hydration phases; C-S-H, C-A-S-H, C-N-A-S-H, and N-A-S-H). The models apply only to the classification of sewer corrosivity adopted from Valix (2021), which has H_2S < 200 ppm as the main corrosive compound this study covers.

6.3 PREVIOUS SERVICE LIFE MODEL

The traditional approach to predicting the corrosion rate is a semi-empirical model method by Pomeroy (1990), as shown in Equation 6.1.

$$C_r = \frac{11.5k\phi_{sw}}{A} \qquad \text{Equation 6.1}$$

The parameter of the model identified as C_r = corrosion rate (mm/year); k = correction factor related to the acid formation based on climate conditions, ϕ_{sw} = sulphide flux at the air-wall interface [g $H_2S/(m^2$ hr)]; and A = alkalinity of the sewer pipe material express as (g $CaCO_3$/g concrete). The Pomeroy model is constructed based on the loss of concrete material by the acid production rate and the amount of reactive material that consumes the acid. If the rate of acid

formation is slow, the k appears to be closed unity, but it may be as low as 0.3 to 0.4 in rapid acid production (Pomeroy, 1990).

Another service life model was developed by Wells and Melchers (2015), as shown in Equation 6.2, using a semi-empirical method. This model is developed based on an Ordinary Portland Cement (OPC) concrete cube. The corrosion resistance performance of the OPC cubes was tested in a live sewer in Sydney, Perth, and Melbourne. Based on the corrosion resistance performance and environmental conditions such as H_2S, temperature, and relative humidity, the corrosion rate equation of the OPC cube is formulated.

$$C = A \times [H_2S]^{0.5} \times \frac{(0.1602H - 0.1355)}{(1 - 0.9770H)} \times e^{(-45000/RT)} \qquad \text{Equation 6.2}$$

Where: where C is the rate of corrosion (mm yr^{-1}), [H_2S] is the concentration of hydrogen sulphide in the sewer atmosphere (ppm), H is the relative humidity of the sewer atmosphere (%), R is the universal gas constant (= 8.314 J mol^{-1} K^{-1}) and T is the temperature of the sewer atmosphere (K).

The development of the service life model was based on OPC concrete and the environmental condition and alkalinity of the OPC. The rate of corrosion model is restricted to OPC only. Considering the parameters involved in the service life prediction model, it should involve environmental conditions and lining material properties. The research gap in this chapter involves with

1. Lack of sample preparation to obtain realistic and reliable corrosion resistance performance data.
2. Lack of various environmental conditions involved in the development of the service life prediction model

3. Lack of consideration of hydration product and chemical composition of binder and aggregate
4. Lack of consideration of properties of fresh geopolymer such alkalinity, porosity, and unconfined compressive strength (UCS)

This chapter aims to develop the service life prediction model for geopolymer mortar using the semi-empirical method. The service life prediction model will be developed based on sewer environmental conditions, binder and aggregate chemical composition, and initial chemical and physical properties. This service life prediction model of geopolymer mortar is performed for the first time in this study.

6.4 SERVICE LIFE MODELS

Failure prediction models are established to foresee the estimated service life of the mortar with respect to the material corrosion resistance against aggressive sewer environmental conditions. Figure 6-1a shows the example of corrosion performance plotted between the corrosion depth and time at different corrosion classifications, as presented in Chapter 5. Generally, the plot of corrosion depth over time presents 3 phases; lag phase, corrosion stage I (R_1), and corrosion stage II (R_2), as shown in section 5.2.3.2.3. However, the corrosion depth over time may present all the phases due to the different corrosion rates at different corrosion classifications. At C1 and C2, the plot shows three (3) corrosion phases, while C3, C4, and C5 show a partial corrosion phase.

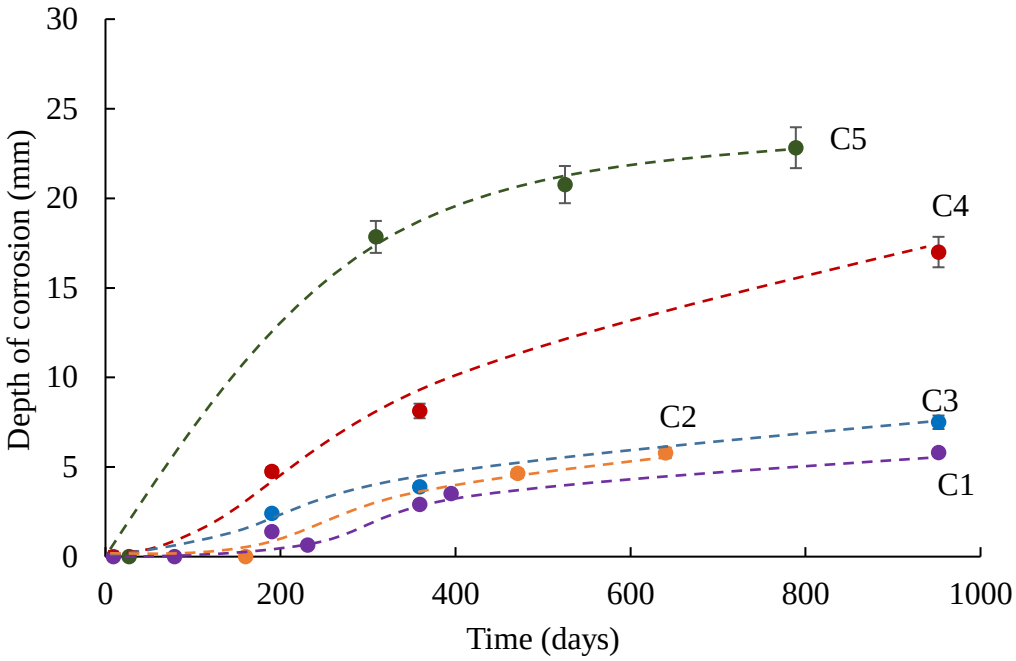

Figure 6-1 Corrosion of geopolymer coating (OGPm-3) as a function of time and sewer classifications

Based on the corrosion performance data, a conceptual model for the corrosion of cement mortar is proposed in Figure 6-2. The service life (t_L) of the protective mortar is defined by the time from when it is first established to the time when it fails to act as a corrosion barrier. The mortar provides a barrier against the corrosive media by neutralising acids that permeate the mortar. As a result of an acid attack, decalcification of the mortar will cause the cement's alkalinity and pH to decline and cause the loss of cement's hydraulic properties.

The mortar is assumed to have failed either when it can no longer provide a corrosion barrier against the aggressive sewer environment or if its compressive strength is less than required to support external loads. As shown in Figure 6-2, the overall service period is characterised by three hypothetical stages. The first stage describes the corrosion initiation period (t_i), where little to no corrosion occurs. This is followed by the propagation periods when the corrosion front starts to migrate inwards into the mortar. Two propagation periods, t_{Pi} and t_{Pf}, have been proposed, corresponding to a rapid rate of corrosion (R_1) followed by a slower rate of corrosion

(R_2), respectively. It is proposed that as corrosion progresses, there will be a build-up of a corroded layer that, in time, may hamper and slow the corrosion rate. This aspect of the conceptual model was evaluated in this study. Overall, the total service life is given as the sum of these individual periods:

$$t_L = t_i + t_{Pi} + t_{Pf} \qquad \text{Equation 6-3}$$

The corrosion will progress until the mortar can no longer act as a barrier against the corrosive environment. The condition may either be that the acid has fully permeated the mortar and has reached the concrete asset or that the remaining strength of the mortar is insufficient to support the load. The latter applies only if the mortar is also required to provide structural strength to the asset.

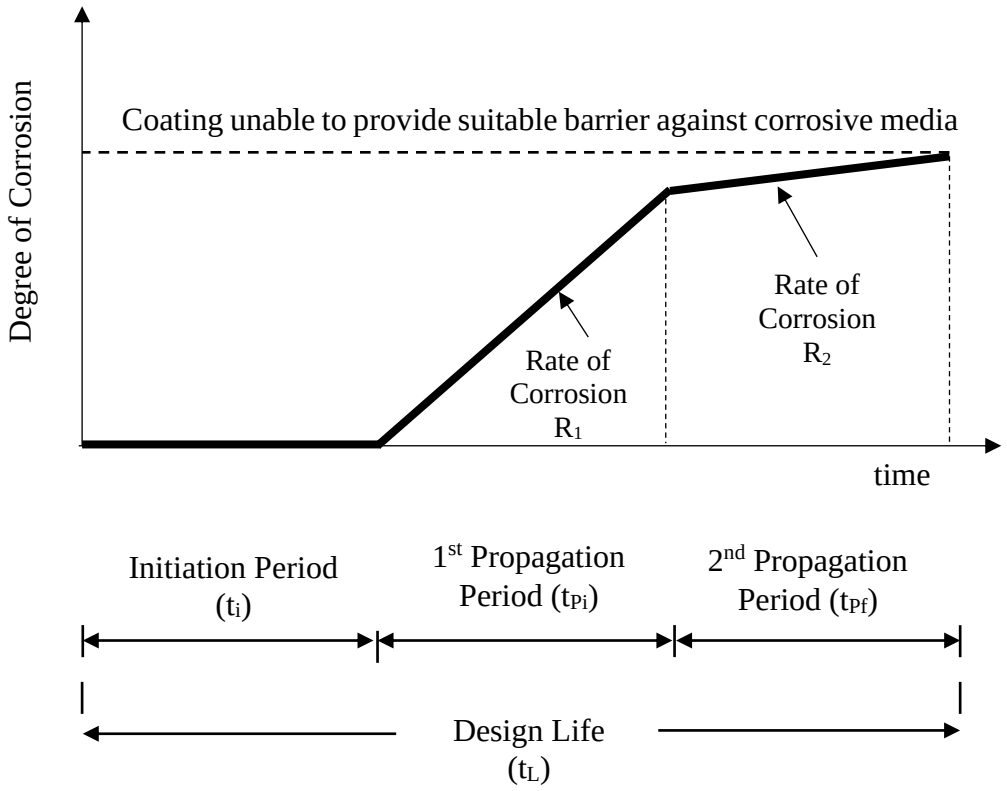

Figure 6-2. Conceptual model of cement mortar corrosion

6.4.1 ERROR ANALYSIS OF THE MODELS

Error functions were defined to determine the significance of each parameter to the predictive models and establish the fit of the experimental data to the models (see Table 6-1). The process for the analysis follows the method outlined by Valix (Valix et al., 2006). The sum of squared total (SST), the sum of squares for regression (SSR), and the sum of squared errors (SSE) were computed from the (n) number of mortars tested (see Equation 6-4 to Equation 6-6). The variance of the random errors (s_e) between the fitted model and the observed data can be measured from the value of SSE averaged with the degree of freedom according to Equation 6-7. This is also referred to as the mean square error (MSE). The significance of the independent variable used in the model is established using a partial F-test. The reduced error sum of the squares ($R(M_1/M_2)$ is calculated by taking the difference between the error sum of the squares of the full model is, SSE_F, and that of the reduced model containing k predictors is SSE_i (see Equation 6-8). The F-statistics for determining the statistical significance of the chosen subset of predictor variables is calculated using Equation 6-9. The goodness of fit of the experimental data is established from the coefficient of determination (R^2) using Equation 6-10. The values of R^2 vary from 0 to 1.0. The R^2 value is closer to 1.0, the greater the fit of the data to the model. However, it should be emphasised that the validity of the fit can be compromised with multiple parameters. The value of R^2 increases as the number of independent variables increases regardless of the significance or lack thereof of the added variable to the dependent variable. To overcome this misleading representation by R^2, a variant called the adjusted- R^2 that adjusts for the number of variables (p) in the fitted model is also reported. This is estimated using Equation 6-11. Correction of the variance of the random errors based on the reduced model through the mean square error is calculated using Equation 6-12.

An additional definition of the parameters used in Table *6-1* is shown below.

Parameters	**Description**
k	Number of predictor variables in the reduced model
n	number of data
p	Number of predictor variables in the model
p-values	probability
SSE_F	error sum of the squares of the full model
SSE_i	error sum of the squares of the reduced model containing k predictors
Y_{mean}	Average of the measured corrosion variable (e.g., depth of corrosion)
$Y_{measured}$	Experimentally measured corrosion variable (e.g., depth of corrosion)
$Y_{predicted}$	Predicted corrosion variable (e.g., depth of corrosion)

Table 6-1. Error functions

Error Functions	Description	Equations	
SST	sum of squared total	$SST = \sum_{i=1}^{n} (Y_{measured} - Y_{mean})^2$	Equation 6-4
SSR	sum of squares for regression	$SSR = \sum_{i=1}^{n} (Y_{predicted} - Y_{mean})^2$	Equation 6-5
SSE	sum of squared errors	$SSE = \sum_{i=1}^{n} (Y_{measured} - Y_{predicted})^2$	Equation 6-6
s_e	mean square error	${s_e}^2 = MSE = \frac{SSE}{degree\ of\ freedom}$	Equation 6-7
$R(M_1/M_2$	Reduced error sum of the squares	$R\left(\frac{M_1}{M_2}\right) = SSE_F - SSE_i$	Equation 6-8
F	F-statistics	$F = \frac{\frac{R(\frac{M_1}{M_2})}{p-k}}{\frac{SSE_F}{n-p-1}} = \frac{MSR(\frac{M_1}{M_2})}{MSE}$	Equation 6-9
R^2	Coefficient determination	$R^2 = 1 - \frac{SSE}{SST}$	Equation 6-10
adjusted -R_a^2	Adjusted coefficient determination	$adjusted\ R^2 = 1 - \frac{(n-1)SSE}{(n-p-1)SST}$	Equation 6-11
corrected -s_e	Corrected mean square error	$corrected - {s_e}^2 = MSE = \frac{SSE}{(n-p-1)}$	Equation 6-12

6.4.2 MODEL OF THE CORROSION INITIATION PERIOD

The initiation period represents the time from the establishment of the mortar to the period when corrosion is activated and begins to migrate into the mortar structure. Generally, the initiation period is dictated by the microbial production of the aggressive acids on the mortar surface. According to the successive growth theory, various micro-organisms that exhibit pH-dependent growth work cooperatively in bringing the surface pH of the cementitious materials from around pH 12 to pH conditions that allow the successive growth of the different organisms and, therefore the generation of different biogenic acids (Mori et al., 1992, Islander et al., 1991b, Okabe et al., 2007b, Valix et al., 2012). The concept of microbiome growth is shown in Figure 6-3. As shown, sewer corrosion is characterised by the attack from sewer gases, fungi and their organic acids, neutrophiles with their sulphuric acid, and finally, acidophiles with sulphuric acid. Corrosion is not dictated by an attack of one type of biogenic acid but rather an integrated attack of the acids. Sewer gases, including H_2S, CO_2, NO_2, and SO_2, play an essential role in reducing the mortar pH in the initial phase of corrosion. When hydrolysed in humid sewer environments, these sewer gases will form weak acids, specifically H_2CO_3, HNO_3 and H_2SO_3 (Sand, 1997b). Because these hydrolysis gases and H_2S originate from the sewage, they will participate in the corrosion of the crown and walls of mortar sewer pipes regardless of the mortar surface pH and microbe population on its surface. Hence, sewer gases are likely to contribute in an integrative manner to the biogenic acids generated as a result of successive growth.

The biogenic acids that accumulated on the surface of an epoxy mortar installed in sewers are shown in Figure 6-4. As shown, the quantity of acids that are generated by successive growth only becomes significant below pH 9.0, with the more aggressive H_2SO_4 being generated below pH 4.0. These are consistent with the pH growth optimum for acidophiles which oxidise H_2S and sulphur compounds (e.g., S_2O_3 and S) to sulphuric acid, have their growth optimum at pH

0.0 to 5.5 (Okabe et al., 2007b, Hernandez et al., 2002); neutrophils which promote the conversion of thiosulphate to elemental sulphur grow optimally at pH 5.5 to 8.0 (Islander et al., 1991b), and fungi growth at pH 4.0 to 6.0 (Valix et al., 2012, Gu et al., 1997, Cho and Mori, 1995). These results infer that the corrosion initiation is likely to be dominated by sewer gas attack.

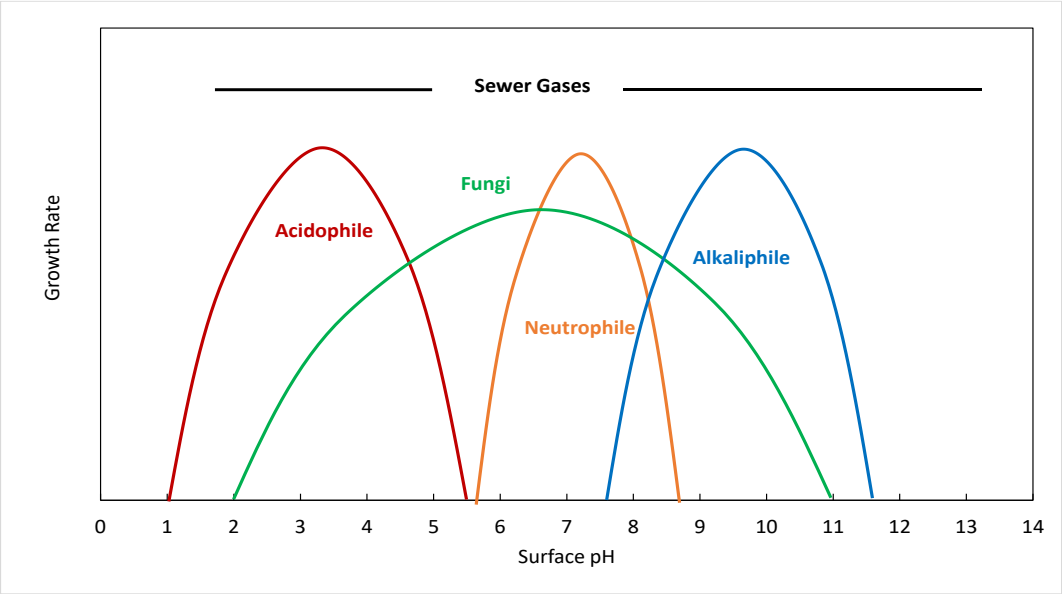

Figure 6-3. pH dependence of microbiome growth

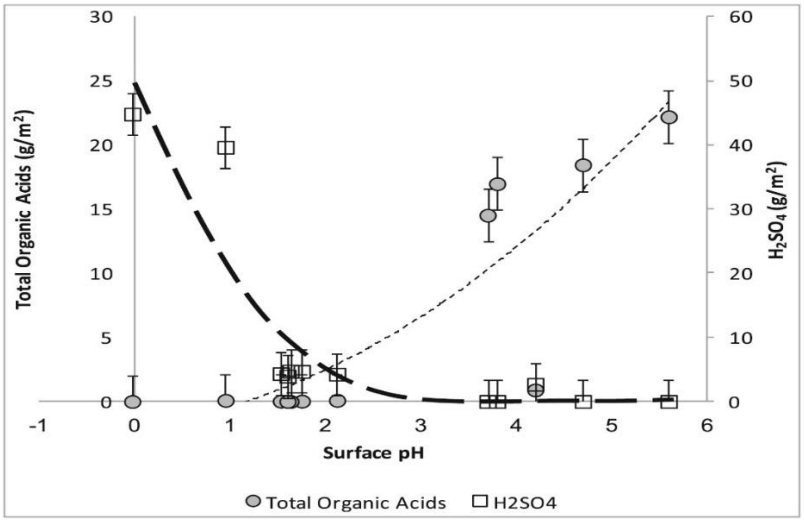

Figure 6-4. Biogenic acid generation as a function of pH on polymeric coatings installed in sewers for 18 months (Valix and Shanmugarajah, 2015)

The depth of corrosion for a geopolymer mortar exposed to conditions corresponding to corrosivity classification is reported in Table 6-2. As shown, the initiation period decreases with increasing corrosivity. Since the H_2S concentration increases with classification while CO_2 has an inverse correlation, it would be presumed that the H_2S concentration significantly impacts the corrosion initiation period.

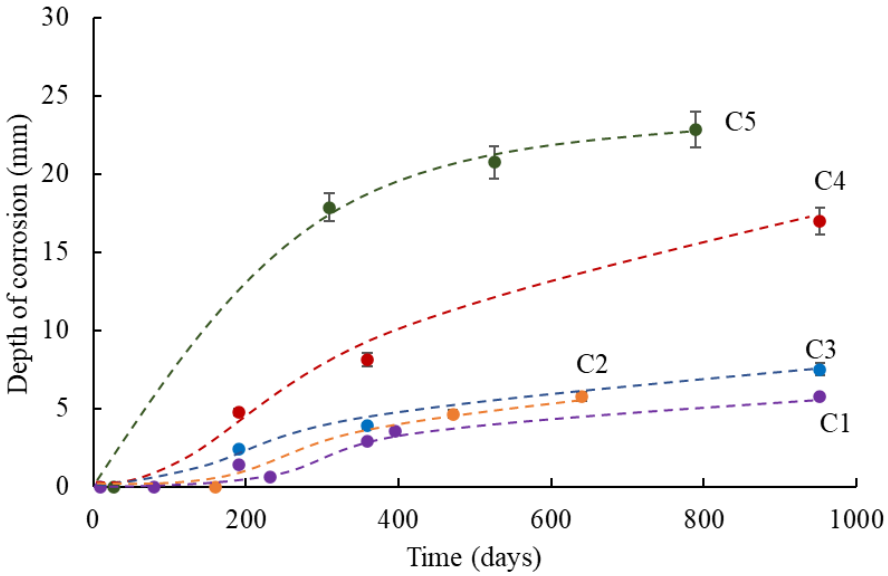

Figure 6-5. Corrosion of geopolymer coating (OGPm-3) as a function of time and sewer classifications

Table 6-2. Environmental conditions for OGPm-3

Classification	H_2S (ppm)	CO_2 (ppm)	T(°C)	RH (%)
C1	1.6	9393	24.0	99.0
C2	26	9418	21.3	99.0
C3	94	7500	18.5	99.0
C4	155	2520	20.2	99.0
C5	164	1970	26.0	99.0

H_2S contributes to the partial reduction of mortar pH by reacting with $Ca(OH)_2$ to form CaS (Hudon et al., 2011, Cerny and Rovnanikova, 2002):

$$Ca(OH)_2 + H_2S \rightarrow CaS + 2H_2O$$ Equation 6-13

It can also react with any carbonate cement (e.g., calcite) to form calcium sulphide and calcium bicarbonate:

$$2CaCO_3 + H_2S \rightarrow CaS + Ca(HCO_3)_2$$ Equation 6-14

Both reactions achieve a pH of around 9.0, and thus, H_2S impact on corrosion is considered low (Hudon et al., 2011, Cerny and Rovnanikova, 2002). Nonetheless, the reduction in pH allows corrosion to propagate as fungi grow and generate organic acid. The known minimum pH for mortar neutralisation by H_2S is consistent with pH when significant biogenic is generated in the sewer (see Figure 6-4).

Carbonation of the mortar will occur when CO_2 dissolves in water to form a weak carbonic acid solution (H_2CO_3):

$$CO_2 + H_2O \rightarrow H_2CO_3$$ Equation 6-15

The carbonic acid solution reacts first with calcium hydroxide (C-H) and calcium silicate hydrate (C-S-H) to form calcium carbonate or calcite:

$$Ca(OH)_2 + H_2CO_3 \rightarrow CaCO_3 + 2H_2O$$ Equation 6-16

$$CaO \cdot SiO_2 \cdot 2H_2O + H_2CO_3 \rightarrow CaCO_3 + Si(OH)_2 + 2H_2O$$ Equation 6-17

The minimum pH generated by carbonation is about 8.2. Hence, the impact of carbonation on corrosion is often considered low. It has been suggested that the optimum rates of carbonation occur when the relative humidity (RH) is in the range of 50% to 75%; carbonation effectively stops when mortar is saturated (ACI-201, 2001, Elsalamawy et al., 2019). The relative humidity observed in this study is from 95-100%; therefore, carbonation is not expected to contribute significantly to the initial reduction in mortar surface pH and the initial corrosion period.

The resistance of the mortars to change pH as a result of carbonic acid attack and H_2S adsorption will depend on the mortar acid neutralisation capacity and cement chemistry. The

semi-empirical model has been proposed to predict the period for corrosion initiation (t_i) of the alkali-activated binder and geopolymer mortar as a function of sewer corrosivity (C_{ti}) and geopolymer mortar durability (F_{tiG}) (see Table 6-3). The corrosivity is defined by the environmental conditions, specifically H_2S, CO_2, %RH and temperature. These conditions were assumed to have reached a steady state and would remain relatively constant for the duration of the mortar service life.

Table 6-3. Semi-empirical model for the corrosion initiation period

Model	**Equation**	
Corrosion Initiation Period (t_i)	$t_i = k_{tiG} C_{ti} F_{tiG}$	Equation 6-18
Corrosivity (C_{ti})	$C_{ti} = [H_2S]^{c1\_tiG}[CO_2]^{c2\_tiG}[RH]^{c3\_tiG} e^{(-\frac{E_{C\_tiG}}{RT})}$	Equation 6-19
Mortar durability (F_{tiG})	$F_{tiG} = HB_{tiG} A_{tiG} \beta^{f1\_tiG} UCS^{f2\_tiG} \theta^{f3\_tiG}$	Equation 6-20
Binder hydrate composition (HB_{tiG})	$HB_{tiG} = [HB_1]^{b1\_tiG}[HB_2]^{b2\_tiG}[HB_3]^{b3\_tiG}[HB_4]^{b4\_tiG}$	Equation 6-21
Aggregate composition (A_{tiC})	$A_{tiC} = [A_{Al_2O_3}]^{a1\_tiG}[A_{CaO}]^{a2\_t1G}[A_{SiO_2}]^{a3\_tiG}$	Equation 6-22

where

k_{tiG}	Constant for the corrosion initiation period
$[H_2S]$	hydrogen sulphide concentration (ppm)
$[CO_2]$	carbon dioxide concentration (ppm)
[RH]	relative humidity (%)
T	gas temperature (K)
E_{C_tiG}	Sum of the activation energies associated with the interaction (adsorption and reaction) between corrosive gases and mortar surface $\Sigma E_{H2S}+ E_{CO2}+\ldots$
R	Gas constant 8.3145 J/mol. K
β	acid neutralisation capacity (millimoles H^+/g substrate)
UCS	Unconfined compressive strength (MPa)
θ	porosity
HB_1	Hydrate composition phase 1 (e.g., C-S-H) (wt.%)
HB_2	Hydrate composition phase 2 (e.g., C-A-S-H) (wt.%)
HB_3	Hydrate composition phase 3 (e.g., C-N-A-S-H) (wt.%)
HB_4	Hydrate composition phase 4 (e.g., N-A-S-H) (wt.%)
A_{Al2O3}	Al_2O_3 content of the aggregate (wt.%) estimated by XRF
A_{CaO}	CaO content of the aggregate (wt.%) estimated by XRF
A_{SiO2}	SiO_2 content of the aggregate (wt.%) estimated by XRF
$c_{i(i=1,2,3)\_tiG}$	order of reaction as a function of the environmental corrosivity parameters for the corrosion initiation period
$f_{i(i=1,2,3)\_tiG}$	order of reaction as a function of mortar durability parameters for the corrosion initiation period
$b_{i(i=1,2,3,4)\_tiC}$	order of reaction as a function of mortar hydrate composition for the corrosion initiation period
$a_{i(i=1,2,3)\_tiC}$	order of reaction as a function of mortar aggregate composition for the corrosion initiation period

The properties that define mortar durability have been proposed to include binder hydrate composition (HB), acid neutralisation capacity (β), compressive strength (UCS), and porosity (θ). It was assumed that the remaining sound concrete would retain these properties through its service life and could, therefore, be used to infer the durability or corrosion resistance of the mortar through its life. The impact of these properties will be examined statistically below. The measured corrosion initiation periods are fitted to the model for the corrosion initiation period (see Table 6-3) in Figure 6-6. The corresponding fitted parameters are shown in Table 6-4.

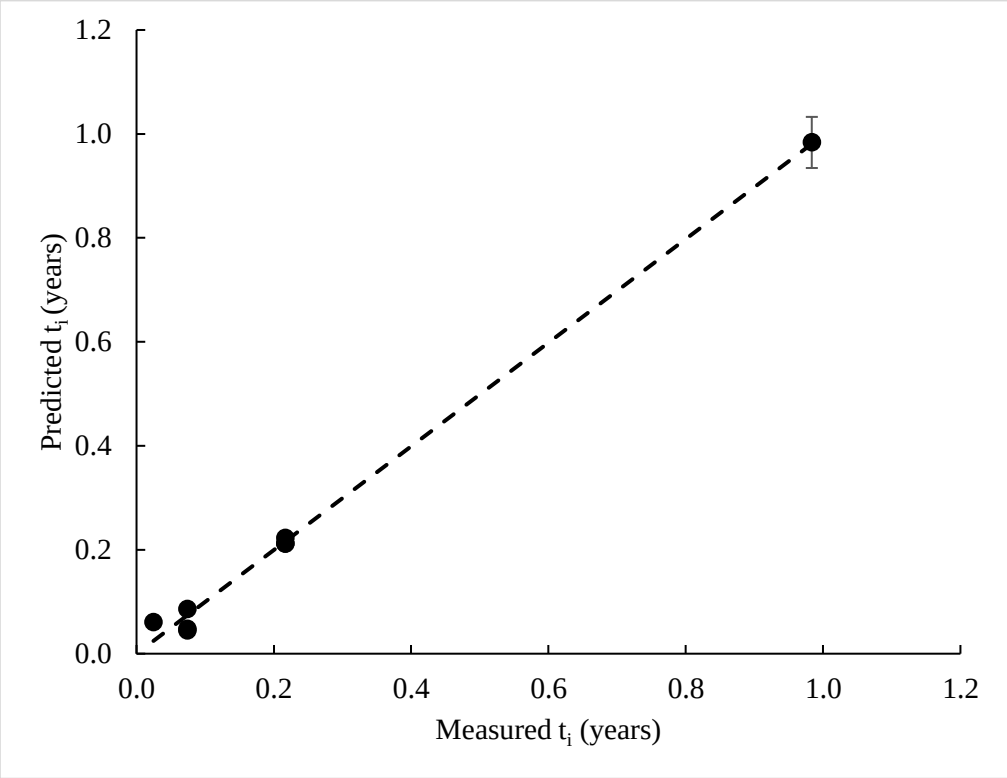

Figure 6-6. Corrosion data fitted to the corrosion initiation period model (see Table 6-3)

Table 6-4. Fitted parameters for the corrosion initiation period model (Table 6-3)

Parameters	**Values**	**Parameters**	**Values**
k_{tiG}	2.2		
Corrosivity		***Binder hydrate composition***	
c_{1_t1G}	-0.319	b_{1_tiG}	0.40
c_{2_t1G}	-0.49	b_{2_tiG}	0.26
c_{3_t1G}	0.0	b_{3_tiG}	0.65
$E_{C\text{-}tiG}$	800	b_{4_tiG}	0.60
Mortar durability		***Aggregate composition***	
f_{1_tiG}	0.0	a_{1_tiG}	0.0
f_{2_tiG}	0.0	a_{2_tiG}	0.0
f_{3_tiG}	0.0	a_{3_tiG}	

The significance of the independent variables used in the model for the corrosion initiation period was established using a partial F-test. Only parameters that showed non-zero orders were included in the assessment. The F-test parameters for the model are reported in Table 6-5. The F-statistics was used to test the null hypothesis that the variances of the reduced and full models are equal. The significance of the observed F-test was measured from the p-value or significance probability. The p-values were estimated using Microsoft Excel. If the p-value is less than the conventional 0.05 level, then the null hypothesis was rejected, and the conclusion was that the two variances differed significantly. The variable removed in the reduced model was a statistically significant predictor in the predictive model. As shown in Table *6-5*, all the p-values are below 0.05, except for HB_2 and HB_4, inferring that all the remaining parameters in the model are statistically significant.

Table 6-5. Statistical significance analysis of Model 1 parameters (n = 11, p = 8)

Parameters	Degree of Freedom	SSE	R(M1/M2)	MSE	F	p-value
Full	2	0.003		$1.53x10^{-3}$		
H_2S	1	0.33	0.32	0.32	211	0.0047
CO_2	1	8118	8118	8118	$5.31x10^{6}$	0.0000
T	1	1.00	0.98	0.98	643.11	0.0016
Constant, k_{tiG}	1	1.08	0.35	0.35	226.40	0.0044
HB_1	1	0.17	0.17	0.17	109.56	0.0090
HB_2	1	0.01	0.01	0.01	3.76	0.1920
HB_3	1	0.28	0.28	0.28	183.00	0.0054
HB_4	1	0.03	0.03	0.03	17.99	0.0513

The measures of the statistical fit of the model are R^2 of 0.99, adjusted- R^2 of 0.98 and s_e of 0.04. These statistical parameters suggest that the model adequately fits or captures the mortar corrosion initiation period behaviour. The proposed Model 1 – Corrosion initiation period for alkali-activated binder including geopolymers is simplified as follows:

$$t_i = 2.2\frac{e^{\left(\frac{800}{T}\right)}[H_{B1}]^{0.40}[H_{B3}]^{0.65}}{[H_2S]^{0.319}[CO_2]^{0.49}} \qquad \text{Equation 6-23}$$

The fitted parameters suggest that both the neutralisation by H_2S adsorption and carbonic acid are the primary factors that contribute to the initial pH reduction of the mortars. It appears that the cement chemistry specifically hydrates 1 and 3 in the binder, contributed to the resistance in surface pH reduction rather than acid neutralisation capacity. This may, in effect, be due to pH reduction being partly attributed to H_2S adsorption. In general, it appears that hydration phases 1 and 3, which are C-S-H and Al substituted C-S-H, are more resistant to H_2S adsorption and carbonic acid compared to the geopolymer phase.

6.4.3 CORROSION PROPAGATION MODELS BASED ON THE DEPTH OF CORROSION

Two solid-liquid kinetic models have been proposed to predict the rate of mortar corrosion (Levenspiel, 1999). These are based on the shrinking core model (SCM) and shrinking particle model (SPM). The core shrinking model is used to describe the process where the material, in this case, mortar binder, is being consumed by acid (e.g., H_2SO_4) attack and the remaining sound mortar is shrinking but leaves an inert porous corrosion layer. At the same time, the particle shrinking model describes the process where no corrosion layer remains. Figure 6-7 shows an example of the cross-section of a corroded geopolymer mortar that has been sprayed with a Universal pH indicator. There is a distinct sound mortar region with a layer of corroded material where pH has been reduced to around pH 1-2. This is typical of most of the corroded mortar analysed in this study and suggests the process is consistent with the core-shrinking model.

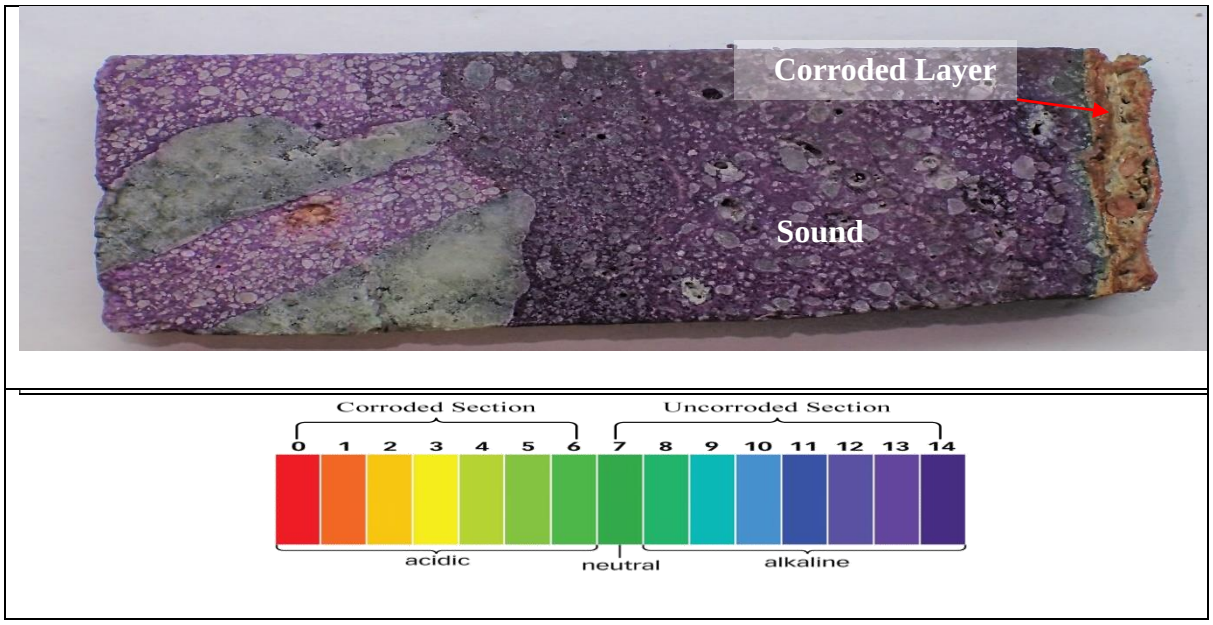

Figure 6-7. Example of a cross-section of corroded geopolymer demonstrating core-shrinking model

The kinetics of mortar corrosion, for this study, was therefore modelled based on the core shrinking model. It was assumed the material consists of an unreactive matrix (aggregates)

with reactive components (binder) that may consist of $Ca(OH)_2$ and C-S-H, C-A-S-H, N-C-A-S-H, N-A-S-H and CAC hydrates (e.g., C_2AH_8). The corrosion proceeds by the migration of biogenic acids through the porous corrosion layer until this reaches and reacts with the sound mortar. The model assumes the reaction proceeds at a sharp interface with a reaction boundary that gradually moves inward, leaving a corrosion layer while the core or the sound mortar remains the same. Figure 6-7 shows that, in general, this is true, although there is a layer in between the corroded and sound sections that shows there are transitional materials that are partly corroded. The rate of corrosion is determined or controlled by the slowest step in the process. Initially, in the absence of a corrosion layer, the rate of corrosion will be controlled primarily by the surface chemical reaction (assuming the delivery of the acid to the mortar surface is rapid). As corrosion occurs and with the build-up of the corrosion layer, the inward movement of the corrosion boundary may begin to be impacted by diffusional resistance. This will be dictated by the relative speed of the chemical corrosion reaction to acid diffusion through the corrosion layer. Given the sound mortar has a constant acid neutralisation capacity, the rate of chemical corrosion reaction will likely depend on the corrosivity of the environment. The rate of corrosion will be controlled either by the rate of chemical reaction and/or the mass transport of the acid through the corrosion layer. The shrinking core models are based on specific geometries (spherical, cylindrical, and flat slabs). The mortar assets consist of circular and square pipes and access chambers with an internal diameter of 0.8 to 2.8 m. Protective lining mortars that are applied on these assets were assumed to be represented as flat slabs. The shrinking core model equations of the determining steps for mortar with flat geometry can be written as follows (Szekely et al., 1976):

Pore diffusion controlled

$$X_f{}^2 = k_d t \ or \ X_f = k_d{}^{1/2} t^{1/2} \qquad \text{Equation 6-24}$$

Chemical reaction controlled

$$X_f = k_c t \qquad \text{Equation 6-25}$$

Where k_d and k_c are rate constants, t is time, and X_f is the fraction of material that reacted or, in the case of mortar, the amount of Al^{3+} that has been leached. For this study, the fraction of the depth of corrosion ($\Delta X/X°$) based on the original thickness ($X°$) of the mortar asset was correlated to the change in mass of ($\Delta M_{Al3+}/M_{Al}^{3+0}$) in the mortar from:

$$\frac{\Delta M_{Al^{3+}}}{M_{Al^{3+}}{}^{o}} = \rho_{mortar} A\,(1-\theta)\frac{\Delta x}{x^0} \qquad \text{Equation 6-26}$$

The fraction of mortar that corroded is given as:

$$X_f = \frac{\Delta X}{X^0} = \frac{\Delta M_{Al^{3+}}}{M_{Al^{3+}}{}^{o}\rho_{mortar} A\,(1-\theta)} \qquad \text{Equation 6-27}$$

Where $M_{Al}^{3+\circ}$ is the original mass of Al^{3+} in the mortar, ρ is the mortar density, θ is the original mortar porosity, and A is the area of corrosion. It is assumed the movement of the corrosion front is very slow, which is a valid assumption considering that the corrosion of mortar occurs over several years (> 20 years). Because of the slow movement of the corrosion boundary, it can be assumed the rate of mass transport is at a steady state. The advancement of the corrosion boundary is determined by the factors that contribute to the corrosion resistance of the mortar (F) (see Equation *6-21*) it encounters from the remaining sound mortar (see Figure 6-8).

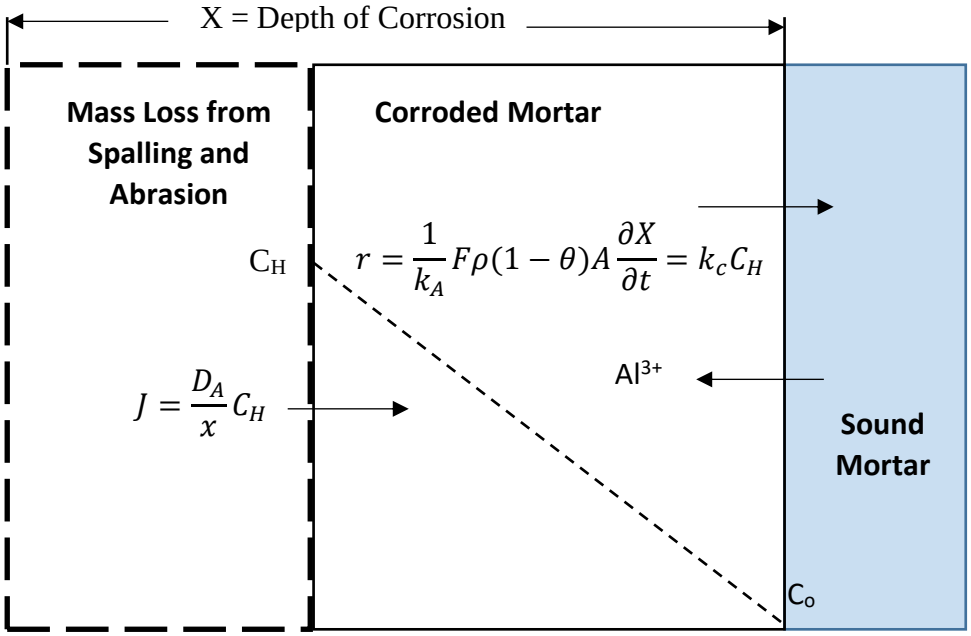

Figure 6-8. Schematic of the core shrinking model for corroding geopolymer and/or alkali-activated mortar

Under quasi-steady state conditions, the rate of aluminium leaching is equal to the rate of volume or porosity changes, and this is equal to the diffusion flux (J) or rate of mass transfer of the corroding acids through the corrosion layer as defined by Fick's first law:

$$J = r \qquad \text{Equation 6-28}$$

The rate expression shown in Figure 6-8 is for one corrodent. However, in the sewer, various biogenic acids attack the mortar. In the absence of biogenic acid concentration, the precursors that contribute to the formation of biogenic acids were used. Although there are various precursors for this study, these were assumed to be H_2S, CO_2, and humidity.

$$J_i = \frac{F}{k_A}\frac{\partial C_{Al3+}}{\partial t} = \frac{F\rho(1-\theta)A}{k_A}\frac{\partial X}{\partial t} = \prod_{i=1}^{w}\frac{D_A}{X}(C_{Hi} - C_{oi}) = \prod_{i=1}^{w}\frac{D_A}{X}C_{Hi} \qquad \text{Equation 6-29}$$

In this study, it was assumed that the differences in the diffusion coefficients of the precursors are negligible, and these can be represented by one constant diffusion coefficient D_A. D_A is the effective diffusion coefficient of the acids through the mortar with time, F represents the factors

that control the durability of the mortar, C_{Hi} is the biogenic acid precursor concentration, X is the depth of corrosion, and t is the period of corrosion. Since the surface chemical reaction is fast under mass transfer control, It was also assumed C_o is negligible. That is, most of the acid that penetrates through the corroded section is consumed at the interface of the sound mortar.

Corrosion at the surface of the sound mortar can be controlled by factors including the acid neutralisation capacity of the mortar and the corrosivity of the acid. The rate of corrosion under the surface reaction-controlled condition is given as:

$$r = \prod_{i=1}^{w} k_{ci} {C_{Hi}}^{ni} \qquad \text{Equation 6-30}$$

Where k_{Ci} is the chemical rate constant and is the order of reaction for the corroding biogenic acid precursor concentration C_{Hi}. The depth of corrosion was defined by the difference between the original sound mortar and the remaining sound mortar. The depth of corrosion would consist of both the remaining corroded section and material loss from abrasion and spalling. Continuous removal of mortar material from abrasion can increase the rate of corrosion as the barrier for the acid to reach the sound mortar is reduced. Abrasion effects are difficult to model but could be simulated by assuming an upper limit to the thickness of the corrosion layer above the sound mortar. To maintain this upper limit thickness, the mass loss is assumed to be directly related to the pH profile that remains constant across the mortar. Mortar with pH below 8.0 would be unsound and would be more susceptible to abrasion and spalling. To maintain this constant pH profile across the mortar, it is assumed that the biological system in the sewer continuously replenishes the acid concentration.

Monitoring the accumulation of biogenic sulphuric acid in epoxy in Figure 6-9 shows the acid build-up appears to reach a steady state after 12 months. These are significant results because, under steady-state conditions, it could be presumed the surface pH profile across the mortar

would be constant in the long term. In view of this, the impact of abrasion could also be assumed to be constant.

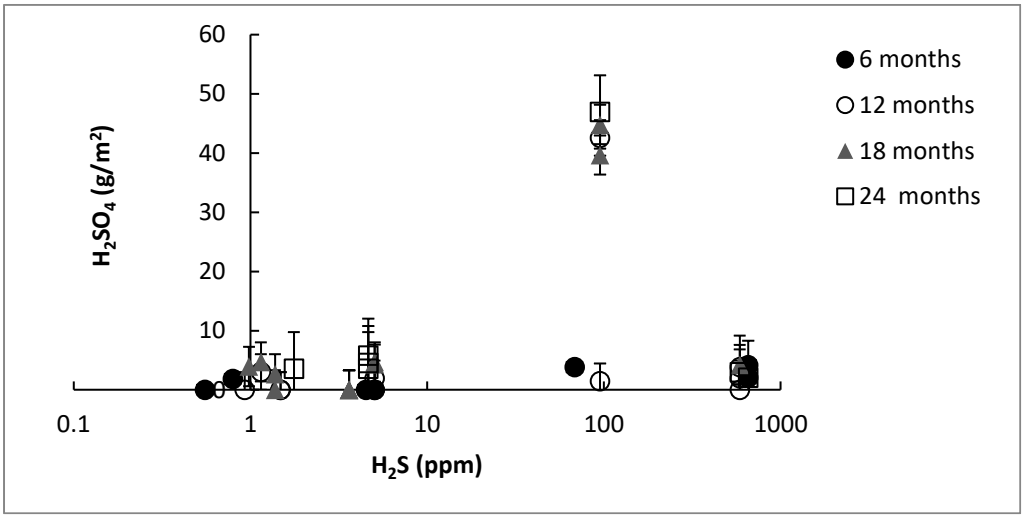

Figure 6-9. Cumulative sulphuric acid generated in epoxy mortars installed in large-diameter sewer pipes at various H_2S concentrations and with time (Valix and Shanmugarajah, 2015)

This is considered in the rate of chemical mortar corrosion (r) as a function of acid concentration with the first order of reaction given as:

$$r = \frac{1}{k_A} F\rho(1-\theta)A\frac{\partial X}{\partial t} = \prod_{i=1}^{w} k_{ci} {C_{Hi}}^{ni} \qquad \text{Equation 6-31}$$

Where k_A is the rate of mortar abrasion. The value of k_A will depend on the mortar mix design and cement chemistry. The value of k_A is likely to be close to 1.0 because the locations in the assets attacked by gas phase corrosion considered in this study are only intermittently exposed to sewage flow. Therefore, material loss is most likely to occur by spalling rather than abrasion. Spalling is considered to be slow. Under these conditions, the value of k_A was assumed to be constant.

The corrosivity of sewer conditions is dependent on various environmental parameters. The key precursors that determine the acid production were defined based on H_2S and CO_2 concentrations and the relative humidity (Valix, 2021). A semi-empirical model for the rate of

mortar corrosion under chemical control was proposed based on the following power law model:

$$\frac{\partial X}{\partial t} = \frac{k_A}{FA\prod_{i=1}^{y}\rho_{OGPi}(1-\theta_{OGPi})}\prod_{i=1}^{w} k_{ci}{C_{Hi}}^{ni} \qquad \text{Equation 6-32}$$

Where ρ_{OGPi} and θ_{OGPi} represent the density and porosity of OGP mortars and y represents the number of mortars.

Where the rate constant is defined according to the Arrhenius equation:

$$k_{Ci} = A_{ci}e^{(-\frac{E_{Ci}}{RT})} \qquad \text{Equation 6-33}$$

Substituting Equation 6-33 into Equation 6-32 gives:

$$\frac{\partial X}{\partial t} = \frac{k_A}{FA\prod_{i=1}^{y}\rho_{Gi}(1-\theta_{Gi})}\prod_{i=1}^{w}[C_{Hi}]^{n_i}A_{ci}e^{(-\frac{E_{ci}}{RT})} = \frac{K_C}{F\prod_{i=1}^{y}\rho_{Gi}(1-\theta_{Gi})}[H_2S]^{c1}[CO_2]^{c_2}[RH]^{c_3}e^{(-\frac{E_C}{RT})} \qquad \text{Equation 6-34}$$

where

$A_{Ci\ (i=1,2,3)}$	frequency factor for chemically controlled corrosion for each corrodent
C_{Hi}	the concentration of environmental parameters or precursor for sewer corrosivity (H_2S) (ppm), CO_2 (ppm) and relative humidity (%))
$c_{i\ (i=1,2,3)}$	orders of reaction relative the environmental parameters
$E_{Ci(i=1,2,3)}$	the activation energy for the reaction of each corroded (J/mol)
Ec	Overall activation energy $Ec = \Sigma E_{ci}$
Kc	Overall constant, $K_c = k_A(\Pi A_{Ci})/A$
R	8.3145 J/mol. K
X	depth of corrosion (mm)
w	number of corrodents or chemicals that contribute to corrosion

Integrating Equation 6-34 gives the semi-empirical model for predicting the depth of corrosion under a chemically controlled reaction (X_c):

$$X_c = \frac{K_C}{F\prod_{i=1}^{y}\rho_{Gi}(1-\theta_{Gi})}[H_2S]^{c_1}[CO_2]^{c_2}[RH]^{c_3}e^{(-\frac{E_C}{RT})}t^d \qquad \text{Equation 6-35}$$

Under the mass transfer-controlled condition, Equation 6-29 was amended to consider the mass loss to provide the proposed semi-empirical model:

$$\frac{\partial X}{\partial t} = k_A\frac{D_A}{FX\prod_{i=1}^{y}\rho_{Gi}(1-\theta_{Gi})}\prod_{i=1}^{w}[C_{Hi}] \qquad \text{Equation 6-36}$$

The diffusion constants (D_A) for the biogenic acid precursors are expressed in terms of the Arrhenius equation as follows:

$$D_A = A_D e^{(-\frac{E_D}{RT})} \qquad \text{Equation 6-37}$$

Expanding Equation 6-36 to include the corrosivity precursors gives:

$$\frac{\partial X}{\partial t} = k_A\frac{\prod A_{Di}}{\rho_i A(1-\theta)F_D X}[C_{Hi}]e^{(-\frac{\prod E_{Di}}{RT})} = \frac{K_{Di}}{X}[H_2S][CO_2][RH]e^{(-\frac{\prod E_{Di}}{RT})} \qquad \text{Equation 6-38}$$

Integrating Equation 6-38 gives the semi-empirical model for predicting the depth of corrosion under mass transfer-controlled reaction (X_D):

$$X_D = \left[\frac{K_D}{F\prod_{i=1}^{y}\rho_{Gi}(1-\theta_{Gi})}\right]^{1/2}[H_2S]^{1/2}[CO_2]^{1/2}[RH]^{1/2}e^{(-\frac{E_D}{2RT})}t^{1/2} \qquad \text{Equation 6-39}$$

where

E_D	The activation energy of the diffusion of the acid precursor (J/mol)
K_D	Overall constant for Equation 6-38, $K_D = k_A A_D$
X_D	Depth of corrosion under pore diffusion-controlled conditions (mm)

6.4.4 RATE-DETERMINING STEP AND MODEL FITTING

6.4.4.1 RATE DETERMINING STEP - PROPAGATION STAGE 1

The rate-determining step of the mortar corrosion under propagation stage 1, as defined in Figure 6-2, was established for the various sewer classifications by plotting the corrosion data using Equation 6-24 and Equation 6-25 (see Figure 6-10 a-d). As suggested, Equation 6-24 applies to pore diffusion-controlled conditions, while Equation 6-25 applies to chemical-controlled conditions. The data fit was evaluated from the correlation of regression (R^2) (see Figure 6-11). The value of R^2 varies from 0-1, and the closer the value to 1.0, the better the fit. The R^2 values of C1, C2, and C5 did not vary significantly between the chemical and pore diffusion-controlled mechanisms. It appears the kinetics of corrosion at the propagation stage 1 under the various corrosion classifications is controlled by both the combined chemical and pore diffusion steps.

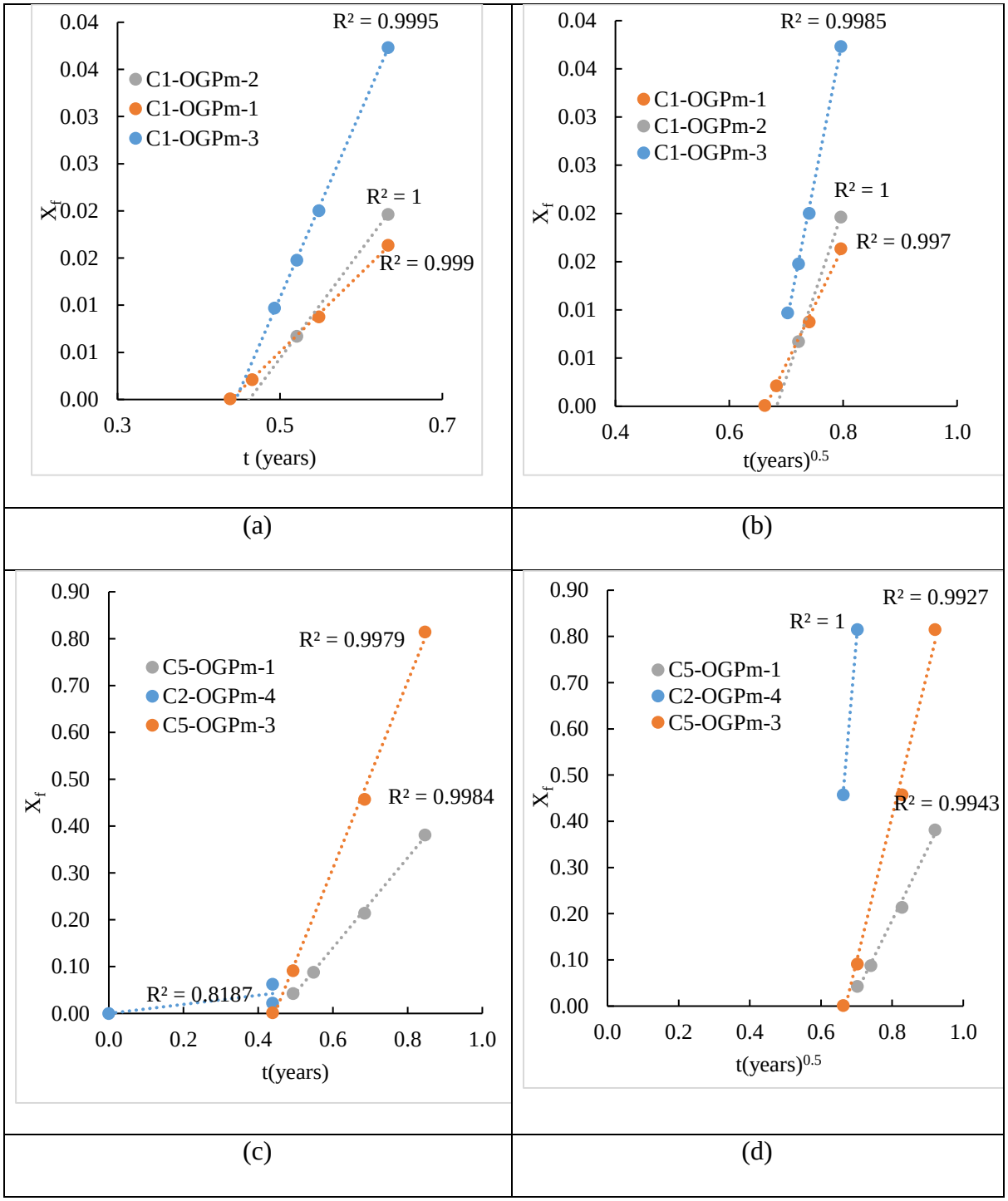

Figure 6-10. The plot of mortar corrosion data under propagation stage 1 fitted to the core shrinking model based on: a) chemical controlled (C1), b) pore diffusion-controlled reaction (C1), c) chemical controlled (C2, C5) and d) pore diffusion-controlled reaction (C2, C5)

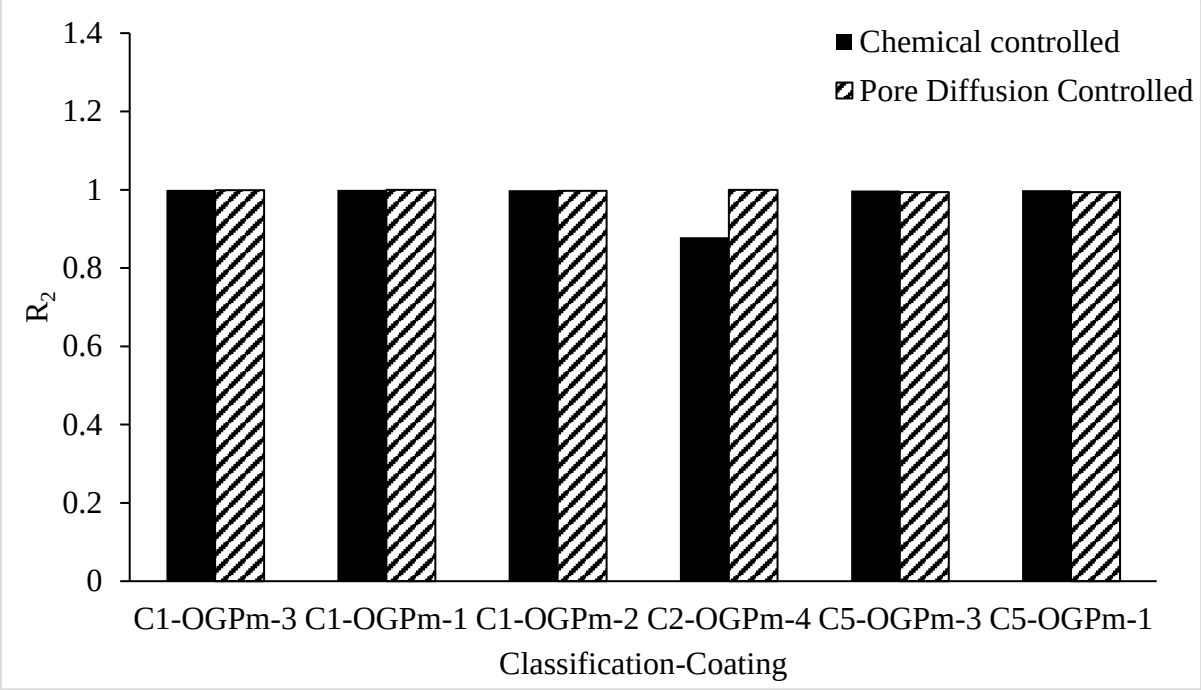

Figure 6-11. R^2 of fitted mortar corrosion data under propagation stage 1 to core shrinking models

Equation 6-35 and Equation 6-39 were combined to provide the mixed control model:

$$X_{S1\_G} = X_C + \gamma X_D \qquad \text{Equation 6-40}$$

Where γ is a constant

The following semi-empirical model was proposed to predict the depth of corrosion at the first stage of corrosion propagation (X_{S1_G}) (see Table 6-6) under chemical and pore diffusion-controlled corrosion. The depth of corrosion is dependent on the corrosivity of the environment (C_{S1_G}), durability properties of the mortar (F_{S1_G}) and service period (t).

Table 6-6. Model for Stage 1 Corrosion Propagation of Alkali Activated Binders (AAB) including Geopolymers under Mixed Chemical and Pore Diffusion Controlled

Model	**Equation**	
Depth of Corrosion Prediction at Stage 1 Corrosion Propagation (X_{S1_G})	$X_{S1\_G} = K_{S1\_G} C_{S1\_G} F_{S1\_G} (-p_{1\_S1G} t^{p_{2\_S1G}} + p_{3\_S1G} t - p_{4\_S1G})$	Equation 6-41
Corrosivity (C_{S1_G})	$C_{S1\_G} = [H_2S]^{c1\_S1G} [CO_2]^{c2\_S1G} [RH]^{c3\_S1G} e^{(\frac{E_{C\_S1G}}{RT})}$	Equation 6-42
Mortar durability (F_{S1_G})	$F_{S1\_G} = F \prod_{i=1}^{y} \rho_{Gi} (1 - \theta_{Gi}) = B_{S1\_G} A_{S1\_G} \beta^{f1\_S1G} UCS^{f2\_S1G} \theta^{f3\_S1G}$	Equation 6-43
Binder hydrate composition (B_{S1_G})	$HB_{tiG} = [HB_1]^{b1\_S1G} [HB_2]^{b2\_S1G} [HB_3]^{b3\_S1G} (-b_{4\_S1G} [HB_4]^{b_{5\_S1G}} + b_{6\_S1G} [HB_4] - b_{7\_S1G})$	Equation 6-44
Aggregate composition (A_{S1_G})	$A_{S1\_G} = [A_{Al_2O_3}]^{a1\_S1G} [A_{CaO}]^{a2\_S1G} [A_{SiO_2}]^{a3\_S1G}$	Equation 6-45

Where:

X_{S1_G}	Depth of Corrosion Prediction at Stage 1 Corrosion Propagation
K_{S1_G}	Constant for depth of corrosion prediction model for stage 1 corrosion propagation
C_{S1_G}	Sewer Corrosivity
F_{S1_G}	Mortar durability
t	Exposure time
$p_{i(1,2,3,4)\_S1G}$	Constant parameters for time
$[H_2S]$	hydrogen sulphide concentration (ppm)
$[CO_2]$	carbon dioxide concentration (ppm)
[RH]	relative humidity (%)
T	gas temperature (K)
E_{C_S1G}	Sum of the activation energies associated with the interaction (adsorption and reaction) between corrosive gases and mortar surface $\Sigma E_{H2S}+ E_{CO2}+\ldots$
R	Gas constant 8.3145 J/mol. K
e	Natural exponential
$c_{i(i=1,2,3)\_S1G}$	order of reaction as a function of the environmental corrosivity parameters for stage 1 corrosion propagation
B_{S1_G}	Binder hydrate composition
A_{S1_G}	Aggregate composition
β	acid neutralisation capacity (millimoles H^+/g substrate)
UCS	Unconfined compressive strength (MPa)
θ	porosity
$f_{i(i=1,2,3)\_S1G}$	order of reaction as a function of mortar durability parameters for stage 1 corrosion propagation
HB_1	Hydrate composition phase 1 (e.g., C-S-H) (wt.%)
HB_2	Hydrate composition phase 2 (e.g., C-A-S-H) (wt.%)
HB_3	Hydrate composition phase 3 (e.g., C-N-A-S-H) (wt.%)
HB_4	Hydrate composition phase 4 (e.g., N-A-S-H) (wt.%)
$b_{i(i=1,2,3,4,5,6,7)\_S1G}$	order of reaction as a function of AAB and geopolymer mortar binder hydrate composition for stage 1 corrosion propagation
$[A_{Al2O3}]$	Al_2O_3 content of the aggregate (wt.%) estimated by XRF
$[A_{CaO}]$	CaO content of the aggregate (wt.%) estimated by XRF
$[A_{SiO2}]$	SiO_2 content of the aggregate (wt.%) estimated by XRF
$a_{i(i=1,2,3)\_S1G}$	order of reaction as a function of AAB and geopolymer mortar aggregate composition for stage 1 corrosion propagation

6.4.4.2 FITTING AND PARAMETER SIGNIFICANCE ANALYSIS OF CORROSION PROPAGATION STAGE 1 MODEL

The mortar corrosion data based on the depth of corrosion that fell under corrosion propagation 1 were fitted to the stage 1 corrosion propagation model (see Table 6-6) in Figure 6-12. The model parameters were determined by the solver "add-in" function of the Microsoft Excel spreadsheet program by minimising the sum of squared errors (SSE).

The significance of the independent variable used in the model was established using a partial F-test (see section 6.4.1). The F-test parameters for the model are reported in Table 6-7. The F-statistics was used to test the null hypothesis that the variances of the reduced and full models are equal. The significance of the observed F-test was measured from the p-value or significance probability. The p-values were estimated using Microsoft Excel. If the p-value is less than the conventional 0.05 level, then the null hypothesis was rejected, and the conclusion was that the two variances differed significantly. The variable removed in the reduced model was a statistically significant predictor in the predictive failure model for stage 1 corrosion. As shown, all the p-values are below 0.05, inferring that all the parameters in the model are statistically significant except for the Al_2O_3 composition of the aggregate.

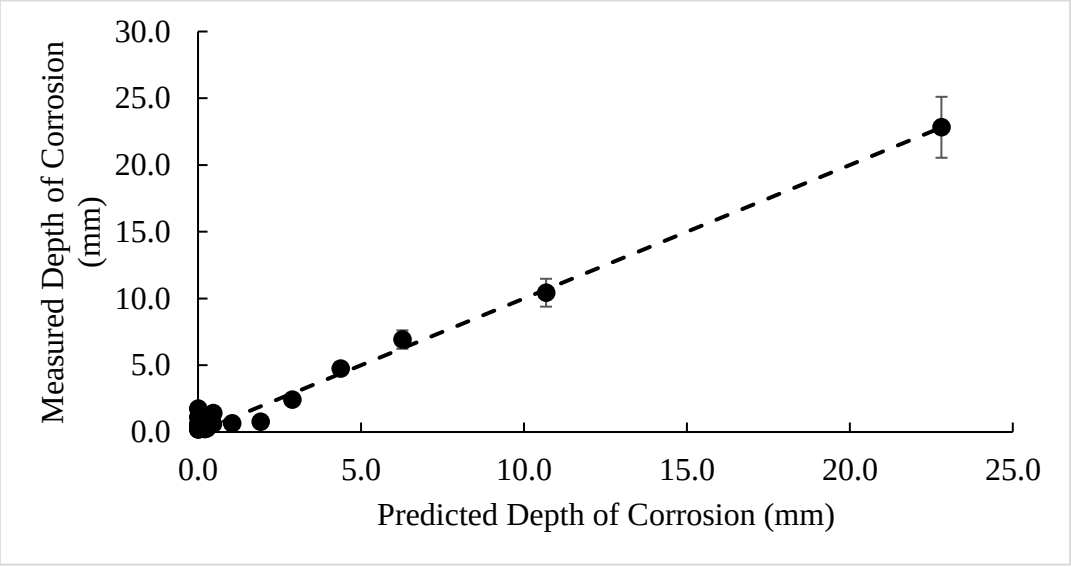

Figure 6-12. Mortar data under propagation stage 1 fitted to Model 2 – mixed chemical and pore diffusion- controlled model (see Equation 6-41)

Table 6-7. Fitted parameters for mortar corrosion data under propagation stage 1

Parameters	**Values**	**Parameters**	**Values**
K_{S1G}	3029		
Corrosivity		***Binder composition***	
c_{1_S1G}	0.5	b_{1_S1G}	0.27
c_{2_S1G}	0.057	b_{2_S1G}	0.91
c_{3_S1G}	0.164	b_{3_S1G}	2.63
$E_{C\text{-}SiG}$	-983	b_{4_S1G}	0.03
		b_{5_S1G}	0.003
		b_{6_S1G}	0.147
		b_{7_S1G}	0.002
Mortar durability		***Aggregate composition***	
f_{1_S1G}	0.226	a_{1_S1G}	0.0
f_{2_S1G}	0.186	a_{2_S1G}	0.443
f_{3_S1G}	0.51	a_{3_S1G}	0.254
Time			
p_{1_S1G}	0.254		
p_{2_S1G}	0.79		
p_{3_S1G}	0.30		
p_{4_S1G}	$3.73x10^{-5}$		

Table 6-8 Statistical significance analysis of Model 2 parameters fitted to propagation stage 1 corrosion data (n = 17, p = 15)

Parameters	Degree of Freedom	SSE	$R(M_1/M_2)$	MSE	F	p-value
Full	1	8.2		8.21		
H_2S	1	606.4	598.2	598.2	3.91×10^5	0.0000
CO_2	1	358	350	350	2.29×10^5	0.0000
RH	1	5.17×10^5	5.17×10^5	5.17×10^5	3.38×10^8	0.0000
T	1	207	198.8	198.8	1.30×10^5	0.0000
Constant, K_M	1	714	705.8	705.8	4.62×10^5	0.0000
HB1	1	19.7	11.8	11.5	7.52×10^3	0.0001
HB2	1	181	173	173	1.13×10^5	0.0000
HB3	1	75	66.7	66.69	4.36×10^4	0.0000
HB4	1	1.74×10^5	1.74×10^5	1.74×10^5	1.14×10^8	0.0000
Al_2O_3 (Ag)	1	8.2	0.01	0.01	3.47	0.2037
CaO (Ag)	1	244.7	236.5	236.5	1.55×10^5	0.0000
SiO_2 (Ag)	1	322	313.8	313.8	2.05×10^5	0.0000
β	1	22	13.8	13.8	9.02×10^3	0.0001
UCS	1	2.58×10^4	2.58×10^4	2.58×10^4	1.69×10^7	0.0000
θ	1	142	133.8	133.8	8.75×10^4	0.0000

The measures of the statistical fit of the model are R^2 of 0.98, adjusted- R^2 of 0.75 and s_e of 2.87. These statistical parameters suggested that the model adequately fits or captures the mortar corrosion behaviour under propagation stage 1. However, the lower adjusted R^2 suggests the number of parameters slightly biased the fit. This can be rectified by increasing the number of data points.

6.4.4.3 RATE DETERMINING STEP - PROPAGATION STAGE 2

The rate-determining step of the mortar corrosion under propagation stage 2 was established for the various sewer classifications by plotting the corrosion data using Equation 6-24 and Equation 6-25 (see Figure 6-13 a-h). The fit of the data was evaluated from the correlation of regression (R^2) (see Figure 6-14). As shown, the R^2 value between C1 to C5 did not vary

significantly between the chemical and pore diffusion-controlled mechanisms, suggesting the kinetics of corrosion under the propagation stage 2 under the various classifications where H_2S < 200 ppm are controlled by both the combined chemical and pore diffusion steps. It should be noted that above 200 ppm H_2S, the rate of corrosion could be higher, and this may drive diffusion-controlled kinetics. However, the greater bacteriostatic effect of higher concentration may limit the corrosion driving a chemically controlled kinetics. It is anticipated that the proposed modelling could be made more comprehensive as more kinetic data are made available from these conditions.

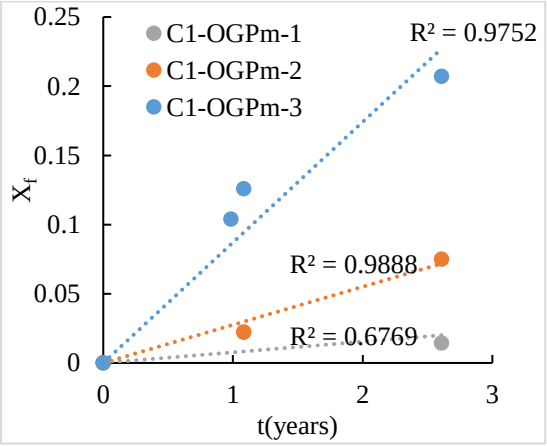

(a)

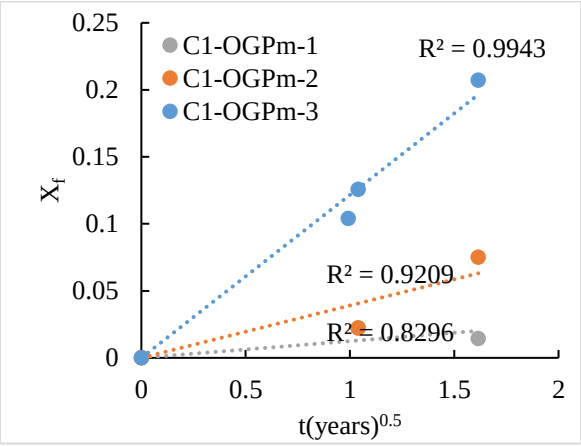

(b)

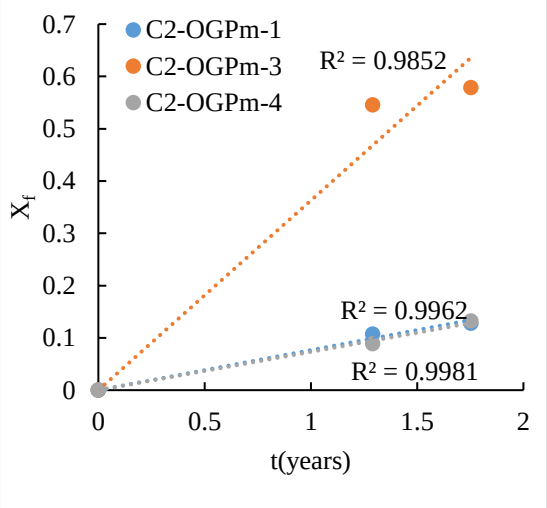

(c)

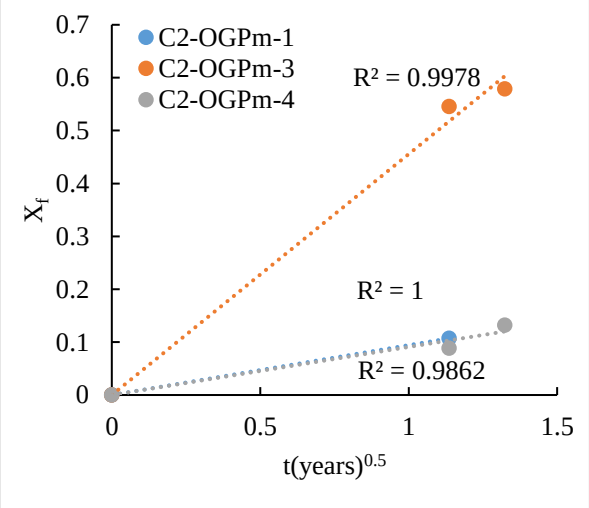

(d)

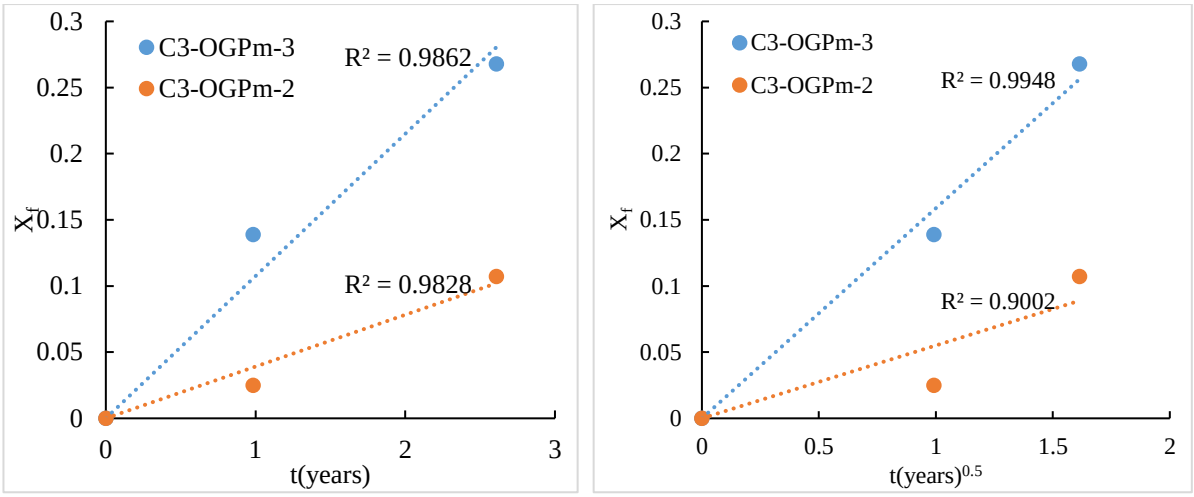

(e)

(f)

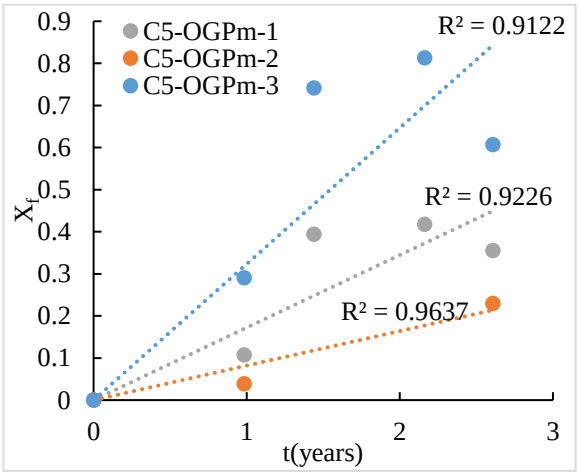

(g)

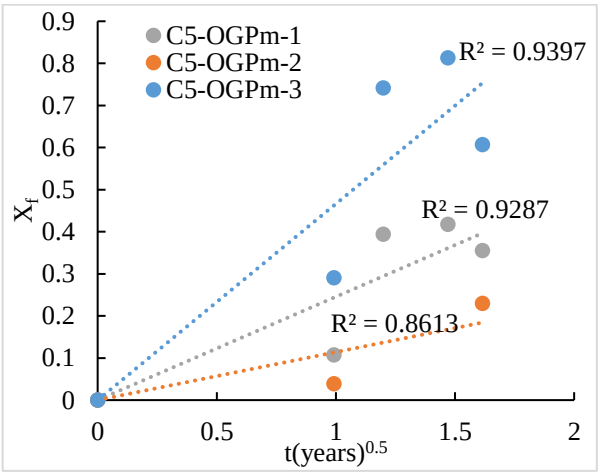

(h)

Figure 6-13. Plot of mortar corrosion data under propagation stage 2 fitted to the core shrinking model based on: a) chemical-controlled (C1), b) pore diffusion-controlled (C1), c) chemical-controlled (C2) and d) pore diffusion-controlled reaction (C2), e) chemical controlled (C3), f) pore diffusion-controlled reaction (C3), g) chemical controlled (C5) and h) pore diffusion-controlled reaction (C5)

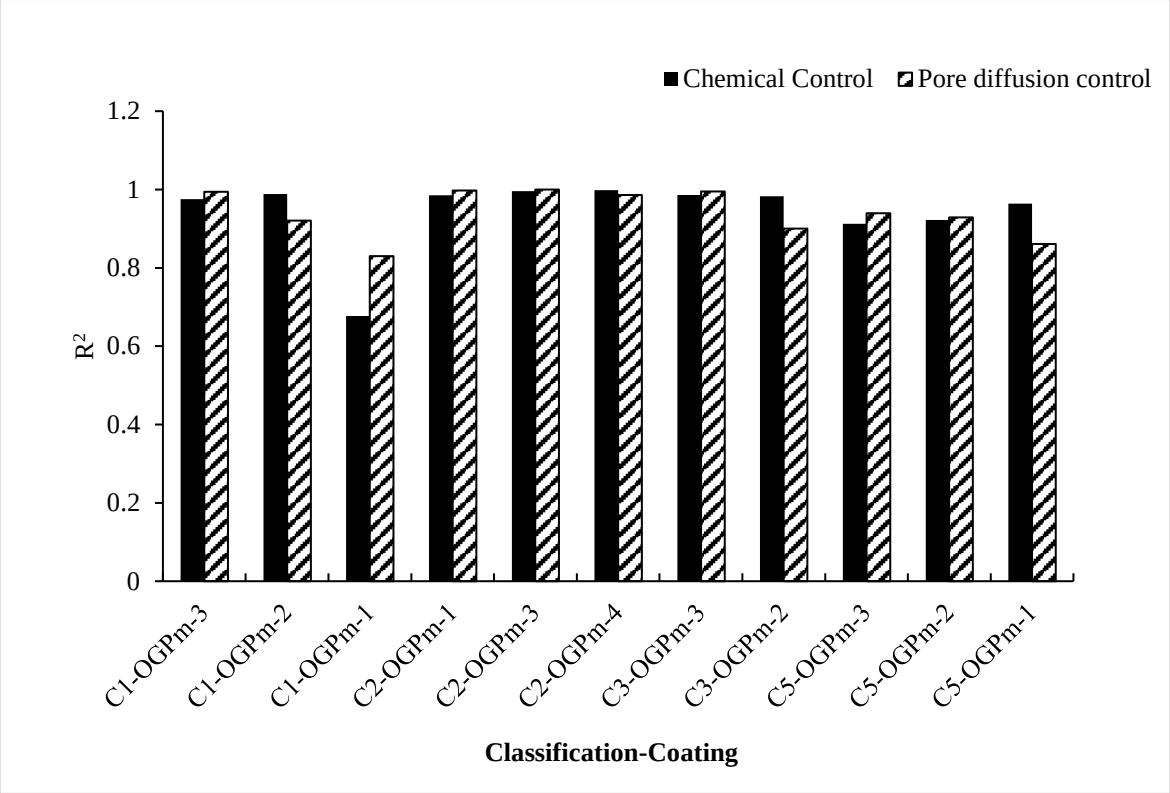

Figure 6-14. R^2 of fitted mortar corrosion data under propagation stage 2 to core shrinking models

Following the model for stage 1 corrosion propagation (see Table 6-9), the following semi-empirical model was proposed to predict corrosion depth at the second stage of corrosion propagation (X_{S2_G}) under chemical and pore diffusion-controlled corrosion. The depth of corrosion, as shown, is also dependent on the corrosivity of the environment (C_{S2_G}), durability properties of the mortar (F_{S2_G}) and service period (t).

Table 6-9. Model for Stage 2 Corrosion Propagation of AAB and Geopolymer Mortar under Mixed Chemical and Pore Diffusion Controlled

Model	**Equation**	
Depth of Corrosion Prediction at Stage 2 Corrosion Propagation (X_{S2_G})	$X_{S2\_G} = K_{S2\_G} C_{S2\_G} F_{S2\_G} (-p_{1\_S2G} t^{p_{2\_S2G}} + p_{3\_S2G} t - p_{4\_S2G})$	Equation 6-46
Corrosivity (C_{S2_G})	$C_{S2\_G} = [H_2S]^{c1\_S2G} [CO_2]^{c2\_S2G} [RH]^{c3\_S2G} e^{(-\frac{E_{C\_S2G}}{RT})}$	Equation 6-47
Mortar durability (F_{S2_G})	$F_{S2\_G} = F \prod_{i=1}^{y} \rho_{Gi}(1-\theta_{Gi}) = B_{S2\_G} A_{S2\_G} \beta^{f1\_S2G} UCS^{f2\_S2G} \theta^{f3\_S2G}$	Equation 6-48
Binder hydrate composition (B_{S2_G})	$HB_{tiG} = [HB_1]^{b1\_S2G} [HB_2]^{b2\_S2G} [HB_3]^{b3\_S2G} (-b_{4\_S2G} [HB_4]^{b_{5\_S2G}} + b_{6\_S2G} [HB_4] - b_{7\_S2G})$	Equation 6-49
Aggregate composition (A_{S2_G})	$A_{S2\_G} = [A_{Al_2O_3}]^{a1\_S2G} [A_{CaO}]^{a2\_S2G} [A_{SiO_2}]^{a3\_S2G}$	Equation 6-50

Where:

X_{S2_G}	Depth of Corrosion Prediction at Stage 2 Corrosion Propagation
K_{S2_G}	Constant for depth of corrosion prediction model for stage 2 corrosion propagation
C_{S2_G}	Sewer Corrosivity
F_{S2_G}	Mortar durability
t	Exposure time
$p_{i(1,2,3,4)\_S1G}$	Constant parameters for time
$[H_2S]$	hydrogen sulphide concentration (ppm)
$[CO_2]$	carbon dioxide concentration (ppm)
[RH]	relative humidity (%)
T	gas temperature (K)
E_{C_S2G}	Sum of the activation energies associated with the interaction (adsorption and reaction) between corrosive gases and mortar surface $\Sigma E_{H2S} + E_{CO2} + \ldots$
R	Gas constant 8.3145 J/mol. K
e	Natural exponential
$c_{i(i=1,2,3)\_S2G}$	order of reaction as a function of the environmental corrosivity parameters for stage 2 corrosion propagation
B_{S2_G}	Binder hydrate composition
A_{S2_G}	Aggregate composition
β	acid neutralisation capacity (millimoles H^+/g substrate)
UCS	Unconfined compressive strength (MPa)
θ	porosity
$f_{i(i=1,2,3)\_S1G}$	order of reaction as a function of mortar durability parameters for stage 2 corrosion propagation
HB_1	Hydrate composition phase 1 (e.g., C-S-H) (wt.%)
HB_2	Hydrate composition phase 2 (e.g., C-A-S-H) (wt.%)
HB_3	Hydrate composition phase 3 (e.g., C-N-A-S-H) (wt.%)
HB_4	Hydrate composition phase 4 (e.g., N-A-S-H) (wt.%)
$b_{i(i=1,2,3,4,5,6,7)\_S2G}$	order of reaction as a function of AAB and geopolymer mortar binder hydrate composition for stage 2 corrosion propagation
$[A_{Al2O3}]$	Al_2O_3 content of the aggregate (wt.%) estimated by XRF
$[A_{CaO}]$	CaO content of the aggregate (wt.%) estimated by XRF
$[A_{SiO2}]$	SiO_2 content of the aggregate (wt.%) estimated by XRF
$a_{i(i=1,2,3)\_S2G}$	order of reaction as a function of AAB and geopolymer mortar aggregate composition for stage 2 corrosion propagation

6.4.4.4 FITTING AND PARAMETER SIGNIFICANCE ANALYSIS OF CORROSION PROPAGATION STAGE 2 MODEL

The mortar corrosion data based on the corrosion depth under corrosion propagation were also fitted to the stage 2 corrosion model (see Table 6-10). The fit of the data is shown in Figure 6-15. The model parameters for propagation stage 2 were determined by the solver "add-in" function of the Microsoft Excel spreadsheet program by minimising the sum of squared errors (SSE). The significance of the independent variable used in the model was established using a partial F-test. The F-test parameters for the model are reported in Table 6-10. The F-statistics was used to test the null hypothesis that the variances of the reduced and full models are equal. The significance of the observed F-test was measured from the p-value or significance probability. The p-values were estimated using Microsoft Excel. If the p-value is less than the conventional 0.05 level, then the null hypothesis was rejected, and the conclusion was that the two variances differed significantly, and the variable removed in the reduced model was a statistically significant predictor in the failure predictive at stage 2. As shown, all the p-values are below 0.05, inferring that all the parameters in the model are statistically significant.

The measures of the statistical fit of the model to the corrosion data under propagation stage 2 are R^2 of 0.90, adjusted- R^2 of 0.82 and s_e of 4.0. These statistical parameters suggest the model adequately fits of captures the mortar corrosion behaviour under stage 2 corrosion propagation. This degree of fit also provides some assurance that the assumption of the pore resistance remains constant with time.

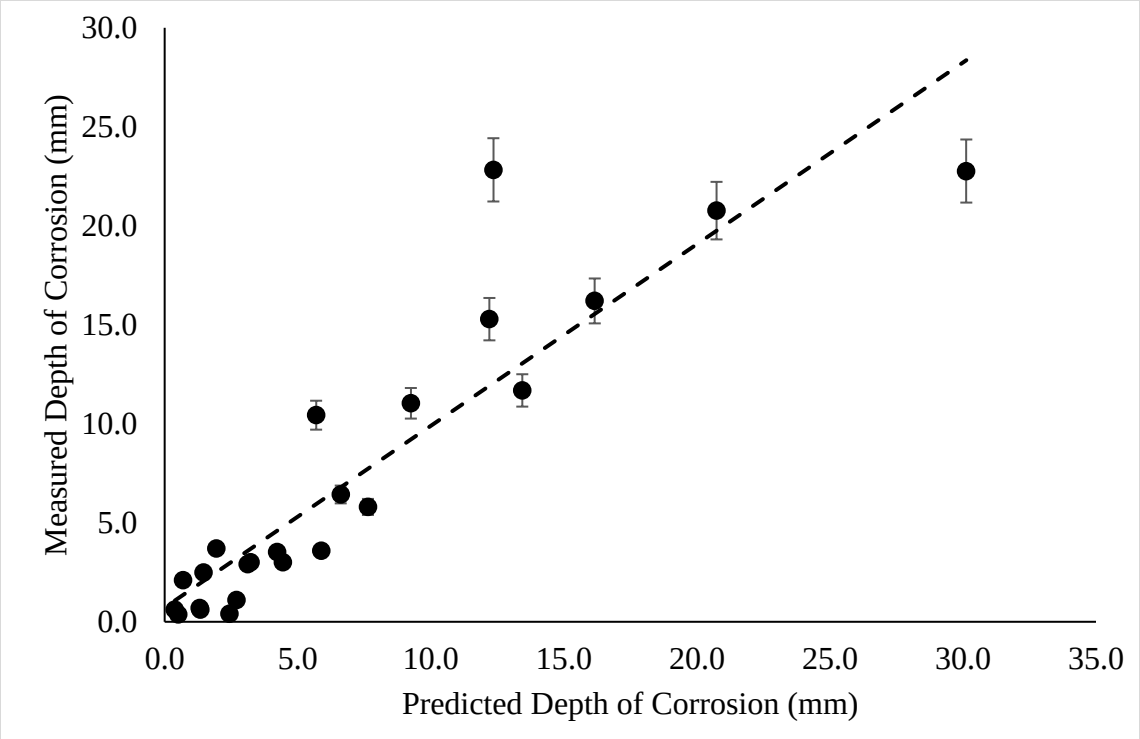

Figure 6-15. Mortar data under propagation stage 2 fitted to Model 2 – mixed chemical and pore diffusion-controlled model (see equation 25)

Table 6-10 Fitted parameters for AAB and geopolymer mortar corrosion data under propagation stage 2

Parameters	Values	Parameters	Values
K_{S2G}	1.72		
Corrosivity		***Binder composition***	
c_{1_S2G}	0.348	b_{1_S2G}	0.08
c_{2_S2G}	0.438	b_{2_S2G}	0.072
c_{3_S2G}	3.24	b_{3_S2G}	0.108
$E_{C\text{-}S2G}$	-925	b_{4_S2G}	0.355
		b_{5_S2G}	0.018
		b_{6_S2G}	0.0
		b_{7_S2G}	0.0
Mortar durability		***Aggregate composition***	
f_{1_S2G}	0.19	a_{1_S2G}	0.28
f_{2_S2G}	0.163	a_{2_S2G}	0.018
f_{3_S2G}	1.80	a_{3_S2G}	0.11
Time			
p_{1_S2G}	0.51		
P_{2_S2G}	0.92		
P_{3_S2G}	0.0		
P_{4_S2G}	0.0		

Table 6-11. Statistical significance analysis of Model 2 parameters fitted to propagation stage 2 data (n = 30, p = 15)

Parameters	Degree of Freedom	SSE	$R(M_1/M_2)$	MSE	F	p-value
Full	14	227		16		
H_2S	1	1624	1397	1397	9.14×10^5	0.0000
CO_2	1	1.85×10^6	1.85×10^6	1.85×10^6	1.21×10^9	0.0000
RH	1	1.13×10^6	1.13×10^6	1.13×10^6	7.41×10^8	0.0000
T	1	2488	2261	2261	1.48×10^6	0.0000
Constant, K_M	1	586	359	359	2.35×10^5	0.0000
HB1	1	228	1	1	654	0.0015
HB2	1	228	1	1	654	0.0015
HB3	1	231	4	4	2617	0.0004
HB4	1	8317	8090	8090	5.29×10^6	0.0000
Al_2O_3 (Ag)	1	516	289	289	1.89×10^5	0.0000
CaO (Ag)	1	228	1	1	654	0.0015
SiO_2 (Ag)	1	547	320	320	2.09×10^5	0.0000
β	1	269	42	42	2.75×10^4	0.0000
UCS	1	4.02×10^7	4.02×10^7	4.02×10^7	2.63×10^{10}	0.0000
θ	1	541	314	314	2.05×10^5	0.0000

6.4.5 SENSITIVITY ANALYSIS

A sensitivity analysis, also known as a what-if analysis, is a technique used to examine the impact of changes in independent variables on the dependent variable. It helps in understanding how variations in the input variables affect the output of a model. By systematically altering the independent variables within defined ranges, sensitivity analysis provides the sensitivity of the

dependent variable to the service life prediction model. In this section, the impact of changes in environmental conditions (H_2S, CO_2, Temperature, and %RH) and durability parameters (chemical and physical properties) were examined.

6.4.5.1 IMPACT OF SEWER ENVIRONMENTAL CONDITIONS

The effect of changes in H_2S, CO_2, %RH and T under C1 of sewer corrosivity classification (See section 5.2.2 in chapter 5) on the OGPm-1 sample as presentative lining mortar sample were assessed based on the predictive corrosion depth as shown in Figure *5-20*. the corrosion depth at ten years changed by 47 % (10 mm to 15 mm) when H_2S increased from 5 ppm to 15 ppm while keeping the CO_2 at 9500 ppm, T at 28 °C, and 99 %RH. This finding aligns with the performance result in Chapter 5, indicating the effectiveness of H_2S in an increase of depth of corrosion. The effect of changes in the CO_2 concentration from 9400 to 9500 ppm reduced the corrosion depth by 0.23 % (15 mm to 14.97 mm) while keeping the H_2S at 15 ppm, T at 28 °C, and 99 %RH. It could change the corrosion depth significantly. However, significant changes in the depth of corrosion were noted when CO_2 concentration was increased by several orders of magnitude. For example, increasing the CO_2 concentration from 8000 to 10000 ppm reduced corrosion depth by 4.76 %. The reduction of corrosion depth with increasing the CO_2 concentration results in $CaCO_3$ formation and slows down the reaction of further acid attacks by pore blocking (Grengg et al., 2020). The effect of the change of temperature from 15 °C to 28 °C increased the corrosion depth by 12.75% (13.28 mm to 14.97 mm) while keeping the H_2S at 15 ppm, CO_2 at 9500 ppm, and 99 %RH. The effect of the change of %RH from 95 %RH to 99 %RH increased the corrosion depth by 13.73 % (13.16 mm to 14.97 mm) while keeping the H_2S at 15 ppm, CO_2 at 9500 ppm, and T at 28 °C. The temperature and the %RH were effects in the increase of corrosion depth by approximately 13-14 %. Higher temperatures can enhance the diffusion of the corrosive compound and the rate of

reaction. While higher humidity can promote corrosion due to condensed humidity can transfer corrosive compounds and facilitating their penetration into the mortar matrix, promoting chemical reactions that lead to mortar deterioration. Moreover, high humidity levels and temperature can accelerate the growth of microorganisms, such as sulphur-reducing bacteria, which produce corrosive byproducts that can further deteriorate the mortar (Qiu et al., 2022).

Overall, these results highlight the significant impact of environmental conditions on the corrosion performance of mortar. The study revealed that environmental parameters such as H_2S concentration, CO_2 exposure, relative humidity (%RH), and temperature (T) are interrelated and cannot be considered in separation. Each parameter influences the corrosive environment in its own way, and their combined effects play a key role in mortar degradation. For instance, H_2S and CO_2 can react with high humidity leading to the formation of corrosive acids. Meanwhile, high humidity levels can facilitate the absorption of moisture and corrosive substances into the mortar, accelerating degradation processes. Temperature variations can also influence the rate of chemical reactions and moisture evaporation, further impacting corrosion rate. Therefore, management of these sewer environmental factors are needed in developing effective strategies to enhance the corrosion resistance performance of mortar in various applications.

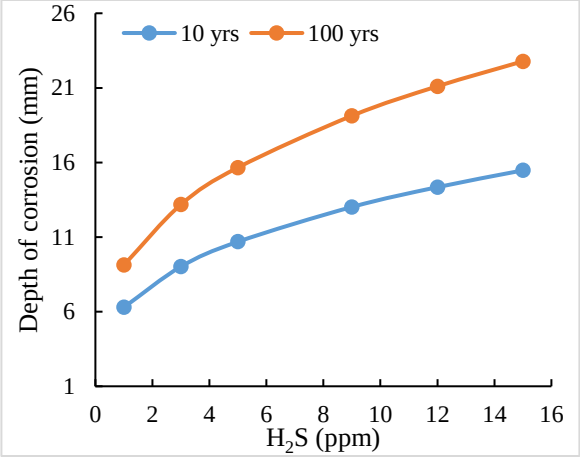

CO_2 at 9500 ppm, T at 28 °C, and 99 %RH

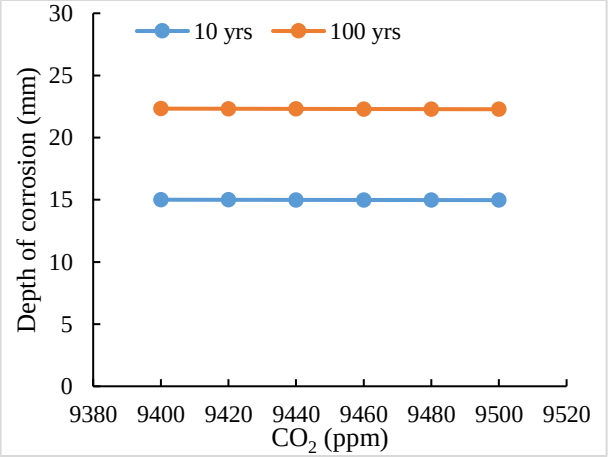

H_2S at 15 ppm, T at 28 °C, and 99 %RH

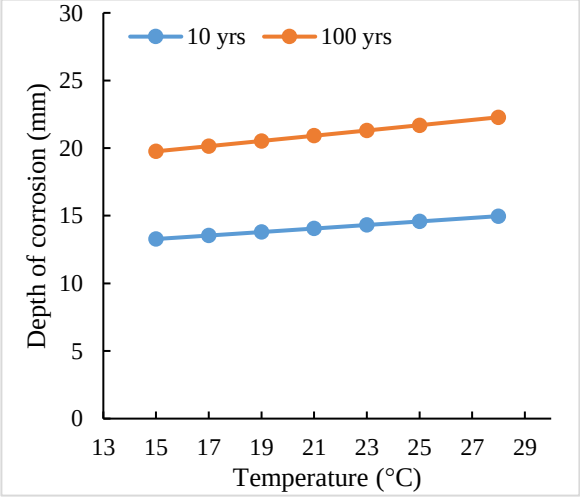

15 ppm H_2S, 9500 ppm CO_2, and 99 %RH

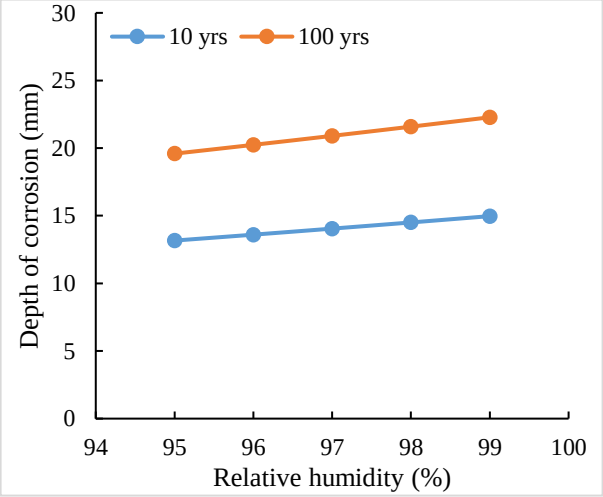

15 ppm H_2S, 9500 ppm CO_2, and T = 28 °C

Figure 6-16 Impact of changes in the relative humidity on the depth of corrosion as a function of service life under Category 1 exposure conditions

6.4.5.2 IMPACT OF DURABILITY PARAMETER

Mortar corrosion is a complex process involving multiple factors, such as sewer environmental conditions and the chemical and physical properties of the mortar. The physical and chemical properties of mortar, such as UCS, porosity, ANC, Hydration product, and aggregate, play key roles in determining its corrosion resistance performance. Sensitivity analysis enables a systematic exploration of these properties and their impact on the corrosive behaviour of mortar.

6.4.5.2.1 PHYSICAL PROPERTIES

The physical properties were determined by the sensitivity of UCS and porosity impacted on the corrosion performance under C1 of sewer corrosivity classification, which has environmental conditions (15 ppm H_2S, 9500 ppm CO_2, T at 28 °C, and 99 %RH) and chemical properties (ANC at 1 mmol H^+ /g substrate,0.68 wt.% C-S-H, 0.42 wt.% C-A-S-H, 0.99 wt.% C-N-A-S-H, and 0.69 wt.% N-A-S-H, 0.36 wt.% Al_2O_3.in aggregate, 0.10 wt.% CaO in the aggregate, and 96.95 wt.% SiO_2 in aggregate) constant.

The corrosion depth at 10 years was reduced by 95% (21.3 mm to 1.1 mm) when initial UCS increased from 30 MPa to 120 MPa while keeping the porosity at 22.3 vol.% constant, along with environmental conditions and chemical properties, as shown in Figure 6-17 (left). Higher UCS values were generally associated with improved corrosion resistance performance, as shown in the effect of UCS in Chapter 5. higher UCS indicates a denser and more compact mortar structure, limiting the pathways for moisture and corrosive substances to penetrate. Changing porosity increased corrosion depth by 9.2 % (13.79 mm to 15.07 mm) while keeping UCS at 35 MPa constant, along with environmental conditions and chemical properties, as shown in Figure 6-17 (right). It observed that higher porosity allows for increased moisture absorption and the penetration of corrosive compounds into the mortar.

The results indicate that higher UCS values and lower porosity levels are associated with improved corrosion resistance. This suggests that a denser and more compact mortar with lower porosity has a better capability to resist corrosive environments. Aiken et al. (2018) and Luna Galiano et al. (2016) found a relationship between porosity and UCS. It found that the geopolymers with lower porosity had greater compressive strength. Moreover, Aiken et al. (2018), Khan et al. (2020b), and Grengg et al. (2020) have also found that the corrosion resistance performance was impacted by

porosity and UCS after being exposed to a sewer environment. Therefore, the interdependence of porosity and UCS highlights the importance of considering both factors together when assessing the corrosion resistance performance of mortar.

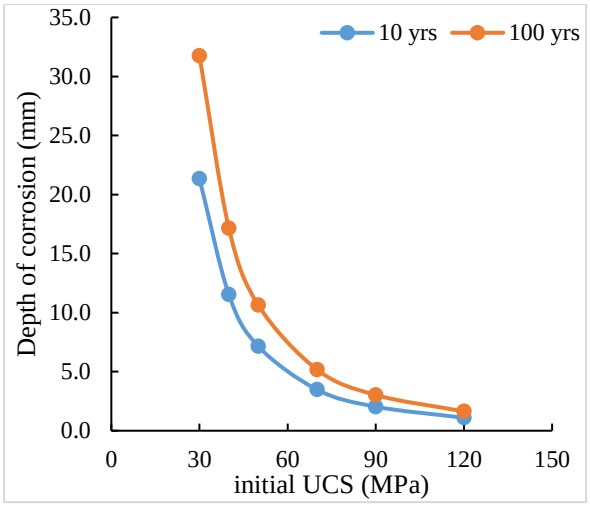

(a) Initial UCS

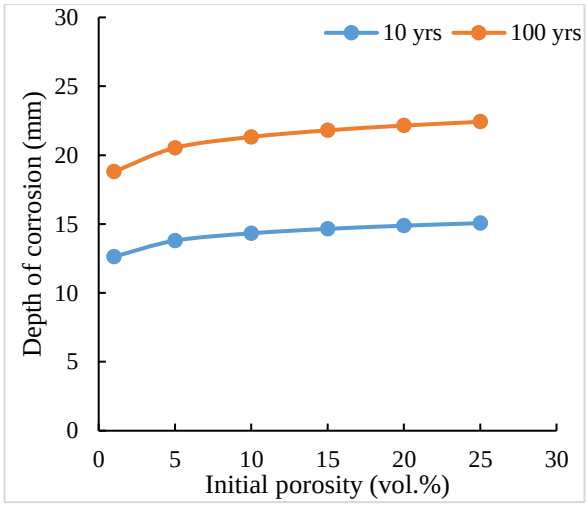

(b) Initial Porosity

Figure 6-17 Impact of changes in UCS and porosity on the depth of corrosion as a function of service life under Category 1 exposure conditions (C1:15 ppm H_2S, 9500 ppm CO_2, T= 28 °C and 99 %RH) and chemical properties (ANC at 1 mmol H^+ /g substrate,0.68 wt.% C-S-H, 0.42 wt.% C-A-S-H, 0.99 wt.% C-N-A-S-H, and 0.69 wt.% N-A-S-H, 0.36 wt.% Al_2O_3.in aggregate, 0.10 wt.% CaO in the aggregate, and 96.95 wt.% SiO_2 in aggregate)

6.4.5.2.2 CHEMICAL PROPERTIES

The sensitivity or impact of chemical properties on acid corrosion resistance performance was determined by changing the ANC and amount of hydration products under C1 of sewer corrosivity classification in the environmental conditions (15 ppm H_2S, 9500 ppm CO_2, T at 28 °C, and 99 %RH) and physical properties (35.4 MPa UCS and 22.3 vol.% porosity) of mortar was kept constant. The chemical properties (ANC at 1 mmol H^+ /g substrate,0.68 wt.% C-S-H, 0.42 wt.% C-A-S-H, 0.99 wt.% C-N-A-S-H, and 0.69 wt.% N-A-S-H, 0.36 wt.% Al_2O_3.in aggregate, 0.10

wt.% CaO in the aggregate, and 96.95 wt.% SiO_2 in aggregate) were changed individually. The change in each chemical parameter is discussed below.

ANC

The corrosion depth at 10 years was increased by 68% (15 mm to 25 mm) when the ANC increased from 1 mmol H^+ /g substrate to 3 mmol H^+ /g substrate while keeping environmental conditions and physical properties constant, as shown in Figure 6-18. This result highlights the significance of the ANC as an important parameter for assessing a mortar's capability to neutralise acids and combat corrosion. The ANC was strongly linked with the CaO content in the mortar, indicating that higher CaO levels contribute to a greater ANC. This association between ANC and CaO content suggests a higher ANC can provide effective acid neutralisation and protection in short-term acid exposure. However, it is essential to consider the long-term effects of sewer environments on the mortar. Over time, in the presence of sulfuric acid attacks, the CaO in the mortar gradually converts to $CaSO_4$, an expansive corrosion product. This transformation leads to an increase in the corrosion depth. The predicted result suggested that higher ANC values were associated with more severe increases in corrosion depth over the long term. However, this needs to note that this section is analysed based on the modelling to understand the impact of ANC under certain geopolymer and environmental conditions. Therefore, the impact of the ANC in actual field applications was not perfectly the same because corrosion data were obtained from different types of geopolymer, which have different ANC values. However, the impact of the ANC in the field corrosion data and predicted data revealed the same suggestion that higher ANC of more than 4.2 mmol H^+ /g substrate (see Figure *5-40*) impacted the corrosion resistance performance by increasing the depth of corrosion. These results suggested that consideration of Ca content in the

geopolymer mortar is necessary in order to control the ANC, ensuring effective corrosion resistance performance in short-term and long-term sewer environments.

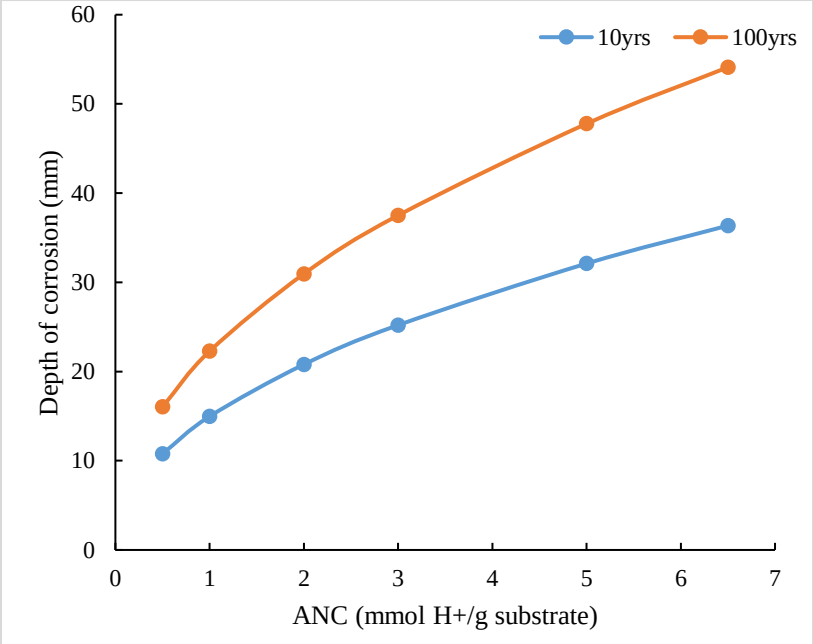

Figure 6-18 Impact of changes in ANC on the depth of corrosion as a function of service life under Category 1 exposure conditions (15 ppm H_2S, 9500 ppm CO_2, T at 28 °C, and 99 %RH) and physical properties (35.4 MPa UCS and 22.3 vol.% porosity) and The chemical properties (0.68 wt.% C-S-H, 0.42 wt.% C-A-S-H, 0.99 wt.% C-N-A-S-H, and 0.69 wt.% N-A-S-H, 0.36 wt.% Al_2O_3.in aggregate, 0.10 wt.% CaO in the aggregate, and 96.95 wt.% SiO_2 in aggregate)

Hydration products

Figure 6-19 shows the impact of hydration products on the depth of corrosion at 10 years and 100 years. The corrosion depth at 10 years was reduced by 75 % (9.43 mm to 1.83 mm) when the C-S-H increased from 1 wt.% substrate to 4 wt.% while keeping environmental conditions and physical properties constant. While the effect of changes in the C-A-S-H concentration from 0.4 wt.% to 2 wt.% reduced the corrosion depth by 7 % (15.02 mm to 13.83 mm). The effect of changes

in the C-N-A-S-H concentration from 0.6 wt.% to 4 wt.% reduced the corrosion depth by 81 % (23.2 mm to 4.40 mm). At the same time, the effect of changes in the N-A-S-H concentration from 0.2 wt.% to 1.5 wt.% reduced the corrosion depth by 16.5 % (16.73 mm to 13.97 mm). Overall, increasing the hydration product enhanced the corrosion resistance performance of mortar. However, increasing the C-S-H and C-N-A-S-H impacted the corrosion depth by reducing the depth of corrosion by 75-81 %, while increasing the C-A-S-H and N-A-S-H reduced the corrosion depth by 7-16.5%.

Chemical composition of Aggregate

Figure 6-20 shows the impact of the chemical composition of aggregate on the corrosion of mortar based on corrosion depth. The corrosion depth at 10 years of mortar is not affected by changing the concentration of SiO_2 content in aggregate. At the same time, the corrosion depth was increased by 27 % (18.7 mm to 23.7 mm) when the content of Al_2O_3 in aggregate increased from 1 wt.% to 3 %wt. At the same time, the effect of changing the CaO content in aggregate from 1 wt.% to 10 wt.% was observed to decrease the corrosion depth by 15% (13 mm to 11 mm). It was observed that both Al_2O_3 and CaO significantly affected the depth of corrosion.

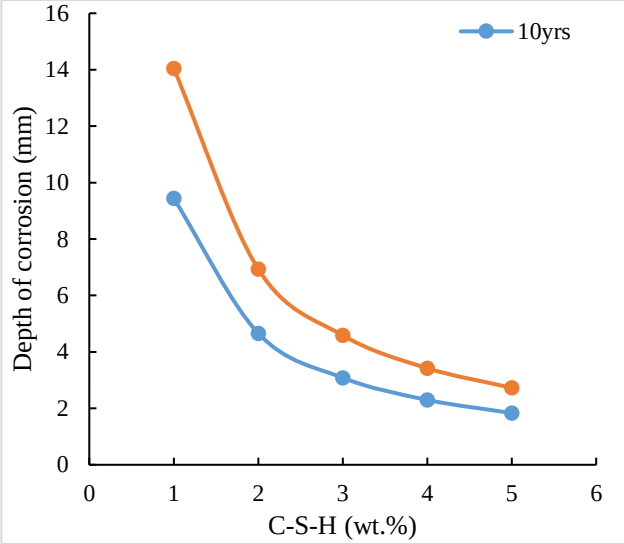

(a) C-S-H

0.42 wt.% C-A-S-H, 0.99 wt.% C-N-A-S-H, and 0.69 wt.% N-A-S-H

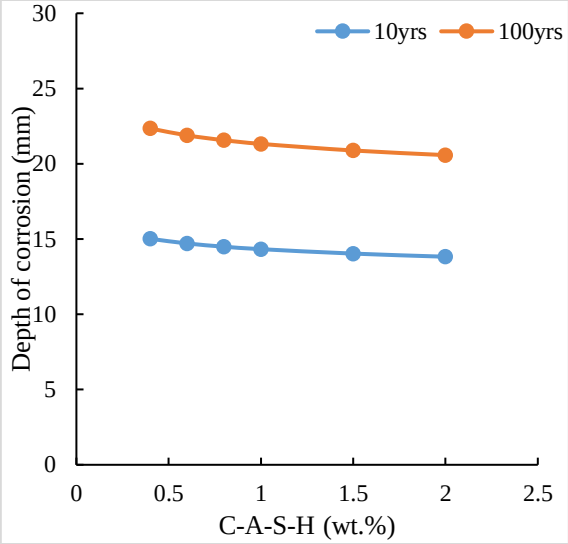

(b) C-A-S-H

0.68 wt.% C-S-H, 0.99 wt.% C-N-A-S-H, and 0.69 wt.% N-A-S-H

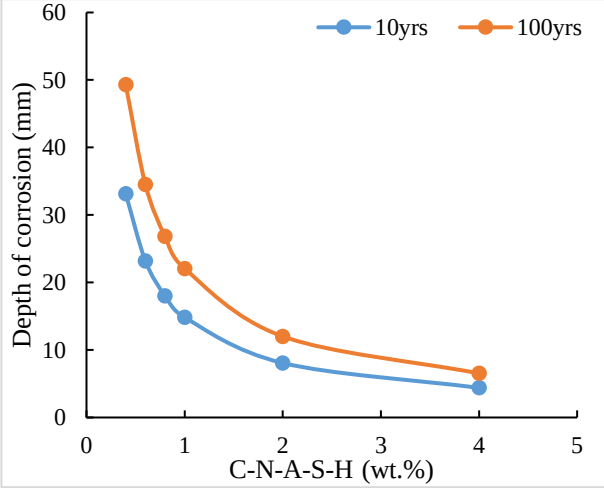

(c) C-N-A-S-H

0.68 wt.% C-S-H, 0.42 wt.% C-A-S-H, and 0.69 wt.% N-A-S-H

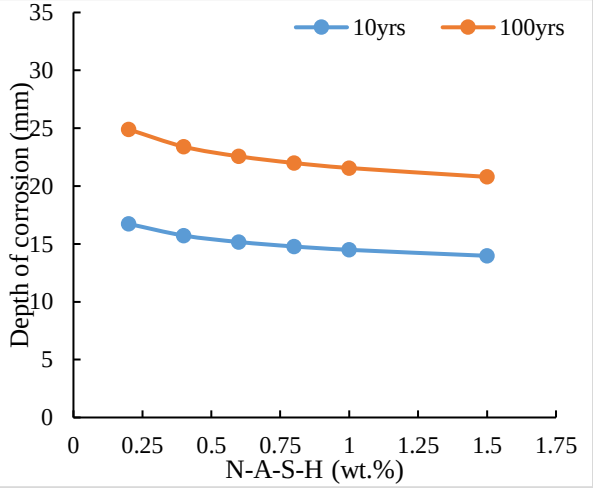

(d) N-A-S-H

0.68 wt.% C-S-H, 0.42 wt.% C-A-S-H, and 0.99 wt.% C-N-A-S-H

Figure 6-19 Impact of changes C-S-H, C-A-S-H, C-N-A-S-H, and N-A-S-H on the depth of corrosion as a function of service life under Category 1 exposure conditions (15 ppm H_2S, 9500 ppm CO_2, T at 28 °C, and 99 %RH) and physical properties (35.4 MPa UCS and 22.3 vol.% porosity) and The chemical properties (ANC at 1 mmol H+ /g substrate, 0.36 wt.% Al_2O_3.in aggregate, 0.10 wt.% CaO in the aggregate, and 96.95 wt.% SiO_2 in aggregate)

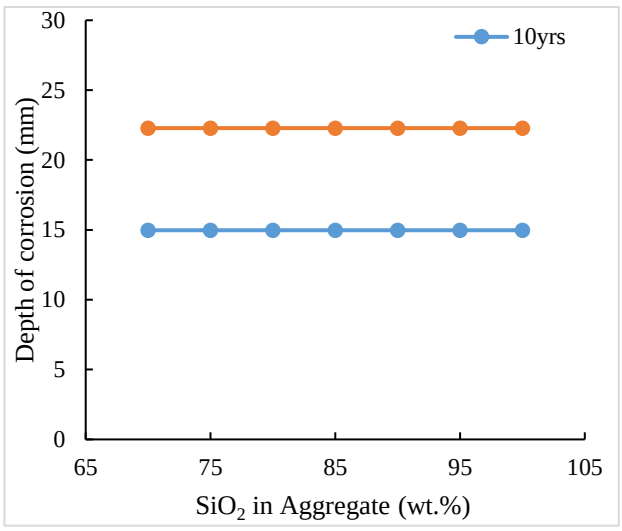

(a) SiO_2

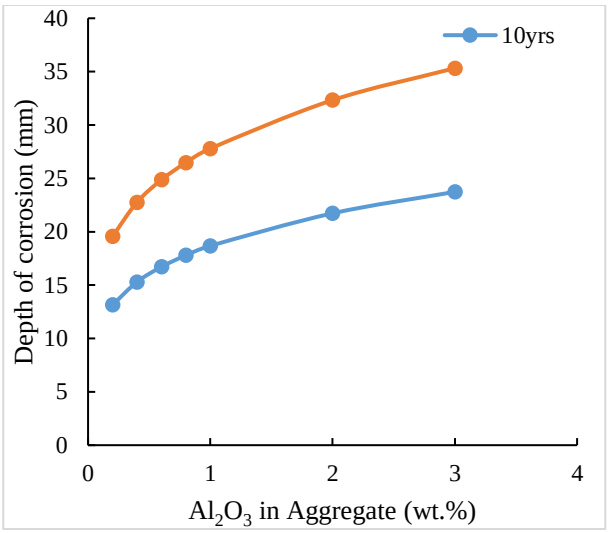

(b) Al_2O_3

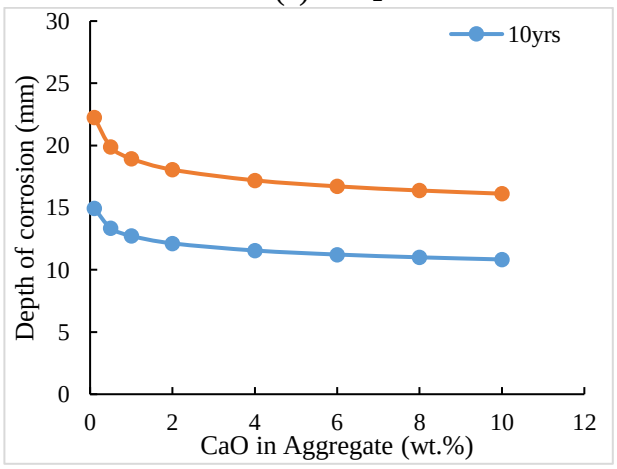

(c) CaO

Figure 6-20 Impact of changes in the chemical composition of aggregate SiO2, Al_2O_3 and CaO on the depth of corrosion as a function of service life under Category 1 exposure conditions (15 ppm H_2S, 9500 ppm CO_2, T at 28 °C, and 99 %RH) and physical properties (35.4 MPa UCS and 22.3 vol.% porosity) and The chemical properties (ANC at 1 mmol H+ /g substrate,0.68 wt.% C-S-H, 0.42 wt.% C-A-S-H, 0.99 wt.% C-N-A-S-H, and 0.69 wt.% N-A-S-H)

6.4.6 VERIFICATION OF SERVICE LIFE PREDICTION MODEL

Verifying a service life prediction model is essential to assess its accuracy and reliability in estimating durability and corrosion resistance performance. This section verified the service life prediction model for geopolymer lining mortar by correlating the model prediction and observed data. To verify the model, the measured corrosion depth data of OGPm-1, OGPm-2, OGPm-3, and

OGPm-4 from the field test under various sewer corrosivity classifications were plotted against the predicted corrosion depth data with the diagonal line as shown in Figure 6-21. The correlation observed that the measured and predicted data did not perfectly align with the diagonal line. Some points deviate slightly above or below the line, indicating a prediction error. Despite the deviations, there is a generally positive trend where the predicted corrosion data increases as the measured corrosion data increases. The service life prediction model was also used to predict the depth of corrosion, which was not included in the development of the model as verified data. It was observed that the verified corrosion depth fit along with the diagonal line well. Figure 6-22 shows the difference between the actual corrosion depth and the predicted corrosion depth. The difference between the two measurements mostly does not exceed 2.5 mm. This indicates a relatively accurate prediction of the corrosion depth by the model. The close agreement between the actual and predicted values shows that the model effectively estimates the corrosion performance of the mortar.

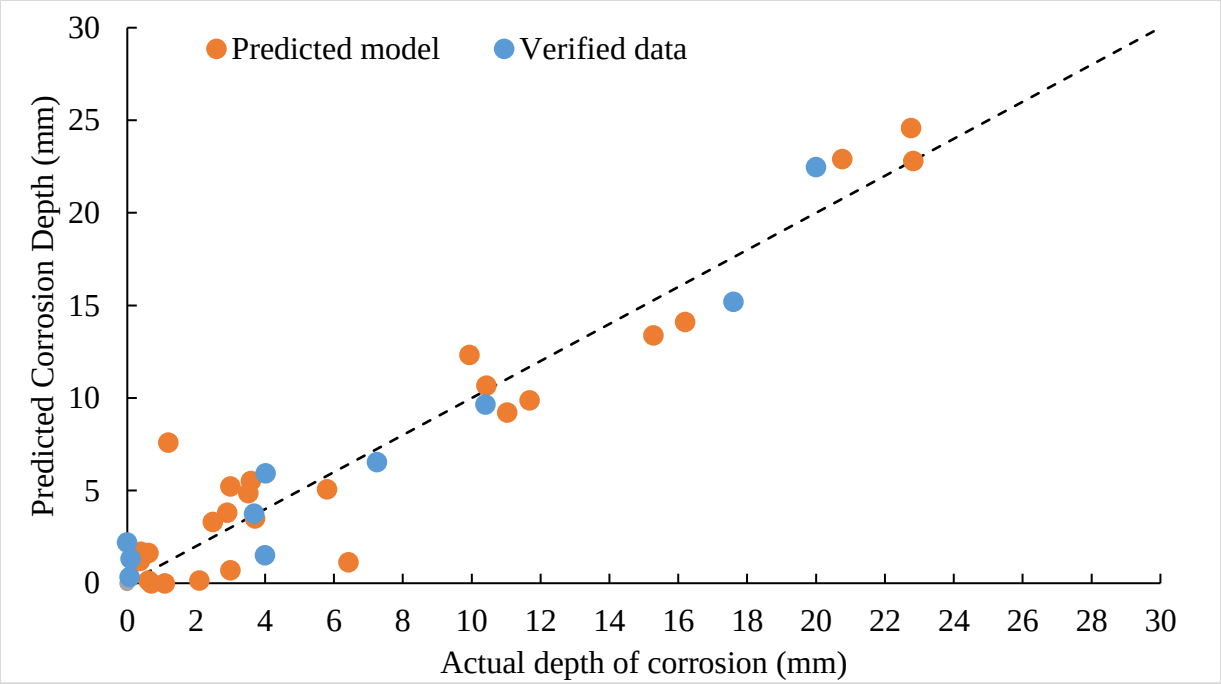

Figure 6-21 Correlation between predicted corrosion depth and actual corrosion depth

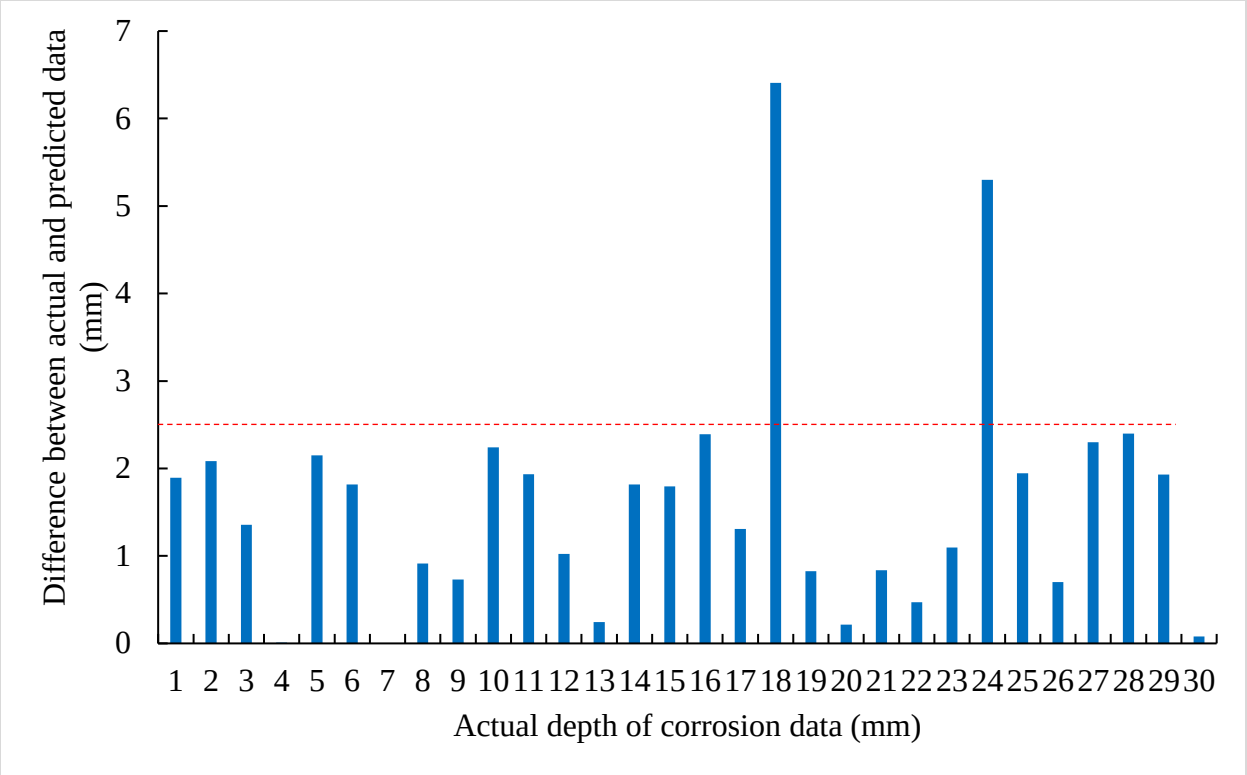

Figure 6-22 Difference between actual and predicted corrosion depth

6.5 SUMMARY

This chapter developed the service life prediction model for alkali-activated binder mortar, including geopolymer. This study is the first time the service model has been developed by considering real scenarios of field application, live sewer environmental conditions, and their physical and chemical properties.

A service life prediction model was developed based on corrosion depth over time, which was characterised by three stages of corrosion, with shrinking cored model assumption. The three corrosion stages were i). initiation period, ii). stage 1 corrosion propagation, and iii). stage 2 corrosion propagation. Each stage of corrosion was individually modelled employing a semi-

empirical model using the power law model and a solid-liquid kinetic based on the shrinking core model.

At the initial corrosion period, The semi-empirical model has been proposed to predict the period for corrosion initiation (t_i) as a function of sewer corrosivity (C_{ti}) and geopolymer mortar durability (F_{tiG})

$$t_i = k_{tiG} C_{ti} F_{tiG}$$

At stage 1 and stage 2 of corrosion, The semi-empirical model has been proposed to predict the corrosion depth as a function of sewer corrosivity (C_{ti}), geopolymer mortar durability (F_{tiG}), and time as shown below.

$$\text{Stage 1} : X_{S1\_G} = K_{S1\_G} C_{S1\_G} F_{S1\_G} (-p_{1\_S1G} t^{p_{2\_S1G}} + p_{3\_S1G} t - p_{4\_S1G})$$

$$\text{Stage 2} : X_{S2\_G} = K_{S2\_G} C_{S2\_G} F_{S2\_G} (-p_{1\_S2G} t^{p_{2\_S2G}} + p_{3\_S2G} t - p_{4\_S2G})$$

Where: t = time, C= sewer corrosivity, F = mortar durability, K = Constant for depth of corrosion prediction model, p = Constant parameters for time

The final service life was defined as $t = t_i + t$ (stag 1) + t (stage 2)

The full model parameters of the initial period, stage 1, and stage 2 of corrosion were presented in Table 6-3, Table 6-6, and Table 6-9, respectively. The model parameters in each stage of corrosion were determined by the solver "add-in" function of the Microsoft Excel spreadsheet program by minimising the sum of squared errors (SSE). The fitted parameters of the initial period, stage 1, and stage 2 of corrosion were presented in Table 6-4, Table 6-7, and Table 6-10, respectively.

To establish the fit of these models, an independent variable significance test was statistically performed for each model using a partial F-test and justified with the p-value. If the p-value is less

0.05, the independent variable was found to be a significant predictor in the predictive model. While the p-value is more than 0.05, the independent variable is rejected from the full model. The goodness of fit of the final models was determined using R^2, adjusted-R^2 and mean-square error (se), as presented below.

For the initial corrosion period: R^2 of 0.99, adjusted-R^2 of 0.98 and s_e of 0.04

For stage 1 corrosion propagation: R^2 of 0.98, adjusted-R^2 of 0.75 and s_e of 2.87

For Stage 2 corrosion propagation: R^2 of 0.90, adjusted-R^2 of 0.82 and s_e of 4.0

These statistical parameters suggested that the model adequately fits with the mortar corrosion behaviour under all stages of corrosion. The sensitivity of the change in sewer corrosivity (H_2S, CO_2, relative humidity, and temperature) and mortar durability parameters (porosity, UCS, ANC, C-S-H, C-A-S-H, C-N-A-S-H, N-A-S-H) showed the relative impact on the depth of corrosion. The corrosion depth prediction models were verified by comparing the predicted and 10% of the external data. The verified corrosion depth was observed to be a reliable fit along with the diagonal line. It is important to note that this study presents the first development of a service life prediction model for alkali-activated mortar, including geopolymer, that considers real-world field applications, encompassing varied live sewer corrosivity classifications and mortar durability. The selection criteria input in the service life prediction model were the mortar durability and sewer corrosivity. The mortar durability could be predicted from porosity, UCS, ANC, binder hydrations (C-S-H, C-A-S-H, C-N-A-S-H, and N-A-S-H), and chemical composition of aggregate (CaO, SiO_2, and Al_2O_3) and sewer corrosivity conditions, as defined by sewer environmental conditions, could be predicted from H_2S, CO_2, temperature, and %RH.

7 CONCLUSION AND RECOMMENDATIONS

7.1 CONCLUSIONS

This study developed a service life prediction model for alkali-activated mortars, including geopolymer mortars, that could be used in selecting and designing protective lining mortars that are fit for protecting concrete sewer assets.

The key outcome of this study concerning the specific objectives is described below.

1. Comparative corrosion resistance performance of various commercial geopolymers with calcium aluminate cement mortar representing different sewer corrosion classifications

The results of this study provide valuable corrosion data into the comparative corrosion resistance performance of various commercial geopolymers mortar (OGPm) and calcium aluminate cement mortar (CACm) in different sewer corrosion classifications, encompassing the entire range from C1 (very low corrosivity) - C5 (very high corrosivity) of sewer corrosivity classifications. The corrosion resistance performance was determined based on the corrosion depth and residual UCS with time.

Upon mortar sample analysis, it was observed that the corrosion resistance performance of the OGPm in the field varied significantly depending on exposed sewer environment conditions, their chemical compositions, and inherent physical and chemical properties. The corrosion depth of OGPm obtained varied from 0 % to 58 % from the original thickness, depending on the type of geopolymer and sewer corrosivity environment during the field test. Comparing the corrosion resistance performance among the geopolymer using the service life prediction model, it observed that the corrosion depth of OGPm-1, OGPm-2, OGPm-3, and OGPm-4 were presented at 20.2%, 3.2 %, 59.9 %, and 14.8 %, respectively, under C1 sewer corrosivity classification (15 ppm H_2S, 9500 ppm CO_2, 28 °C, and 99 %RH) for 10 years with 25 mm of

the initial thickness of lining. These results indicated that the OGPm-2 exhibited the highest acid resistance among the tested geopolymer samples. This suggests that OGPm-2 is expected to have the most extended service life compared to the other geopolymers.

In contrast, CACm presented the highest corrosion resistance performance across sewer corrosivity classification. CACm exhibited corrosion depth varied from 0 % to 36 % from the original thickness, depending on sewer corrosivity classifications. The CACm exhibited minimal corrosion depth and high residual UCS, indicating its suitability for application in various sewer corrosion classifications. The excellent performance of CACm can be attributed to its chemical and physical properties, which resist the corrosive compound generated under sewer environments.

The comparative evaluation of OGPm and CACm in different sewer corrosion classifications highlighted that the CACm presented better corrosion resistance performance than OGPm. Despite the CACm performing better than OGPm, some of the OGPm performed comparably with the CACm, such as OGPm-2. Moreover, the performance of geopolymer at low sewer corrosivity classification was performed comparably with CACm. Therefore, OGPm can be selected for high sewer corrosivity classification but must consider its chemical and physical properties.

2. Selection criteria for alkali-activated mortars, including geopolymer for sewer rehabilitation

The different types of lining mortar, denoted as OGPm-1, OGPm-2, OGPm-3, and OGPm-4, were exposed to different live sewer corrosivity classifications to obtain long-term corrosion resistance performance tests. The corrosion resistance performance of the lining mortars was determined based on corrosion depth over time. The corrosion depth was correlated with the

sewer environment and chemical and physical properties to determine the selection criteria for lining mortar.

Effect of Sewer Environmental Conditions

The corrosion depth was correlated with sewer environmental conditions, specifically H_2S, CO_2, %RH, and temperature. It was observed that H_2S significantly impacted the corrosion depth. The CO_2 was observed to have less impact compared to H_2S due to the carbonation can significantly impact at 50 to 75 %RH, while the live sewer in this study was observed to have 95-99 %RH. The temperature and %RH facilitated the absorption of moisture and corrosive substances into the mortar, accelerating degradation processes and supporting the growth of microorganisms.

Effect of Chemical and Physical Properties

The deterioration of the lining mortar in this study was primarily attributed to the formation of gypsum. This can be associated with a low ANC (acid neutralization capacity), which leads to the decalcification of essential hydration products such as C-S-H, C-A-S-H, and C-N-A-S-H. Interestingly, it was also observed that certain geopolymers with lower C-S-H and C-A-S-H content still exhibited high corrosion depths. This can be attributed to the high initial porosity of the mortar, which allows acid to penetrate the mortar matrix and react with the binder. The initial porosity of the geopolymer was found to be influenced by the presence of N-A-S-H. An increase in N-A-S-H content resulted in higher initial porosity. Therefore, when selecting alkali-activated mortar, including geopolymer, it is essential to consider factors such as ANC, hydration product composition, porosity, and UCS to ensure optimal corrosion resistance performance and durability.

3. Service life of the geopolymer under the sewer environment?

The durability and service life of geopolymers as a protective lining for sewer asset rehabilitation under live sewer environments are essential for selecting alkali-activated mortar, including geopolymers. This study developed a service life prediction model for geopolymers using a semi-empirical method as observed corrosion was noted to be divided into three stages. These are lag phases (corrosion initiation period), stage 1 of corrosion (rapid corrosion rate), and stage 2 of corrosion (slow corrosion rate). These three stages were modelled separately. The lag phase was modelled based on the mortar acid neutralisation capacity and cement chemistry. The subsequent stages 1 and 2 of the corrosion were modelled based on the chemical rate equation with the temperature dependence of the rate constant based on the Arrhenius law. The assumption was that the extent of corrosion could be directly related to corrosivity and durability factors.

This study inferred the corrosivity factors from sewer environmental conditions (H_2S, CO_2, temperature, and %RH). At the same time, the durability factors were inferred from physical and chemical properties (porosity, UCS, ANC, Hydration products (C-S-H, C-A-S-H, C-N-A-S-H, and N-A-S-H) and chemical composition of aggregate (CaO, SiO_2, and Al_2O_3). Data from measured corrosion and corresponding corrosivity durability factors were fitted using an Excel solver. The fit of the model was then established by the partial F-test and p-value. The final models were integrated to generate the following final service model.

Further validation of the models showed well-predicted corrosion depth. These results show the assumption that mortar durability could be predicted from porosity, UCS, ANC, binder hydrations (C-S-H, C-A-S-H, C-N-A-S-H, and N-A-S-H), and chemical composition of aggregate (CaO, SiO_2, and Al_2O_3) and service life of the mortar exposed to specific corrosivity conditions as defined by sewer environmental conditions could be predicted from H_2S, CO_2, temperature, and %RH with 95% confidence level.

The service life prediction model can be utilised for selecting alkali-activated mortar, including geopolymer, by inputting the chemical and physical properties of the specific alkali-activated mortar, including the geopolymer and sewer environmental conditions. The model output presented the predicted corrosion depth over time at particular chemical and physical properties and exposure to live sewer environmental conditions. This selection method ensures the lining mortar is appropriate for the sewer application in the desired service life.

7.2 RECOMMENDATIONS

1. Accelerated corrosion test in the laboratory – The acid immersion test conducted in this study focused exclusively on using sulphuric acid at pH 1 to simulate corrosive conditions. However, it is essential to acknowledge that in real corrosion scenarios, the presence of carbon dioxide (CO_2) can also contribute to the deterioration of the lining mortar. Therefore, incorporating carbonation before the acid corrosion test would provide valuable information regarding the combination of corrosion mechanisms between carbonation and acid attacks. This test could enhance our understanding of the overall corrosion mechanism.

2. Service life prediction model – This study has successfully developed an empirical service life prediction model for lining alkali-activated mortar, including geopolymer, based on a specific set of sewer environmental conditions and the chemical and physical properties of the lining mortar, including geopolymer mortar. However, it is essential to note that the predictive model can be improved by expanding the scope of the study. Increasing the number of sample observations and including a wider range of alkali-activated mortars will provide a more comprehensive dataset, leading to a more accurate and reliable service life prediction model. Therefore, future research should aim to broaden the sample size and incorporate different types of alkali-activated mortars to refine further and validate the service life prediction model.

8 REFERENCES

14429, C. T. 2005. CHARACTERIZATION OF WASTE - LEACHING BEHAVIOUR TESTS - INFLUENCE OF PH ON LEACHING WITH INITIAL ACID/BASE ADDITION. Comite Europeen de Normalisation.

ABALOUCH, I., SAKAMI, S., ELABBASSI, F.-E. & BOUKHATTEM, L. 2021. Effects of Recycled Fine Glass Aggregates on Alkali Silica Reaction and Thermo-Mechanical Behavior of Modified Concrete. *Applied Sciences* [Online], 11.

ABOULAYT, A., SOUAYFAN, F., ROZIERE, E., JAAFRI, R., CHERKI EL IDRISSI, A., MOUSSA, R., JUSTINO, C. & LOUKILI, A. 2020. Alkali-activated grouts based on slag-fly ash mixtures: From early-age characterization to long-term phase composition. *Construction and Building Materials,* 260**,** 120510.

ACI-201 2001. Guide to Durable Concrete. *In:* COMMITTEE, A. C. I. (ed.). Farmington Hills, MI, USA,.

ADESANYA, E., EZU, A., NGUYEN, H., RÖßLER, C., SREENIVASAN, H., OHENOJA, K., KINNUNEN, P. & ILLIKAINEN, M. 2023. Hydration of blended ladle slag and calcium aluminate cement. *Journal of Building Engineering,* 66**,** 105855.

ADESANYA, E., OHENOJA, K., LUUKKONEN, T., KINNUNEN, P. & ILLIKAINEN, M. 2018. One-part geopolymer cement from slag and pretreated paper sludge. *Journal of Cleaner Production,* 185**,** 168-175.

AHMAD, M. R., LAO, J., DAI, J.-G., XUAN, D. & POON, C. S. 2022. Upcycling of air pollution control residue waste into cementitious product through geopolymerization technology. *Resources, Conservation and Recycling,* 181**,** 106231.

AIKEN, T. A., KWASNY, J., SHA, W. & SOUTSOS, M. N. 2018. Effect of slag content and activator dosage on the resistance of fly ash geopolymer binders to sulfuric acid attack. *Cement and Concrete Research,* 111**,** 23-40.

AL-SWAIDANI, A. M., ALIYAN, S. D. & ADARNALY, N. 2016. Mechanical strength development of mortars containing volcanic scoria-based binders with different fineness. *Engineering Science and Technology, an International Journal,* 19**,** 970-979.

ALBITAR, M., MOHAMED ALI, M. S., VISINTIN, P. & DRECHSLER, M. 2017. Durability evaluation of geopolymer and conventional concretes. *Construction and Building Materials,* 136**,** 374-385.

ALEXANDER, A. E. & SHASHIKALA, A. P. 2022. Studies on the microstructure and durability characteristics of ambient cured FA-GGBS based geopolymer mortar. *Construction and Building Materials,* 347**,** 128538.

ALEXANDER, M. G. & FOURIE, C. 2011. Performance of sewer pipe concrete mixtures with portland and calcium aluminate cements subject to mineral and biogenic acid attack. *Materials and Structures,* 44**,** 313-330.

ALI, H. A., XUAN, D., LU, J.-X. & POON, C. S. 2022. Enhancing the resistance to microbial induced corrosion of alkali-activated glass powder/GGBS mortars by calcium aluminate cement. *Construction and Building Materials,* 341**,** 127912.

ALIQUES-GRANERO, J., TOGNONVI, M. T. & TAGNIT-HAMOU, A. 2019. Durability study of AAMs: Sulfate attack resistance. *Construction and Building Materials,* 229**,** 117100.

ALLAHVERDI, A. & SKVARA, F. 2001. Nitric acid attack on hardened paste of geopolymeric cements, Part 2. *Ceramics Silikaty,* 45**,** 143-150.

ALZEEBAREE, R., ÇEVIK, A., NEMATOLLAHI, B., SANJAYAN, J., MOHAMMEDAMEEN, A. & GÜLŞAN, M. E. 2019. Mechanical properties and durability of unconfined and confined geopolymer concrete with fiber reinforced

polymers exposed to sulfuric acid. *Construction and Building Materials,* 215**,** 1015-1032.
ALZRAIEE, H., BAKRY, I. & ZAYED, T. 2015. Destructive Analysis-Based Testing for Cured-in-Place Pipe. *Journal of Performance of Constructed Facilities,* 29**,** 04014095.
AMRAN, Y. H. M., ALYOUSEF, R., ALABDULJABBAR, H. & EL-ZEADANI, M. 2020. Clean production and properties of geopolymer concrete; A review. *Journal of Cleaner Production,* 251**,** 119679.
ANA, E., BAUWENS, W., PESSEMIER, M., THOEYE, C., SMOLDERS, S., BOONEN, I. & DE GUELDRE, G. 2009. An investigation of the factors influencing sewer structural deterioration. *Urban Water Journal,* 6**,** 303-312.
ARAGAW, T. A. 2018. *Concise Introduction to Cement Chemistry and Manufacturing,* San Rafael, UNITED STATES, Morgan & Claypool Publishers.
ARIFFIN, M. A. M., BHUTTA, M. A. R., HUSSIN, M. W., MOHD TAHIR, M. & AZIAH, N. 2013. Sulfuric acid resistance of blended ash geopolymer concrete. *Construction and Building Materials,* 43**,** 80-86.
ARULMOLY, B., KONTHESINGHA, C. & NANAYAKKARA, A. 2021. Performance evaluation of cement mortar produced with manufactured sand and offshore sand as alternatives for river sand. *Construction and Building Materials,* 297**,** 123784.
AS1012.9:2014 2014. AS 1012.9:2014: Methods of testing concrete, Method 9: Compressive strength tests - Concrete, mortar and grout specimens. https://subscriptions.techstreet.com/products/825025: Standards Australia.
ASSI, L. N., CARTER, K., DEAVER, E. & ZIEHL, P. 2020. Review of availability of source materials for geopolymer/sustainable concrete. *Journal of Cleaner Production,* 263**,** 121477.
ASSI, L. N., EDDIE DEAVER, E. & ZIEHL, P. 2018. Effect of source and particle size distribution on the mechanical and microstructural properties of fly Ash-Based geopolymer concrete. *Construction and Building Materials,* 167**,** 372-380.
ASTM-C39/C39M-21 2021. Standard Test Method for Compressive Strength of Cylindrical Concrete Specimens. ASTM International: ASTM International.
ASTM-C109/C109M-21 2021. C109/C109M − 21:Standard Test Method for Compressive Strength of Hydraulic Cement Mortars (Using 2-in. or [50 mm] Cube Specimens). ASTM International: ASTM International.
ASTM-C144-18 2019. Standard Specification for Aggregate for Masonry Mortar. ASTM International: ASTM International.
ASTM-C618 2022. ASTM C618-22: Standard Specification for Coal Fly Ash and Raw or Calcined Natural Pozzolan for Use in Concrete. ASTM International: ASTM International.
ASTM-C642 2013. Standard Test Method for Density, Absorption, and Voids in Hardened Concrete. ASTM International.
ASTMC192/C192M 2019. ASTM C192/C192M −19 Standard Practice for Making and Curing Concrete Test Specimens in the Laboratory. ASTM International: ASTM International.
ATIŞ, C. D., GÖRÜR, E. B., KARAHAN, O., BILIM, C., İLKENTAPAR, S. & LUGA, E. 2015. Very high strength (120MPa) class F fly ash geopolymer mortar activated at different NaOH amount, heat curing temperature and heat curing duration. *Construction and Building Materials,* 96**,** 673-678.
ATTIOGBE, E. K. & RIZKALLA, S. H. 1988. RESPONSE OF CONCRETE TO SULFURIC-ACID ATTACK. *Aci Materials Journal,* 85**,** 481-488.
AUGUET, O., PIJUAN, M., BATISTA, J., BORREGO, C. M., GUTIERREZ, O. & VOORDOUW, G. 2015. Changes in Microbial Biofilm Communities during

Colonization of Sewer Systems. *Applied and Environmental Microbiology,* 81**,** 7271-7280.
AUSTRALIA, C. I. O. 2010. Shotcreting in Australia, Second Edition. TechMedia Publishing Pty Ltd.
AZIZ, I. H., ABDULLAH, M. M. A. B., MOHD SALLEH, M. A. A., AZIMI, E. A., CHAIPRAPA, J. & SANDU, A. V. 2020. Strength development of solely ground granulated blast furnace slag geopolymers. *Construction and Building Materials,* 250**,** 118720.
BADAPALLI, P. K., KOTTALA, R. B., RAJASEKHAR, M., RAMACHANDRA, M. & KRUPAVATHI, C. 2022. Modeling of comparative studies on surface micro morphology of Aeolian, River, Lake, and Beach sand samples using SEM and EDS/EDAX. *Materials Today: Proceedings,* 50**,** 655-660.
BARTON, L. L. & FAUQUE, G. D. 2009. Chapter 2 Biochemistry, Physiology and Biotechnology of Sulfate-Reducing Bacteria. *Advances in Applied Microbiology.* Academic Press.
BASHAR, I. I., ALENGARAM, U. J., JUMAAT, M. Z. & ISLAM, A. 2014. The effect of variation of molarity of alkali activator and fine aggregate content on the compressive strength of the fly ash: palm oil fuel ash based geopolymer mortar. *Advances in Materials Science and Engineering,* 2014.
BEAINO, S., EL HAGE, P., SONNIER, R., SEIF, S. & EL HAGE, R. 2022. Novel Foaming-Agent Free Insulating Geopolymer Based on Industrial Fly Ash and Rice Husk. *Molecules* [Online], 27.
BEALL, C. 2012. Mortar and Grout. *Masonry Design and Detailing.* 6th ed. ed. New York: McGraw-Hill Education.
BEDDOE, R. E. & DORNER, H. W. 2005. Modelling acid attack on concrete: Part I. The essential mechanisms. *Cement and Concrete Research,* 35**,** 2333-2339.
BEHNOOD, A., VAN TITTELBOOM, K. & DE BELIE, N. 2016. Methods for measuring pH in concrete: A review. *Construction and Building Materials,* 105**,** 176-188.
BERGADO, D., ANDERSON, L., MIURA, N. & BALASUBRAMANIAM, A. Soft ground improvement in lowland and other environments. 1996. AsCE.
BERGER, C., LOHAUS, J., WITTNER, A. & SCHÄFER, R. 2003. Zustand der Kanalisation in Deutschland. *WASSERWIRTSCHAFT WASSERTECHNIK***,** 10-17.
BERNAL, S. A., PROVIS, J. L., WALKLEY, B., SAN NICOLAS, R., GEHMAN, J. D., BRICE, D. G., KILCULLEN, A. R., DUXSON, P. & VAN DEVENTER, J. S. 2013. Gel nanostructure in alkali-activated binders based on slag and fly ash, and effects of accelerated carbonation. *Cement and Concrete Research,* 53**,** 127-144.
BERTRON, A. 2013. General Introduction to Part I. *Performance of Cement-Based Materials in Aggressive Aqueous Environments.*
BICZOK, I. & BLASOVSZKY, N. 1964. Concrete corrosion and concrete protection.
BROUGH, A. R. & ATKINSON, A. 2002. Sodium silicate-based, alkali-activated slag mortars: Part I. Strength, hydration and microstructure. *Cement and Concrete Research,* 32**,** 865-879.
C1894-19, A. 2019. Standard Guide for Microbially Induced Corrosion of Concrete Products. ASTM: ASTM.
CALISKAN, S. 2003. Aggregate/mortar interface: influence of silica fume at the micro- and macro-level. *Cement and Concrete Composites,* 25**,** 557-564.
CAO, Y.-F., TAO, Z., PAN, Z. & WUHRER, R. 2018. Effect of calcium aluminate cement on geopolymer concrete cured at ambient temperature. *Construction and Building Materials,* 191**,** 242-252.

CASTILLO, H., COLLADO, H., DROGUETT, T., SÁNCHEZ, S., VESELY, M., GARRIDO, P. & PALMA, S. 2021. Factors affecting the compressive strength of geopolymers: A review. *Minerals,* 11**,** 1317.

CERNY, R. & ROVNANIKOVA, P. 2002. *Transport Processes in Concrete,* London, CRC Press.

CHATVEERA, B. & LERTWATTANARUK, P. 2014. Evaluation of nitric and acetic acid resistance of cement mortars containing high-volume black rice husk ash. *Journal of environmental management,* 133**,** 365-373.

CHEN, K., WU, D., FEI, S., PAN, C., SHEN, X., ZHANG, C. & HU, J. 2022. Resistance of blended alkali-activated fly ash-OPC mortar to mild-concentration sulfuric and acetic acid attack. *Environmental Science and Pollution Research***,** 1-15.

CHEN, K., WU, D., XIA, L., CAI, Q. & ZHANG, Z. 2021. Geopolymer concrete durability subjected to aggressive environments – A review of influence factors and comparison with ordinary Portland cement. *Construction and Building Materials,* 279**,** 122496.

CHEN, M.-C., WANG, K. & XIE, L. 2013. Deterioration mechanism of cementitious materials under acid rain attack. *Engineering Failure Analysis,* 27**,** 272-285.

CHINDAPRASIRT, P., HOMWUTTIWONG, S. & SIRIVIVATNANON, V. 2004. Influence of fly ash fineness on strength, drying shrinkage and sulfate resistance of blended cement mortar. *Cement and Concrete Research,* 34**,** 1087-1092.

CHINDAPRASIRT, P., PAISITSRISAWAT, P. & RATTANASAK, U. 2014. Strength and resistance to sulfate and sulfuric acid of ground fluidized bed combustion fly ash–silica fume alkali-activated composite. *Advanced Powder Technology,* 25**,** 1087-1093.

CHO, K. S. & MORI, T. 1995. A NEWLY ISOLATED FUNGUS PARTICIPATES IN THE CORROSION OF CONCRETE SEWER PIPES. *Water Science and Technology,* 31**,** 263-271.

CHOWDHURY, S., MOHAPATRA, S., GAUR, A., DWIVEDI, G. & SONI, A. 2021. Study of various properties of geopolymer concrete – A review. *Materials Today: Proceedings,* 46**,** 5687-5695.

CHUGHTAI, F. & ZAYED, T. 2008. Infrastructure condition prediction models for sustainable sewer pipelines. *Journal of Performance of Constructed Facilities,* 22**,** 333-341.

CIOFFI, R., MAFFUCCI, L. & SANTORO, L. 2003. Optimization of geopolymer synthesis by calcination and polycondensation of a kaolinitic residue. *Resources, Conservation and Recycling,* 40**,** 27-38.

COHEN, M. D. & MATHER, B. 1991. SULFATE ATTACK ON CONCRETE - RESEARCH NEEDS. *Aci Materials Journal,* 88**,** 62-69.

COLLEPARDI, M. 2003. A state-of-the-art review on delayed ettringite attack on concrete. *Cement & Concrete Composites,* 25**,** 401-407.

CONG, P. & CHENG, Y. 2021. Advances in geopolymer materials: A comprehensive review. *Journal of Traffic and Transportation Engineering (English Edition),* 8**,** 283-314.

CONG, P. & MEI, L. 2021. Using silica fume for improvement of fly ash/slag based geopolymer activated with calcium carbide residue and gypsum. *Construction and Building Materials,* 275**,** 122171.

CONG, T. D., PHUONG, T., VU, M. T. & NGUYEN, T. H. 2023. Effect of Calcium Hydroxide on Compressive Strength and Microstructure of Geopolymer Containing Admixture of Kaolin, Fly Ash, and Red Mud. *Applied Sciences* [Online], 13.

CRIADO, M., FERNÁNDEZ-JIMÉNEZ, A. & PALOMO, A. 2007. Alkali activation of fly ash: Effect of the SiO2/Na2O ratio: Part I: FTIR study. *Microporous and mesoporous materials,* 106**,** 180-191.

CWIRZEN, A. 2020. 10 - Properties of SCC with industrial by-products as aggregates. *In:* SIDDIQUE, R. (ed.) *Self-Compacting Concrete: Materials, Properties and Applications.* Woodhead Publishing.

DAMION, T., CEPURITIS, R. & CHAUNSALI, P. 2022. Sulfuric acid and citric acid attack of calcium sulfoaluminate-based binders. *Cement and Concrete Composites,* 130**,** 104524.

DAMION, T. & CHAUNSALI, P. 2022. Evaluating acid resistance of Portland cement, calcium aluminate cement, and calcium sulfoaluminate based cement using acid neutralisation. *Cement and Concrete Research,* 162**,** 107000.

DAMVERGIS, C. 2014. Sewer systems: Failures and rehabilitation. *Water Utility Journal,* 8**,** 17-24.

DARVISH, P., ALENGARAM, U. J., POH, Y. S., IBRAHIM, S. & YUSOFF, S. 2020. Performance evaluation of palm oil clinker sand as replacement for conventional sand in geopolymer mortar. *Construction and Building Materials,* 258**,** 120352.

DAVIDOVITS, J. 1991. Geopolymers: inorganic polymeric new materials. *Journal of Thermal Analysis and calorimetry,* 37**,** 1633-1656.

DAVIDOVITS, J. Properties of geopolymer cements. First international conference on alkaline cements and concretes, 1994. Kiev State Technical University, Ukraine: Scientific Research Institute on …, 131-149.

DAVIDOVITS, J. 2020. Geopolymer Chemistry and Applications. 5-th edition. *J. Davidovits.–Saint-Quentin, France,* 5.

DAVIDOVITS, J. & CORDI, S. 1979. Synthesis of new high temperature geo-polymers for reinforced plastics/composites. *Spe Pactec,* 79**,** 151-154.

DAVIS, J. L., NICA, D., SHIELDS, K. & ROBERTS, D. J. 1998. Analysis of concrete from corroded sewer pipe. *International Biodeterioration & Biodegradation,* 42**,** 75-84.

DE BELIE, N., MONTENY, J., BEELDENS, A., VINCKE, E., VAN GEMERT, D. & VERSTRAETE, W. 2004. Experimental research and prediction of the effect of chemical and biogenic sulfuric acid on different types of commercially produced concrete sewer pipes. *Cement and Concrete Research,* 34**,** 2223-2236.

DE SCHUTTER, G. & POPPE, A. M. 2004. Quantification of the water demand of sand in mortar. *Construction and Building Materials,* 18**,** 517-521.

DIAMOND, S. & KINTER, E. B. 1965. Mechanisms of soil-lime stabilization. *Highway research record,* 92**,** 83-102.

DONG, J., WANG, L. & ZHANG, T. 2014. Study on the strength development, hydration process and carbonation process of NaOH-activated Pisha Sandstone. *Construction and Building Materials,* 66**,** 154-162.

DORNER, H. Acid resistance of high performance concrete. 38th research colloquium, German Committee for Reinforced Concrete (DAfStb), Munich, 2000. 77-86.

DORNER, H. & BEDDOE, R. Prognosis of concrete corrosion due to acid attack. 9th International Conference of Building Materials, Brisbane, Australia, 2002.

DUAN, P., YAN, C. & ZHOU, W. 2017. Compressive strength and microstructure of fly ash based geopolymer blended with silica fume under thermal cycle. *Cement and Concrete Composites,* 78**,** 108-119.

DUXSON, P. 2009. 3 - Geopolymer precursor design. *In:* PROVIS, J. L. & VAN DEVENTER, J. S. J. (eds.) *Geopolymers.* Woodhead Publishing.

DUXSON, P., FERNÁNDEZ-JIMÉNEZ, A., PROVIS, J. L., LUKEY, G. C., PALOMO, A. & VAN DEVENTER, J. S. J. 2006. Geopolymer technology: the current state of the art. *Journal of Materials Science,* 42**,** 2917-2933.

DUXSON, P., PROVIS, J. L., LUKEY, G. C., SEPAROVIC, F. & VAN DEVENTER, J. S. J. 2005. 29Si NMR Study of Structural Ordering in Aluminosilicate Geopolymer Gels. *Langmuir,* 21**,** 3028-3036.

EL MOGAHZY, Y. E. 2009. 13 - Development of technical textile products: materials and applications. *In:* EL MOGAHZY, Y. E. (ed.) *Engineering Textiles.* Woodhead Publishing.

ELSALAMAWY, M., MOHAMED, A. R. & KAMAL, E. M. 2019. The role of relative humidity and cement type on carbonation resistance of concrete. *Alexandria Engineering Journal,* 58**,** 1257-1264.

EN14429:2015 2015. Characterization of Waste–Leaching Behaviour Tests–Influence of pH on Leaching with Initial Acid/base Addition. European Committee for Standardization (CEN): European Committee for Standardization (CEN).

FAN, W., ZHUGE, Y., MA, X., CHOW, C. W. K., GORJIAN, N., OH, J.-A. & DUAN, W. 2020. Durability of Fibre-Reinforced Calcium Aluminate Cement (CAC)–Ground Granulated Blast Furnace Slag (GGBFS) Blended Mortar after Sulfuric Acid Attack. *Materials,* 13**,** 3822.

FAN, Y., HU, Z. & LUAN, H. 2012. Deterioration of tensile behavior of concrete exposed to artificial acid rain environment. *Interaction and multiscale mechanics,* 5**,** 41-56.

FENNER, R. A. 2000. Approaches to sewer maintenance: a review. *Urban Water,* 2**,** 343-356.

FERNÁNDEZ-JIMÉNEZ, A. & PALOMO, A. 2005. Mid-infrared spectroscopic studies of alkali-activated fly ash structure. *Microporous and Mesoporous Materials,* 86**,** 207-214.

FLETCHER, R. A., MACKENZIE, K. J. D., NICHOLSON, C. L. & SHIMADA, S. 2005. The composition range of aluminosilicate geopolymers. *Journal of the European Ceramic Society,* 25**,** 1471-1477.

FOŘT, J., NOVOTNÝ, R., VEJMELKOVÁ, E., TRNÍK, A., ROVNANÍKOVÁ, P., KEPPERT, M., POMMER, V. & ČERNÝ, R. 2019. Characterization of geopolymers prepared using powdered brick. *Journal of Materials Research and Technology,* 8**,** 6253-6261.

GAMEIRO, A., SANTOS SILVA, A., FARIA, P., GRILO, J., BRANCO, T., VEIGA, R. & VELOSA, A. 2014. Physical and chemical assessment of lime–metakaolin mortars: Influence of binder:aggregate ratio. *Cement and Concrete Composites,* 45**,** 264-271.

GAO, X., YU, Q. L., LAZARO, A. & BROUWERS, H. J. H. 2017. Investigation on a green olivine nano-silica source based activator in alkali activated slag-fly ash blends: Reaction kinetics, gel structure and carbon footprint. *Cement and Concrete Research,* 100**,** 129-139.

GARBACZ, A., COURARD, L. & KOSTANA, K. 2006. Characterization of concrete surface roughness and its relation to adhesion in repair systems. *Materials Characterization,* 56**,** 281-289.

GARBACZ, A., GÓRKA, M. & COURARD, L. 2005. Effect of concrete surface treatment on adhesion in repair systems. *Magazine of Concrete Research,* 57**,** 49-60.

GARCÍA-LODEIRO, I., FERNÁNDEZ-JIMÉNEZ, A., BLANCO, M. T. & PALOMO, A. 2008. FTIR study of the sol–gel synthesis of cementitious gels: C–S–H and N–A–S–H. *Journal of Sol-Gel Science and Technology,* 45**,** 63-72.

GARCÍA-LODEIRO, I., FERNÁNDEZ-JIMÉNEZ, A. & PALOMO, A. 2013. Variation in hybrid cements over time. Alkaline activation of fly ash–portland cement blends. *Cement and Concrete Research,* 52**,** 112-122.

GIAMPAOLO, C., LO MASTRO, S., POLETTINI, A., POMI, R. & SIRINI, P. 2002a. Acid neutralisation capacity and hydration behaviour of incineration bottom ash-Portland cement mixtures. *Cement and Concrete Research,* 32**,** 769-775.

GIAMPAOLO, C., MASTRO, S. L., POLETTINI, A., POMI, R. & SIRINI, P. 2002b. Acid neutralisation capacity and hydration behaviour of incineration bottom ash–Portland cement mixtures. *Cement and Concrete Research,* 32**,** 769-775.

GOMAA, E., SARGON, S., KASHOSI, C., GHENI, A. & ELGAWADY, M. A. 2020. Mechanical Properties of High Early Strength Class C Fly Ash-Based Alkali Activated Concrete. *Transportation Research Record,* 2674**,** 430-443.

GÖRHAN, G. & KÜRKLÜ, G. 2014. The influence of the NaOH solution on the properties of the fly ash-based geopolymer mortar cured at different temperatures. *Composites Part B: Engineering,* 58**,** 371-377.

GOROSPE, K., BOOYA, E., GHAEDNIA, H. & DAS, S. 2019. Effect of various glass aggregates on the shrinkage and expansion of cement mortar. *Construction and Building Materials,* 210**,** 301-311.

GRENGG, C., MITTERMAYR, F., UKRAINCZYK, N., KORAIMANN, G., KIENESBERGER, S. & DIETZEL, M. 2018. Advances in concrete materials for sewer systems affected by microbial induced concrete corrosion: A review. *Water Res,* 134**,** 341-352.

GRENGG, C., UKRAINCZYK, N., KORAIMANN, G., MUELLER, B., DIETZEL, M. & MITTERMAYR, F. 2020. Long-term in situ performance of geopolymer, calcium aluminate and Portland cement-based materials exposed to microbially induced acid corrosion. *Cement and Concrete Research,* 131**,** 106034.

GU, J.-D. 2003. Microbiological deterioration and degradation of synthetic polymeric materials: recent research advances. *International Biodeterioration & Biodegradation,* 52**,** 69-91.

GU, J. D., LU, C., MITCHELL, R., THORP, K. & CRASTO, A. 1997. Fungal degradation of fiber-reinforced composite materials. *Materials Performance,* 36**,** 37-42.

GUO, X., SHI, H. & DICK, W. A. 2010. Compressive strength and microstructural characteristics of class C fly ash geopolymer. *Cement and Concrete Composites,* 32**,** 142-147.

GUTIERREZ, O., MOHANAKRISHNAN, J., SHARMA, K. R., MEYER, R. L., KELLER, J. & YUAN, Z. 2008. Evaluation of oxygen injection as a means of controlling sulfide production in a sewer system. *Water research,* 42**,** 4549-4561.

GUTIERREZ, O., SUDARJANTO, G., REN, G., GANIGUE, R., JIANG, G. & YUAN, Z. 2014. Assessment of pH shock as a method for controlling sulfide and methane formation in pressure main sewer systems. *Water Res,* 48**,** 569-78.

HADI, M. N. S., AL-AZZAWI, M. & YU, T. 2018. Effects of fly ash characteristics and alkaline activator components on compressive strength of fly ash-based geopolymer mortar. *Construction and Building Materials,* 175**,** 41-54.

HAJIMOHAMMADI, A., PROVIS, J. L. & VAN DEVENTER, J. S. J. 2008. One-Part Geopolymer Mixes from Geothermal Silica and Sodium Aluminate. *Industrial & Engineering Chemistry Research,* 47**,** 9396-9405.

HAJIMOHAMMADI, A., PROVIS, J. L. & VAN DEVENTER, J. S. J. 2010. Effect of Alumina Release Rate on the Mechanism of Geopolymer Gel Formation. *Chemistry of Materials,* 22**,** 5199-5208.

HANJITSUWAN, S., PHOO-NGERNKHAM, T. & DAMRONGWIRIYANUPAP, N. 2017. Comparative study using Portland cement and calcium carbide residue as a promoter in bottom ash geopolymer mortar. *Construction and Building Materials,* 133**,** 128-134.

HARDJITO, D., CHEAK, C. C. & ING, C. L. 2008. Strength and setting times of low calcium fly ash-based geopolymer mortar. *Modern applied science,* 2**,** 3-11.

HARDJITO, D., WALLAH, S. E., SUMAJOUW, D. M. & RANGAN, B. V. 2004. On the development of fly ash-based geopolymer concrete. *Materials Journal,* 101**,** 467-472.

HAWARI, A., ALKADOUR, F., ELMASRY, M. & ZAYED, T. 2017. Simulation-Based Condition Assessment Model for Sewer Pipelines. *Journal of Performance of Constructed Facilities,* 31**,** 04016066.

HAWARI, A., ALKADOUR, F., ELMASRY, M. & ZAYED, T. 2020. A state of the art review on condition assessment models developed for sewer pipelines. *Engineering Applications of Artificial Intelligence,* 93**,** 103721.

HE, J., JIE, Y., ZHANG, J., YU, Y. & ZHANG, G. 2013. Synthesis and characterization of red mud and rice husk ash-based geopolymer composites. *Cement and Concrete Composites,* 37**,** 108-118.

HE, P., ZHANG, B., LU, J.-X. & POON, C. S. 2021. Reaction mechanisms of alkali-activated glass powder-ggbs-CAC composites. *Cement and Concrete Composites,* 122**,** 104143.

HEIKAL, M., RADWAN, M. M. & AL-DUAIJ, O. K. 2015. Physico-mechanical characteristics and durability of calcium aluminate blended cement subject to different aggressive media. *Construction and Building Materials,* 78**,** 379-385.

HERNANDEZ, M., MARCHAND, E. A., ROBERTS, D. & PECCIA, J. 2002. In situ assessment of active Thiobacillus species in corroding concrete sewers using fluorescent RNA probes. *International Biodeterioration & Biodegradation,* 49**,** 271-276.

HERRMANN, A., KOENIG, A. & DEHN, F. 2018. Structural concrete based on alkali-activated binders: Terminology, reaction mechanisms, mix designs and performance. *Structural Concrete,* 19**,** 918-929.

HEWLETT, P. & LISKA, M. 2019. *Lea's chemistry of cement and concrete*, Butterworth-Heinemann.

HOSAN, A., HAQUE, S. & SHAIKH, F. 2016. Compressive behaviour of sodium and potassium activators synthetized fly ash geopolymer at elevated temperatures: A comparative study. *Journal of Building Engineering,* 8**,** 123-130.

HUDON, E., MIRZA, S. & FRIGON, D. 2011. Biodeterioration of Concrete Sewer Pipes: State of the Art and Research Needs. *Journal of Pipeline Systems Engineering and Practice,* 2**,** 42-52.

HUMAD, A. M., KOTHARI, A., PROVIS, J. L. & CWIRZEN, A. 2019. The Effect of Blast Furnace Slag/Fly Ash Ratio on Setting, Strength, and Shrinkage of Alkali-Activated Pastes and Concretes. *Frontiers in Materials,* 6.

HUO, R., LI, S. & DING, Y. 2018. Experimental Study on Physicochemical and Mechanical Properties of Mortar Subjected to Acid Corrosion. *Advances in Materials Science and Engineering,* 2018**,** 3283907.

HUSEIEN, G. F., MIRZA, J., ISMAIL, M., GHOSHAL, S. K. & ARIFFIN, M. A. M. 2018. Effect of metakaolin replaced granulated blast furnace slag on fresh and early strength properties of geopolymer mortar. *Ain Shams Engineering Journal,* 9**,** 1557-1566.

HVITVED-JACOBSEN, T. 2001. *Sewer processes: microbial and chemical process engineering of sewer networks*, CRC press.

HVITVED-JACOBSEN, T., VOLLERTSEN, J. & NIELSEN, A. H. 2013. *Sewer processes: microbial and chemical process engineering of sewer networks*, CRC press.

HVITVED-JACOBSEN, T., VOLLERTSEN, J., YONGSIRI, C., NIELSEN, A. & ABDUL-TALIB, S. Sewer microbial processes, emissions and impacts. 3rd International Conference on sewer processes and networks, April, 2002. 15-17.

HYEOK-JUNG, K., KANG, S.-P. & CHOE, G.-C. 2018. Effect of red mud content on strength and efflorescence in pavement using alkali-activated slag cement. *International Journal of Concrete Structures and Materials,* 12**,** 1-9.

IBRAHIM, M. & MASLEHUDDIN, M. 2021. An overview of factors influencing the properties of alkali-activated binders. *Journal of Cleaner Production,* 286**,** 124972.

IDEKER, J. H., SCRIVENER, K. L., FRYDA, H. & TOUZO, B. 2019. 12 - Calcium Aluminate Cements. *In:* HEWLETT, P. C. & LISKA, M. (eds.) *Lea's Chemistry of Cement and Concrete (Fifth Edition).* Butterworth-Heinemann.

ISLAM, A., ALENGARAM, U. J., JUMAAT, M. Z. & BASHAR, I. I. 2014. The development of compressive strength of ground granulated blast furnace slag-palm oil fuel ash-fly ash based geopolymer mortar. *Materials & Design (1980-2015),* 56**,** 833-841.

ISLANDER, R. L., DEVINNY, J. S., MANSFELD, F., POSTYN, A. & HONG, S. 1991a. Microbial ecology of crown corrosion in sewers

Journal of Environmental Engineering-Asce, 117**,** 751-770.

ISLANDER, R. L., DEVINNY, J. S., MANSFELD, F., POSTYN, A. & HONG, S. 1991b. Microbial ecology of crown corrosion in sewers. *Journal of Environmental Engineering-Asce,* 117**,** 751-770.

ISMAIL, I., BERNAL, S. A., PROVIS, J. L., HAMDAN, S. & VAN DEVENTER, J. S. J. 2012. Microstructural changes in alkali activated fly ash/slag geopolymers with sulfate exposure. *Materials and Structures,* 46**,** 361-373.

ISMAIL, I., BERNAL, S. A., PROVIS, J. L., SAN NICOLAS, R., HAMDAN, S. & VAN DEVENTER, J. S. J. 2014. Modification of phase evolution in alkali-activated blast furnace slag by the incorporation of fly ash. *Cement and Concrete Composites,* 45**,** 125-135.

ISTUQUE, D. B., SORIANO, L., AKASAKI, J. L., MELGES, J. L. P., BORRACHERO, M. V., MONZÓ, J., PAYÁ, J. & TASHIMA, M. M. 2019. Effect of sewage sludge ash on mechanical and microstructural properties of geopolymers based on metakaolin. *Construction and Building Materials,* 203**,** 95-103.

JACOBS, F. 2019. Durability of concrete in structural members. *Beton- Und Stahlbetonbau,* 114**,** 383-391.

JAIN, V., BIESINGER, M. C. & LINFORD, M. R. 2018. The Gaussian-Lorentzian Sum, Product, and Convolution (Voigt) functions in the context of peak fitting X-ray photoelectron spectroscopy (XPS) narrow scans. *Applied Surface Science,* 447**,** 548-553.

JAMIL, M. S., LI, Z., ABUGHARARA, A. & BUTT, S. 2022. Effect of Particle Gradation on the Strength Properties of Cemented Paste Backfill (CPB).

JAVED, U., UDDIN AHMED SHAIKH, F. & KUMAR SARKER, P. 2022. Microstructural investigation of thermo-mechanically processed lithium slag for geopolymer precursor using various characterization techniques. *Construction and Building Materials,* 342**,** 127952.

JEGAN, M., ANNADURAI, R. & KANNAN RAJKUMAR, P. R. 2023. A state of the art on effect of alkali activator, precursor, and fibers on properties of geopolymer composites. *Case Studies in Construction Materials,* 18**,** e01891.

JENSEN, H., BIGGS, C. A. & KARUNAKARAN, E. 2016. The importance of sewer biofilms. *WIREs Water,* 3**,** 487-494.

JENSEN, H. S., NIELSEN, A. H., HVITVED-JACOBSEN, T. & VOLLERTSEN, J. 2009. Modeling of Hydrogen Sulfide Oxidation in Concrete Corrosion Products from Sewer Pipes. *Water Environment Research,* 81**,** 365-373.

JIA, L., GUO, J., ZHOU, Z., FU, Y. & YAO, K. 2019. Experimental investigation on strength development of lime stabilized loess. *RSC Advances,* 9**,** 19680-19689.

JIANG, G., KELLER, J. & BOND, P. L. 2014. Determining the long-term effects of H2S concentration, relative humidity and air temperature on concrete sewer corrosion. *Water Research,* 65**,** 157-169.

JIANG, G., SUN, X., KELLER, J. & BOND, P. L. 2015a. Identification of controlling factors for the initiation of corrosion of fresh concrete sewers. *Water Research,* 80**,** 30-40.

JIANG, G., SUN, X., KELLER, J. & BOND, P. L. 2015b. Identification of controlling factors for the initiation of corrosion of fresh concrete sewers. *Water Res,* 80**,** 30-40.

JIANG, G. M., KELLER, J., BOND, P. L. & YUAN, Z. G. 2016. Predicting concrete corrosion of sewers using artificial neural network. *Water Research,* 92**,** 52-60.

JIANG, T. & JIN, Y. 2022. Phase Analysis of Alkali-Activated Slag Hybridized with Low-Calcium and High-Calcium Fly Ash. *Sustainability* [Online], 14.

JOBBÁGY, M. & REGAZZONI, A. E. 2011. Dissolution of nano-size Mg–Al–Cl hydrotalcite in aqueous media. *Applied Clay Science,* 51**,** 366-369.

JOHN, S. K., NADIR, Y. & GIRIJA, K. 2021. Effect of source materials, additives on the mechanical properties and durability of fly ash and fly ash-slag geopolymer mortar: A review. *Construction and Building Materials,* 280**,** 122443.

JONKERS, H. M. & SCHLANGEN, E. 2008. Development of a bacteria-based self healing concrete. *Tailor Made Concrete Structures,* 1**,** 425-430.

JOSEPH, A. P., KELLER, J., BUSTAMANTE, H. & BOND, P. L. 2012. Surface neutralization and H2S oxidation at early stages of sewer corrosion: Influence of temperature, relative humidity and H2S concentration. *Water Research,* 46**,** 4235-4245.

KAPELUSZNA, E., KOTWICA, Ł., RÓŻYCKA, A. & GOŁEK, Ł. 2017. Incorporation of Al in C-A-S-H gels with various Ca/Si and Al/Si ratio: Microstructural and structural characteristics with DTA/TG, XRD, FTIR and TEM analysis. *Construction and Building Materials,* 155**,** 643-653.

KARRI, S. K., PONNADA, M. R. & VEERNI, L. 2022. Development of eco-friendly GGBS and SF based alkali-activated mortar with quartz sand. *Journal of Building Pathology and Rehabilitation,* 7**,** 100.

KAUFMANN, J., FRECH, K., SCHUETZ, P. & MÜNCH, B. 2013. Rebound and orientation of fibers in wet sprayed concrete applications. *Construction and Building Materials,* 49**,** 15-22.

KAUR, M., SINGH, J. & KAUR, M. 2018. Synthesis of fly ash based geopolymer mortar considering different concentrations and combinations of alkaline activator solution. *Ceramics International,* 44**,** 1534-1537.

KAUSHAL, V., NAJAFI, M., LOVE, J. & QASIM SYED, R. 2020. Microbiologically Induced Deterioration and Protection of Concrete in Municipal Sewerage System: Technical Review. *Journal of Pipeline Systems Engineering and Practice,* 11**,** 03119002.

KHALE, D. & CHAUDHARY, R. 2007. Mechanism of geopolymerization and factors influencing its development: a review. *Journal of Materials Science,* 42**,** 729-746.

KHALIQ, W. & KHAN, H. A. 2015. High temperature material properties of calcium aluminate cement concrete. *Construction and Building Materials,* 94**,** 475-487.

KHAN, H. A. 2019. *Durability of alkali-activated mortar in sewage environment.* UNSW Sydney.

KHAN, H. A., CASTEL, A. & KHAN, M. S. 2020a. Corrosion investigation of fly ash based geopolymer mortar in natural sewer environment and sulphuric acid solution. *Corrosion Science,* 168**,** 108586.

KHAN, H. A., CASTEL, A. & KHAN, M. S. H. 2020b. Corrosion investigation of fly ash based geopolymer mortar in natural sewer environment and sulphuric acid solution. *Corrosion Science,* 168.

KHAN, H. A., CASTEL, A., KHAN, M. S. H. & MAHMOOD, A. H. 2019a. Durability of calcium aluminate and sulphate resistant Portland cement based mortars in aggressive sewer environment and sulphuric acid. *Cement and Concrete Research,* 124**,** 105852.

KHAN, H. A., KHAN, M. S., CASTEL, A. & SUNARHO, J. 2018. Deterioration of alkali-activated mortars exposed to natural aggressive sewer environment. *Construction and Building Materials,* 186**,** 577-597.

KHAN, I., XU, T., CASTEL, A., GILBERT, R. I. & BABAEE, M. 2019b. Risk of early age cracking in geopolymer concrete due to restrained shrinkage. *Construction and Building Materials,* 229**,** 116840.

KHATIB, J. M., BAALBAKI, O. & ELKORDI, A. A. 2018. 15 - Metakaolin. *In:* SIDDIQUE, R. & CACHIM, P. (eds.) *Waste and Supplementary Cementitious Materials in Concrete.* Woodhead Publishing.

KIM, D., YI, S. & LEE, W. Life cycle assessment of sewer system: Comparison of pipe materials. The World Congress on Advances in Civil, Environmental, and Materials Research, 2012.

KIM, T., KIM, J. H. & JUN, Y. 2019. Properties of Alkali-Activated Slag Paste Using New Colloidal Nano-Silica Mixing Method. *Materials* [Online], 12.

KIM, Y.-Y., LEE, K.-M., BANG, J.-W. & KWON, S.-J. 2014. Effect of W/C Ratio on Durability and Porosity in Cement Mortar with Constant Cement Amount. *Advances in Materials Science and Engineering,* 2014**,** 273460.

KLOPROGGE, J. T., DUONG, L. V., WOOD, B. J. & FROST, R. L. 2006. XPS study of the major minerals in bauxite: Gibbsite, bayerite and (pseudo-)boehmite. *Journal of Colloid and Interface Science,* 296**,** 572-576.

KNOTKOVÁ, D. K., K., 2007. Chapter 3: Corrosivity of atmo-spheres – derivation and use of information. *In:* MONCMANOVÁ, A. (ed.) *Environmental deterioration of materials.* Southhampton, Boston: WIT Press.

KODAGODA, S. & THIYAGARAJAN, K. 2018. Performance Monitoring of Liners: Parameter Identification. *Deliverables/31_UTS_Literature_Review_FINAL. pdf*.

KOHANKAR KOUCHESFEHANI, Z., DARABNOUSH TEHRANI, A., NAJAFI, M. & SYAR, J. 2020. Laboratory testing of invert-cut corrugated metal pipes renewed with polymeric spray applied pipe lining. *Transportation Geotechnics,* 25**,** 100413.

KOMLJENOVIĆ, M., TANASIJEVIĆ, G., DŽUNUZOVIĆ, N. & PROVIS, J. L. 2020. Immobilization of cesium with alkali-activated blast furnace slag. *Journal of Hazardous Materials,* 388**,** 121765.

KONG, L., ZHAO, W., XUAN, D., WANG, X. & LIU, Y. 2022. Application potential of alkali-activated concrete for antimicrobial induced corrosion: A review. *Construction and Building Materials,* 317**,** 126169.

KRIVENKO, P., DROCHYTKA, R., GELEVERA, A. & KAVALEROVA, E. 2014. Mechanism of preventing the alkali–aggregate reaction in alkali activated cement concretes. *Cement and Concrete Composites,* 45**,** 157-165.

KUMAR, S. & KUMAR, R. 2011. Mechanical activation of fly ash: Effect on reaction, structure and properties of resulting geopolymer. *Ceramics International,* 37**,** 533-541.

KUMAR, S., KUMAR, R. & MEHROTRA, S. P. 2010. Influence of granulated blast furnace slag on the reaction, structure and properties of fly ash based geopolymer. *Journal of Materials Science,* 45**,** 607-615.

KURDA, R., DE BRITO, J. & SILVESTRE, J. D. 2019. Carbonation of concrete made with high amount of fly ash and recycled concrete aggregates for utilization of CO2. *Journal of CO2 Utilization,* 29**,** 12-19.

KURDOWSKI, W. 2014. *Cement and concrete chemistry*, Springer Science & Business.

KURI, J. C., KHAN, M. N. N. & SARKER, P. K. 2022. Workability, strength and microstructural properties of ground ferronickel slag blended fly ash geopolymer mortar. *Journal of Sustainable Cement-Based Materials,* 11**,** 75-87.

LAFHAJ, Z., GOUEYGOU, M., DJERBI, A. & KACZMAREK, M. 2006. Correlation between porosity, permeability and ultrasonic parameters of mortar with variable water/cement ratio and water content. *Cement and Concrete Research,* 36**,** 625-633.

LAHOTI, M., TAN, K. H. & YANG, E.-H. 2019. A critical review of geopolymer properties for structural fire-resistance applications. *Construction and Building Materials,* 221**,** 514-526.

LECOMTE, I., HENRIST, C., LIÉGEOIS, M., MASERI, F., RULMONT, A. & CLOOTS, R. 2006. (Micro)-structural comparison between geopolymers, alkali-activated slag cement and Portland cement. *Journal of the European Ceramic Society,* 26**,** 3789-3797.

LEDUC, L. G. & FERRONI, G. D. 1994. THE CHEMOLITHOTROPHIC BACTERIUM THIOBACILLUS-FERROOXIDANS. *Fems Microbiology Reviews,* 14**,** 103-119.

LEE, L. S. & ESTRADA, H. 2020. Aggregates. *Materials for Civil Engineering: Properties and Applications in Infrastructure.* First edition. ed. New York: McGraw-Hill Education.

LEE, N. K. & LEE, H. K. 2016. Influence of the slag content on the chloride and sulfuric acid resistances of alkali-activated fly ash/slag paste. *Cement and Concrete Composites,* 72**,** 168-179.

LEE, W. & VAN DEVENTER, J. 2003. Use of infrared spectroscopy to study geopolymerization of heterogeneous amorphous aluminosilicates. *Langmuir,* 19**,** 8726-8734.

LEVENSPIEL, O. 1999. *Chemical Reaction Engineering,* New York, John Wiley & Sons.

LI, X., KAPPLER, U., JIANG, G. & BOND, P. L. 2017. The Ecology of Acidophilic Microorganisms in the Corroding Concrete Sewer Environment. *Frontiers in Microbiology,* 8**,** 683.

LI, Z., GAO, Y., ZHANG, J., ZHANG, C., CHEN, J. & LIU, C. 2021. Effect of particle size and thermal activation on the coal gangue based geopolymer. *Materials Chemistry and Physics,* 267**,** 124657.

LIEW, Y.-M., HEAH, C.-Y., MOHD MUSTAFA, A. B. & KAMARUDIN, H. 2016. Structure and properties of clay-based geopolymer cements: A review. *Progress in Materials Science,* 83**,** 595-629.

LIGUORI, B., CAPASSO, I., DE PERTIS, M., FERONE, C. & CIOFFI, R. 2017. Geopolymerization Ability of Natural and Secondary Raw Materials by Solubility Test in Alkaline Media. *Environments,* 4.

LING, A. L., ROBERTSON, C. E., HARRIS, J. K., FRANK, D. N., KOTTER, C. V., STEVENS, M. J., PACE, N. R. & HERNANDEZ, M. T. 2014. Carbon Dioxide and Hydrogen Sulfide Associations with Regional Bacterial Diversity Patterns in Microbially Induced Concrete Corrosion. *Environmental Science & Technology,* 48**,** 7357-7364.

LING, A. L., ROBERTSON, C. E., HARRIS, J. K., FRANK, D. N., KOTTER, C. V., STEVENS, M. J., PACE, N. R. & HERNANDEZ, M. T. 2015. High-Resolution Microbial Community Succession of Microbially Induced Concrete Corrosion in Working Sanitary Manholes. *PLOS ONE,* 10**,** e0116400.

LIU, J. & VIPULANANDAN, C. 2001. Evaluating a polymer concrete coating for protecting non-metallic underground facilities from sulfuric acid attack. *Tunnelling and Underground Space Technology,* 16**,** 311-321.

LIU, Z. & KLEINER, Y. 2013. State of the art review of inspection technologies for condition assessment of water pipes. *Measurement,* 46**,** 1-15.

LLOYD, R. R., PROVIS, J. L. & VAN DEVENTER, J. S. J. 2012. Acid resistance of inorganic polymer binders. 1. Corrosion rate. *Materials and Structures,* 45**,** 1-14.

LONG, T., WANG, Q., GUAN, Z., CHEN, Y. & SHI, X. 2017. Deterioration and microstructural evolution of the fly ash geopolymer concrete against MgSO4 solution. *Advances in Materials Science and Engineering,* 2017.

LONGHI, M. A., WALKLEY, B., RODRÍGUEZ, E. D., KIRCHHEIM, A. P., ZHANG, Z. & WANG, H. 2019. New selective dissolution process to quantify reaction extent and product stability in metakaolin-based geopolymers. *Composites Part B: Engineering,* 176**,** 107172.

LUNA GALIANO, Y., FERNÁNDEZ PEREIRA, C. & IZQUIERDO, M. 2016. Contributions to the study of porosity in fly ash-based geopolymers. Relationship between degree of reaction, porosity and compressive strength. *Materiales de construcción, 66 (324)*.

LUO, J., CHEN, X., CRUMP, J., ZHOU, H., DAVIES, D. G., ZHOU, G., ZHANG, N. & JIN, C. 2018. Interactions of fungi with concrete: Significant importance for bio-based self-healing concrete. *Construction and Building Materials,* 164**,** 275-285.

LUO, Y., KLIMA, K., BROUWERS, H. & YU, Q. 2022a. Effects of ladle slag on Class F fly ash geopolymer: Reaction mechanism and high temperature behavior. *Cement and Concrete Composites,* 129**,** 104468.

LUO, Y., KLIMA, K. M., BROUWERS, H. J. H. & YU, Q. 2022b. Effects of ladle slag on Class F fly ash geopolymer: Reaction mechanism and high temperature behavior. *Cement and Concrete Composites,* 129**,** 104468.

LUUKKONEN, T., ABDOLLAHNEJAD, Z., YLINIEMI, J., KINNUNEN, P. & ILLIKAINEN, M. 2018a. Comparison of alkali and silica sources in one-part alkali-activated blast furnace slag mortar. *Journal of Cleaner Production,* 187**,** 171-179.

LUUKKONEN, T., ABDOLLAHNEJAD, Z., YLINIEMI, J., KINNUNEN, P. & ILLIKAINEN, M. 2018b. One-part alkali-activated materials: A review. *Cement and Concrete Research,* 103**,** 21-34.

MA, C., LONG, G., SHI, Y. & XIE, Y. 2018. Preparation of cleaner one-part geopolymer by investigating different types of commercial sodium metasilicate in China. *Journal of Cleaner Production,* 201**,** 636-647.

MA, S. L., ZHANG, Z. Q. & LIU, X. M. 2022. Comprehensive Understanding of Aluminosilicate Phosphate Geopolymers: A Critical Review. *Materials,* 15.

MACKENZIE L. DAVIS, P. D. P. E. B. 2020. INTRODUCTION. 2nd edition. ed. New York: McGraw-Hill Education.

MAJIDI, B. 2013. Geopolymer technology, from fundamentals to advanced applications: a review. *Materials Technology,* 24**,** 79-87.

MAKRIS, K. F., LANGEVELD, J. & CLEMENS, F. H. L. R. 2020. A review on the durability of PVC sewer pipes: research vs. practice. *Structure and Infrastructure Engineering,* 16**,** 880-897.

MARAGKOS, I., GIANNOPOULOU, I. P. & PANIAS, D. 2009. Synthesis of ferronickel slag-based geopolymers. *Minerals Engineering,* 22**,** 196-203.

MARQUARDT, D. W. 1963. An Algorithm for Least-Squares Estimation of Nonlinear Parameters. *Journal of the Society for Industrial and Applied Mathematics,* 11**,** 431-441.

MATALKAH, F. & SOROUSHIAN, P. 2022. CO2 treatment of ground granulated blast furnace slag for enhancing geopolymer properties. *Journal of Materials Research and Technology,* 17**,** 2457-2465.

MATSUNAGA, T., KIM, J. K., HARDCASTLE, S. & ROHATGI, P. K. 2002. Crystallinity and selected properties of fly ash particles. *Materials Science and Engineering: A,* 325**,** 333-343.

MCDONALD, S. E. & ZHAO, J. Q. 2020. Condition assessment and rehabilitation of large sewers. *Underground Infrastructure Research.* CRC Press.

MEDUPIN, R. O., ABUBAKRE, O. K., ABDULKAREEM, A. S., MURIANA, R. A., KARIIM, I. & BADA, S. O. 2017. Thermal and physico-mechanical stability of recycled high density polyethylene reinforced with oil palm fibres. *Engineering Science and Technology, an International Journal,* 20**,** 1623-1631.

MEHDIPOUR, I. & KHAYAT, K. H. 2017. Effect of particle-size distribution and specific surface area of different binder systems on packing density and flow characteristics of cement paste. *Cement and Concrete Composites,* 78**,** 120-131.

MEHTA, P. K. 1983. Mechanism of sulfate attack on portland cement concrete—Another look. *Cement and Concrete Research,* 13**,** 401-406.

MEHTA, P. K. & MONTEIRO, P. J. M. 2014. Aggregates. *Concrete: Microstructure, Properties, and Materials.* 4th ed. ed. New York: McGraw-Hill Education.

MERMERDAŞ, K., MANGURI, S., NASSANI, D. E. & OLEIWI, S. M. 2017. Effect of aggregate properties on the mechanical and absorption characteristics of geopolymer mortar. *Engineering Science and Technology, an International Journal,* 20**,** 1642-1652.

MIKHAILOV, A. A., TIDBLAD, J. & KUCERA, V. 2004. The classification system of ISO 9223 standard and the dose-response functions assessing the corrosivity of outdoor atmospheres. *Protection of Metals,* 40**,** 541-550.

MIKHAILOVA, O., DEL CAMPO, A., ROVNANIK, P., FERNÁNDEZ, J. F. & TORRES-CARRASCO, M. 2019. In situ characterization of main reaction products in alkali-activated slag materials by Confocal Raman Microscopy. *Cement and Concrete Composites,* 99**,** 32-39.

MOHAMED, O. A. 2022. Effect of immersing geopolymer slag-fly ash mortar in sulfuric acid on strength development and stability of mass. *Construction and Building Materials,* 341**,** 127786.

MOHAMMADI, M. M., NAJAFI, M., KERMANSHACHI, S., KAUSHAL, V. & SERAJIANTEHRANI, R. 2020. Factors Influencing the Condition of Sewer Pipes: State-of-the-Art Review. *Journal of Pipeline Systems Engineering and Practice,* 11**,** 03120002.

MOHAMMED RAZZAQ, A., MAJID, D. L., ISHAK, M. R. & BASHEER, U. M. 2017. Effect of Fly Ash Addition on the Physical and Mechanical Properties of AA6063 Alloy Reinforcement. *Metals* [Online], 7.

MOHIT, M., RANJBAR, A. & SHARIFI, Y. 2021. Mechanical and microstructural properties of mortars incorporating ceramic waste powder exposed to the hydrochloric acid solution. *Construction and Building Materials,* 271**,** 121565.

MONTEIRO, P. J., MILLER, S. A. & HORVATH, A. 2017. Towards sustainable concrete. *Nature materials,* 16**,** 698.

MONTENY, J., VINCKE, E., BEELDENS, A., DE BELIE, N., TAERWE, L., VAN GEMERT, D. & VERSTRAETE, W. 2000. Chemical, microbiological, and in situ test methods for biogenic sulfuric acid corrosion of concrete. *Cement and Concrete Research,* 30**,** 623-634.

MORI, T., NONAKA, T., TAZAKI, K., KOGA, M., HIKOSAKA, Y. & NODA, S. 1992. Interactions of nutrients, moisture and ph on microbial corrosion of concrete sewer pipes. *Water Research,* 26**,** 29-37.

NAZARI, A., BAGHERI, A. & RIAHI, S. 2011. Properties of geopolymer with seeded fly ash and rice husk bark ash. *Materials Science and Engineering: A,* 528**,** 7395-7401.

NAZEMI, M. K. & VALIX, M. 2016. Evaluation of acid diffusion behaviour of amine-cured epoxy coatings by accelerated permeation testing method and prediction of their service life. *Progress in Organic Coatings,* 97**,** 307-312.

NEVAREZ, L., VASSEUR, V., LE MADEC, A., LE BRAS, M. A., COROLLER, L., LEGUÉRINEL, I. & BARBIER, G. 2009. Physiological traits of Penicillium glabrum

strain LCP 08.5568, a filamentous fungus isolated from bottled aromatised mineral water. *International Journal of Food Microbiology,* 130**,** 166-171.

NG, C., ALENGARAM, U. J., WONG, L. S., MO, K. H., JUMAAT, M. Z. & RAMESH, S. 2018. A review on microstructural study and compressive strength of geopolymer mortar, paste and concrete. *Construction and Building Materials,* 186**,** 550-576.

NG, T. S. & FOSTER, S. J. 2013. Development of a mix design methodology for high-performance geopolymer mortars. *Structural Concrete,* 14**,** 148-156.

NIELSEN, A. H., LENS, P., HVITVED-JACOBSEN, T. & VOLLERTSEN, J. 2005a. Effects of aerobic-anaerobic transient conditions on sulfur and metal cycles in sewer biofilms. *Biofilms,* 2**,** 81-91.

NIELSEN, A. H., YONGSIRI, C., HVITVED-JACOBSEN, T. & VOLLERTSEN, J. 2005b. Simulation of sulfide buildup in wastewater and atmosphere of sewer networks. *Water Science and Technology,* 52**,** 201-208.

OJOVAN, M. I. & LEE, W. E. 2005. Chapter 15 - Immobilisation of Radioactive Wastes in Cement. *In:* OJOVAN, M. I. & LEE, W. E. (eds.) *An Introduction to Nuclear Waste Immobilisation.* Oxford: Elsevier.

OKABE, S., ODAGIRI, M., ITO, T. & SATOH, H. 2007a. Succession of Sulfur-Oxidizing Bacteria in the Microbial Community on Corroding Concrete in Sewer Systems. *Applied and Environmental Microbiology,* 73**,** 971.

OKABE, S., ODAGIRI, M., ITO, T. & SATOH, H. 2007b. Succession of sulfur-oxidizing bacteria in the microbial community on corroding concrete in sewer systems. *Applied and environmental microbiology,* 73**,** 971-980.

OPILA, M. C. 2011. *Structural condition scoring of buried sewer pipes for risk-based decision making,* University of Delaware.

PACHECO-TORGAL, F., CASTRO-GOMES, J. & JALALI, S. 2008. Alkali-activated binders: A review: Part 1. Historical background, terminology, reaction mechanisms and hydration products. *Construction and building Materials,* 22**,** 1305-1314.

PAL, S. C., MUKHERJEE, A. & PATHAK, S. R. 2003. Investigation of hydraulic activity of ground granulated blast furnace slag in concrete. *Cement and Concrete Research,* 33**,** 1481-1486.

PALOMO, A., GRUTZECK, M. W. & BLANCO, M. T. 1999. Alkali-activated fly ashes: A cement for the future. *Cement and Concrete Research,* 29**,** 1323-1329.

PALOMO, Á., KAVALEROVA, E., FERNÁNDEZ-JIMÉNEZ, A., KRIVENKO, P., GARCÍA-LODEIRO, I. & MALTSEVA, O. 2015. A review on alkaline activation: new analytical perspectives.

PARK, K., LEE, H., PHELAN, S., LIYANAARACHCHI, S., MARLENI, N., NAVARATNA, D., JEGATHEESAN, V. & SHU, L. 2014. Mitigation strategies of hydrogen sulphide emission in sewer networks–a review. *International Biodeterioration & Biodegradation,* 95**,** 251-261.

PARK, S., NEIZERT, T., KIM, Y. & LEE, S. 2017. Properties of Lightweight Composites Using Industry Wastes with NaOH Alkaline Activator. *Journal of Asian Architecture and Building Engineering,* 16**,** 619-624.

PART, W. K., RAMLI, M. & CHEAH, C. B. 2015. An overview on the influence of various factors on the properties of geopolymer concrete derived from industrial by-products. *Construction and Building Materials,* 77**,** 370-395.

PARTHIBAN, D., VIJAYAN, D. S., KODA, E., VAVERKOVA, M. D., PIECHOWICZ, K., OSINSKI, P. & DUC, B. V. 2022. Role of industrial based precursors in the stabilization of weak soils with geopolymer – A review. *Case Studies in Construction Materials,* 16**,** e00886.

PASUPATHY, K., BERNDT, M., CASTEL, A., SANJAYAN, J. & PATHMANATHAN, R. 2016. Carbonation of a blended slag-fly ash geopolymer concrete in field conditions after 8years. *Construction and Building Materials,* 125**,** 661-669.

PAUDEL, S. R., YANG, M. & GAO, Z. 2020. pH Level of Pore Solution in Alkali-Activated Fly-Ash Geopolymer Concrete and Its Effect on ASR of Aggregates with Different Silicate Contents. *Journal of Materials in Civil Engineering,* 32**,** 04020257.

PAVÍA, S. & TOOMEY, B. 2008. Influence of the aggregate quality on the physical properties of natural feebly-hydraulic lime mortars. *Materials and Structures,* 41**,** 559-569.

PAZOKI, M., ABDOLI, M., GHASEMZADE, R., DALAEI, P. & AHMADI PARI, M. 2016. Comparative evaluation of poly urethane and poly vinyl chloride in lining concrete sewer pipes for preventing biological corrosion. *International Journal of Environmental Research,* 10**,** 305-312.

PENG, H., CUI, C., CAI, C. S., LIU, Y. & LIU, Z. 2019. Microstructure and microhardness property of the interface between a metakaolin/GGBFS-based geopolymer paste and granite aggregate. *Construction and Building Materials,* 221**,** 263-273.

PETERSEN, S. P. & AHRING, B. K. 1990. Analysis of sulfate in sewage sludge using ion chromatographic techniques. *Journal of Microbiological Methods,* 12**,** 225-230.

PHOO-NGERNKHAM, T., CHINDAPRASIRT, P., SATA, V., PANGDAENG, S. & SINSIRI, T. 2013. Properties of high calcium fly ash geopolymer pastes with Portland cement as an additive. *International Journal of Minerals, Metallurgy, and Materials,* 20**,** 214-220.

PHOO-NGERNKHAM, T., SATA, V., HANJITSUWAN, S., RIDTIRUD, C., HATANAKA, S. & CHINDAPRASIRT, P. 2015. High calcium fly ash geopolymer mortar containing Portland cement for use as repair material. *Construction and Building Materials,* 98**,** 482-488.

POMEROY, R. D. 1990. The problem of hydrogen sulphide in sewers. *Clay Pipe Development Association. Ltd., London, 2 nd edition(edited by A. G. Boon), 1990, 24*.

POTGIETER-VERMAAK, S., POTGIETER, J., MONAMA, P. & VAN GRIEKEN, R. 2006. Comparison of limestone, dolomite and fly ash as pre-treatment agents for acid mine drainage. *Minerals Engineering,* 19**,** 454-462.

POWERS, M. C. 1953. A new roundness scale for sedimentary particles. *Journal of Sedimentary Research,* 23**,** 117-119.

PROVIS, J. L., PALOMO, A. & SHI, C. 2015. Advances in understanding alkali-activated materials. *Cement and Concrete Research,* 78**,** 110-125.

PROVIS, J. L. & VAN DEVENTER, J. S. 2013. *Alkali activated materials: state-of-the-art report, RILEM TC 224-AAM,* Springer Science & Business Media.

PROVIS, J. L. & VAN DEVENTER, J. S. J. 9.3 Acid Attack. *Geopolymers - Structure, Processing, Properties and Industrial Applications.* Woodhead Publishing.

PROVIS, J. L. & VAN DEVENTER, J. S. J. 11.3.1 Mixture Design. *Geopolymers - Structure, Processing, Properties and Industrial Applications.* Woodhead Publishing.

PUERTAS, F. & FERNÁNDEZ-JIMÉNEZ, A. 2003. Mineralogical and microstructural characterisation of alkali-activated fly ash/slag pastes. *Cement and Concrete Composites,* 25**,** 287-292.

PULIGILLA, S., CHEN, X. & MONDAL, P. 2019. Does synthesized C-S-H seed promote nucleation in alkali activated fly ash-slag geopolymer binder? *Materials and Structures,* 52**,** 65.

PULIGILLA, S. & MONDAL, P. 2013. Role of slag in microstructural development and hardening of fly ash-slag geopolymer. *Cement and Concrete Research,* 43**,** 70-80.

PULIGILLA, S. & MONDAL, P. 2015. Co-existence of aluminosilicate and calcium silicate gel characterized through selective dissolution and FTIR spectral subtraction. *Cement and Concrete Research,* 70**,** 39-49.

QIAN, G., DENG, M., LAN, X., XU, Z. & TANG, M. 2002. Alkali carbonate reaction expansion of dolomitic limestone aggregates with porphyrotopic texture. *Engineering Geology,* 63**,** 17-29.

QIU, Y., ZHOU, Y., CHANG, Y., LIANG, X., ZHANG, H., LIN, X., QING, K., ZHOU, X. & LUO, Z. 2022. The Effects of Ventilation, Humidity, and Temperature on Bacterial Growth and Bacterial Genera Distribution. *International Journal of Environmental Research and Public Health,* 19**,** 15345.

QU, F., LI, W., WANG, K., ZHANG, S. & SHENG, D. 2021. Performance deterioration of fly ash/slag-based geopolymer composites subjected to coupled cyclic preloading and sulfuric acid attack. *Journal of Cleaner Production,* 321**,** 128942.

RAJABIPOUR, F., MARAGHECHI, H. & FISCHER, G. 2010. Investigating the alkali-silica reaction of recycled glass aggregates in concrete materials. *Journal of Materials in Civil Engineering,* 22**,** 1201-1208.

RAMOS, F. J. H. T. V., VIEIRA, M. D. F. M., TIENNE, L. G. P. & AGUIAR, V. D. O. 2020. Evaluation and characterization of geopolymer foams synthesized from blast furnace with sodium metasilicate. *Journal of Materials Research and Technology,* 9**,** 12019-12029.

REN, J., ZHANG, L., WALKLEY, B., BLACK, J. R. & SAN NICOLAS, R. 2022. Degradation resistance of different cementitious materials to phosphoric acid attack at early stage. *Cement and Concrete Research,* 151**,** 106606.

REVATHI, T. & JEYALAKSHMI, R. 2021. Fly ash–GGBS geopolymer in boron environment: A study on rheology and microstructure by ATR FT-IR and MAS NMR. *Construction and Building Materials,* 267**,** 120965.

RICHARDSON, I., BROUGH, A., GROVES, G. & DOBSON, C. 1994a. The characterization of hardened alkali-activated blast-furnace slag pastes and the nature of the calcium silicate hydrate (CSH) phase. *Cement and Concrete Research,* 24**,** 813-829.

RICHARDSON, I. G., BROUGH, A. R., GROVES, G. W. & DOBSON, C. M. 1994b. The characterization of hardened alkali-activated blast-furnace slag pastes and the nature of the calcium silicate hydrate (C-S-H) phase. *Cement and Concrete Research,* 24**,** 813-829.

ROBERTS, D. J., NICA, D., ZUO, G. & DAVIS, J. L. 2002. Quantifying microbially induced deterioration of concrete: initial studies. *International Biodeterioration & Biodegradation,* 49**,** 227-234.

ROGHANIAN, N. & BANTHIA, N. 2019. Development of a sustainable coating and repair material to prevent bio-corrosion in concrete sewer and waste-water pipes. *Cement and Concrete Composites,* 100**,** 99-107.

RONG-RONG, Z. & DONG-DONG, M. 2020. Effects of Curing Time on the Mechanical Property and Microstructure Characteristics of Metakaolin-Based Geopolymer Cement-Stabilized Silty Clay. *Advances in Materials Science and Engineering,* 2020**,** 9605941.

ROSAS-CASAREZ, C. A., ARREDONDO-REA, S. P., GÓMEZ-SOBERÓN, J. M., ALAMARAL-SÁNCHEZ, J. L., CORRAL-HIGUERA, R., CHINCHILLAS-CHINCHILLAS, M. D. J. & ACUÑA-AGÜERO, O. H. 2014. Experimental study of XRD, FTIR and TGA techniques in geopolymeric materials. *Int. J. Adv. Comput. Sci. Appl,* 4**,** 221-226.

RYPAROVÁ, P., PROŠEK, Z., SCHREIBEROVÁ, H., BÍLÝ, P. & TESÁREK, P. 2021. The role of bacterially induced calcite precipitation in self-healing of cement paste. *Journal of Building Engineering,* 39**,** 102299.

SABERIAN, M., ZHANG, J., GAJANAYAKE, A., LI, J., ZHANG, G. & BOROUJENI, M. 2022. Life cycle assessment (LCA) of concrete containing waste materials: comparative studies. *Handbook of Sustainable Concrete and Industrial Waste Management.* Elsevier.

SAMANTASINGHAR, S. & SINGH, S. P. 2018. Effect of synthesis parameters on compressive strength of fly ash-slag blended geopolymer. *Construction and Building Materials,* 170**,** 225-234.

SANCHEZ, F., BARNA, R., GARRABRANTS, A., KOSSON, D. S. & MOSZKOWICZ, P. 2000. Environmental assessment of a cement-based solidified soil contaminated with lead. *Chemical Engineering Science,* 55**,** 113-128.

SAND, W. 1997a. Microbial mechanisms of deterioration of inorganic substrates—A general mechanistic overview. *International Biodeterioration & Biodegradation,* 40**,** 183-190.

SAND, W. Microbial mechanisms of deterioration of inorganic substrates - A general mechanistic overview. 1997b. 183-190.

SARGENT, P. 2015. 21 - The development of alkali-activated mixtures for soil stabilisation. *In:* PACHECO-TORGAL, F., LABRINCHA, J. A., LEONELLI, C., PALOMO, A. & CHINDAPRASIRT, P. (eds.) *Handbook of Alkali-Activated Cements, Mortars and Concretes.* Oxford: Woodhead Publishing.

SATA, V., SATHONSAOWAPHAK, A. & CHINDAPRASIRT, P. 2012. Resistance of lignite bottom ash geopolymer mortar to sulfate and sulfuric acid attack. *Cement and Concrete Composites,* 34**,** 700-708.

SCRIVENER, K. L., CABIRON, J.-L. & LETOURNEUX, R. 1999. High-performance concretes from calcium aluminate cements. *Cement and Concrete Research,* 29**,** 1215-1223.

SCRIVENER, K. L. & CAPMAS, A. 1998. 13 - Calcium Aluminate Cements. *In:* HEWLETT, P. C. (ed.) *Lea's Chemistry of Cement and Concrete (Fourth Edition).* Oxford: Butterworth-Heinemann.

SCRIVENER, K. L., CRUMBIE, A. K. & LAUGESEN, P. 2004. The Interfacial Transition Zone (ITZ) Between Cement Paste and Aggregate in Concrete. *Interface Science,* 12**,** 411-421.

SENHADJI, Y., SIAD, H., ESCADEILLAS, G., BENOSMAN, A. S., CHIHAOUI, R., MOULI, M. & LACHEMI, M. 2019. Physical, mechanical and thermal properties of lightweight composite mortars containing recycled polyvinyl chloride. *Construction and Building Materials,* 195**,** 198-207.

SHAMSAI, A., PEROTI, S., RAHMANI, K. & RAHEMI, L. 2012. Effect of water-cement ratio on abrasive strength, porosity and permeability of nano-silica concrete. *World Applied Sciences Journal,* 17**,** 929-933.

SHEHAB-ELDEEN, T. & MOSELHI, O. 2001. A decision support system for rehabilitation of sewer pipes. *Canadian Journal of Civil Engineering,* 28**,** 394-401.

SHI, C., ROY, D. & KRIVENKO, P. 2003. *Alkali-activated cements and concretes,* CRC press.

SHI, C. & XIE, P. 1998. Interface between cement paste and quartz sand in alkali-activated slag mortars. *Cement and Concrete Research,* 28**,** 887-896.

SHILL, S. K., AL-DEEN, S., ASHRAF, M. & HUTCHISON, W. 2020. Resistance of fly ash based geopolymer mortar to both chemicals and high thermal cycles simultaneously. *Construction and Building Materials,* 239**,** 117886.

SHIRANI, S., CUESTA, A., DE LA TORRE, A. G., DIAZ, A., TRTIK, P., HOLLER, M. & ARANDA, M. A. G. 2020. Calcium aluminate cement conversion analysed by ptychographic nanotomography. *Cement and Concrete Research,* 137**,** 106201.

SHOAEI, P., MUSAEEI, H. R., MIRLOHI, F., AMERI, F. & BAHRAMI, N. 2019. Waste ceramic powder-based geopolymer mortars: Effect of curing temperature and alkaline solution-to-binder ratio. *Construction and Building Materials,* 227**,** 116686.

SIDDIQUE, R. & KLAUS, J. 2009. Influence of metakaolin on the properties of mortar and concrete: A review. *Applied Clay Science,* 43**,** 392-400.

SITARZ, M., HAGER, I. & CHOIŃSKA, M. 2020. Evolution of Mechanical Properties with Time of Fly-Ash-Based Geopolymer Mortars under the Effect of Granulated Ground Blast Furnace Slag Addition. *Energies* [Online], 13.

SMITH, M. R., COLLIS, L., FOOKES, P. G., SIMS, J. L. I., SMITH, M. R. & WEST, G. 2001a. 8. Aggregates for concrete. *Geological Society, London, Engineering Geology Special Publications,* 17**,** 199.

SMITH, M. R., COLLIS, L., FOOKES, P. G., SIMS, J. L. I., SMITH, M. R. & WEST, G. 2001b. 9. Aggregates for mortar. *Geological Society, London, Engineering Geology Special Publications,* 17**,** 225.

STANASZEK-TOMAL, E. & FIERTAK, M. 2016. Biological Corrosion in the Sewage System and the Sewage Treatment Plant. *Procedia Engineering,* 161**,** 116-120.

STRAUSS RAMBO, D. A., UKRAINCZYK, N., DE ANDRADE SILVA, F., KOENDERS, E., TOLEDO FILHO, R. D. & DA FONSECA MARTINS GOMES, O. 2019. Calcium-aluminate mortars at high temperatures: Overcoming adverse conversion effects using clinker aggregates. *Cement and Concrete Composites,* 96**,** 212-224.

STURM, P., GLUTH, G. J. G., JÄGER, C., BROUWERS, H. J. H. & KÜHNE, H. C. 2018. Sulfuric acid resistance of one-part alkali-activated mortars. *Cement and Concrete Research,* 109**,** 54-63.

SULISTIYONO, E., HANDAYANI, M., PRASETYO, A., IRAWAN, Y., FEBRIANA, E., SEMBIRING, S. & YUSTANTI, E. Identification of Quartz Sand From the Hills of Gunung Walat at Sukabumi Regency for Raw Materials of Nano Silica Precipitate. IOP Conference Series: Materials Science and Engineering, 2020. IOP Publishing, 012048.

SUN, B., YE, G. & DE SCHUTTER, G. 2022. A review: Reaction mechanism and strength of slag and fly ash-based alkali-activated materials. *Construction and Building Materials,* 326**,** 126843.

SUN, X. 2015. Improving the understanding of concrete sewer corrosion through investigations of the gaseous hydrogen sulfide uptake and transformation processes in the corrosion layer.

SZEKELY, J., EVANS, J. W. & SOHN, H. Y. 1976. *Gas-Solid Reactions,* New York.

TACIROĞLU, M. V., ERGEZER, F., BAYKAL, T., ERISKIN, E. & TERZI, S. 2022. Investigation of waste quartz sand as filler in hot-mix asphalt. *Construction and Building Materials,* 342**,** 128004.

TAYLOR, G. 2011. 13 Sprayed concrete for repairing concrete structures. *Concrete Repair: A Practical Guide***,** 212.

TEMUUJIN, J., VAN RIESSEN, A. & MACKENZIE, K. J. D. 2010. Preparation and characterisation of fly ash based geopolymer mortars. *Construction and Building Materials,* 24**,** 1906-1910.

THOKCHOM, S., GHOSH, P. & GHOSH, S. 2009. Effect of water absorption, porosity and sorptivity on durability of geopolymer mortars. *ARPN Journal of engineering and Applied Sciences,* 4**,** 28-32.

UKRAINCZYK, N., MUTHU, M., VOGT, O. & KOENDERS, E. 2019. Geopolymer, Calcium Aluminate, and Portland Cement-Based Mortars: Comparing Degradation Using Acetic Acid. *Materials,* 12**,** 3115.

UL HAQ, E., KUNJALUKKAL PADMANABHAN, S. & LICCIULLI, A. 2014. Synthesis and characteristics of fly ash and bottom ash based geopolymers–A comparative study. *Ceramics International,* 40**,** 2965-2971.

USHA, S., NAIR, D. G. & VISHNUDAS, S. 2016. Feasibility Study of Geopolymer Binder from Terracotta Roof Tile Waste. *Procedia Technology,* 25**,** 186-193.

USMAN KANKIA, M., BALOO, L., MOHAMMED, B. S., HASSAN, S. B., HARUNA, S., DANLAMI, N., AFFIANA ISHAK, E. & NURLIYANA SAMAHANI, W. 2021. Effects of petroleum sludge ash in fly ash-based geopolymer mortar. *Construction and Building Materials,* 272**,** 121939.

VAFAEI, M. & ALLAHVERDI, A. 2017. Durability of Geopolymer Mortar Based on Waste-Glass Powder and Calcium Aluminate Cement in Acid Solutions. *Journal of Materials in Civil Engineering,* 29.

VAFAEI, M., ALLAHVERDI, A., DONG, P. & BASSIM, N. 2018. Acid attack on geopolymer cement mortar based on waste-glass powder and calcium aluminate cement at mild concentration. *Construction and Building Materials,* 193**,** 363-372.

VALENCIA SAAVEDRA, W. G. & MEJÍA DE GUTIÉRREZ, R. 2017. Performance of geopolymer concrete composed of fly ash after exposure to elevated temperatures. *Construction and Building Materials,* 154**,** 229-235.

VALIX, M. 2011. Survey and Review of Current Rehabilitation and Coating Technologies for Many Entry Sewer Pipes and Manholes with Protective Coatings.

VALIX, M. 2021. CORROSION CLASSIFICATION OF SEWERS. Water Services Association of Australia.

VALIX, M., CHEUNG, W. H. & ZHANG, K. 2006. Role of heteroatoms in activated carbon for removal of hexavalent chromium from wastewaters. *Journal of Hazardous Materials,* 135**,** 395-405.

VALIX, M., CHEUNG, A.W., SENDANAYAKA, R. C. AND NAZEMI, M.K. Corrosion of lined concrete. Final Conference of RILEM TC 253-MCI: Microorganisms-Cementitious Materials Interactions, 25-26 June 2018 2018 Tolouse, France.

VALIX, M., MINEYAMA, H., CHEN, C., CHEUNG, W. H., SHI, J. & BUSTAMANTE, H. 2011. Effect of film thickness and filler properties on sulphuric acid permeation in various commercially available epoxy mortar coatings. *Water Science and Technology,* 64**,** 1864-1869.

VALIX, M. & SHANMUGARAJAH, K. 2015. Biogenic acids produced on epoxy linings installed in sewer crown and tidal zones. *Water Research,* 80**,** 217-226.

VALIX, M., ZAMRI, D., MINEYAMA, H., CHEUNG, W. H., SHI, J. & BUSTAMANTE, H. 2012. Microbiologically Induced Corrosion of Concrete and Protective Coatings in Gravity Sewers. *Chinese Journal of Chemical Engineering,* 20**,** 433-438.

VAN JAARSVELD, J. G. S., VAN DEVENTER, J. S. J. & LORENZEN, L. 1998. Factors affecting the immobilization of metals in geopolymerized flyash. *Metallurgical and Materials Transactions B,* 29**,** 283-291.

VON GREVE-DIERFELD, S., LOTHENBACH, B., VOLLPRACHT, A., WU, B., HUET, B., ANDRADE, C., MEDINA, C., THIEL, C., GRUYAERT, E. & VANOUTRIVE, H. 2020. Understanding the carbonation of concrete with supplementary cementitious materials: a critical review by RILEM TC 281-CCC. *Materials and structures,* 53**,** 1-34.

WAFA, F. F. 1994. ACCELERATED SULFATE ATTACK ON CONCRETE IN A HOT CLIMATE. *Cement Concrete and Aggregates,* 16**,** 31-35.

WAHLSTRÖM, M., LAINE-YLIJOKI, J. & KAARTINEN, T. 2009. *Acid neutralization capacity of waste-specification of requirement stated in landfill regulations*, Nordic Council of Ministers.

WALKLEY, B., SAN NICOLAS, R., SANI, M.-A., REES, G. J., HANNA, J. V., VAN DEVENTER, J. S. & PROVIS, J. L. 2016. Phase evolution of C-(N)-ASH/NASH gel blends investigated via alkali-activation of synthetic calcium aluminosilicate precursors. *Cement and Concrete Research,* 89**,** 120-135.

WANG, D. L., CHEN, M. L. & TSANG, D. D. C. W. 2020a. Chapter 5 - Green remediation by using low-carbon cement-based stabilization/solidification approaches. *In:* HOU, D. (ed.) *Sustainable Remediation of Contaminated Soil and Groundwater.* Butterworth-Heinemann.

WANG, H.-Y., TSAI, S.-L., HUNG, C.-C. & JIAN, T.-Y. 2022a. Research on engineering properties of cement mortar adding stainless steel reduction slag and pozzolanic materials. *Case Studies in Construction Materials,* 16**,** e01144.

WANG, H., WU, H., XING, Z., WANG, R. & DAI, S. 2021. The effect of various Si/Al, Na/Al molar ratios and free water on micromorphology and macro-strength of metakaolin-based geopolymer. *Materials,* 14**,** 3845.

WANG, T., WU, K., KAN, L. & WU, M. 2020b. Current understanding on microbiologically induced corrosion of concrete in sewer structures: a review of the evaluation methods and mitigation measures. *Construction and Building Materials,* 247**,** 118539.

WANG, Y., LIU, X., ZHANG, W., LI, Z., ZHANG, Y., LI, Y. & REN, Y. 2020c. Effects of Si/Al ratio on the efflorescence and properties of fly ash based geopolymer. *Journal of Cleaner Production,* 244**,** 118852.

WANG, Y., ZHONG, H. & ZHANG, M. 2022b. Experimental study on static and dynamic properties of fly ash-slag based strain hardening geopolymer composites. *Cement and Concrete Composites,* 129**,** 104481.

WELLS, T. & MELCHERS, R. E. 2014. An observation-based model for corrosion of concrete sewers under aggressive conditions. *Cement and Concrete Research,* 61-62**,** 1-10.

WELLS, T. & MELCHERS, R. E. 2015. Modelling concrete deterioration in sewers using theory and field observations. *Cement and Concrete Research,* 77**,** 82-96.

WILLEY, J., SHERWOOD, L. M. & WOOLVERTON, C. J. 2016. *Prescott's Microbiology,* NY, UNITED STATES, McGraw-Hill Higher Education.

WIRAHADIKUSUMAH, R., ABRAHAM, D. M., ISELEY, T. & PRASANTH, R. K. 1998. Assessment technologies for sewer system rehabilitation. *Automation in Construction,* 7**,** 259-270.

WONG, L. S. 2022. Durability Performance of Geopolymer Concrete: A Review. *Polymers* [Online], 14.

WONG, V., JERVIS, W., FISHBURN, B., NUMATA, T., JOE, W., RAWAL, A., SORRELL, C. C. & KOSHY, P. 2021. Long-Term Strength Evolution in Ambient-Cured Solid-Activator Geopolymer Compositions. *Minerals* [Online], 11.

WSA161-2021 2021. Water Industry Standard for Alkali Activated Binder Including Geopolymer Cement Mortar used for the renovation of wastewater structures and large diameter pipes Version 1.0. Water industry standards: Water industry standards.

WSA-201 2017. Manual for selection and application of protective coatings Docklands VIC 3008, Australia: Water Services Association of Australia Limited.

WSAA 2017. Manual for selection and application of protective coatings.

WSSA 2021. Water Industry Standard for Alkali Activated Binder Including Geopolymer Cement Mortar used for the renovation of wastewater structures and large diameter pipes Version 1.0. Water Services Association of Australia: Water Services Association of Australia.

WU, L., HU, C. & LIU, W. 2018a. The Sustainability of Concrete in Sewer Tunnel—A Narrative Review of Acid Corrosion in the City of Edmonton, Canada. *Sustainability,* 10.

WU, L., HU, C. & LIU, W. V. 2018b. The Sustainability of Concrete in Sewer Tunnel—A Narrative Review of Acid Corrosion in the City of Edmonton, Canada. *Sustainability,* 10.

WU, M., WANG, T., WU, K. & KAN, L. 2020. Microbiologically induced corrosion of concrete in sewer structures: A review of the mechanisms and phenomena. *Construction and Building Materials,* 239**,** 117813.

XIE, Y., LIN, X., JI, T., LIANG, Y. & PAN, W. 2019. Comparison of corrosion resistance mechanism between ordinary Portland concrete and alkali-activated concrete subjected to biogenic sulfuric acid attack. *Construction and Building Materials,* 228**,** 117071.

XUE, X., LIU, Y.-L., DAI, J.-G., POON, C.-S., ZHANG, W.-D. & ZHANG, P. 2018. Inhibiting efflorescence formation on fly ash–based geopolymer via silane surface modification. *Cement and Concrete Composites,* 94**,** 43-52.

YAGHOUBI, M., ARULRAJAH, A., DISFANI, M. M., HORPIBULSUK, S., DARMAWAN, S. & WANG, J. 2019. Impact of field conditions on the strength development of a geopolymer stabilized marine clay. *Applied Clay Science,* 167**,** 33-42.

YAN, J., MORENO, L. & NERETNIEKS, I. 2000. The long-term acid neutralizing capacity of steel slag. *Waste Management,* 20**,** 217-223.

YANG, K.-H., SONG, J.-K., ASHOUR, A. F. & LEE, E.-T. 2008. Properties of cementless mortars activated by sodium silicate. *Construction and Building Materials,* 22**,** 1981-1989.

YANG, K., YANG, C., MAGEE, B., NANUKUTTAN, S. & YE, J. 2016. Establishment of a preconditioning regime for air permeability and sorptivity of alkali-activated slag concrete. *Cement and Concrete Composites,* 73**,** 19-28.

YANG, M., ZHENG, Y., LI, X., YANG, X., RAO, F. & ZHONG, L. 2022. Durability of alkali-activated materials with different C–S–H and N-A-S-H gels in acid and alkaline environment. *Journal of Materials Research and Technology,* 16**,** 619-630.

YASERI, S., MASOOMI VERKI, V. & MAHDIKHANI, M. 2019. Utilization of high volume cement kiln dust and rice husk ash in the production of sustainable geopolymer. *Journal of Cleaner Production,* 230**,** 592-602.

YIP, C. K., LUKEY, G. C. & VAN DEVENTER, J. S. J. 2005. The coexistence of geopolymeric gel and calcium silicate hydrate at the early stage of alkaline activation. *Cement and Concrete Research,* 35**,** 1688-1697.

YOUNG, D. 2021. Mortars: materials, mixes and methods. *In:* AUSTRALIA, H. C. O. (ed.). www.heritagecouncil.vic.gov.au.: www.heritagecouncil.vic.gov.au.

YUAN, H., DANGLA, P., CHATELLIER, P. & CHAUSSADENT, T. 2015. Degradation modeling of concrete submitted to biogenic acid attack. *Cement and Concrete Research,* 70**,** 29-38.

YUAN, H. F., DANGLA, P., CHATELLIER, P. & CHAUSSADENT, T. 2013. Degradation modelling of concrete submitted to sulfuric acid attack. *Cement and Concrete Research,* 53**,** 267-277.

ZAPATA, J. F., AZEVEDO, A., FONTES, C., MONTEIRO, S. N. & COLORADO, H. A. 2022. Environmental Impact and Sustainability of Calcium Aluminate Cements. *Sustainability* [Online], 14.

ZHANG, L., DE SCHRYVER, P., DE GUSSEME, B., DE MUYNCK, W., BOON, N. & VERSTRAETE, W. 2008. Chemical and biological technologies for hydrogen sulfide emission control in sewer systems: a review. *Water research,* 42**,** 1-12.

ZHANG, P., GAO, Z., WANG, J., GUO, J., HU, S. & LING, Y. 2020. Properties of fresh and hardened fly ash/slag based geopolymer concrete: A review. *Journal of Cleaner Production,* 270**,** 122389.

ZHANG, Y., SARAVANAKUMAR, K. & ÇOPUROĞLU, O. 2022. EDS Microanalysis of Unhydrated Blast Furnace Slag Grains in Field Concrete with Different Service Life. *Microscopy and Microanalysis,* 28**,** 1493-1503.

ZHAO, X., LIU, C., ZUO, L., WANG, L., ZHU, Q. & WANG, M. 2019. Investigation into the effect of calcium on the existence form of geopolymerized gel product of fly ash based geopolymers. *Cement and Concrete Composites,* 103**,** 279-292.

ZHU, H., WANG, T., WANG, Y. & LI, V. C. 2021a. Trenchless rehabilitation for concrete pipelines of water infrastructure: A review from the structural perspective. *Cement and Concrete Composites,* 123**,** 104193.

ZHU, X., LI, W., DU, Z., ZHOU, S., ZHANG, Y. & LI, F. 2021b. Recycling and utilization assessment of steel slag in metakaolin based geopolymer from steel slag by-product to green geopolymer. *Construction and Building Materials,* 305**,** 124654.

ZHUANG, H. J., ZHANG, H. Y. & XU, H. 2017. Resistance of geopolymer mortar to acid and chloride attacks. *Procedia Engineering,* 210**,** 126-131.

ZHUANG, X. Y., CHEN, L., KOMARNENI, S., ZHOU, C. H., TONG, D. S., YANG, H. M., YU, W. H. & WANG, H. 2016. Fly ash-based geopolymer: clean production, properties and applications. *Journal of Cleaner Production,* 125**,** 253-267.